



Centre for Doctoral Training (CDT)  
in Oil and Gas



**Improving the assessment of seismic hazard in the  
North Sea**

**Christopher Brooks**

**A thesis submitted for the degree of Doctor of  
Philosophy**

**May 2021**

## **Acknowledgements**

First, I would like to sincerely thank John Douglas for his supervision of my PhD. John's supervision has always been thorough, constructive and timely, especially during the first year of my project when my understanding of engineering seismology was limited and I sent more than my fair share of confused emails. Secondly, I would like to thank Zoe Shipton as my secondary supervisor. Zoe's supervision has been positive and encouraging, and was really helpful during the start of my project when the transition from an undergraduate to a doctoral student was a daunting task. Thirdly, I would like to thank John Underhill, Lorna Morrow and Anna Clark at the NERC CDT for Oil and Gas for providing a large proportion of the funding for my project, as well organising the CDT training courses and the annual CDT conference. Fourth, I would like to thank Dino Bindi for providing the North Sea ground-motion data from the EIDA database hosted at GFZ Potsdam. The provision of this ground-motion dataset helped me to really get my project rolling, and took considerable time on Dino's behalf to prepare for me. Fifth, I would like to thank Conrad Lindholm for providing the seismogenic source zone model used by Bungum et al. (2000). This source model was very helpful due to forming the basis of my North Sea seismic hazard calculations. Sixth, I would like to thank Hilmar Bungum. for providing invaluable and constructive feedback on some of my first chapters of research. Seventh, I would like to thank Enrico Tubaldi for his useful feedback and suggestions from the perspective of a structural engineer during my annual project reviews. Finally, I would like to thank my family and friends for their support and encouragement.

## **Abstract**

The following PhD thesis provides a comprehensive reassessment of probabilistic seismic hazard assessment (PSHA) in the North Sea. PSHA provides probabilistic representations of the expected ground-shaking at sites of interest, which can be used to assess the seismic risk for structures located at (or proximal to) said sites. In the North Sea, the seismic risk for offshore infrastructure including (1) oil and gas platforms and (2) wind turbine facilities must be considered. The seismic risk of this offshore infrastructure is important to consider because certain levels of seismic damage can result in negative impacts upon (1) the environmental health of the North Sea, (2) the personal health of employees on or near the considered infrastructure and (3) the economic health of governments and corporations which are reliant upon this infrastructure.

The most recent publically available North Sea PSHA was undertaken by Bungum et al. (2000). Two decades have passed since this study, since which substantial developments in PSHA have been made, and additional North Sea ground-motion data has been collected. Furthermore, the 2001 Ekofisk earthquake was the first hydrocarbon production induced earthquake in the North Sea to have been deemed of engineering significance for platforms in the region, but was not considered within the Bungum et al. (2000) study.

In this investigation, North Sea PSHA is reassessed in several ways. Firstly, a pre-existing ground-motion prediction equation (GMPE) which performs well in the North Sea is identified as a base model for a North Sea GMPE using an additional 20 years of ground-motion records available since the Bungum et al. (2000) study. This base model GMPE is then improved incrementally through the constraint of North Sea path and site effects using novel techniques. Following the development of this North Sea GMPE, the seismogenic source model of Bungum et al. (2000) is updated using an additional two decades of North Sea earthquake observations. The impact of the North Sea GMPE and the updated source model are evaluated using (1) macroseismic earthquake observations and (2) assessment of the seismic risk of offshore infrastructure in the region.

The updated PSHA formulation developed within this investigation results in moderate but significant differences in the seismic risk for offshore infrastructure in the North Sea. These seismic risk estimates are potentially more appropriate than those computed using the Bungum et al. (2000) PSHA formulation due to the additional ground-motion data and the PSHA advancements available since the Bungum et al. (2000) PSHA study.

Ultimately, the improved seismic hazard estimates potentially help to better assess the structural health of offshore North Sea infrastructure, and subsequently minimise the likelihood of levels of seismic damage which could be detrimental to the North Sea environment or the personnel and/or economies operating within the region.

## **Peer-Reviewed Journal Publications Resulting from Work Undertaken in this PhD Project**

Chapter 5 contains work published in:

Brooks, C. and Douglas, J. (2020) Influence of the Site-Specific Component of Kappa on the Magnitude-Dependency of Within-Event Aleatory Variabilities in Ground-Motion Models. *Seismological Research Letters*, **92**(1), pp.238-245.

Chapters 3 and 4 contain work published in:

Brooks, C., Douglas, J. and Shipton, Z. (2020). Improving earthquake ground-motion predictions for the North Sea. *Journal of Seismology*, **24**(2), pp.343-362.

## **Funding Acknowledgements**

This PhD project was undertaken as part of the Natural Environment Research Council (NERC) Centre for Doctoral Training (CDT) in Oil & Gas [grant number NE/M00578X/1]. It is sponsored by the University of Strathclyde whose support is gratefully acknowledged.

## Table of Contents

Section	Page Number(s)
List of Figures.....	1-6
List of Tables.....	7-9
List of Abbreviations.....	10-12
List of Mathematical Symbols.....	13-16
1.0 Introduction to Seismic Hazard Assessment in the North Sea.....	17-25
2.0 North Sea Seismicity.....	26-55
3.0 Ground-Motion Prediction Equations for the North Sea.....	56-96
4.0 Improving GMPE Performance in the North Sea.....	97-136
5.0 Investigation of High Frequency Ground-Motion Variability with the Site-Specific Component of Kappa.....	137-162
6.0 Constructing a North Sea Ground-Motion Prediction Equation Logic Tree.....	163-185
7.0 Reassessment of North Sea Seismic Source Model Parameters.....	186-204
8.0 Assessing the Seismic Risk for Critical Infrastructure in the North Sea.....	205-224
9.0 Conclusions for Reassessment of North Sea Seismic Hazard.....	225-228
10.0 References.....	229-256
Appendix A: Basic Earthquake Terminology.....	257-263
Appendix B: Overview of Probabilistic Seismic Hazard Assessment.....	264-275
Appendix C: Site Effects and Site Response Analysis.....	276-284
Appendix D: Induced Seismicity Mechanisms Associated with Hydrocarbon Production.....	285-295
Appendix E: Statistical Methods Used for Constraining Site Effects in the North Sea.....	296-304

## List of Figures

**Figure 1.0** *Spatial distribution of hydrocarbon fields in the North Sea.*

**Figure 1.1** *Spatial distribution of offshore wind farm development in northwestern Europe.*

**Figure 1.2** *Wind turbine collapse due to ground-shaking in Japan (left) and New Zealand (right).*

**Figure 1.3** *Slider system for the Trans-Alaska pipeline and the horizontal displacement resulting from the 2002 Denali earthquake fault rupture.*

**Figure 1.4** *Final composite map produced through appraisal of past UKCS seismic hazard efforts.*

**Figure 2.0** *Seismicity of Norway and Britain and the adjoining offshore areas.*

**Figure 2.1** *Geographical locations of north-western Europe oil and gas fields.*

**Figure 2.2** *Map showing locations of the Ekofisk and Valhall fields.*

**Figure 2.3** *Differential bathymetry data for the Ekofisk field.*

**Figure 2.4** *Vertical section showing locations of 328 micro-earthquakes detected by the seismic array operational in the Valhall field between June 1 and July 27, 1988.*

**Figure 2.5** *Number of earthquakes per year and volume of hydrocarbons produced per year in the Groningen field.*

**Figure 2.6** *Map illustrating the spatial distribution of earthquake focal depths, hydrocarbon fields and faults in the United Kingdom economic sector of the North Sea.*

**Figure 2.7** *Number of earthquakes per year and volume of hydrocarbons produced per year in the North Sea.*

**Figure 2.8** *Number of earthquakes per year ( $M_L \geq 3$ ) and volume of hydrocarbons produced per year in the North Sea.*

**Figure 2.9** *Number of earthquakes per year ( $M_L \geq 4$ ) and volume of hydrocarbon produced per year in the North Sea.*

**Figure 2.10** *North Sea and United Kingdom ( $M_L \geq 2.5$ ) Gutenberg-Richter Distributions.*

**Figure 2.11** *Normalised North Sea and United Kingdom ( $M_L \geq 2.5$ ) Gutenberg-Richter Distributions.*

**Figure 2.12** *North Sea earthquake focal depth distribution.*

**Figure 2.13** *United Kingdom earthquake focal depth distribution.*

**Figure 2.14** *North Sea earthquake focal depth distribution ( $M_L \geq 2.5$ ).*

**Figure 2.15** *United Kingdom Sea earthquake focal depth distribution ( $M_L \geq 2.5$ ).*

**Figure 2.16** Map illustrating the spatial distribution of earthquake focal depths, hydrocarbon fields and faults in the United Kingdom economic sector of the North Sea.

**Figure 2.17** Focal depth distribution for earthquakes occurring off the East Anglian coast.

**Figure 2.18** North Sea ( $M_L \geq 2.5$  earthquakes) and the North Sea ( $M_L \geq 2.5$  but excluding potentially induced earthquakes originating in the United Kingdom economic sector) Gutenberg-Richter Distributions.

**Figure 2.19** Normalised North Sea ( $M_L \geq 2.5$  earthquakes) and North Sea ( $M_L \geq 2.5$  but excluding potentially induced earthquakes originating in the United Kingdom economic sector) Gutenberg-Richter Distributions.

**Figure 3.0** Acceleration time series for the 1997 Umbria-Marche seismic sequence, central Italy recorded at analogue station NCR (top) and digital station NCR2 (bottom).

**Figure 3.1** Example of spurious spikes in a digitised record.

**Figure 3.2** Example of baseline shift and its effect on the velocity time series.

**Figure 3.3** Example of low-cut filtering with a 0.02 Hz cut-off (left) and a 0.01 Hz cut-off (right).

**Figure 3.4** Example of acceleration time series with similar PGAs ( $105 - 112 \text{ cm/s}^2$ ) but different PGVs and PGDs.

**Figure 3.5** Acceleration time series with bracketed duration (bottom) and corresponding Husid plot with significant duration (top).

**Figure 3.6** Fourier amplitude spectra for acceleration time series recorded for different sized earthquakes recorded at the same site and similar source-to-site distances.

**Figure 3.7** Acceleration response (SA), velocity response spectra (SV) and displacement spectra (SD) for 4 arbitrary acceleration time series.

**Figure 3.8** Spatial distributions of the earthquake epicentres and seismograph stations in the preliminary and North Sea datasets.

**Figure 3.9** Magnitude-distance distributions, PGA residuals with respect to magnitude and PGA residuals with respect to distance for the preliminary and North Sea datasets.

**Figure 3.10** PGA Residual analysis of the North Sea dataset with respect to local magnitude and epicentral distance, using the Akkar et al. (2014)  $R_{jb}$  GMPE.

**Figure 3.11** PGA Residual analysis of the North Sea dataset with respect to local magnitude and epicentral distance, using the Toro et al. (1997) GMPE.

**Figure 3.12** SA(0.1 s) Residual analysis of the North Sea dataset with respect to local magnitude and epicentral distance, using the Toro et al. (1997) GMPE.

**Figure 3.13** *SA(0.5 s) Residual analysis of the North Sea dataset with respect to local magnitude and epicentral distance, using the Toro et al. (1997) GMPE.*

**Figure 3.14** *SA(1.0 s) Residual analysis of the North Sea dataset with respect to local magnitude and epicentral distance, using the Abrahamson et al. (2014) GMPE.*

**Figure 3.15** *SA(0.1 s) Residual analysis of the North Sea dataset with respect to local magnitude and epicentral distance, using the Toro et al. (1997) GMPE.*

**Figure 3.16** *SA(0.5 s) Residual analysis of the North Sea dataset with respect to local magnitude and epicentral distance, using the Toro et al. (1997) GMPE.*

**Figure 3.17** *SA(1.0 s) Residual analysis of the North Sea dataset with respect to local magnitude and epicentral distance, using the Toro et al. (1997) GMPE.*

**Figure 3.18** *PGV Residual analysis of the North Sea dataset with respect to local magnitude and epicentral distance, using the Toro et al. (1997) GMPE.*

**Figure 3.19** *PGA Seismic hazard curves comparing components of Bungum et al. (2000)'s logic-tree approach with the Akkar et al. (2014)  $R_{jb}$  GMPE at a moderate hazard site ( $\lambda = 0.0501$ , longitude = 4, latitude = 64) within the North Sea.*

**Figure 3.20** *(a) PGA hazard contour map for the Norwegian economic sector of the North Sea computed using the Bungum et al. (2000) logic-tree approach for a return period of 475 years, (b) PGA hazard contour map for the Norwegian economic sector of the North Sea computed using the Akkar et al. (2014)  $R_{jb}$  GMPE with the model standard deviations for a return period of 475 years, (c) Ratio between the North Sea PGA seismic hazard contour map computed using the Akkar et al. (2014)  $R_{jb}$  GMPE and the North Sea PGA seismic hazard contour map computed using the Bungum et al., (2000) logic-tree approach.*

**Figure 3.21** *PGA Residual analysis of the independent dataset with respect to local magnitude and epicentral distance, using the  $R_{jb}$  variant of the Akkar et al. (2014) GMPE.*

**Figure 4.0** *Clustered  $\Delta S_2 S_5$  vectors following 1000 iterations of the k-means algorithm.*

**Figure 4.1** *Silhouette plot of the clustered  $\Delta S_2 S_5$  vectors (iterations = 1000, k = 3).*

**Figure 4.2** *Mean  $\Delta S_2 S_5$  vectors following 1000 iterations of the k-means algorithm.*

**Figure 4.3** *Cluster amplification functions for the  $\Delta S_2 S_5$  vectors.*

**Figure 4.4** *Intra-cluster standard deviations of  $\delta S_2 S_5$  per period.*

**Figure 4.5** *Spatial distribution of the sites assigned to each cluster.*

**Figure 4.6** *V/H spectra for the geometric average of the offshore SEMS sites and select onshore records.*

**Figure 4.7** *Recomputed (response spectra) site transfer functions for the offshore North Sea sites considered by Rognlien (1987).*

**Figure 4.8** *North Sea region with 3x3 grid overlay.*

**Figure 4.9** *Computed North Sea apparent attenuation rates (per km) for a spectral period of 0.5 s.*

**Figure 4.10** *(a) Inputted checkerboard matrix, (b) reconstructed checkerboard matrix.*

**Figure 4.11** *Percentage difference between the reconstructed checkerboard matrix and the inputted checkerboard matrix.*

**Figure 4.12** *Mean attenuation rates for each grid cell, computed using different size North Sea datasets.*

**Figure 4.13** *Standard deviation reductions in the site-corrected intra-event residuals following implementation of the 9 computed apparent attenuation rates.*

**Figure 4.14** *Computed apparent attenuation rates for each grid cell over the considered spectral periods.*

**Figure 4.15** *Map of the inputted North Sea source zones and the evaluated sites.*

**Figure 4.16** *PGA seismic hazard curves generated using the CRISIS seismic hazard software and the Monte Carlo PSHA program (MATLAB) for an example (low hazard) test site (longitude = 20, latitude = 58).*

**Figure 4.17** *Pre- and Post-Correction Seismic Hazard Curves for Evaluated Sites 1 and 2.*

**Figure 4.18** *Pre- and Post-Correction Seismic Hazard Curves for Evaluated Sites 3 and 4.*

**Figure 4.19** *Pre- and post-correction uniform hazard response spectra for the evaluated sites.*

**Figure 5.0** *Seismic hazard curve demonstrating the impact of modifying  $\sigma$  within a PSHA.*

**Figure 5.1** *Fourier amplitude spectrums of ground-motion at a particular distance and site condition for earthquakes of magnitudes 5 and 7 based on a standard seismological model and the corresponding time-series for these ground-motion spectrums.*

**Figure 5.2** *Source scaling for single corner frequency  $\omega$ -square model.*

**Figure 5.3** *Geometrical spreading function developed by Boore and Atkinson (1995).*

**Figure 5.4** *Illustration of  $Q(f)$ .*

**Figure 5.5** *Observed duration (once source duration is subtracted) for earthquakes from an arbitrary region.*

**Figure 5.6** *Site amplification vs. frequency.*

**Figure 5.7** *Combined effect of the site amplification and the path-independent attenuation.*

**Figure 5.8** Schematic of the time-domain procedure.

**Figure 5.9** Comparison of waveforms and peak surface velocity (PSV) response spectra for time-domain simulations using the box and exponential (shaped) windows to shape the noise.

**Figure 5.10** The target spectrum, the spectrum from a single realisation and the spectrum from an average of 640 realisations. The simulations were undertaken using an arbitrary seismological model. Taken from Boore (2003).

**Figure 5.11** (a)  $\phi$  for PGA from the simulated ground-motions, (b)  $\phi$  for PGA from the considered GMPEs, (c)  $\phi$  for SA(0.2 s) from the simulated ground-motions, (d)  $\phi$  for SA(0.2 s) from the considered GMPEs, (e)  $\phi$  for SA(1 s) from the simulated ground-motions and (f)  $\phi$  for SA(1 s) from the considered GMPEs.

**Figure 5.12** (a) Rate of change of  $\phi$  with respect to magnitude for PGA, (b) rate of change of  $\phi$  with respect to magnitude for SA(0.2 s) and (c) rate of change of  $\phi$  with respect to magnitude for SA(1 s).

**Figure 6.0** PGA seismic hazard curves computed using the considered GMPE logic trees.

**Figure 6.1** SA(1.0 s) seismic hazard curves computed using the considered GMPE logic trees.

**Figure 6.2** PGA seismic hazard curves computed using the Tromans et al. (2019) GMPE logic tree and the Tromans et al. (2019 with the Grunthal et al. (2018) stress drop scaling factors.

**Figure 6.3** SA(1.0 s) seismic hazard curves computed using the Tromans et al. (2019) GMPE logic tree and the Tromans et al. (2019 with the Grunthal et al. (2018) stress drop scaling factors.

**Figure 6.4** PGA seismic hazard curves computed using the Tromans et al. (2019) GMPE logic tree and the Tromans et al. (2019 with the modified GMPE weights stress drop scaling factors.

**Figure 6.5** SA(1.0 s) seismic hazard curves computed using the Tromans et al. (2019) GMPE logic tree and the Tromans et al. (2019 with the modified GMPE weights stress drop scaling factors.

**Figure 6.6** PGA seismic hazard curves computed using the Tromans et al. (2019) GMPE logic tree with both modifications and the GMPE logic trees considered for modification to the North Sea.

**Figure 6.7** SA(1.0) seismic hazard curves computed using the Tromans et al. (2019) GMPE logic tree and the Tromans et al. (2019 with the modified GMPE weights stress drop scaling factors.

**Figure 7.0** Seismogenic source zonation model of Bungum et al. (2000) with the original  $a$ -values ( $a_{B2000}$ ).

**Figure 7.1** Frequency magnitude distribution of the declustered, non-duplicative and combined North Sea catalogue.

**Figure 7.2** Stepp (1972) plot for the declustered, non-duplicative ( $M_L \geq 2.1$ ) and combined North Sea catalogue.

**Figure 7.3** *Magnitude and spatial distribution of the UNSEC.*

**Figure 7.4** *Frequency magnitude distribution of the UNSEC.*

**Figure 7.5** *(a) North Sea PGA seismic hazard map computed using the (normalised) updated source parameters computed within this investigation and (b) North Sea PGA seismic hazard map computed using the (normalised) original source parameters of Bungum et al. (2000).*

**Figure 7.6** *PGA seismic hazard curves for the considered North Sea sites.*

**Figure 7.7** *Spatial distribution of MDPs within the compiled dataset.*

**Figure 7.8** *Isoseismal contours (EMS-98 scale) generated for the 1979/06/14 21:24:12 and 2009-11-10 02:29:57 earthquakes.*

**Figure 7.9** *Plots of cumulative number of MDPs (intensity  $\geq 1$ ) against time.*

**Figure 7.10** *Intensity hazard curves computed from the MDPs and the North Sea PSHA calculations.*

**Figure 8.0** *Conversion from fragility curves to DPM.*

**Figure 8.1** *General framework of fragility analysis.*

**Figure 8.2** *Schematic representation of the fragility curve generation procedure: (a) response statistics, (b) probability of exceeding a limit state at a specific ground-motion intensity, (c) discrete fragility information for a predetermined limit state and (d) continuous fragility function.*

**Figure 8.3** *Simple schematic diagram of a fixed-steel jacket platform.*

**Figure 8.4** *Simple two-dimensional schematic of a 5-MW offshore wind turbine.*

**Figure 8.5** *Spatial distribution of offshore wind farm development in northwestern Europe.*

**Figure 8.6** *Considered fragility curves for (a) FSJ platforms and (b) 5-MW offshore wind turbines.*

**Figure 8.7** *Seismic hazard curves for sites in the North Sea.*

**Figure 8.8** *Ground-motion intensity vs.  $R_{jb}$  for an  $M_L$  6.5 earthquake using the Akkar et al. (2014) GMPE.*

**Figure 8.9** *Ground-motion intensity vs.  $R_{jb}$  for an  $M_L$  4.2 earthquake using the Akkar et al. (2014) GMPE.*

## List of Tables

**Table 2.0** *Normalised  $a$  and  $b$  parameters for the North Sea and United Kingdom ( $M_L \geq 2.5$ ) earthquakes.*

**Table 2.1** *Some earthquakes potentially related to hydrocarbon production and associated hydrocarbon fields in the United Kingdom economic sector.*

**Table 2.2** *Comparison of the  $a$  and  $b$  parameters for the North Sea ( $M_L \geq 2.5$  earthquakes) and the North Sea ( $M_L \geq 2.5$  but excluding potentially induced earthquakes originating in the United Kingdom economic sector) earthquake catalogues.*

**Table 2.3** *Questions, answers and associated scores provided within the Verdon et al. (2019) framework.*

**Table 2.4** *Evidence assessment and answer rating, and answer and corresponding (modified) score for each question within the Verdon et al. (2019) framework.*

**Table 3.0** *Table of some notable GMPEs (up to 2020) which were developed to predict ground-shaking resulting from induced seismicity.*

**Table 3.1** *GMPE testing fit criteria.*

**Table 3.2** *GMPEs considered within residual analysis of the North Sea dataset.*

**Table 3.3** *Parameters determined from residual analysis for each GMPE with regards to the North Sea dataset for PGA.*

**Table 3.4** *Parameters determined from residual analysis for each GMPE with regards to the North Sea dataset for SA(0.1 s).*

**Table 3.5** *Parameters determined from residual analysis for each GMPE with regards to the North Sea dataset for SA(0.5 s).*

**Table 3.6** *Parameters determined from residual analysis for each GMPE with regards to the North Sea dataset for SA(1.0 s).*

**Table 3.7** *Parameters determined from residual analysis for each GMPE with regards to the North Sea dataset for PGV.*

**Table 3.8** *Ranking of each GMPE based on performance for all ground-motion intensity measures considered.*

**Table 4.0** *Quantitative descriptions of the terminology used by Rognlien (1987) to describe the strength of each distinct soil layer within each considered site's subsurface profile.*

**Table 4.1** *Basic subsurface profiles for each offshore North Sea site considered by Rognlien (1987).*

**Table 4.2** *Explanation of how traversing a grid cell with either a negative or positive apparent attenuation rate affects the corresponding intra-event residual.*

**Table 4.3** *Number of travel path passes for each grid cell in Fig. 5.8.*

**Table 4.4** *Computed apparent attenuation rate (per km) for each grid cell*

**Table 4.5** *Intra-event residual standard deviations following each adjustment to the base model GMPE.*

**Table 4.6** *Matches per grid cell (computed attenuation vs expected attenuation).*

**Table 4.7** *Intra-event residual standard deviations following each adjustment to the base model GMPE.*

**Table 5.0** *Parameters of the Bora et al. (2017) stochastic model for Europe and the considered  $\kappa_0$  distributions.*

**Table 5.1** *GMPEs for which  $\phi$  (or  $\sigma$ ) was compared to  $\phi$  computed from the stochastic simulations.*

**Table 6.0** *GMPE logic trees for regions surrounding the North Sea.*

**Table 6.1** *Distributions of predicted PGA and SA(1.0 s) for return periods of 475 years and 2475 years at the high hazard site.*

**Table 6.2**  *$U_R$  for the predicted ground-motion for a given return period at the high hazard site.*

**Table 6.3** *Results of North Sea GMPE testing.*

**Table 6.4**  *$U_R$  for the predicted ground-motion for return periods of 475 years and 2475 years using the modified forms of the Tromans et al. (2019) GMPE logic tree at the high hazard site and the low hazard site.*

**Table 6.5** *Distributions of predicted PGA and SA(1.0 s) for return periods of 475 years and 2475 years using the Tromans et al. (2019) GMPE logic tree and the Tromans et al. (2019) GMPE logic tree with the Grunthal et al. (2018) stress drop scaling factors at the high hazard site and the low hazard site.*

**Table 6.6** *Modified GMPE weights for the Tromans et al. (2019) GMPE logic tree.*

**Table 6.7** *Distributions of predicted PGA and SA(1.0 s) for return periods of 475 years and 2475 years using the Tromans et al. (2019) GMPE logic tree and the Tromans et al. (2019) GMPE logic tree with modified GMPE weights at the high hazard site and the low hazard site.*

**Table 6.8** *Distributions of predicted PGA and SA(1.0 s) for return periods of 475 years and 2475 years using the Tromans et al. (2019) GMPE logic tree and the Tromans et al. (2019) GMPE logic tree with the Grunthal et al. (2018) stress drop scaling factors and the modified GMPE weights at the high hazard site and the low hazard site.*

**Table 6.9**  $U_R$  for the predicted ground-motion for return periods of 475 years and 2475 years for the Tromans et al. (2019) GMPE logic tree with the combined modifications and the GMPE logic trees considered for modification to the North Sea.

**Table 7.0** Parameters for the Reasenber (1985) declustering algorithm.

**Table 7.1** Number of observed earthquakes in each time window for each magnitude interval.

**Table 7.2** Number of observed events for each source zone and (normalised) original and updated  $a$ -values.

**Table 8.0** Damage state definitions for steel moment frames as defined by the National Institute of Building Science.

**Table 8.1** Damage state definitions for a 5-MW offshore wind turbine.

**Table 8.2** Mean AFOEs for each damage state considered for FSJ platforms in the North Sea.

**Table 8.3** Mean AFOEs for each damage state considered for 5-MW wind turbines in the North Sea.

**Table 8.4** Ground-motion intensities at select distances for an  $M_L$  6.5 earthquake using the Akkar et al. (2014) GMPE.

**Table 8.5** Probability of exceeding each FSJ damage state (PoE) for the expected SA at each site from an  $M_L$  6.5 earthquake using the Akkar et al. (2014) GMPE.

**Table 8.6** Probability of exceeding each 5-MW wind turbine damage state (PoE) for the expected PGA at each site from an  $M_L$  6.5 earthquake using the Akkar et al. (2014) GMPE.

**Table 8.7** Ground-motion intensities at select distances for an  $M_L$  4.2 earthquake using the Akkar et al. (2014) GMPE.

**Table 8.8** Probability of exceeding each FSJ damage state (PoE) for the expected PGA at each site from an  $M_L$  4.2 earthquake using the Akkar et al. (2014) GMPE.

## List of Abbreviations

AFOE = Annual frequency of exceedance

AK2014 = Akkar et al. (2014) ground-motion prediction equation

API = American Petroleum Institute

ASCE = American Society of Civil Engineers

B17 = Bora et al. (2017) (stochastic parameters)

B2000 = Bungum et al. (2000) ground-motion prediction equation

BGS = British Geological Survey

CCS = Carbon capture storage

CENA = Central and eastern North America

CO6 = Chandler et al. (2006) (stochastic parameters)

DPM = Damage probability matrix

DRP = Damage return period

DPM = Damage probability matrix

E11 = Edwards et al. (2011) (stochastic parameters)

EIDA = European integrated data archive

ELSR = Equivalent-linear site response

EMS-98 = European macroseismic scale

ESHM13 = European seismic hazard model 2013

ESR = Evidence strength ratio

EU = European Union

FAS = Fourier amplitude spectrum

FEMA = Federal Emergency Management Agency

FMD = Frequency magnitude distribution

FSJ = Fixed-Steel Jacket (platform)

GEUS = Geological Survey of Denmark and Greenland

GMIM = Ground-motion intensity measure

GMM = Ground-motion model

GMPE = Ground-motion prediction equation

GR = Gutenberg-Richter (distribution)

HSE = Health and Safety Executive

HVSR = Horizontal to vertical ratio (of ground-motion components)

IAR = Induced assessment ratio

IDR = Inter-level drift ratio

IPE = Intensity prediction equation

ISO = International Organisation of Standardisation

MCE = Maximum credible earthquake

MDP = Macroseismic data point

MECE = Mutually exclusive and collectively exhaustive

NES = Norwegian economic sector

NIBS = National Institute of Building Science

NORSAR = Norwegian Seismological Array

p.a. = per annum

PC = Principal component

PCA = Principal component analysis

PGA = Peak ground acceleration

PGD = peak ground displacement

PGV = Peak ground velocity

PoE = Probability of exceedance

PSHA = Probabilistic seismic hazard assessment

SA = Spectral acceleration

SEMS = Seafloor earthquake measuring system

SFA = Seismic fragility analysis

SHARE = Seismic hazard harmonisation in Europe (project)

SRL = Surface rupture length

SRW = Surface rupture width

UHRS = Uniform hazard response spectrum

UKCS = United Kingdom continental shelf

UKES = United Kingdom economic sector

UNSEC = Updated North Sea earthquake catalogue

USGS = United States Geological Service

UTM = Universal transverse mercator (zone)

## List of Mathematical Symbols

$A$  = amplification function considered in  $G$

$a$  = overall rate of seismicity within a region (parameter within a Gutenberg Richter distribution)

$a_{B2000}$  = original a-values for the Bungum et al. (2000) seismogenic source model

$a_{upd}$  = updated a-values for the Bungum et al. (2000) seismogenic source model

$A_R$  = geographical area of considered region for computation of normalised a value

$b$  = ratio of small earthquakes to large earthquakes in a region (parameter within a Gutenberg Richter distribution)

$b_{B2000}$  = original b-value for the Bungum et al. (2000) seismogenic source model

$b_{upd}$  = regional updated b-value for the Bungum et al. (2000) seismogenic source model

$C$  = constant required for source spectrum considered in stochastic simulations

$C_V$  = velocity of primary waves in the water layer

$c_Q$  = seismic velocity used when determining  $Q$

$D$  = path-independent attenuation function considered in  $G$

$D_{hypo}$  = hypocentral depth

$E$  = source spectrum (for ground-motion spectrum considered in stochastic simulations)

$F$  = Fourier transform function

$f_c$  = corner frequency

$f_p$  = resonant frequency of the water layer

$ft1, ft2$  = reference frequencies considered in  $Q$

$F_S$  = effect of the free surface considered in determination of  $C$

$f_0$  = fundamental period of a site's subsurface profile

$f_1$  = primary frequency

$f_2$  = secondary frequency

$G$  = site effect function (for ground-motion spectrum considered in stochastic simulations)

$GM_{15}$  = 15<sup>th</sup> fractile of the predicted ground-shaking for a given return period

$GM_{85}$  = 85<sup>th</sup> fractile of the predicted ground-shaking for a given return period

$G_0$  = initial shear modulus of a distinct soil layer within a site's subsurface profile (MPa)

$H_w$  = water layer thickness

$H_{800}$  = depth to bedrock where shear wave velocity equals 800 m/s

$I$  = ground-motion intensity filter for computation of considered ground-motion intensity measure(s) in stochastic simulations

$k$  = optimal number of clusters for k-means clustering

$m$  = earthquake magnitude (non-scale specific)

$M_c$  = magnitude of completeness

$M_L$  = Local magnitude of an earthquake

$M_{max}$  = largest earthquake magnitude in the cluster (Reasenberg declustering)

$M_w$  = moment magnitude of an earthquake

$M_0$  = seismic moment

$N$  = earthquake count (within a Gutenberg Richter distribution)

$p$  = near-source density

$P$  = path effect function (for ground-motion spectrum considered in stochastic simulations)

$P_{ies}$  = distance (in km) through grid cell  $i$  for a straight line travel path of source  $e$  to site  $s$

$p_s$  = density in proximity to earthquake source in determination of  $C$

$PSA$  = pseudo-acceleration spectrum

$PSV$  = pseudo-velocity spectrum

$\rho_1$  = probability of detecting the next clustered earthquake used for the computation of the look-ahead time within Reasenberg declustering

$Q$  = attenuation function considered in  $P$

$Qr1, Qr2$  = attenuation values corresponding to  $ft1, ft2$  in  $Q$

$Q_0$  = anelastic attenuation

$r_{fact}$  = number of crack radii surrounding each earthquake within later earthquakes that are treated as part of the considered cluster within Reasenberg declustering

$R_{hypo}$  = hypocentral source-to-site distance

$R_{epi}$  = epicentral source-to-site distance

$R_{jb}$  = Joyner-Boore source-to-site distance

$RotD50$  = median value of the response spectra of the two horizontal components of ground-motion projected onto all redundant azimuths

$R_{rup}$  = rupture source-to-site distance

$R_x$  = horizontal distance from site to top edge of the rupture, measured normal to the strike of the fault

$R_{y0}$  = horizontal distance from site to termination of the rupture, measured parallel to strike of the fault

$R_0$  = reference distance considered in  $Z$  and determination of  $C$

$R_1, R_2$  = reference distances considered in  $Z$

$R_{\theta\phi}$  = radiation pattern (considered in determination of  $C$ )

$S$  = displacement source spectrum (for ground-motion spectrum considered in stochastic simulation)

$SA$  = response spectrum

$SD$  = displacement spectrum

$S_u$  = shear strength of a distinct soil layer within a site's subsurface profile

$SV$  = velocity spectrum

$T_c$  = time interval considered within the Stepp (1972) method for assessment of magnitude completeness

$T_{gm}$  = ground-motion duration considered in stochastic simulations

$t_n$  = system period

$T_1$  = first natural period of a structure

$U_R$  = relative uncertainty for a ground-motion prediction equation logic tree

$V$  = gain considered in computation of  $I$  for response spectra in stochastic simulations

$V_C$  = partition of shear-wave energy into horizontal components (considered in determination of  $C$ )

$V_S$  = shear-wave velocity

$V_S, av$  = average shear-wave velocity of the soil column structure

$V_{S30}$  = shear-wave velocity in the upper 30 m of a site's subsurface profile

$x_k$  = incremental increase of the lower cut-off magnitude within Reasenberg declustering

$x_{meff}$  = effective lower magnitude cut-off considered within Reasenberg declustering

$Y$  = ground-motion spectrum (for ground-motion spectrum considered in stochastic simulations)

$Z$  = depth per distinct layer within a site's subsurface profile, or geometrical spreading function considered in  $P$

$Z_{obs}$  = observed ground-motion (base log10)

$Z_p$  = path-corrected intra-event residual (base log10)

$Z_{pred}$  = predicted ground-motions (base log10)

$Z_s$  = site-corrected intra-event residual (base log10)

$\beta$  = near-source shear wave velocity

$\Delta S2S_s$  = vector comprising the  $\delta S2S_s$  scalar computed for each spectral period considered

$\Delta t$  = sampling frequency

$\Delta\sigma$  = static earthquake stress drop

$\xi$  = damping coefficient

$\kappa$  = kappa

$\kappa_0$  = site-specific component of kappa

$\lambda$  = mean rate of earthquake occurrence

$\lambda_{DS}$  = probability of exceedance for a given damage state

$\delta_i$  = ground-motion residual (base log10)

$\delta_Q$  = apparent attenuation per km

$\delta_\lambda$  = standard deviation of the mean rate of earthquake occurrence

$\delta S2S_s$  = average (intra-event) ground-motion prediction equation residual for a single site

$\Phi$  = intra-event ground-motion residual standard deviation (base log10)

$\sigma$  = total ground-motion residual standard deviation (base log10)

$\phi S2S_s$  = standard deviation of the site-to-site (intra-event) ground-motion prediction equation residuals

$\omega_n$  = natural angular frequency of the system

$\tau$  = inter-event ground-motion residual standard deviation (base log10)

$\tau_{max}$  = maximum look-ahead time for the building of clusters (Reasenberg declustering)

$\tau_{min}$  = minimum look-ahead time for identifying clusters when the first earthquake is not clustered (Reasenberg declustering)

$|dH(x)|$  = absolute value of the derivative of the hazard curve at the site for which the fragility information and hazard information are being convolved to determine the mean annual frequency of exceeding a given damage state

## 1.0 Introduction to Seismic Hazard Assessment in the North Sea

The North Sea borders the United Kingdom, Norway and northwestern Europe (Fig. 1.0), and contains considerable amounts of offshore infrastructure. A great amount of this infrastructure is a result of the extensive and historic hydrocarbon production in the region, and therefore comprises largely of oil and gas platforms and pipelines (Wood Mackenzie, 2017). Production began in the North Sea in 1967 when British Petroleum installed the first offshore platform in the region at the Sole A hydrocarbon field (Fig. 1.0; Oil and Gas UK, 2012). Total hydrocarbon production in the North Sea has risen from ~8000 barrels of oil equivalent per day (boe/d) in 1975 to a peak of ~5.4 million boe/d in 2000, before having subsequently decreased sharply and levelled off to ~1.6 million boe/d since 2016 (Data-ogauthority.opendata.arcgis.com, 2020). Such considerable levels of production have resulted in the deployment of large numbers of offshore platforms throughout the many producing (or once-producing) hydrocarbon fields in the region (Fig. 1.0), with 556 platforms having been installed as of 2012 throughout these fields (Oil and Gas UK, 2012).

In addition to hydrocarbon production infrastructure, the increasing global demand for renewable energy has led to the increased deployment of offshore wind turbine facilities in the North Sea, with wind energy (as of 2017) providing 10.4% of total energy demand for the European Union (EU), and 97% of European wind turbines being deployed in the North Sea (Northsearegion.eu, 2017). The offshore environment of the North Sea is ideal for the deployment of wind turbines due to (1) the consistently high wind speeds and (2) the remoteness of their deployment locations limiting their visibility to populations who could potentially object to their construction otherwise (Mo et al., 2017). The locations of offshore wind turbine facilities in the North Sea are provided in Fig. 1.1.

The many platforms, pipelines and wind turbine facilities deployed in the North Sea mean there is considerable amounts of critical offshore infrastructure<sup>1</sup> in the region. It is important to minimise the damage to critical infrastructure deployed in the North Sea because it can be detrimental to (1) the environmental health of the North Sea, (2) the personal health of employees operating on or near the damaged infrastructure and (3) the operations and financial status of the corporations and governments which rely upon the infrastructure (Sakai et al. 2017; Romeo, 2013). Infrastructure damage can potentially result from ground-shaking generated by earthquakes. High levels of ground-shaking could result in significant direct damage to the critical infrastructure in the North Sea, potentially including the collapse of platforms and wind turbines (e.g. Fig. 1.2) or the rupturing of pipelines (Romeo, 2013; Sakai et al. 2017). Furthermore, indirect damage can be caused by secondary effects such as soil liquefaction, soil densification and landslides (Romeo, 2013). The engineering (seismic) risk of critical North Sea infrastructure to earthquakes is therefore important to consider.

---

<sup>1</sup> Critical infrastructure refers to assets which are vital for the functioning of a country's economy or national security, and/or which damage to could result in endangerment of the population's health.

The potential impacts of ground-shaking and the associated importance of considering the seismic risk for offshore North Sea infrastructure are well demonstrated at other locations, albeit onshore, although the challenges of the offshore environment for the deployment/construction of infrastructure (e.g. the supersaturation of the seafloor sediments and the presence of the water layer) potentially indicate that the damage resulting from ground-shaking at offshore locations is more severe than for onshore locations<sup>2</sup>. For example, in 2002, an earthquake of (moment) magnitude 7.9 (the 2002 Denali Fault earthquake) struck the Trans-Alaska oil pipeline in Alaska, which at the time provided 17% of the domestic oil supply for the United States (United States Geological Survey, 2003). No damage was observed resulting from this earthquake, but the fault rupture resulted in horizontal ground-displacement of approximately 4.5 m (United States Geological Survey, 2003). This lack of observed damage is attributed to the implementation of Teflon shoes which can slide on horizontal steel beams (Fig. 1.3). This slider solution was deployed based on seismic design specifications resulting from geological studies undertaken in the 1970s by the United States Geological Survey (USGS). When the USGS undertook these studies, the cost was approximately \$3 million. If the pipeline had collapsed, the combined financial cost due to economic losses, and the repair and environmental remediation costs would far exceed \$100 million (United States Geological Survey, 2003), demonstrating the significant potential (economic) loss reduction which can be achieved if sufficient seismic design/hazard studies are undertaken.

An earthquake engineering analysis can be used to assess whether a structure can withstand a given level of ground-shaking and maintain a certain level of structural integrity (Baker, 2015). To determine the intensities of ground-shaking considered within an earthquake engineering analysis, the large uncertainties associated with the location, magnitude and resulting ground-shaking of potential earthquakes must be accounted for (Baker, 2015). Probabilistic seismic hazard assessment (PSHA) quantifies and assimilates these uncertainties to provide probabilistic representations of the future intensities of ground-shaking that could occur for the considered region. Overviews of earthquake terminology and PSHA are provided in Appendices A and B respectively.

PSHAs are generally undertaken for onshore locations where buildings are frequently constructed, rather than offshore locations, of which there is often not much engineering interest due to a lack of infrastructure and limited populace. However, for offshore locations with critical infrastructure such as the North Sea, PSHA must still be undertaken. Of the 556 offshore platforms installed in the North Sea, at least 52 have already been decommissioned (Oil and Gas UK, 2012). Despite the apparent onset of decommissioning in the North Sea many operators throughout the world are looking to operate offshore platforms beyond their initial design life of ~25 years (Kammula and Sriramula, 2014). At least half of the 288 platforms present in the United Kingdom Continental Shelf (UKCS) of the North Sea have

---

<sup>2</sup> See Chapter 4 for more details on the influence of local offshore site conditions on incident ground-motions.

already exceeded their design life (Stacey et al., 2008)<sup>3</sup>, and therefore will be more structurally vulnerable to ground-shaking from North Sea earthquakes than during this initial 25 year period (Kammula and Sriramula, 2014). These offshore platforms will therefore require assessment of their structural health if they are not decommissioned.

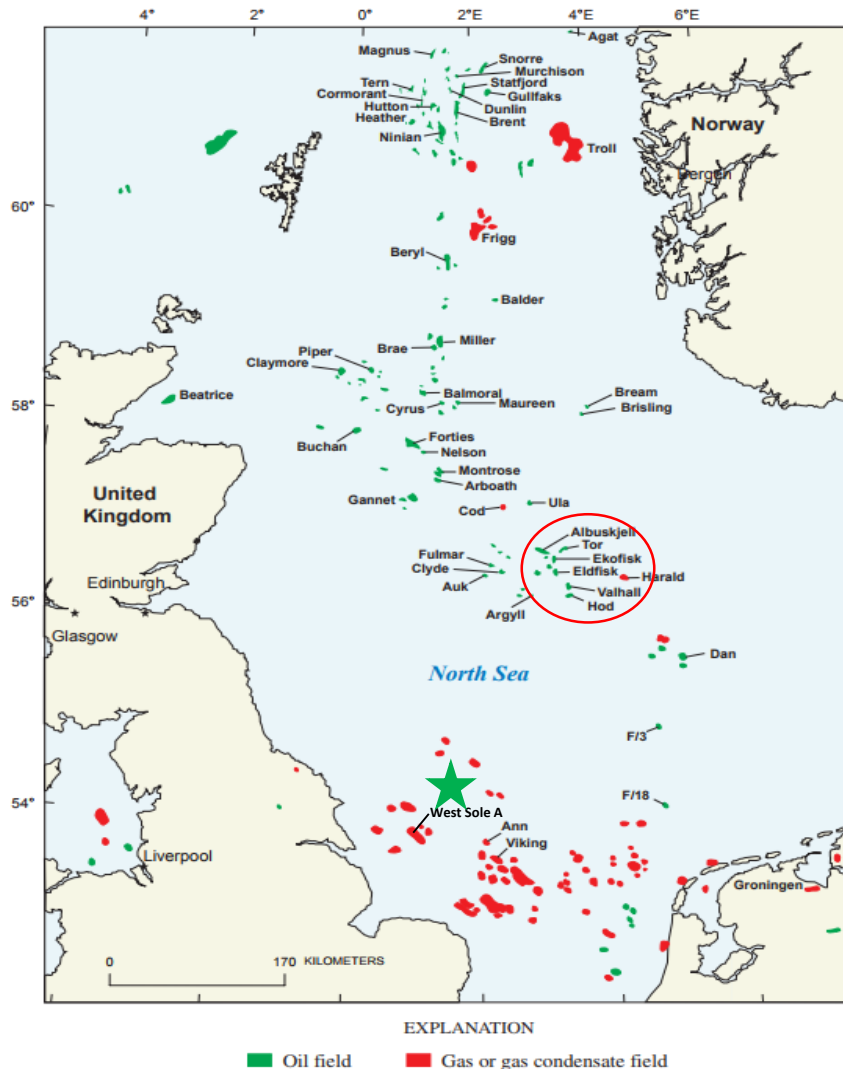


**Figure 1.0** Spatial distribution of hydrocarbon fields in the North Sea. Green star is the approximate location of the 1931 Dogger Bank earthquake. Taken from Gautier, (2013).

In addition to more conventional offshore infrastructure, the engineering risk for newer, developing technologies in the North Sea to ground-shaking in the region must be considered. The storage of recaptured CO<sub>2</sub> within either depleted hydrocarbon reservoirs or aquifers (carbon capture and storage (CCS) sites) is an important example of such technologies. The primary concern associated with CCS sites being subjected to earthquakes is the hydraulic integrity of the cap rock being comprised (Verdon, 2014). If the cap rock of a CCS site is compromised, massive volumes of CO<sub>2</sub> could potentially be

<sup>3</sup> More recent design life statistics were sought for platforms in the North Sea but were not available in the public domain. The total number of FSJ platforms which have exceeded their design life in the region is likely substantially higher now.

released into the surrounding environment. Such an instance would be a catastrophic result for a CCS project within the North Sea. The North Sea is considered an excellent region for CO<sub>2</sub> storage due to (1) its proximity to many European countries investing in CCS technology and (2) the many viable geological repositories in the region (Strachan, 2011). Consequently, the long term viability of CCS in the North Sea in terms of engineering risk to ground-shaking must also be considered, although such viability is not assessed within this investigation, with priority being given to the locally far more abundant offshore platforms and wind turbine facilities.

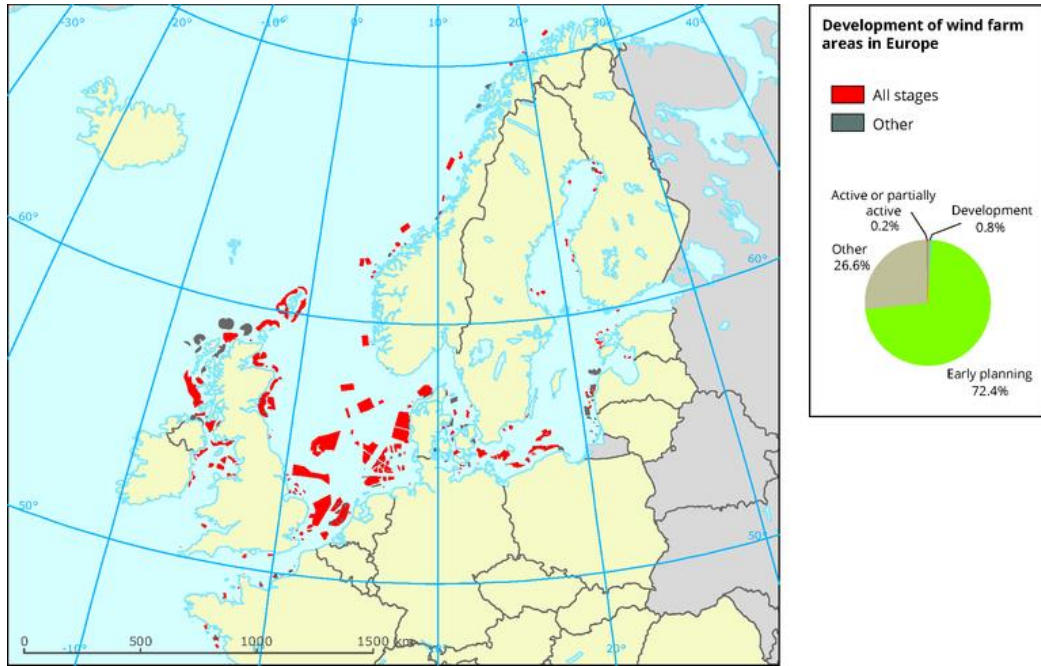


**Figure 1.1** Spatial distribution of offshore wind farm development in northwestern Europe. Taken from eea.europa.eu. (2015). This image has not been modified and is available for reuse under the creative commons license (CC BY 2.5 DK) as per [https://creativecommons.org/licenses/by/2.5/dk/deed.en\\_GB](https://creativecommons.org/licenses/by/2.5/dk/deed.en_GB):



**Figure 1.2** Wind turbine collapse due to ground-shaking in Japan (left) and New Zealand (right). Taken from Asareh (2015).



**Figure 1.3** Slider system for the Trans-Alaska pipeline and the horizontal displacement resulting from the 2002 Denali earthquake fault rupture. Taken from United States Geological Survey (2003).

### 1.1 Previous PSHAs for the North Sea

There have been a number of PSHAs for the North Sea. A common output of PSHA is a horizontal PGA hazard contour map for a specified probability of exceedance per annum (p.a.) (e.g. Fig. 1.4) (Mallard et al., 2003).

One of the earliest investigations into seismic hazard analysis in the North Sea was undertaken for the United Kingdom Health and Safety Executive (HSE) in 1986 (Principia Mechanica Ltd, 1986) as part of a larger effort to estimate seismic hazard for the entirety of the United Kingdom continental shelf (UKCS), with these estimates improved upon by further HSE reports published in 1993 (Musson et al., 1993), 1997 (BGS & Ove Arup and Partners, 1997), and 2002 (EQE International, 2002). The seismic hazard of the United Kingdom sector of the North Sea is characterised by these HSE commissioned reports, whilst the Norwegian sector is characterised by Bungum et al. (2000).

The 1986, 1997 and 2002 HSE reports, along with Bungum et al. (2000)'s study were appraised by the HSE in 2003 (Mallard et al., 2003). In this appraisal the individual strengths and weaknesses of each study's approach were assessed to provide a weighting to each report's hazard results (as a means of providing a simplistic alternative to a more complex logic-tree approach PSHA). This resulted in a

composite hazard contour map which was compared against site-specific seismic hazard analyses throughout coastal areas of the UK. The composite hazard contour map for a  $10^{-4}$  p.a. probability of exceedance was evaluated by comparison to a stopgap (provisional) hazard contour map, which was produced specifically for the appraisal from the North Sea earthquake catalogue.

Further to this, Mallard et al. (2003) developed an additional composite  $10^{-4}$  p.a. hazard contour map by taking the greater PGA hazard value per each geographical point plotted on the composite  $10^{-4}$  p.a. hazard contour map and the provisional map. Mallard et al. (2003) compared this additional composite map to the EQE International (2002) map. Relatively small and explainable differences were observed between these maps, however there was also clearly area-specific bifurcation throughout the UKCS, including the North Sea (EQE International Ltd, 2002). For example, in the northern North Sea, the additional composite map was found to differ by up to 0.12 g, whereas in the southern North Sea, the additional composite map was found to differ by up to -0.06 g. A final composite map taking the greater of the PGA hazard values per point plotted of either this composite map or the EQE International (2002) map was then constructed (Fig. 1.4). This final composite hazard contour map was concluded by the HSE appraisal as being the most suitable hazard contour map for the UKCS (and thus the UK sector of the North Sea) until more extensive seismic hazard analysis is carried out.

It should also be noted that the most recent PSHA for the United Kingdom was undertaken by Mosca et al. (2020), two decades later than the most recent North Sea PSHA by Bungum et al. (2000). This recent United Kingdom PSHA was carried out to provide updated seismic hazard estimates for upcoming revisions to the Eurocode 8 seismic zoning procedure (see BS EN 1998,2004 for more details on this seismic zoning procedure). The United Kingdom inherently has a far larger population than the North Sea, and therefore contains far more buildings for which seismic hazard calculations must be undertaken. Consequently, despite extensive networks of critical offshore infrastructure being present within the North Sea, reassessment of the seismic hazard in the United Kingdom has likely taken priority due to the considerably greater population present in the region.

## 1.2 The 2001 Ekofisk Earthquake

Despite the HSE appraisal deeming their final composite map as suitable until a more extensive North Sea PSHA is undertaken, the appraisal notes that the 2001 local magnitude ( $M_L$ ) 4.2 Ekofisk earthquake as a significant development since the publication of their composite map. Prior to the 2001 Ekofisk earthquake, seismic hazard in the North Sea was considered to be of limited engineering significance due to natural seismicity in the region being predominantly moderate<sup>4</sup> (Mallard et al., 2003).

The Ekofisk earthquake led to an increased interest in the engineering significance of North Sea seismicity due to the combination of three factors. Firstly, macroseismic surveying following the

---

<sup>4</sup> See Chapter 2 for an overview of seismicity in the North Sea.

Ekofisk earthquake noted the resultant ground-shaking as being described as strongly felt on the Ekofisk field platforms, as well as being felt but to a weaker extent on platforms in the Eldfisk and Embla fields 30 km south of Ekofisk and the Tor field 20 km north-east (Fig. 1.0) (Ottemöller et al., 2005). Secondly, a shallow focal depth of less than 3 km was determined. This shallow source depth was attributed to the induced nature of the earthquake, with the earthquake having originated within the overburden of the Ekofisk reservoir, where seismic slip was enabled by hydraulic jacking up of the reservoir, itself facilitated by unintentional mass water injection (Zoback & Zinke, 2002; Ottemöller et al., 2005; Cesca et al., 2011)<sup>5</sup>. Finally, the computed seismic moment of the event was considered relatively large ( $M_0 = 5 \times 10^{15}$  N m) for a moderate size earthquake. This surprisingly large seismic moment was deemed to have “important implications for evaluating the response of the oil and gas infrastructure proximal to the Ekofisk field from an engineering point of view” despite no structural damage resulting from the associated ground-shaking (Ottemöller et al., 2005). Furthermore, the ground-motions from induced earthquakes can be large because they occur at shallow focal depths, and therefore can be experienced by critical facilities at short hypocentral distances (Atkinson, 2015), as was most probably the case for the Ekofisk earthquake. The hazard associated with induced earthquakes could therefore potentially be significant.

Considering the potentially significant seismic hazard presented by induced seismicity in the North Sea, and that the 2001 Ekofisk earthquake (the only induced earthquake to be deemed of engineering significance in the region) is not accounted for in past North Sea PSHAs (Mallard et al., 2003), current seismic hazard assessment for the region is potentially inadequate. Therefore, considering this, and that the most recent North Sea PSHA (Bungum et al., 2000) is over two decades old, the reassessment of PSHA for the North Sea is undertaken in this investigation. The rationale for reassessment of North Sea PSHA is further validated by the offshore seismic hazard maps within the current industry standards for offshore seismic design (API RP 2EQ, 2014) implementing the results of a PSHA undertaken for onshore Norway (NORSAR and NGI, 1998), rather than specifically for the North Sea region, which is again over two decades ago. Finally, the reassessment of North Sea PSHA is appropriate because of the improvements in GMPE and PSHA development could help to better estimate the hazard resulting from the potential occurrence of an earthquake similar to 1931  $M_L$  6.1 Dogger Bank earthquake. The 1931 Dogger Bank earthquake occurred approximately 100 km off the coast of Yorkshire (Fig. 1.0), with the most severe observed structural damage being the rotation of a church spire in Filey, a coastal community on the Yorkshire coastline (Ritsema and Gürpınar, 1983). The damage resulting from this earthquake was limited due to the earthquake occurring far from any built infrastructure at the time, but the occurrence of a similar earthquake could potentially result in significant damage to offshore infrastructure now deployed in the North Sea (see Fig. 1.0; Fig. 1.1).

---

<sup>5</sup> For a detailed summary of the 2001 Ekofisk event see Chapter 2.

### 1.3 Reassessment of North Sea PSHA

The reassessment of North Sea seismic hazard requires consideration of the individual aspects of North Sea PSHA.

The selected ground-motion prediction equation (GMPE) is a key variable within a PSHA. Bungum et al. (2000) use the Toro et al. (1997) and Ambraseys et al. (1996) GMPEs in a GMPE logic tree<sup>6</sup>. These GMPEs are over two decades old, with many advancements in GMPE development having been accomplished since their publication. Furthermore, over 20 years of additional North Sea ground-motions have been recorded<sup>7</sup> since the Bungum et al. (2000) study. Therefore, a viable way of improving North Sea PSHA is to develop a new GMPE for the region (Chapters 3 – 4).

North Sea seismic hazard can also be better estimated through the improvement of other aspects of PSHA. For example, the existing GMPE logic trees for regions with seismicity similar to the North Sea can be considered (Chapter 6), and the seismogenic source model can be reassessed in light of new data (Chapter 7). The seismic hazard estimates computed using an updated North Sea PSHA formulation can then be used to reassess the corresponding seismic risk for critical infrastructure in the region (Chapter 8). Before North Sea PSHA is reassessed, basic overviews are provided of (1) seismicity in the region (Chapter 2), and (2) the processing of ground-motion records (Chapter 3).

---

<sup>6</sup> See Appendix B for more details on GMPEs and Chapter 6 for more details on GMPE logic trees.

<sup>7</sup> See Chapter 3 for an overview of ground-motion records and the processing of them to characterise seismic hazard.

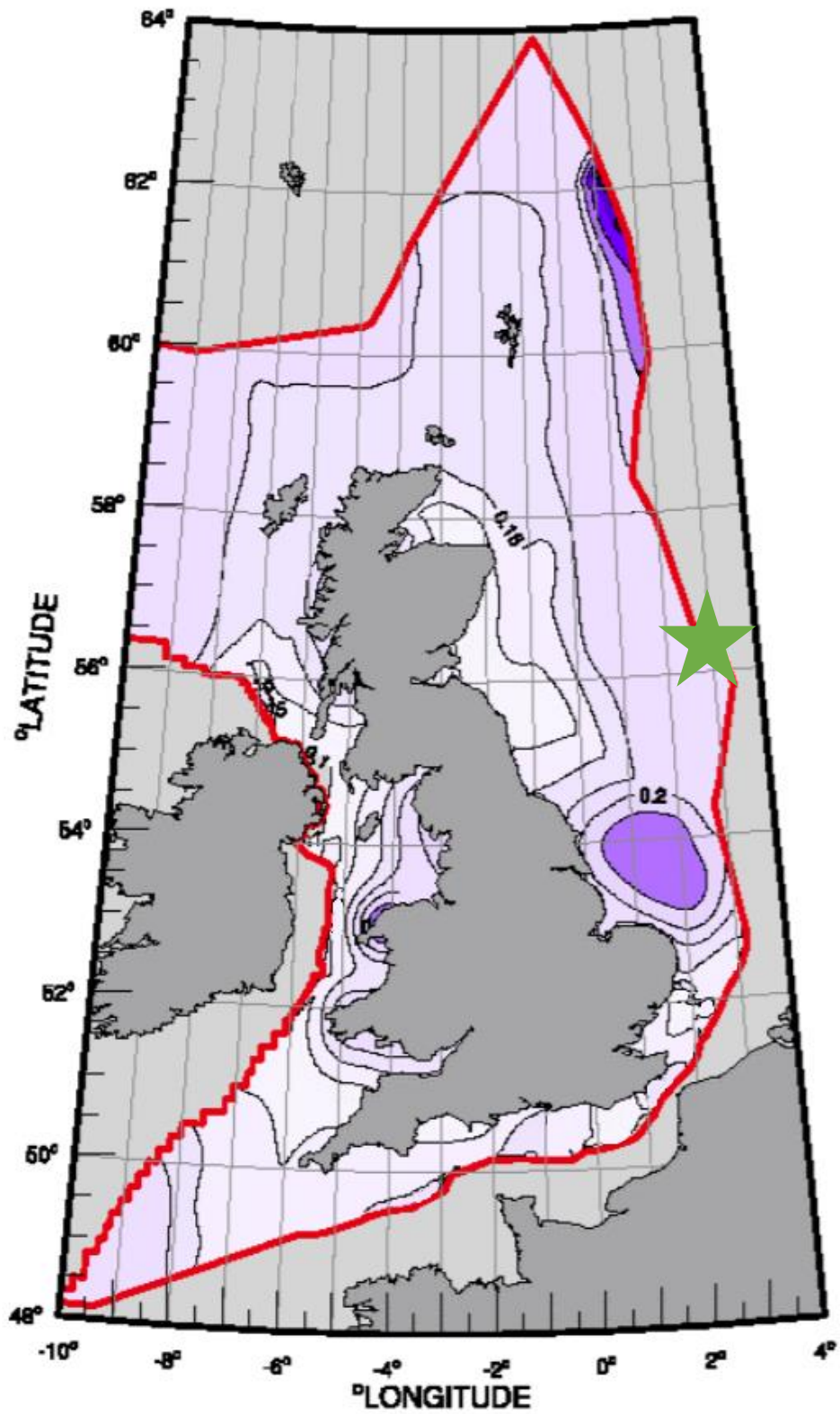


**Figure 1.4** Final composite map produced through appraisal of past UKCS seismic hazard efforts. PGA is in g. Ekofisk earthquake epicentre marked approximately with green star. Return period = 1,000 years. Adapted from Mallard et al., 2003.

## 2.0 North Sea Seismicity

The following chapter provides a brief overview of (1) natural seismicity in the North Sea, (2) induced seismicity in the North Sea and (3) a simple statistical assessment of the likelihood of future induced earthquakes in the region.

### 2.1 Natural Seismicity in the North Sea

The North Sea is not close to any major tectonic plate boundaries and thus is considered an intraplate region of the Eurasian plate (i.e. it is situated upon a passive continental margin). As a result of this, natural (tectonic) seismicity throughout the region is relatively modest (although still significant) compared to other areas in the world (Ritsema and Gürpınar, 1983). The first earthquake of which observations are available within the North Sea was the 23 April 1449 earthquake within the southern extent of the region, proximal to the Belgium coast, having been felt definitely by the population of Canterbury (Musson, 2008). The distribution of natural seismicity in the North Sea is reasonably well defined by the areal extents of the United Kingdom and Norwegian national economic sectors (Fig. 2.0). The offshore earthquakes are considerably concentrated to the immediate west of the rifted passive continental margin of central Norway and the northern apex of the Viking Graben (Fig. 2.0; Bungum et al., 2000). Despite the limited monitoring of North Sea seismicity, this tight earthquake distribution (especially west of Norway) is suggestive of the North Sea natural seismicity being elevated in comparison to the surrounding areas (Ritsema and Gürpınar, 1983). Additionally, whilst the natural seismicity of the North Sea is generally regarded as moderate, there have been several larger earthquakes observed historically, including the 1927 Viking Graben earthquake of local magnitude ( $M_L$ ) 5.3 and the 1931 Dogger Bank earthquake of  $M_L$  6.1. Further to this, there is a lack of evidence to suggest a larger (although unlikely to occur) natural earthquake (e.g.  $M_L \sim 7.0$ ) can be ruled out in the future (Ritsema and Gürpınar, 1983).

It should be noted that our knowledge of seismicity in the North Sea is potentially influenced by the detection threshold (minimum detectable magnitude) for earthquakes in the region. The detection threshold of a network is determined by station distribution, background noise and instrument sensitivity (Ford et al., 1987). Additionally, in areas of the United Kingdom where monitoring is not continuous, such as the Scottish Highlands, the detection capabilities are dependent on the population density, as local inhabitants notice and subsequently report smaller earthquakes to the British Geological Survey (BGS) (Ford et al., 1987). The influence of this detection threshold is evident from the BGS earthquake catalogue's bulletins. From 1967 to 1978, a single  $M_L \leq 2.5$  earthquake ( $M_L$  1.8 in 1977) was detected in the North Sea (Burton and Neilson, 1980), whereas in 2017 alone 6  $M_L \leq 2.5$  earthquakes were detected (Ford, 2018). Consequently, it is clear that the North Sea earthquake catalogue is significantly influenced by detection threshold, and therefore annual rates of seismicity in past years are likely higher than those suggested by the corresponding BGS bulletins.

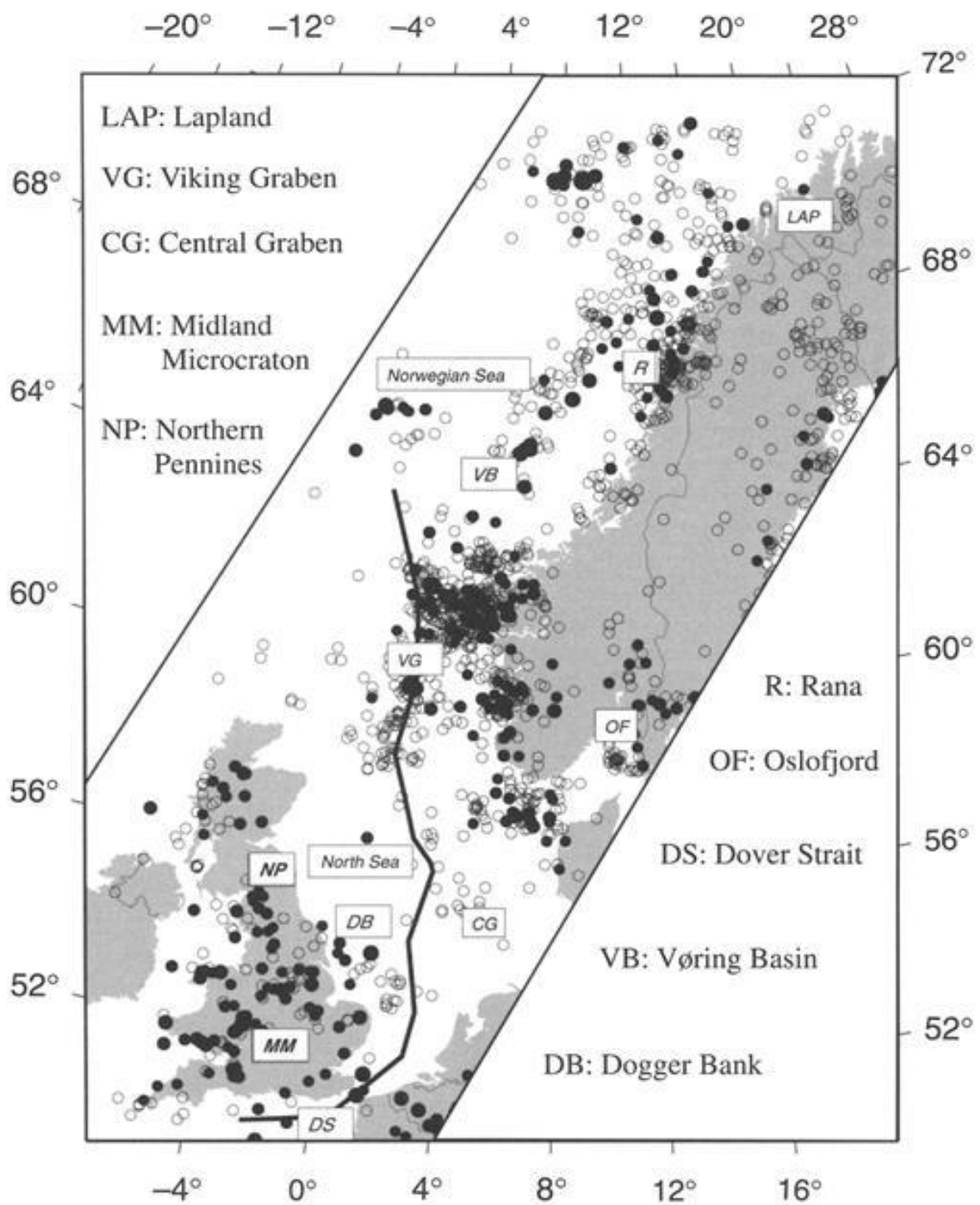


**Figure 2.0** *Seismicity of Norway and Britain and the adjoining offshore areas.* Earthquakes with magnitudes below 4.0 are marked with open circles. The thick line indicates the national (economic) sector line. Taken from Bungum et al. (2000).

## 2.2 Induced Seismicity in the North Sea

The determined engineering significance of the 2001 Ekofisk earthquake for oil and gas platforms in the North Sea (Ottemöller et al., 2005) is a key driving factor for the reassessment of PSHA in the region. Therefore, it is useful to provide overviews of the most prominent examples of induced seismicity in the North Sea. Overviews are also provided for geologically similar regions which are also in northwestern Europe: (1) the Groningen natural gas field of the Netherlands and (2) the natural gas reservoirs of northern Germany (Fig. 2.1). The geomechanical mechanisms associated with hydrocarbon induced seismicity are described in more detail in Appendix D.

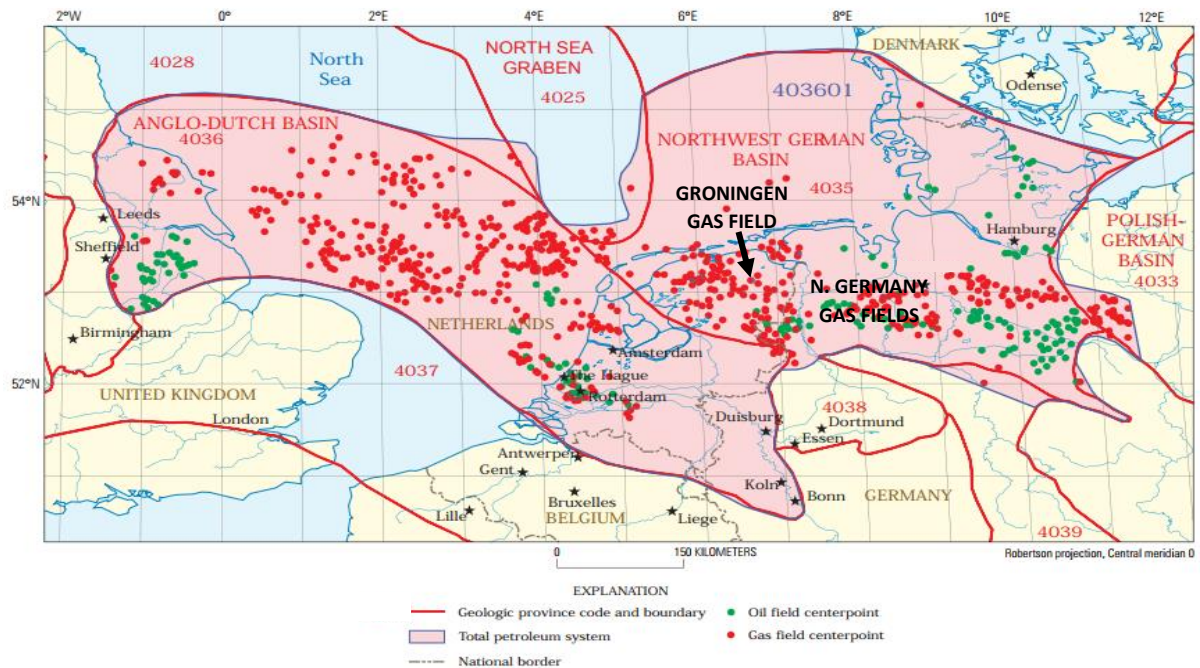


**Figure 2.1** Geographical locations of north-western Europe oil and gas fields. The Anglo-Dutch Basin and Northwest German Basin are sub-basins of the Southern Permian Basin. Adapted from Gautier (2003).

### 2.2.1 The 2001 Ekofisk Earthquake

The 7 May 2001 earthquake within the Ekofisk field (Fig. 2.2) is the most prominent observed case of induced seismicity in the North Sea. A comprehensive investigation of the 2001 Ekofisk event was undertaken by Ottemöller et al. (2005). They concluded that the local magnitude ( $M_L$ ) 4.2, shallow depth ( $\leq 3$  km) Ekofisk event resulted from unintentional water injection into the overburden.

The Ekofisk field was discovered in 1969, with production subsequently starting in July 1971. By the end of 2004 approximately  $17.2 \times 10^6$  m<sup>3</sup> oil and  $2.7 \times 10^6$  m<sup>3</sup> gas had been produced from the field, with such production aided by substantial fluid (gas and water) injection. In addition to fluid injection as a means of secondary recovery, injection of water to counteract field-wide subsidence through repressurisation was initiated in 1987. Reservoir depletion by fluid extraction can result in reduced pore pressures, and thus increased effective normal stresses acting upon the reservoir, resulting in differential compaction of the reservoir which is observed as subsidence (Segall, 1985).

In addition to these instances of controlled water injection, unintentional water injection was discovered following the discovery of elevated pressures in the overburden, which were detected during investigation by ConocoPhillips into possible production performance issues resulting from the Ekofisk earthquake (Ottemöller et al. (2005)). This investigation found that a water injector on the north-eastern flank of the field was injecting 2385 m<sup>3</sup>/d of cold water into the Ekofisk reservoir overburden. This unintentional water injection was responsible for the abnormally high pressures within the overburden observed close to the water injector. Furthermore, the position of the water injector matched where uplift was observed in the north-east periphery of the field, as revealed by the differential bathymetric data (Fig. 2.3). The correlation between the location of uplift, the abnormally high overburden pressures and the proximity of the injection site suggests that the unintentional water injection resulted in hydraulic jacking up of the Ekofisk overburden. The pressure of the injected water was greater than the minimum horizontal stress of the Ekofisk overburden, resulting in the weakening of the uplifted area of the overburden. Considering (1) the over-pressurised zone of uplift (Fig. 2.3) was weakened horizontally and (2) the plausibility of a Coulomb type failure criterion for fluid injection related seismicity, seismic slip was likely first generated in the north-western flank of the overburden (Ottemöller et al., 2005). No seismic events of considerable magnitude had previously occurred in association with the Ekofisk overburden. Therefore, Ottemöller et al. (2005) proposed that without the unintentional water injection into the overburden, the 2001 Ekofisk earthquake would not have occurred.

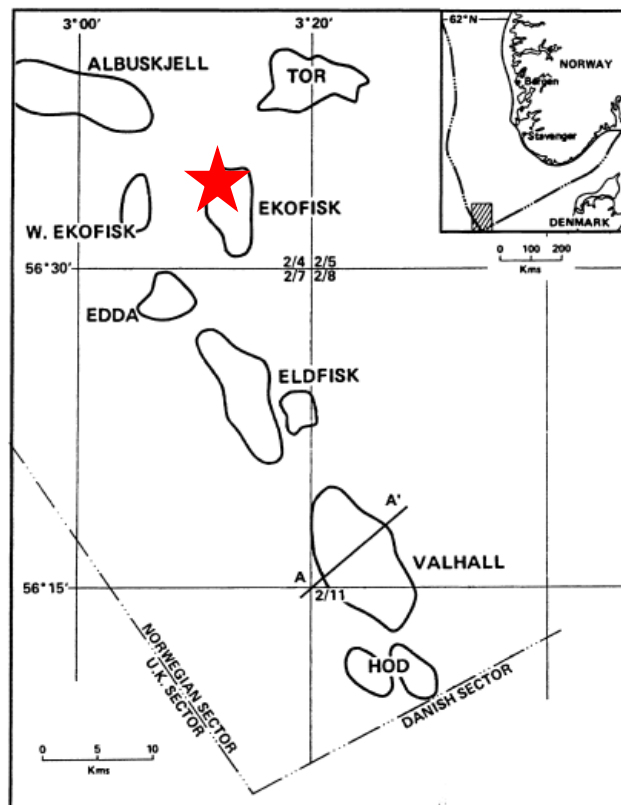


**Figure 2.2** Map showing locations of the Ekofisk and Valhall fields. Red star is the location of the Ekofisk earthquake. Adapted from Ottemöller et al. (2005).

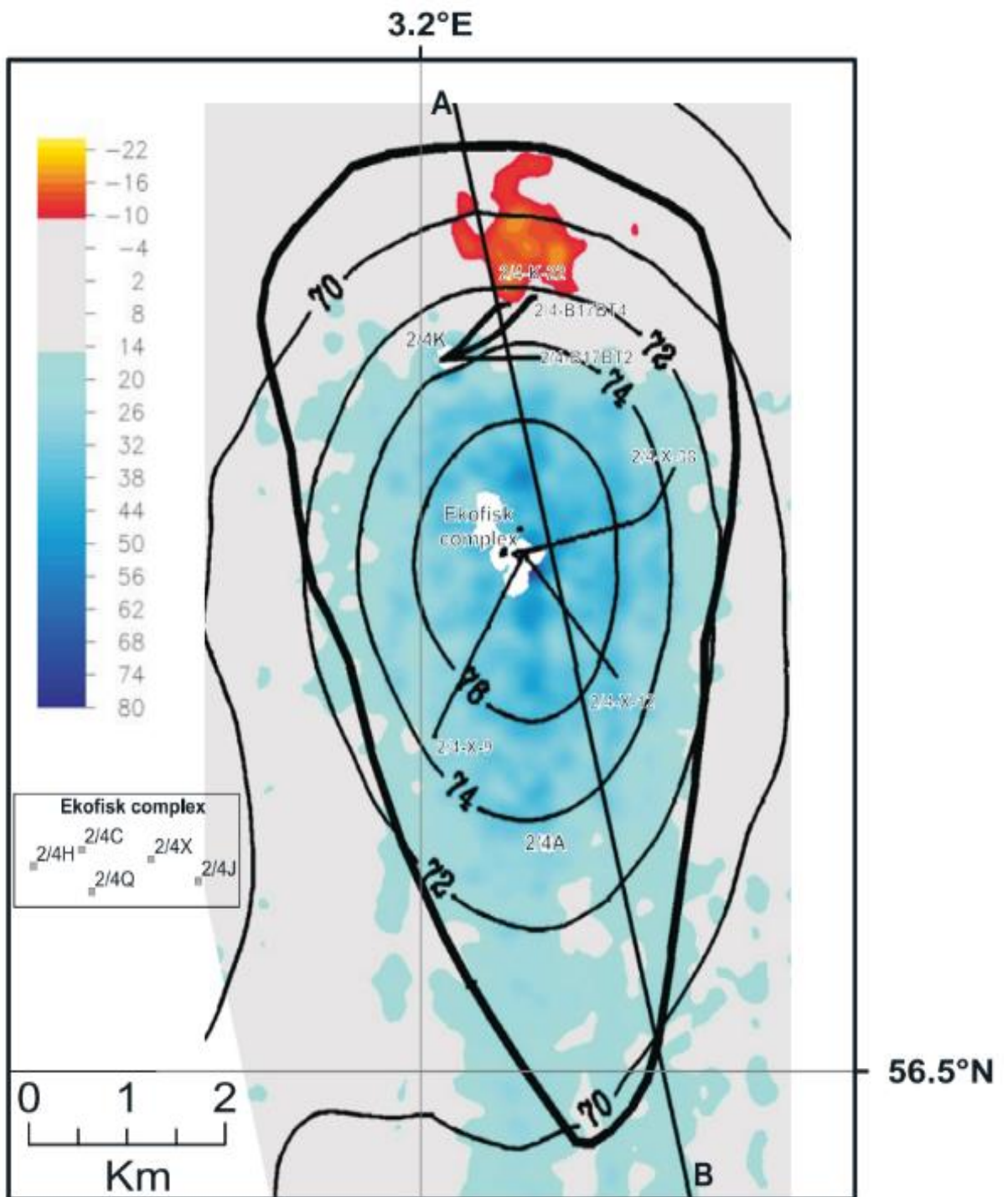


**Figure 2.3** Differential bathymetry data for the Ekofisk field. The total subsidence as of 2001 is shown in decimetres by the black contour lines. The blue shaded areas indicate the regions of positive subsidence (compaction). The red shaded areas indicate regions of negative subsidence (uplift). Surface projections of the producing wells are indicated by the thin black lines. Additionally, the platform locations for the Ekofisk complex are plotted on the inset map. Taken from Ottemöller et al. (2005).

### 2.2.2 The Valhall Field

Alongside the Ekofisk field, investigation has been undertaken into the impact of hydrocarbon production on stress changes and potentially associated seismicity within the Valhall field (Fig. 2.1).

Unlike within the Ekofisk field, no moderate (or larger) size earthquakes have been detected, however seismic monitoring over a period of 57 days in 2000 recorded 572 micro-seismic ( $M_L < 2$ ) events (Kristiansen et al., 2000). Since production started in 1982, 28 of the 102 production well casings within the field have experienced tubular deformation (Kristiansen et al., 2002; Suckale, 2009). The majority (~60%) of such deformations took place within the Valhall reservoir overburden (Kristiansen et al., 2002). Additionally, from June 1 1998 to July 27 1998, 328 micro-seismic events were recorded by a seismic array operating within the Valhall field, and were located to have occurred predominantly above the reservoir (Fig. 2.4). These spatial correlations are supportive of hydrocarbon production resulting in reservoir compaction, and thus perturbing the stress field in the overburden due to poroelastic effects. Zoback and Zinke (2002) demonstrated that the increase in horizontal compressive stresses (~0.2 MPa) above the Valhall reservoir in response to hydrocarbon production contributed only 1% of the associated reduction in compressive horizontal stresses (~20 MPa) within the reservoir. This increase in horizontal compressive stresses within the overburden potentially induced reverse faulting above the reservoir, inducing the observed micro-earthquakes (Segall, 1989).

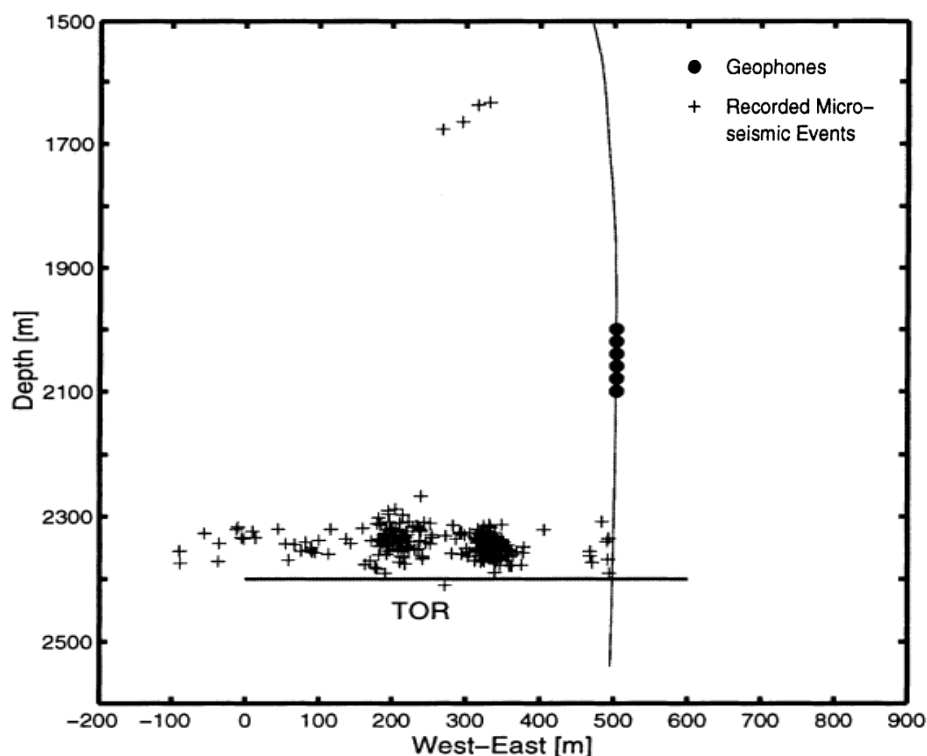


**Figure 2.4** Vertical section showing locations of 328 micro-earthquakes detected by the seismic array operational in the Valhall field between June 1 and July 27, 1998. The thin black line represents well path. The thick black line represents the boundary between the overburden and the overlying reservoir. Tor refers to the Tor formation within which the Valhall reservoir is located (rather than the Tor field shown in Fig. 2.2). Taken from Zoback and Zinke (2002).

### 2.2.3 Northwestern Europe

The most prominent hydrocarbon production related induced seismicity in northwestern Europe has occurred in the Groningen natural gas field of the Netherlands (Fig. 2.1). The Groningen natural gas field is estimated to have had 75% of the gas reserves initially in place produced as of January 2015 (Van Thienen-Visser and Breunese, 2015). As of January 2016, 271 earthquakes of  $M_L$  1.5 or greater had been observed (Coppersmith, 2016), the first of which was 28 years after production started in the previously aseismic Groningen field (van Eck et al., 2006). The largest observed earthquake so far was the 2012  $M_L$  3.6 Huizinge earthquake (Coppersmith, 2016). The earthquakes of the Groningen natural gas field are induced by reservoir compaction, itself a result of gas production (van Eck et al., 2006; van Thienen-Visser and Breunese, 2015). Gas production inducing these earthquakes is supported by (1) the observed correlation between production and the delayed onset of earthquakes in the region (Fig. 2.5) and (2) the average focal depth of the 179 earthquakes being only 2.5 km, which correlates with the average Groningen reservoir depth (van Eck et al., 2006).

In addition to the Groningen field of the Netherlands, there has also been induced seismicity associated with hydrocarbon production observed in northern Germany. The natural gas reservoirs of both the northern Netherlands (including the Groningen field) and northern Germany (in addition to the southern North Sea) are located within the Rotliegend (sandstone) formation of the Southern Permian Basin (Dahm et al., 2007). Northern Germany, similarly to the Groningen field is largely considered aseismic, with tectonic earthquakes being sparse and isolated (Dahm et al., 2007; Plenefisch et al., 2014). Despite this low seismic activity, 35 earthquakes ( $M_L$  1.9 – 4.5) were observed from 1976 to 2013 (Plenefisch et al., 2014). These earthquakes are considered as induced, firstly due to their close proximity to one another, and secondly due to having occurred following the onset of gas production in the region (Plenefisch et al., 2014).

The seismic hazard presented by induced earthquakes in both the Groningen field and northern Germany have been investigated in previous studies. For the Groningen field, the ground-shaking resulting from induced earthquakes has been estimated to be capable of approaching a peak ground acceleration (PGA) of 0.25 g over a 100 year return period (van Eck et al., 2006). However, despite only non-structural damage having been observed so far in Groningen from these earthquakes, a PGA above 0.1 g is capable of causing moderate structural damage to engineered structures, and hence the seismic hazard presented by the induced seismicity within the Groningen field is significant (van Eck et al., 2006; Stevenson, 2003). For northern Germany, limited studies on the seismic hazard presented by induced earthquakes in the region have been undertaken, although Gestermann et al. (2015) note that the observation of an  $M_L$  4.5 earthquake despite the low background seismicity means further study of the seismic hazard presented by induced earthquakes in northern Germany is necessary. The significance of the seismic hazard to local infrastructure within both the Groningen field and northern Germany is therefore further justification for the reassessment of North Sea seismic hazard.

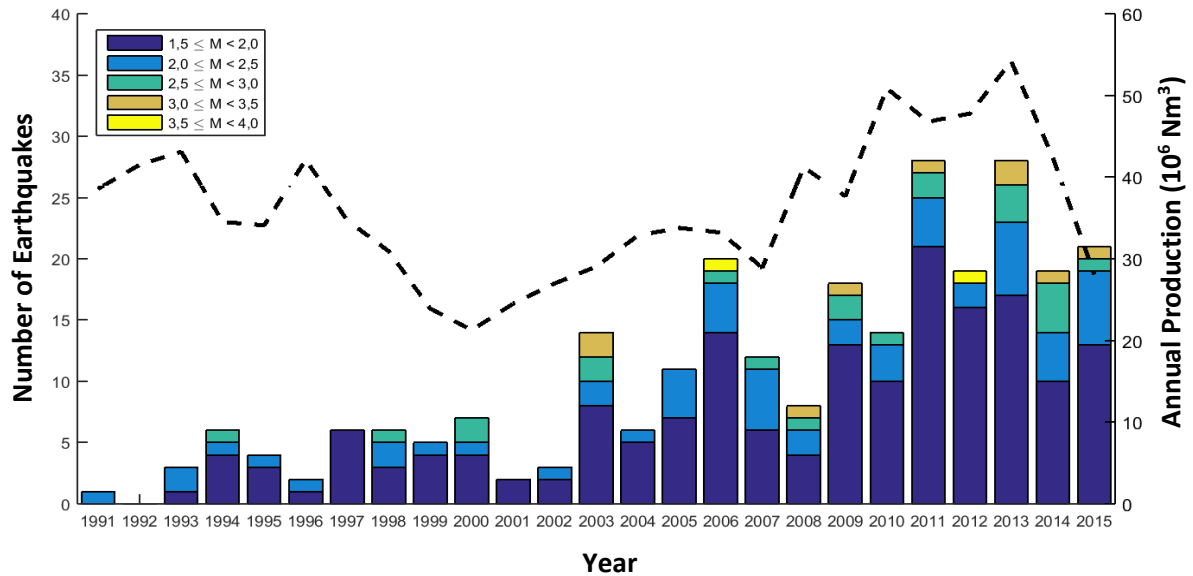


**Figure 2.5** Number of earthquakes per year and volume of hydrocarbons produced per year in the Groningen field. Taken from Nlog.nl (2016).

### 2.3 Are Further Induced Earthquakes Likely in the North Sea?

Although the engineering significance of the 2001 Ekofisk earthquake has led to a renewed interest in re-evaluating North Sea seismic hazard (Ottemöller et al., 2005), the likelihood of further North Sea earthquakes occurring as a result of hydrocarbon production is associated with much uncertainty.

The apparent spatial correlation in the United Kingdom economic sector of the North Sea<sup>8</sup> between the geographical locations of earthquake epicentres and hydrocarbon production points<sup>9</sup> (Fig. 2.6) is potentially suggestive of induced seismicity occurring in the region. This is because the extended production of mature basins has been shown to contribute to the occurrence of induced earthquakes (e.g. Grasso, 1992). This spatial correlation is therefore also potentially indicative of future induced earthquakes occurring if hydrocarbon production ramps up again in the North Sea (Fig. 2.7). However, these hydrocarbon production points are situated close to faults (Fig. 2.6), most likely because faults often act as hydrocarbon migration pathways (Pang et al., 2003). Consequently, this spatial correlation is more likely between the faults and the earthquakes, rather than the earthquake epicentres and the hydrocarbon production points. This is further supported by the lack of a correlation between the volume of hydrocarbons produced per annum and the corresponding number of earthquakes observed per annum (Fig. 2.7; Fig. 2.8; Fig. 2.9). Therefore, the apparent spatial correlation between the geographical locations of earthquake epicentres and hydrocarbon production points is likely not indicative of future induced earthquakes occurring in the North Sea region.

<sup>8</sup> Only the spatial correlation between earthquakes and hydrocarbon field production points in the United Kingdom economic sector of the North Sea is considered here. Earthquakes originating in the Norwegian economic sector are not considered here because hydrocarbon field production point data is not readily-available for this sector.

<sup>9</sup> Hydrocarbon field production points are used as proxies for hydrocarbon reservoir locations. This data was readily available from the Oil and Gas Authority's open access database (see [Data-ogauthority.opendata.arcgis.com](http://Data-ogauthority.opendata.arcgis.com), 2020).

As discussed above, a correlation between the occurrence of earthquakes and hydrocarbon production is observed within both the Groningen natural gas field of the Netherlands and Northern Germany. However, in both cases there is a significant delay between the onset of hydrocarbon production, and the first occurrence of induced earthquakes (van Eck et al., 2006; Gestermann et al., 2015). For the Groningen field, seismicity was first observed 28 years after production began (van Eck et al., 2006). In northern Germany, seismicity was first observed 20 years after production began (Gestermann et al., 2015). For both the Groningen field and northern Germany, this delay is attributed to reservoir pressure depletion, which over time results in reservoir compaction, leading to seismic slip which generates (induced) earthquakes (Gestermann et al., 2015; van Thienen-Visser and Breunese, 2015). Alongside time-dependent compaction, van Thienen-Visser et al. (2016) suggest that the creep of surrounding rocks and delayed pressure diffusion are factors which could influence the stress redistribution within the Groningen field, and therefore also the observed delay in seismicity. Consequently, such factors could also be responsible for the contrast in delay periods for the first occurrence of anthropogenic earthquakes following the onset of production within both the Groningen field and Northern Germany's gas fields, as well as between hydrocarbon fields in general.

A delay in the occurrence of induced seismicity following hydrocarbon production could also be present within the North Sea, but as of yet this delay period is not easily identifiable (e.g. Fig. 2.7). Commercial offshore hydrocarbon production in the North Sea began in 1967 (Oil and Gas UK, 2012), but unlike the Groningen field or northern Germany, the North Sea was not an aseismic region prior to the onset of this hydrocarbon production (Ritsema and Gürpınar, 1983). The North Sea not being a naturally aseismic region therefore makes it difficult to determine if a delay period occurred between the onset of hydrocarbon production and the first occurrence of North Sea induced seismicity, or any other potential correlation between hydrocarbon production and the frequency of induced North Sea earthquakes. Additionally, significant amounts of oil are produced in the North Sea whereas in the Groningen field and northern Germany only gas is produced, which could also contribute to a less clear delay period being identifiable due to causing temporal differences in geo-mechanical processes. Further still, the mechanism for induced seismicity within both the Groningen field and northern Germany is known to be fluid extraction, whereas for the North Sea, other mechanisms such as fluid injection (Ekofisk) are in play (Ottemöller et al., 2005). A further complication in the identification of (1) a delay in the onset of seismicity and (2) a correlation between production and induced earthquake frequency is that the extent of seismic monitoring within the North Sea has varied significantly throughout time, and thus so has the detection threshold (personal correspondence with Dr. Brian J. Baptie, Team Leader of the BGS Earthquake Seismology Team). Therefore, the number of earthquakes per year is likely influenced by this (e.g. there was probably more  $M_L$  2 – 3 earthquakes for 1978 – 1980 than suggested by Fig. 2.7).

Currently there seems to be no correlation between North Sea hydrocarbon production and the occurrence of earthquakes. However, there have likely been induced earthquakes in the North Sea prior to the 2001 Ekofisk earthquake. If so, these earlier induced earthquakes could have potentially already been accounted for within prior North Sea PSHAs. The 2001 Ekofisk earthquake was the first induced North Sea earthquake to be considered of engineering significance to oil and gas infrastructure in the region (see above). The 2001 Ekofisk earthquake could potentially be indicative of the characteristics of induced seismicity within the region beginning to alter to more frequently being of engineering significance (i.e. moderate size earthquakes with shallow focal depths) due to dramatic stress perturbations within the maturing reservoirs occurring as production continues in the region (e.g. Noreng, 1980; Kemp, 2005; Suckale, 2009). Therefore, whilst previous North Sea PSHAs have potentially accounted for induced earthquakes prior to the 2001 Ekofisk earthquake, consideration of the potentially evolving nature of induced earthquakes in the region (i.e. post-Ekofisk earthquakes) could be critical to the survivability of offshore North Sea infrastructure in the future.

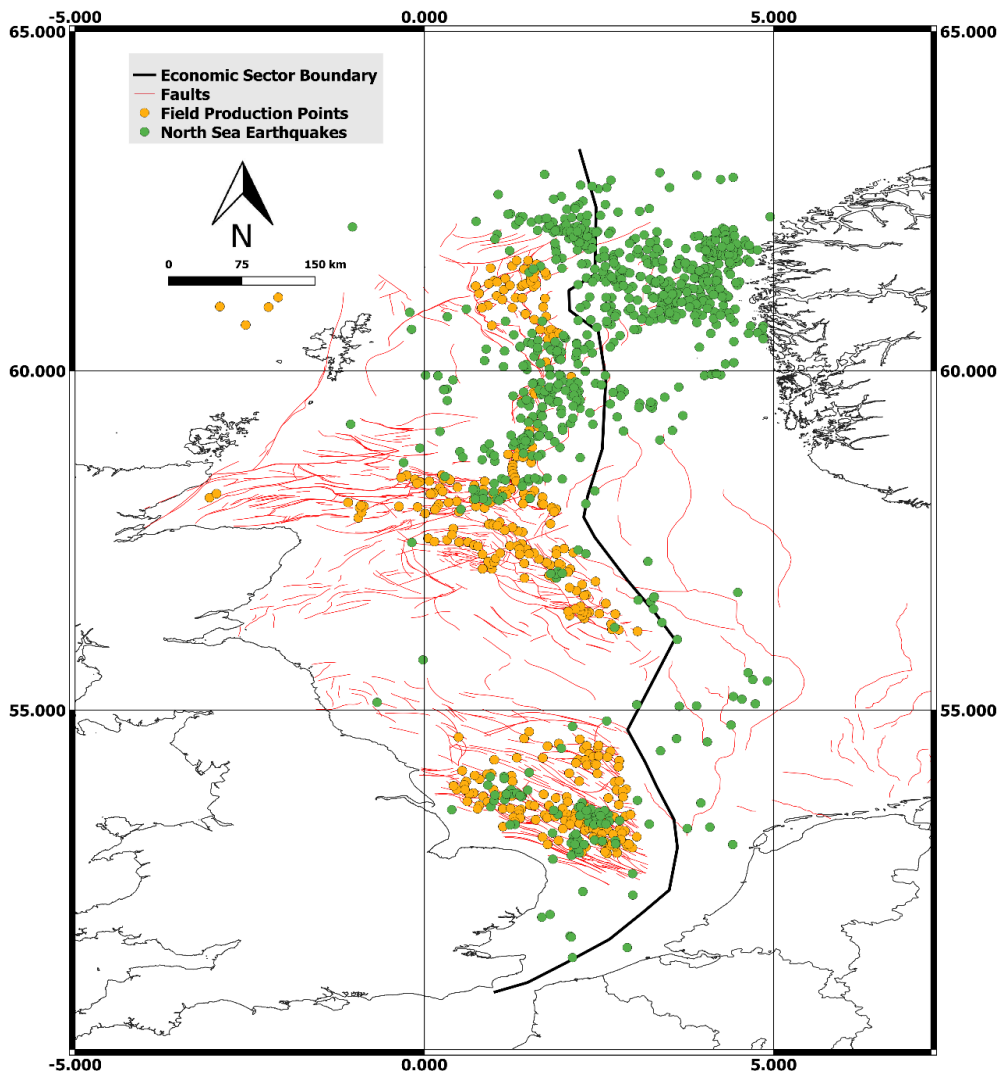


**Figure 2.6** Map illustrating the spatial distribution of earthquake focal depths, hydrocarbon fields and faults in the United Kingdom economic sector of the North Sea. Fault data obtained from Europe-geology.eu. (2019).

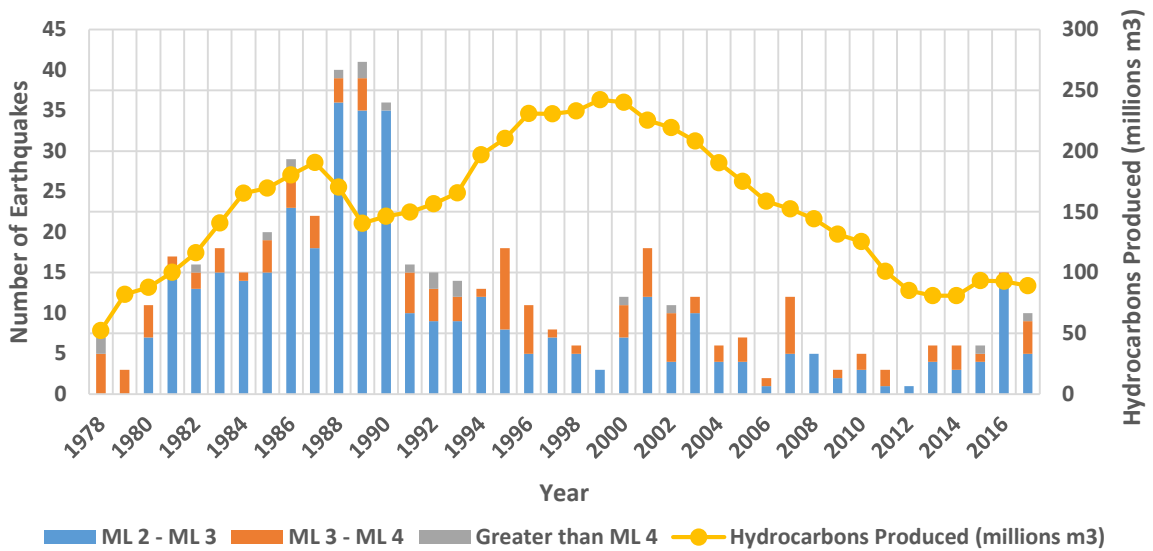


**Figure 2.7** Number of earthquakes per year and volume of hydrocarbons produced per year in the North Sea. Earthquakes per year data is from the BGS Earthquake Catalogue (Earthquakes.bgs.ac.uk, 2020a). Volumes of hydrocarbons produced per year data is from the Oil and Gas Authority Open Data (Data-authority.opendata.arcgis.com, 2020).

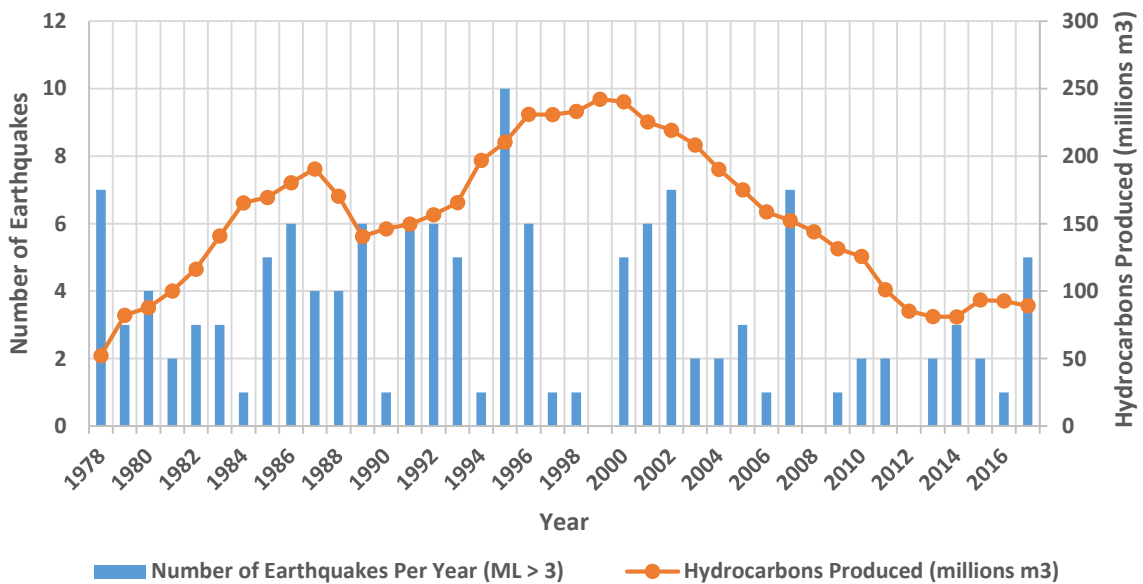


**Figure 2.8** Number of earthquakes per year ( $M_L \geq 3$ ) and volume of hydrocarbons produced per year in the North Sea. Earthquakes per year data is from the BGS Earthquake Catalogue (Earthquakes.bgs.ac.uk, 2020a). Volumes of oil produced per year data is from the Oil and Gas Authority Open Data (Data-authority.opendata.arcgis.com, 2020).

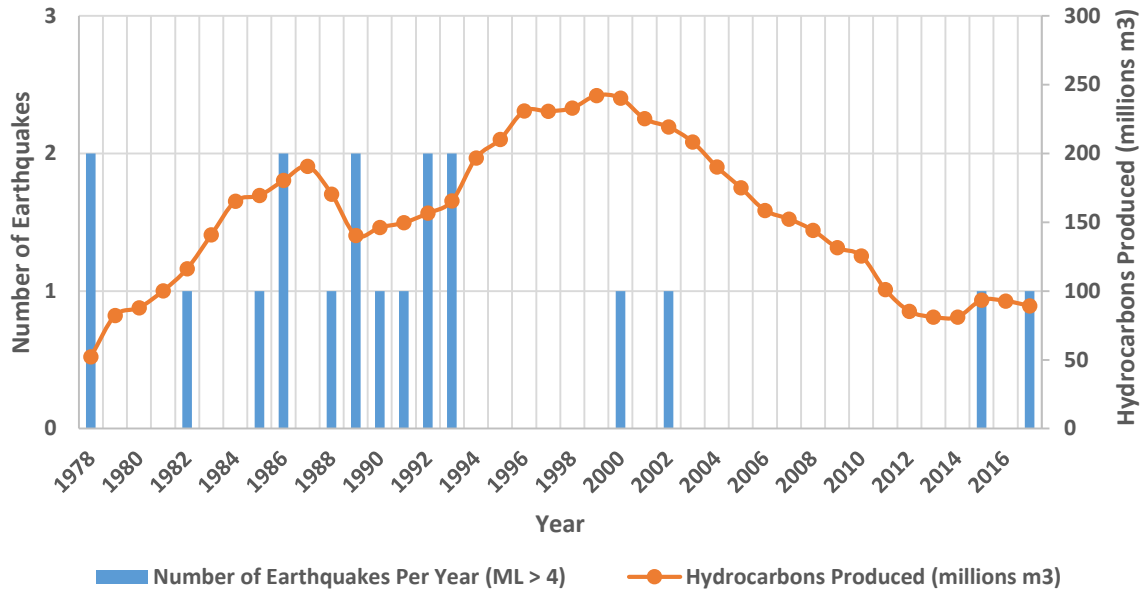


**Figure 2.9** Number of earthquakes per year ( $M_L \geq 4$ ) and volume of hydrocarbon produced per year in the North Sea. Earthquakes per year data is from the BGS Earthquake Catalogue (Earthquakes.bgs.ac.uk, 2020a). Volume of hydrocarbons produced per year data is from the Oil and Gas Authority Open Data (Data-ogauthority.opendata.arcgis.com, 2020).

## 2.4 Conclusions for North Sea Seismicity Summary

The natural seismicity in the North Sea is small to moderate in terms of earthquake size. However, future induced earthquakes are likely to occur in the region due to the continued perturbation of reservoirs by hydrocarbon production, and these earthquakes could add to the already moderate seismic hazard presented by tectonic North Sea earthquakes. Furthermore, as discussed in Chapter 1, the most recent North Sea PSHA appraisal (Mallard et al., 2003) has not accounted for the 2001 Ekofisk earthquake. The 2001 Ekofisk earthquake is potentially indicative of the evolution of North Sea induced earthquakes to a greater state of engineering significance in the region. This therefore provides additional impetus for the reassessment of North Sea PSHA, so as to capture the seismic hazard associated with these potentially evolving induced earthquakes.

## 2.5 Characterisation of North Sea and United Kingdom Earthquakes

Despite the seismicity of the North Sea being relatively elevated compared to that of the United Kingdom (Ritsema and Gürpinar, 1983), the limited seismic monitoring of the North Sea has resulted in the region having a significantly less complete earthquake catalogue than the United Kingdom. The more limited seismic monitoring in the North Sea is due to the instruments which record earthquakes generally being located onshore, resulting in offshore earthquakes (e.g. in the North Sea) being more difficult to detect than onshore earthquakes (e.g. in the United Kingdom). However, as time has passed the detection threshold (the minimum detectable magnitude) for earthquakes in the North Sea has improved. For example, from 1967 to 1978, a single earthquake of  $M_L < 2.5$  was detected in the North Sea ( $M_L$  1.8 in 1977 - Burton and Neilson, 1980), whereas in 2017 alone 6 earthquakes of  $M_L \leq 2.5$  were

detected (Ford, 2018). The clear influence of the detection threshold on the North Sea earthquake catalogue means the annual rates of North Sea seismicity in past years are likely higher than those suggested by the corresponding BGS bulletins. Therefore, earthquakes below the magnitude of completeness (the detection threshold magnitude) are not considered when assessing earthquake rates. Considering the seismicity is elevated in the North Sea compared to the neighbouring United Kingdom, the characterisation of potential differences in the earthquakes of these regions is of interest to this investigation, especially with respect to induced seismicity due to the increased interest it is receiving within the seismic hazard assessment community.

The two datasets used within this comparison of North Sea and United Kingdom earthquakes are the BGS earthquake catalogues for these regions respectively (see Earthquakes.bgs.ac.uk (2020a) for access to this database<sup>10</sup>). After separating the database into earthquakes originating in the North Sea and the United Kingdom, further processing comprised of removing earthquakes with (apparent) local magnitudes of 0 and/or focal depths of 0 km. These entries in the earthquake catalogue result from earthquakes in which the depth could not be determined because of a lack of nearby stations, so the focal depth was fixed to 0 km, or alternatively the magnitude could not be determined because of few instruments or high noise levels, and so was also fixed to a local magnitude of 0.

### **2.5.1 Comparison of North Sea and United Kingdom Magnitude Distributions**

Comparison of the Gutenberg-Richter magnitude distributions<sup>11</sup> of North Sea and United Kingdom earthquakes (Fig. 2.10) provides further insight into the seismicity of each region. To mitigate the higher magnitude of completeness in the North Sea and therefore ensure a fair comparison, earthquakes of only  $M_L \geq 2.5$  or greater were used for catalogue completeness.

The North Sea is thought to have a higher rate of seismicity than the United Kingdom (Ritsema and Gürpinar, 1983). At a glance, the magnitude distributions are supportive of the North Sea having a higher rate of seismicity than the United Kingdom. Slightly more earthquakes of  $M_L \geq 2.5$  have occurred in the North Sea compared to the United Kingdom (273 earthquakes vs. 237 earthquakes respectively), with two  $M_L \geq 6.0$  earthquakes having been observed in the North Sea, compared to none within the United Kingdom (Fig. 2.10). However, the  $b$  parameter of a magnitude distribution is representative of the ratio of small earthquakes to large earthquakes, and the North Sea  $b$  parameter is slightly larger than the United Kingdom  $b$  parameter (0.72 vs. 0.64), which supports the North Sea actually having (proportionally) fewer large earthquakes than the adjacent United Kingdom. The  $a$  parameter of a magnitude distribution is indicative of the overall rate of seismicity within a region. The North Sea  $a$  parameter is slightly higher than the United Kingdom  $a$  parameter (4.25 vs. 3.92 respectively), which suggest the North Sea is more seismically active overall than the United Kingdom.

---

<sup>10</sup> This analysis was undertaken in 2019, and therefore more recent data was not available at the time.

<sup>11</sup> See Appendix B for an overview of Gutenberg-Richter magnitude distributions.

As discussed above, comparison of the North Sea and United Kingdom magnitude distributions appears to support the North Sea having a higher rate of seismicity overall than the North Sea due to the  $a$  parameter being larger for the North Sea. However, these  $a$  parameter values do not take into account the considerably smaller geographical area of the United Kingdom ( $\sim 248,352 \text{ km}^2$ ) compared to that of the North Sea ( $\sim 570,000 \text{ km}^2$ ). Therefore, a more appropriate comparison is undertaken by normalising the  $a$  parameter of each region (the  $b$  parameter of each region inherently cannot be normalised due to being a ratio). To compute the normalised  $a$  parameter for each region (Tab. 2.0) one plots a modified form of the Gutenberg-Richter distribution equation (Fig. 2.11):

$$\log_{10}\left(\frac{N}{A_r}\right) = a - b(M_L) \quad (3.0)$$

Where  $N$  is the earthquake count,  $M_L$  is the corresponding local magnitude and  $A_r$  is the geographical area ( $\text{km}^2$ ) of the region being considered. The North Sea's normalised  $a$  parameter is slightly smaller than the United Kingdom's  $a$  parameter (Fig. 2.11; Tab. 2.0), suggesting the North Sea is less seismically active than the United Kingdom when the geographical area of each region is considered.

Ultimately, the magnitude distributions enable a brief yet effective characterisation of the differences in the magnitudes of earthquakes originating in the North Sea and the United Kingdom. Analysis of the distributions (Fig. 2.10; Fig. 2.11; Tab. 2.0) indicate that earthquakes of larger maximum magnitudes can (probably) occur in the North Sea, but that the overall rate of seismicity is greater in the United Kingdom than the North Sea, and that a greater proportion of earthquakes are classified as large seismic events than small seismic events in the United Kingdom than in the North Sea.

**Table 2.0** Normalised  $a$  and  $b$  parameters for the North Sea and United Kingdom ( $M_L \geq 2.5$ ) earthquakes.

Region	Area ( $\text{km}^2$ )	# Earthquakes	# Earthquakes per $\text{km}^2$	a value	b value	Normalised a value
N. Sea	570,000	273	4.79E-04	4.25	0.72	-1.51
UK	248,352	237	9.54E-04	3.92	0.64	-1.47

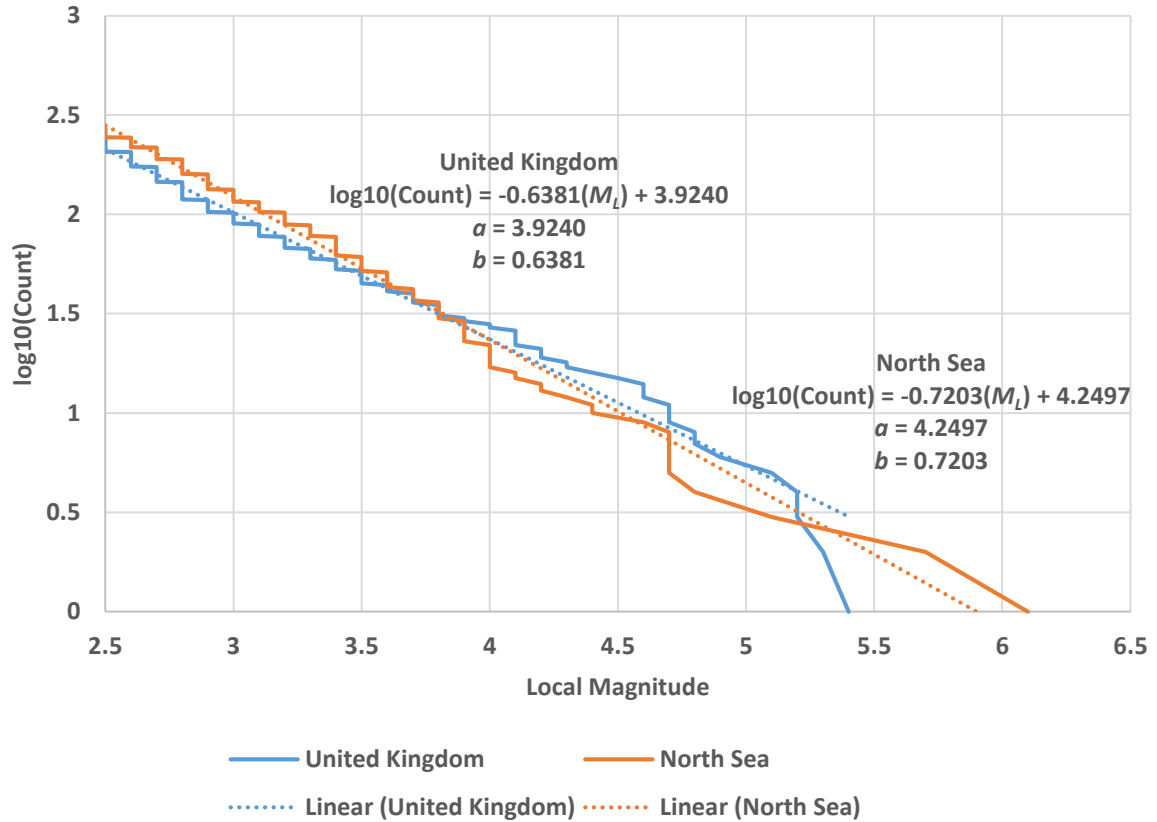


**Figure 2.10** North Sea and United Kingdom ( $M_L \geq 2.5$ ) Gutenberg-Richter Distributions.

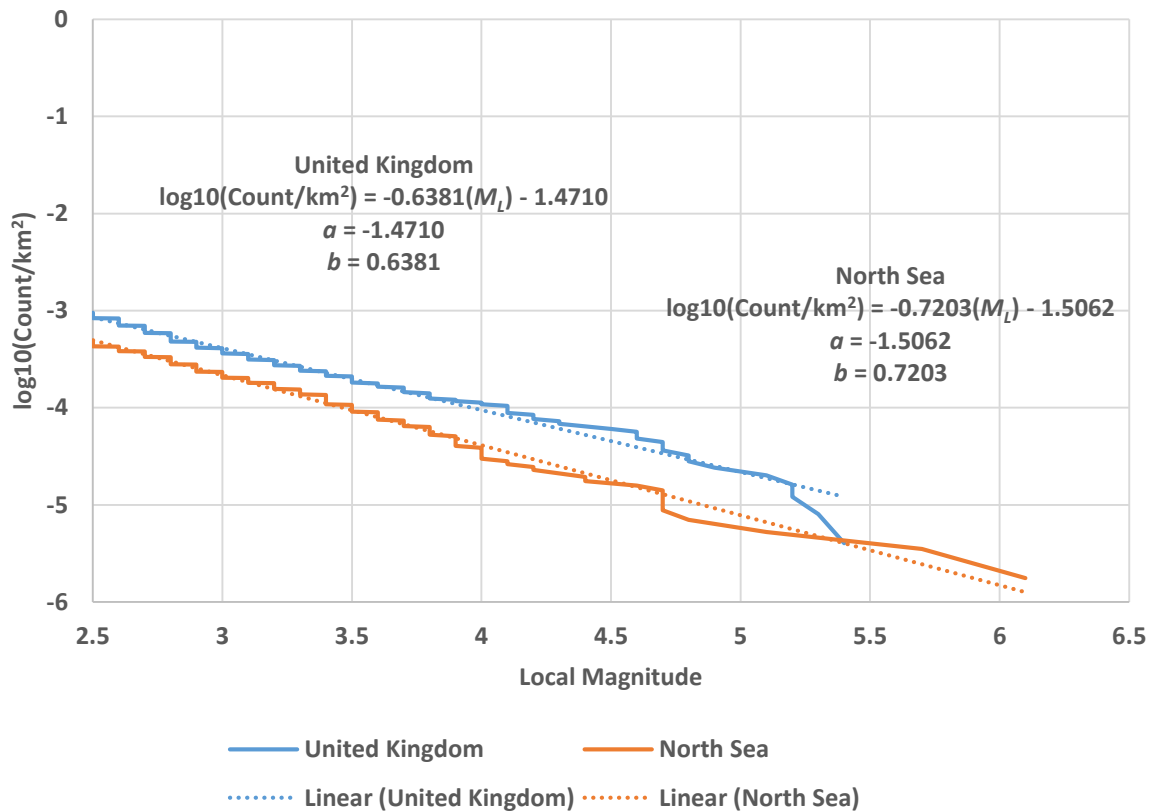


**Figure 2.11** Normalised North Sea and United Kingdom ( $M_L \geq 2.5$ ) Gutenberg-Richter Distributions.

## 2.5.2 Comparison of North Sea and United Kingdom Earthquake Focal Depths

Statistical analysis of the focal depths of earthquakes originating in the North Sea and the United Kingdom can provide great insight into the respective natures of seismic events in these regions. In a hydrocarbon production context, a shallow ( $\sim < 5$  km) focal depth is indicative of an earthquake being anthropogenic in origin (e.g. Grasso, 1992; Suckale, 2009). This is because it suggests the earthquake's focal mechanism is associated with production induced stress changes at (or surrounding) hydrocarbon reservoir level, as observed in the case of the 2001  $M_L$  4.2 Ekofisk earthquake, which occurred at a focal depth of less than 3 km (Ottemöller et al., 2005).

In the context of this investigation, the most obvious contrast between the raw North Sea and United Kingdom focal depth distributions (Fig. 2.12 vs Fig. 2.13 respectively) is the greater number of earthquakes with a focal depth of less than 5 km in the United Kingdom than the North Sea (2995 earthquakes vs. 166 earthquakes respectively). However, considering the higher magnitude of completeness in the North Sea compared to the United Kingdom, comparison of focal depths has only been undertaken for earthquakes with magnitudes of greater than  $M_L$  2.5 (Fig. 2.14; Fig. 2.15). Therefore, the ratios (Fig. 2.14; Fig. 2.15), rather than the frequencies for the specified focal depth bins are a more appropriate parameter for comparison of focal depths between the two regions. There is a considerable contrast in the proportions of earthquakes which occurred at a depth of less than 5 km within the United Kingdom compared to within the North Sea ( $\sim 38\%$  vs.  $\sim 18\%$  respectively). This observation is intriguing considering the potential spatial correlation between North Sea earthquake epicentres and hydrocarbon field production point locations<sup>12</sup> within the United Kingdom economic sector (UKES)<sup>13</sup> of the North Sea (Fig. 2.6). This correlation could suggest a moderate amount of production related seismicity occurs within the North Sea, and so the ratios observed here are interesting as they suggest otherwise. However, as discussed above in section 2.3, these production points are situated proximal to faults (Fig. 2.6), likely due to faults often acting as hydrocarbon migration pathways (e.g. Pang et al., 2003), and therefore the spatial correlation is more likely between the faults and the earthquake epicentres, rather than the earthquake epicentres and the nearby hydrocarbon production. This spatial correlation being between earthquake epicentres and faults rather than earthquake epicentres and production points is also supported by the North Sea focal depth distribution. Furthermore, one is assuming the spatial correlation observed within the UKES is also representative of the spatial distribution between earthquake epicentres and production points in the Norwegian economic sector (NES). Consequently, it is highly tenuous to assume induced seismicity should be prominent in the North Sea based on this apparent spatial correlation between earthquake epicentres

---

<sup>12</sup> Hydrocarbon field production points are used as proxies for hydrocarbon reservoir locations. This data was readily available from the Oil and Gas Authority's open access database (see [Data-ogauthority.opendata.arcgis.com](https://data-ogauthority.opendata.arcgis.com), 2020).

<sup>13</sup> Only the spatial correlation between earthquakes and hydrocarbon field production points in the UKES of the North Sea is considered here. Earthquakes originating in the NES are not considered here because hydrocarbon field production point data is not (currently) available for this sector.

and zones of hydrocarbon production alone. Regardless, it is surprising how much the proportions of earthquakes with focal depths less than 5 km contrast between the North Sea and the United Kingdom.

As discussed above, the apparent spatial correlation between hydrocarbon production and nearby earthquakes alone is a tenuous indicator of the presence of induced earthquakes in the North Sea. However, because induced earthquakes associated with hydrocarbon production often occur at shallow focal depths (less than 5 km), the distribution of earthquake focal depths for earthquakes originating close to production points (Fig. 2.16) was considered here as an additional analysis for determining whether induced seismicity is present in the North Sea. Once again, the UKES is assumed to be representative of the entire North Sea region. From Fig. 2.16, it appears that in the northern North Sea there is no readily apparent trend in earthquake focal depths with (horizontal) distance from the hydrocarbon fields. However, within the southern North Sea off the East Anglian coast there appears to be a slight trend, in which focal depths are overall shallower the closer the corresponding earthquake's origin is to a hydrocarbon reservoir. The focal depth distribution for earthquakes occurring proximal to the east Anglian coast (Fig. 2.17) shows a higher proportion of these earthquakes occur at shallow depths (< 5 km) compared to those occurring in the entire North Sea (~ 37% vs. ~ 22% respectively), indicating the potential presence of elevated induced seismicity in the area.

## **2.6 Identification of Potentially Induced North Sea Earthquakes**

To identify a handful of potentially induced earthquakes originating in the UKES of the North Sea an additional spatial analysis was undertaken. The horizontal distances between each earthquake and hydrocarbon field production point were calculated, and then all earthquakes with focal depths greater than 5 km and corresponding horizontal distances greater than 10 km were filtered out. Earthquakes with focal depths greater than 5 km were filtered out because such earthquakes likely did not originate at (or surrounding) reservoir level, and so are unlikely to be the result of hydrocarbon production. Horizontal distances greater than 10 km were filtered out because hydrocarbon production is less likely to induce earthquakes at larger distances (Dahm et al., 2015). The shortest horizontal distance for each remaining earthquake was selected (the nearest production point is likely associated with the hydrocarbon field within which the corresponding earthquake originated in). This spatial analysis resulted in the identification of 27 earthquakes originating in the United Kingdom sector which are potentially of an induced nature (Tab. 2.1; Fig. 2.16).

It should be noted that a high level of uncertainty is associated with the automatic computation of focal depths for shallow earthquakes (Havskov and Ottemöller, 2010), and therefore many earthquakes within the BGS database used in this comparative analysis could in fact occupy say the 5.0 – 10 km focal depth bin, rather than the < 5 km focal depth bin. Therefore, the observations (and subsequent interpretations) of this analysis should be treated with caution due to this. One way of quantifying the uncertainty in the determination of focal depths is the comparison of those determined for the 2001 Ekofisk earthquake.

The focal depth of the 2001 Ekofisk event was determined both by the BGS (automatic procedure) and by Ottemöller et al. (2005) (careful re-evaluation for a specific earthquake). The focal depth determined by the BGS automatic procedure was 1 km, whereas the focal depth determined by Ottemöller et al. (2005) was less than 3 km. Therefore, in this instance the focal depth has an uncertainty of approximately  $\pm 2$  km, demonstrating the uncertainty associated with the determination of focal depths for shallow earthquakes.

### **2.6.1 Impact of Potentially Induced Earthquakes on North Sea Seismic Activity**

An additional analysis which can be undertaken is the contribution of induced earthquakes to the overall seismicity within the North Sea. A simple way of estimating this is to plot the Gutenberg-Richter distribution of the North Sea earthquake catalogue excluding the potentially induced earthquakes (Tab. 2.1) and comparing it to the Gutenberg-Richter distribution of the complete North Sea earthquake catalogue (Fig. 2.18). Despite the geographical area being the same for both Gutenberg-Richter distributions (i.e. they are the same region), area-normalised distributions were also computed (Fig. 2.19) to enable potential comparison of this analysis with other regions also experiencing induced seismicity in the future.

The magnitude distribution for the entire North Sea earthquake catalogue has a slightly larger  $b$  parameter than the magnitude distribution for the North Sea earthquake catalogue excluding the potentially induced earthquakes (Tab. 2.2; Fig. 2.18). This slightly larger  $b$  parameter suggests the (potentially) induced North Sea earthquakes have a small contribution to the number of larger magnitude earthquakes occurring in the North Sea. This is expected however, as within most hydrocarbon fields, earthquakes induced by hydrocarbon production are thought to be largely limited to being of small to moderate magnitude (Suckale, 2009).

The magnitude distribution for the entire North Sea earthquake catalogue also has a marginally larger  $a$  parameter than the magnitude distribution for the North Sea earthquake catalogue excluding the potentially induced earthquakes (Tab. 2.2; Fig. 2.19). The marginal difference between these two  $a$  parameter values is suggestive that induced seismicity in the UKES contributes only a small amount to the overall seismicity within the North Sea. As discussed above, the  $a$  parameter is indicative of the overall seismicity of a region. Therefore, considering the magnitude distributions compared here are for the North Sea, but one simply has some of the potentially induced earthquakes originating in the region excluded, the larger  $a$  parameter for the magnitude distribution for the entire North Sea earthquake catalogue is unsurprising.

**Table 2.1** *Some earthquakes potentially related to hydrocarbon production and associated hydrocarbon fields in the United Kingdom economic sector.*

<b>yyyy-mm-dd</b>	<b>hh:mm:ss.ss</b>	<b>Lat.</b>	<b>Lon.</b>	<b><math>M_L</math></b>	<b>Depth (km)</b>	<b>Assoc. Hydrocarbon Field</b>
11/08/2005	04:02:12.7	52.88	2.13	1.8	5.0	Camelot Central South
30/08/2007	22:24:30.5	52.86	2.10	2	5.0	Camelot Central South
20/04/1992	06:36:09.4	56.22	2.72	2.2	5.0	Duncan
06/09/1993	02:28:31.8	53.07	2.55	2.3	3.8	Yare
26/01/2014	15:22:56.7	53.74	1.18	2.3	4.0	Newsham
02/02/1986	03:53:38.8	59.30	1.38	2.3	0.3	Harding
03/08/1988	21:26:01.3	59.65	1.67	2.3	4.0	Linnhe
21/09/1987	08:07:18.7	59.82	1.56	2.3	5.0	Bruce
15/09/1994	11:41:36.4	52.95	2.21	2.4	1.4	Camelot North East
22/06/2004	15:42:52.1	53.12	2.18	2.4	4.3	Perenco
05/03/2016	04:16:59.6	53.37	2.36	2.4	5.0	Victor
27/12/1990	03:16:48.8	53.68	1.15	2.4	1.8	West Sole
06/10/1987	02:55:42.5	59.22	1.62	2.4	0.2	Devenick
13/01/1988	15:21:53.0	59.72	1.64	2.4	1.0	Bruce
28/05/2007	05:27:07.8	53.37	2.44	2.5	5.0	Viking B
29/03/2005	02:38:39.7	53.76	1.25	2.5	5.0	Viking B
24/03/1990	16:11:58.5	53.49	2.41	2.7	0.5	Johnston
04/12/2010	01:53:25.3	53.99	1.14	2.7	2.0	Viking A
14/02/1971	18:44:05.4	58.30	1.40	2.9	5.0	West Sole
15/06/1981	12:52:43.8	60.11	1.66	2.9	1.1	Thelma
15/06/1986	21:27:07.4	53.04	2.10	3	1.0	Rhum
12/08/2005	08:05:10.2	53.54	2.38	3	5.0	Perenco
22/11/2002	01:40:22.0	53.03	2.74	3.1	5.0	Wenlock
24/07/2007	01:01:19.0	57.00	1.88	3.2	5.0	Tristan
19/09/1986	16:31:10.4	53.52	2.32	3.7	4.4	Elgin
16/05/1998	23:54:56.3	53.02	2.16	3.8	0.2	Perenco
04/06/2007	17:34:45.9	57.01	1.81	3.9	5.0	Elgin

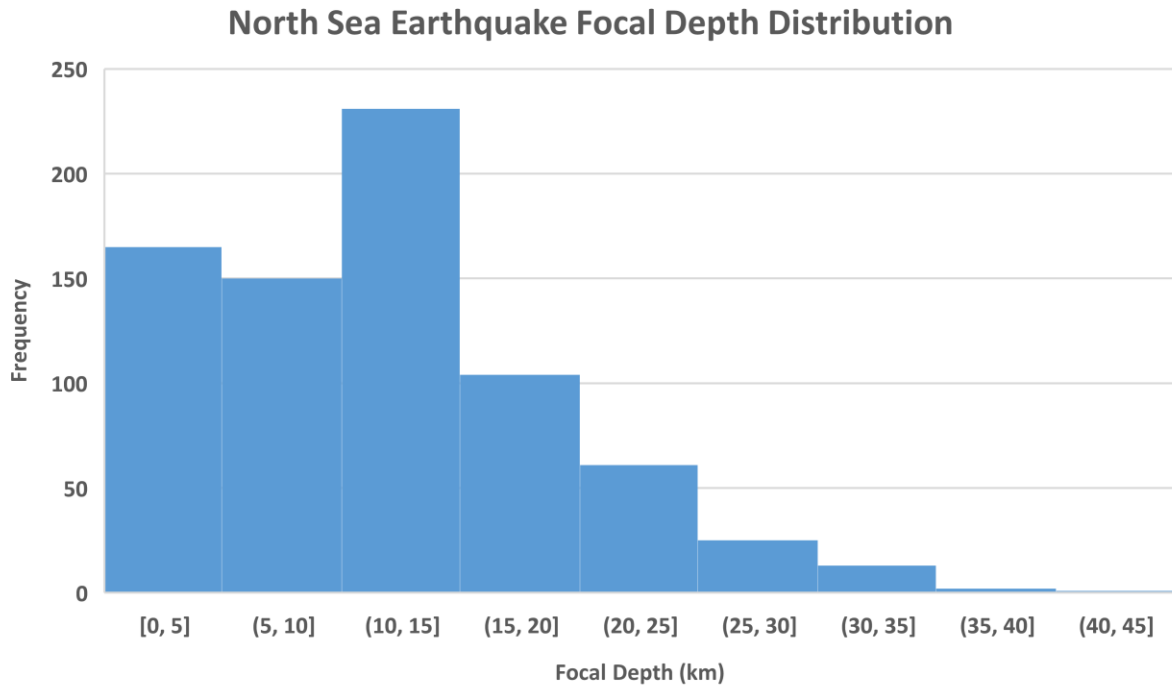


**Figure 2.12** *North Sea earthquake focal depth distribution.*

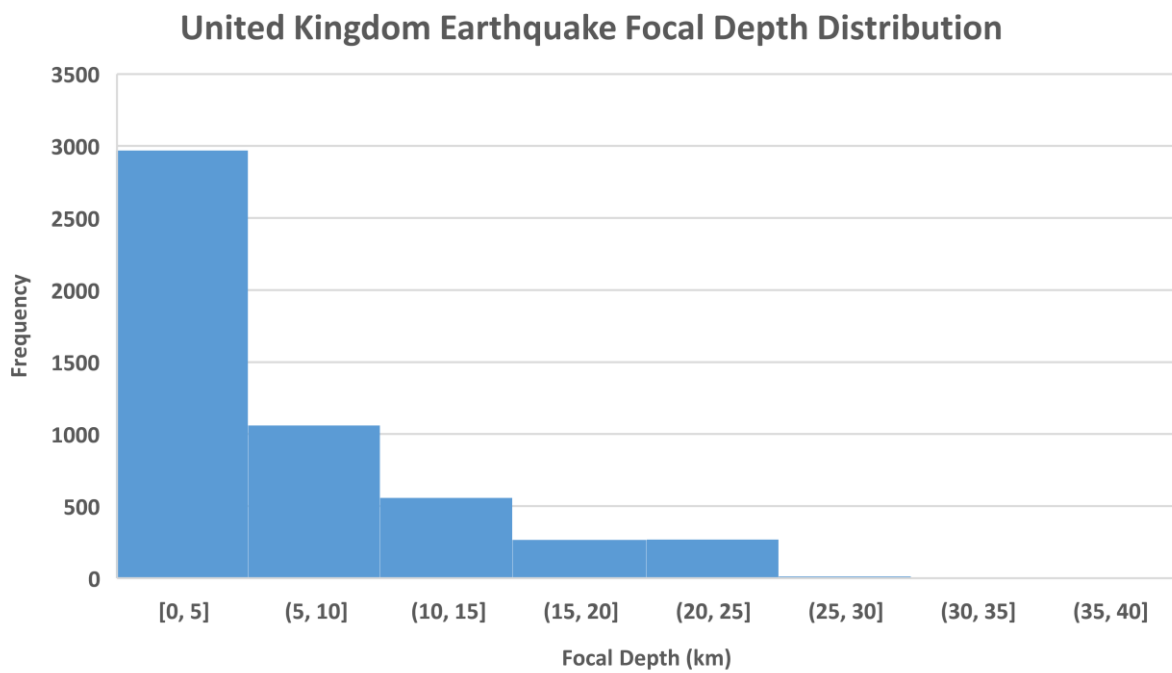


**Figure 2.13** *United Kingdom earthquake focal depth distribution.*

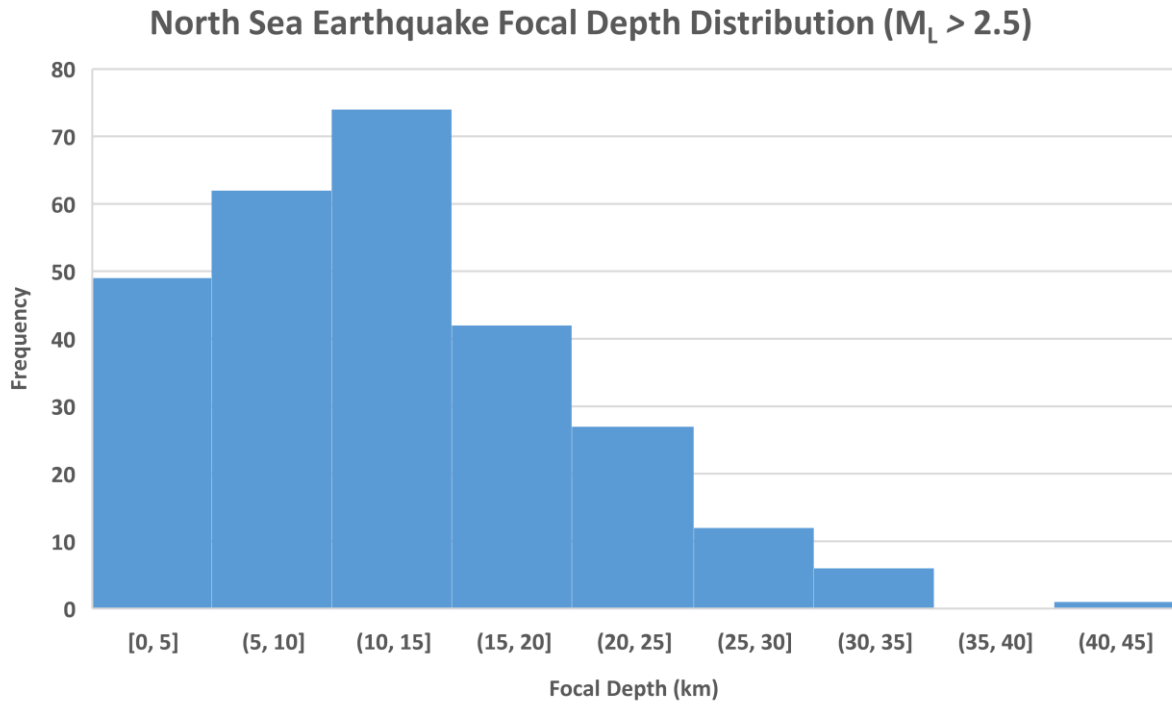


**Figure 2.14** North Sea earthquake focal depth distribution ( $M_L \geq 2.5$ ).

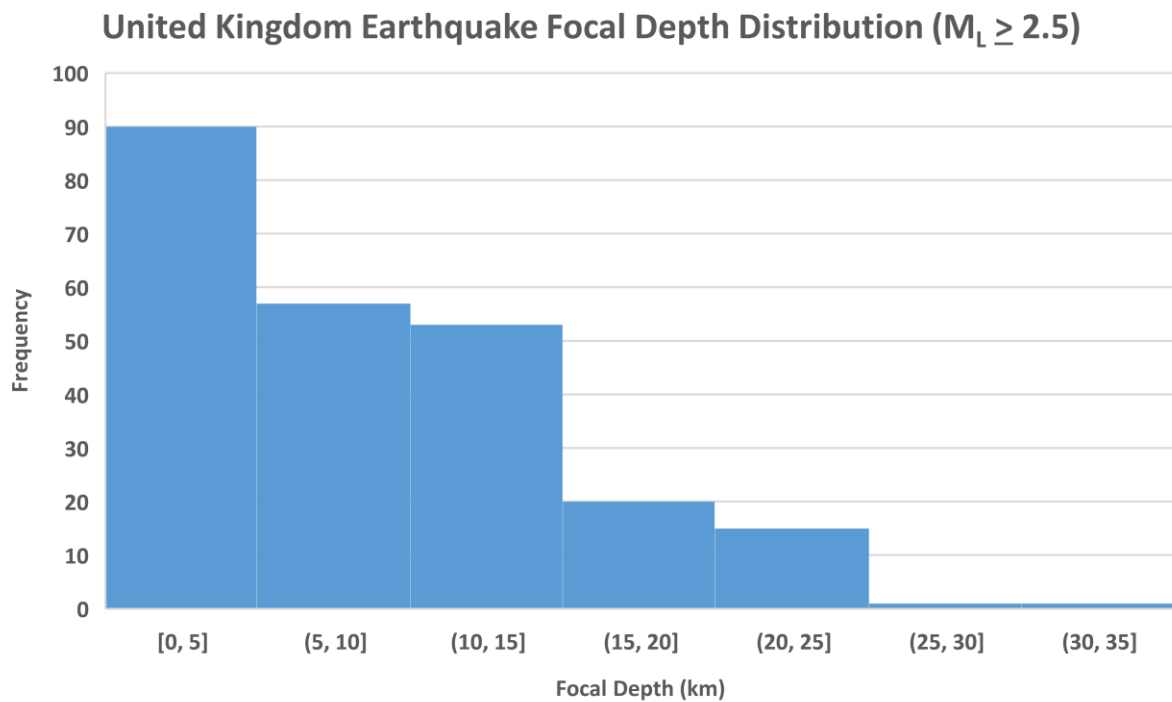


**Figure 2.15** United Kingdom Sea earthquake focal depth distribution ( $M_L \geq 2.5$ ).

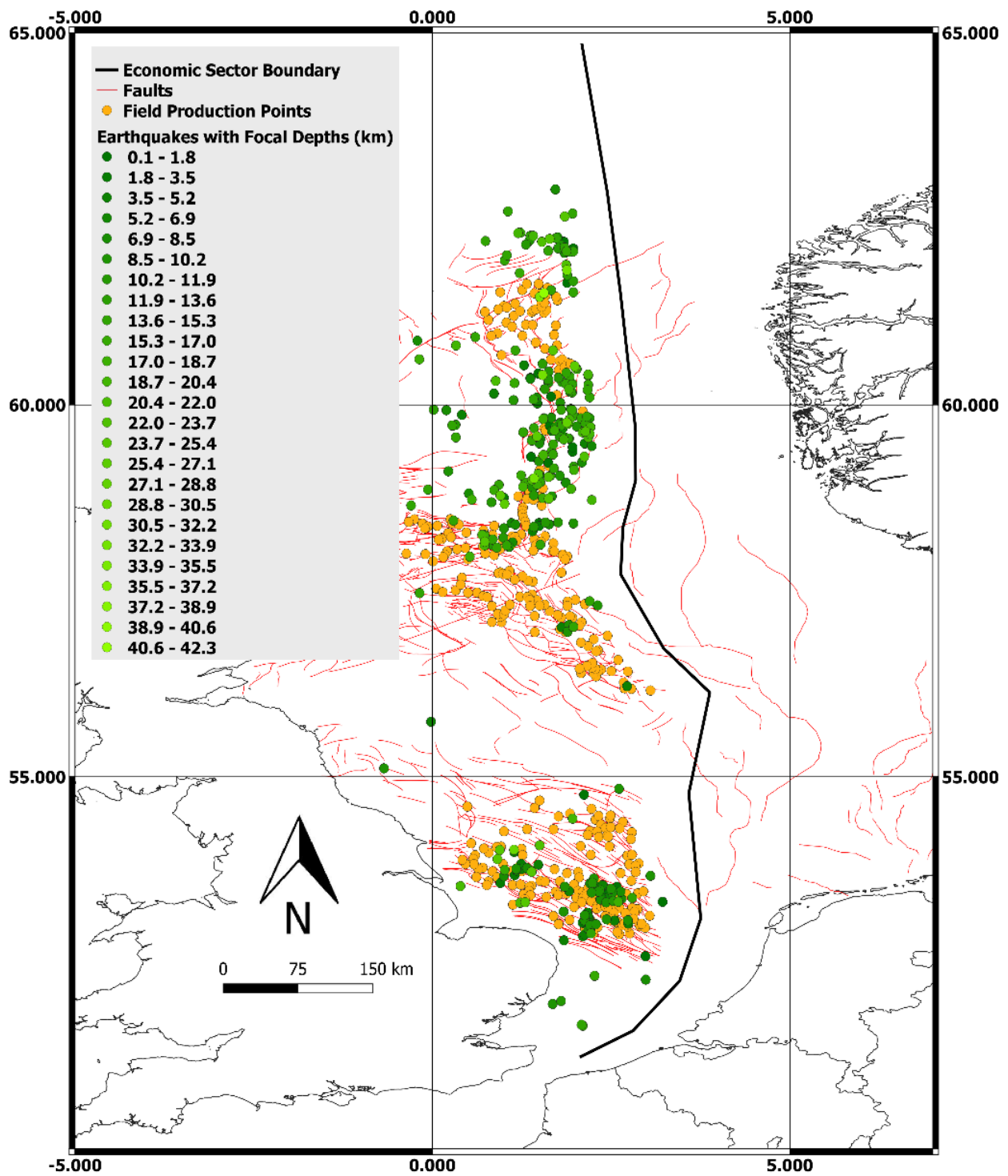


**Figure 2.16** Map illustrating the spatial distribution of earthquake focal depths, hydrocarbon fields and faults in the United Kingdom economic sector of the North Sea. Fault data obtained from Europe-geology.eu. (2019).

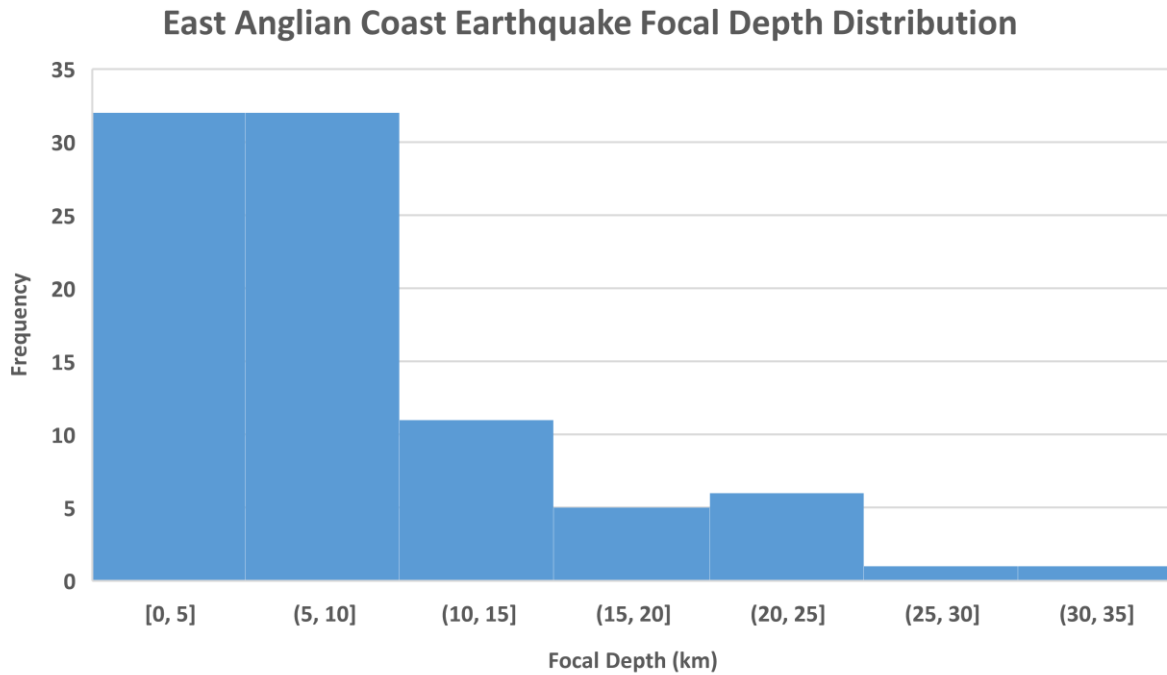


**Figure 2.17** Focal depth distribution for earthquakes occurring off the East Anglian coast.

**Table 2.2** Comparison of the *a* and *b* parameters for the North Sea ( $M_L \geq 2.5$  earthquakes) and the North Sea ( $M_L \geq 2.5$  but excluding potentially induced earthquakes originating in the United Kingdom economic sector) earthquake catalogues. See Tab. 2.1 for list of potentially induced earthquakes.

Region	Area (km <sup>2</sup> )	# Earthquakes	# Earthquakes per km <sup>2</sup>	a value	b value	Normalised a value
N. Sea	570,000	273	4.79E-04	4.25	0.72	-1.51
N. Sea (excluding induced earthquakes)	570,000	260	4.56E-04	4.21	0.71	-1.55

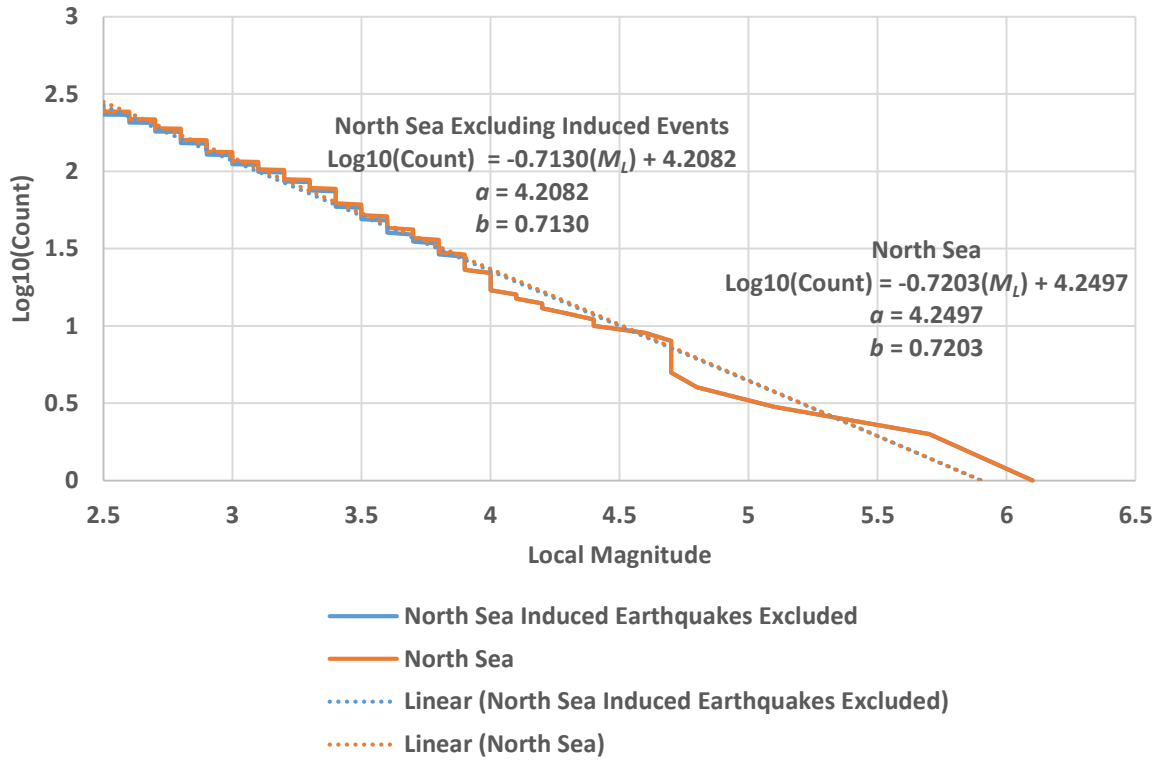


**Figure 2.18** North Sea ( $M_L \geq 2.5$  earthquakes) and the North Sea ( $M_L \geq 2.5$  but excluding potentially induced earthquakes originating in the United Kingdom economic sector) Gutenberg-Richter Distributions. See Tab. 2.1 for list of potentially induced earthquakes.

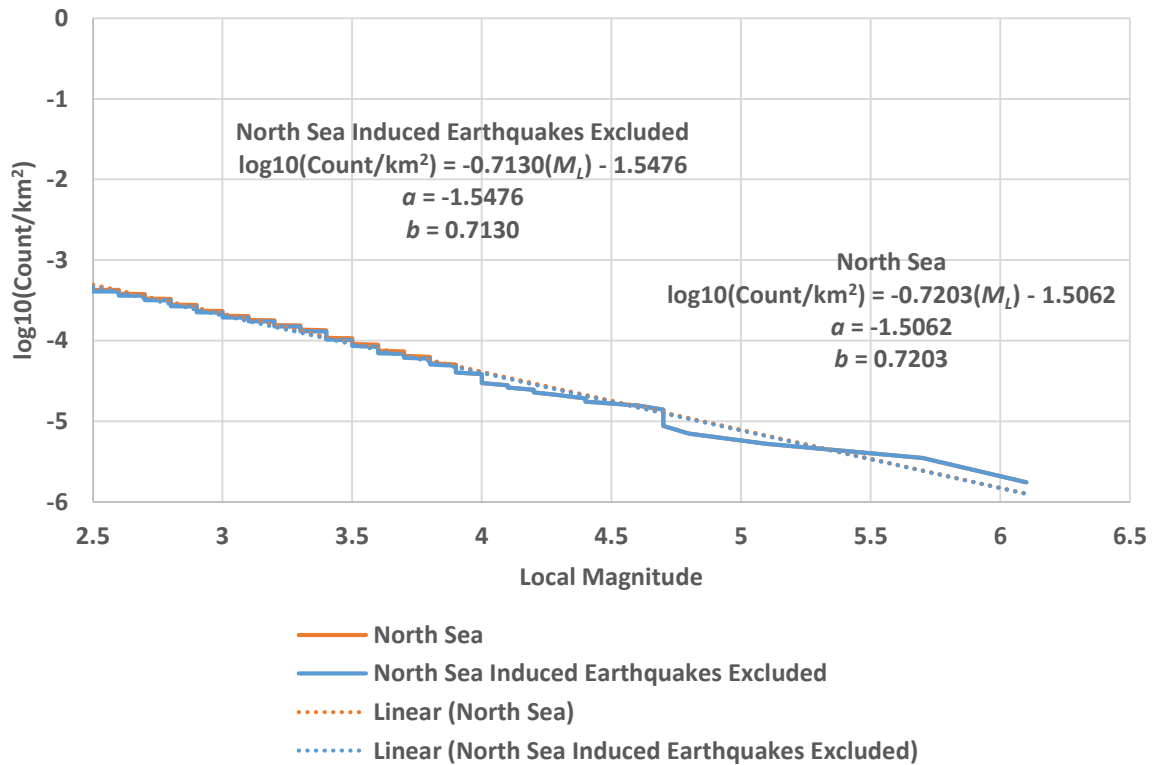


**Figure 2.19** Normalised North Sea ( $M_L \geq 2.5$  earthquakes) and North Sea ( $M_L \geq 2.5$  but excluding potentially induced earthquakes originating in the United Kingdom economic sector) Gutenberg-Richter Distributions. See Tab. 2.1 for list of potentially induced earthquakes.

## 2.7 Discriminating Between Tectonic and Induced North Sea Earthquakes

The simple three-dimensional spatial analysis identified 27 potentially induced North Sea earthquakes. However, as discussed above, use of solely the spatial correlation between earthquake epicentres and hydrocarbon field production points is tenuous evidence for the identification of induced earthquakes. The technical framework of Verdon et al. (2019) was applied to provide an additional means of discerning whether these 27 earthquakes were induced or tectonic in origin. The first qualitative framework for assessing induced seismicity was provided by Davis and Frohlich (1993), with this approach and derivatives of it (e.g. Davis et al., 1995; Frohlich et al. 2016) being in widespread application today (e.g. Montalvo-Arrieta et al., 2018; Grigoli et al., 2018). The Verdon et al. (2019) framework (see below for more details) addresses perpetual weaknesses within these previous frameworks through (1) addressing whether the available evidence in fact supports the case for natural rather than induced seismicity, (2) weighting questions according to the relative influence of the factor considered in each question, (3) providing a means of accounting for ambiguity or uncertainty in the evidence and (4) providing final outcomes which are easily understood by all stakeholders regardless of their technical knowledge regarding seismicity and seismic hazard. To best utilise the Verdon et al. (2019) framework, North Sea hydrocarbon production data (Fig. 2.7) was considered in addition to the BGS North Sea earthquake catalogue and the production point location data. It should be noted that geostatistical approaches for discriminating between induced and tectonic earthquakes such as those proposed by Dahm et al. (2015) and Pollyea et al. (2018) were considered, but the lack of well-specific pressure data for each North Sea hydrocarbon field meant these approaches were not feasible.

The Verdon et al. (2019) framework provides 7 questions, each with a set of qualitative answers (Tab. 2.3). For each question, the answer most supportive of an induced origin for the considered seismicity is assigned a positive score, and the answer most supportive of a tectonic origin a negative score. Before each question is answered, an evidence assessment is undertaken, in which the ability to answer the question based on the available information is considered, resulting in the provision of an “answer rating” (Tab. 2.4). Based on the answer rating, the score associated with each possible answer for the question is modified (Tab. 2.3). This information-dependent adjustment of each question results in the questions for which more information is available contributing more to the outputs of the framework than questions for which little information is available. For questions which not enough information is available to effectively answer, an answer rating of 0% is given, and the associated question is omitted from the assessment. Once each applicable question has been answered, the Induced Assessment Ratio (IAR) and Evidence Strength Ratio (ESR) are computed. The IAR reflects whether the considered seismicity is either positive or negative. A positive score indicates the considered seismicity is induced, and a negative score indicates the considered seismicity is tectonic. The IAR is computed as follows:

$$IAR = \frac{\text{Summed score}}{|\text{Maximum points given available data}|} * 100 \quad (3.1)$$

where the maximum points given available data is the maximum number of positive points available if the summed score is positive, and the maximum number of negative points available if the summed score is negative. The ESR represents the strength of the available data for assessing whether the considered seismicity is induced or tectonic. The ESR is the ratio of the maximum score that can be given with the available data to the maximum score that would be possible if all the required data was available:

$$ESR = \frac{(|\text{Maximum-ve points given available data}| + |\text{Maximum+ve points given available data}|)}{\text{Total number of +ve and -ve points that can be scored in the framework}} * 100 \quad (3.2)$$

The IAR for the 27 considered earthquakes was negative (-18 %), suggesting these events are more likely (albeit only slightly) of a tectonic origin than an induced one. A tectonic origin is supported by similar seismicity having occurred within the North Sea prior to the onset of hydrocarbon production in the region (Fig. 2.7). An induced origin is supported by the spatial correlation between the earthquake hypocentres and the zones of hydrocarbon production (Tab. 2.4). The ESR for the assessment is approximately 62%, reflecting the insufficient information to answer questions 1, 2, 4, 5 and 6 with complete certainty, and questions 3 and 7 at all (Tab. 2.4). Therefore, whilst the IAR suggests the considered earthquakes are more likely tectonic than induced in origin, the ESR indicates a reasonable degree of uncertainty in this conclusion. The IAR supporting a tectonic origin despite the proximity of hydrocarbon production to the earthquakes in terms of both focal depth and horizontal distance further demonstrates that a spatial correlation between earthquakes and zones of hydrocarbon production alone is a tenuous indicator of induced seismicity.

**Table 2.3** *Questions, answers and associated scores provided within the Verdon et al. (2019) framework.* The modified scores for the answers to each question, according to the evidence assessment (see Tab. 2.4), are given within brackets.

Question	Answer A	Answer B	Answer C	Answer D	Answer E
1. Has there been previous seismicity at the same site, or regional setting?	Earthquakes have previously occurred in vicinity to the site, with similar rates and magnitudes: <b>-5 (-4)</b>	Earthquakes have previously occurred within the same regional setting, with similar rates and magnitude: <b>-2 (-1.6)</b>	Earthquakes have not occurred at similar rates or magnitudes within the regional setting: <b>+5 (+4)</b>	Past earthquakes have occurred at similar depths within the regional setting: <b>-3 (-2.4)</b>	Earthquakes are significantly shallower than any past events that have been observed within the regional setting: <b>+3 (+2.4)</b>
2. Is there temporal co-incidence between the onset of events and industrial activities?	The earthquake sequence began prior to the commencement of industrial activity: <b>-15 (-14.1)</b>	The earthquake sequence did not begin until a significant period of time after the cessation: <b>-5 (-4.5)</b>	The earthquake sequence began while the industrial activity was ongoing: <b>+5 (+4.5)</b>	N/A	N/A
3. Are the observed seismic events temporally correlated with the injection and/or extraction activities?	The earthquakes are co-incident with the industrial activity, but there is minimal correlation: <b>-4 (N/A)</b>	There is some temporal correlation between the seismicity and the industrial activity: <b>+4 (N/A)</b>	There is strong temporal correlation between the seismicity and the industrial activity (e.g., between rates of injection and rates of seismicity): <b>+15 (N/A)</b>	N/A	N/A
4. Do the events occur at similar depths to the activities?	Earthquakes do not occur at the same depth, and there is no plausible mechanism by which stress or pressure changes could be transferred to these depths: <b>-4 (-2)</b>	Earthquakes do not occur at the same depth, but plausible mechanisms exist by which stress or pressure changes could be transferred to these depths: <b>+2 (+1)</b>	Earthquakes occur at similar depths to the industrial activity: <b>+3 (+1.5)</b>	N/A	N/A
5. Is there spatial co-location between events and activities?	Earthquakes are distant to the activities, given the putative causative mechanism: <b>-10 (-9)</b>	Earthquakes are sufficiently close to the activities, given the putative causative mechanism: <b>+5 (+4)</b>	If earthquake loci change with time, this change is consistent with the industrial activity: <b>+10 (+9)</b>	N/A	N/A
6. Is there a plausible mechanism to explain the events?	No significant pore pressure increase or decrease has occurred that can be linked in a plausible manner to the event hypocentral position: <b>-5 (-3.75)</b>	Some pore pressure or poro-elastic stress change has occurred that can be linked in a plausible manner to the event hypocentral position: <b>+2 (+1.5)</b>	A large pore pressure or poro-elastic stress change has occurred, that can be linked in a plausible manner to the event hypocentral position: <b>+5 (+3.75)</b>	N/A	N/A
7. Do the source mechanisms indicate an induced event mechanism?	The source mechanisms are consistent with the regional stress conditions: <b>0 (N/A)</b>	Source mechanisms are not consistent with the regional conditions, but are consistent with a putative causative mechanism (e.g. thrust faults above a subsiding reservoir): <b>+4 (N/A)</b>	N/A	N/A	N/A

**Table 2.4** Evidence assessment and answer rating, and answer and corresponding (modified) score for each question within the Verdon et al. (2019) framework.

Question	Evidence Assessment and Answer Rating	Answer and Score
1	The BGS North Sea earthquake catalogue is extensive and focal depths are provided for each earthquake, although the uncertainty in these focal depths is unknown. As discussed, the relative incompleteness of the BGS catalogue prior to hydrocarbon production means earthquakes which potentially occurred at the sites of interest were not recorded. Considering this, and the focal depth uncertainty, an answer rating of <b>80%</b> is given.	Similar earthquakes are known to have previously occurred in the region, although not at every site at which the considered earthquakes originate. Therefore, <b>Answer B (-1.6)</b> was selected for this question. Answer B more so supports the considered earthquakes as being tectonic rather than induced. The spatial correlation between the earthquake epicentres and the faults is further indicative of a tectonic origin..
2	The North Sea earthquake catalogue precedes the onset of hydrocarbon production in the region (e.g. Fig. 2.7). Therefore, the required information is available to establish whether seismicity was present in the North Sea prior to hydrocarbon production. The incompleteness of the BGS's North Sea earthquake catalogue prior to hydrocarbon production means many earthquakes were not recorded. The rates of earthquakes computed from the BGS catalogue are therefore likely not representative of the true seismicity present in the North Sea, and the rates of the 27 considered earthquakes cannot be compared to those computed from the BGS catalogue. An answer rating of <b>90%</b> is therefore assigned to reflect that although this question can be fundamentally answered, the rates of seismicity prior to hydrocarbon production in the North Sea cannot be compared to the rates of the 27 potentially induced earthquakes.	Seismicity similar to the considered earthquakes (in terms of magnitude and focal depth) is known to have occurred prior to the onset of hydrocarbon production in the North Sea (e.g. Fig. 2.7). <b>Answer A (-14.1)</b> is therefore selected.  It should be noted that although Fig. 2.7 could be interpreted as showing an (initial) increase in seismicity as hydrocarbon production begins, this apparent correlation is in fact due to the improvement of the detection threshold in the North Sea coinciding with the onset of hydrocarbon production. The emphasis should be placed upon the 1750 to 1971 year range, in which despite no hydrocarbon production occurring, earthquakes with similar magnitudes (and focal depths) to the 27 considered earthquakes are observed.
3	Annual production data from 1978 onwards is available for the North Sea region (Fig. 2.7). Local production data is not available for each hydrocarbon production point. Considering perturbation from hydrocarbon production is thought to only induce earthquakes up to 10 km from the well location, local production data is required to answer this question. An answer rating of <b>0%</b> is therefore assigned for this question.	N/A
4	The 2001 Ekofisk earthquake focal depths determined by Ottemöller et al. (2005) and the BGS instruments demonstrate that there is considerable uncertainty associated with the focal depths. However, the BGS does provide a focal depth for each earthquake in the North Sea catalogue (Fig. 2.12), and therefore this information should be utilised, albeit with caution. An answer rating of <b>50%</b> is therefore given.	The 27 earthquakes identified as potentially induced in the simple spatial analysis inherently all have focal depths of less than 5 km. Therefore, all of the considered earthquakes occur at similar depths to those of hydrocarbon reservoirs in which pressure perturbations occur due to production. <b>Answer C (+1.5)</b> is selected.
5	The 2001 Ekofisk epicentre determined by Ottemöller et al. (2005) and the BGS catalogue show minimal difference (geometrical average of the differences in lat. and lon. is ~ 2%). The uncertainty in the epicentre of the 2001 Ekofisk earthquake is therefore seemingly minimal. However, the uncertainty in the epicentre of each considered North Sea earthquake is likely not as small. Therefore, an answer rating of <b>90%</b> is assigned to this question. An insufficient number of potentially induced earthquakes are associated with each hydrocarbon field to determine if the earthquake epicentres are changing systemically with ongoing hydrocarbon production. Therefore, Answer C is removed.	The 27 earthquakes identified as potentially induced in the simple spatial analysis are inherently within 10 km of the hydrocarbon production points. Therefore, all of the considered earthquakes occur sufficiently close for hydrocarbon production to be the responsible mechanism. <b>Answer B (+4.5)</b> is therefore selected.
6	Pressure perturbation data is not readily available for the hydrocarbon fields thought to be associated with the considered earthquakes, although the presence of hydrocarbon fields close to the earthquakes is suggestive of hydrocarbon production being a potential mechanism for the induction of the considered earthquakes. Therefore, an answer rating of <b>75%</b> is given to reflect the presence of hydrocarbon production throughout the North Sea being used as a proxy for local pressure data.	The presence of a hydrocarbon field within 10 km of each of the considered earthquakes suggests hydrocarbon production could be the mechanism responsible for said earthquakes. Hydrocarbon production is known to result in reservoir scale pressure perturbations (e.g. Grasso, 1992), and therefore the pressure perturbations are likely large in scale. Therefore, <b>Answer C (+3.75)</b> is selected.
7	Individual focal mechanisms could not be determined for each of the considered earthquakes. Therefore, this question cannot be answered and an answer rating of <b>0%</b> is given.	N/A

## 2.8 Conclusions for Characterisation of North Sea and United Kingdom Earthquakes

In conclusion, there are numerous differences between North Sea and United Kingdom earthquakes. The magnitude distributions of the two areas suggest that the rate of seismicity in the United Kingdom is actually greater than the rate of seismicity in the North Sea, which conflicts with the North Sea being considered as more seismically active than the United Kingdom (Ritsema and Gürpınar, 1983). Although the normalised  $a$  values suggesting the United Kingdom is actually more seismically active, larger earthquakes can occur in the North Sea, as shown by the observation of two  $M_L > 6.0$  earthquakes in the North Sea compared to none in the United Kingdom.

The simple spatial correlation between North Sea earthquake epicentres and hydrocarbon production points could be argued to indicate a relatively significant proportion of North Sea earthquakes are of an induced nature. However, this appears not to be the case based on the focal depth distributions. The predominantly deep focal depth distributions suggest this spatial correlation is more likely between the earthquakes and the nearby geological faults which the field production points are situated on or proximal to, rather than the field production points themselves. Consequently, two-dimensional spatial correlations between earthquake epicentres and zones of hydrocarbon production are determined to be tenuous indicators of induced seismicity. This can be attributed to induced seismicity being generated by complex reservoir-scale stress variations, and consequently not being adequately captured by such a simplistic spatial analysis.

An additional spatial analysis incorporating earthquake focal depths lead to the identification of 27 North Sea earthquakes potentially induced by hydrocarbon production in the UKES. If these 27 earthquakes are excluded from the North Sea magnitude distribution, it can be inferred that (1) induced earthquakes originating in the UKES contribute minimally to the number of larger earthquakes in the North Sea and (2) that induced earthquakes originating in the UKES comprise only a small amount of the total earthquakes originating in the North Sea (assuming these 27 earthquakes are in fact induced in origin).

To determine whether potentially induced earthquakes from the entire North Sea contribute significantly to the number of larger earthquakes in the region or the number of earthquakes observed in the region in general, three-dimensional spatial analysis incorporating focal depths needs to be undertaken for the NES of the North Sea to identify potentially induced earthquakes in this sector also. This additional spatial analysis would require production point location data for the Norwegian economic sector, which as of completion of this analysis is not publically accessible.

The 27 North Sea earthquakes identified as being potentially induced were evaluated within the Verdon et al. (2019) induced seismicity framework. The results of this framework suggest the 27 earthquakes are more likely of a tectonic origin, further supporting the notion that spatial correlations between

earthquakes and zones of hydrocarbon production alone are insufficient evidence for induced seismicity.

Finally, it should be reiterated that the results of this comparison of North Sea and United Kingdom earthquakes are potentially influenced by two factors: (1) the lack of seismic monitoring in the North Sea region compared to the United Kingdom and (2) the uncertainty associated with automatic focal depth computation. However, as discussed within the analysis, considerable efforts are undertaken to mitigate these factors, resulting in the analysis providing a sufficient summary of both tectonic and induced seismicity in the North Sea and the neighbouring United Kingdom.

### 3.0 Ground-Motion Prediction Equations for the North Sea

As briefly discussed in Chapter 1, ground-motion prediction equations (GMPEs) are one of the most important aspects of probabilistic seismic hazard assessment (PSHA). Within the most recent North Sea PSHA by Bungum et al. (2000), a simple GMPE logic tree, comprising of the Toro et al. (1997) and the Ambraseys et al. (1996) GMPEs with equal weights was used to predict ground-shaking. Bungum et al. (2000) selected a logic-tree approach to help account for the significant epistemic uncertainty resulting from a lack of knowledge regarding North Sea earthquakes. This lack of knowledge was caused by a lack of North Sea ground-motion records. Ground-motion records for North Sea earthquakes are now more readily available, enabling a more substantial GMPE evaluation process than was possible by Bungum et al. (2000).

In this chapter, pre-existing GMPEs are evaluated using the additional ground-motion data which is now available for North Sea earthquakes, so as to identify an appropriate base model for modification to better predict the ground-shaking in the region. This GMPE evaluation procedure (see section 3.6) is also provided in Brooks et al. (2020). Prior to this, an overview of ground-motion records is provided. An overview is also provided for GMPEs developed specifically for predicting the ground-shaking resulting from induced earthquakes due to the engineering significance of the 2001 Ekofisk earthquake.

#### 3.1 Signal Processing of Acceleration Time Series

The primary focus of seismic design is the balance between the potential for ground-shaking to cause damage (seismic demand) and the capabilities of structures to resist this damage (seismic capacity). The seismic capacity of engineered structures can be assessed through experimentation, analytical modelling and post-earthquake field observations, whereas the seismic demand has been determined primarily from acceleration time series (Boore and Bommer, 2005).

Acceleration time series (also known as ground-motion or strong-motion records) are the acceleration of the ground sampled many dozens of times per second in three mutually orthogonal directions (Pacor and Luzi, 2014). For several decades, the reference ground-motion for earthquake engineers and engineering seismologists was the El Centro earthquake acceleration time series which was recorded in California in 1940. Following the Loma Prieta (1989), Northridge (1994) and Kobe (1995) earthquakes, hundreds of acceleration time series were made available through databases accessible through the Internet (Pacor et al., 2011). This huge increase in the availability of acceleration time series highlighted the considerable variability of ground-motion based on (but not limited to) earthquake size and focal mechanism, source-to-site distance<sup>14</sup> and azimuthal positioning of site relative to source, properties of the propagation medium and the geology underlying the considered site. The ability to evaluate acceleration time-series and identify the main characteristics that can potentially result in damage to

---

<sup>14</sup> Site refers to the location where an earthquake was observed (in this case the location of the recording station).

structures (the seismic hazard) is a key input in the mitigation of seismic risk. To this end, acceleration time series are used in non-linear regression to develop GMPEs, or for the derivation of a point-source model to generate synthetic ground-motions within stochastic simulations<sup>15</sup>, from which a GMPE can then be fitted instead. Here, several aspects of acceleration time series are discussed: (1) issues associated with instrumental characteristics, (2) evaluation of data quality and record processing and (3) the computation of acceleration, velocity and displacement values from the processed data. The discussion of such concepts below is largely summarised from Pacor and Luzi (2014).

### 3.1.1 Analog and Digital Recording Instruments for Recording an Acceleration Time Series

Acceleration time series are recorded by two types of instruments (Trifunac and Todorovska, 2001):

1. Analogue accelerographs, which are optical-mechanical devices that produce traces of the ground-motion on film or paper. Analogue accelerographs were in use from the early 1930s to the end of the twentieth century, and have several drawbacks: (1) they operate on standby, only recording once triggered by ground-motions above a specific acceleration threshold, and therefore not preserving the pre- and post-earthquake time series (Fig. 3.0), (2) the natural frequency of the implemented transducers is often limited to  $\sim 25$  Hz, which limits the usable frequency band and (3) if numerical analyses are planned, the traces of the ground-motion must be digitised.
2. Digital accelerographs, which record ground-motion continuously in a digital medium (e.g. cassettes or solid-state memory), and have been in use since the 1980s. A significant benefit of digital accelerographs is that due to continuously recording they preserve the pre- and post-earthquake segments of the time series (Fig. 3.0). The precision of the recorded ground-motion depends on the instrument settings (e.g. sampling rate).

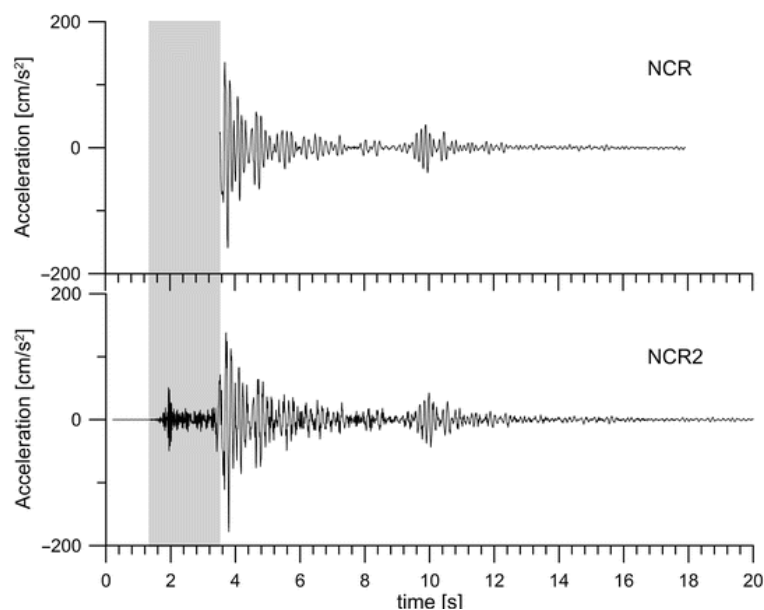


**Figure 3.0** Acceleration time series for the 1997 Umbria-Marche seismic sequence, central Italy recorded at analogue station NCR (top) and digital station NCR2 (bottom). Taken from Pacor and Luzi (2014).

<sup>15</sup> See Chapter 5 for more details on the stochastic method.

### 3.1.2 Processing of an Acceleration Time Series

It must be emphasised that digitised acceleration time series are not identical reproductions of the incident ground-motion, as they contain noise of various origins, at both high and low frequencies. The purpose of signal processing is the quantification and removal of the noise present in the record, so as to provide a reliable estimate of the true ground-motion. The key stages of processing are as follows

#### Step 1: Quality Check of Acceleration Time Series

Prior to data processing a quality check of the considered record is undertaken, where one can determine if the record should be discarded or retained for further processing. Douglas (2003) reports the features which identify an acceleration time series as of poor quality (see Table I of Douglas, 2003) based on an analysis of the acceleration time series within the European Strong-Motion Database (Ambraseys et al., 2004). The primary indicators of a poor quality record (referred to as nonstandard errors) deduced from Douglas (2003) are: (1) insufficient digitiser resolution, (2) S-wave trigger threshold for analogue instruments (e.g. Fig. 3.0), (3) insufficient sampling rate, (4) early termination during coda, (5) the presence of spurious spikes (Fig 3.1) and (6) baseline shift (the presence of multiple baselines resulting in unphysical velocities and displacements – Boore, 2003; Fig 3.2). Some of these nonstandard errors do not correspond to the usual sources of noise, and therefore can be visually identified and remedied before further processing is undertaken. For example, “spikes” in a digitised record (Fig. 3.1) can be replaced with the mean of the accelerations of the adjacent data points either side of the spike, and baseline shifts (Fig. 3.2) can be accounted for using baseline adjustments (see Boore and Bommer, 2005 for more details on such adjustments).

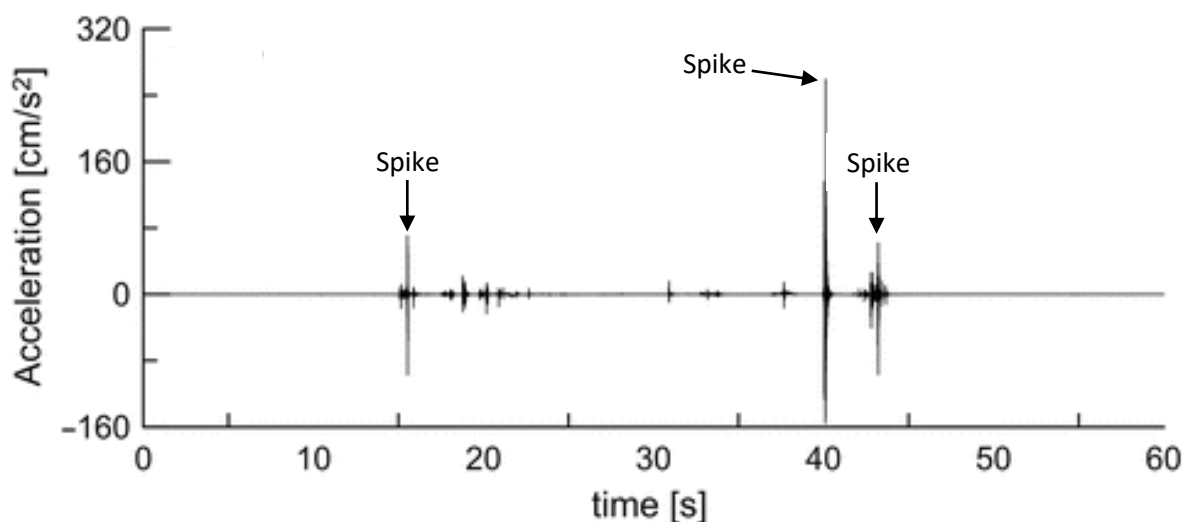


**Figure 3.1** Example of spurious spikes in a digitised record. Adapted from Pacor and Luzi (2014).

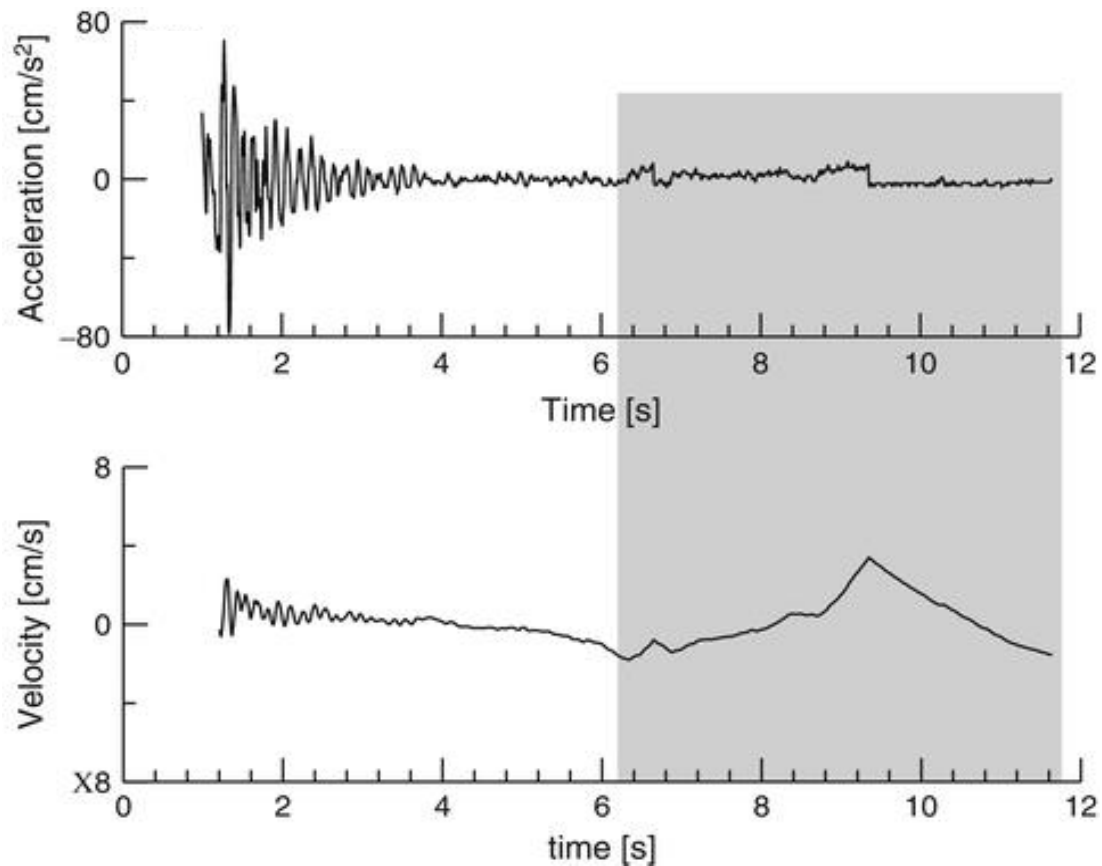


**Figure 3.2** Example of baseline shift and its effect on the velocity time series. The grey box highlights the differences. Taken from Pacor and Luzi (2014).

## Step 2: Filtering of an Acceleration Time Series

The filtering of a record conventionally takes the form of removing most of the signal at frequencies where the Fourier amplitude spectrum (FAS – see below for more detail on FAS) indicates a low signal-to-noise ratio. Filters to remove signal at the desired frequencies can be applied in either the frequency domain or the time domain (exactly the same result should be obtained in either case).

For the removal of low frequency noise ( $< 1$  Hz), a low-cut (high-pass) filter can be applied to a record (Fig. 3.3). Low frequency noise can strongly influence the computed ground-motion velocities, displacements and response spectral ordinates, and consequently most studies consider the effects of a high pass filter. For example, in Fig. 3.3, the application of a high-pass filter of 0.01 Hz provides unrealistic velocities and displacements, whereas a high-pass filter of 0.02 Hz provides more reasonable values. The low frequency cut-off (the lowest frequency for which the data are reliable in terms of signal-to-noise ratio) is most commonly determined from picking the frequency at which the FAS for the record deviates from the tendency to decay in proportion to the reciprocal of the frequency squared, based on a seismological model of the radiated energy (i.e. a source model, such as the Brune 1970; 1971 stress drop model – see Chapter 5 for more details on such models). The identified frequency is referred to as the (low-cut) corner frequency.

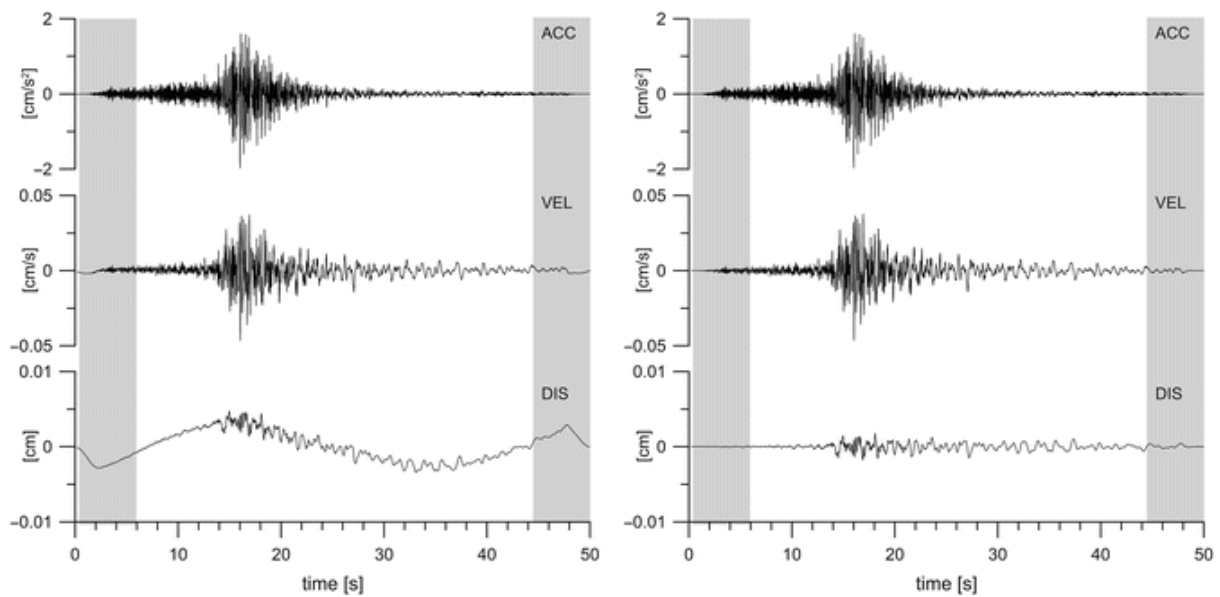


**Figure 3.3** Example of low-cut filtering with a 0.01 Hz cut-off (left) and a 0.02 Hz cut-off (right). Taken from Pacor and Luzi (2014).

Generally, the removal of high frequency noise ( $> 20$  Hz) using high-cut (low-pass) filters is only considered for select engineering problems such as the design of non-structural elements, sensitive equipment and pipework (e.g. in nuclear power facilities). It should be noted that the sampling rate of the instrument determines the upper usable frequency (the Nyquist frequency) of a record, which is equal to  $1/2\Delta t$ , where  $\Delta t$  is the sampling interval. This is important to consider because a high-cut filter applied at frequencies greater than the Nyquist frequency will have no effect on the record. In summary, whilst low-cut filters strongly influence the computed ground-motion intensity measures (GMIMs), high-cut filtering is sometimes not necessary.

### Step 3: Computation of Ground-Motion Intensity Measures from a Processed Acceleration Time Series

Following the processing of an acceleration time series GMIMs can be computed. GMIMs are computed in both the time and frequency domains to capture various features of the acceleration time series record.

#### Time Domain Ground-Motion Intensity Measures

The most commonly considered ground-motion intensity measure is peak ground acceleration (PGA), which is the (absolute) maximum ground acceleration observed on the acceleration time series. PGA is usually computed for each mutually orthogonal component of the ground-motion. It can be computed directly from either a raw or processed record because PGAs change minimally due to the processing procedure. It should be noted that although PGA is widely considered in earthquake engineering due to being directly related to the inertial force, it poorly characterises the ground-motion. Fig. 3.4 demonstrates that records with the same PGA can be very different for other GMIMs depending on the

earthquake magnitude, source-to-site distance and the geological conditions below the considered site amongst other factors.

The peak ground velocity (PGV) is the (absolute) maximum ground velocity observed following an initial integration of the acceleration time series, and peak ground displacement (PGD) is the maximum ground displacement observed following an additional integration of the acceleration time series. Like for PGA, a value is computed for PGV and PGD for each mutually orthogonal component of the ground-motion. However, unlike for PGA, the computed PGV and PGD are strongly influenced by the band-pass filtering. PGD is especially dependent on the specified low-cut corner frequency.

A preliminary assessment of the frequency content of an acceleration time series can be inferred from the ratio of PGA to PGV. Low PGA/PGV ratios are generally suggestive of earthquakes with low predominant frequencies, broad response spectra and longer durations.

The duration of an acceleration time series is commonly used to identify the portion of the record in which the ground-motion amplitude can potentially cause damage to engineering structures. Multiple definitions have been proposed, and are demonstrated in Fig. 3.5:

1. Bracketed duration (Bolt, 1973): a threshold PGA value is fixed (usually 0.05 g or 0.1 g), above which the motion is considered to have relevance for earthquake engineering purposes. The duration is defined as the time interval between the first and last exceedance of this threshold PGA value.
2. Significant duration (Husid, 1967; Trifunac and Brady, 1975): the time interval over which the integral of the square of ground-acceleration (Husid plot – see Fig. 3.5) is within a given range of its total value (conventionally between 5% and 95% or 5% and 75%).

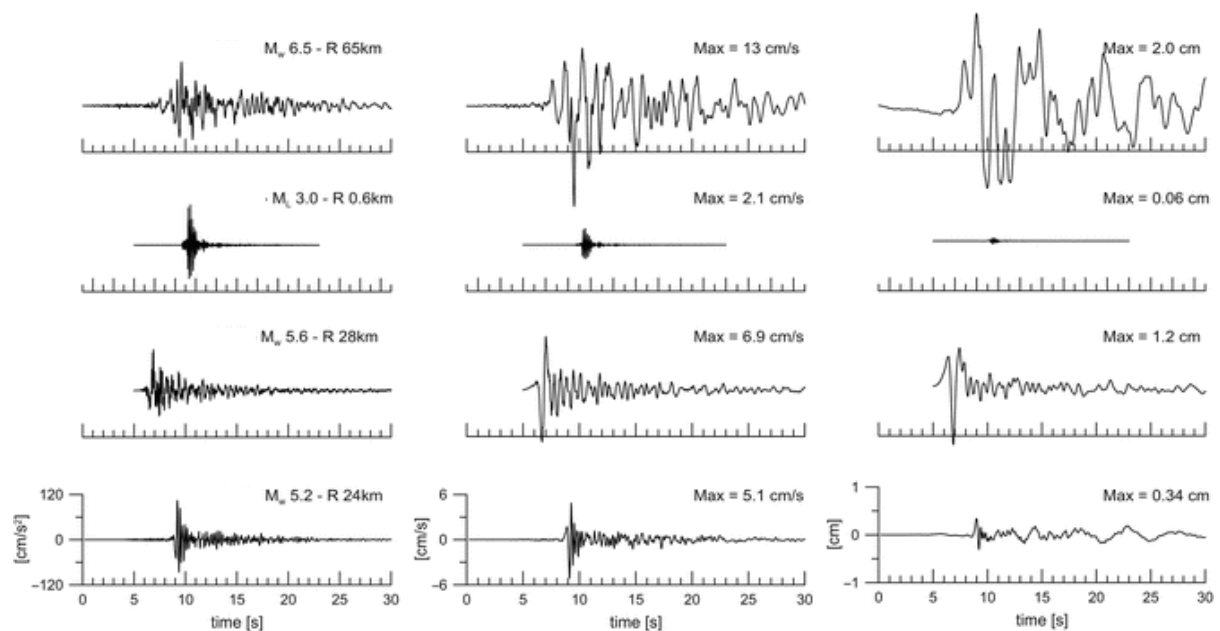


**Figure 3.4** Example of acceleration time series with similar PGAs ( $105 - 112 \text{ cm/s}^2$ ) but different PGVs and PGDs. Taken from Pacor and Luzi (2014).

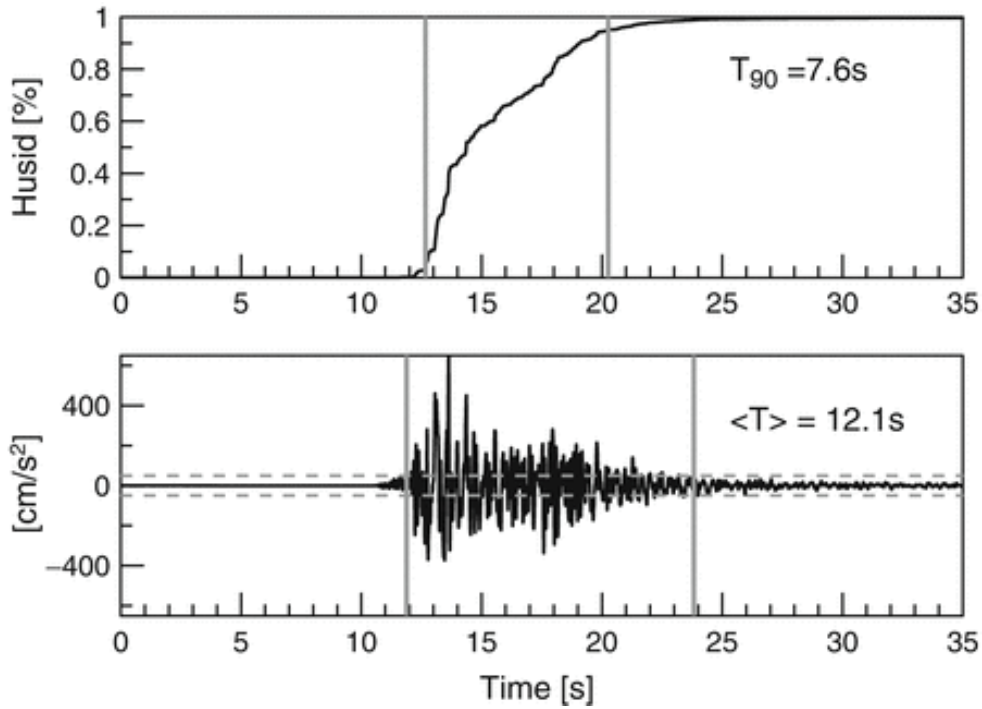


**Figure 3.5** Acceleration time series with bracketed duration (bottom) and corresponding Husid plot with significant duration (top). Values within 5% and 95% of the integral of the square of ground-acceleration were considered. Taken from Pacor and Luzi (2014).

### Frequency Domain Ground-Motion Intensity Measures

As discussed briefly above, the frequency content of an acceleration time series can be computed using the Fourier transform<sup>16</sup>. For an acceleration time series  $a(t)$  with total duration  $t_d$ , the Fourier transform is defined as follows:

$$F(f) = \int_0^{t_d} a(t)e^{-i2\pi ft} dt \quad (3.0)$$

where because  $F(f)$  is a complex function it can be expressed in the form  $F(f) = A(f) - iB(f)$ :

$$A(f) = \int_0^{t_d} a(t) \cos(2\pi ft) dt; B(f) = \int_0^{t_d} a(t) \sin(2\pi ft) dt \quad (3.1)$$

Of considerable use to engineering seismologists is the Fourier amplitude spectra, which is defined as:

$$FAS = \sqrt{A^2 + B^2} \quad (3.2)$$

The FAS is used for investigating the ground-motion amplitude and energy content at different frequencies. Acceleration time series from large earthquakes and/or soft sites usually feature larger motions at low frequencies than from small events and/or from rock sites (e.g. Fig. 3.6). FAS are commonly used to decompose the observed ground-motion into spectral functions describing source, path and site effects (see Chapter 5 for more details on these functions).

<sup>16</sup> The Fourier transform of a function is a complex-valued function of frequency, with the absolute magnitude representing the amount of frequency present in the original function, whose argument is the phase offset of the basic sinusoid in that frequency (see Cooley and Turkey, 1965 for more details on the Fourier transform).

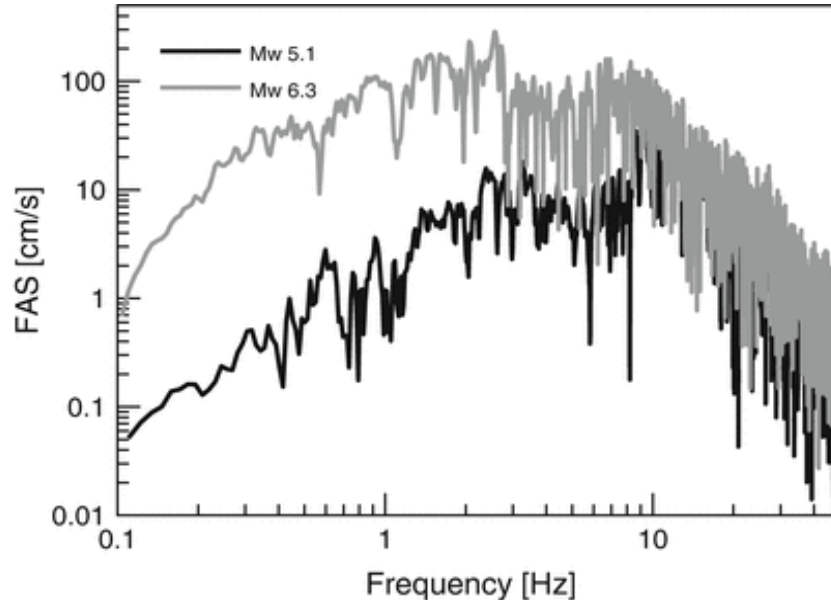


**Figure 3.6** Fourier amplitude spectra for acceleration time series recorded for different sized earthquakes recorded at the same site and similar source-to-site distances. Taken from Pacor and Luzi (2014).

### Response Spectra

For the determination of seismic demand, the most important representation of ground-motion at a site is the response spectrum, in terms of absolute acceleration, relative velocity or relative displacement. The response spectrum is defined as the maximum response amplitude of a single-degree-of-freedom (SDOF) system, subject to a (displacement, velocity or acceleration) time series as a function of system period  $t_n$ . The response spectrum can be computed for different damping ratios  $\zeta$  (usually assumed to be equal to 5% of the critical damping for most structures). The maximum amplitude of the response is computed by integrating the equation of motion of the SDOF system:

$$\ddot{x}(t) = -\omega_n^2 y(t) - 2\xi\omega_n^2 \dot{y}(t) \quad (3.3)$$

where  $y(t)$  and  $\dot{y}(t)$  are the relative displacement and velocity of the oscillator with respect to the ground,  $\ddot{x}(t)$  is the absolute acceleration of the oscillator given by  $\dot{y}(t) + a(t)$ , and  $\omega_n (= \frac{2\pi}{T})$  is the natural angular frequency of the oscillator. When acceleration, velocity or displacement is considered the following definitions are introduced:

$$\text{Displacement spectrum (relative):} \quad SD(t_n, \xi) = \max_t |y(t)| \quad (3.4)$$

$$\text{Velocity spectrum (relative):} \quad SV(t_n, \xi) = \max_t |\dot{y}(t)| \quad (3.5)$$

$$\text{Acceleration spectrum (absolute):} \quad SA(t_n, \xi) = \max_t |\ddot{x}(t)| \quad (3.6)$$

Acceleration response spectra are commonly used by earthquake engineers because multiplication of  $\ddot{x}$  by mass  $m$  is equal to the maximum force imposed on an engineering structure. Fig. 3.7 provides example SA, SV and SD response spectra for some arbitrary acceleration time series.

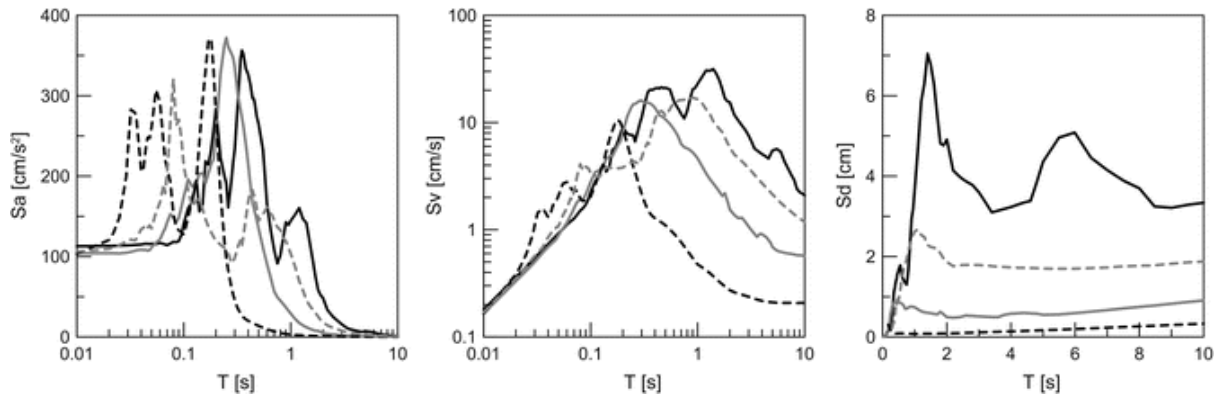


**Figure 3.7** Acceleration response spectra ( $S_a$ ), velocity response spectra ( $S_v$ ) and displacement spectra ( $S_d$ ) for 4 arbitrary acceleration time series. Different axis scales are used to emphasise the different spectral shapes associated with each type of response spectrum. Taken from Pacor and Luzi (2014).

At period  $T = 0$  s, the spectral displacement and spectral velocity are zero, and the spectral acceleration is equal to the PGA, which is why PGA is largely used in seismic design codes to anchor design spectra. Conversely, when  $T$  approaches infinity, the spectral acceleration approaches zero and spectral displacement approaches the PGD.

The pseudo-acceleration and pseudo-velocity spectra are also commonly used in practice. These pseudo spectra are defined as functions of the displacement spectrum:

$$\text{Pseudo-acceleration spectrum:} \quad PSA(t_n, \xi) = \left(\frac{2\pi}{t_n}\right)^2 SD(t_n, \xi) \quad (3.7)$$

$$\text{Pseudo-velocity spectrum:} \quad PSV(t_n, \xi) = \left(\frac{2\pi}{t_n}\right) SD(t_n, \xi) \quad (3.8)$$

For small damping values and intermediate to high frequencies, the pseudo spectra are good approximations of the absolute response spectra, and for an un-damped oscillator the pseudo spectra are exact matches to the absolute response spectra. For very low frequencies the pseudo spectra and absolute spectra are considerably different because velocity spectrum tends to PGV and pseudo-velocity spectrum tends to zero (Hudson, 1979).

The response spectrum provides an indication of the maximum response amplitude for a SDOF system when subjected to a time series as a function of system period, whereas the FAS provides an indication of the frequency content from an observed (or simulated) earthquake. Therefore, through considering both the response spectra and the FAS, a comprehensive overview of the seismic hazard at a considered site can be determined.

### 3.2 Ground-Motion Prediction Equations for Induced Seismicity

GMPEs predict ground-motion intensities as a function of magnitude, distance and other input parameters<sup>17</sup> (e.g. site conditions), and are usually developed for specific areas using an associated ground-motion record dataset (Baker, 2015). However, in addition to being developed for specific localities, GMPEs are also developed for (or to incorporate) specific types of seismicity within regions. One of the most important types of seismicity (both in the context of this investigation and GMPE development in general) is induced/anthropogenic seismicity. Induced seismicity is of engineering significance for the North Sea (i.e. the 2001 Ekofisk earthquake), and therefore GMPEs developed for predicting the ground-shaking from anthropogenic earthquakes are reviewed here.

There are numerous types of induced seismicity (e.g. geothermal, mining and hydrocarbon production related – for more details see Wilson et al., 2015), with GMPEs being developed to predict the ground-shaking resulting from specific forms of induced seismicity in certain regions. For example, Rashedi and Mahani (2017) developed a GMPE specifically for hydrocarbon induced seismicity so as to assess the seismic risk for dams in western Canada, and Bommer et al. (2016) developed a GMPE for induced seismicity in the Groningen field of the Netherlands (again hydrocarbon production related – see Chapter 2) to arrest safety concerns of the local population.

Currently, there is a handful of notable GMPEs developed to predict ground-shaking associated with anthropogenic earthquakes (Tab. 3.0). The characteristics of these GMPEs are noticeably similar, which can be attributed to induced earthquakes being largely similar to one another. Firstly, for each GMPE the applicable magnitude range is generally limited to small and moderate magnitudes because induced earthquakes are themselves predominantly small to moderate in size (local magnitude ( $M_L$ )  $\leq 4.5$ ) (Suckale, 2009). Secondly, these GMPEs have relatively small maximum applicable distances because nearby earthquakes result in greater ground-shaking at the considered site(s), and therefore are of greater engineering significance than further away earthquakes. Furthermore, ground-motions resulting from induced earthquakes are generally small and therefore likely to be of limited ground-shaking intensity at source-to-site distances beyond  $\sim 20$  km (Suckale, 2009), and the ground-motion data used for the development of these GMPEs is often recorded close to the source of the induced seismicity, so there is a lack of records from large distances (e.g. McGarr and Fletcher, 2005; Bommer et al., 2016). Thirdly, hypocentral distance ( $R_{hyp}$ ) and epicentral distance ( $R_{epi}$ ) are the preferred distance metrics for the majority of these GMPEs, being chosen over Joyner-Boore distance ( $R_{jb}$ ) and rupture distance ( $R_{rup}$ ) because they enable earthquakes to be treated as point sources, and thus simplifying the subsequent hazard calculations (Dost et al., 2013). Finally, GMPEs for induced seismicity are more often developed for regions where there are sufficient records and where there is a need for engineering purposes (i.e. seismic risk calculations). Prominent examples of such regions include Oklahoma in the United States

---

<sup>17</sup> See Appendix B for a basic overview of GMPEs.

(e.g. Bydlon et al., 2017) and the Groningen natural gas field in The Netherlands (e.g. Bommer et al., 2016).

The development of GMPEs for induced seismicity has taken three key pathways: (1) the conventional method in which non-linear regression of observed ground-motion records produces an empirical GMPE, (2) the stochastic method in which a point-source model is derived from observed ground-motion records and used to produce simulated ground-motion records to which a GMPE is then fitted (again through non-linear regression) and (3) the modification of existing GMPEs developed for tectonic (i.e. non-anthropogenic) earthquakes to predict the ground-shaking from anthropogenic earthquakes.

There are several GMPEs which were developed through non-linear regression of ground-motion records corresponding to induced earthquakes (Tab. 3.0). The use of many ground-motion records ensures the functional form of the GMPE is well constrained (Baker, 2015), resulting in a GMPE which can be used in confidence for seismic hazard calculations. Consequently, the regions in which empirical GMPEs for induced earthquakes have been developed are those in which extensive (or at least adequate) seismic monitoring efforts are in place, an example of which is McGarr and Fletcher (2005)'s GMPE.

The McGarr and Fletcher (2005) GMPE was developed for use in the area surrounding the Cottonwood Tract in central Utah, and was developed as the basis for assessing seismic hazard to the Joes Valley Dam from nearby coal mining activity. From late 2000 to early 2001 a nearby seismic network operated by the University of Utah monitored the earthquakes resulting from this local coal mining. Consequently, McGarr and Fletcher (2005) were able to utilise a set of high quality ground-motion records to construct their empirical GMPE, which was found to effectively predict the coal mining-related ground-shaking experienced by the Joes Valley Dam (Arabasz et al., 2005), illustrating how sufficient seismic monitoring (to acquire an appropriate dataset) is critical to developing a satisfactory empirical GMPE. The Bommer et al. (2017a) GMPE for the Groningen field is another example of the need for complete ground-motion datasets to develop competent empirical models for predicting induced seismicity. This GMPE is an update of the Bommer et al. (2016) GMPE. Improved seismic monitoring in the Groningen field enabled the addition of more small earthquakes to the ground-motion dataset, enabling the minimum applicable magnitude of the Bommer et al. (2016) GMPE to be extended from  $M_L$  2.5 to  $M_L$  1.8 (Bommer et al., 2017a).

Whilst empirical GMPEs have successfully been developed for induced seismicity (Tab. 3.0), the dependency of the empirical GMPE development method on the availability of an extensive ground-motion record database is problematic. For example, whilst the McGarr and Fletcher (2005) GMPE has an applicable magnitude range of  $M_L$  0.98 to  $M_L$  4.2, the upper magnitude limit was due to the addition of two supplementary ground-motion records of an  $M_L$  4.2 earthquake from Willow Creek mine, Wyoming. The use of supplementary records from another region shows how poor magnitude coverage

(i.e. database incompleteness) severely hampers the construction of empirical GMPEs for induced seismicity. The requirement of a complete ground-motion record database is especially troublesome for areas in which induced seismicity has not yet been observed, or is only recently emerging as potentially problematic (e.g. the North Sea), as such areas are likely to lack sufficient seismic monitoring.

The dependency of empirical GMPEs on complete ground-motion datasets has led to the emergence of more GMPEs for induced seismicity being developed using the stochastic method (Tab. 3.0). In effect, the stochastic method distils the ground-motion parameters obtained from observed ground-motions within a region to produce a stochastic (input) model from which many simulated ground-motions can be generated and a GMPE can be fitted to (Boore, 2003). Therefore, whilst the stochastic method still requires observed ground-motions, the need for a complete ground-motion dataset is minimised (due to the generation of many simulated ground-motions), and consequently is suitable for use in areas experiencing induced seismicity but lacking in seismic monitoring (e.g. the North Sea). In addition to generating many (synthetic) ground-motion records, the stochastic method permits the extrapolation of GMPEs to larger magnitudes. For example, Bommer et al. (2017b) used stochastic simulations to extrapolate the maximum magnitude of their GMPE (for the Groningen field) from  $M_L$  3.6 (the Huizinge earthquake – the largest observed earthquake in the region) to  $M_L$  6.5 (the largest magnitude of interest to hazard calculations for the region). However, there is additional epistemic uncertainty associated with extrapolating to larger magnitudes than within the observed ground-motions (Bommer et al., 2017b). Bommer et al. (2017b) accounted for this additional epistemic uncertainty through introducing magnitude-dependent stress parameter models (in addition to magnitude-independent stress parameter models) and the construction of alternative (higher and lower) models through the variation of the stress parameter itself. The majority of stochastic GMPEs for induced seismicity have been developed to predict ground-shaking associated with hydrocarbon production, predominantly within the Groningen field, but also to a marginally lesser extent within Oklahoma and Kansas (Tab. 3.0). Douglas et al. (2013) developed several stochastic GMPEs for ground-motions associated with geothermal energy production in northwestern Europe. Several stochastic models were developed as a means of accounting for epistemic uncertainty associated with the prediction of median ground-motions due to model selection (in contrast to the measures taken by Bommer et al., 2017b to account for the epistemic uncertainty associated with magnitude extrapolation). Douglas et al. (2013) fitted the GMPEs to this data, and aleatory variability was computed through statistical analysis of the observed ground-motion data (Douglas et al., 2013).

Conventionally, stochastic simulations are used to generate ground-motions from which GMPEs can be fitted, although stochastic simulations are not always used in this manner. Atkinson (2015) developed an empirical GMPE from the Next Generation of Ground-Motion Attenuation Models for the western United States (NGA West) (tectonic) ground-motion record database, and then ratified this GMPE using simulated induced earthquake ground-motion records. This is the only known GMPE for induced

seismicity developed through this approach (using stochastic simulations to generate ground-motion records for induced earthquakes, so as to evaluate an empirical GMPE for the prediction of induced seismicity), but has been included to provide a thorough summary of GMPEs for induced seismicity. Additionally, it should be noted that Gupta et al. (2017) modified the Atkinson (2015) GMPE to be applicable up to distances of 200 km through the incorporation of the geometric spreading term of the Shahjouei and Pezeshk (2016) tectonic GMPE.

Efforts to modify GMPEs developed for tectonic earthquakes to fit ground-motions from induced earthquakes associated with reservoir depletion (hydrocarbon production) were first undertaken by Dost et al. (2013) and Bourne et al. (2015) for the Groningen natural gas field of The Netherlands. In the case of Dost et al. (2013), the lack of recordings of  $M_w \geq 3.6$  induced earthquakes lead to the evaluation of empirical GMPEs from regions with seismicity reasonably similar to the seismicity occurring in the Groningen field (i.e. shallow focal depth, short source-to-site distance earthquakes). Dost et al. (2013) found Akkar et al. (2014)'s pan-European model to be the most suitable GMPE for predicting induced seismicity in the Groningen field following modification to fit PGA and PGV values from 8 recorded anthropogenic earthquakes in the area. Similarly, Bourne et al. (2015) used a combination of ground-motion records indigenous to the Groningen field in addition to supplementary ground-motion records from areas with similar (although tectonic) seismicity to adjust an existing empirical GMPE developed for naturally occurring earthquakes (the Akkar et al., 2014 GMPE) to fit the seismicity of the Groningen field. Both the Dost et al. (2013) GMPE and the Bourne et al. (2015) GMPE are considered within their respective studies to be suitable preliminary models for predicting induced ground-shaking in the Groningen field.

Atkinson and Assatourians (2017) tested how well several GMPEs developed using ground-motion records from tectonic earthquakes predict ground-shaking resulting from seismicity induced by hydrocarbon production in central and eastern North America (CENA). Atkinson and Assatourians (2017) identified three GMPEs as being suitable for predicting anthropogenic ground-shaking in CENA: (1) Abrahamson et al. (2014); (2) Atkinson (2015) and (3) Yenier and Atkinson (2015). These GMPEs were found to predict median ground-motions reasonably well for the magnitude range (3.5 – 6) and distance range (0 – 50 km) deemed by Atkinson and Assatourians (2017) to be of interest for hazard calculations associated with induced earthquakes. Atkinson and Assatourians (2017) show that these models can be used as proxies for GMPEs specifically developed for induced seismicity, rather than selecting them as suitable GMPEs for modification to better account for anthropogenic earthquakes, as is undertaken by Dost et al. (2013) and Bourne et al. (2015).

### 3.2.1 The Development of GMPEs for Induced Seismicity in the North Sea

The development of an original North Sea GMPE would prove challenging due to the limited seismic monitoring in the region resulting in an insufficient size ground-motion dataset for the development of a GMPE from the ground-up. Consequently, the development of a GMPE specifically for predicting the induced seismicity associated with hydrocarbon production in the region would prove even more difficult. This difficulty would primarily arise from the selection of only ground-motion records associated with induced seismicity further reducing the size of the ground-motion dataset available for the development of a North Sea GMPE. Furthermore, the development of North Sea GMPE for induced seismicity would require separating induced and tectonic earthquakes in an earthquake catalogue of tens to hundreds of North Sea earthquakes, which would prove difficult due to the North Sea not being aseismic prior to the onset of hydrocarbon production in the region, unlike in the Groningen field, which was aseismic prior to gas production (van Eck et al., 2006). Such difficulties are demonstrated in Chapter 2, where the identification of 27 potentially induced earthquakes was associated with much uncertainty.

The difficulty associated with differentiating induced and tectonic earthquakes is also well documented within the literature. Atkinson (2018) showed that the average macroseismic intensities of earthquake can be used to differentiate between tectonic and induced origins due to induced earthquakes having smaller average macroseismic intensities beyond a source-to-site distance of 10 km, but noted that this method had several caveats which still make the identification of induced earthquakes highly challenging. Firstly, due to the predicted intensity signatures being closely related to the focal depths, there is the possibility of misidentifying tectonic earthquakes with shallow focal depths as induced (Atkinson, 2018). Secondly, the intensity signatures of large ( $M_L > 6$ ) induced and tectonic earthquakes are expected to be similar due to the effects of focal depths on stress parameter becoming less prominent (Atkinson, 2018). Finally, this approach has been developed for average intensities, so probably will not be very effective for use on specific earthquakes. Douglas et al. (2013) showed with multiple regional ground-motion datasets that tectonic and induced GMPEs are statistically indistinguishable, further illustrating the difficulties associated with identifying anthropogenic earthquakes within areas like the North Sea which experience both tectonic and induced seismicity.

Considering the challenges associated (1) with developing a North Sea GMPE from the ground up and (2) the developing of GMPE specifically for induced seismicity, the modification of an existing GMPE to predict ground-shaking associated with all seismicity within the region is the most suitable approach for improving North Sea PSHA going forward.

**Table 3.0** Table of some notable GMPEs (up to 2020) which were developed to predict ground-shaking resulting from induced seismicity. SA = spectral acceleration.

- “~” = Value not explicitly stated and therefore inferred from the corresponding publication.
- “Emp.” = GMPE developed using the empirical (conventional) method of performing non-linear regression on observed ground-motion records (in this context records associated with induced earthquakes).
- “Stoch.” = GMPE developed using the stochastic point-source model simulation method.
- “Mod.” = GMPE developed by modifying a GMPE original constructed for predicting ground-shaking associated with tectonic earthquakes to fit the ground-shaking associated with induced earthquakes.

Reference	Region	Type of Induced Seismicity	$M_{min}$	$M_{max}$	$M$ scale	$r_{min}$	$r_{max}$	$r$ scale	IM	Dev. Method
McGarr and Fletcher (2005)	Central Utah	Coal Mining	0.98	4.2	$M_w$	0.5	10	$R_{hyp}$	PGV, PGA, SA	Emp.
Bommer et al. (2006)	El Salvador	Geothermal Energy	~0.3	~4.4	$M_L$	~0	~30	$R_{hyp}$	PGV	Mod.
Srinivasan et al. (2008)	Kolar Gold Fields, South India	Gold Mining	0	3	$M_L$	0	5	$R_{hyp}$	PGA	Emp.
Douglas et al. (2013)	Northwestern Europe	Geothermal Energy	1	4	$M_w$	0	20	$R_{hyp}$	PGV, PGA, SA	Stoch.
Dost et al. (2013)	Groningen Gas Field, The Netherlands	Hydrocarbon Production	~ 1.5	~ 5	$M_w$	~ 0	~ 50	$R_{hyp}$	PGV, PGA	Mod.
Sharma et al. (2013)	Northern California	Geothermal Energy	1.3	3.3	$M_w$	0.5	20	$R_{hyp}$	PGV, PGA, SA	Emp.
Atkinson (2015)	Western United States of America	Hydrocarbon Production	3	6	$M_w$	0	40	$R_{hyp}$	PGV, PGA, SA	Emp. + Stoch.
Bourne et al. (2015)	Groningen Gas Field, The Netherlands	Hydrocarbon Production	~ 1.5	~ 6.5	$M_w$	~ 0	~ 15	$R_{hyp}$	PGV, PGA	Mod.
Bommer et al. (2015)	Groningen Gas Field, The Netherlands	Hydrocarbon Production	1.0	6.5	$M_w$	0	60	$R_{epi}$	SA	Stoch.
Bommer et al. (2016)	Groningen Gas Field, The Netherlands	Hydrocarbon Production	2.5	3.6	$M_L$	0	30	$R_{epi}$	PGV	Emp.
Bommer et al. (2017a)	Groningen Gas Field, The Netherlands	Hydrocarbon Production	1.8	3.6	$M_L$	0	35	$R_{epi}$	PGV	Emp.
Bommer et al. (2017b)	Groningen Gas Field, The Netherlands	Hydrocarbon Production	2.5	6.5	$M_L$	0	60	$R_{epi}$	SA	Stoch.
Bydlon et al. (2017)	North-Central Oklahoma and South-Central Kansas	Hydrocarbon Production	3	4	$M_w$	0	200	$R_{hyp}$	PGV, PGA, SA	Stoch.
Gupta et al. (2017)	Central and Eastern United States	Hydrocarbon Production	3	5.5		0	200	$R_{hyp}$	PGV, PGA, SA	Emp. + Stoch. + Mod.
Rashedi and Mahani (2017)	Western Canada	Hydrocarbon Production	3.5	4.6	$M_w$	~ 0	~ 1000	$R_{epi}$	PGV, PGA	Emp.
Yenier et al. (2017)	Oklahoma	Hydrocarbon Production	3	6	$M_w$	3	150	$R_{rup}$	PGV, PGA, SA	Emp.
Bommer et al. (2018)	Groningen Gas Field, The Netherlands	Hydrocarbon Production	2.5	~ 7	$M_L$	~ 0	~ 40	$R_{rup}$	PGV, SA	Stoch.

**Continuation of Table 3.0** Table of some notable GMPEs (up to 2020) which were developed to predict ground-shaking resulting from induced seismicity.

<i>Reference</i>	<i>Region</i>	<i>Type of Induced Seismicity</i>	$M_{min}$	$M_{max}$	$M$ scale	$r_{min}$	$r_{max}$	$r$ scale	<i>IM</i>	<i>Dev. Method</i>
Edwards et al. (2018)	Groningen Gas Field, The Netherlands	Hydrocarbon Production	2	7	$M_w$	0	60	$R_{epi}$	PGV, PGA, SA	Stoch.
Mahani and Kao (2018)	Northeast British Columbia, Canada	Hydrocarbon Production	1.5	3.8	$M_L$	0	45	$R_{hyp}$	PGV, PGA, SA	Emp.
Sharma and Convertito (2018)	The Geysers, USA	Geothermal Energy	0.7	3.3	$M_w$	0.1	73	$R_{hyp}$	PGV, PGA, SA	Emp.
Novakovic et al. (2018)	Oklahoma	Hydrocarbon Production	3.5	5.8	$M_w$	2	500	$R_{hyp}$	PGV, PGA, SA	Emp.
Bydlon et al. (2019)	North-Central Oklahoma and South-Central Kansas	Hydrocarbon Production	3	5.8	$M_w$	0	40	$R_{hyp}$	PGV, PGA, SA	Stoch.
Zalachoris and Rathje (2019)	Texas, Oklahoma and Kansas	Hydrocarbon Production	3	5.8	$M_w$	0	500	$R_{hyp}$	PGV, PGA, SA	Mod.

### 3.3 Testing of Existing Ground-Motion Prediction Equations within the North Sea

The following work on the evaluation of North Sea GMPEs is also provided in Brooks et al. (2020).

As discussed above, to modify an existing GMPE, a base model must first be identified. Here, an extensive residual analysis is undertaken to identify the best performing GMPEs for the North Sea. Residual analysis computes ground-motion residuals,  $\delta_i$ :

$$\delta_i = Z_{obs} - Z_{pred} \quad (3.8)$$

where  $Z_{obs}$  and  $Z_{pred}$  are the observed and predicted ground-motion in either base natural log or base log10. The ground-motion residual is defined as the difference between the observed and predicted ground-motion, and is representative of the component of ground-motion not explained by the GMPE. Logarithms of the observed and predicted ground-motion are taken because ground-motion amplitudes are assumed to be log-normally distributed with a mean of zero and a standard deviation of  $\sigma$  (Strasser et al, 2009). A negative residual indicates over-prediction and a positive residual indicates under-prediction (by the GMPE).

### 3.4 Preparation of the North Sea Dataset

Before GMPE testing, a dataset of North Sea ground-motion records (henceforth referred to as the North Sea dataset) was prepared. The preliminary data used for the compilation of the North Sea dataset was extracted from the European Integrated Data Archive (EIDA) broadband strong motion record database. This dataset was provided by Dr. Dino Bindi (GFZ Potsdam). The preliminary dataset covered the entirety of north-western Europe (Fig. 3.8), and comprised of 38,562 ground-motion records for 773 unique rupture events and 634 seismograph stations. A band-pass filter of 1-10 Hz was applied to remove noise from the ground-motion records in this preliminary dataset. The corner-frequencies (1 Hz, 10 Hz) of this filter were constrained using several signal-to-noise ratios.

The first stage of preparing the North Sea dataset was to remove all ground-motion records pertaining to earthquakes of  $M_L < 2.5$  or source-to-site distances greater than 500 km from the preliminary dataset (Fig. 3.8; Fig. 3.9). To remove potentially erroneous ground-motion records from the preliminary dataset, initial residual analysis was carried out using MATLAB. The GMPE chosen for this initial residual analysis was the Bragato and Slejko (2005) GMPE. The Bragato and Slejko (2005) GMPE covers a similar magnitude range to that of the preliminary dataset and requires few input parameters, thus justifying its selection. From this residual analysis, all records associated with base log10 residuals smaller than -2 or greater than 2 were removed from the dataset (Fig. 3.8; Fig. 3.9). From the preliminary residual analysis, a moderate increase in residuals with distance is observed, resulting in a greater under-prediction of the corresponding peak ground acceleration (PGA) values by the Bragato and Slejko (2005) GMPE (Fig. 3.9). The Bragato and Slejko (2005) GMPE is designed for north-east Italy, a more tectonically active region than the North Sea (Bragato and Slejko, 2005). The anelastic attenuation

modelled in the Bragato and Slejko (2005) GMPE for north-east Italy is (probably) higher than the anelastic attenuation in the North Sea. Therefore, at larger distances the ground-motions are also higher than expected, explaining the observed (absolute) increase in residuals with distance.

Following preliminary residual analysis all earthquakes originating from outside of the North Sea were removed. Very few events in the southern North Sea remained post-residual analysis. The seismicity in the southern North Sea is potentially very different to the seismicity in the northern North Sea. Consequently, the few remaining southern North Sea earthquakes were also removed. This geographical filtering resulted in a significantly smaller (but high quality) dataset comprising of 120 ground-motion records for 50 unique rupture events and 17 seismograph stations (Fig. 3.8; Fig. 3.9). Finally, the ground-motion records checked for noise contamination by inspection of observed vs predicted spectra, of which such contamination was found to be minimal.

It should be noted that the North Sea dataset is inherently limited because offshore seismic monitoring in the North Sea is minimal. Therefore, following the filtering process very few near-source ( $< 50$  km source-to-site distance) or larger magnitude ( $M_L > 4.0$ ) ground-motion records are available (Fig. 3.9). The relative lack of large magnitude, offshore data increases the uncertainty associated with calibrating GMPEs for predicting higher levels of hazard. Furthermore, the North Sea dataset is limited to magnitudes below those which are of high interest to seismic hazard calculations for offshore infrastructure in the North. This therefore represents a significant (but acknowledged) weakness in this analysis. Data from near-source seismometers (i.e. seismometers installed on offshore platforms or seafloor seismic monitoring networks) was sought, however such data was not accessible. The distribution of earthquakes within the North Sea dataset is also noticeably different both geographically and temporally to the dataset used within the Bungum et al. (1997) PSHA; the ground-motion records within the North Sea dataset pertain exclusively to earthquakes originating in the northern North Sea and are from 1988 onwards, whereas the records in the Bungum et al. (2000) dataset cover the northern and southern North Sea, and in fact terminate at around 1988 (personal correspondence with Hilmar Bungum). Consequently, this represents a source of uncertainty for the comparison of more recent GMPEs to the GMPEs used in the Bungum et al. (2000) logic tree, as one is assuming North Sea earthquakes behave consistently over long periods time.

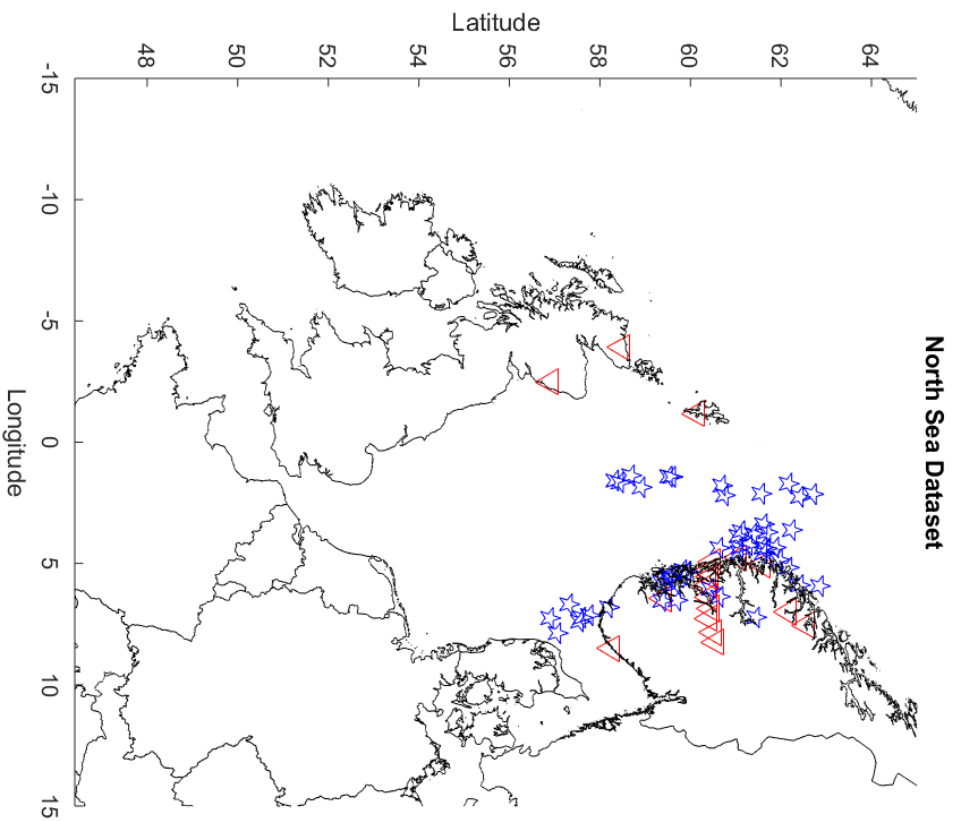
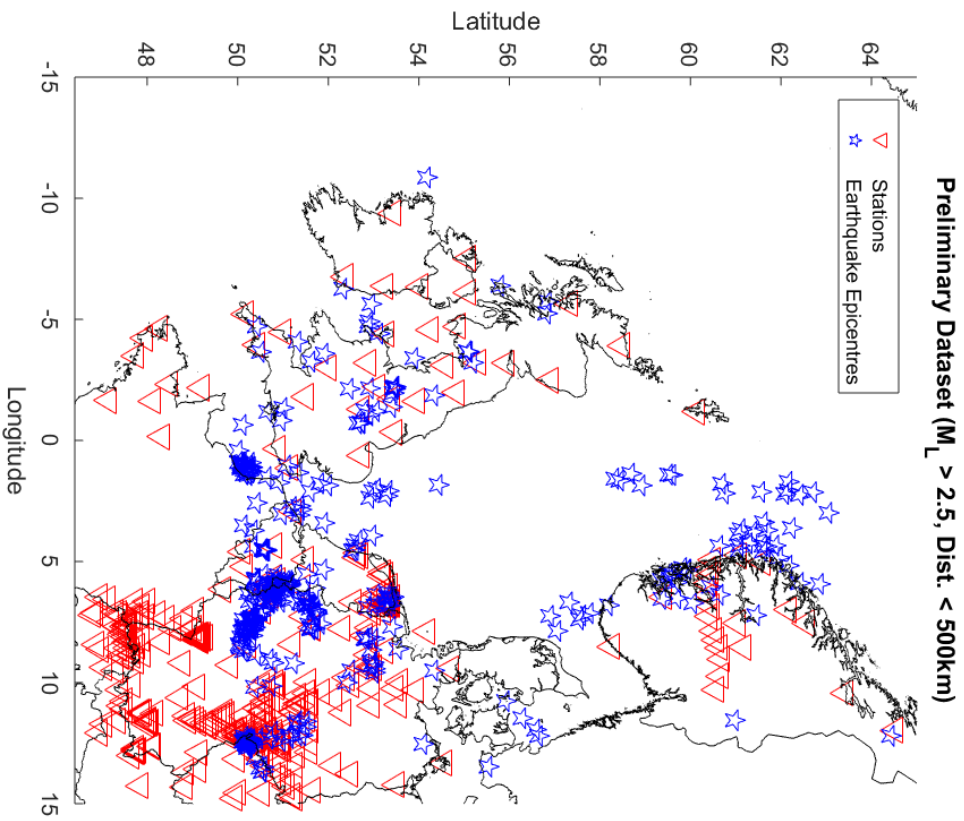


**Figure 3.8** Spatial distributions of the earthquake epicentres and seismograph stations in the preliminary and North Sea datasets.

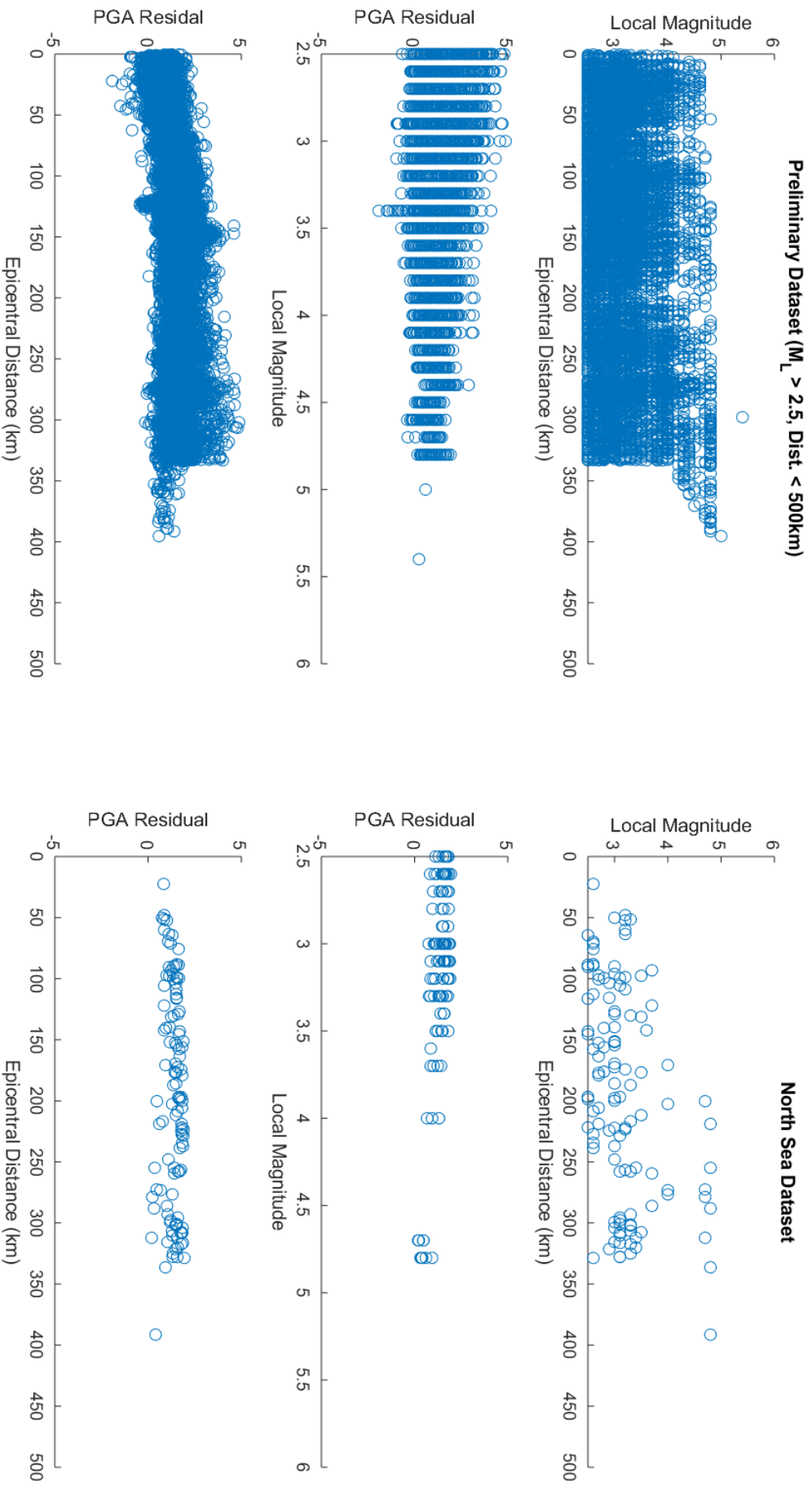


**Figure 3.9** Magnitude-distance distributions, PGA residuals with respect to magnitude and PGA residuals with respect to distance for the preliminary and North Sea datasets. The residuals were computed using the Bragato and Slejko (2005) GMPE.

### 3.5 North Sea GMPE Testing Methodology

Following the compilation of the North Sea dataset, GMPE testing was undertaken using the Python/OpenQuake-based *gmpe-smtk* toolkit (Global Earthquake Model Foundation, 2019). This toolkit enabled quick and effective comparison of the North Sea ground-motion records with numerous GMPEs, providing an efficient and error-free method of identifying the most appropriate GMPEs for the North Sea. The toolbox generated residuals were computed in natural log base. This residual analysis evaluated GMPE performance for various ground-motion intensity measures: (1) PGA, (2) spectral acceleration (SA) for various spectral periods (0.1 s, 0.5 s and 1 s) and (3) PGV.

GMPE testing within the *gmpe-smtk* toolkit was undertaken with 16 GMPEs (Tab. 3.1). The 16 GMPEs were chosen primarily on the basis that they were developed for use in Europe, and approximately suitable in terms of magnitude range and source-to-site distances of the North Sea dataset. Equality between RotD50 and geometric mean was assumed for the considered GMPEs which were developed for RotD50. This assumption is justified by the relations observed between these two horizontal-component ground-motion intensity measures by Boore and Kishida (2017). The GMPE evaluation method used is similar to that described within McNamara et al. (2018): The fit of each model was determined through the minimum trend in residuals. The residuals of the dataset were evaluated with respect to magnitude and distance. The inter-event standard deviation ( $\tau$ ), intra-event standard deviation ( $\Phi$ ), bias (mean residual) of each model and p-values with respect to both magnitude and distance were also considered. In this study a p-value of less than 0.1 is considered as statistically significant, thus representing a trend of over- or under-predicting PGA with respect to either magnitude or distance. However, a p-value of 0.05 is a more common choice. The inter-event standard deviation is associated with event specific factors e.g. randomness in the source process. The intra-event standard deviation represents the variability associated with record specific factors (e.g. site amplification) for the same event. Fits were assigned to each GMPE for each ground-motion intensity measure considered using the criteria described in Tab. 3.1. It should be noted that despite the Ambraseys et al. (1996) GMPE comprising one half of the Bungum et al. (2000) GMPE logic tree, this GMPE is not currently available within the OpenQuake engine, and therefore could not be evaluated in this GMPE testing procedure.

For the use of the processed North Sea dataset within the *gmpe-smtk* toolkit, the data had to be manipulated into flat files. Several source and site parameters were approximated for on the basis that none of the events in the processed dataset possessed magnitudes greater than  $M_L$  4.8. Therefore, these parameters were determined using the following assumptions:

1. The distance from the site (station) to the fault rupture ( $R_{rup}$ )  $\sim$  hypocentral distance ( $R_{hyp}$ )
2.  $R_{hyp}$  was determined through the following relationship:

$$R_{hyp} = \sqrt{R_{epi}^2 + D_{hyp}^2} \quad (3.9)$$

3. The Joyner-Boore distance ( $R_{jb}$ )  $\sim$  epicentral distance ( $R_{epi}$ )
4. The horizontal distance from the site to the top edge of the rupture measured normal to the strike of the fault ( $R_x$ )  $\sim -R_{epi}$  (this approximation negates hanging wall effects)
5. The horizontal distance from the site to the termination of the rupture measured parallel to the strike of the fault ( $R_{y0}$ )  $\sim R_{epi}$
6. Depth to top of rupture  $\sim$  hypocentral depth ( $D_{hyp}$ )
7. Surface rupture length (SRL) and width (SRW) were assumed to have an aspect ratio of 1. These values were approximated from the following relationship determined by Wells and Coppersmith (1994) (see table 2A of Wells and Coppersmith (1994) for more details):

$$m = a + b * \log(SRL) \quad (3.10)$$

where  $m$  represents the earthquake's magnitude and  $a$  and  $b$  are constants determined from regression (5.16 and 1.12 respectively). This relationship is the most appropriate for use with the North Sea dataset because it is applicable to events with strike-slip focal mechanisms.

8. A uniform value of the average shear-wave velocity of the top 30m,  $V_{s30}$ , of 600m/s was assumed for all stations (due to a lack of available subsurface geotechnical information for each site), corresponding to an upper 30m comprising of tens of metres of very dense sand, gravel or very stiff clay, according to the Eurocode 8 earthquake design code (BS EN 1998, 2004).

9. The moment magnitude ( $M_w$ ) used by all of the GMPEs considered is equivalent to the  $M_L$  or body-wave magnitude ( $m_b$ ) listed within the EIDA database. Within this investigation a large proportion of the raw data used was provided with magnitudes measured on the  $M_L$  scale ( $\sim$  90% of ground-motion records). However, considering that (1) earthquakes originating in the North Sea are limited in size (i.e. they are highly improbable to be so large the  $M_L$  scale underestimates the size of them) and (2) only ground-motion records pertaining to seismographs within 500 km of the earthquakes are included within the database, the use of  $M_L$  rather than  $M_w$  should not be problematic (Kramer, 2014). It should be noted however that certain studies have shown that  $M_L$  only scales well with  $M_w$  for earthquakes of a limited size. For example, Edwards et al. (2010) determined that for Switzerland  $M_L$  only scales with  $M_w$  from approximately 3.5 to 7.

**Table 3.1** GMPE testing fit criteria.

GMPE Fit	Conditions for GMPE fit
Good	$-1.5 \leq \text{bias} \leq 1.5$ & p-value (mag) $\geq 0.01$ & p-value (dist) $\geq 0.01$
Moderate	$-2.5 \leq \text{bias} \leq 2.5$ & p-value (mag) $\geq 0.0001$ & p-value (dist) $\geq 0.0001$
Poor	bias $< -2.5$ or bias $> 2.5$ or p-value (mag) $< 0.00001$ or p-value (dist) $< 0.00001$

**Table 3.2** GMPEs considered within residual analysis of the North Sea dataset.

GMPE	Region(s)	Moment Magnitude Range	Distance Range (km)	Reference
Ambraseys et al., 1996	Europe	4.0 – 7.5	0 – 200 ( $R_{jb}$ )	Ambraseys, N., Simpson, K. and Bommer, J.J. (1996). Prediction of Horizontal Response Spectra in Europe. <i>Earthquake Engineering &amp; Structural Dynamics</i> , <b>25</b> (4), pp.371-400.
Abrahamson et al., 2014	Global: active crustal regions	5.0 – 8.5	0 – 200 ( $R_{rup}$ , $R_{jb}$ , $R_x$ and $R_{y0}$ )	Abrahamson, N.A., Silva, W.J. and Kamai, R. (2014). Summary of the ASK14 ground motion relation for active crustal regions. <i>Earthquake Spectra</i> , <b>30</b> (3), pp.1025-1055.
Akkar and Bommer, 2010	Europe/ Mediterranean/ Middle East	4.0 – 7.6	0 – 200 ( $R_{jb}$ )	Akkar, S. and Bommer, J.J. (2010). Empirical equations for the prediction of PGA, PGV and spectral accelerations in Europe, the Mediterranean region and the Middle East. <i>Seismological Research Letters</i> , <b>81</b> (2), pp. 195-206.
Akkar and Cagnan, 2010	Turkey	3.5 – 7.6	0 – 200 ( $R_{jb}$ )	Akkar, S. and Çağnan, Z. (2010). A local ground motion predictive model for Turkey and its comparison with other regional and global ground motion models. <i>Bulletin of the Seismological Society of America</i> , <b>100</b> (6), pp.2978-2995.
Akkar et al., 2014 ( $R_{epi}$ ) Akkar et al., 2014 ( $R_{hyp}$ ) Akkar et al., 2014 ( $R_{jb}$ )	Europe/Middle East	4.0 – 7.6	0 – 200 ( $R_{epi}$ , $R_{hyp}$ and $R_{jb}$ )	Akkar, S., Sandikkaya, M. A. and Bommer, J.J. (2014). Empirical ground motion models for point- and extended-source crustal earthquake scenarios in Europe and the Middle East. <i>Bulletin of Earthquake Engineering</i> , <b>12</b> (1), pp.359-387.
Boore and Atkinson, 2008	Global: active crustal regions	5.0 – 8.0	0 – 200 ( $R_{jb}$ )	Boore, D.M. and Atkinson, G. (2008). Ground motion prediction equations for the average horizontal component of PGA, PGV, and 5%-damped PSA at spectral periods between 0.01s and 10.0s. <i>Earthquake Spectra</i> , <b>24</b> (1), pp.99-138.
Boore et al., 2014	Global: active crustal regions	3.0 – 8.5	0 – 400 ( $R_{jb}$ )	Boore, D.M., Stewart, J.P., Seyhan, E. and Atkinson, G. (2014). NGA-West 2 equations for predicting PGA, PGV, and 5%-damped PSA for shallow crustal earthquakes. <i>Earthquake Spectra</i> , <b>30</b> (3), pp.1057-1085.
Bindi et al., 2017 ( $R_{jb}$ ) Bindi et al., 2017 ( $R_{hyp}$ )	Global: active crustal regions	3.0 – 8.0	0 – 300 ( $R_{jb}$ , $R_{hyp}$ )	Bindi, D., Cotton, F., Kotha, S.R., Bosse, C., Stromeyer, D. and Grünthal, G. (2017). Application-driven ground motion prediction equation for seismic hazard assessments in non-cratonic moderate-seismicity areas. <i>Journal of Seismology</i> , <b>21</b> , pp.1201-1218.
Campbell and Bozorgnia, 2014	Global: active crustal regions	3.0 – 8.5	0 – 300 ( $R_{rup}$ , $R_{jb}$ and $R_x$ )	Campbell, K.W. and Bozorgnia, Y. (2014). NGA-West2 ground motion model for the average horizontal components of PGA, PGV, and 5%-damped linear acceleration response spectra. <i>Earthquake Spectra</i> , <b>30</b> (3), pp.1087-1115.
Chiou and Youngs, 2014	Global: active crustal regions	3.0 – 8.5	0 – 300 ( $R_{rup}$ , $R_{jb}$ and $R_x$ )	Chiou, B.S.J. and Youngs, R.R. (2014). Update of the Chiou and Youngs NGA model for the average horizontal component of peak ground motion and response spectra. <i>Earthquake Spectra</i> , <b>30</b> (3), pp.1117-1153.
Cauzzi et al., 2015	Global: active crustal regions	4.5 – 8.0	0 – 150 ( $R_{rup}$ )	Cauzzi, C., Faccioli, E., Vanini, M. and Bianchini, A. (2015). Updated predictive equations for broadband (0.01–10 s) horizontal response spectra and peak ground motions, based on a global dataset of digital acceleration records. <i>Bulletin of Earthquake Engineering</i> , <b>13</b> (6), pp.1587-1612.
Rietbrock et al., 2013	United Kingdom	2.0 – 6.5	0 - 400 ( $R_{jb}$ )	Rietbrock, A., Strasser, F., Edwards, B. (2013). A Stochastic Earthquake Ground Motion Prediction Model for the United Kingdom. <i>Bulletin of the Seismological Society of America</i> , <b>103</b> (1), pp.57-77.
Toro et al., 1997	Central and Eastern North America	5.0 – 8.0	0 – 500 ( $R_{jb}$ )	Toro, G., Abrahamson, N. and Schneider, J. (1997). Model of Strong Ground Motions from Earthquakes in Central and Eastern North America: Best Estimates and Uncertainties. <i>Seismological Research Letters</i> , <b>68</b> (1), pp.41-57.
Toro et al., 2002	Central and Eastern North America	5.0 – 8.0	0 – 500 ( $R_{jb}$ )	Toro, G. (2002). <i>Modification of the Toro et al. (1997) Attenuation Equations for Large Magnitudes and Short Distances</i> . Risk Engineering, Inc.

### 3.6 North Sea GMPE Testing with Respect to Peak Ground Acceleration

The North Sea dataset was first evaluated using the PGA ground-motion intensity measure (Tab. 3.3). Of the GMPEs evaluated, three appear to provide reasonably good fits for PGA based on the bias, tau, phi and p-values with respect to magnitude and distance. The three GMPEs which provide good fits are the Akkar et al. (2014) GMPE using epicentral distance ( $R_{epi}$ ), the Akkar et al. (2014) GMPE using hypocentral distance ( $R_{hyp}$ ) and the Akkar et al. (2014) GMPE using the distance to the surface projection of the rupture ( $R_{jb}$ ).

The  $R_{jb}$  variant of the Akkar et al. (2014) GMPE provides the best fit for predicting PGA of these three GMPEs. This GMPE provides the lowest bias, inter-event standard deviation and intra-event standard deviation. This GMPE also shows (overall) the smallest trends with respect to both magnitude and distance. The p-values for these trends are both greater than 0.1, and thus can be approximately considered as representing statistically insignificant trends (i.e. no significant over- or under-prediction of PGA at larger magnitudes or smaller distances) (Fig. 3.10).

The Akkar et al. (2014)  $R_{epi}$  GMPE, the Akkar et al. (2014)  $R_{hyp}$  GMPE and the Akkar et al. (2014)  $R_{jb}$  GMPE provide good fits to the observed PGA values for likely several reasons. These GMPEs are pan-European with regards to tectono-geographic applicability, and were developed for shallow focal depth earthquakes. Interestingly, despite these models being applicable down to magnitude ranges of  $M_w$  4 and distances of up to 200 km (Tab. 3.2) and the North Sea dataset largely comprising of (1) earthquakes smaller than  $M_w$  4 and (2) approximately 52% of these earthquakes occurring at distances greater than 200 km, comparatively small statistical trends with respect to both distance and magnitude were determined for these models.

In addition to concluding that the  $R_{jb}$  variant of the Akkar et al. (2014) GMPE is the most suitable GMPE for the North Sea dataset when predicting PGA, testing of the 16 GMPEs shows that the Toro et al. (1997) GMPE (and the Toro et al. (2002) GMPE) predicts PGA poorly in the North Sea (Tab. 3.3). The poor fit of the Toro et al. (1997) GMPE is due to: (1) significant over-prediction and (2) the occurrence of statistically significant trending with respect to both magnitude and distance (Fig. 3.11)<sup>18</sup>.

The constant over-prediction by the Toro et al. (1997) GMPE is most likely the result of the GMPE being primarily applicable to very hard rock sites of very low near-surface attenuation in central and eastern North America ( $\kappa = 0.006$  s for calibration of the Toro et al. (1997) GMPE to these sites) (Toro et al., 2002). Anelastic seismic attenuation is likely greater within the North Sea than in central and eastern North America, as is supported by the observations of poor  $Lg$  wave<sup>19</sup> propagation within

---

<sup>18</sup> Considerably more data points appear on the residual plots pertaining to the Toro et al. (1997) GMPE than for the residual plots pertaining to the other GMPEs tested in this investigation. This is because the Toro et al. (1997) GMPE is programmed within the *gmpe-smtk* toolbox to output only the "total" residuals, unlike the other GMPEs tested here which are programmed to output the inter-event and intra-event residuals.

<sup>19</sup>  $Lg$  waves are effectively a guided waveform which only propagates efficiently in continental (or continental thickness) crust (Chiu and Snyder, 2015).

the North Sea's crust due to the presence of the Central and Viking Grabens in the continental structure of the region (Gregersen and Vaccari, 1993; Sargeant and Ottemöller, 2009). Kennett and Mykkeltveit (1984) showed that when attenuation is superimposed upon these structures, no more than 20% of the energy of the *Lg* waves reaches the far side of such structures. This elevated anelastic seismic attenuation explains the constant over-prediction of ground-motion intensities by the Toro et al. (1997) GMPE.

The considerable over-prediction by the Toro et al. (1997) GMPE for PGA is likely minimised by the equal contribution of the Ambraseys et al. (1996) GMPE within Bungum et al. (2000)'s logic tree. This minimising contribution by the Ambraseys et al. (1996) GMPE is indicated by the seismic hazard curve computed with Bungum et al. (2000)'s logic tree (see Fig. 3.19 below) predicting lower annual frequencies of exceedance (AFOE) for a given level of PGA than the hazard curve computed with Toro et al. (1997) GMPE and higher AFOE for a given level of PGA than the hazard curve computed with the Ambraseys et al. (1996) GMPE. The over-prediction of the Toro et al. (1997) also suggests the uncertainty associated with the differences in the geographical and temporal distributions of the North Sea dataset and the Bungum et al. (2000) dataset is minimal, effectively validating the comparison of more recent GMPEs to the components of the Bungum et al. (2000) logic tree through residual analysis with the North Sea dataset.

It should also be noted that for all ground-motion intensity parameters considered in this analysis that the database-derived intra-event and inter-event uncertainties of each considered GMPE are moderately elevated in comparison to the uncertainties predefined as functions of source-to-site distance and magnitude for each model (Tab. 3.3). These elevated standard deviation values can be attributed to: (1) the considered GMPEs having been developed for regions other than the North Sea, (2) the ground-motion records comprising the North Sea dataset largely pertaining to small size earthquakes recorded at large source-to-site distances (previous studies have found that ground-motions from small events and/or large distances are more variable than those from larger events and/or short distances), (3) uncertainties in the magnitude and distance estimates in the North Sea dataset and (4) the aforementioned lack of information on the near-surface site conditions at the seismometers.

**Table 3.3** Parameters determined from residual analysis for each GMPE with regards to the North Sea dataset for PGA. I.V.D. = Input variable dependent (to compute these standard deviations see the referenced studies).

GMPE	Bias	$\tau$	$\Phi$	$\tau(\text{model})$	$\Phi(\text{model})$	p-value (mag)	p-value (dist)	Model Fit
Abrahamson et al., 2014	1.151	0.637	0.653	I.V.D	I.V.D	$1.164 \times 10^{-4}$	$4.486 \times 10^{-1}$	Moderate
Akkar and Bommer, 2010	-0.008	0.667	0.881	0.099	0.261	$5.708 \times 10^{-6}$	$1.235 \times 10^{-3}$	Poor
Akkar and Cagnan, 2010	1.741	0.760	0.784	0.516	0.653	$1.376 \times 10^{-5}$	$6.317 \times 10^{-5}$	Poor
Akkar et al., 2014 ( $R_{epi}$ )	1.307	0.604	0.778	0.358	0.638	$3.946 \times 10^{-2}$	$4.321 \times 10^{-1}$	Good
Akkar et al., 2014 ( $R_{hyp}$ )	0.988	0.569	0.775	0.347	0.648	$1.802 \times 10^{-1}$	$7.757 \times 10^{-1}$	Good
Akkar et al., 2014 ( $R_{jb}$ )	0.381	0.536	0.750	0.350	0.620	$3.488 \times 10^{-1}$	$7.468 \times 10^{-1}$	Good
Boore and Atkinson, 2008	-0.672	0.598	1.040	0.265	0.502	$6.233 \times 10^{-1}$	$4.361 \times 10^{-7}$	Poor
Boore et al., 2014	1.801	0.735	0.774	I.V.D.	I.V.D.	$3.388 \times 10^{-6}$	$1.499 \times 10^{-1}$	Poor
Bindi et al., 2017 ( $R_{jb}$ )	2.107	0.762	0.896	0.495	0.631	$8.516 \times 10^{-2}$	$5.481 \times 10^{-3}$	Moderate
Bindi et al., 2017 ( $R_{hyp}$ )	1.985	0.717	0.841	0.502	0.638	$9.166 \times 10^{-2}$	$3.101 \times 10^{-2}$	Moderate
Campbell and Bozorgnia, 2014	1.459	0.882	0.800	I.V.D.	I.V.D.	$1.284 \times 10^{-2}$	$2.503 \times 10^{-3}$	Moderate
Chiou and Youngs, 2014	1.377	0.985	0.867	I.V.D.	I.V.D.	$4.802 \times 10^{-1}$	$9.119 \times 10^{-6}$	Poor
Cauzzi et al., 2015	0.467	0.640	0.868	0.259	0.221	$5.863 \times 10^{-4}$	$7.213 \times 10^{-1}$	Poor
Rietbrock et al., 2013	0.150	0.476	0.581	Stochastic	Stochastic	$4.024 \times 10^{-1}$	$9.363 \times 10^{-3}$	Moderate
Toro et al., 1997	-2.369	0.853 (total)		I.V.D.		$6.093 \times 10^{-1}$	$4.670 \times 10^{-7}$	Poor
Toro et al., 2002	-4.323	1.164 (total)		I.V.D.		$1.459 \times 10^{-6}$	$4.517 \times 10^{-3}$	Poor

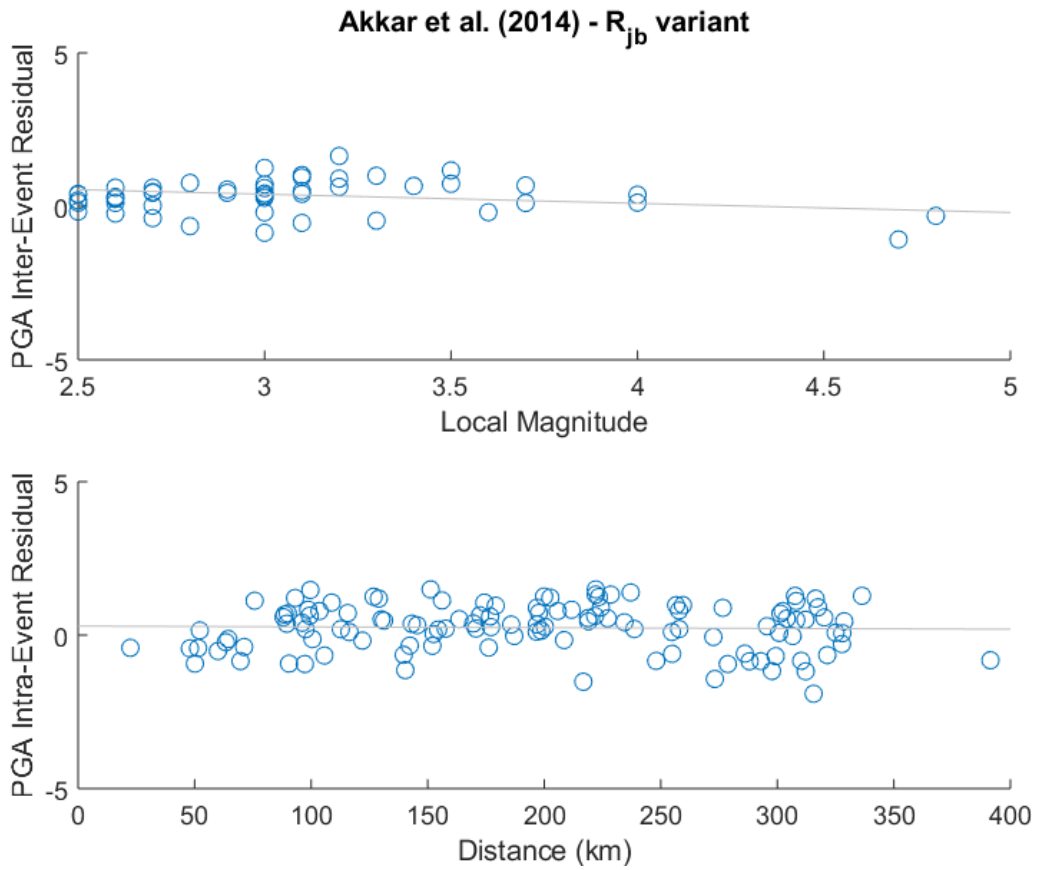


**Figure 3.10** *PGA Residual analysis of the North Sea dataset with respect to local magnitude and epicentral distance, using the Akkar et al. (2014)  $R_{jb}$  GMPE.*

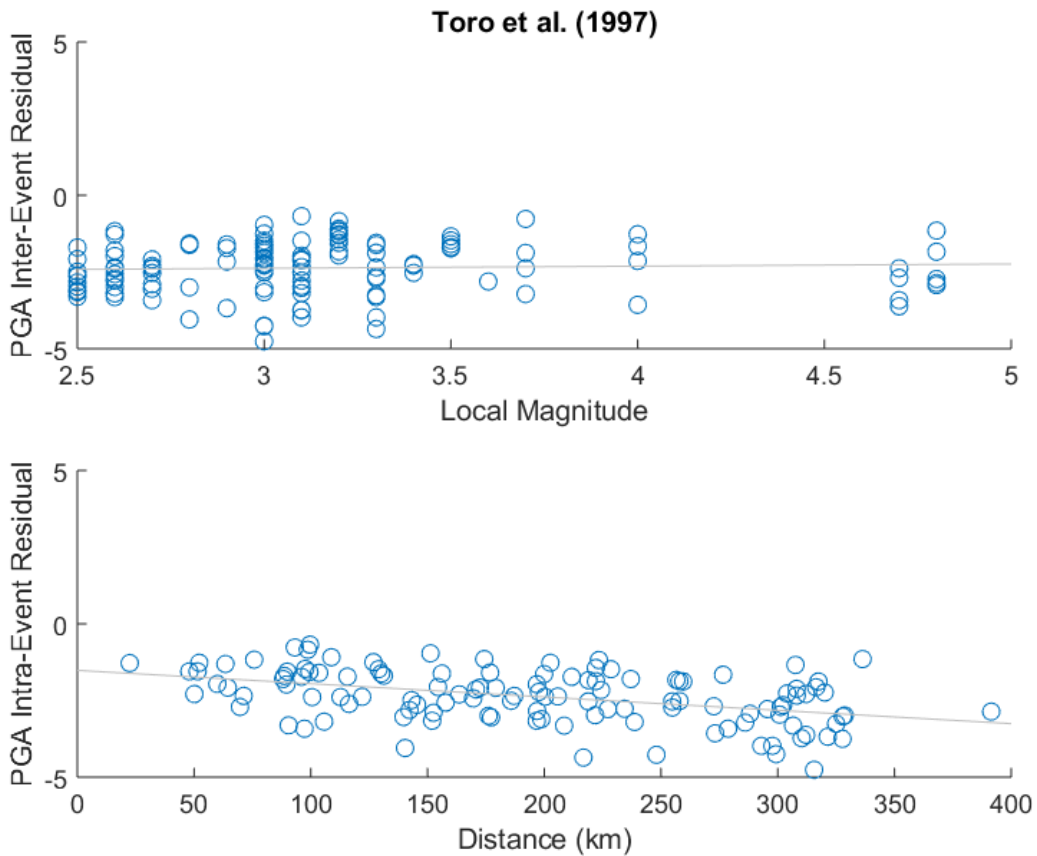


**Figure 3.11** *PGA Residual analysis of the North Sea dataset with respect to local magnitude and epicentral distance, using the Toro et al. (1997) GMPE.*

### 3.7 North Sea GMPE Testing with Respect to Spectral Acceleration

Residual analysis was also undertaken for the North Sea data subset with respect to spectral acceleration at spectral periods of 0.1 s, 0.5 s and 1.0 s with 5% damping.

Overall, both the p-values (with respect to both magnitude and distance) and bias decrease with increasing spectral period. Consequently, in general a decrease in how well the batch of tested GMPEs (Tab. 3.3) fit to the North Sea dataset is observed with an increase in the spectral period (tab 5.4; tab 5.5; tab 5.6). The GMPEs which provide the best fits at the selected spectral periods are largely the same select group as those that provide the best fits to the PGA ground-motion intensity measure.

For a spectral period of 0.1 s all variants of the Akkar et al. (2014) GMPE provide good fits, as they do for predicting PGA. Additionally, the Akkar and Cagnan (2010) GMPE and the Rietbrock et al. (2013) GMPE provide good fits despite only providing a moderate fit when predicting PGA (e.g. Fig. 3.12).

For a spectral period of 0.5 s no GMPEs evaluated provide good fits to the North Sea dataset, although the Abrahamson et al. (2014) GMPE, the Rietbrock et al. (2013) GMPE, the Cauzzi et al. (2015) GMPE and all variants of the Akkar et al., 2014 GMPE provide moderate fits (e.g. Fig. 3.13).

For a spectral period of 1.0 s, all GMPEs tested provide poor fits aside from the Abrahamson et al. (2014) GMPE, which provides a moderate fit (Fig. 3.14). For the majority of the GMPEs, the poor fits are due to significant statistical trends with respect magnitude (Tab. 3.6). For example, the Rietbrock et al., 2013 GMPE and all the variants of Akkar et al., 2014 GMPE provide low bias values, as well as statistically insignificant trends with respect to distance, but considerably larger (statistically significant) trends with respect to magnitude.

Overall, for predicting spectral acceleration values in the North Sea, all variants of the Akkar et al. (2014) GMPE and the Rietbrock et al. (2013) GMPE are the most appropriate GMPEs; these are the only GMPEs of those tested which provide both good fits for spectral periods of 0.1 s and moderate fits for spectral periods of 0.5 s. These GMPEs provide poor fits for spectral periods of 1.0 s, however as discussed above all of the GMPEs considered here bar the Abrahamson et al. (2014) GMPE do for larger spectral periods.

Another key observation is that the Toro et al. (1997) GMPE significantly over-predicts for SA(0.1 s) (Fig. 3.15). The Toro et al. (1997) GMPE does however provide a better fit to SA(0.1 s) than it does for PGA, especially with regards to magnitude and distance dependency (i.e. larger p-values are observed for PGA). At higher spectral periods (0.5 s and 1.0 s) the Toro et al. (1997) GMPE slightly to moderately under-predicts (Fig. 3.16; Fig. 3.17). However, the corresponding p-values with respect to both magnitude and distance are significantly smaller than for PGA or other spectral periods, thus meaning the overall fit is poor for Toro et al., 1997 at these spectral periods also. Interestingly, the overall bias of the Toro et al. (1997) GMPE decreases with increasing spectral period (i.e. the bias is largest when

using the Toro et al. (1997) GMPE to predict PGA, and decreases as the spectral acceleration increases from 0.1 s through to 1.0 s). This trend will need further investigation, as usually GMPEs provide better fits at smaller spectral periods (as is generally observed in this analysis – see Tab. 3.8), rather than larger spectral periods as is the case here for the Toro et al. (1997) GMPE.

**Table 3.4** Parameters determined from residual analysis for each GMPE with regards to the North Sea dataset for SA(0.1 s). I.V.D. = Input variable dependent (to compute these standard deviations see the referenced studies).

GMPE	Bias	$\tau$	$\Phi$	$\tau(\text{model})$	$\Phi(\text{model})$	p-value (mag)	p-value (dist)	Model Fit
Abrahamson et al., 2014	1.583	0.730	0.734	I.V.D	I.V.D	$2.609 \times 10^{-1}$	$4.870 \times 10^{-4}$	Moderate
Akkar and Bommer, 2010	1.027	0.661	0.924	0.117	0.273	$9.939 \times 10^{-4}$	$1.581 \times 10^{-1}$	Moderate
Akkar and Cagnan, 2010	1.239	0.554	0.706	0.518	0.700	$3.989 \times 10^{-1}$	$7.086 \times 10^{-1}$	Good
Akkar et al., 2014 ( $R_{epi}$ )	1.297	0.605	0.782	0.416	0.685	$8.684 \times 10^{-1}$	$2.630 \times 10^{-1}$	Good
Akkar et al., 2014 ( $R_{hyp}$ )	1.255	0.604	0.792	0.412	0.694	$3.642 \times 10^{-1}$	$2.874 \times 10^{-1}$	Good
Akkar et al., 2014 ( $R_{jb}$ )	0.626	0.553	0.762	0.407	0.667	$9.833 \times 10^{-2}$	$9.681 \times 10^{-2}$	Good
Boore and Atkinson, 2008	-0.048	0.650	1.046	0.313	0.520	$4.463 \times 10^{-1}$	$4.463 \times 10^{-7}$	Poor
Boore et al., 2014	2.007	0.734	0.829	I.V.D.	I.V.D.	$4.701 \times 10^{-1}$	$4.721 \times 10^{-4}$	Moderate
Bindi et al., 2017 ( $R_{jb}$ )	2.184	0.789	0.961	0.577	0.680	$9.122 \times 10^{-1}$	$4.514 \times 10^{-6}$	Poor
Bindi et al., 2017 ( $R_{hyp}$ )	2.067	0.741	0.900	0.582	0.684	$8.052 \times 10^{-1}$	$3.310 \times 10^{-5}$	Poor
Campbell and Bozorgnia, 2014	1.662	0.941	0.874	I.V.D.	I.V.D.	$3.062 \times 10^{-1}$	$9.615 \times 10^{-7}$	Poor
Chiou and Youngs, 2014	1.683	1.119	0.956	I.V.D.	I.V.D.	$4.777 \times 10^{-3}$	$2.366 \times 10^{-8}$	Poor
Cauzzi et al., 2015	0.732	0.687	0.892	0.286	0.243	$4.366 \times 10^{-3}$	$1.371 \times 10^{-1}$	Moderate
Rietbrock et al., 2013	0.128	0.539	0.641	Stochastic	Stochastic	$2.826 \times 10^{-1}$	$1.020 \times 10^{-2}$	Good
Toro et al., 1997	-1.989	0.839 (total)		I.V.D.		$7.976 \times 10^{-2}$	$3.232 \times 10^{-2}$	Moderate
Toro et al., 2002	-3.645	1.145 (total)		I.V.D.		$7.500 \times 10^{-9}$	$3.992 \times 10^{-1}$	Poor

**Table 3.5** Parameters determined from residual analysis for each GMPE with regards to the North Sea dataset for SA(0.5 s). I.V.D. = Input variable dependent (to compute these standard deviations see the referenced studies).

GMPE	Bias	$T$	$\Phi$	$\tau(\text{model})$	$\Phi(\text{model})$	p-value (mag)	p-value (dist)	Model Fit
Abrahamson et al., 2014	-0.210	0.714	0.778	I.V.D	I.V.D	$4.530 \times 10^{-4}$	$5.962 \times 10^{-1}$	Moderate
Akkar and Bommer, 2010	-0.259	0.812	1.007	0.117	0.273	$3.582 \times 10^{-11}$	$1.651 \times 10^{-2}$	Poor
Akkar and Cagnan, 2010	0.380	0.899	0.810	0.518	0.700	$2.639 \times 10^{-10}$	$6.953 \times 10^{-4}$	Poor
Akkar et al., 2014 ( $R_{epi}$ )	-0.028	0.694	0.837	0.416	0.685	$4.086 \times 10^{-4}$	$1.638 \times 10^{-1}$	Moderate
Akkar et al., 2014 ( $R_{hyp}$ )	-0.087	0.666	0.842	0.412	0.694	$2.622 \times 10^{-3}$	$2.898 \times 10^{-2}$	Moderate
Akkar et al., 2014 ( $R_{jb}$ )	-0.502	0.672	0.843	0.407	0.651	$6.175 \times 10^{-3}$	$6.076 \times 10^{-2}$	Moderate
Boore and Atkinson, 2008	-4.093	1.232	1.201	0.265	0.555	$2.974 \times 10^{-1}$	$1.129 \times 10^{-2}$	Poor
Boore et al., 2014	0.482	0.954	0.879	I.V.D	I.V.D	$1.341 \times 10^{-20}$	$4.951 \times 10^{-1}$	Poor
Bindi et al., 2017 ( $R_{jb}$ )	0.483	0.817	0.893	0.378	0.639	$4.617 \times 10^{-6}$	$9.118 \times 10^{-1}$	Poor
Bindi et al., 2017 ( $R_{hyp}$ )	0.346	0.777	0.862	0.379	0.648	$5.668 \times 10^{-6}$	$4.491 \times 10^{-1}$	Poor
Campbell and Bozorgnia, 2014	0.360	0.833	0.918	I.V.D	I.V.D	$1.537 \times 10^{-5}$	$2.079 \times 10^{-1}$	Poor
Chiou and Youngs, 2014	0.097	0.778	0.739	I.V.D	I.V.D	$3.485 \times 10^{-9}$	$7.852 \times 10^{-1}$	Poor
Cauzzi et al., 2015	-0.290	0.609	0.853	0.299	0.217	$8.924 \times 10^{-3}$	$2.619 \times 10^{-1}$	Moderate
Rietbrock et al., 2013	0.109	0.774	0.894	Stochastic	Stochastic	$3.784 \times 10^{-3}$	$2.797 \times 10^{-2}$	Moderate
Toro et al., 1997	0.392	1.443 (total)		I.V.D.		$3.486 \times 10^{-23}$	$1.894 \times 10^{-8}$	Poor
Toro et al., 2002	-3.896	1.083 (total)		I.V.D.		$6.810 \times 10^{-1}$	$1.575 \times 10^{-3}$	Poor

**Table 3.6** Parameters determined from residual analysis for each GMPE with regards to the North Sea dataset for SA(1.0 s). I.V.D. = Input variable dependent (to compute these standard deviations see the referenced studies).

GMPE	Bias	$\tau$	$\Phi$	$\tau(\text{model})$	$\Phi(\text{model})$	p-value (mag)	p-value (dist)	Model Fit
Abrahamson et al., 2014	-0.071	0.812	0.734	I.V.D	I.V.D	$2.120 \times 10^{-4}$	$1.117 \times 10^{-1}$	Moderate
Akkar and Bommer, 2010	0.819	1.246	1.117	0.148	0.290	$1.156 \times 10^{-13}$	$2.129 \times 10^{-3}$	Poor
Akkar and Cagnan, 2010	0.640	1.090	0.717	0.641	0.649	$2.377 \times 10^{-13}$	$6.649 \times 10^{-5}$	Poor
Akkar et al., 2014 ( $R_{epi}$ )	0.011	0.795	0.784	0.397	0.692	$6.107 \times 10^{-7}$	$1.952 \times 10^{-1}$	Poor
Akkar et al., 2014 ( $R_{hyp}$ )	-0.068	0.753	0.791	0.383	0.702	$3.802 \times 10^{-6}$	$4.881 \times 10^{-2}$	Poor
Akkar et al., 2014 ( $R_{jb}$ )	-0.369	0.758	0.761	0.394	0.679	$5.163 \times 10^{-6}$	$9.032 \times 10^{-2}$	Poor
Boore and Atkinson, 2008	-2.895	1.063	0.959	0.318	0.573	$5.662 \times 10^{-4}$	$3.631 \times 10^{-2}$	Poor
Boore et al., 2014	0.295	1.058	0.754	I.V.D.	I.V.D.	$3.574 \times 10^{-19}$	$7.445 \times 10^{-1}$	Poor
Bindi et al., 2017 ( $R_{jb}$ )	0.320	0.912	0.746	0.480	0.621	$8.711 \times 10^{-8}$	$9.065 \times 10^{-1}$	Poor
Bindi et al., 2017 ( $R_{hyp}$ )	0.196	0.875	0.719	0.478	0.633	$1.343 \times 10^{-7}$	$3.996 \times 10^{-1}$	Poor
Campbell and Bozorgnia, 2014	0.154	0.995	0.807	I.V.D.	I.V.D.	$8.008 \times 10^{-8}$	$4.192 \times 10^{-1}$	Poor
Chiou and Youngs, 2014	0.038	0.928	0.701	I.V.D.	I.V.D.	$5.810 \times 10^{-14}$	$5.605 \times 10^{-1}$	Poor
Cauzzi et al., 2015	0.010	0.724	0.908	0.296	0.231	$8.605 \times 10^{-5}$	$6.492 \times 10^{-2}$	Poor
Rietbrock et al., 2013	0.199	1.016	1.084	Stochastic	Stochastic	$5.301 \times 10^{-5}$	$3.612 \times 10^{-2}$	Poor
Toro et al., 1997	0.950	1.561 (total)		I.V.D.		$3.097 \times 10^{-33}$	$7.669 \times 10^{-8}$	Poor
Toro et al., 2002	-3.152	1.083 (total)		I.V.D.		$4.041 \times 10^{-5}$	$1.077 \times 10^{-5}$	Poor

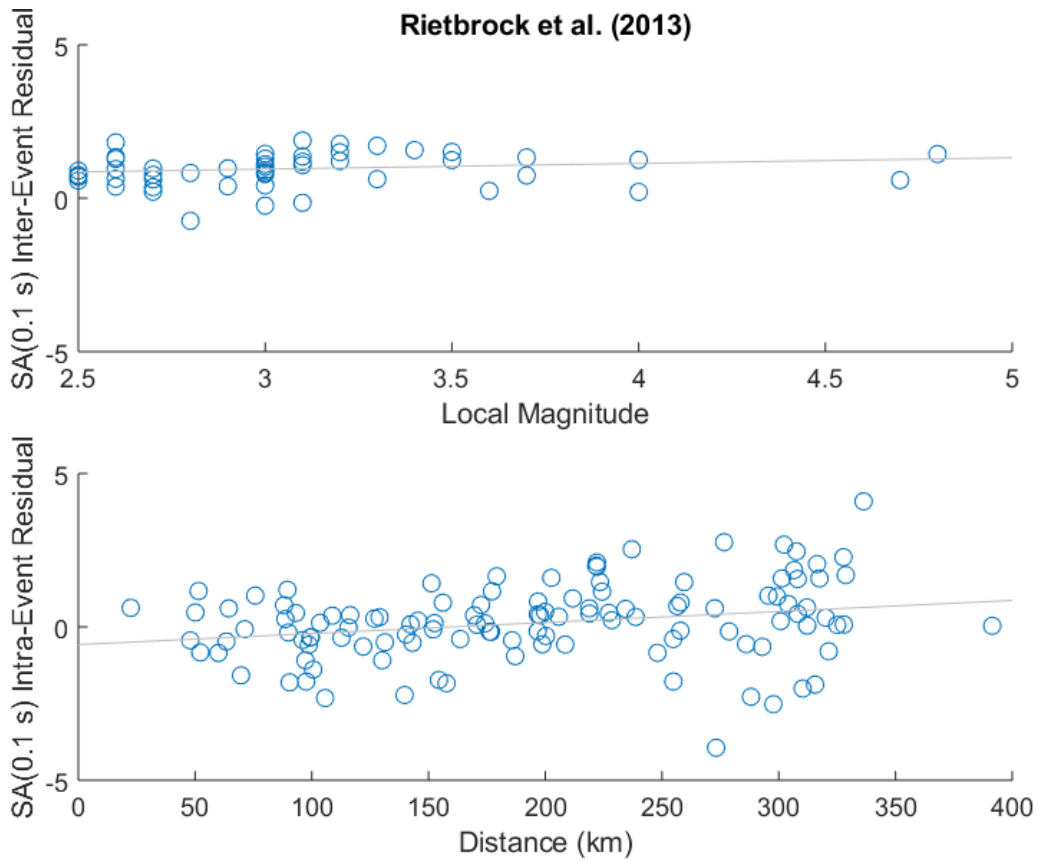


**Figure 3.12** *SA(0.1 s) Residual analysis of the North Sea dataset with respect to local magnitude and epicentral distance, using the Rietbrock et al. (2013) GMPE.*

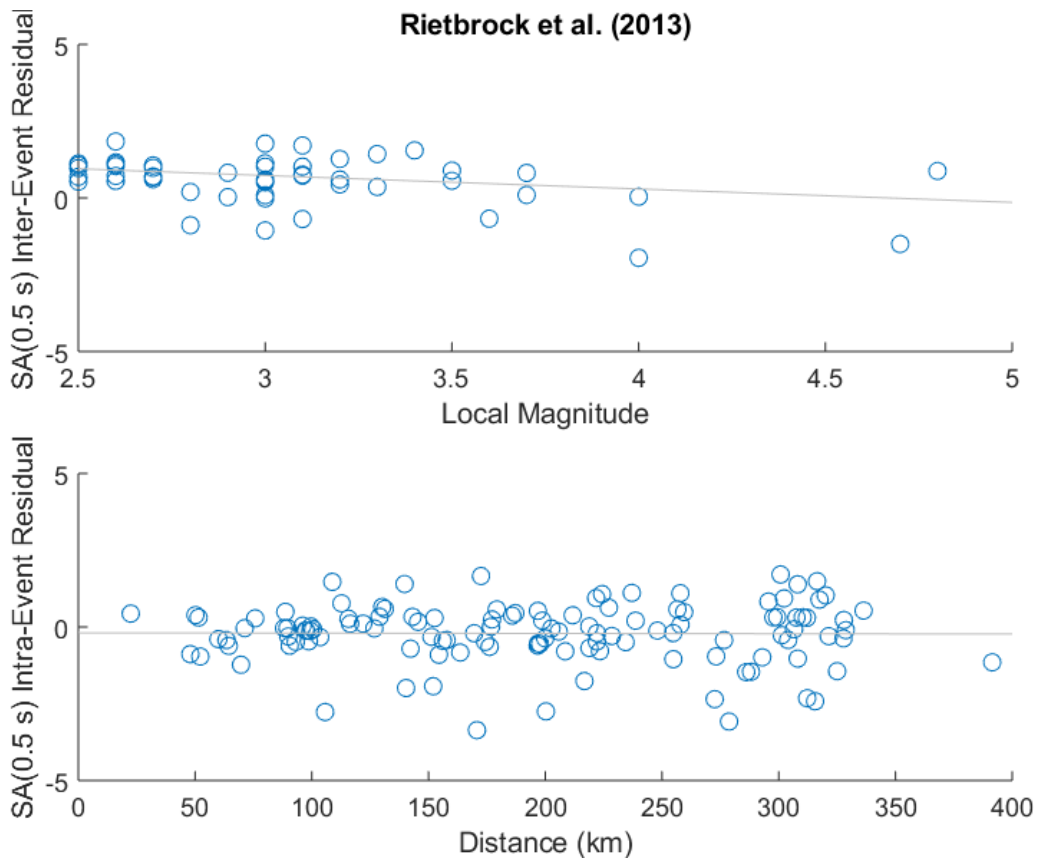


**Figure 3.13** *SA(0.5 s) Residual analysis of the North Sea dataset with respect to local magnitude and epicentral distance, using the Rietbrock et al. (2013) GMPE.*

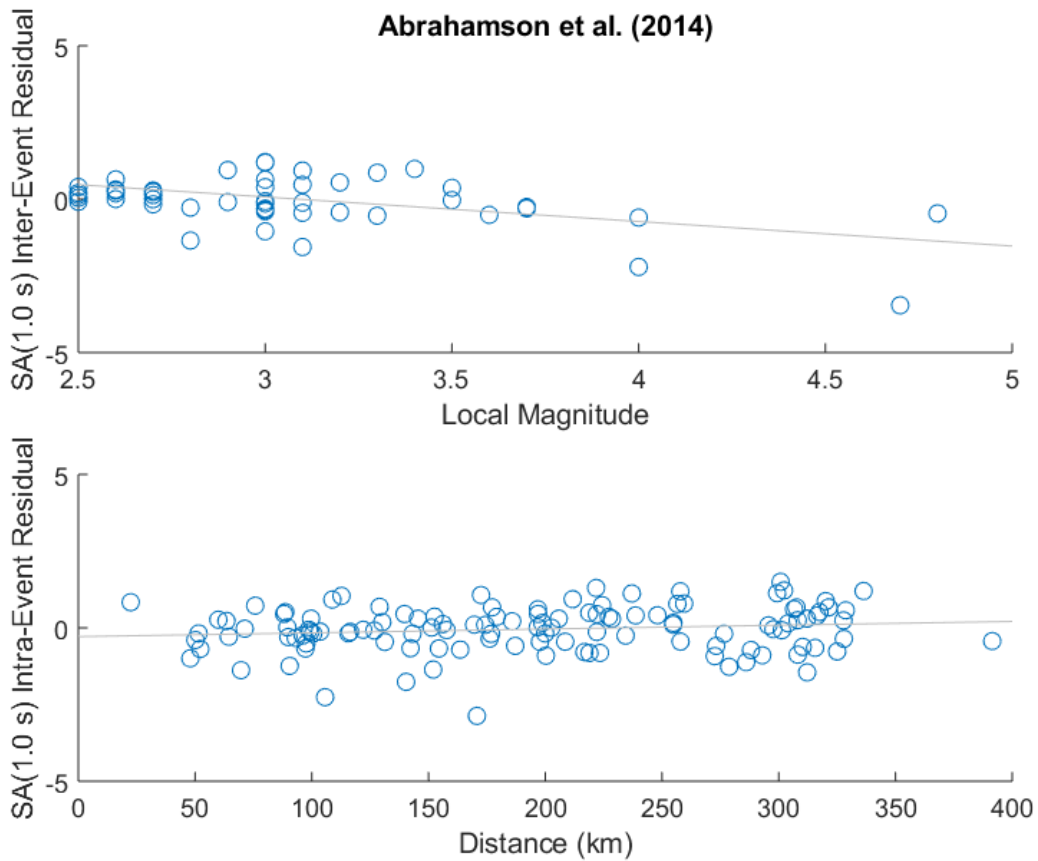


**Figure 3.14** *SA(1.0 s) Residual analysis of the North Sea dataset with respect to local magnitude and epicentral distance, using the Abrahamson et al. (2014) GMPE.*

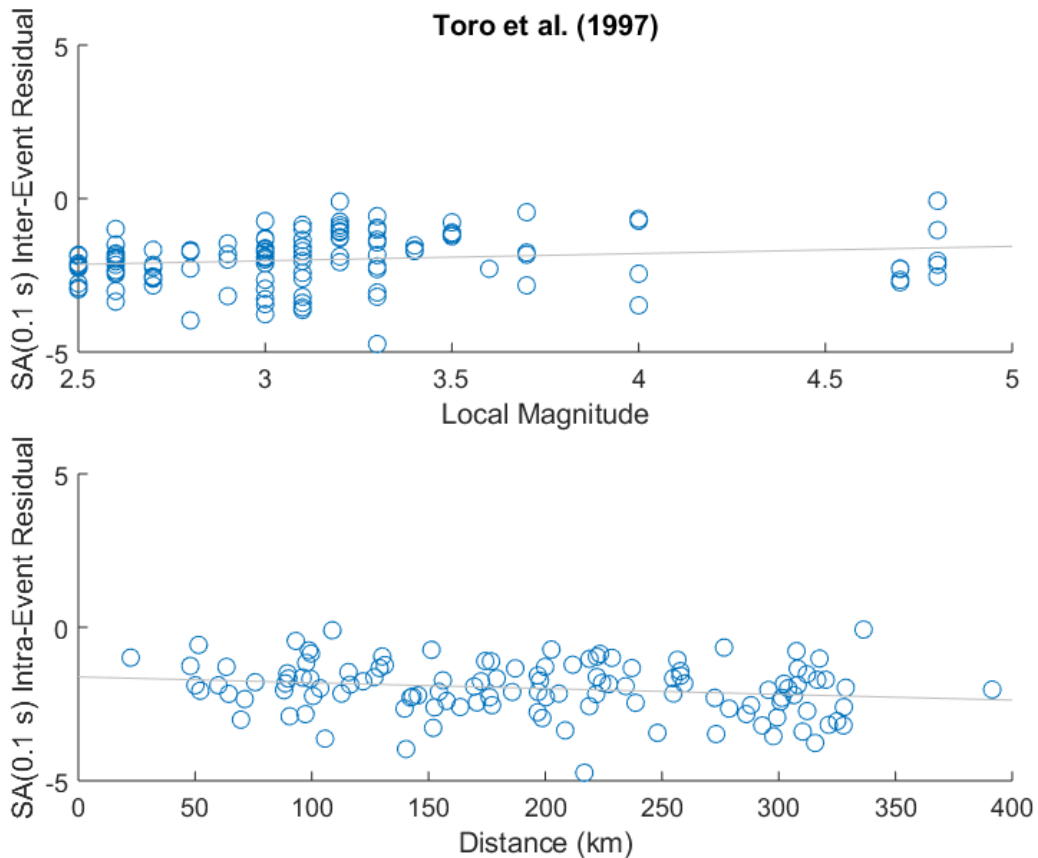


**Figure 3.15** *SA(0.1 s) Residual analysis of the North Sea dataset with respect to local magnitude and epicentral distance, using the Toro et al. (1997) GMPE.*

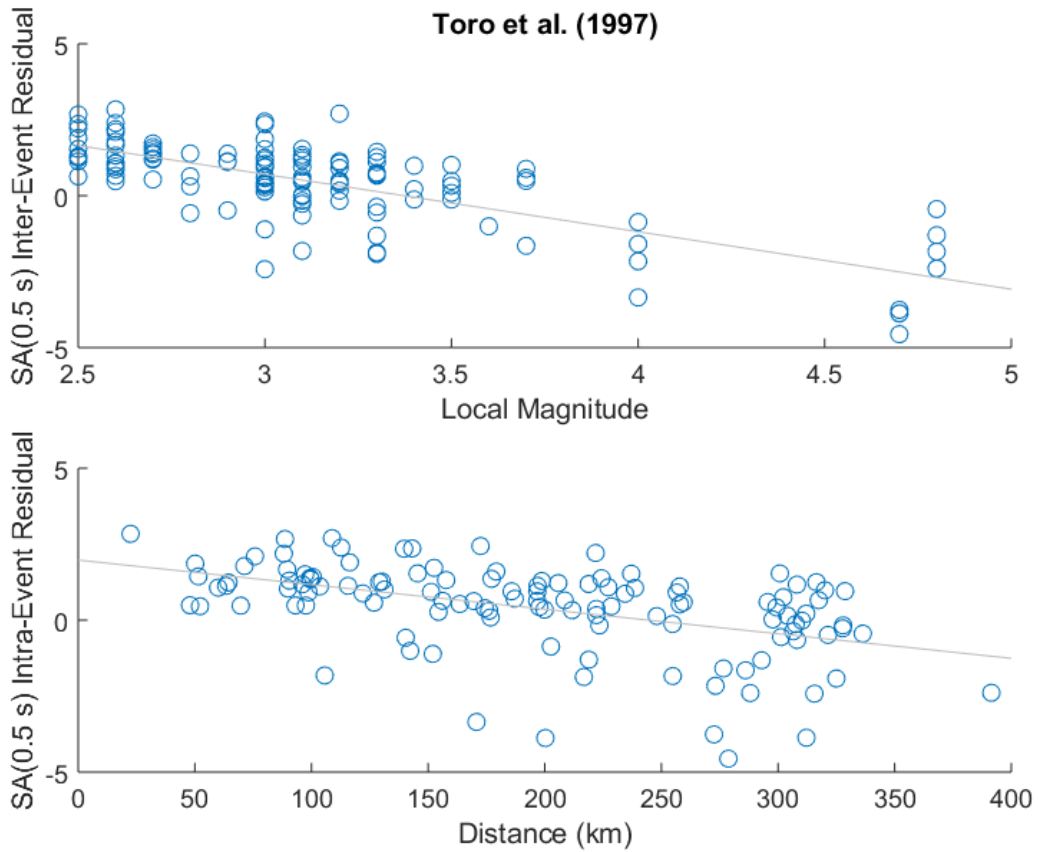


**Figure 3.16** SA(0.5 s) Residual analysis of the North Sea dataset with respect to local magnitude and epicentral distance, using the Toro et al. (1997) GMPE.

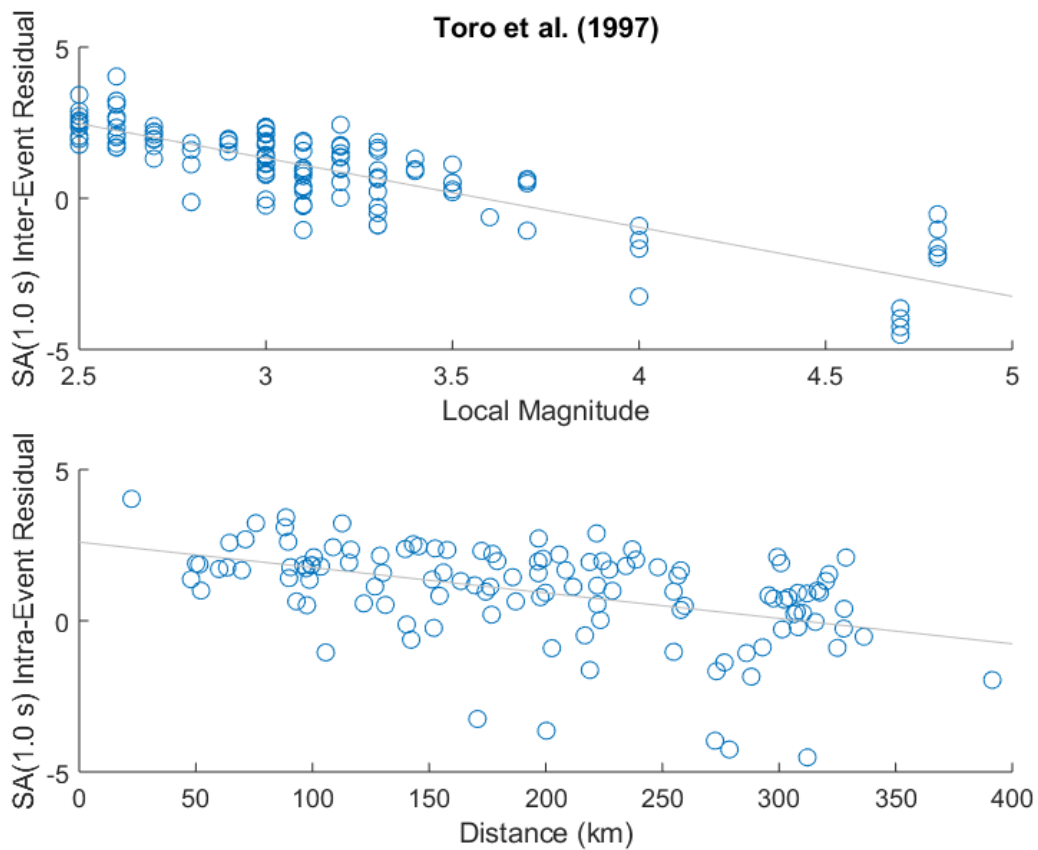


**Figure 3.17** SA(1.0 s) Residual analysis of the North Sea dataset with respect to local magnitude and epicentral distance, using the Toro et al. (1997) GMPE.

Of the GMPEs considered, only the Rietbrock et al. (2013) GMPE provides a good fit when predicting PGV (Fig. 3.18), and only the Cauzzi et al. (2010) GMPE provides a moderate fit. Consequently, of the GMPEs tested in this analysis, the Rietbrock et al. (2013) GMPE can be considered the most appropriate for predicting PGV hazard levels in the North Sea.

The majority of the GMPEs considered show low – moderate bias, however as with the residual analysis results for the intensity measure SA(1.0 s) many show statistically significant trends with respect to magnitude (Tab. 3.7). Considering only a small component of the database records is likely contaminated with noise (see above on database preparation), such statistically significant trends can be attributed to the poor fit of the models.

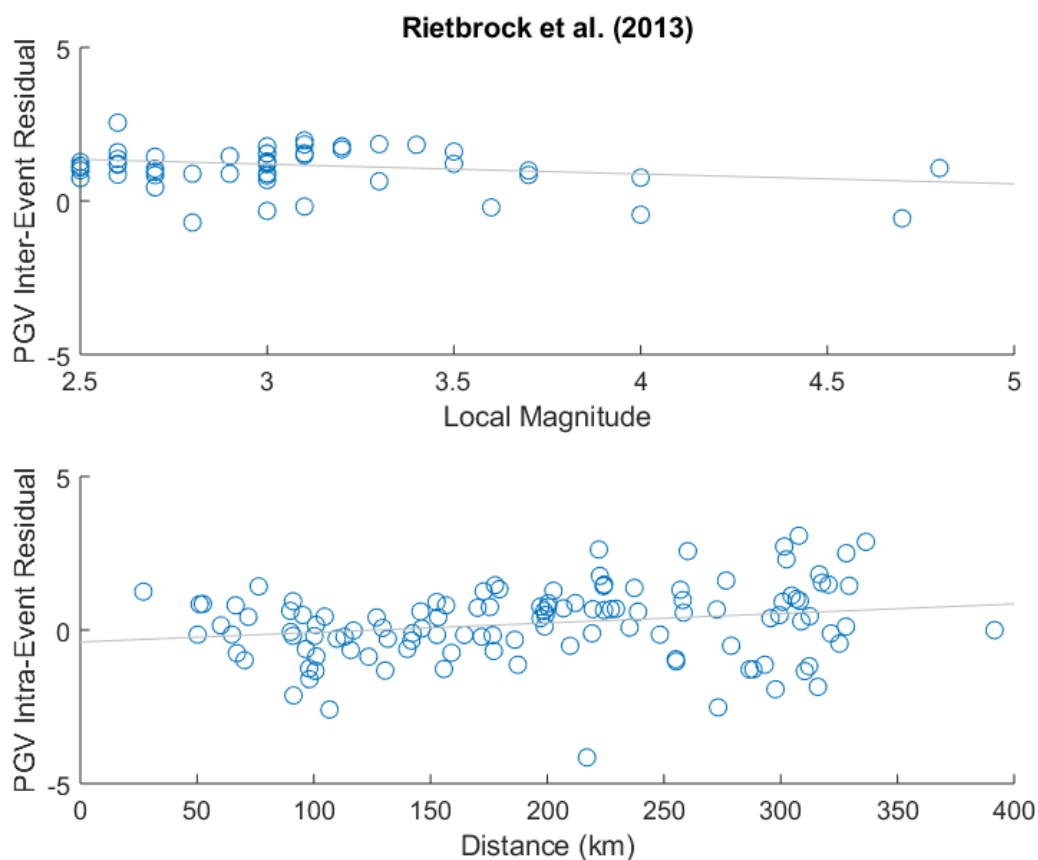


**Figure 3.18** PGV Residual analysis of the North Sea dataset with respect to local magnitude and epicentral distance, using the Rietbrock et al. (2013) GMPE.

**Table 3.7** Parameters determined from residual analysis for each GMPE with regards to the North Sea dataset for PGV. I.V.D. = Input variable dependent (to compute these standard deviations see the referenced studies).

GMPE	Bias	$\tau$	$\Phi$	$\tau(\text{model})$	$\Phi(\text{model})$	p-value (mag)	p-value (dist)	Model Fit
Abrahamson et al., 2014	0.191	0.793	0.799	I.V.D	I.V.D	$1.905 \times 10^{-7}$	$9.820 \times 10^{-8}$	Poor
Akkar and Bommer, 2010	0.171	0.931	1.046	0.108	0.256	$6.174 \times 10^{-11}$	$8.295 \times 10^{-5}$	Poor
Akkar and Cagnan, 2010	1.928	1.154	0.942	0.526	0.615	$2.114 \times 10^{-12}$	$2.037 \times 10^{-6}$	Poor
Akkar et al., 2014 ( $R_{epi}$ )	0.655	0.817	0.864	0.349	0.614	$3.362 \times 10^{-8}$	$2.554 \times 10^{-2}$	Poor
Akkar et al., 2014 ( $R_{hyp}$ )	0.586	0.749	0.851	0.331	0.628	$2.323 \times 10^{-7}$	$1.321 \times 10^{-1}$	Poor
Akkar et al., 2014 ( $R_{jb}$ )	0.128	0.749	0.831	0.331	0.601	$3.940 \times 10^{-7}$	$4.033 \times 10^{-7}$	Poor
Boore and Atkinson, 2008	-2.606	1.148	1.017	0.286	0.500	$1.610 \times 10^{-4}$	$9.981 \times 10^{-3}$	Poor
Boore et al., 2014	0.997	0.936	0.789	I.V.D.	I.V.D.	$2.231 \times 10^{-23}$	$2.386 \times 10^{-2}$	Poor
Bindi et al., 2017 ( $R_{jb}$ )	-	-	-	-	-	-	-	-
Bindi et al., 2017 ( $R_{hyp}$ )	-	-	-	-	-	-	-	-
Campbell and Bozorgnia, 2014	0.501	0.751	0.844	I.V.D.	I.V.D.	$8.457 \times 10^{-7}$	$2.287 \times 10^{-1}$	Poor
Chiou and Youngs, 2014	0.503	0.777	0.751	I.V.D.	I.V.D.	$1.244 \times 10^{-8}$	$8.260 \times 10^{-1}$	Poor
Cauzzi et al., 2015	-0.246	0.643	0.840	0.240	0.221	$9.309 \times 10^{-4}$	$5.840 \times 10^{-2}$	Moderate
Rietbrock et al., 2013	0.219	0.681	0.809	Stochastic	Stochastic	$6.113 \times 10^{-2}$	$1.844 \times 10^{-1}$	Good
Toro et al., 1997	-	-	-	-	-	-	-	-
Toro et al., 2002	-	-	-	-	-	-	-	-

### 3.8 Evaluation of North Sea GMPE Testing Results

Following GMPE testing, each GMPE was assigned an overall score to rank their performance when evaluated with the North Sea dataset (Tab. 3.8). The four highest scoring GMPEs were the Rietbrock et al. (2013) GMPE and the three variants of the Akkar et al. (2014).

Of this suite of GMPEs, the Akkar et al. (2014) GMPE variants are considered more appropriate for use in the North Sea than the Rietbrock et al. (2013) GMPE, despite scoring lower overall than the Rietbrock et al. (2013) GMPE. The higher score of the Rietbrock et al. (2013) GMPE is the result of this GMPE providing a good fit to PGV. The PGV ground-motion intensity measure is of less significance in this investigation because the earthquakes generated in the North Sea are predominantly small to moderate in size (i.e. the generated seismic waves from North Sea earthquakes are predominantly of higher frequencies). If the contribution of PGV fit to the score of each GMPE is discounted, the Akkar et al. (2014) GMPE variants score highest. Of the Akkar et al. (2014) GMPE variants, the distance to the surface projection of the rupture ( $R_{jb}$ ) variant is the best performing GMPE overall in the North Sea region based on its superior performance when predicting PGA (Fig. 3.11). Consequently, for the remainder of the investigation, the  $R_{jb}$  variant of the Akkar et al. (2014) GMPE is treated as the base model to which adjustments are made to improve the prediction of North Sea ground-motions.

**Table 3.8** Ranking of of each GMPE based on performance for all ground-motion intensity measures considered.

GMPE	PGA	SA(0.1 s)	SA(0.5 s)	SA(1.0 s)	PGV	Mean Score for GMPE Fit
Abrahamson et al., 2014	2	2	2	2	1	1.80
Akkar and Bommer, 2010	1	2	1	1	1	1.20
Akkar and Cagnan, 2010	1	3	1	1	1	1.40
Akkar et al., 2014 ( $R_{epi}$ )	3	3	2	1	1	2.00
Akkar et al., 2014 ( $R_{hyp}$ )	3	3	2	1	1	2.00
Akkar et al., 2014 ( $R_{jb}$ )	3	3	2	1	1	2.00
Boore and Atkinson, 2008	1	1	1	1	1	1.00
Boore et al., 2014	1	2	1	1	1	1.20
Bindi et al., 2017 ( $R_{jb}$ )	2	1	1	1	0	1.00
Bindi et al., 2017 ( $R_{hyp}$ )	2	1	1	1	0	1.00
Campbell and Bozorgnia, 2014	2	1	1	1	1	1.20
Chiou and Youngs, 2014	1	1	1	1	1	1.00
Cauzzi et al., 2015	1	2	2	1	2	1.60
Rietbrock et al., 2013	2	3	2	1	3	2.20
Toro et al., 1997	1	2	1	1	0	1.00
Toro et al., 2002	1	1	1	1	0	0.80

*Good fit = 3, moderate fit = 2, poor fit = 1, GMPE does not predict associated ground-motion intensity measure = 0.*

### 3.9 Comparative North Sea Seismic Hazard Calculations

Following identification of the  $R_{jb}$  variant of the Akkar et al. (2014) GMPE as the most appropriate GMPE for predicting ground-shaking in the North Sea, hazard curves were computed for an example North Sea location (Fig. 3.19) using the *CRISIS* seismic hazard software (Ordaz et al., 2015). To replicate the PGA outputs of Bungum et al. (2000)'s logic tree approach, the mean outputs of the Toro et al. (1997) GMPE and the Ambraseys et al. (1996) GMPE were used.

The hazard curves are largely representative of the GMPE testing results; the  $R_{jb}$  variant of the Akkar et al. (2014) GMPE (with the GMPE's default standard deviations) predicts considerably lower AFOE for higher levels of PGA compared to Bungum et al. (2000)'s logic tree approach. The lower AFOE computed using the  $R_{jb}$  variant of the Akkar et al. (2014) GMPE provide strong grounds for the development of a new North Sea GMPE.

Use of the larger database-derived inter-event and intra-event standard deviations for the  $R_{jb}$  variant of the Akkar et al. (2014) also has a moderate impact on the seismic hazard calculations for this example North Sea location; for an AFOE of  $10^{-3}$ , the predicted PGA is approximately 30% larger with the database-derived standard deviations than the GMPE's reported standard deviations. In North Sea PSHA calculations with the  $R_{jb}$  variant of the Akkar et al. (2014), the model's default standard deviations should be used for now until more work has been carried out.

Hazard maps were also computed using the *CRISIS* seismic hazard software. These hazard maps were computed for the Norwegian economic sector of the North Sea, as originally done so within the Bungum et al. (2000) PSHA. The input files for the source zone coordinates and the corresponding seismicity parameters were provided by Conrad Lindholm (NORSAR). The hazard maps, like the hazard curves are representative of the GMPE testing results, with the relative over-prediction resulting from the Toro et al. (1997) GMPE being clearly observed (Fig. 3.20).

Because of the sparsity of ground-motion records from moderate and large ( $M_L > 5$ ) earthquakes within the North Sea dataset the performance of the  $R_{jb}$  variant of the Akkar et al. (2014) GMPE was also evaluated using a small dataset of ground-motion records that are not in EIDA from larger North Sea earthquakes (8 ground-motion records for 5 earthquakes of sizes  $M_L$  4.4, 4.4, 5.3, 5.7 and 6.1 recorded at distances of approximately 300 – 700 km), including the  $M_L$  5.3 Viking Graben event of 1927 and the  $M_L$  6.1 Dogger Bank event of 1931. This ground-motion data was collated from Bungum et al. (2003), the Norwegian Seismological Array (NORSAR) and the Norwegian National Seismic Network (NNSN). These additional data are of poorer quality with less reliable metadata, and consequently were not incorporated within the original residual analysis because they could potentially bias the results from the EIDA (North Sea) dataset. Using this independent dataset, the  $R_{jb}$  variant of the Akkar et al. (2014) GMPE was found to provide a good fit overall for PGA, with a bias of 0.712 and no statistically significant trending with respect to either magnitude or distance being observed (Fig. 3.21). This good

fit with the independent dataset provides external validation of the selection of the  $R_{jb}$  variant of the Akkar et al. (2014) GMPE as the base model GMPE based on its performance with the North Sea dataset. It should be noted that the evaluation of each of the 16 considered GMPEs with the independent dataset is unnecessary, as the GMPE which provides the best fit overall to the observed North Sea ground-motions will not change, considering the  $R_{jb}$  variant of the Akkar et al. (2014) GMPE provides the best overall fit for the (significantly larger) North Sea dataset and a good fit for the (far smaller) independent dataset.

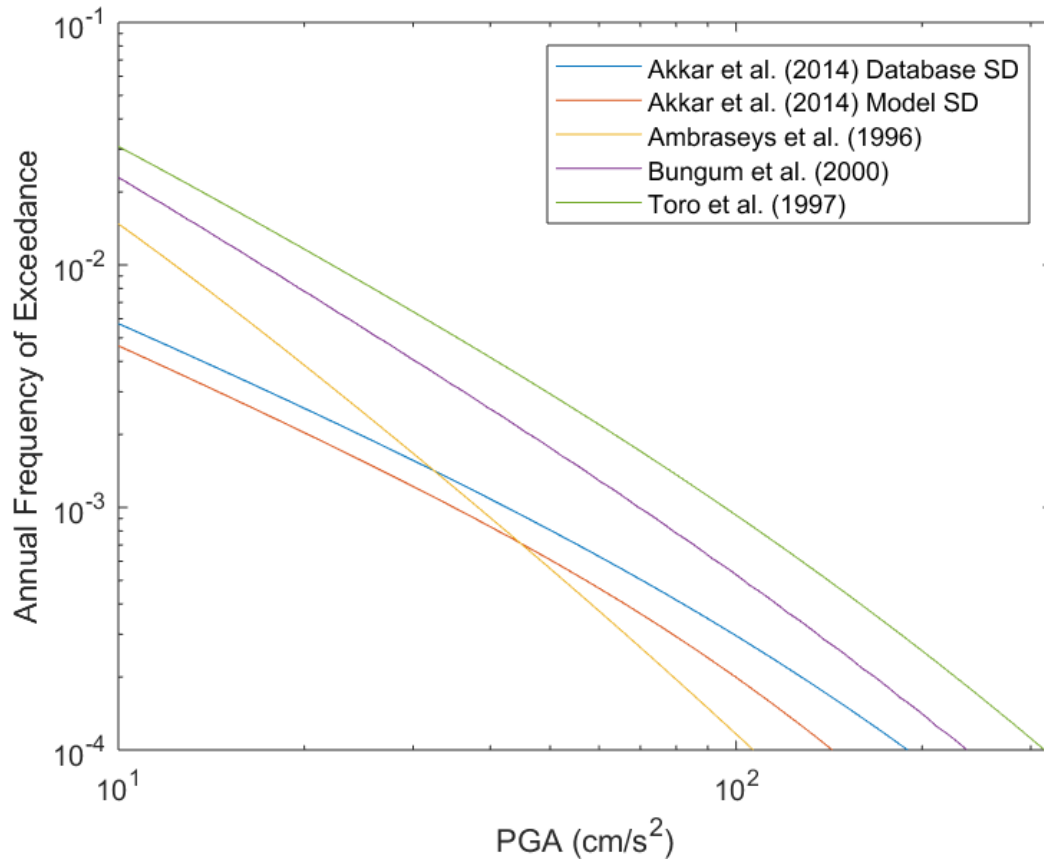


**Figure 3.19** PGA Seismic hazard curves comparing components of Bungum et al. (2000)'s logic-tree approach with the Akkar et al. (2014)  $R_{jb}$  GMPE at a moderate hazard site ( $\lambda = 0.0501$ , longitude = 4, latitude = 64) within the North Sea.

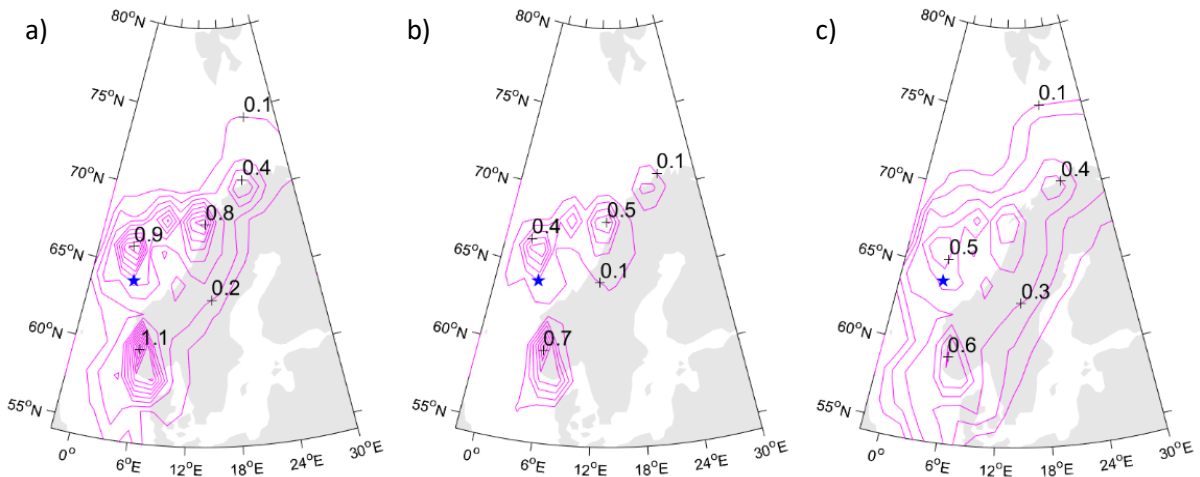


**Figure 3.20** (a) PGA hazard contour map for the Norwegian economic sector of the North Sea computed using the Bungum et al. (2000) logic-tree approach for a return period of 475 years, (b) PGA hazard contour map for the Norwegian economic sector of the North Sea computed using the Akkar et al. (2014)  $R_{jb}$  GMPE with the model standard deviations for a return period of 475 years, (c) Ratio between the North Sea PGA seismic hazard contour map computed using the Akkar et al. (2014)  $R_{jb}$  GMPE and the North Sea PGA seismic hazard contour map computed using the Bungum et al., (2000) logic-tree approach. PGA is in  $m/s^2$ . The blue star represents the site considered in Fig. 3.19.

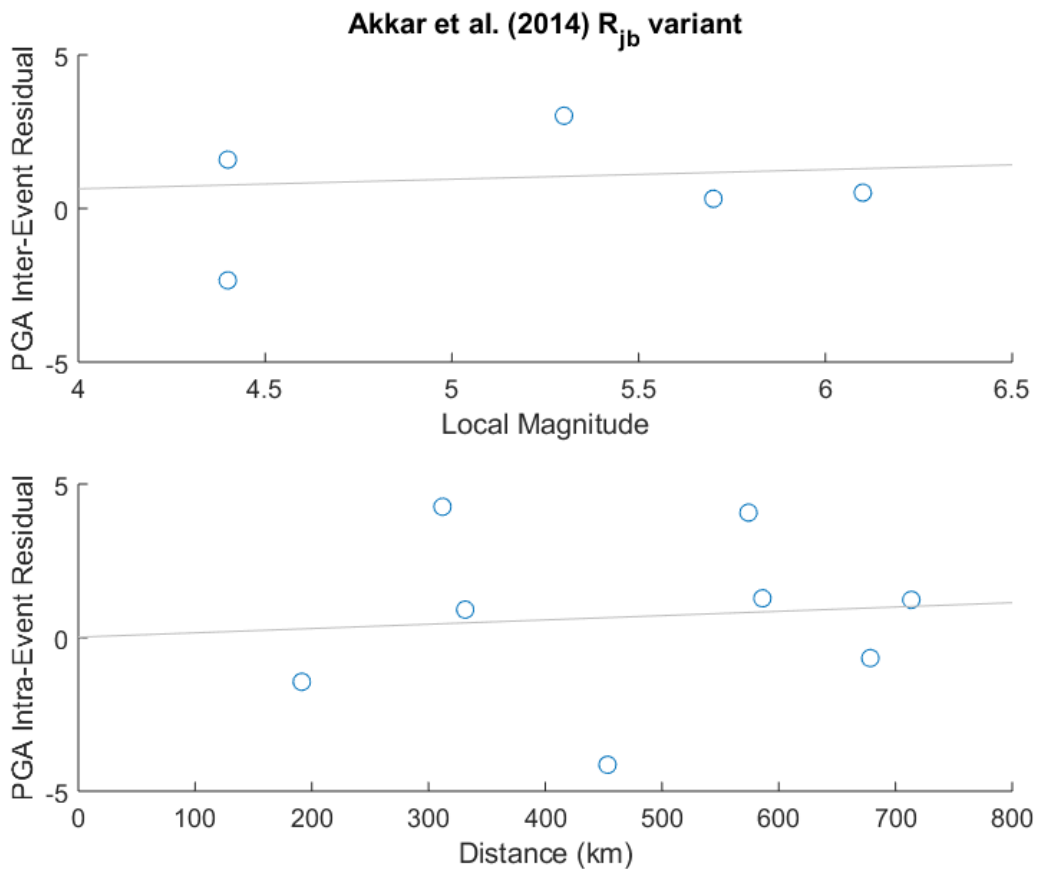


**Figure 3.21** PGA Residual analysis of the independent dataset with respect to local magnitude and epicentral distance, using the  $R_{jb}$  variant of the Akkar et al. (2014) GMPE.

### 3.10 Conclusions for North Sea GMPE Testing

The GMPE testing concluded that no single GMPE provides an overall good fit to the North Sea dataset. However, the  $R_{jb}$  variant of the Akkar et al. (2014) GMPE was found to predict well for the PGA, SA(0.1 s) and SA(0.5 s) ground-motion intensity measures. Consequently, the  $R_{jb}$  variant of the Akkar et al. (2014) GMPE was determined to be the best existing GMPE for predicting seismic hazard in the North Sea overall. The viability of this GMPE as an alternative to models currently used for North Sea PSHA is supported by the hazard calculations and the GMPE testing with the independent dataset of larger magnitude earthquakes. The  $R_{jb}$  variant of the Akkar et al. (2014) GMPE is henceforth treated as a base model to which incremental improvements in GMPE performance are implemented, so as to develop a GMPE better suited for use in the North Sea. Furthermore, the Akkar et al. (2014) GMPE was identified by both Dost et al. (2013) and Bourne et al. (2015) as an appropriate base model for modification to better predict (hydrocarbon production induced) ground-shaking in the Groningen natural gas field. This consistent identification of the Akkar et al. (2014) GMPE as a suitable base model for a region of reasonably similar seismicity to the North Sea<sup>20</sup> is supportive of the GMPE being appropriate for modification to the North Sea region too.

---

<sup>20</sup> Albeit an area where a considerably larger proportion of earthquakes are known to be of an induced nature.

#### 4.0 Improving GMPE Performance in the North Sea

Following the testing of existing ground-motion prediction equations (GMPEs) in the North Sea, the best performing GMPE (the Joyner-Boore distance ( $R_{jb}$ ) variant of the Akkar et al., 2014 GMPE) was designated as a base model to which incremental improvements in GMPE performance were implemented, so as to develop a GMPE better suited for use in the region. These improvements were made through relaxing the ergodic assumption with respect to site and path in the region using novel techniques for improving probabilistic seismic hazard assessment (PSHA) calculations.

In the context of PSHA, the assumption of ergodicity suggests that the aleatory variability associated with the ground-shaking predicted by a GMPE for a specific source-path-site combination is equal to the aleatory variability observed in an entire strong motion dataset comprising of multiple source-path-site combinations (Anderson and Brune, 1999; Walling and Abrahamson, 2012). The assumption of ergodicity is made because of the short history of earthquake observations, and consequently the lack of many repeated source-path-site combinations in ground-motion record databases (Anderson and Brune, 1999).

The application of the ergodic assumption when developing GMPEs potentially results in unnecessarily large uncertainties for predicted ground-shaking in PSHAs where source, path and site effects are repeated. Larger uncertainties can significantly impact seismic hazard estimates, especially for critical facilities, which are usually designed for long return periods (Bommer and Abrahamson, 2006). Therefore, to reduce the aleatory variability associated with predicting ground-shaking the relaxation of the ergodic assumption can be undertaken for PSHAs with repeated source, path and site effects. The relaxation of the ergodic assumption consequently provided a means of implementing small yet significant improvements in the performance of the base GMPE in the North Sea region.

Alongside the identification of the base model GMPE using residual analysis, this work to constrain site and path effects to provide incremental improvements in GMPE performance (in the North Sea) is also provided in Brooks et al. (2020).

#### 4.1 Constraining Site Effects in the North Sea

The intensities of ground-shaking resulting from a single earthquake vary between sites due to local site conditions (Sanchez-Sesma, 1987). Local site conditions determine the extent of amplification experienced by incident ground-motions at a specific site, resulting in said variability observed amongst many sites.

For localities with similar subsurface conditions similar site effects on incident ground-motions are expected (Sanchez-Sesma, 1987). Generally, if the subsurface comprises soil or soft rock, the ground-motions experience larger amplification than if the subsurface comprises of hard rock (Bowden and Tsai, 2017). Consequently, incident ground-motions at localities are often computed using site effects assigned to site classes, where each class is associated with specific subsurface conditions. Site classification schemes therefore enable simple yet effective adjustments to ground-motions incident at many sites of interest within PSHA calculations. These adjustments effectively result in the partial relaxation of the ergodic assumption with respect to site, subsequently leading to improved GMPE performance.

In design codes, site classification schemes often define classes using the  $V_{S30}$  site-response parameter (the time-averaged shear-wave velocity through the top 30 m of the site soil profile). For example, in the Eurocode 8 design code (BS EN 1998, 2004), the subsurface conditions of a site are determined using the  $V_{S30}$  site-response parameter, and then a corresponding elastic design spectrum is used for the design of infrastructure which could be built on the site. However, despite its widespread use, the  $V_{S30}$  site-response parameter is still largely considered limited in its ability to effectively capture site amplification over a large period range, as is often present in the context of engineering seismology (e.g. Castellaro et al., 2008). Consequently, several efforts have been undertaken to provide rigorous site classification schemes which incorporate additional site-response parameters. For example, Pitilakis et al. (2013) composed a site classification scheme which takes into account  $H_{800}$  (depth to bedrock where  $V_s = 800$  m/s),  $V_{s,av}$  (average shear-wave velocity of the soil column structure) and  $f_0$  (the fundamental period), and Gallipoli and Mucciarelli (2009) composed a site classification scheme using  $V_{S10}$  (the time-averaged shear-wave velocity through the top 10 m of the site soil profile) and the horizontal to vertical spectral ratios (HVSr) in addition to  $V_{S30}$ .

Significant challenges are associated with using such site classifications schemes, the most prominent of which being the requirement of an abundance of *a priori* information regarding the site conditions for determining the site class criteria. To circumvent this dependency on *a priori* site information, Kotha et al. (2018) developed a novel data-driven method for site classification. This data-driven method uses a variety of statistical techniques to determine an optimal number of site classes using only the intra-event residuals of a selected GMPE as *a priori* information, and then known site-response parameters

(e.g.  $V_{s30}$ ,  $H_{800}$ ) are used as *a posteriori* information to assign characteristic subsurface conditions to each class<sup>21</sup>.

Considering the lack of reliable *a priori* information for each site in the North Sea dataset, the Kotha et al. (2018) methodology is ideal for constraining site effects in the North Sea, so as to improve the performance of the base model GMPE (the  $R_{jb}$  variant of the Akkar et al., 2014 GMPE) in the region. It should be prefaced that the sites within the North Sea dataset are exclusively onshore sites. Therefore, the site classes determined here using the Kotha et al. (2018) technique require augmentation to be applicable to the offshore sites in the North Sea, where critical offshore infrastructure are located.

## 4.2 Methodology for Constraining Onshore Site Effects in the North Sea

The Kotha et al. (2018) site classification method incorporates principal component analysis (PCA) and k-means clustering (Jolliffe, 2013; Aggarwal, 2014) to derive site classes, and is described below. For detailed overviews of PCA and k-means clustering see Appendix E. The Kotha et al. (2018) site classification method incorporates nomenclature defined by Al Atik et al. (2010). The relevant nomenclature is as follows: (1)  $\delta S2S_s$  - the average (intra-event) GMPE residual for one site, which represents the site-specific random effects (2)  $\Delta S2S_s$  - a vector comprising the  $\delta S2S_s$  scalar computed for each spectral period considered and (3)  $\phi S2S_s$  - the standard deviation of the site-to-site (intra-event) GMPE residuals.

As will be demonstrated below, the considerably smaller dataset used in this investigation introduces some subjectivity into the statistical techniques the Kotha et al. (2018) method incorporates, therefore constraining the study in this regard.

PCA is used to reduce the multi-dimensionality of an  $\Delta S2S_s$  vector dataset to produce principal component scores. The principal component scores represent the variability observed in the  $\Delta S2S_s$  vector dataset. The first 2 principal component scores represent the bulk of the variability in a dataset for which PCA is performed (Aggarwal, 2014). The plotting of these first 2 principal component scores is representative of the variability observed in the  $\Delta S2S_s$  vector dataset in a two-dimensional space (e.g. Fig. 4.0).

The representation of the bulk variability of the  $\Delta S2S_s$  vector dataset in a two-dimensional space enables clustering of the  $\Delta S2S_s$  vectors using the k-means algorithm (e.g. Fig. 4.0). The k-means clustering assigns each  $\Delta S2S_s$  vector to a cluster comprising of similar  $\Delta S2S_s$  vectors. The k-means clustering of  $S2S_s$  vectors therefore effectively groups sites with similar site-specific random effects over the range of spectral periods considered.

---

<sup>21</sup> The assignment of characteristic subsurface conditions to each class is not required if applying this approach to sites with strong-motion data. However, this final step is necessary for applying the method to sites with only geotechnical information available (as is generally the case for engineering infrastructure).

For each cluster, the means of the  $\Delta S2S_s$  vectors within that cluster are calculated to produce cluster-specific  $\Delta S2S_s$  vectors. The  $\Delta S2S_s$  vectors effectively act as amplification functions relative to one another, from which the response spectra computed for each site can be adjusted. For the  $\Delta S2S_s$  vectors to act as amplification functions relative to one another, a reference cluster must be chosen. This reference cluster should ideally display small site response at all considered spectral periods. Conventionally, outcropping hard bedrock sites ( $V_{s30} > 800\text{m/s}$ ) are used as reference sites, for which seismic hazard estimates are computed and then scaled using the appropriate site amplification function (Kotha et al., 2018).

Within this investigation, the North Sea  $\Delta S2S_s$  vector dataset comprises of 17  $\Delta S2S_s$  vectors (one for each site). The North Sea  $\delta S2S_s$  scalars were computed for each spectral period considered (0 s, 0.1 s, 0.5 s, 1.0 s and 2.0 s)<sup>22</sup> with the  $R_{jb}$  variant of the Akkar et al. (2014) GMPE - the GMPE determined to best predict North Sea seismicity overall and the North Sea dataset. The Kotha et al. (2018) methodology was subsequently applied to this North Sea  $\Delta S2S_s$  vector dataset. PCA was performed to produce a two-dimensional representation of the bulk variability observed in the North Sea  $\Delta S2S_s$  vector dataset. PCA resulted in the reduction of the  $\Delta S2S_s$  vector dataset to five principal components. The first two principal components represent approximately 90% of the variability in the  $\Delta S2S_s$  vector dataset. K-means clustering was then run for 1000 iterations, resulting in successful convergence with two clusters<sup>23</sup> (Fig. 4.0). Cluster 1 contained 10 sites and Cluster 2 contained 7 sites. Cluster 1 was chosen to be the reference cluster for the computation of the other cluster's amplification function due to cluster 1's residuals implying small site response at all considered spectral periods (Fig. 4.1). The intra-cluster standard deviations of  $\delta S2S_s$  for each spectral period considered (i.e.  $\phi S2S_s$ ) were also computed (Fig. 4.4). The spatial distribution of the sites within each cluster are shown in Fig. 4.4.

Following the partitioning of the North Sea  $\Delta S2S_s$  vector dataset into clusters, and the subsequent computation of cluster amplification functions, characteristic geotechnical conditions should be defined for each cluster. However, minimal information was available for the subsurface conditions of each site in the North Sea dataset. In the Kotha et al. (2018) study, an abundance of geotechnical information enabled rigorous assignment of characteristic site conditions for each cluster, including the computation of two-dimensional kernel distributions of the geotechnical site characteristics, from which representative ranges for each cluster could be identified. In comparison, here the only geotechnical site characteristic which could be reliably assigned (albeit again from the ground-motion data) is the spectral

---

<sup>22</sup> The GMPEs tested were only evaluated up to a spectral period of 1.0 s; however, considering the relatively good performance of the  $R_{jb}$  variant of the Akkar et al. (2014) GMPE at a spectral period of 1.0 s compared to the other GMPEs tested, it is likely this GMPE is still the most appropriate.

<sup>23</sup> Silhouette analysis revealed the optimal number of clusters to be two (i.e.  $k = 2$ , Fig. E.6). Three or more clusters would have been preferable due to providing more site classes, but the negative silhouette values resulting from partitioning the (small) dataset into more than two clusters indicated this was not viable for the most effective clustering of the  $\Delta S2S_s$  vector dataset. For a detailed overview of silhouette analysis see Appendix E.

period corresponding to peak amplification, which for Cluster 2 was determined to be 0.5 s, thereby matching the period determined by the analysis using  $\Delta S2S_s$ . Because of the lack of geotechnical information, it can only be said that Cluster 1 represents the reference cluster and that Cluster 2 represents the amplification cluster.

Sites of interest in future PSHA, but not included in the clustering procedure can theoretically be assigned to a site class derived from the Kotha et al. (2018) method based on known site parameters, and the most appropriate cluster amplification function can be applied to response spectra computed for the site. However, Kotha et al. (2018) suggest that for their cluster site amplification functions to be applicable to new sites, additional site-response parameters should be developed and further geotechnical information for certain clustered sites must be obtained. Kotha et al. (2018) suggest such actions because using only the site-response parameters available during their study results in some clusters being indistinguishable (e.g. similar  $V_{S30}$  distributions are observed for significantly different site amplification functions). Considering the far smaller size of the dataset used in this study compared to the dataset used by Kotha et al. (2018), such recommendations are clearly necessary for the application of the cluster amplification functions computed in this investigation to new North Sea sites for which no ground-motions records are available.

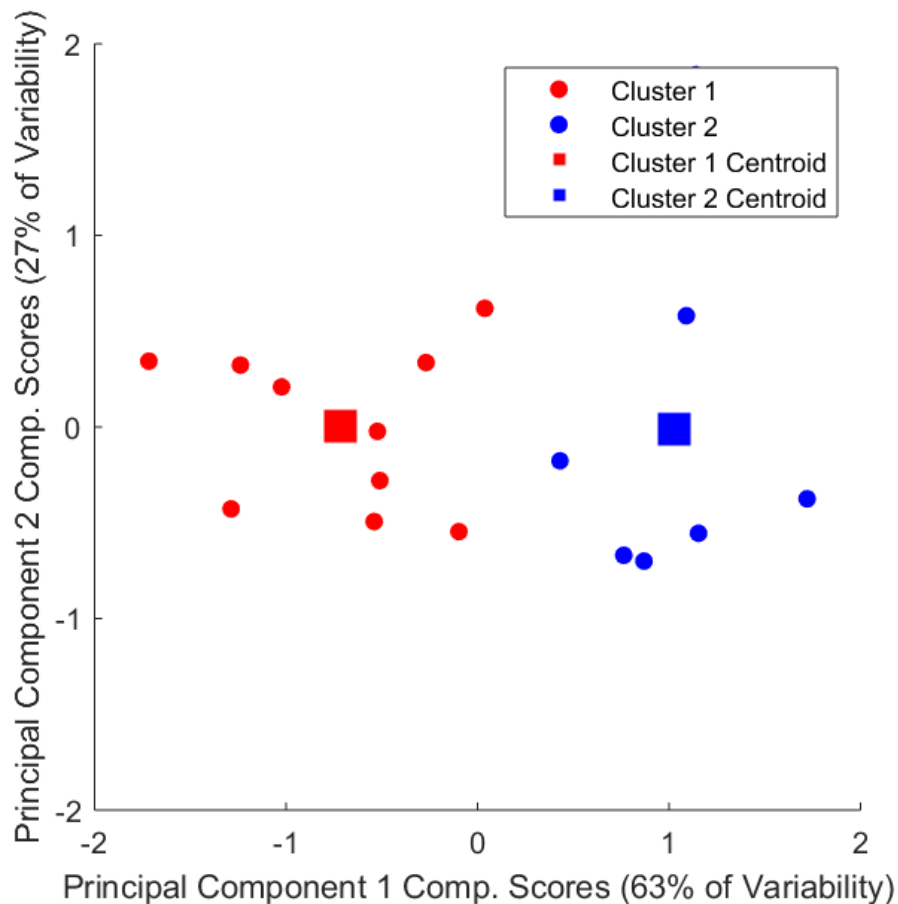


**Figure 4.0** Clustered  $\Delta S2S_s$  vectors following 1000 iterations of the k-means algorithm.

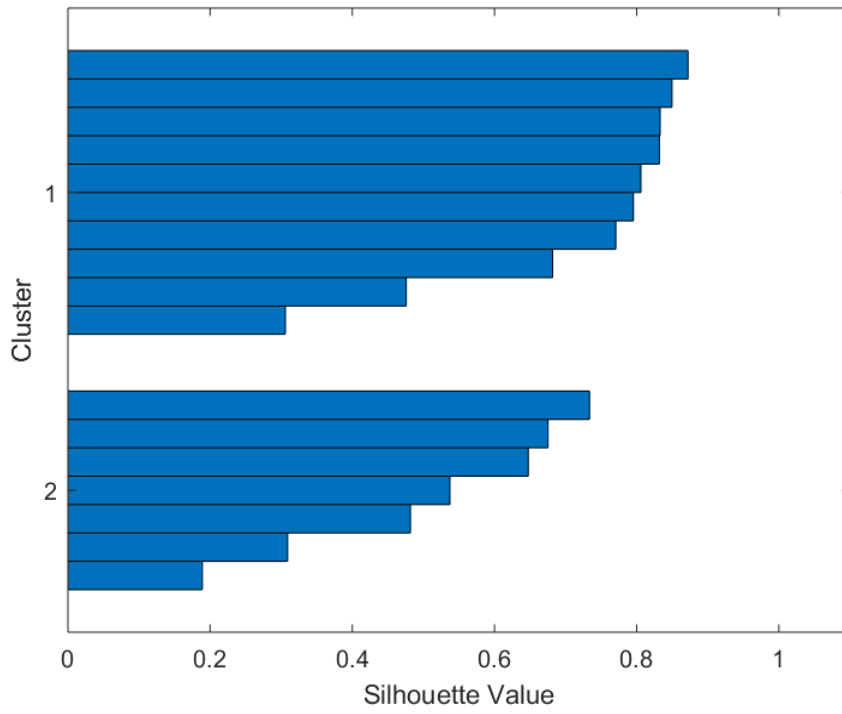


**Figure 4.1** Silhouette plot of the clustered  $\Delta S2S_s$  vectors (iterations = 1000,  $k = 3$ ).

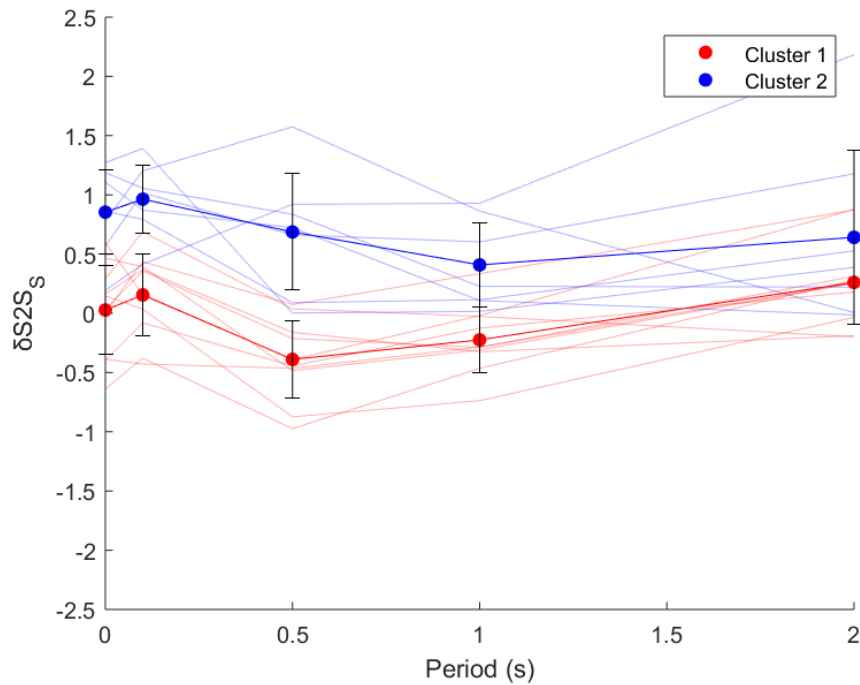


**Figure 4.2** Mean  $\Delta S2S_s$  vectors following 1000 iterations of the  $k$ -means algorithm. Error bars represent plus/minus one standard deviation. Feint lines represent pre-clustering  $\Delta S2S_s$  vectors.

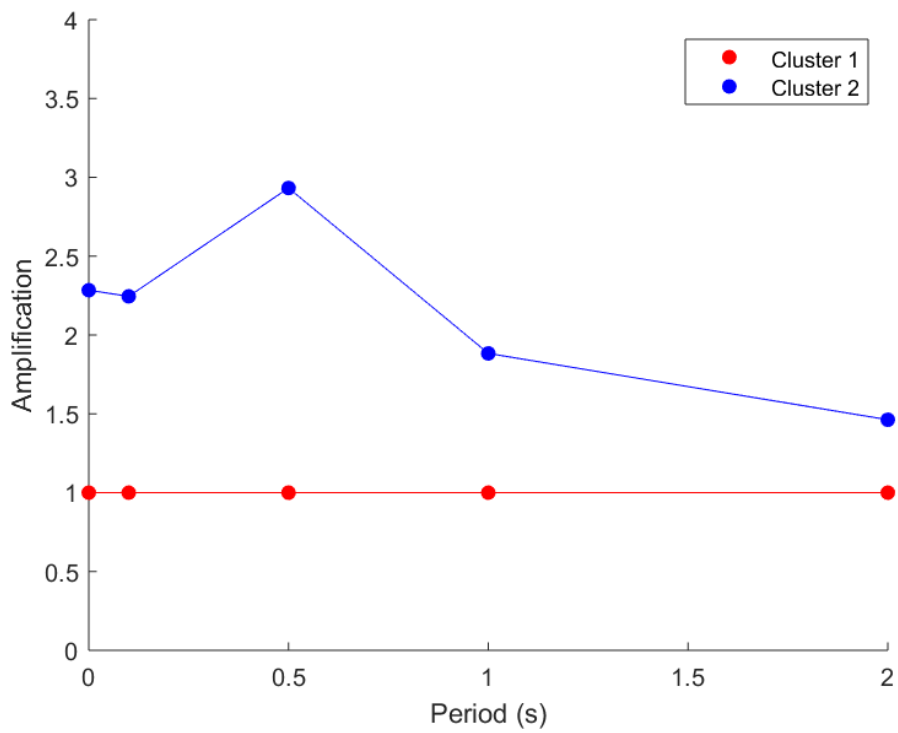


**Figure 4.3** Cluster amplification functions for the  $\Delta S2S_s$  vectors.

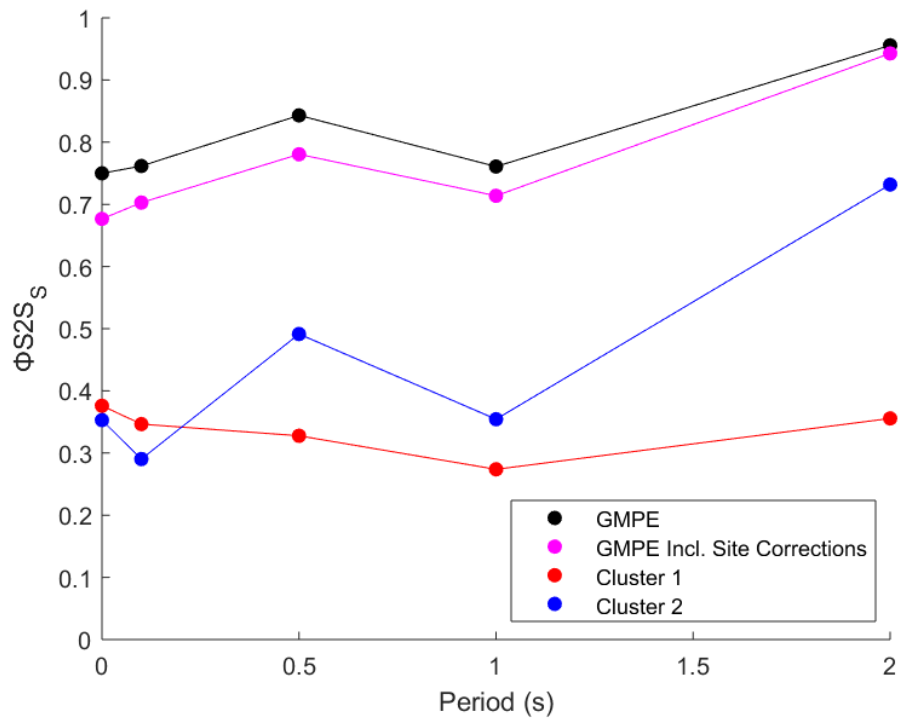


**Figure 4.4** Intra-cluster standard deviations of  $\delta S2S_s$  per period.

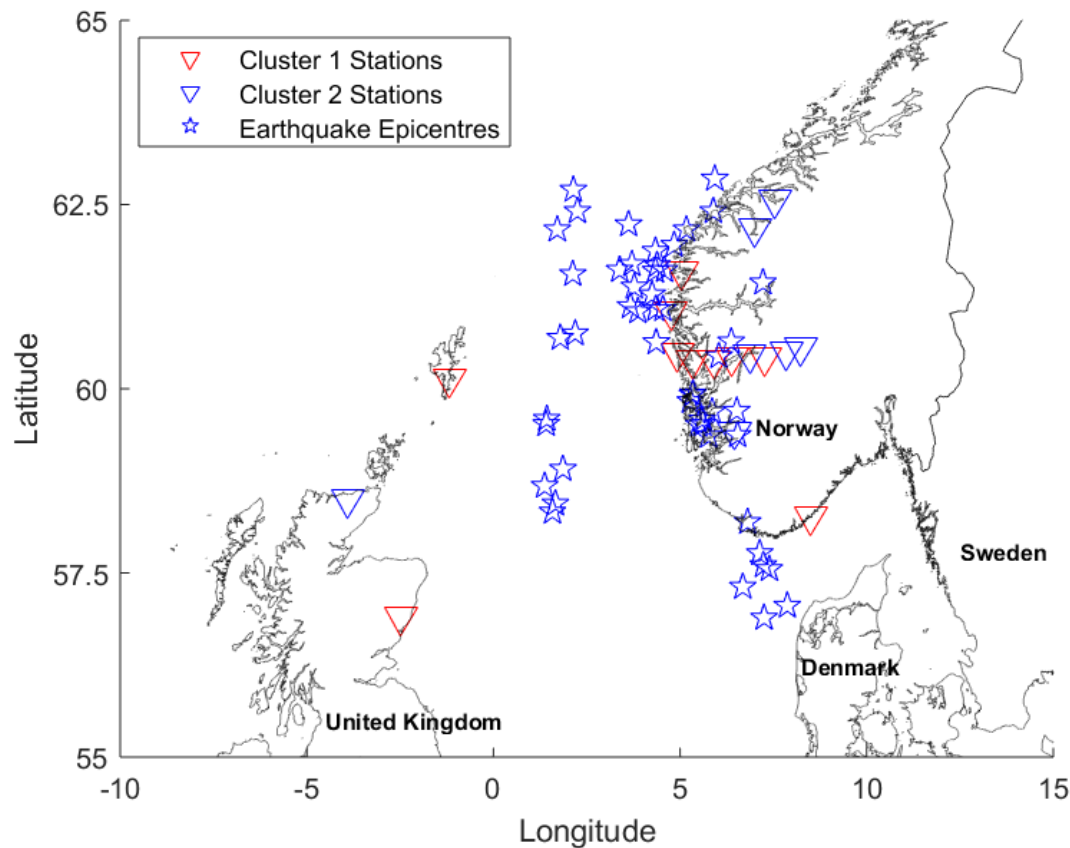


**Figure 4.5** *Spatial distribution of the sites assigned to each cluster.*

### 4.3 Results for Constraining Onshore Site Effects in the North Sea

The partitioning of the  $\Delta S2S_s$  vectors dataset into distinct site classes, with corresponding site amplification functions can be considered moderately successful. The k-means clustering produced two reasonably distinct amplification functions, with significant overlap only occurring for the  $\Delta S2S_s$  vectors (from which the amplification functions are calculated) at a period of 2.0 s (Fig. 4.2), which can be attributed to the high intra-cluster standard deviation for  $\delta S2S_s$  values at a period of 2.0 s (Fig. 4.4). This high standard deviation is evident from the visual representation of the  $\Delta S2S_s$  vector clustering (Fig. 4.2), where the  $\Delta S2S_s$  vectors assigned to cluster 2 are visibly less similar than the  $\Delta S2S_s$  vectors assigned to cluster 1. Consequently, it can be concluded that overall cluster 1 (the reference cluster) represents a more similar set of  $\Delta S2S_s$  vectors than cluster 2 (the amplification cluster), which represents the remaining, higher amplification  $\Delta S2S_s$  vectors of less similar  $\Delta S2S_s$  vectors.

A significant benefit observed within the Kotha et al. (2018) study is also observed in this analysis; the intra-cluster site-to-site response variability for each considered period is overall significantly smaller than the pre-clustered overall site-to-site response (Fig. 4.4) – this reduction is approximately 58% on average for cluster 1, and approximately 43% for cluster 2. The smallest reduction in intra-event standard deviation is observed at a period of 2.0 s for cluster 2 (~ 22%). This can be attributed to the

poorer clustering observed in cluster 2 compared to cluster 1 (see Fig. 4.2). This overall reduction in the standard deviations is primarily the result of the clustering of the  $\Delta S_2 S_s$  vector dataset. This reduction can also be attributed to (1) the relatively small size of the dataset and (2) the dataset comprising many small earthquakes (the greater variability in the ground-shaking associated with smaller earthquakes (Ambraseys et al., 2005) results in a more significant variability reduction following clustering).

As mentioned above, if more geotechnical site characteristics were available for the sites within the North Sea dataset, the clustering could be evaluated in terms of the variability observed in the site conditions within each cluster's assigned sites. Consequently, each cluster was only given a simple description: cluster 1 is the reference cluster which likely comprises sites with harder, more intact bedrock and a thinner soil layer, and cluster 2 is the amplification cluster which likely comprises sites with softer, less intact bedrock and a thicker soil layer.

Importantly, the site amplification functions improve the performance of the  $R_{jb}$  variant of the Akkar et al. (2014) GMPE in the North Sea. This improved performance is primarily indicated by small but largely consistent reductions in the variability in the intra-event residuals when incorporating the computed cluster amplification functions (Fig. 4.4). The largest reduction in  $\delta S_2 S_s$  is observed at a period of 0 s (~ 10%), although considerable reductions are still observed for periods of 0.1 s, 0.5 s and 1.0 s (~ 8%, ~ 7% and ~ 6% respectively). A smaller reduction in  $\delta S_2 S_s$  variability is observed at 2.0 s (~1%, Fig. 4.4), which can be attributed to site effects having smaller impacts at longer periods (longer periods are more affected by source and path effects). Overall, this reduction in the variability observed in the intra-event residuals suggests the clustering of the  $\Delta S_2 S_s$  vector dataset provides an effective means of partially relaxing the ergodic assumption with respect to site, therefore improving GMPE performance in the North Sea region.

#### **4.4 Conclusions for Constraining Onshore Site Effects in the North Sea**

The ergodic assumption was relaxed with respect to site through the constraining of North Sea onshore site effects. The constraining of site effects was achieved through clustering analysis of the  $\Delta S_2 S_s$  vector dataset. This cluster analysis can be considered as moderately successful due to the cluster amplification functions reducing the variability in site-to-site response for onshore sites in the North Sea region (Fig. 4.4). However, the lack of geotechnical information for the sites in the North Sea dataset prevented the evaluation of the clustering in terms of how similar the site conditions are for the sites within each cluster, resulting in simpler descriptions of the clusters as either representative of high or low amplification subsurface conditions. This lack of geotechnical information highlights the need for abundant *post posteriori* information to maximise the effectiveness of the Kotha et al. (2018) site classification method. As discussed above, more detailed geotechnical descriptions for each cluster would enable onshore sites in the North Sea region which were not included in the original analysis for

which no ground-motions have been observed, but the site conditions are known to be assigned the appropriate cluster amplification functions, and therefore be corrected for site effects in a future North Sea PSHA. Further work on the cluster functions is required for their application to offshore North Sea sites, where critical infrastructure such as wind turbine facilities and oil and gas platforms are deployed in the region.

#### **4.5 Constraining Offshore Site Effects in the North Sea**

Site effects were successfully constrained above for onshore sites within the North Sea region through the computation of cluster amplification functions. However, critical infrastructure within the North Sea region (e.g. wind turbine facilities and oil and gas platforms) are primarily situated at offshore locations. The computed cluster amplification functions are therefore insufficient for estimating local effects at typical sites of interest in a North Sea PSHA. More detailed geotechnical descriptions for each cluster amplification function would permit additional onshore North Sea sites (for which no ground-motions have been recorded, but site conditions are known) to be assigned the most appropriate cluster amplification function. However, for offshore sites, the presence of additional local site effects resulting from the marine environment must be considered, and consequently offshore sites within the North Sea cannot be assigned an appropriate cluster amplification function simply through the acquisition of a site-specific geotechnical description. The additional site effects associated with the marine environment are the result of (1) the presence of the water layer and (2) the supersaturation of near-surface sediments on the seafloor (Chen et al., 2017).

The presence of both the water layer and the supersaturation of seafloor sediments were examined by Boore and Smith (1999), in which 8 earthquakes recorded at 6 offshore sites in Southern California were analysed. The data analysed by Boore and Smith (1999) was recorded using instruments installed on the seafloor for the Seafloor Earthquake Measuring System (SEMS) project. The analysis within this investigation comprised of comparing the ratio of vertical to horizontal response spectra ( $V/H$ ) computed for each of the 6 offshore sites to the  $V/H$  computed for onshore sites which recorded the same earthquakes, so as to determine whether offshore ground-motions are significantly different to onshore ground-motions. Ground-motions are affected by many variables including earthquake size, source-to-site distance, fault focal mechanism and local site conditions. Boore and Smith (1999) used  $V/H$  to compare offshore and onshore ground-motions because it should effectively reduce any differences in the incident ground-motions to solely the local site conditions. The use of  $V/H$  computed from ambient noise to investigate local site effects was first proposed by Nogoshi and Igarashi (1971) and popularised by Nakamura (1989). Atakan and Havskov (1996) demonstrated that this technique is viable for the evaluation of seafloor site response using  $V/H$  computed from earthquakes recorded by two ocean bottom seismograph (OBS) networks situated in the North Sea (see section 4.7 below).

Boore and Smith (1999) found that the presence of the water layer strongly reduced the vertical component of incident *P*-waves because compressional waves can propagate through the water layer. This reduction is not observed for incident *S*-waves because transverse waves cannot propagate through the water layer. This reduction in the vertical component was observed at higher frequencies (above ~ 3 Hz), but was most prominent for the resonant frequency of the water layer<sup>24</sup>. This reduction in the vertical component (at higher frequencies) resulted in *V/H* computed for the offshore SEMS sites being smaller than for the onshore sites (Fig. 4.6). The horizontal component was found to experience minimal modification at all considered frequencies due to *S*-waves not being able to propagate through the water layer. For the engineering of offshore oil and gas platforms horizontal ground-motions with periods greater than 1.0 s are generally of far greater importance than higher frequency (smaller period) ground-motions (Boore and Smith, 1999)<sup>25</sup>. The natural period of offshore oil and gas platforms is approximately 1.5 – 4.0 s (Boore and Smith, 1999). The lower frequency components of ground-motion incident at the offshore SEMS sites were found to not be directly affected by the presence of the water layer. Therefore, the presence of the water layer was determined by Boore and Smith (1999) to be of minimal importance when determining the nature of the lower frequency ground-motions incident at offshore sites, which are of considerably greater importance for the engineering of offshore structures.

The good agreement between *V/H* for the offshore SEMS sites and onshore sites at lower frequencies (Fig. 4.6) indicates that the differences in *V/H* are primarily a function of the sediments underlying the sites, rather than the presence or absence of the water layer. This suggestion was subsequently evaluated by comparing *V/H* of offshore SEMS sites with additional onshore sites with *S*-wave velocities similar to those of the offshore SEMS sites. Boore and Smith (1999) observed differences at larger periods in *V/H* between the additional onshore sites and the original onshore sites, which were attributed to the variations in the *S*-wave velocities beneath these sites. The *S*-wave velocities of the additional onshore sites were considerably lower than those of an average soil site. Boore and Smith (1999) determined that this lends further support to *V/H* at larger periods being more strongly controlled by the *S*-wave velocities of the near-seafloor sediments rather than the presence or absence of the water layer.

Since Boore and Smith (1999), few studies have been undertaken to examine the effects of the offshore environment on ground-motions. Hatayama (2004) used two-dimensional numerical modelling to investigate the influence of the water layer on incident ground-motions, also determining that the water layer has a significant impact on the *P*-wave component of ground-motions recorded on the seafloor.

---

<sup>24</sup> The resonant frequency of the water layer,  $f_p = C_v/4H$ , where  $C_v$  is the velocity of *P*-waves in the water layer (assumed to be ~1500 m/s) and  $H_w$  is the water layer thickness in metres (Boore and Smith, 1999).

<sup>25</sup> Offshore wind turbines also have relatively large natural periods in the horizontal direction (~ 3 s), and therefore like oil and gas platforms are not particularly vulnerable to higher frequency ground-motions (Kaydia, 2019). However, offshore wind turbines possess reasonably high natural frequencies in the vertical direction (4 - 7 Hz), and therefore are vulnerable to even moderate ground-shaking (Kaydia, 2019). Kjølraug and Kaynia (2015) suggest that engineering offshore wind turbines to be resilient to these higher frequency vertical ground-motions is vital for their long-term structural integrity.

Diao et al. (2014) investigated the propagation of  $P$ - and  $SV$ - (vertical shear) waves at the water layer boundary using 4 additional earthquakes recorded by the SEMS project instruments. The findings of this study were also largely in agreement with those of Boore and Smith (1999). Zhang and Zheng (2019) studied the differences in offshore and onshore ground-motions by comparing more than 1,000 seafloor ground-motions predominantly recorded by 6 seafloor seismometers belonging to the Kyoshin Network (K-NET) off the coast of Sagami Bay in Japan to onshore ground-motions pertaining to the same earthquakes. Zhang and Zheng (2019) compared the ground-motions using PGA, the vertical and horizontal response spectra and  $V/H$ . For PGA, Zhang and Zheng (2019) observed that for the same earthquake with identical (epicentral) source-to-site distances, the offshore horizontal PGA experiences greater amplification than its onshore counterpart. The offshore  $V/H$  PGA was found to be considerably smaller than the onshore  $V/H$  PGA. The offshore  $V/H$  PGA was determined to be smaller than the onshore  $V/H$  PGA because for PGA the offshore environment effectively amplifies the horizontal component of ground-motion and reduces the vertical component of ground-motion. For both the vertical and horizontal response spectra, it was observed that (1) the spectral plateau occurs at larger periods for offshore records than onshore records and (2) for moderate and large periods the offshore ground-motions experience greater amplification than the onshore ground-motions. The greater amplification experienced at moderate and large periods is significant for the seismic design of bottom-fixed offshore structures due to them possessing large natural periods (Zhang and Zheng, 2019). Additionally, Zhang and Zheng (2019) observed that for periods longer than 2 s, offshore and onshore  $V/H$  are comparable, which is in agreement with the findings of Boore and Smith (1999) (Fig. 4.6).

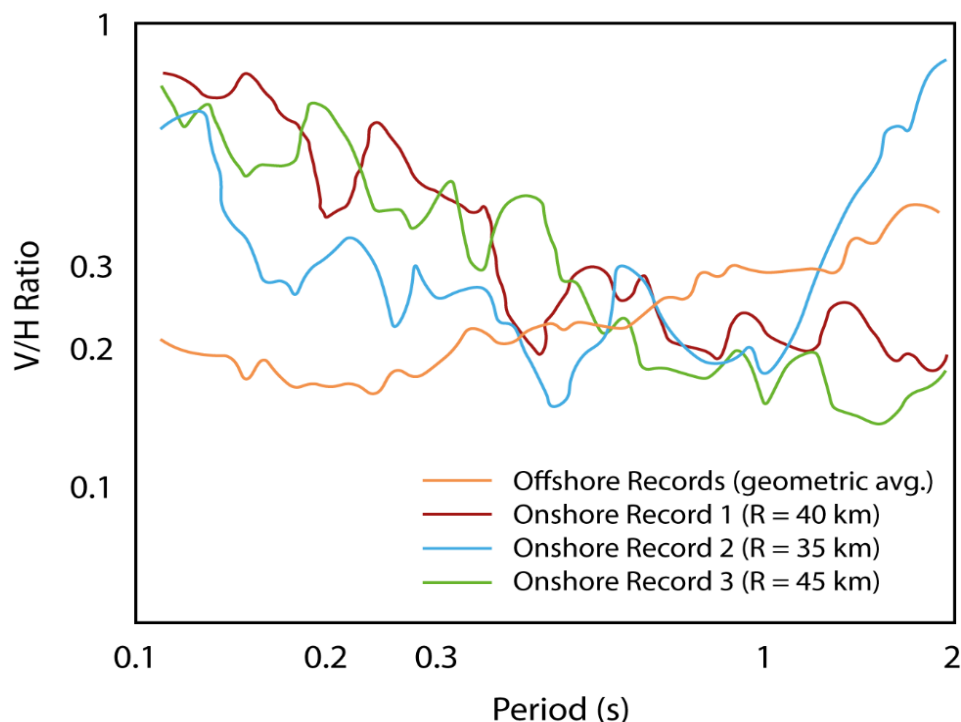


**Figure 4.6**  $V/H$  spectra for the geometric average of the offshore SEMS sites and select onshore records. The onshore sites are underlain by soils with  $S$ -wave velocities similar to those estimated to lie beneath the SEMS sites. Adapted from Boore and Smith (1999).

#### 4.6 The Application of $V/H$ in Offshore Seismic Design

The studies briefly discussed above used  $V/H$  to investigate offshore local site effects. The primary use of  $V/H$  is the estimation of the vertical component of ground-motion incident at a site of interest, based on the estimate computed for the horizontal component using PSHA (Boore and Smith, 1999). Prior to extensive investigation into the vertical component of ground-motion, the International Organisation of Standardisation (ISO)'s original offshore seismic design standard (ISO19901-2, 2004) recommended the use of a fixed  $V/H$  of 0.5 for all periods. The characteristics of vertical ground-motion have since been well examined. Many of the characteristics of  $V/H$  identified in the studies discussed below are demonstrated in Fig. 4.6.

A series of studies by Niazi and Bozorgnia (1990, 1991, 1992), Bozorgnia and Niazi (1993) and Bozorgnia et al. (1995, 1996) identified that  $V/H$  is (1) highly sensitive to period and the distance from the fault, (2) that a distinct peak where  $V/H$  exceeds  $2/3$  is observed within the low period range and (3) that  $V/H$  is usually less than  $2/3$  for larger periods in the near-source region. Importantly,  $V/H$  characteristically peaking at larger than  $2/3$  for smaller periods and usually being less than  $2/3$  for larger periods suggests the use of a unified  $V/H$  for all periods potentially results in the underestimation (for smaller periods) or overestimation (for larger periods) of the predicted vertical component of ground-motion. Watabe et al. (1990) identified a systematic relationship between the amplitudes of the vertical and horizontal components of ground-motion, and first proposed that an estimate of the vertical response spectra should be obtainable from the horizontal response spectra through the development of simple relationships between the three components of ground-motion (two horizontal and one vertical). These investigations into the vertical component of ground-motion all determined that  $V/H$  is strongly a function of period, with the smaller periods possessing higher ratios than the larger periods. These observations were consistent with the differences identified in the spectral shapes of the vertical and horizontal ground-motion components. These differences in the spectral shapes of the vertical and horizontal components result in  $V/H$  (1) possessing a maximum in the period range of 0.05 – 0.1 s and a minimum in the period range of 0.4 – 0.8 s and (2) for the largest considered periods gradually increasing with period. A concise summary of the proposed seismological explanations for the observed characteristics of the  $V/H$  parameter is provided by Campbell and Bozorgnia (2004).

Several of the studies regarding  $V/H$  discussed above have proposed the reassessment of using a fixed  $V/H$  for the estimation of vertical ground-motion. Campbell (1985) first proposed such reassessment based on the findings of Bureau (1981) and Campbell (1982), who first recognised that  $V/H$  computed using ground-motions recorded in the near-source region from large earthquakes are significantly different to  $V/H$  computed using ground-motions recorded at large source-to-site distances from small

earthquakes. Based on the findings of these studies<sup>26</sup>, the ISO's most recent offshore seismic design standard (ISO19901-2, 2016) recommends the use of a period-dependent  $V/H$  for estimating vertical ground-motions, rather than the use of a fixed  $V/H$  as recommended in the original standard (ISO19901-2, 2004).

GMPEs for predicting the horizontal and vertical components of ground-motion have been developed using near-source ground-motion data. Many of these GMPEs have been used to evaluate  $V/H$ , and were developed for individual earthquakes (e.g. Bozorgnia and Niazi (1993) for the 1989 Loma Prieta earthquake), specific regions (e.g. Niazi and Bozorgnia (1991, 1992) for Taiwan) and for global application (e.g. Ambraseys and Douglas, 2003). Campbell and Bozorgnia (2003) developed a mutually consistent set of GMPEs for the vertical and horizontal components of ground-motion which largely confirm the empirical observations for  $V/H$  discussed above. Bozorgnia and Campbell (2004) developed a GMPE for directly predicting  $V/H$  using the set of GMPEs developed in Campbell and Bozorgnia (2003). Bozorgnia and Campbell (2019) further built upon the GMPEs developed by Campbell and Bozorgnia (2003) and Bozorgnia and Campbell (2004) through developing a  $V/H$  GMPE which separates the variability in the predicted  $V/H$  into intra-event and inter-event components. Additional GMPEs for directly predicting  $V/H$  have also been developed by Gülerce and Abrahamson (2011), Bommer et al. (2011) and Akkar et al. (2014).

#### **4.7 Offshore Site Effects in the North Sea**

Limited studies into offshore site effects in the North Sea have been undertaken. As discussed above, Atakan and Havskov (1996) demonstrated that the use of  $V/H$  for evaluating site effects is viable for offshore environments, doing so using  $V/H$  computed from earthquakes recorded by two North Sea OBS networks. As part of the Earthquake Loading on the Norwegian Continental Shelf (ELOCS) project (Bungum and Selnes, 1987), Rognlien (1987) performed site response analysis for 8 offshore North Sea sites to study the variation in local site effects in the region. Geotechnical information was acquired for each of these 8 sites. The equivalent-linear method was used for these site response analyses<sup>27</sup>. Two site response analyses were performed for each of the 8 offshore sites using the *SHAKE* site response software (Schnabel et al., 1972). For the first analysis each site was subjected to the same low-amplitude ground-motion with an annual rate of occurrence of  $10^{-2}$  and for the second analysis each site was subjected to the same high-amplitude ground-motion with an annual rate of occurrence rate of  $10^{-4}$ . For the low-amplitude ground-motion, the east-west component of a ground-motion record of the Friuli earthquake (6/5/1976) from a seismograph station in Ljubljana, Slovenia was used. The ground-

---

<sup>26</sup> The most important of such findings being that the use of a unified  $V/H$  for all periods potentially results in the underestimation (for smaller periods) or overestimation (for larger periods) of the predicted vertical component of ground-motion (due to  $V/H$  characteristically peaking at larger than  $2/3$  for smaller periods and usually being less than  $2/3$  for larger periods).

<sup>27</sup> See Appendix C for an overview of site response analysis.

motion record was scaled to  $PGA = 0.05$  g. For the high-amplitude ground-motion, the north-south component of a ground-motion record of the Friuli earthquake (6/5/1976) from a seismograph station in Tolmezzo, Italy was used. The ground-motion record was scaled to  $PGA = 0.20$  g. The ground-motion records used for the site response analyses were recorded on bedrock. These ground-motions could therefore be treated as bedrock ground-motions, which could then be scaled by the subsurface conditions of each site to produce corresponding rock outcrop ground-motions, providing a means of determining the local site effects for each site. The local site effects for each of the 8 sites were expressed as response spectra site transfer functions<sup>28</sup>.

Rognlien (1987) determined that local soil conditions on the Norwegian Continental Shelf can amplify incident ground-motions by up to a factor 6 for the low-amplitude ground-motion and up to a factor of 5 for the high-amplitude ground-motion, with a high level of variability between sites. The low period range was found to generally be amplified more for the low-amplitude ground-motion than for the high-amplitude ground-motion, whereas the high period range was found to generally be amplified more for the high-amplitude ground-motion than for the low-amplitude ground-motion. An increase in soil stiffness was found to result in an increase in free-field response for the low period range and a decrease in free-field response for the high period range. Due to the variability in site-to-site response observed by Rognlien (1987), the Health and Safety Executive (HSE) report on seismic hazard for the United Kingdom's continental shelf (EQE International Ltd, 2002) specifies period-dependent ranges for the bedrock-to-surface amplification ratios used for estimating offshore North Sea site response, rather than specific values.

The cluster amplification functions computed above cannot be assigned to offshore sites within the North Sea for which subsurface conditions are known without (1) more detailed geotechnical descriptions for each cluster amplification function and (2) consideration of the additional site effects resulting from the marine environment. The acquisition of detailed geotechnical descriptions for each cluster amplification function is currently not possible due to this requiring in-depth investigation of the site conditions present at each of the 17 (onshore) sites originally clustered. The marine environment has been shown by the studies discussed above to have a pronounced effect on incident vertical ground-motions. Considering that the cluster amplification functions cannot currently be applied to offshore North Sea sites, the period-dependent  $V/H$  ratios for estimating offshore vertical ground-motions recommended within the ISO's most recent offshore seismic design standard (ISO19901-2, 2016) are the most practical available means of accounting for the site effects resulting from the marine environment. The HSE's period-dependent ranges for bedrock-to-surface amplification on the United Kingdom's continental shelf (EQE International Ltd, 2002) are also viable for estimating offshore site

---

<sup>28</sup> Only response spectra transfer functions were considered within this investigation (as opposed to Fourier amplitude spectra transfer functions) because the response spectra is the most important singular representation of ground-motion at a site.

effects in the North Sea. For offshore North Sea sites for which geotechnical information is available the site transfer functions computed by Rognlien (1987) may be applicable if the subsurface conditions of the site of interest are similar to one of the 8 sites Rognlien (1987) evaluated.

The site transfer functions provided by Rognlien (1987) have been recomputed for 7 of the 8 sites considered within the original investigation (Fig. 4.7). The site omitted within this recomputation of the site transfer functions (“Site H”) was not included because the site is geographically located outside the primary region of focus for this investigation into North Sea seismic hazard (the central northern North Sea). The site transfer functions were recomputed for a high-amplitude ground-motion using the geotechnical site profiles provided within the original investigation (Tab. 4.0; Tab. 4.1), the *STRATA* site response software (Kottke and Rathje, 2008) and the equivalent-linear site response method. For the high-amplitude ground-motion, the north-south component of a ground-motion record from a local magnitude ( $M_L$ ) 5.2 earthquake originating near Bursa, Turkey (18/07/1979) recorded from a nearby (within 10 km) seismograph station (station name: AI\_145\_DUR\_KGI) was used. This ground-motion record was chosen because (1) like the ground-motion records used within the original analysis by Rognlien (1987) the ground-motion was recorded on bedrock, (2) the source-to-site distance is small<sup>29</sup> and (3) the average shear-wave velocity of the top 30 m ( $V_{s30}$ ) of the station recording this ground-motion is similar to the average  $V_{s30}$  of the Rognlien (1987) sites considered in this recomputation of the site transfer functions.

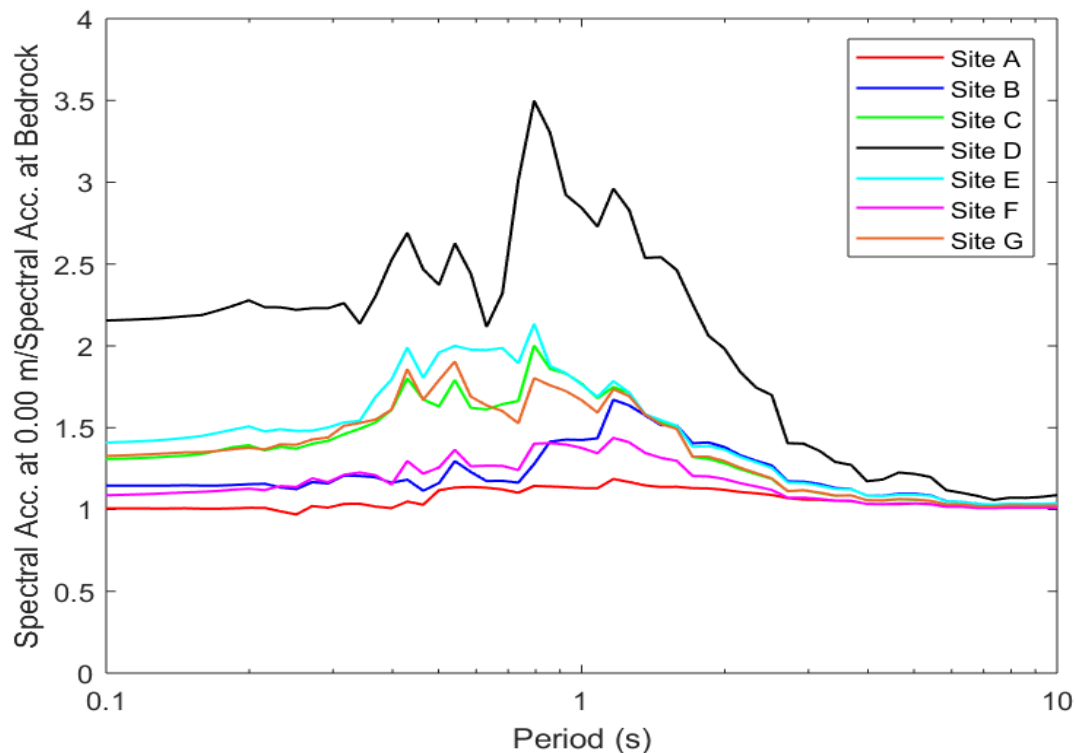


**Figure 4.7** *Recomputed (response spectra) site transfer functions for the offshore North Sea sites considered by Rognlien (1987). Subsurface profiles for each site are provided in Tab. 4.1.*

<sup>29</sup> A small source-to-site distance minimises the impact of path effects on the incident ground-motion.

The recomputed site transfer functions are similar to those computed by Rognlien (1987) for a high-amplitude ground-motion. The high-amplitude ground-motion experiences considerably greater amplification at Site D than at the other considered sites, which can be attributed to Site D being the only site underlain predominantly by soft and highly plastic clay. The high-amplitude ground-motion experiences the least amplification at Site A, which can be attributed to Site A being underlain primarily by dense sand. The high-amplitude ground-motion experiences minimal amplification at Site B and Site F because Site B is underlain by dense sand overlying stiff clay and Site F is underlain by stiff clay.

#### **4.8 Conclusions for Constraining Offshore Site Effects in the North Sea**

Limited work has been undertaken regarding the effects of the marine environment on seismic hazard. The majority of these studies have utilised  $V/H$  to evaluate the effects of the water layer and the super-saturated seafloor sediments on incident ground-motions.  $V/H$  is smaller for offshore sites than onshore sites due to the water layer strongly reducing the vertical component of incident P-waves, especially at the resonant frequency of the water column (Boore and Smith, 1999; Hatayama, 2004). The lower frequency components of ground-motion incident at offshore sites are unaffected directly by the presence of the water layer (Boore and Smith, 1999). Larger period ground-motions are more significant for the seismic design of conventional offshore structures, and therefore the water layer is of minimal importance for estimating the ground-shaking at offshore sites (Boore and Smith, 1999). For larger periods, offshore ground-motions are more affected by the S-wave velocities of the soils immediately underlying the sites of interest (within a PSHA) than the presence or absence of the water layer (Boore and Smith, 1999).

Considering that the computed cluster amplification functions cannot currently be assigned to offshore sites, the most practical available means of accounting for offshore site effects in the North Sea are the use of the period-dependent  $V/H$  ratios recommended within the ISO's most recent offshore seismic design standard (ISO19901-2, 2016) and the period-dependent ranges for bedrock-to-surface amplification on the United Kingdom's continental shelf provided by the HSE (EQE International Ltd, 2002). If sufficient geotechnical information is available for an offshore North Sea site, the site transfer functions computed by Rognlien (1987) may be applicable. The site transfer functions have been recomputed within this investigation for 7 of the 8 considered sites. The recomputed site transfer functions are similar to those computed by Rognlien (1987) for a high-amplitude ground-motion.

**Table 4.0** *Quantitative descriptions of the terminology used by Rognlien (1987) to describe the strength of each distinct soil layer within each considered site's subsurface profile.*

<b>Terminology</b>	<b><math>S_u</math> (shear strength – kPa)</b>
Very soft	< 12.5
Soft	12.5 – 25
Medium	25 – 50
Stiff	50 – 100
Very stiff	100 – 200
Hard	200 – 400
Very hard	> 400

**Table 4.1** Basic subsurface profiles for each offshore North Sea site considered by Rognlien (1987). Quantitative descriptions of the terminology used to describe the strength of each distinct soil layer are provided in Tab. 4.0.

Site	Z (Depth of Distinct Layers - m)	Soil Description	$G_0$ (initial shear modulus)
A	0 – 26	Dense, fine sand	30 – 230
	26 – 38.5	Hard clay	175 – 235
	38.5 – 85	Dense, fine sand	270 – 370
	$Z > 85$	Hard clay	$G_0 > 225$
B	0 – 22	Dense, fine sand	25 – 155
	22 – 74	Very stiff, silty clay	115 – 195
	74 – 90	Dense sand and silt	250 – 300
	90 – 120	Hard, silty clay	300 – 375
C	0 – 5	Very soft, silty clay	$G_0 < 12$
	5 – 32	Medium dense sandy, clayey silt	20 – 70
	32 – 48	Very stiff silty clay	90 – 175
	48 – 68	Fine dense sand	~ 300
	$Z > 68$	Hard silty clay	$G_0 > 200$
D	0 – 24	Soft, very silty clay	1 – 26
	24 – 64	Stiff, silty and sandy clay	65 – 150
	64 – 120	Hard, silty clay	210 – 230
E	2 – 9	Soft, silty clay	5 – 20
	9 – 28	Dense, silty sand	45 – 75
	28 – 108	Very stiff clay	75 – 200
F	0 – 13	Stiff, silty clay	20 – 90
	13 – 17	Dense sand	~ 185
	17 – 55	Very stiff, sandy clay	125 – 180
	55 – 80	Hard, sandy clay	200 – 350
G	0 – 9	Soft/medium silty and sandy clay	10 – 34
	9 – 19	Stiff/very stiff silty and sandy clay	50 – 75
	19 – 42	Stiff/very stiff silty clay	90 – 150
	42 – 90	Hard silty and sandy clay	170 – 300
	$Z > 90$	Hard plastic normally consolidated clay	$G_0 > 350$

#### 4.9 Constraining Path Effects in the North Sea

Following application of the cluster amplification functions to the intra-event GMPE residuals (computed using the base model GMPE – the  $R_{jb}$  variant of the Akkar et al., 2014 GMPE), site effects for the North Sea dataset were found to be sufficiently constrained<sup>30</sup>. Source effects (e.g. source size and shape) had been constrained by the magnitude term and style-of-faulting terms implemented in the Akkar et al. (2014) GMPE (see equation 2 of Akkar et al. (2014) for more details). Consequently, the intra-event residuals were now considered as effectively representative of exclusively the path effects for each ground-motion record in the North Sea dataset.

Path effects represent the energy dissipated as seismic waves propagate through the subsurface due to seismic attenuation (Kennett, 2009). Seismic attenuation occurs through three mechanisms: (1) geometric spreading, (2) anelastic attenuation and (3) scattering. Through the implementation of a geometric spreading term in the Akkar et al. (2014) GMPE distance-related path effects had already been constrained (see equation 2 of Akkar et al. (2014) for more details). The Akkar et al. (2014) GMPE does not implement an anelastic attenuation term nor a scattering term<sup>31</sup>, and therefore neither anelastic attenuation or scattering path effects were explicitly constrained<sup>32</sup>. Each site-corrected intra-event residual could therefore now be treated as effectively representative of solely the apparent attenuation (anelastic attenuation plus scattering) path effects for each ground-motion record (in the North Sea dataset).

Each intra-event residual was used to relax the ergodic assumption with respect to path (and therefore improve GMPE performance) through determining repeat apparent attenuation effects for the North Sea region. Repeat apparent attenuation effects were determined through implementing a tomographic inversion methodology based on Dawood and Rodriguez-Marek (2013)'s study on relaxing the ergodic assumption with respect to path in Japan.

#### 4.10 Methodology for Constraining Path Effects in the North Sea

Prior to the implementation of the Dawood and Rodriguez-Marek (2013) methodology the latitude and longitudes of the earthquake epicentres and the stations were converted to northings and eastings relative to the corresponding Universal Transverse Mercator (UTM) zone(s). This conversion ensured the curvature of the earth was accounted for even in the two-dimensional visualisation of a tomographic

---

<sup>30</sup> The Akkar et al. (2014) GMPE utilises a non-linear site amplification term (see equation 3 of Akkar et al. (2014) for more details). However, the lack of information for subsurface conditions in our investigation led to the choice to assign a uniform  $V_{S30}$  value of 600 m/s for all sites in the North Sea dataset, effectively resulting in the non-linear site amplification term being nullified.

<sup>31</sup> An anelastic attenuation term and a scattering term were not implemented due to a poor range of source-to-site distances for the ground-motion records in the dataset used for the GMPE's development, which is required to effectively constrain these path effect terms for a GMPE's functional form (Akkar et al., 2014).

<sup>32</sup> The geometric spreading term of the Akkar et al. (2014) GMPE potentially accounts for some of the apparent attenuation because the regression analysis undertaken for the development of the GMPE determines the model that best fits the data given the assumed functional form.

problem. Following this conversion, the modified Dawood and Rodriguez-Marek (2013) methodology was implemented. This methodology comprised of four stages:

1. Firstly, a grid of an appropriate resolution was imposed over the region for which repeat apparent attenuation effects were to be determined. For each grid cell an apparent attenuation rate was computed. This grid had to also overlay the travel paths of the associated ground-motion records (Fig. 4.8).

Ideally, the resolution of the grid had to be small enough that each grid cell captured significant yet particular variabilities in apparent attenuation over the region, but large enough that a sufficient number of travel paths also passed through each grid cell. A higher number of passes for each grid cell resulted in a better constrained attenuation rate for the associated grid cell (Dawood and Rodriguez-Marek, 2013).

Within the Dawood and Rodriguez-Marek (2013) study, the grid cell resolution was set at 25 km per grid cell. Within this investigation, the grid resolution was set at approximately 250 km per grid cell, resulting in a 3x3 grid overlay (Fig. 4.8). This reduction in grid resolution compared to the Dawood and Rodriguez-Marek (2013) study is attributed to the significantly smaller ground-motion record used in this investigation compared to the Dawood and Rodriguez-Marek (2013) study (120 records for 50 unique events vs. 7242 records for 117 unique events respectively). The smaller dataset resulted in far poorer coverage of the study region by the associated travel paths, and therefore a lower grid resolution being required to ensure a sufficient number of passes were observed for the majority of grid cells.

2. Secondly, the distance traversed across each grid cell by each travel path was determined. The travel paths are represented as straight lines (Fig. 4.8). For the travel paths to be represented as straight lines, it was assumed that the seismic waves are travelling at constant velocities. This assumption represents a significant source of simplification in the Dawood and Rodriguez-Marek (2013) methodology, which near-certainly does not hold true, but is implemented regardless so as to simplify the calculations.
3. Thirdly, the apparent attenuation of each grid cell was solved for each considered spectral period (0 s, 0.1 s, 0.5 s and 1.0 s). Within the Dawood and Rodriguez-Marek (2013) study, this is achieved through an iterative mixed-effects regression analysis, whereas in this investigation attenuation rates were solved for using simultaneous linear equations.

In this study, each linear equation is representative of a travel path, where the associated intra-event residual (representative of the apparent attenuation) is equal to the total apparent attenuation segmented over the grid cells which the travel path passes through. Each unknown value represents the apparent attenuation rate per km for a specific grid cell, with each unknown possessing a scaling coefficient equal to the distance (in km) the associated travel path traverses through this grid cell.

Attenuation rates were computed for each grid cell that any travel path passes through, resulting in 9 apparent attenuation rates for each spectral period considered (e.g. Fig. 4.9). These attenuation rates

were then implemented as distance-scaled correction factors for each associated site-corrected intra-event residual, resulting in the partial relaxation of the ergodic assumption with respect to path in the North Sea region. The computed attenuation rates are displayed in Tab. 4.4.

It should be noted that for any grid cell with less than 5 passes the corresponding apparent attenuation rate was considered as poorly constrained, and therefore the attenuation rate for each of these grid cells was replaced with the average apparent attenuation of the other grid cells. This procedure was applied to 1 of the 9 grid cells (grid cell A – see Fig. 4.8; Tab. 4.3). A similar procedure was applied to poorly constrained elements in the Dawood and Rodriguez-Marek (2013) study.

The grid cell apparent attenuation rates, like the GMPE residuals, were computed in base natural log units. If the apparent attenuation rate for each grid cell, each expressed as an attenuation coefficient is considered as a correction applied to each ground-motion record travel path (to reduce the associated site-corrected residual), then a negative grid cell attenuation rate must represent a zone of high attenuation, and a positive grid cell attenuation rate a zone of low attenuation. Equation 4.0 and Tab. 4.2 demonstrate how these corrections are applied:

$$Z_p = Z_s - \sum_{i=1}^n \delta_Q P_{ies} \quad (4.0)$$

where  $Z_p$  represents the path-corrected intra-event residual,  $Z_s$  represents the site-corrected intra-event residual,  $P_{ies}$  represents the distance (in km) through grid cell  $i$  for a straight line travel path of source  $e$  to site  $s$ , and  $\delta_Q$  represents the apparent attenuation per km through each grid cell.

4. Finally, statistical analysis comprising of (1) checkerboard inversion testing and (2) rerunning the tomographic inversion with a smaller dataset was undertaken to determine the appropriateness of the grid overlay resolution for the size of the North Sea dataset.

Checkerboard testing comprises of a simple data inversion. Firstly, a checkerboard pattern matrix of alternating high and low data points (relative to the outputted grid cell attenuation rates in the forward calculation) is inputted (Fig. 4.10), and the forward model (the resolution of the overlain grid and the associated distance coefficients for each travel path) is used to invert the checkerboard matrix, resulting in the computation of synthetic site-corrected residuals. Perturbations in the form of random sampling from a Gaussian noise distribution (with a standard deviation equal to that observed within the checkerboard matrix) are then added to these synthetic residuals. The perturbed synthetic residuals are then inputted into the forward model to reconstruct the original checkerboard pattern (Fig. 4.10). The percentage difference between each grid cell in the reconstructed matrix and the inputted checkerboard matrix (Fig. 4.11) provides an indication of how well the attenuation rate of each grid cell has been constrained using the forward model. A large difference is indicative of a grid cell being poorly constrained, and a small difference is indicative of a grid cell having been well constrained.

It should be noted that the checkerboard test has several weaknesses: (1) adding perturbations in the form of Gaussian noise with a specified standard deviation is likely not representative of the noise in the observed dataset (Rawlinson et al., 2014), (2) the use of an identical model for both the data inversion and the reconstruction will inherently result in a favourable reconstruction of the checkerboard matrix (Rawlinson et al., 2014) and (3) results can depend strongly on the inputted structure (Rawlinson et al., 2014), with L ev eque et al. (1993) demonstrating that this sometimes leads to smaller-scale structures (surprisingly) being better reconstructed than larger-scale structures. These inherent weaknesses for the checkerboard test led to the choice to rerun the tomographic inversion with smaller datasets for further verification of the viability of the chosen grid resolution.

Rerunning the tomographic inversion with a smaller dataset simply comprised of removing records from the North Sea dataset and re-computing the grid cell apparent attenuation rates using these reduced size datasets. As discussed in detail below, if reasonably similar results can be computed with smaller datasets (e.g. Fig. 4.12), this indicates that the grid resolution is appropriate for computing path effects in the North Sea region with the complete North Sea dataset (i.e. it would suggest that the computed attenuation rates are not extensively perturbed by moderate reductions in the size of the dataset).

**Table 4.2** Explanation of how traversing a grid cell with either a negative or positive apparent attenuation rate affects the corresponding intra-event residual.

Intra-Event Residual	Implication of Intra-Event Residual	Effect of Traversing a Grid Cell with a Negative Apparent Attenuation Rate	Effect of Traversing a Grid Cell with a Positive Attenuation Rate
Positive	Under-prediction due to GMPE factoring in an excessive amount of attenuation	Larger residual (i.e. poorer fit) due to factoring in additional attenuation.	Reduced residual (i.e. better fit) due to factoring in less attenuation.
Negative	Over-prediction due to GMPE not factoring in a sufficient amount of attenuation	Reduced residual (i.e. better fit) due to factoring in additional attenuation.	Larger residual (i.e. poorer fit) due to factoring in less attenuation.

**Table 4.3** Number of travel path passes for each grid cell in Fig. 4.8. \*Grid cell A is intercepted once by a marginal amount not clearly observable on the scale of Fig. 4.8.

Grid Cell	A	B	C	D	E	F	G	H	I
Number of Passes	1*	36	56	12	33	70	6	13	19

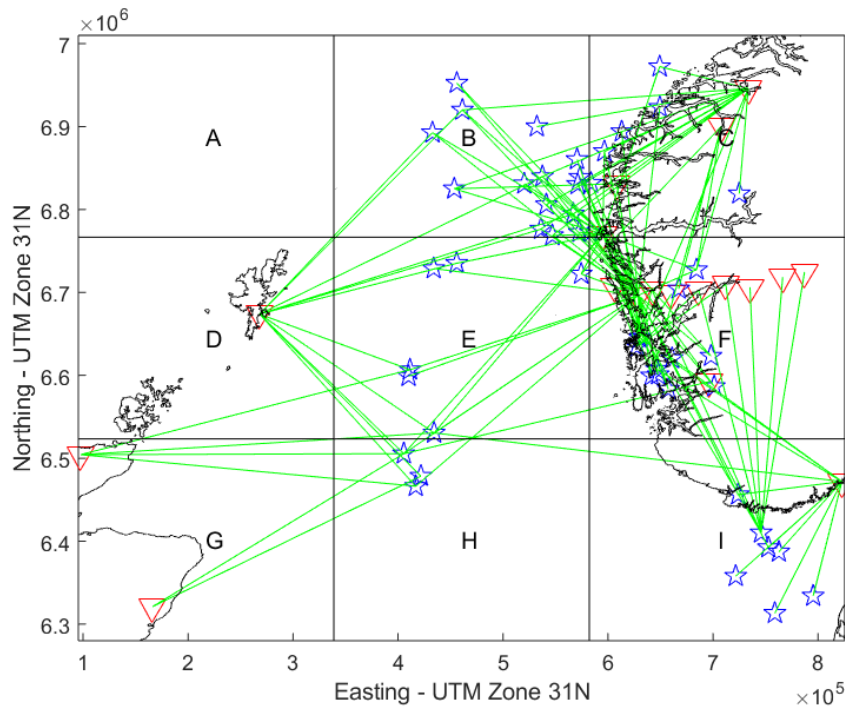


**Figure 4.8** North Sea region with  $3 \times 3$  grid overlay. Blue stars represent the earthquake epicentre locations. Red triangles represent the station locations. Green lines represent travel paths. Bold letters denote each grid cell for which path effects are to be constrained for.

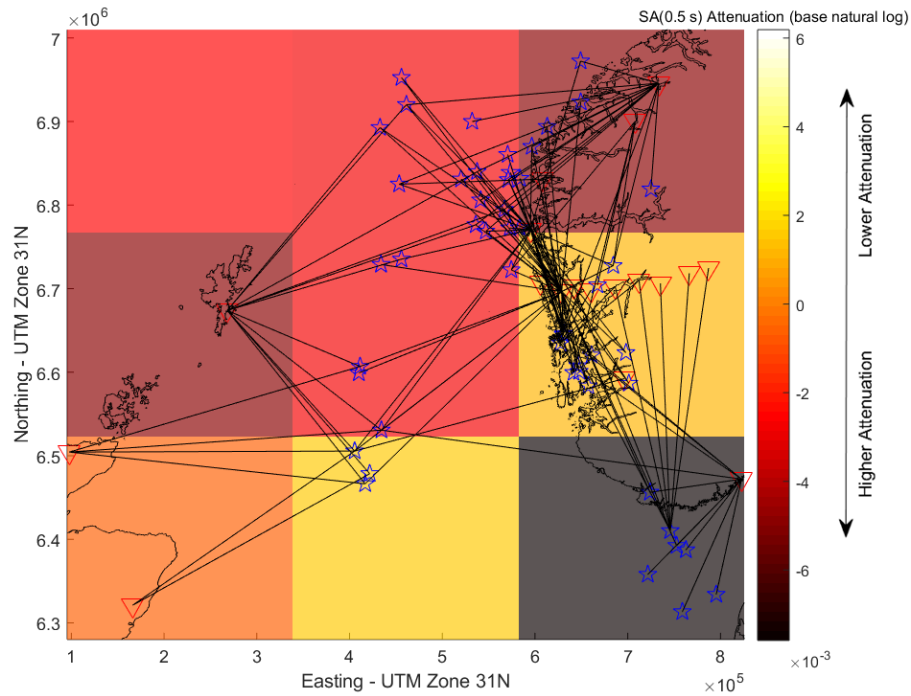


**Figure 4.9** Computed North Sea apparent attenuation rates (per km) for a spectral period of 0.5 s. Blue stars represent the earthquake epicentre locations. Red triangles represent the station locations. Black lines represent travel paths.

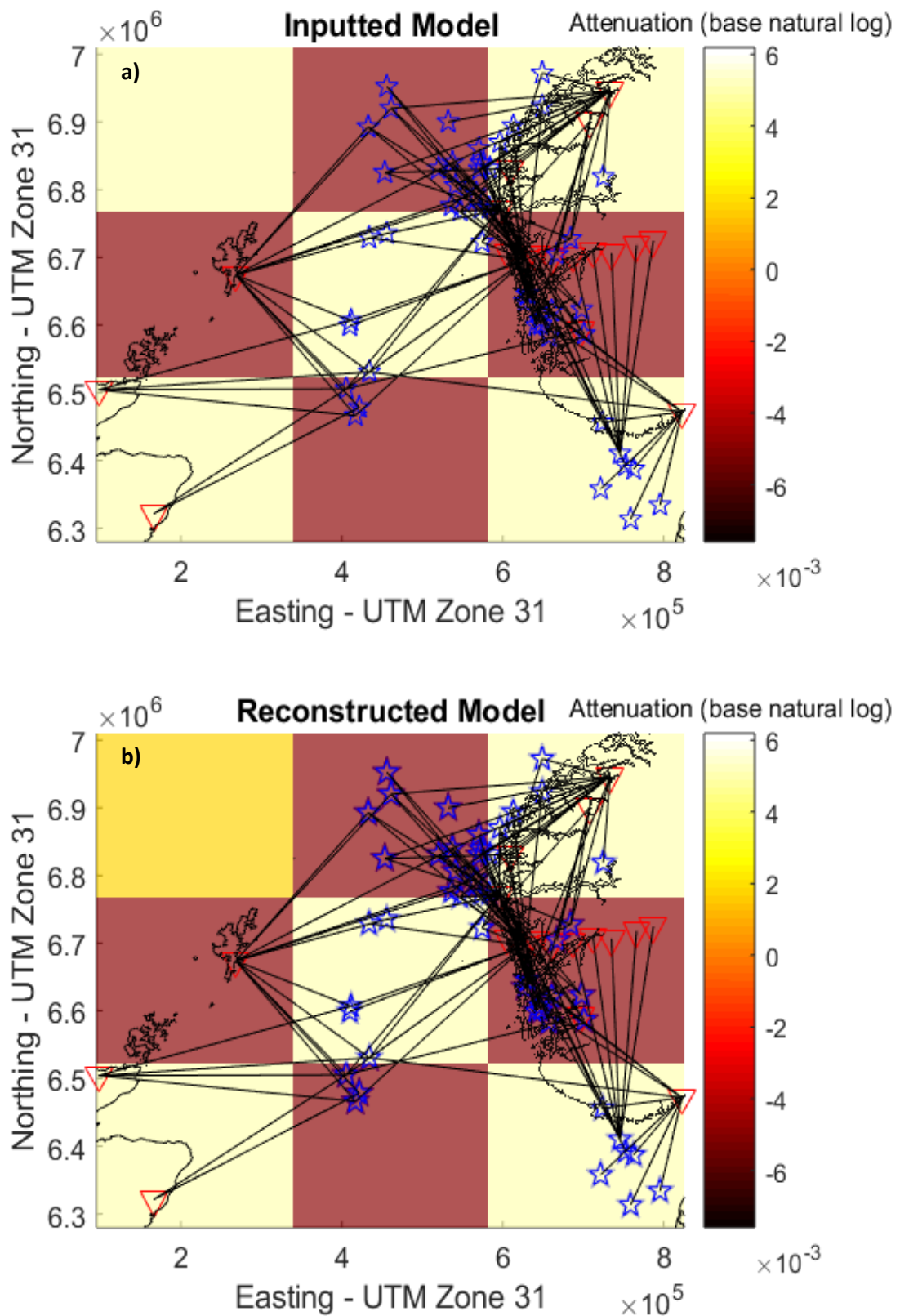


**Figure 4.10** (a) *Inputted checkerboard matrix*, (b) *reconstructed checkerboard matrix*. Blue stars represent the earthquake epicentre locations. Red triangles represent the station locations. Black lines represent travel paths.

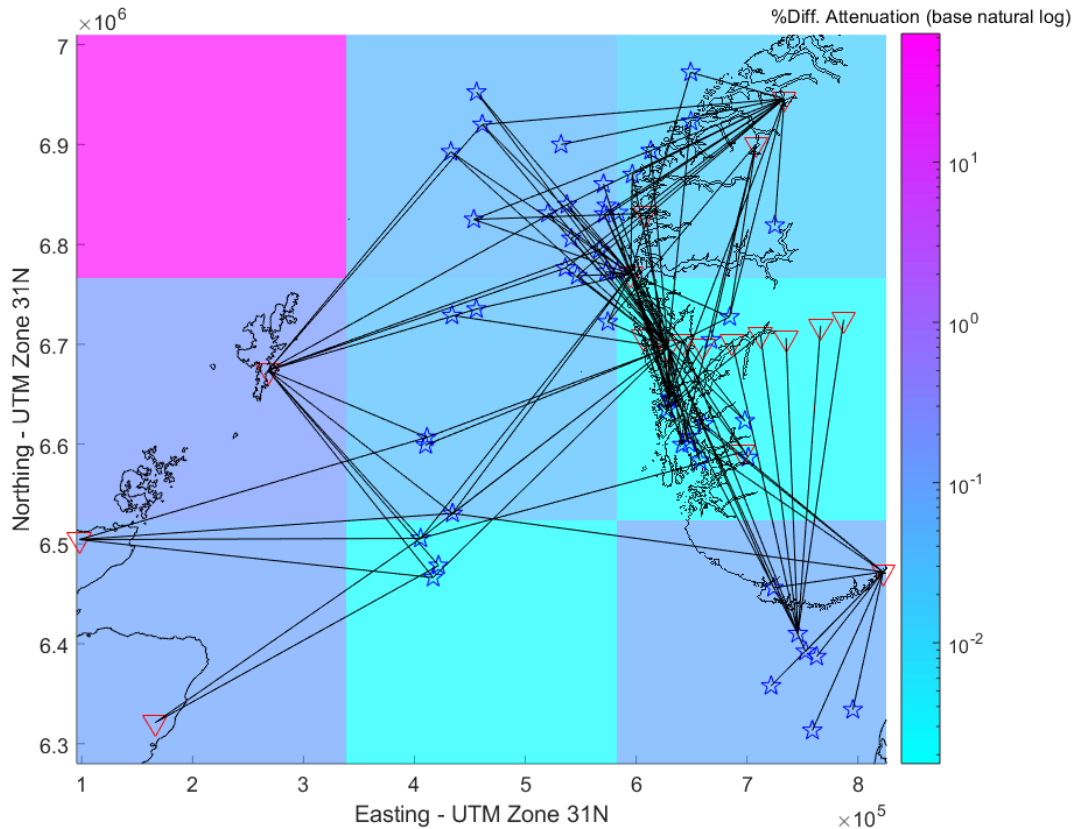


**Figure 4.11** Percentage difference between the reconstructed checkerboard matrix and the inputted checkerboard matrix. Blue stars represent the earthquake epicentre locations. Red triangles represent the station locations. Black lines represent travel paths.

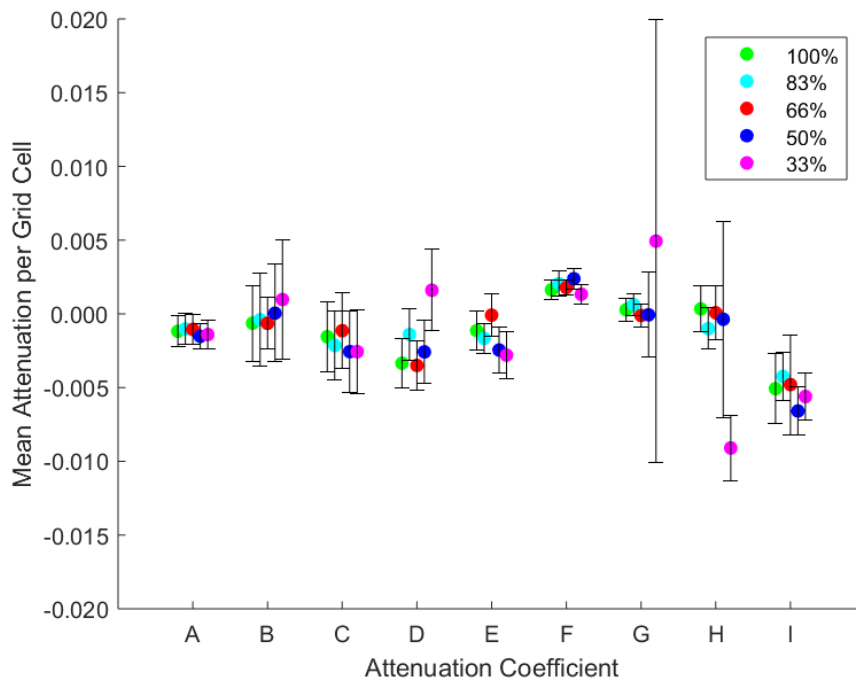


**Figure 4.12** Mean attenuation rates for each grid cell, computed using different size North Sea datasets. These mean values were determined using the computed attenuation rates for each spectral period considered (0 s, 0.1 s, 0.5 s and 1.0 s). The standard deviations represent the variability in the computed attenuation rates for these spectral periods.

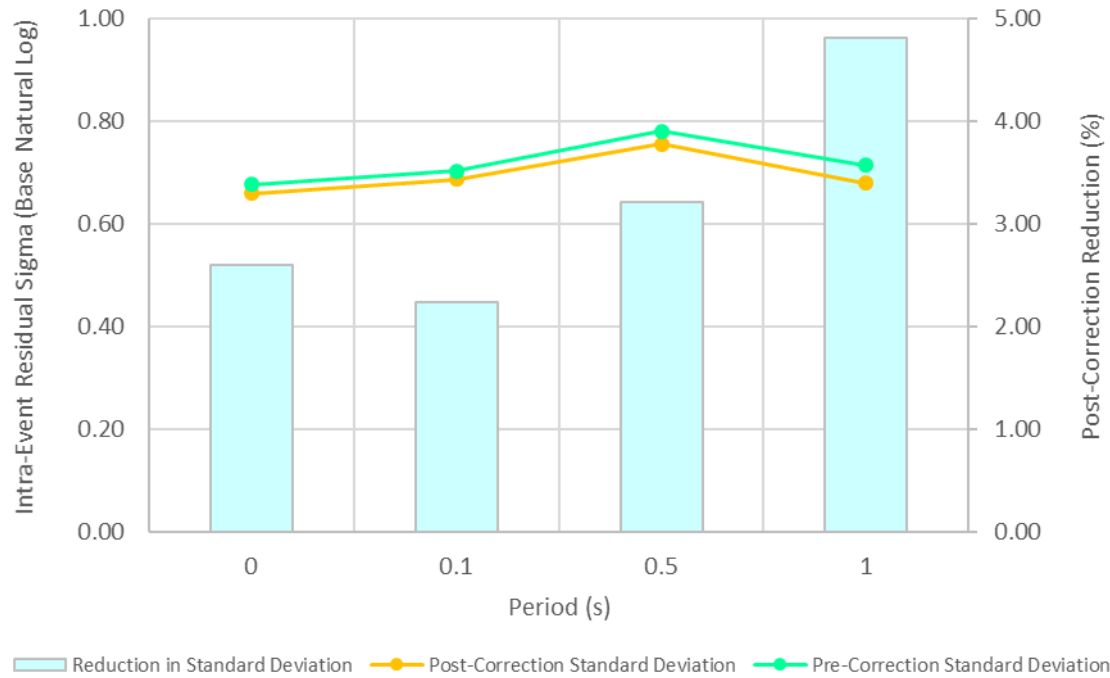


**Figure 4.13** Standard deviation reductions in the site-corrected intra-event residuals following implementation of the 9 computed apparent attenuation rates.

**Table 4.4** Computed apparent attenuation rate (per km) for each grid cell

Period (s)	A	B	C	D	E	F	G	H	I
0	-6.83E-04	1.29E-03	7.54E-04	-4.56E-03	-3.15E-04	1.31E-03	1.57E-04	-1.99E-03	-2.12E-03
0.1	1.56E-04	2.46E-03	6.05E-04	-3.13E-03	5.66E-04	2.75E-03	1.56E-03	-1.63E-04	-3.42E-03
0.5	-2.63E-03	-2.73E-03	-4.93E-03	-4.97E-03	-2.85E-03	1.19E-03	-6.66E-04	1.49E-03	-7.59E-03
1.0	-1.58E-03	-3.56E-03	-2.61E-03	-7.34E-04	-1.95E-03	1.25E-03	7.16E-05	2.01E-03	-7.15E-03

#### 4.11 Results for Constraining Path Effects in the North Sea

The aim of the tomographic inversion was to constrain repeat North Sea path effects, so as to help relax the ergodic assumption with respect to path in the North Sea, and thus improve GMPE performance in the region. With regards to this aim, the tomographic inversion can be considered as successful. The implementation of the 9 computed apparent attenuation rates results in consistently small yet significant (all 2 - 5%) reductions in the standard deviations of the intra-event GMPE residuals ( $\Phi$ ) at all considered spectral periods (Fig. 4.13; Tab. 4.5). Consistent reductions in the standard deviations of the intra-event GMPE residuals indicate the variability in the predicted ground-motion is well reduced. This reduction in variability suggests (1) the ergodic assumption has been partially relaxed with respect to path in the North Sea and (2) GMPE performance has subsequently been improved in the region.

The checkerboard inversion test reconstructs the inputted checkerboard matrix considerably well aside from for grid cell A (Fig. 4.10; Fig. 4.11). The well-achieved reconstruction of the majority of the grid cells can be attributed to an appropriate resolution being used for the grid overlay. The low resolution

grid overlay (250 km per grid cell) ensures the majority of the grid cells each had a sufficient number of passes to be well constrained, whilst still being able to capture (larger scale) particularities in apparent attenuation in the North Sea.

The poor reconstruction of grid cell A (see the significantly larger percentage difference compared to the other grid cells in Fig. 4.11) can be attributed to only one travel path traversing this grid cell (Fig. 4.8; Tab. 4.3), and therefore resulting in the grid cell being poorly constrained. To effectively constrain grid cell A, and further relax the ergodic assumption with respect to path, additional North Sea ground-motion records could be acquired, although this would likely prove difficult due to the limited offshore seismic monitoring in the North Sea region. However, the supplementation of the existing dataset with additional ground-motion records could also permit a higher resolution grid overlay to be used, enabling smaller scale North Sea apparent attenuation particularities to be captured.

The rerunning of the tomographic inversion with smaller size permutations of the North Sea dataset further validates that the chosen grid overlay resolution is an appropriate choice. The tomographic inversion provides reasonably similar results overall with down to only 66% of the North Sea dataset (with respect to their respective means and standard deviations – Fig. 4.12). This similarity suggests that the grid cell attenuation rates were well constrained using the North Sea dataset and the chosen grid overlay (i.e. small to moderate perturbations in the dataset do not drastically change the results of the tomographic inversion with this grid/model).

The rerunning of the tomographic inversion with 50% of the dataset provides considerably different results for select grid cells, and even more so with only 33% of the dataset. However, such different results are expected when rerunning the tomographic inversion with less than half of the original dataset. The largest differences between the results using 66% of the dataset or greater, and less than 66% of the dataset are observed overall in grid cells D, G and H. The larger differences observed for these grid cells can be attributed to the poorer travel path coverage observed within them (Fig. 4.8). Despite each of these grid cells having more than 5 travel path passes, the travel path coverage of each of these grid cells is limited in comparison to the other grid cells<sup>33</sup>. Furthermore, of the grid cells with greater than 5 passes each, grid cells D, G and H do have the least passes (12, 6 and 13 respectively). As a result of this poorer coverage, the computed attenuation rates in grid cells D, G and H are more easily perturbed by rerunning the tomographic inversion with smaller datasets. However, overall, the rerunning of the tomographic analysis with smaller datasets confirms the chosen grid overlay is an appropriate resolution for the coverage provided by the North Sea dataset.

An additional indicator of the computed attenuation rates having been well constrained using this grid overlay resolution is the relatively minimal variation within the attenuation rate for each grid cell over

---

<sup>33</sup> Excluding grid cell A. The differences observed in the computed apparent attenuation rates with smaller datasets are artificially deflated for grid cell A due to the replacement process (discussed above) for grid cells with less than 5 passes.

each considered spectral period (Fig. 4.14). It should also be noted that the attenuation for each grid cell over the considered spectral periods generally appears to follow a pattern of being largest at spectral periods of either 0 s or 0.1 s, and subsequently decreasing at spectral periods of 0.5 s or 1.0 s. This pattern is most likely the result of shorter spectral periods being more affected by anelastic attenuation, and therefore larger attenuation rates being computed for them (Aki and Richards, 2002).

**Table 4.5** *Intra-event residual standard deviations following each adjustment to the base model GMPE.*

Period (s)	Model $\Phi$	North Sea Dataset $\Phi$	Site-Corrected $\Phi$	Site- and Path-Corrected $\Phi$ (see below)
0	0.648	0.775	0.677	0.659
0.1	0.667	0.762	0.703	0.687
0.5	0.651	0.843	0.781	0.755
1.0	0.679	0.761	0.714	0.679
2.0	0.815	0.956	0.943	Not applicable*

\*North Sea path corrections were not computed for a spectral period of 2.0s.

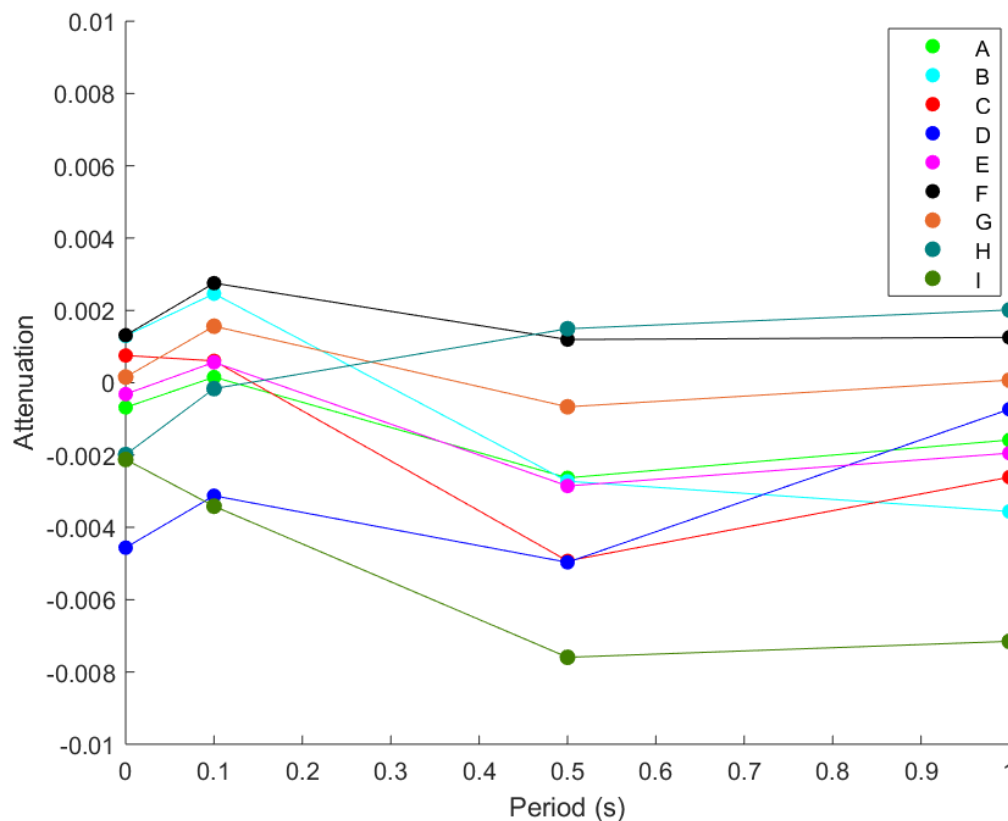


**Figure 4.14** *Computed apparent attenuation rates for each grid cell over the considered spectral periods.*

Alongside validating this tomographic inversion through (1) checkerboard inversion testing and (2) rerunning the analysis with smaller datasets, another good test for validating the results is to compare the computed apparent attenuation rates to what would be expected based on the major geological structures present in the North Sea (Tab. 4.6). Generally, tectonically active areas like faults, grabens and sedimentary basins act as zones of high attenuation, whereas tectonically stable regions like cratons and igneous and metamorphic terrains act as zones of low attenuation (Hearn et al., 2008). The subsurface of the northern North Sea is dominated by grabens and sedimentary basins (Fossen and Hurich, 2008), and therefore is likely to overall be a high attenuation region. Due to the coarse resolution of the grid overlay, the path effects resulting from larger-scale geological structures like basin and non-basin environments are likely far better constrained than the influence of comparatively smaller-scale geological structures like tectonic faults. Therefore, the expected attenuation behaviour within each grid cell is approximated based solely on the presence of basin or non-basin environments.

Grid cells A, B, D, E, G, H and I are dominated by basin environments, whereas grid cells C and F are primarily non-basin environments dominated by the igneous and metamorphic terrains of the Norwegian coastline (Fossen and Hurich, 2005; Fig. 4.9). Therefore, grid cells A, B, D, E, G, H and I are expected to be zones of relatively high attenuation, whilst grid cells C and F are expected to be zones of relatively low attenuation.

The computed attenuation rate for grid cell A is not compared to its expected attenuation behaviour due to the replacement procedure for poorly constrained grid cells having been applied to this cell. For spectral periods of 0 s and 0.5 s the computed attenuation rates for six of the eight remaining grid cells are as would be expected (Fig. 4.9) and for 0.1s, five out of eight, and for 1.0s, four out of eight grid cells, are as would be expected. Therefore, overall the computed attenuation rates correlate reasonably well with what would be expected based on the geological environments present.

This comparison of the expected attenuation rates and the computed attenuation rates is, however, associated with much uncertainty due to: (1) the grid overlay resolution and (2) distinguishing between high and low attenuation zones solely on the presence of basin or non-basin environments within each grid cell. Despite the coarse resolution of the grid overlay resulting in the attenuation effects of smaller geological structures (e.g. faults) not being as well constrained as considerably larger-scale geological structures (e.g. basin and non-basin environments), these smaller-scale structures likely still contribute to the attenuation behaviour within each grid cell. If the grid overlay resolution was higher, the contribution of smaller-scale geological structures would be better constrained, and therefore the attenuation behaviour expected within each grid cell could be approximated based on both the presence of tectonic faults and basin or non-basin environments, reducing the uncertainty in this comparison of expected and computed attenuation rates. A higher grid overlay resolution requires a larger dataset, further validating the need for additional North Sea ground-motion records to improve upon this analysis.

#### 4.12 Conclusions for Constraining Path Effects in the North Sea

The ergodic assumption was relaxed with respect to path through the constraining of North Sea path effects. The constraining of North Sea path effects was achieved through a tomographic inversion analysis, and can also be regarded as successful. This success is indicated by the small but significant and consistent reduction in the standard deviations of the intra-event GMPE residuals over each considered period (Fig. 4.13; Tab. 4.5). The validity of these reductions is largely supported by the two statistical tests carried out to determine the rigidity of the tomographic analysis results (Fig. 4.11; Fig. 4.12). The comparison of the computed attenuation rates to the expected attenuation rates for each grid cell also supports the validity of the tomographic analysis (Fig. 4.9; Tab. 4.6). To expand upon this analysis, a larger ground-motion record dataset with improved travel path coverage of the North Sea region would be required. An expanded dataset would firstly enable further validation of the outputs of the low resolution 3x3 matrix used within this analysis, and secondly the use of a higher resolution for the constraining of smaller particularities in North Sea attenuation, which in turn could further help relax the ergodic assumption with respect to path in the region.

**Table 4.6** *Matches per grid cell (computed attenuation vs expected attenuation)*. Ticks indicate matches. Crosses indicate non-matches. Grid cell A is excluded due to being poorly constrained. PGA = peak ground acceleration, SA = spectral acceleration.

<b>Grid Cell (High/Low Attenuation)</b>	<b>PGA</b>	<b>SA(0.1 s)</b>	<b>SA(0.5 s)</b>	<b>SA(1.0 s)</b>
B (High)	X	X	✓	✓
C (Low)	✓	✓	X	X
D (High)	✓	✓	✓	✓
E (High)	✓	X	✓	✓
F (Low)	✓	✓	✓	✓
G (High)	X	X	✓	X
H (High)	✓	✓	X	X
I (High)	✓	✓	✓	✓
<b>Total Matches</b>	6/8	5/8	6/8	4/8

#### 4.13 Implementation of North Sea Path Corrections into a Monte Carlo Approach Probabilistic Seismic Hazard Assessment

Following the constraining of North Sea path effects through the use of a tomographic inversion to compute attenuation rates, a program undertaking Monte Carlo approach probabilistic seismic hazard assessment (PSHA) was modified to implement them as path corrections.

The following description of the Monte Carlo PSHA approach is summarised from Musson (2000), which should be consulted for further details. The essence of the Monte Carlo approach is to use the seismic source model to generate synthetic earthquake catalogues using the controlled use of random numbers (i.e. a Monte Carlo simulation). The seismic source model can be used to generate synthetic earthquake catalogues because the seismic source model describes (as completely as possible) the spatial and temporal variation of earthquakes within the specified region. Each synthetic earthquake catalogue is therefore representative of the earthquakes which could occur within the specified region based on the seismicity observed there previously. For each earthquake generated within each synthetic catalogue, the ground-motion incident at the site of interest can be simulated using an appropriate GMPE to model attenuation and the scatter of said attenuation within the specified region. Following the generation of many synthetic earthquake catalogues, from the large number of earthquakes simulated, one can calculate the annual probability of exceedance for each level of ground-motion considered by simply counting the number of results exceeding a given level of ground-motion. For example, 100,000 simulations of 100 years of seismicity (i.e. using seismic source zone parameters based on 100 years of observed earthquakes) provides 10,000,000 years of simulated ground-motions. If the largest simulated ground-motion from each of these 10,000,000 years of simulated ground-motions is ordered by size, the level of ground-motion associated with a  $10^{-4}$  annual probability of exceedance is simply the 1001<sup>st</sup> value in these ordered ground-motions.

The implementation of the path corrections into a Monte Carlo PSHA permits assessment of their impact on the predicted seismic hazard. The implementation of the path corrections also permits the use of the base model GMPE (the  $R_{jb}$  variant of the Akkar et al., 2014 GMPE) with the path adjustments for forward modelling. Path corrections were implemented into a Monte Carlo approach PSHA rather than a conventional PSHA due to the mathematical simplicity of Monte Carlo simulations (Musson, 2000) meaning the path corrections could be implemented with relative ease.

Equation 4.1 demonstrates how these attenuation rates can be applied as corrections to the site-corrected intra-event residuals:

$$Z_p = Z_s - \sum_{i=1}^n \delta_i P_{ies} \quad (4.1)$$

where  $Z_p$  represents the path-corrected intra-event residual,  $Z_s$  represents the site-corrected intra-event residual,  $P_{ies}$  represents the distance (in km) through grid cell  $i$  (of the grid of computed attenuation

rates) for a straight line travel path of source  $e$  to site  $s$ , and  $\delta_i$  represents the apparent attenuation per km through each grid cell.

To apply these path corrections to the ground-shaking intensities predicted by a GMPE, a simple modification can be made to equation 4.1:

$$\ln(Y_{corrected}) = \ln(Y) - \sum_{i=1}^n \delta_i P_{ies} \quad (4.2)$$

where  $\ln(Y_{corrected})$  represents the path-corrected predicted ground-motion and  $\ln(Y)$  represents the non-corrected predicted ground-motion.

#### 4.14 Modification of an Existing Monte Carlo PSHA Program

Before the North Sea path corrections could be implemented, the Monte Carlo PSHA program was modified to perform a North Sea PSHA. This process comprised of (1) inputting the 37 North Sea source zones used within the most recent Bungum et al. (2000) North Sea PSHA<sup>34</sup> (Fig. 4.15) and (2) programming the GMPE determined from residual analysis to perform best in the North Sea region (the  $R_{jb}$  variant of the Akkar et al. (2014) GMPE).

Following these simple modifications, the peak ground acceleration (PGA) seismic hazard curves computed by the Monte Carlo PSHA program were compared against those computed in the *CRISIS* seismic hazard software (Ordaz et al., 2015). The hazard curves (e.g. Fig. 4.16) were computed for sites of varying (expected) seismic hazard. Acceptable matches were observed for the test sites and consequently implementation of the path corrections within the Monte Carlo PSHA program could proceed. A match between the seismic hazard curves was considered acceptable if for a given annual frequency of exceedance over the range considered ( $10^{-1}$  to  $10^{-4}$ ), the predicted PGA from the Monte Carlo PSHA and the *CRISIS* PSHA were consistently within  $10 \text{ cm/s}^2$  of one another. The slight differences observed in the PGA for the range of annual frequencies of exceedance considered can be partially attributed to the Monte Carlo PSHA program using point sources with epicentral distance whilst the *CRISIS* PSHA uses finite ruptures with Joyner-Boore distance.

Following validation of the Monte Carlo PSHA program, the path corrections were implemented. To implement the path corrections within a Monte Carlo simulation PSHA, the corrections must be applied to the travel path for each simulated earthquake to the specified site. Consequently, the Monte Carlo PSHA program was modified to: (1) record the distances traversed across each grid cell by each travel path to scale the associated attenuation rates accordingly, (2) sum the distance-scaled corrections and (3) apply the corrections to the predicted ground-shaking intensities for each considered spectral periods (0 s, 0.1 s, 0.5 s and 1.0 s).

---

<sup>34</sup> Kindly provided by Conrad Lindholm.

#### 4.15 Results for the Implementation of North Sea Path Corrections into a Monte Carlo PSHA

Monte-Carlo simulation PSHAs were ran for 4 sites to evaluate the impact of the implemented path corrections. The evaluated sites lie within the grid of computed attenuation rates (Fig. 4.15). Sites in these locations were chosen because to fairly evaluate the impact of the path corrections, the simulated ground-motions must firstly pass through the areas for which path effects have been constrained and secondly be incident at each site from a good spread of azimuthal directions. The impact of the path corrections for each site was evaluated through the comparison of (1) pre- and post-correction seismic hazard curves (Fig. 4.17; Fig. 4.18) and (2) pre- and post-correction uniform hazard response spectrta (UHRS) (Fig. 4.19). The non-corrected predicted ground-motion was calculated using the base model GMPE with the standard deviations computed using the North Sea dataset. The corrected predicted ground-motion was calculated using the base model GMPE with the site- and path-corrected standard deviations. The intra-event residual standard deviations ( $\Phi$ ) used in these calculations are listed in Tab. 4.7.

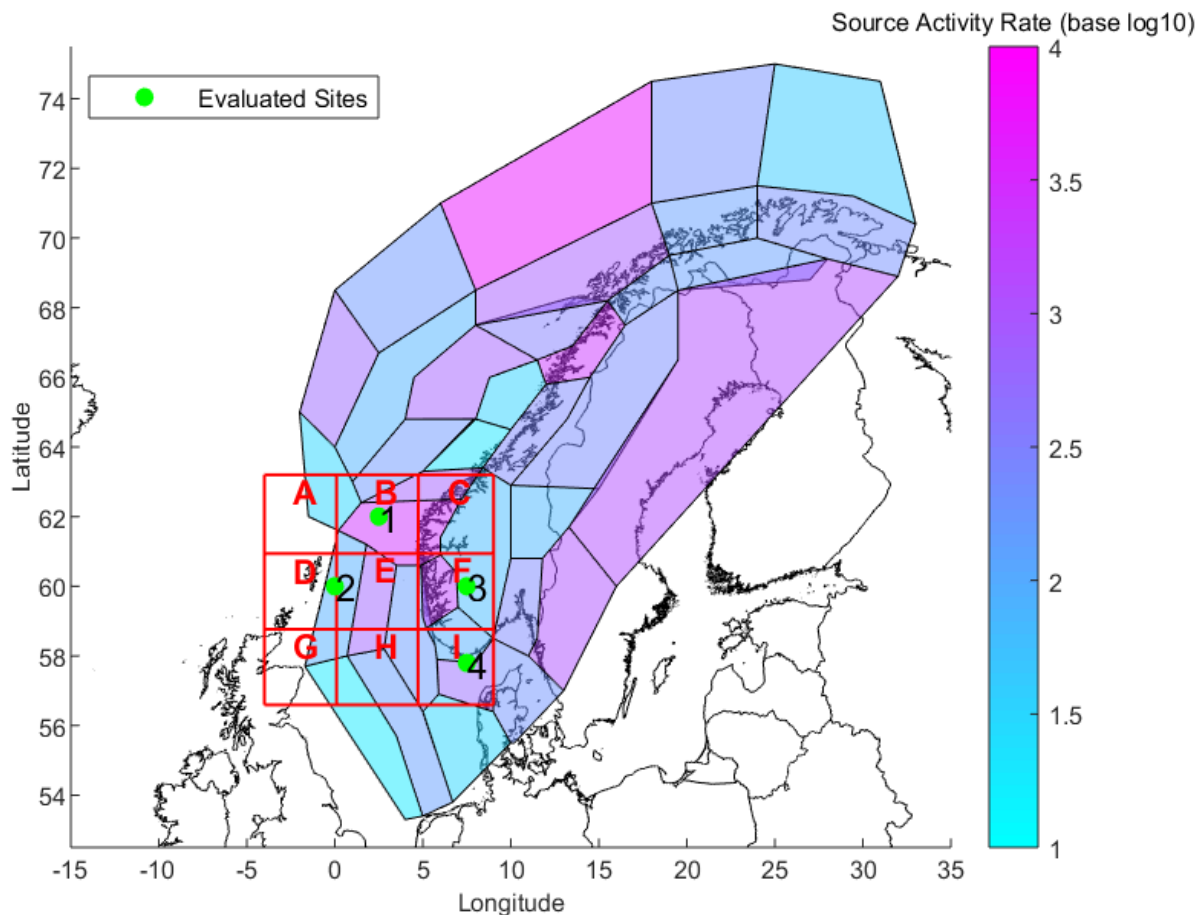


**Figure 4.15** Map of the inputted North Sea source zones and the evaluated sites. The red grid represents the tomographic inversion grid overlay, for which each grid cell (denoted by the corresponding letter) an attenuation rate has been constrained for each spectral period considered.

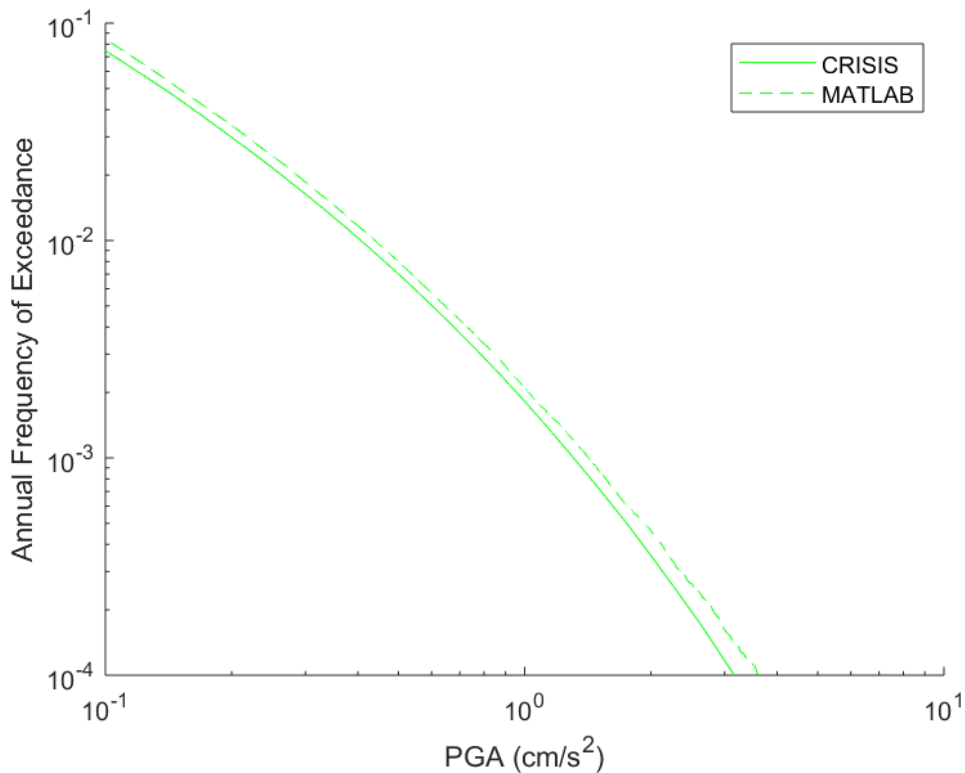


**Figure 4.16** PGA seismic hazard curves generated using the CRISIS seismic hazard software and the Monte Carlo PSHA program (MATLAB) for an example (low hazard) test site (longitude = 20, latitude = 58).

For each considered spectral period, the path corrections result in reasonably consistent modifications to the predicted ground-shaking. For PGA and SA(0.1 s), the path corrections result in reductions in the predicted ground-shaking of approximately 10 – 30%, with the reductions generally being greater for SA(0.1 s) than PGA. For SA(0.5 s), the path corrections result in increases in the predicted ground-shaking of up to approximately 80%. For site 1, below an annual frequency of exceedance of  $10^{-3}$ , reductions in the predicted ground-shaking of up to approximately 30% are observed. For sites 3 and 4, smaller reductions of approximately 5% are observed for the lowest annual frequencies of exceedance considered. For each of the evaluated sites, the magnitude of the correction for SA(0.5 s) is generally greater with increasing annual frequency of exceedance. For SA(1.0 s), the path corrections result in increases in the predicted ground-shaking of up to approximately 120%. As for SA(0.5 s), for each of the evaluated sites the magnitude of the correction for SA(1.0 s) is generally greater with increasing annual frequency of exceedance. The larger corrections observed for SA(0.5 s) and SA(1.0 s) can be attributed to the larger attenuation rates computed for these spectral periods (Tab. 4.4). The larger corrections observed for SA(0.5 s) and SA(1.0 s) are supported by the largest reductions in the standard deviation of the site-corrected intra-event residuals being observed for these spectral periods (Fig. 4.13). The consistency of the corrections for each evaluated site over the range of considered spectral periods can likely be accredited to the most frequently traversed grid cells having more substantial path affects (i.e. larger absolute attenuation rates) than the grid cells less frequently traversed in the simulation.

The impact of the path corrections is well demonstrated by the UHRS computed for the evaluated sites. The UHRS were computed for a practical annual frequency of exceedance ( $10^{-3}$ ) to demonstrate the consistently small-to-moderate yet significant impact of the path-corrections for a realistic range of predicted ground-shaking intensities. Post-path correction, the predicted ground-shaking for PGA and SA(0.1 s) at each site is consistently reduced, and for SA(0.5 s) and SA(1.0 s) the predicted ground-shaking is consistently increased (aside from for site 1 for which it is slightly reduced), as would be expected based on the pre- and post-correction seismic hazard curves.

**Table 4.7** *Intra-event residual standard deviations following each adjustment to the base model GMPE.*

Period (s)	Model $\Phi$	North Sea Dataset $\Phi$	Site-Corrected $\Phi$	Site- and Path-Corrected $\Phi$
0	0.648	0.775	0.677	0.659
0.1	0.667	0.762	0.703	0.687
0.5	0.651	0.843	0.781	0.755
1.0	0.679	0.761	0.714	0.679

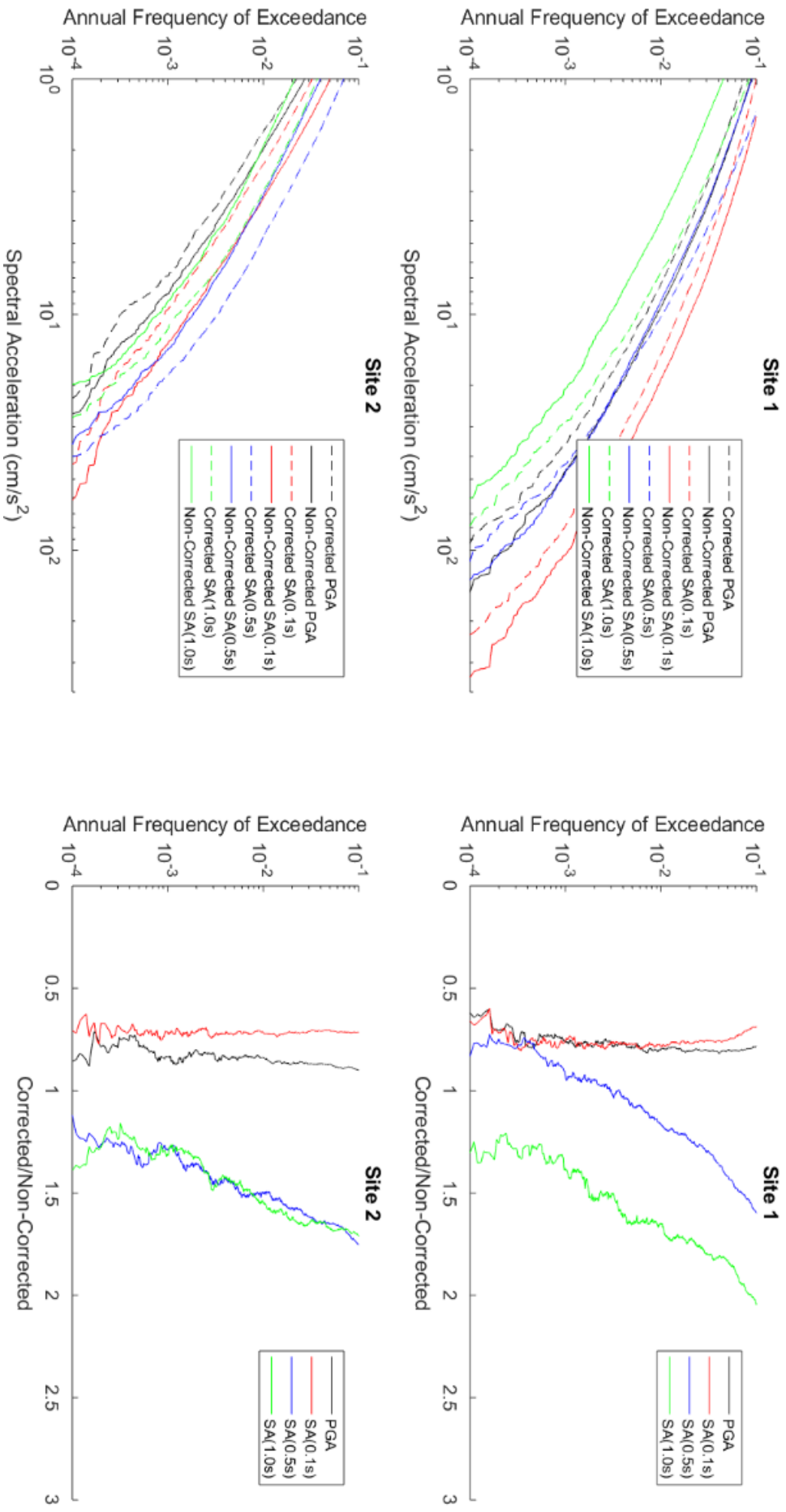
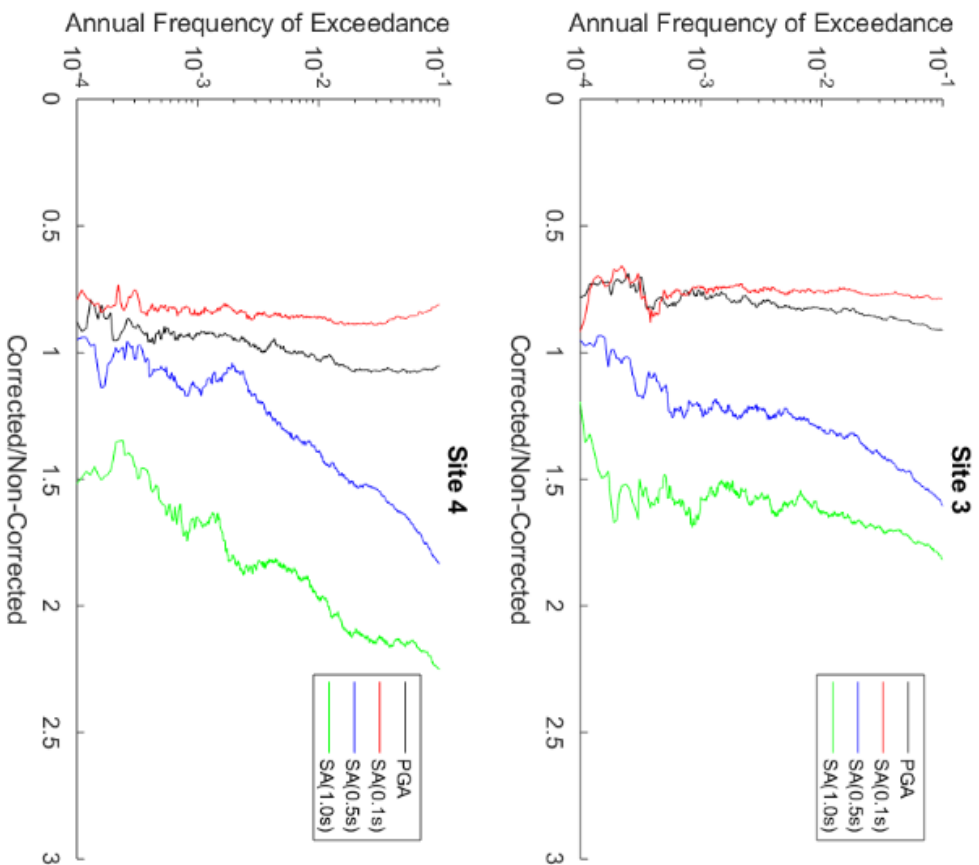
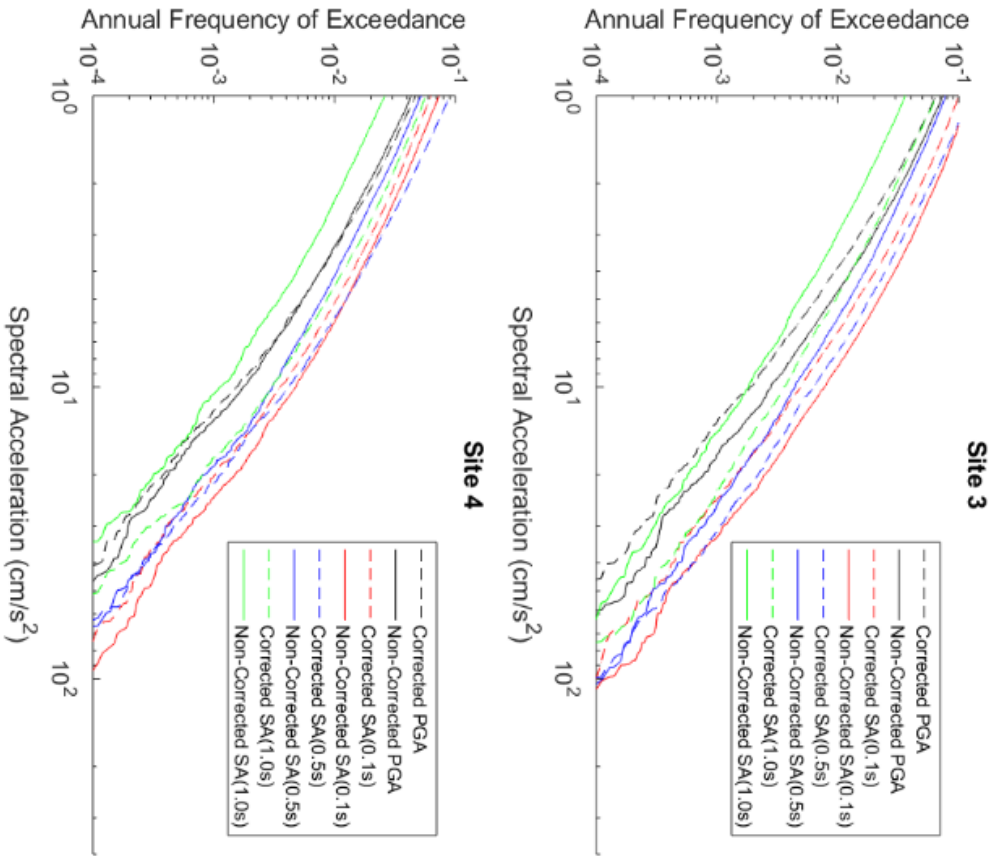


Figure 4.17 Pre- and Post-Correction Seismic Hazard Curves for Evaluated Sites 1 and 2



**Figure 4.18** Pre- and Post-Correction Seismic Hazard Curves for Evaluated Sites 3 and 4.

Uniform Hazard Spectra for Annual Probability of Exceedance = 1E-03

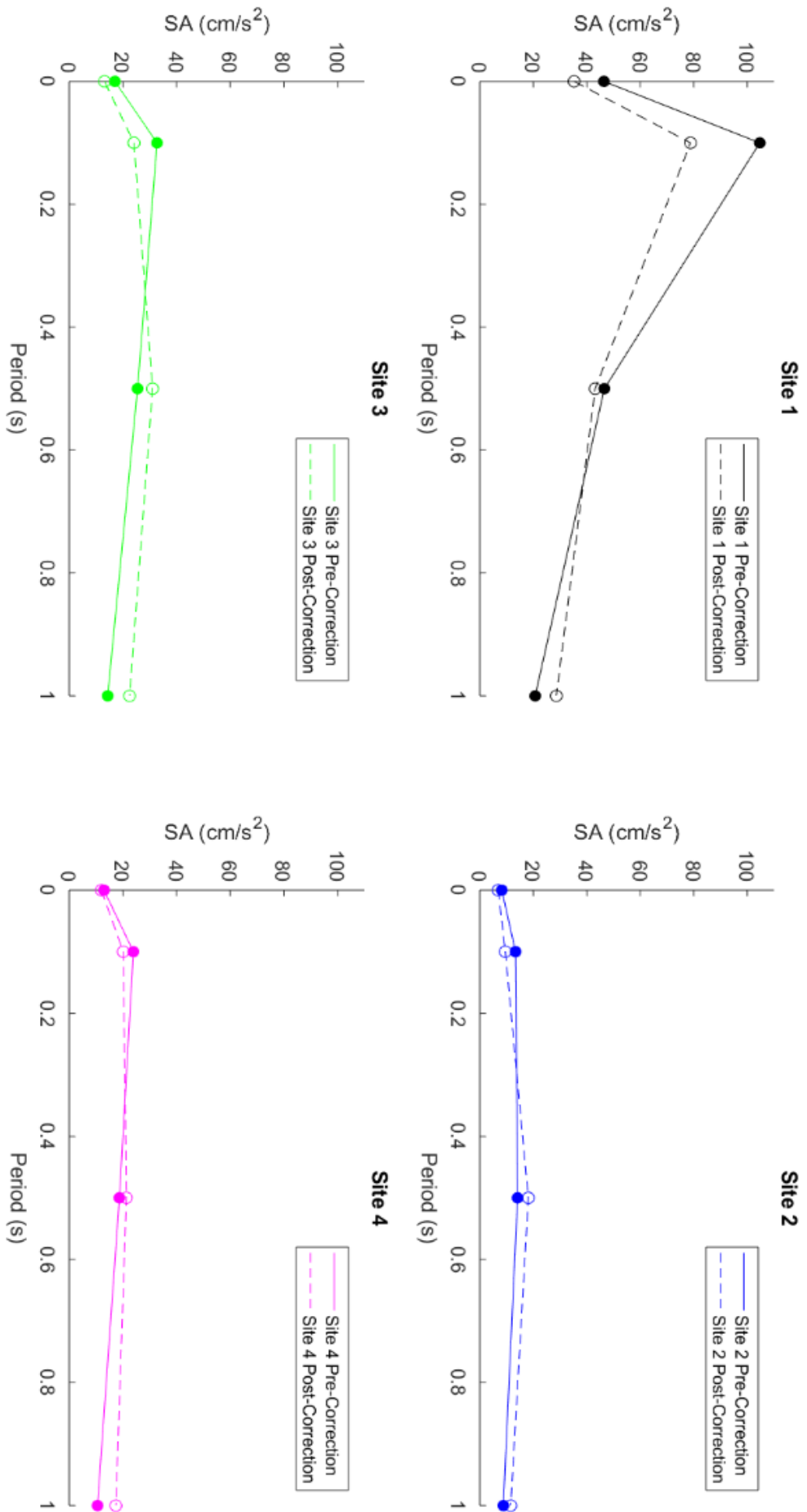


Figure 4.19 Pre- and post-correction uniform hazard response spectra for the evaluated sites.

#### **4.16 Conclusions for the Implementation of North Sea Path Corrections into a Monte Carlo PSHA**

An existing Monte Carlo approach PSHA was successfully modified for North Sea PSHA, as demonstrated by the favourable comparison between the seismic hazard curves computed using both the modified Monte Carlo approach PSHA and the *CRISIS* seismic hazard software. The path corrections were then successfully implemented into the modified Monte Carlo PSHA program, permitting an assessment of their impact on the predicted seismic hazard levels. The path corrections were found to result in small-to-moderate and consistent corrections to the predicted ground-shaking for the considered spectral periods, as demonstrated by the computed seismic hazard curves and UHRS for the evaluated sites. The implementation of the path effects also permits the use of the base GMPE with the path adjustments for forward modelling.

## 5.0 Investigation of High Frequency Ground-Motion Variability with the Site-Specific Component of Kappa

In addition to the reassessment of North Sea seismic hazard, work has been undertaken in this thesis to investigate the influence of the poorly understood site response parameter, kappa (see below) on the variability of ground-motions as predicted by ground-motion prediction equations (GMPEs). This work is also provided in Brooks and Douglas (2020).

GMPEs are most commonly developed through undertaking regression analysis on select sets of instrumentally recorded ground-motion data. The explanatory variables incorporated within a GMPE are a simple representation of the physical processes associated with the generation and subsequent propagation of ground-motions (Douglas and Edwards, 2016). This simple representation of ground-motions therefore results in the observed ground-motions departing from the predicted ground-motion with a seemingly random behaviour (Strasser et al., 2009). To capture this random scatter, the distribution of the ground-motion residuals ( $\delta_i$ ) is considered:

$$\delta_i = Z_{obs} - Z_{pred} \quad (5.0)$$

Where  $Z_{obs}$  and  $Z_{pred}$  are the observed and predicted ground-motions in either base natural log or base log10. Logarithms of the observed and predicted ground-motions are taken because the aleatory variability component of GMPEs is assumed to be log-normally distributed with a mean of zero and a standard deviation of  $\sigma$  (Strasser et al, 2009). The ground-motion residuals are defined as the difference between the observed and predicted ground-motion, and are therefore representative of the component of ground-motion not explained by the GMPE<sup>35</sup>.

Within a probabilistic seismic hazard assessment (PSHA), the uncertainty in the predicted ground-motion is usually separated into epistemic uncertainty (uncertainty with respect to either GMPE selection or parameter selection for the seismological model due to a lack of earthquake knowledge) and aleatory variability (uncertainty due to the randomness of the natural processes being considered). The aleatory variability is generally considered to be represented by the standard deviation of the ground-motion residual distribution ( $\sigma$ ). However, it is difficult to evaluate the extent to which  $\sigma$  is representative of true randomness (intrinsic variability in the ground-motion), or the epistemic uncertainty with respect to GMPE modelling (variables influencing ground-motion which have not yet been incorporated within GMPEs and therefore appear as random scatter) (Strasser et al., 2009).

Conventionally,  $\sigma$  is split into the inter-event and intra-event components of ground-motion variability. The inter-event standard deviation ( $\tau$ ) is representative of the ground-motion variability associated with

---

<sup>35</sup> Ground-motion residuals can therefore be computed using ground-motion data from regions for which GMPEs were not developed to evaluate their appropriateness for use in PSHAs for said regions (e.g. see Chapter 4 in which existing GMPEs were evaluated using North Sea ground-motion data).

event-specific factors (e.g. randomness in the source process) which have not been accounted for in the GMPE. The intra-event standard deviation ( $\phi$ ) is representative of the ground-motion variability associated with record specific factors (e.g. randomness in the local site amplification for given geotechnical parameters). For empirical GMPEs,  $\phi$  is often larger than  $\tau$  (e.g. see Tab. 3.3), and thus the contribution of  $\phi$  to  $\sigma$  is generally greater than that of  $\tau$ .

The value of  $\sigma$  greatly influences the predicted ground-motion outputted by a PSHA, more so at lower annual frequencies of exceedance (AFOE) where the ground-shaking represents levels of seismic hazard of interest within earthquake engineering (Fig. 5.0). Further still, the near universal implementation of the logarithmic transform in GMPE regression analyses results in even minute variations in  $\sigma$  having a noticeable impact on the predicted ground-motion for a given AFOE (the predicted ground-motion will vary exponentially with an incremental change in  $\sigma$ ) (e.g. Toro, 2006). Due to the significant influence of  $\sigma$  on the predicted seismic hazard, several studies (e.g. Bommer et al., 2004; Strasser et al., 2007) have proposed that future work must be undertaken to achieve a better understanding of the nature of  $\sigma$ .

The high-frequency attenuation operator, kappa ( $\kappa$ ) was introduced by Anderson and Hough (1984). This parameter describes the observed fall-off at high frequencies of ground-motion within a Fourier amplitude spectra computed from recorded ground-motion time-series due to attenuation. Anderson and Hough (1984) determined the decay of the Fourier amplitude spectrum to occur above  $f > \sim 2 \text{ Hz}$ , but subsequent studies (e.g. Anderson and Humphreys, 1991) suggested this decay occurs when  $f$  is greater than the corner frequency ( $f_c$ ). Anderson and Hough (1984) observed that  $\kappa$  increases with source-to-site distance, and therefore that  $\kappa$  is related to both the near-surface geotechnical conditions and the regional geological structure. Consequently, Anderson and Hough (1984) computed the site-specific component of kappa ( $\kappa_0$ ) by extrapolating  $\kappa$  values for given source-to-site distances to an epicentral distance ( $R_{epi}$ ) of 0 km to correct for regional anelastic attenuation ( $Q$ ).

Despite having been introduced almost 40 years ago and its widespread use,  $\kappa$  is one of the least understood parameters in engineering seismology, with no universally accepted approach for its estimation (see Ktenidou et al., 2017 for details on the various approaches for  $\kappa$  estimation). The  $\kappa$  parameter is thought to be site-specific, although there is likely a record-specific component of  $\kappa$  due to variations in the azimuth of incident seismic waves at each site (therefore resulting in differentiation of the total and site-specific kappa using the notation of  $\kappa$  and  $\kappa_0$  respectively). The site- and record-specific nature of  $\kappa$  results in this parameter contributing to  $\phi$  within GMPEs. The site-specific component of  $\kappa$  should be measurable from observed ground-motions at each site, and therefore should result in the reduction of  $\phi$ . The influence of  $\kappa_0$  upon the observed scatter within empirical GMPEs is not well understood, especially with respect to how it potentially contributes to the magnitude-dependency of  $\phi$

(see below)<sup>36</sup>. Therefore, this chapter examines the influence of  $\kappa_0$  upon  $\phi$  (the path-dependent attenuation is modelled by the considered attenuation model – see Table 5.0), with an emphasis on investigating the potentially magnitude-dependent nature of this influence. The chapter begins with a comprehensive review of recent studies examining the magnitude-dependency of ground-motion variability, followed by a simple analysis examining (1) the influence of  $\kappa_0$  upon  $\phi$  and (2) how well existing empirical GMPEs capture this influence.

### 5.1 Studies on the Magnitude-Dependency of High Frequency Ground-Motion Variability

Studies such as Idriss et al. (1982), Sadigh et al. (1983), Idriss (1985) and Sadigh et al. (1986) first observed that  $\sigma$  for peak ground acceleration (PGA) decreases with increasing magnitude. However, the values of  $\sigma$  within these studies were computed using only a few ground-motion records pertaining to large magnitude earthquakes. Therefore, the results of these studies were criticised because  $\tau$  was likely poorly constrained<sup>37</sup>. Furthermore, the statistical significance of the decrease in  $\sigma$  was not examined within these studies, with Abrahamson (1988) being the first to clearly demonstrate a negative correlation between  $\phi$  and magnitude. The magnitude-dependency of  $\sigma$  for PGA was first examined in-depth by Youngs et al. (1995) using a random effects regression model, with the magnitude-dependency of  $\tau$  for PGA being found to be stronger than the magnitude-dependency for  $\phi$  for PGA.

Prior to Youngs et al. (1995) several explanations for the magnitude-dependency of  $\sigma$  for PGA had been suggested. Chin and Aki (1991) suggested that the observed magnitude-dependency of  $\sigma$  could be due to non-linear site effects. It should be noted that non-linear site effects more likely affect  $\phi$  rather than  $\tau$ . Chin and Aki (1991) proposed the following. As the amplitude of ground-motions increases with magnitude the damping of the soil correspondingly increases. The increased damping results in the attenuation of the high frequency ground-motions. A reduction in the high frequency ground-motion content reduces the variability in the scatter of PGA. However, Youngs et al. (1995) observed that  $\sigma$  is magnitude-dependent even for ground-motions with a PGA of less than 0.1 g. Therefore, Youngs et al. (1995) concluded although non-linear site effects likely do contribute to the observed magnitude-dependency of  $\sigma$  for PGA, additional effects are required to explain the magnitude-dependency of  $\sigma$  for smaller PGA amplitudes.

Beresnev et al. (1994) suggested that the observed magnitude-dependency of  $\sigma$  is due to a shift in the predominant frequencies as a function of magnitude. Ground-motions from large magnitude earthquakes have smaller predominant frequencies than ground-motions from small magnitude earthquakes. Therefore, Beresnev et al. (1994) reasoned that because (1) PGA is a broadband measure and (2) that low frequency ground-motion is less variable over short distances than high frequency

---

<sup>36</sup> It should be noted that since  $\kappa_0$  is a purely empirical parameter, a physical explanation is likely to be inherently problematic.

<sup>37</sup> It should be noted that the lack of large magnitude ground-motion records does not suggest that  $\tau$  is underestimated, only that  $\tau$  has possibly been less reliably underestimated than if additional large magnitude ground-motion records had been used.

ground-motion then the PGA values computed from ground-motion records with lower predominant frequencies will show less variation than PGA values computed from ground-motion records with higher predominant frequencies. Youngs et al. (1995) determined that a change in predominant frequency cannot account for the magnitude-dependency of  $\sigma$  for PGA because response spectral values (which are narrowband measures) have also been observed to demonstrate a magnitude-dependency for  $\sigma$  (e.g. Abrahamson and Sykora, 1993).

In addition to the contribution of non-linear site effects to the magnitude-dependency of  $\sigma$  proposed by Chin and Aki (1991), Youngs et al. (1995) proposed several additional explanations for the observed magnitude dependency of  $\sigma$  for PGA. The first of these explanations was that the standard deviation of the (static) stress drop<sup>38</sup> parameter ( $\Delta\sigma$ ) is magnitude-dependent:  $\Delta\sigma$  scales the amplitudes of the high frequency components of ground-motions because for a given magnitude, the Brune (1970; 1971) stress drop is proportional to the fault rupture area. Using the relationship between the base natural log of fault rupture area and earthquake magnitude established by Wells and Coppersmith (1994), Youngs et al. (1995) computed residuals from a dataset of ground-motions recorded from earthquakes in California. Youngs et al. (1995) observed from these residuals that the scatter of the base natural log of fault rupture area decreases with increasing earthquake magnitude. A decrease in the variability of  $\Delta\sigma$  with increasing earthquake magnitude would result in a corresponding decrease in  $\tau$  with increasing earthquake magnitude.

The second explanation proposed by Youngs et al. (1995) was that issues relating to earthquake metadata could contribute significantly to the magnitude-dependency of  $\sigma$ . The location and magnitude of small magnitude earthquakes are not as well constrained as those for large magnitude earthquakes. The increased error in the associated independent parameters (source-to-site distance and magnitude) results in increased variability of the selected GMPE for smaller magnitude earthquakes compared to larger magnitude earthquakes. Errors associated with magnitude estimation would manifest within  $\tau$ . Errors associated with source-to-site distance estimation would manifest within  $\tau$  and/or  $\phi$  depending on the spatial distribution of stations relative to earthquake source. However, Youngs et al. (1995) determined that the magnitude-dependency of  $\sigma$  for PGA cannot be attributed solely to the increased metadata errors associated with small magnitude earthquakes because Abrahamson (1988) observed a magnitude-dependency of  $\sigma$  even without consideration of the magnitude or source-to-site distance of the event.

The final explanation proposed by Youngs et al. (1995) was that although the duration of ground-motion should not significantly affect the scatter of PGA, Clough and Penzien (1993) observed using random vibration theory (RVT) stochastic simulations that the scatter of PGA decreases with increasing ground-

---

<sup>38</sup> See below and/or Appendix A for more details on the stress drop parameter.

motion duration, and that an explanation<sup>39</sup> for this was required to help explain the magnitude-dependency of  $\phi$ .

Since Youngs et al. (1995)'s study, additional investigations have been undertaken to better understand the magnitude-dependency of  $\sigma$ . Campbell and Bozorgnia (2003), like Youngs et al. (1995), observed that the ground-motions from small earthquakes are more variable than those from large earthquakes. Ambraseys et al. (2005) observed a lack of statistically significant magnitude-dependency for the scatter of long period ground-motions, suggesting the magnitude-dependency of  $\sigma$  does not hold for longer period ground-motions as it appears to for shorter period ground-motions<sup>40</sup>. Like prior studies, Ambraseys et al. (2005) observed that  $\sigma$  for high frequency ground-motions was magnitude-dependent, although in contrast to Youngs et al. (1995) they assumed that the magnitude-dependency for  $\sigma$  was partitioned equally between  $\tau$  and  $\phi$  (rather than being predominantly associated with  $\tau$  – see above). Ambraseys et al. (2005) assumed an equal partitioning because of the complex mapping of the magnitude-dependency upon both components. For example, the magnitude-dependency could be due to site variability or propagation path variability (thus manifesting in  $\phi$ ), due to the method chosen for the regression analysis<sup>41</sup> of the GMPE (thus manifesting in  $\tau$ ) or as discussed above the estimation of source-to-site distance and magnitude (thus manifesting in  $\tau$  and/or  $\phi$  depending on the spatial distribution of sites relative to the earthquake source).

The complexity of the mapping of the magnitude-dependency onto both  $\tau$  and  $\phi$  is evident from the testing of existing GMPEs using a North Sea ground-motion dataset (see Chapter 4 for more details). For all considered ground-motion intensity measures, the values of  $\tau$  and  $\phi$  computed from the North Sea dataset using each GMPE are moderately elevated compared to the default values. This observation can be attributed to the North Sea dataset being dominated by ground-motions recorded from small magnitude earthquakes, unlike the datasets used for the development of the considered GMPEs, which comprised primarily ground-motions recorded from moderate and large earthquakes. Similar observations have been made in other studies e.g. Beauval et al. (2012).

In contrast to the equal partitioning of the magnitude dependency into  $\tau$  and  $\phi$  by Ambraseys et al. (2005), Bommer et al. (2007) demonstrated that expansion of the magnitude range within the regression

---

<sup>39</sup> Small magnitude earthquakes have high corner frequencies and therefore have shorter durations than large magnitude earthquakes. Ground-motions generated from earthquakes with short rupture durations are more affected by attenuation and kappa than earthquakes with long rupture durations, explaining this observation (e.g. Sumy et al., 2017 – see below for more details).

<sup>40</sup> Ambraseys et al. (2005) note that the observed lack of statistically significant magnitude-dependent scatter for longer period ground-motions could be attributed to the selected filter cut-offs (for the compiling of strong-motion data) resulting in a relatively small number of long period ground-motions compared to short period ground-motions rather than an intrinsic seismological effect.

<sup>41</sup> For example, whether a two stage regression is used to decouple distance- and magnitude-dependency as proposed by Joyner and Boore (1981), or whether a weighted regression is used for the explanatory variables with respect to magnitude as is undertaken within Ambraseys et al. (2005) for  $\sigma$ .

analysis significantly increases  $\tau$  but minimally increases  $\phi$  (see their Fig. 12), lending support to Youngs et al. (1995)'s notion that the magnitude-dependency of  $\tau$  is stronger than the magnitude-dependency of  $\phi$ . Bommer et al. (2007) favour the idea that the metadata issues associated with small earthquakes (see above) are primarily responsible for the larger magnitude-dependency of  $\tau$  than  $\phi$  due to the findings of Rhoades (1997), which show that accounting for magnitude-uncertainty estimates can significantly reduce  $\tau$ . It should also be noted that the results of Bommer et al. (2007) demonstrate that the expanded magnitude range systematically increases  $\phi$  slightly more for high frequency ground-motions than  $\phi$  for low frequency ground-motions (once again see their Fig. 12). The expanded magnitude range likely increases  $\phi$  for a given magnitude because of the inclusion of sites associated with the additional ground-motion records increases the site variability. The increased site variability affects the shorter periods more, so the responsible mechanism must cause greater scatter for high frequency ground-motions. This is suggestive of variation in  $\kappa_0$  potentially being the responsible mechanism.

Bommer et al. (2007) also considered that the increased variability resulting from an increased magnitude range could be due to the incorporation of ground-motion data from different regions because (1) different instruments are often used for recording ground-motions within different regions and (2) ground-motions generated from smaller magnitude earthquakes are more sensitive to differences in regional attenuation (due to differing crustal structures). However, sensitivity analyses indicated that the median ground-motions and associated variability for each regression model was not significantly influenced by the inclusion of individual regional datasets. Chiou and Youngs (2010) demonstrated that through accounting for sub-regional differences in Californian earthquakes that the magnitude-dependency for  $\tau$  can be decreased, suggesting in contrast to Bommer et al. (2007) that regional variation can contribute to the magnitude-dependency for  $\tau$ . These contrasting results suggest the impact of regional variation on the magnitude-dependency of  $\tau$  needs further investigation.

Douglas and Jousset (2011) demonstrated using stochastic simulations that variations in  $\kappa_0$  affect PGA more for small magnitude earthquakes than for large magnitude earthquakes, and proposed that this may contribute to the magnitude-dependency of  $\sigma$  within some existing GMPEs.

Kotha et al. (2017) built upon the  $\Delta\sigma$  explanation for the magnitude-dependency of  $\tau$  provided by Youngs et al. (1995). Through consideration of a standard Brune (1970; 1971) source spectrum model, a more expansive physical explanation is provided. For a given moment magnitude ( $M_w$ ), an increase in  $\Delta\sigma$  lowers  $f_c$ , and increases ground-motion amplitudes for  $f > f_c$  whilst ground-motion amplitudes for  $f < f_c$  remain unmodified. If one considers a primary frequency  $f_1$  and a secondary frequency  $f_2$ , when  $(f_1, f_2) < f_c$  neither  $f_1$  or  $f_2$  is affected by variability in  $\Delta\sigma$ , so their correlations are strong. When  $(f_1, f_2) > f_c$ , ground-motion amplitudes increase monotonically with variation in  $\Delta\sigma$ , so their correlations are also strong. According to this theory, Kotha et al. (2017) state that for large magnitude

earthquakes with a low  $f_c$ , stronger correlations would be expected over a wide range of  $(f_1, f_2) > f_c$  than would be observed for small magnitude earthquakes. This assertion is observed within the correlation coefficients computed by Kotha et al. (2017) over the range of considered values for  $f_2$  (with a fixed  $f_1$ ) for large magnitude earthquakes ( $M_w \geq 5.5$ ) and low magnitude earthquakes ( $M_w < 5.5$ ) (see their Fig. 3), lending support to this more substantial explanation of how  $\Delta\sigma$  influences the magnitude-dependency of  $\tau$ .

Ktenidou et al. (2017) observed that the single-station event corrected (intra-event) standard deviation ( $\phi_{ss}$ ) increases with decreasing magnitude down to  $M_w 2$ . Ktenidou et al. (2017) proposed that this trend of increasing  $\phi$  with decreasing magnitude could be due to the reasons discussed above (e.g. metadata issues relating to estimation of source-to-site distance) or alternatively the influence of  $\kappa_0$ .

The studies discussed above demonstrate that the magnitude-dependency of  $\sigma$  has been reasonably well explained, albeit more so with regards to the magnitude-dependency of  $\tau$  rather than  $\phi$  overall. Considering this, and that (1) magnitude is thought to be the explanatory variable which contributes most significantly to the aleatory uncertainty associated with the prediction of PGA (Sigbjörnsson and Ambraseys, 2003), (2) the influence of  $\kappa_0$  on the higher frequency components of ground-motion, (3) the lack of understanding as to how  $\kappa_0$  contributes to  $\phi$  and (4) the demonstrated magnitude-dependency of PGA variability with variation in  $\kappa_0$  by Douglas and Jousset (2011), a more substantial investigation into how  $\kappa_0$  impacts  $\phi$  for different size earthquakes is required. Therefore, this investigation examines in detail (1) how variation in  $\kappa_0$  influences the variability observed in PGA from earthquakes of different magnitudes and (2) whether this influence could be partly responsible for the heteroscedastic nature of  $\phi$  (w.r.t. magnitude) observed within some empirical GMPEs. A better understanding of how  $\kappa_0$  contributes to the heteroscedastic nature of  $\phi$  within empirical GMPEs is important because, as discussed above, the specified  $\sigma$  has a noticeable impact on the predicted ground-shaking (see Fig. 5.0).

It should be noted that heteroscedastic variance with respect to magnitude has been observed in the ground-motion residuals of several empirical GMPEs which have omitted the inclusion of a heteroscedastic variance model. For example, Kotha et al. (2020) observed heteroscedasticity of  $\tau$  with respect to magnitude, but due to the limited number of large earthquakes compared to the number of small to moderate earthquakes within their dataset, the implementation of a heteroscedastic variance model was not thought currently necessary. However, GMPEs have been developed which successfully account for some of the effects contributing to the heteroscedasticity of  $\sigma$ . Kotha et al. (2019) accounted for the influence of earthquake size on  $\phi$  due to azimuthal variation of ground-motions (small earthquakes have simpler radiation patterns than large earthquakes, resulting in larger  $\phi$  for smaller earthquakes), reducing  $\phi$  within their proposed model. Such an example is highlighted within this study

because failing to capture the influence of earthquake size due to azimuthal variation of ground-motions on  $\phi$  in GMPEs results in greater uncertainty.

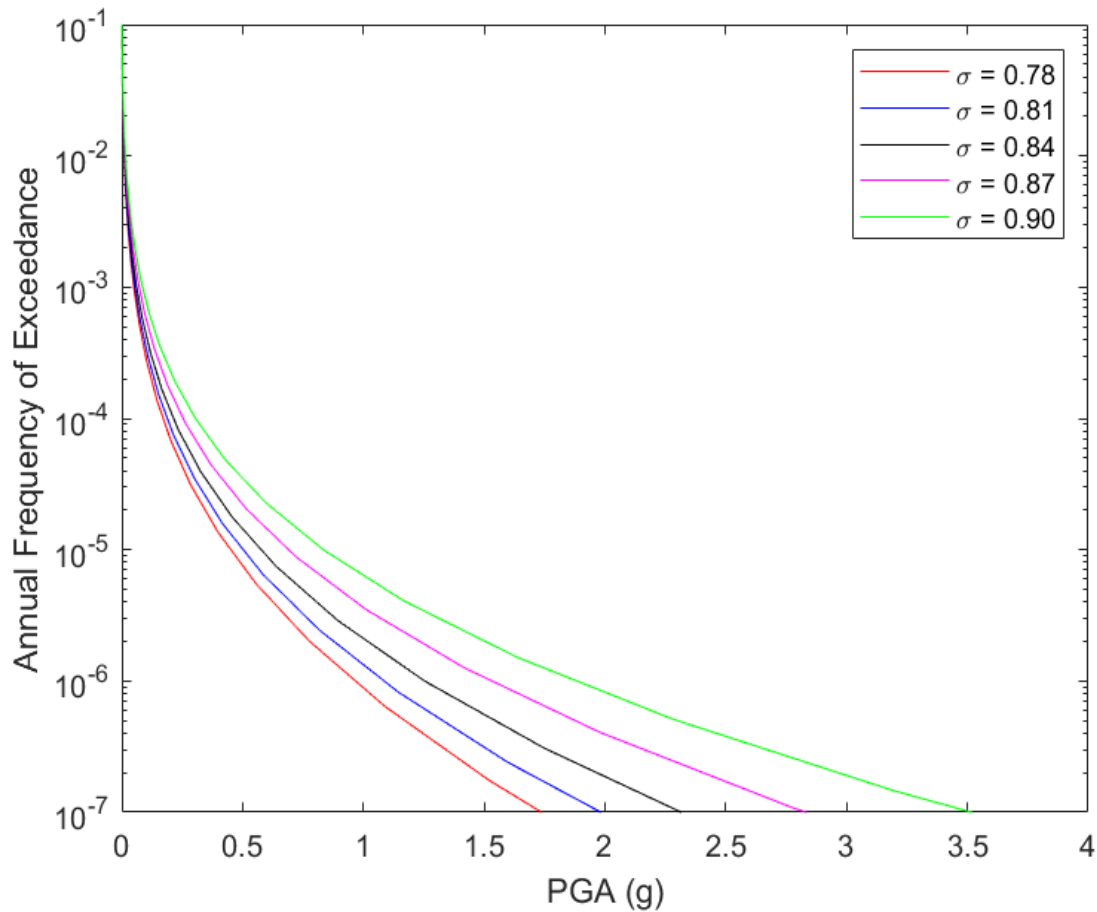


**Figure 5.0** Seismic hazard curve demonstrating the impact of modifying  $\sigma$  within a PSHA. Predicted ground-motion was computed using the Bindi et al. (2017) GMPE for a North Sea site (latitude = 66, longitude = 16,  $\lambda = 0.0758$ ) using the seismic zonation of Bungum et al. (2000).

## 5.2 Methodology for Investigation of High Frequency Ground-Motion Variability with the Site-Specific Component Kappa

To investigate in more detail how high frequency ground-motions vary with changes in  $\kappa_0$ , stochastic simulations were undertaken using the SMSIM ground-motion simulation software (Boore, 2005).

### 5.2.1 Overview of the Stochastic Method for Ground-Motion Simulation

The following overview of the stochastic method for the simulation of ground-motion simulation is summarised from Boore (2003).

The stochastic method uses a point-source earthquake model derived from observed ground-motion records to simulate additional ground-motions. The simulated ground-motions are assumed to be S-waves, since these are the most important to seismic hazard. As discussed in Chapter 4, a GMPE can be fitted to these simulated ground-motion records through non-linear regression, resulting in a stochastic GMPE.

The stochastic method is largely based upon the work of Hanks (1979), McGuire and Hanks (1980) and Hanks and McGuire (1981). They combined seismological models of the spectral amplitude of ground-motion with the treatment of high frequency ground-motions as being effectively random to derive a simple relationship between PGA and stress drop. To derive this relationship between PGA and stress drop, Hanks and McGuire worked under the assumption that (1) the source spectra are described by a single corner-frequency model whose corner frequency depends on earthquake size according to the Brune (1970, 1971) stress drop model and (2) that the acceleration time-histories are band-limited, of finite duration and comprise of white Gaussian noise.

The basis of the stochastic method is illustrated in Fig. 5.1. The top of Fig. 5.1 comprises of spectrums of ground-motion at a particular distance and site condition for earthquakes of magnitudes 5 and 7 based on a standard seismological model. Through assuming the ground-motion of each spectrum are distributed with random phase over a time duration related to the earthquake size and the propagation distance, a corresponding time series can be computed, as displayed in the bottom of Fig. 5.1.

The fundamental component of the stochastic method is the (Fourier amplitude<sup>42</sup>) spectrum of ground-motion (Fig. 5.1). This is because the spectrum of ground-motion is representative of (1) the physics of the earthquake rupture mechanism and (2) the wave propagation required to simulate the ground-motions. The majority of work required for the stochastic method is therefore associated with constructing a model capable of sufficiently describing this spectrum. Conventionally, the spectrum of ground-motion at a site ( $Y(M_0, R, f)$ ) is decomposed into the separate contributions from the earthquake source ( $E$ ), path ( $P$ ), site ( $G$ ) and type of ground-motion ( $I$ ):

$$Y(M_0, R, f) = E(M_0, f)P(R, f)G(f)I(f) \quad (5.0)$$

where  $M_0$  is the seismic moment,  $R$  is the source-to-site distance and  $f$  is the frequency of the ground-motion.

---

<sup>42</sup> See Chapter 3 for an overview of Fourier amplitude spectra.

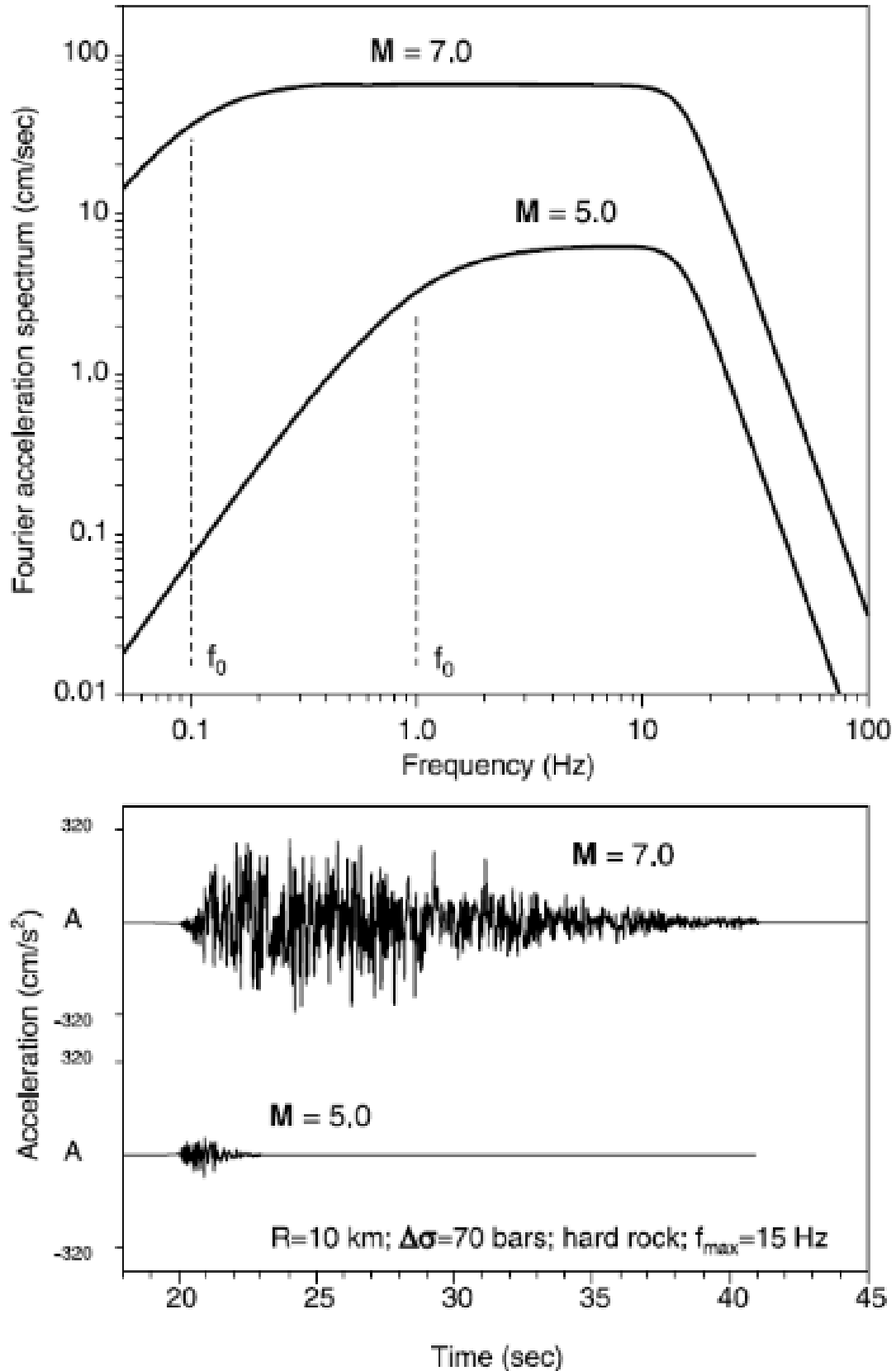


**Figure 5.1** Fourier amplitude spectrums of ground-motion at a particular distance and site condition for earthquakes of magnitudes 5 and 7 based on a standard seismological model and the corresponding time-series for these ground-motion spectrums. Adapted from Boore (2003).

### Step 1 – Modelling of Source Effects $E(M_0, f)$

The shape and amplitude of the earthquake source spectrum need to be specified as a function of earthquake size. The  $\omega$ -square model for amplitude spectral density first proposed by Aki (1967) is often used to model the earthquake source spectrum. Aki (1967) assumed self-similarity for earthquakes to derive a source scaling law, where the scaling of the spectra from one magnitude to another is calculated by specifying the dependence of the corner frequency on seismic moment. Aki (1967) realised that assuming self-similarity for earthquakes therefore implies that:

$$M_0 f_c = \text{constant} \quad (5.1)$$

where the constant is related to the stress drop (Fig. 5.2). Using the Brune (1970; 1971) scaling, the corner frequency is given by:

$$f_0 = 4.9 * 10^6 \beta (\Delta\sigma / M_0)^{\frac{1}{3}} \quad (5.2)$$

where  $\beta$  is the S-wave velocity proximal to the source of the earthquake (in km/s),  $\Delta\sigma$  is the stress drop (in bars) and  $M_0$  is the seismic moment (in dyne-cm).

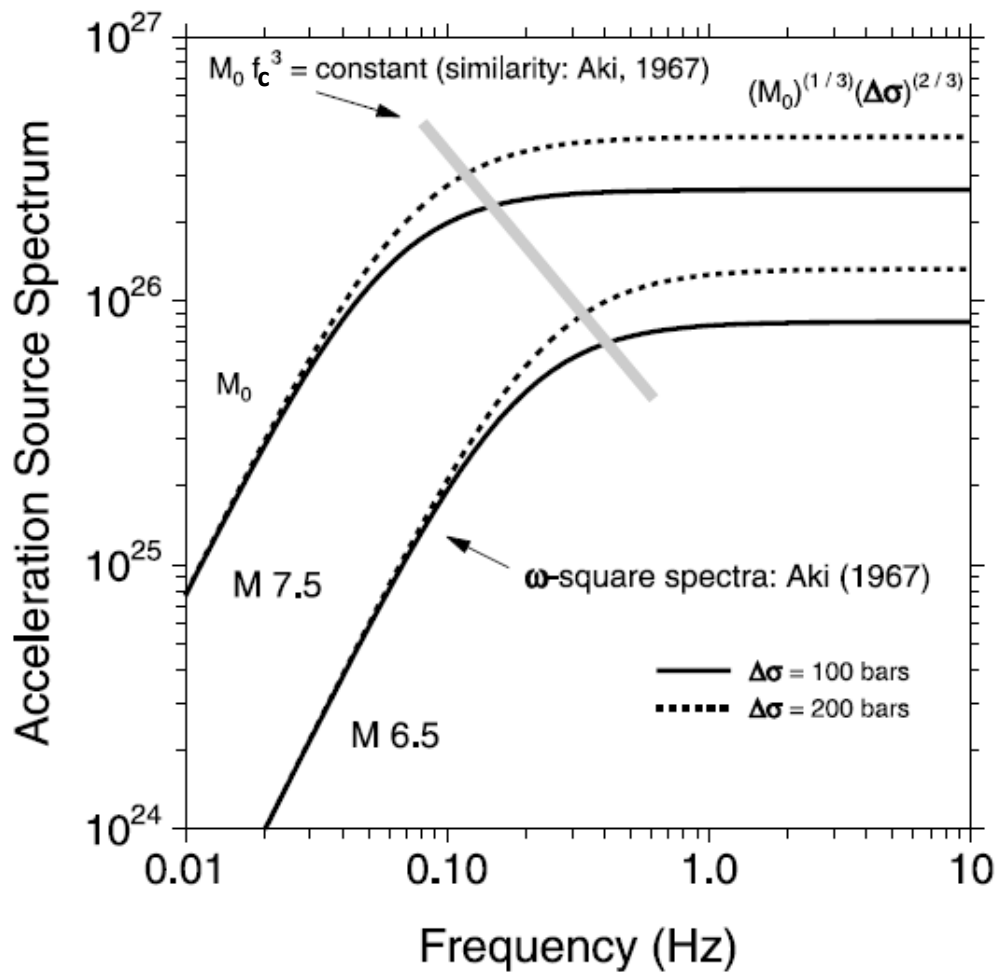


**Figure 5.2** Source scaling for single corner frequency  $\omega$ -square model. For constant stress drop  $M_0 f_0$  is a constant (Aki, 1967). The dependence of the corner frequency ( $f_0$ ) on the seismic moment ( $M_0$ ) (represented by the shaded line) determines the scaling of the spectral shapes. Taken from Boore (2003).

The  $\omega$ -square model is the most commonly used source scaling law, but the source spectra for all models can be given by:

$$E(M_0, f) = CM_0S(M_0, f) \quad (5.3)$$

where  $C$  is a constant given by below (see equation 5.5), and  $S(M_0, f)$  is the displacement source spectrum, given by:

$$S(M_0, f) = S_a(M_0, f) * S_b(M_0, f) \quad (5.4)$$

where the values for  $S_a$  and  $S_b$  are related to the corner frequencies  $f_a$  and  $f_b$ , which in turn are computed from the moment magnitude,  $M_w$ .

The constant  $C$  in equation 5.3 is given by:

$$C = \langle R_{\theta\phi} \rangle V_C F_S / (4\pi p_s \beta_s^3 R_0) \quad (5.5)$$

where  $R_{\theta\phi}$  is the radiation pattern (averaged over an appropriate range of azimuths and take-off angles - see Boore and Boatwright (1984) for more details).  $V_C$  represents the partition of total shear-wave energy into horizontal components ( $V_C = 1/\sqrt{2}$ ).  $F_S$  represents the effect of the free surface (usually taken as 2),  $p_s$  represents the density in proximity to the source and  $R_0$  is a reference distance (usually set to 1 km).

## Step 2 – Modelling of Path Effects ( $P(R, f)$ , *duration*)

For most applications the effects of the travel path can be represented by simple functions which account for geometrical spreading, attenuation (both anelastic and scattering) and the increase of duration with distance (due to wave propagation and scattering). The simplified path effect  $P$  is given by the multiplication of the geometrical spreading function,  $Z(R)$ , and the attenuation function,  $Q(f)$ :

$$P(R, f) = Z(R) \exp\left[-\frac{\pi f R}{Q(f) c_Q}\right] \quad (5.6)$$

where  $c_Q$  is the seismic velocity used when determining  $Q(f)$ , and  $Z(R)$  and is given through a set of continuous straight lines:

$$Z = \begin{cases} \frac{R_0}{R} & R \leq R_1 \\ Z(R_1) \left(\frac{R_1}{R}\right)^{p_1} & R_1 \leq R \leq R_2 \\ Z(R_n) \left(\frac{R_n}{R}\right)^{p_n} & R_n \leq R \end{cases} \quad (5.7)$$

where  $R$  is (usually) taken as the closest distance to the rupture surface ( $R_{rup}$ ) and  $R_1$  and  $R_2$  are reference distances. Through defining  $R$  as the closest distance to the rupture surface rather than as the hypocentral distance ( $R_{hyp}$ ) this method can be applied to extended ruptures. Fig. 5.3 shows an example geometric spreading function composed of three segments.

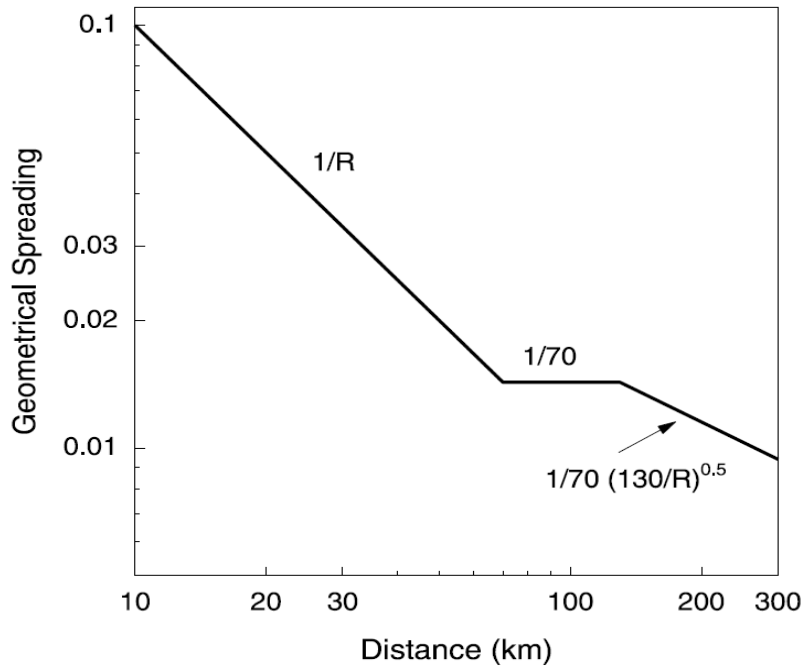


**Figure 5.3** Geometrical spreading function developed by Boore and Atkinson (1995).  $R_0 = 1$ ,  $R_1 = 70$ ,  $R_2 = 130$ ,  $p_1 = 0.0$  and  $p_2 = 0.5$ . Taken from Boore (2003).

The attenuation operator is also made up of three separate line segments (Fig. 5.4). Composing the attenuation operator as three segments is an effective yet simple way of capturing the variation of seismic attenuation ( $Q$ ) over the travel path. The outer lines of the attenuation operator are specified by slopes and intercepts at designated reference frequencies. The middle line joins the outer lines between frequencies  $ft1$  and  $ft2$ . These parameters describing the attenuation operator can be obtained through the analysis of weak-motion data.

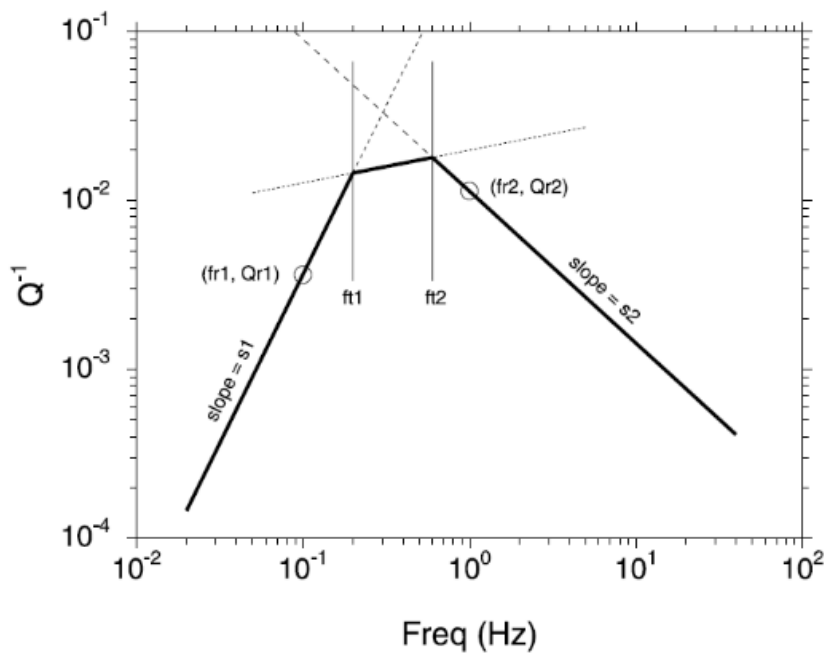


**Figure 5.4** Illustration of  $Q(f)$ . The specification is composed of three line segments in log-log space. Taken from Boore (2003).

The distance-dependent duration is an important function because the peak motions decrease with increasing duration assuming all other parameters remain equal. The spectrum of ground-motion (equation 5.0) does not take into account duration. However, the duration is a function of the path and the source, and therefore it is important to discuss duration. The ground-motion duration ( $T_{gm}$ ) is equal to the sum of the source duration and the path-dependent duration. Both empirical observations and theoretical simulations indicate that the path-dependent part of the duration can be represented by a series of straight-line segments. Fig. 5.5 shows the path-dependent duration function used within Atkinson and Boore (1995). The source duration is related to the inverse of the corner frequency (the larger the duration of the source process the smaller the corner frequency).

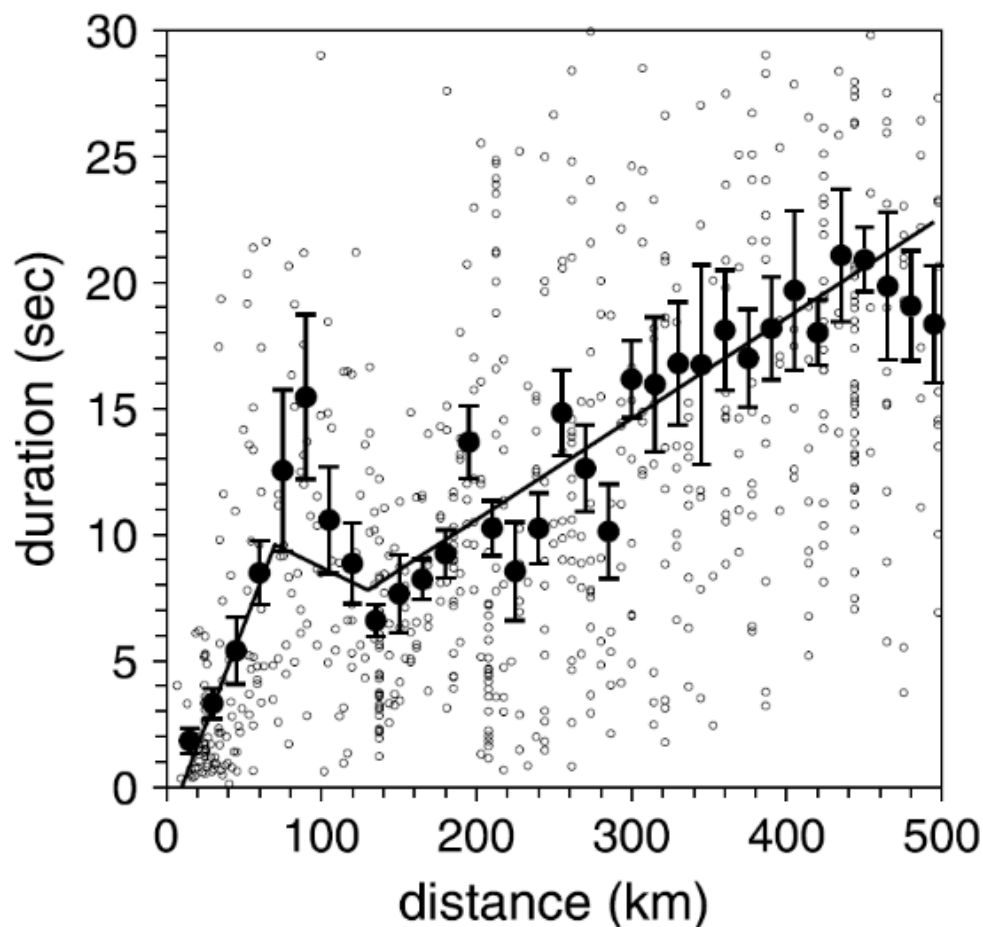


**Figure 5.5** Observed duration (once source duration is subtracted) for earthquakes from an arbitrary region. The solid circles represent averages within 15 km wide bins. The error bars are +/- one standard deviation of the mean. The three-part solid line is the path-dependent duration function developed by Atkinson and Boore (1995). Taken from Boore (2003).

### Step 3 – Modelling of Site Effects $G(f)$

Extensive efforts can be made to account for the modifications of ground-motions due to the local site geology/conditions. In such scenarios site-specific effects can be used. However, in many instances the simulations from the stochastic method are to be used for predicting ground-motions at a generic site

(i.e. a generic rock or generic soil site). In such instances a simplified function is used to describe the frequency-dependent modifications of the seismic spectrum:

$$G(f) = A(f)D(f) \quad (5.8)$$

where  $A(f)$  is the amplification function and  $D(f)$  is the path-independent attenuation function. The amplification function is relative to the source.  $D(f)$  is used to model the path-independent loss of energy. The path-dependent loss of energy is modelled using the exponential function within equation 5.5.  $G$  can also be a function of the amplitude of ground-shaking, but for simplicity non-linear effects are best incorporated through additional, separate site-response calculations. In application, it is also convenient to approximate the amplification by a series of connected line segments (see Fig. 5.6).

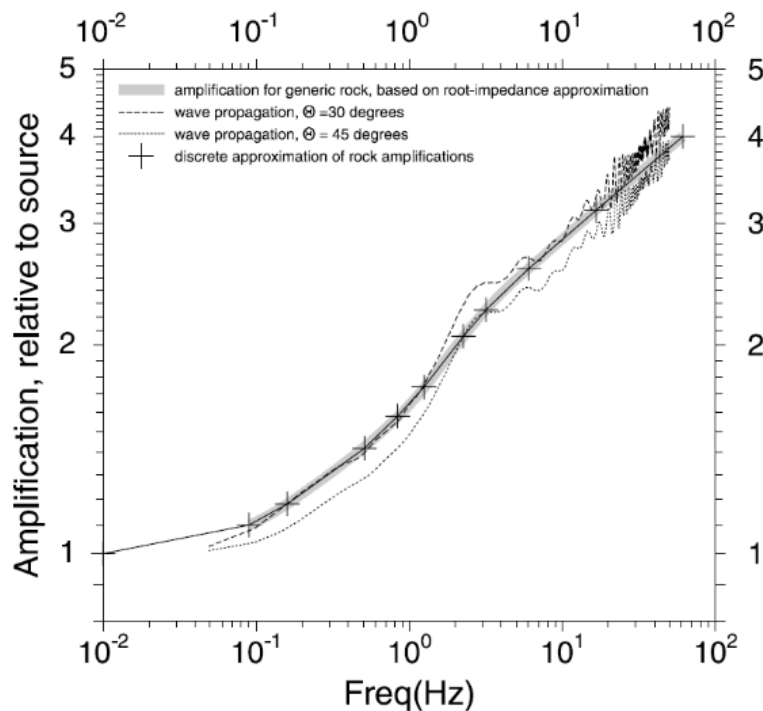


**Figure 5.6** Amplification vs. frequency. The segmented-line function used in the stochastic method is represented by the lines joining the plus symbols. Taken from Boore (2003).

The attenuation function  $D(f)$  in equation 5.8 accounts for the path-independent loss of high-frequency energy in the ground-motions. A simple multiplicative filter can account for the attenuation of the high-frequency motions, for which  $\kappa_0$  is often used:

$$D(f) = \exp(-\pi\kappa_0 f) \quad (5.9)$$

The combined effect of amplification and attenuation for various values of  $\kappa_0$  is shown in Fig. 5.7 for a generic soft rock site.

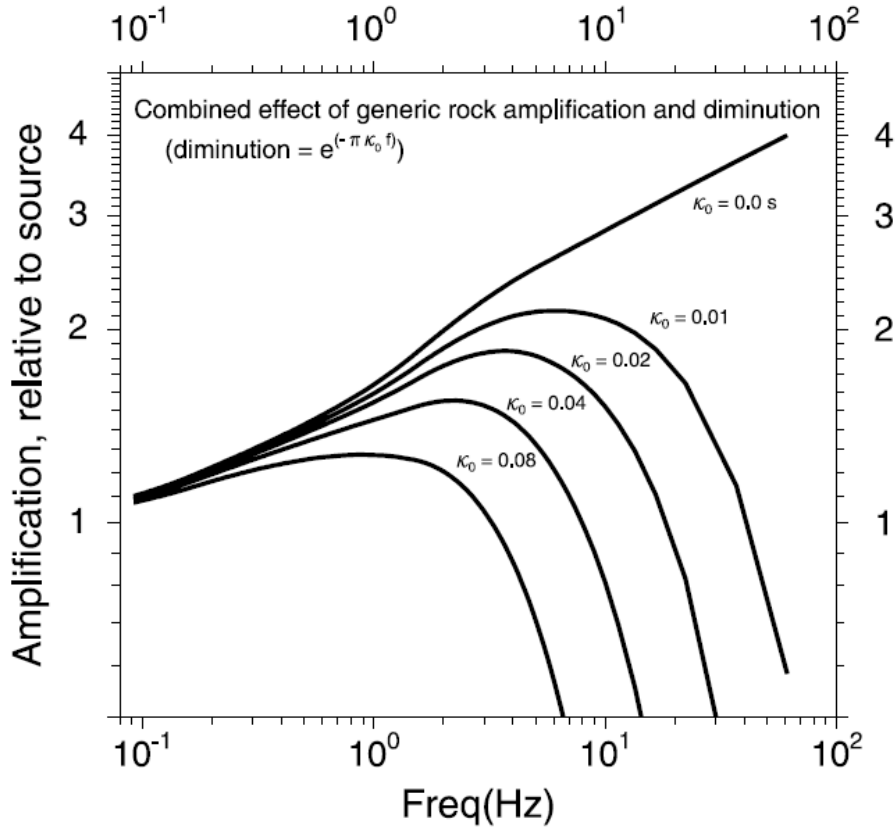


**Figure 5.7** Combined effect of the site amplification and the path-independent attenuation. Taken from Boore (2003).

#### Step 4 - Accounting for Type of Ground-Motion

The type of ground-motion resulting from the stochastic simulation is controlled by the filter,  $I(f)$ :

$$I(f) = (2\pi fi)^n \quad (5.10)$$

where  $i = \sqrt{-1}$  and  $n = 0, 1$  or  $2$  for ground-displacement, velocity or acceleration. For the response of an oscillator with undamped natural frequency  $f_r$ , from which the response spectrum can be derived:

$$I(f) = \frac{-Vf^2}{(f^2 - f_r^2) - 2ff_r\zeta i} \quad (5.11)$$

where  $\zeta$  represents the damping, and  $V$  represents the gain ( $= 1$ ).

#### Step 5 - Obtaining Ground-Motions using the Stochastic Method

When using the stochastic method there are two techniques widely used for obtaining simulated ground-motions: (1) the simulation of time series and (2) the estimation of peak ground-motions using random vibration theory. Here, the time-series simulation method is described.

The steps of the time-series simulation method are illustrated in Fig. 5.8 using an arbitrary seismological model. Firstly, white Gaussian or uniform noise is generated for a duration equal to the duration of the motion (Fig. 5.8a). This noise is then windowed (Fig. 5.8b). Following this, the windowed noise is transformed into the frequency domain (Fig. 5.8c). The spectrum is then normalised by the square-root

of the mean square amplitude spectrum (Fig. 5.8d). The normalised spectrum is multiplied by the ground-motion spectrum  $Y$  (Fig. 5.8e). The resulting spectrum is transformed back to the time domain (Fig. 5.8f). The shaping window applied to Fig. 5.8b can be either a box window or a window providing a more realistic shape for the acceleration time series (Fig. 5.9). An exponential window is commonly used for aesthetic purposes rather than differences in the derived ground-motion intensity parameters.

It should be noted that individual time series realisations should be applied with caution. The spectrum of each individual realisation is not guaranteed to be similar to the target spectrum  $Y(M_0, R, f)$ ; it is the mean of the individual spectra for a large number of simulations which will match the target spectrum (e.g. Fig. 5.10 - the mean of the spectra from 640 realisations is near identical to the target spectrum, but the spectrum of a randomly chosen individual realisation deviates significantly from the mean over the considered frequencies). Additionally, it should be noted that the variability of ground-motion intensity parameters obtained from a suite of simulations is not representative of the variability observed in real (observed) ground-motion intensity parameters. Simulation of the observed variability requires running the simulations using model parameters taken from distribution functions for those model parameters.

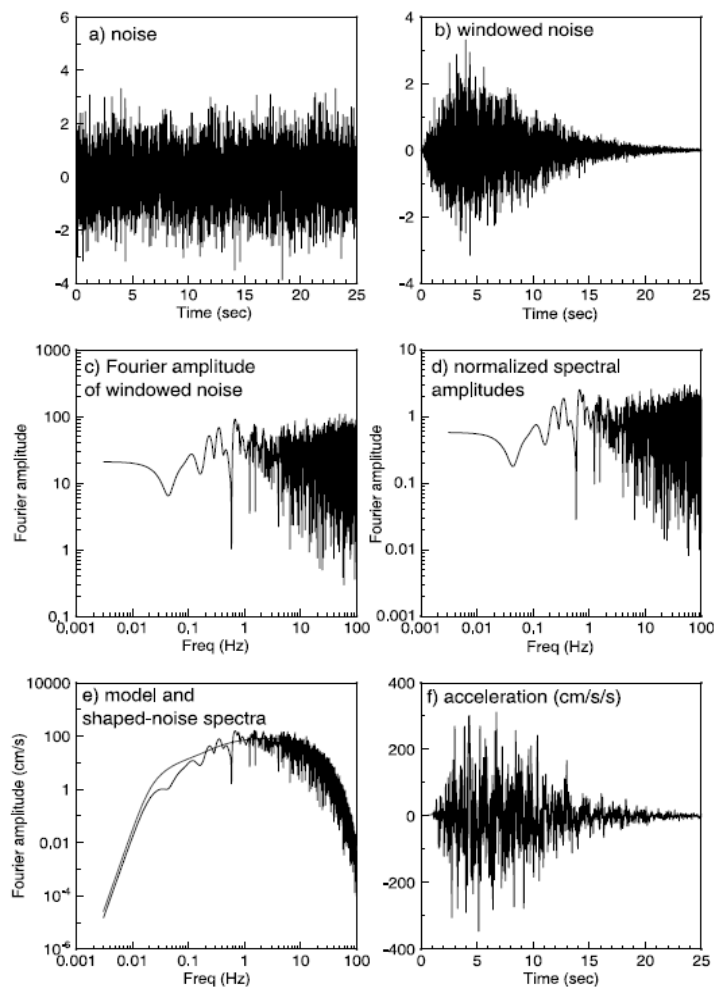


**Figure 5.8** Schematic of the time-domain procedure Taken from Boore (2003).

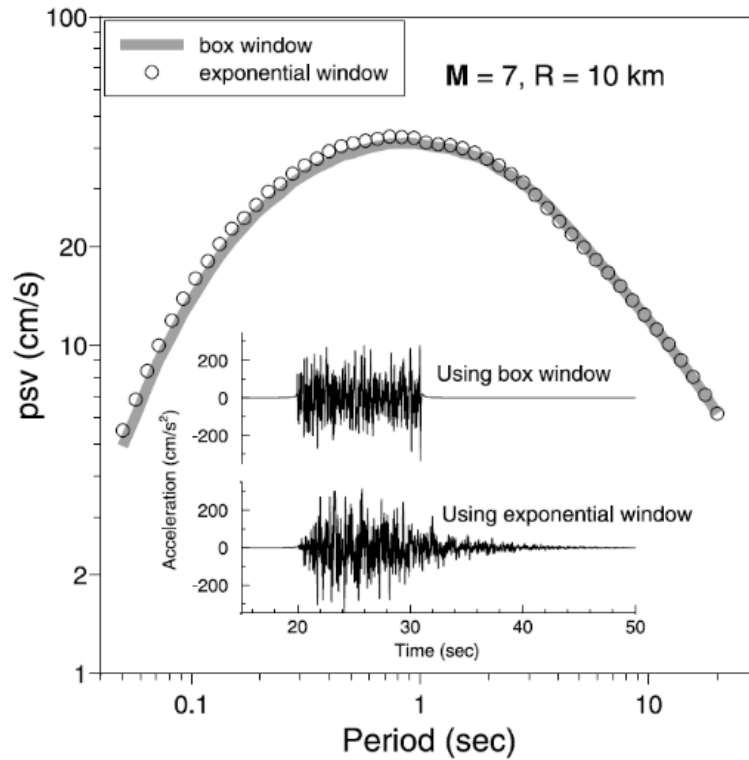


**Figure 5.9** Comparison of waveforms and peak surface velocity (PSV) response spectra for time-domain simulations using the box and exponential (shaped) windows to shape the noise. The response spectra are averages from a suite of 640 simulations. The time series are for a single realisation. The simulations were undertaken using an arbitrary seismological model. Taken from Boore (2003).

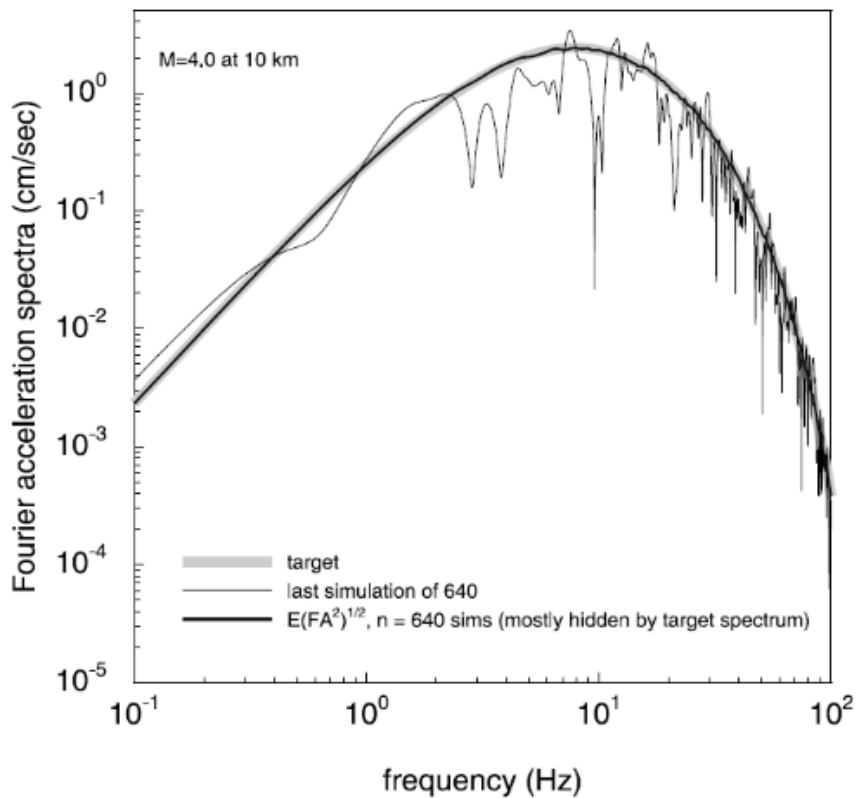


**Figure 5.10** The target spectrum, the spectrum from a single realisation and the spectrum from an average of 640 realisations. The simulations were undertaken using an arbitrary seismological model. Taken from Boore (2003).

## 5.2.2 Stochastic Simulations within SMSIM for Investigation of High Frequency Ground-Motion Variability with the Site-Specific Component of Kappa

Here, stochastic simulations were undertaken using Bora et al. (2017)'s stochastic model for Europe with a Brune (1970; 1971) source spectrum model and  $\kappa_0$  distributions sampled from various published  $\kappa_0$  models (Tab. 5.0). Appropriate  $\kappa_0$  distributions were sampled from the considered  $\kappa_0$  models for an average shear-wave velocity of the top 30 m ( $V_{s30}$ ) of 620 m/s. Bora et al. (2017) state a reference  $V_{s30}$  of 620 m/s was used for the computation of their provided  $\kappa_0$  distribution, and so a  $V_{s30}$  of 620 m/s was used for the computation of the other  $\kappa_0$  distributions too. Considering a different  $V_{s30}$  value is unlikely to affect the results significantly.

For each magnitude  $\phi$  was computed for a hypocentral distance ( $R_{hyp}$ ) of 40 km for PGA and spectral acceleration (SA) for periods of 0.2 s and 1.0 s (Fig. 5.11). The computation of  $\phi$  permits comparison of the variability in ground-motion over the considered moment magnitude range ( $M_w$  1 -  $M_w$  6.5) due to variations in solely  $\kappa_0$ . The  $\phi$  values were computed for  $R_{hyp} = 40$  km to eliminate the influence of regional attenuation. The rate of change of  $\phi$  with respect to magnitude is representative of the magnitude-dependency of the intra-event component of variability of ground-motion, and therefore was also computed (Fig. 5.12). A larger rate of change indicates a greater magnitude-dependency of  $\phi$ .

The computed  $\phi$  are compared to  $\phi$  provided by empirical GMPEs (Fig. 5.11; Fig. 5.12). GMPEs developed for similar magnitude ranges to the magnitude range considered in this investigation (Tab. 5.1) were required to permit determination of whether the magnitude-dependency for  $\phi$  observed in the simulations was similar to that observed in current GMPEs. Empirical GMPEs developed for small magnitude ( $M_w < 3$ ) earthquakes are scarce (even more so those with heteroscedastic  $\sigma$ ) compared to the number of empirical GMPEs developed for moderate to large magnitude earthquakes (from which higher hazard ground-motions are generated). Due to this scarcity of appropriate models, and that  $\phi$  generally contributes more to the total scatter of a GMPE than  $\tau$  (see above), for the considered GMPEs for which  $\phi$  is not provided,  $\sigma$  is considered as an approximation of  $\phi$ .

For each sampled  $\kappa_0$  distribution (see Table 5.0 for details on these  $\kappa_0$  distributions and all other inputted parameters), stochastic simulations were undertaken using: (1) a fixed  $\Delta\sigma$  of 5.65 MPa and (2) a  $\Delta\sigma$  distribution sampled from the Bora et al. (2017) stochastic model (Fig. 5.11; Fig. 5.12; Tab. 5.0). Variation in  $\Delta\sigma$  was considered because the trade-off between the  $\Delta\sigma$  and  $\kappa_0$  parameters<sup>43</sup> means  $\Delta\sigma$  must be varied to determine if it contributes to the magnitude-dependency of  $\phi$ . This trade-off between  $\Delta\sigma$  and  $\kappa_0$  is especially significant for small magnitude earthquakes (which this investigation considers) due to their high corner frequencies resulting in short rupture durations, which in turn results in the

---

<sup>43</sup> The selected value of  $\Delta\sigma$  influences  $k_0$  and *vice versa*, and so these two parameters which both affect the apparent decay of high frequency ground-motion are difficult to constrain simultaneously – e.g. see Anderson and Humphry (1991).

generated ground-motions being more affected by scatter and attenuation (Sumy et al., 2017). Simulations were undertaken with a fixed  $\kappa_0$  of 0.0308 s to examine the effect of varying only stress drop on the magnitude-dependency of  $\phi$  (Fig. 5.11; Fig. 5.12).

**Table 5.0** Parameters of the Bora et al. (2017) stochastic model for Europe and the considered  $\kappa_0$  distributions.

Parameter	Estimate of Parameter
Source Spectrum Model	Brune Point Source
Stress Drop ( $\Delta\sigma$ )	Mean = 5.65 MPa, Standard Deviation = $\ln(0.33)$
Geometric Spreading	$R^{-1.14}$ for $R \leq 70$ km $R^{-0.50}$ for $R > 70$ km
Anelastic Attenuation ( $Q_0$ )	610 for $R \leq 40$ km 1152 for $R > 40$ km
Near-Source Shear Wave Velocity ( $\beta$ )	3500 m/s
Near-Source Density ( $\rho$ )	2800 kg/m <sup>3</sup>
Sampled $\kappa_0$ Distributions*	B17: 0.0341 s, standard deviation 0.024 s (Bora et al., 2017 - $\kappa_0$ model for Europe) C06: 0.0636 s, standard deviation 0.022 s (Chandler et al., 2006 - $\kappa_0$ model for global application) E11: 0.0218 s, standard deviation 0.020 s (Edwards et al., 2011 - $\kappa_0$ for foreland Switzerland)
Site $V_{s30}$	620 m/s

\*The provided means and standard deviations are those for the sampled  $k_0$  values used within the ground-motion simulations, rather than the published means and standard deviations of the considered  $k_0$  distributions.

**Table 5.1** GMPEs for which  $\phi$  (or  $\sigma$ ) was compared to  $\phi$  computed from the stochastic simulations.

GMPE	Region	$M_w$ Range	Distance Range (km)	Heteroscedastic $\sigma$ ?	Structural Periods for which $\sigma$ is Heteroscedastic (s)
Ambraseys et al. (2005)	Europe and Middle East	5.0 - 8.0	0 - 100 ( $R_{jb}$ )	Yes, for both $\tau$ and $\phi$ .	0 - 2.5
Ameri et al. (2017)	France	3.0 - 6.5	0 - 200 ( $R_{epi}$ )	Yes, but for $\tau$ only.	0.01* - 3
Atkinson (2015)	California	3.0 - 5.0	0 - 40 ( $R_{hyp}$ )	No	N/A
Bindi et al. (2007)	Turkey	0.5 - 5.9	0 - 190 ( $R_{hyp}$ )	No	N/A
Bindi et al. (2017)	Active tect. Regions	3.0 - 8.0	0 - 300 ( $R_{hyp}$ )	No	N/A
Bommer et al. (2007)	Europe and Middle East	3.0 - 7.6	0 - 100 ( $R_{jb}$ )	Yes, for both $\tau$ and $\phi$ .	0.00 - 0.50
Boore et al. (2014)	Active tect. Regions	3.0 - 8.0	0 - 400 ( $R_{jb}$ )	Yes, for both $\tau$ and $\phi$ .	0.01* - 10
Chiou et al. (2010)	California	3.0 - 5.5	0 - 200 ( $R_{rup}$ )	No	N/A

\*0.01 s is treated as equivalent to PGA for this investigation.

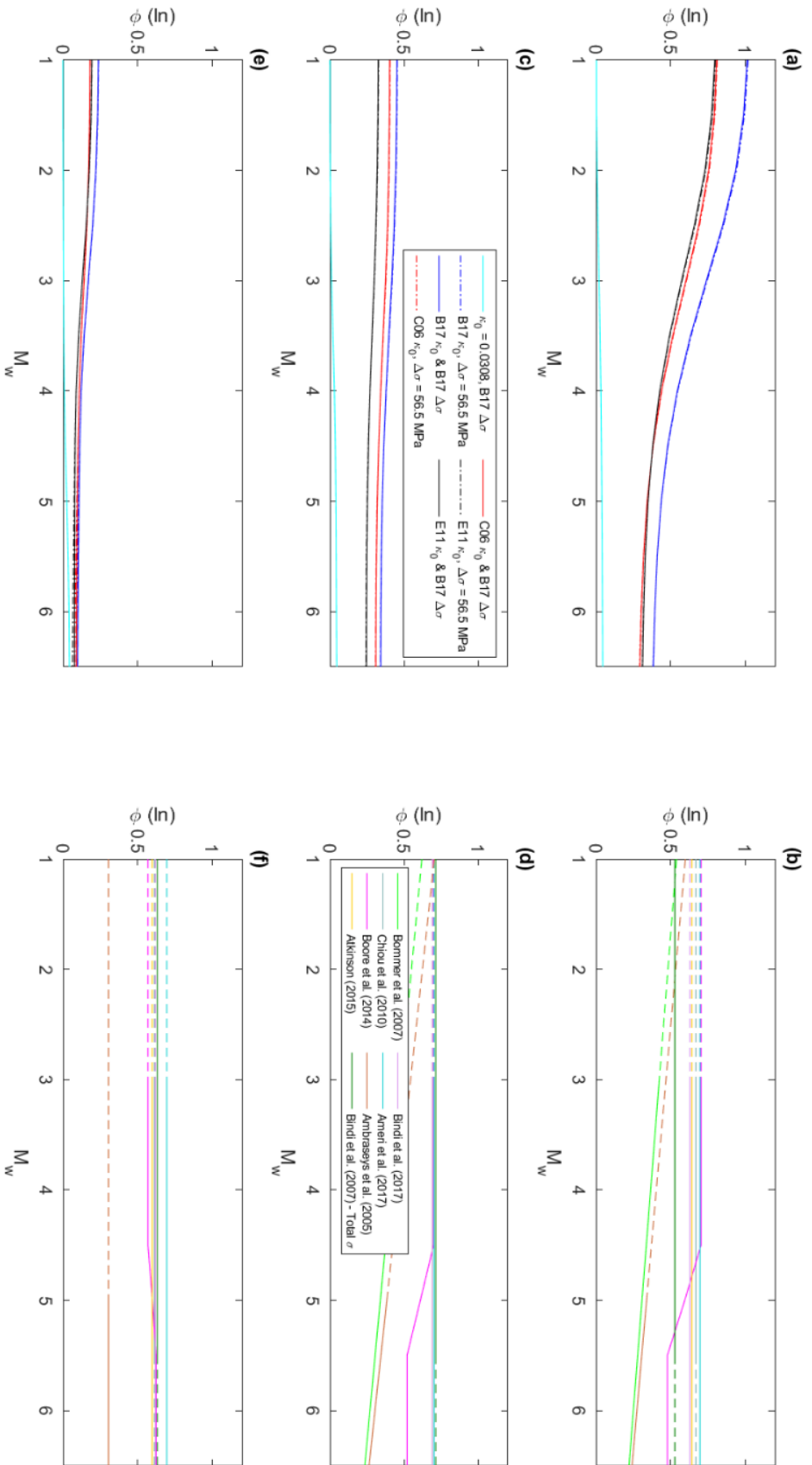


**Figure 5.11** (a)  $\phi$  for PGA from the simulated ground-motions, (b)  $\phi$  for PGA from the simulated GMPEs, (c)  $\phi$  for SA(0.2 s) from the simulated ground-motions, (d)  $\phi$  for SA(0.2 s) from the considered GMPEs, (e)  $\phi$  for SA(1 s) from the simulated ground-motions and (f)  $\phi$  for SA(1 s) from the considered GMPEs. B17 = Bora et al. (2017), C06 = Chandler et al. (2006) and E11 = Edwards et al. (2011). Dashed lines indicate extrapolation of GMPE standard deviation beyond the model's magnitude range.

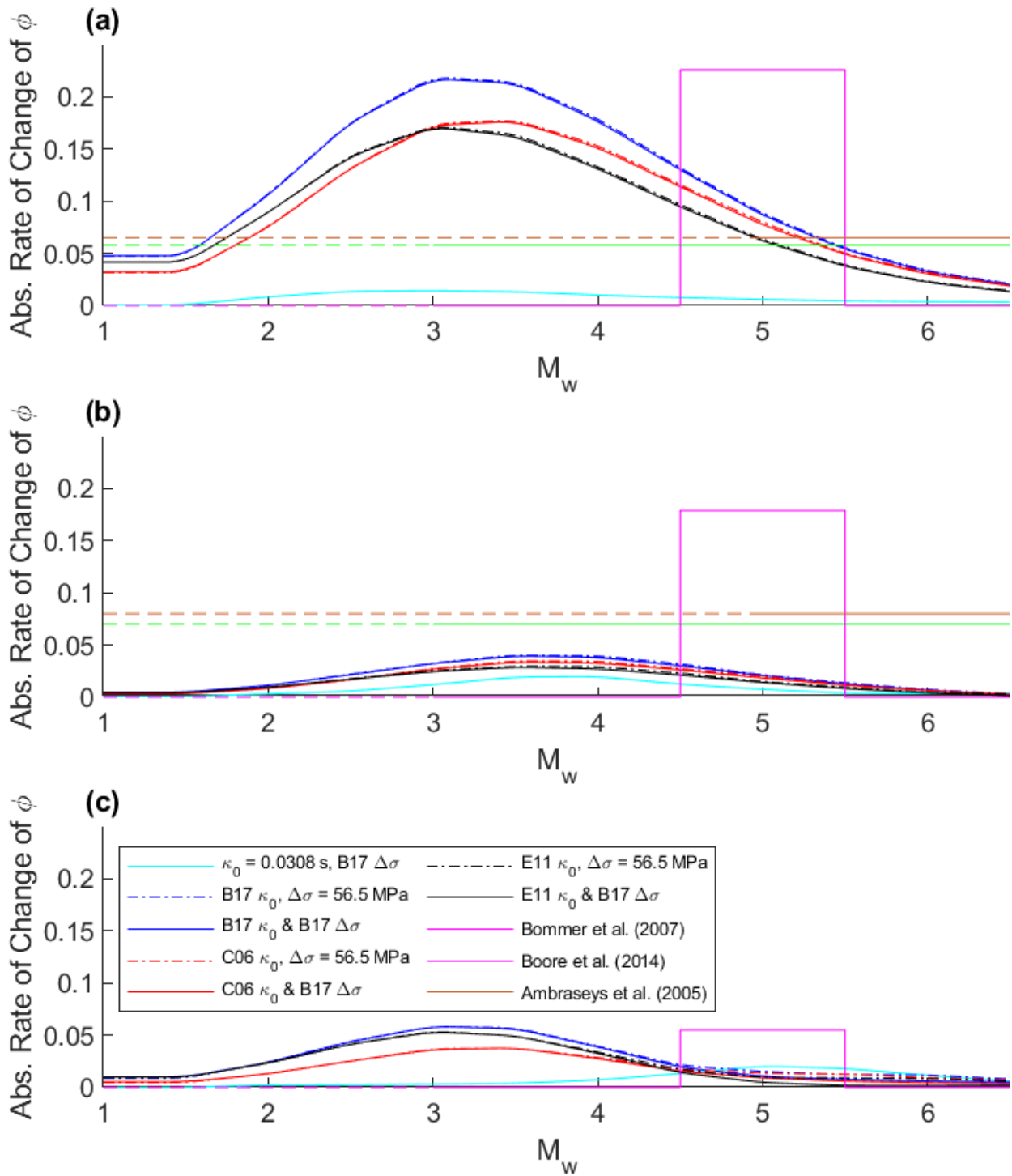


**Figure 5.12** (a) Rate of change of  $\phi$  with respect to magnitude for PGA, (b) rate of change of  $\phi$  with respect to magnitude for SA(0.2 s) and (c) rate of change of  $\phi$  with respect to magnitude for SA(1 s). B17 = Bora et al. (2017), C06 = Chandler et al. (2006) and E11 = Edwards et al. (2011). Dashed lines indicate extrapolation of GMPE standard deviation beyond the model's magnitude range of applicability. The considered GMPEs with homoscedastic  $\phi$  were not plotted. The Ameri et al. (2017) GMPE was not plotted due to only  $\tau$  being heteroscedastic with respect to magnitude.

### 5.3 Results for Investigation of High Frequency Ground-Motion Variability with the Site-Specific Component of Kappa

For a fixed  $\kappa_0$  and a  $\Delta\sigma$  distribution sampled from Bora et al. (2017), the computed  $\phi$  for PGA, SA(0.2 s) and SA(1 s) are small and show minimal magnitude-dependency, with  $\phi$  increasing slightly with magnitude (Fig. 5.11; Fig. 5.12). This weak magnitude-dependency observed when only  $\kappa_0$  is fixed suggests that  $\Delta\sigma$  contributes minimally to the magnitude-dependency of  $\phi$  for PGA, SA(0.2 s) and SA(1 s). The  $\phi$  computed for PGA for a sampled  $\kappa_0$  distribution and a  $\Delta\sigma$  distribution sampled from Bora et al. (2017) show minimal difference to the corresponding  $\phi$  computed with the same  $\kappa_0$  distributions and a fixed  $\Delta\sigma$ . This further supports that  $\Delta\sigma$  has a minimal influence on the magnitude-dependency of  $\phi$  for PGA. The magnitude-dependency of  $\phi$  with a non-fixed  $\kappa_0$  is considerably stronger for PGA than for SA(0.2 s) or SA(1.0) (Fig. 5.12). Variations in  $\kappa_0$  potentially lead to stronger magnitude-dependency of  $\phi$  for PGA than for SA(0.2 s) or SA(1 s) because  $\kappa_0$  describes the decay of specifically high-frequency ground-motions, and therefore PGA is more sensitive to said variations in  $\kappa_0$  than SA(0.2 s) or SA(1 s), resulting in stronger magnitude-dependency being observed for PGA. The seemingly limited influence of  $\Delta\sigma$  on the magnitude-dependency of  $\phi$  observed within this study is supportive of Kotha et al. (2017)'s findings that  $\Delta\sigma$  has a noticeable influence on the magnitude-dependency of  $\tau$ , therefore lending support to their expanded physical explanation of how  $\Delta\sigma$  influences  $\tau$  too. However, due to the complex mapping of magnitude-dependency onto both  $\phi$  and  $\tau$ , an expanded investigation into the influence of  $\Delta\sigma$  on the magnitude-dependency of both components of  $\sigma$  should be undertaken in the future.

The computed  $\phi$  for PGA, SA(0.2 s) and SA(1 s) are all larger for smaller magnitudes because as discussed above, ground-motions generated from smaller earthquakes are more affected by scatter and attenuation, resulting in greater variability in the ground-motions at a given site (Sumy et al., 2017). The magnitude-dependency of  $\phi$  is inherently stronger when a  $\kappa_0$  distribution with greater variability is considered (Fig. 5.12). For example, the maximum magnitude-dependency of  $\phi$  with the Bora et al. (2017)  $\kappa_0$  distribution (highest variability) is approximately 30% stronger than the maximum magnitude-dependency of  $\phi$  with the Edwards et al. (2011)  $\kappa_0$  distributions (lowest variability). The observation of stronger magnitude-dependency of  $\phi$  for PGA than for SA(0.2 s) or SA(1 s) due to solely variation in  $\kappa_0$  (Fig. 5.12) suggests as first proposed by Douglas and Jousset (2011) that  $\kappa_0$  is at least partly responsible for the magnitude-dependent nature of high frequency ground-motion variability within empirical GMPEs with heteroscedastic  $\phi$ .

For PGA the  $\phi$  values computed from the simulated ground-motions are slightly larger at lower magnitudes than the  $\phi$  values provided by the considered GMPEs, whereas for SA(0.2 s) and SA(1 s) the  $\phi$  values computed from the simulated ground-motions are more similar to some of the considered GMPEs (Fig. 5.11), with this being more so for SA(1 s) than for SA(0.2 s). The  $\phi$  values for PGA computed from the simulated ground-motions with the Chandler et al. (2006) and Edwards et al. (2011)

$\kappa_0$  distributions<sup>44</sup> are larger than the  $\phi$  values provided by the considered GMPEs below approximately  $M_w$  2.5. As discussed above, the larger  $\phi$  computed using the Bora et al. (2017)  $\kappa_0$  distribution is inherently due to its wider distribution. Of the considered GMPEs, the models which provide  $\phi$  values most similar to the  $\phi$  values computed from the simulated ground-motions are the Ameri et al. (2017), Chiou et al. (2010), Boore et al. (2014) and Ambraseys et al. (2005) GMPEs. Of these GMPEs, only the Ameri et al. (2017) GMPE was developed for earthquakes of  $M_w < 2.5$  (Tab. 5.1), and consequently was the only one of these three GMPEs which was not extrapolated for  $M_w < 2.5$  (Fig. 5.11). Therefore, extrapolation of GMPEs below their designated magnitude ranges cannot be the sole factor responsible for the difference between  $\phi$  for PGA from the simulated ground-motions and the GMPEs for  $M_w < 2.5$ . The  $\phi$  values for SA(1 s) being smaller/more similar to the  $\phi$  provided by the considered GMPEs than the  $\phi$  values for PGA can be partly attributed to  $\kappa_0$  having a more significant impact on the scatter of PGA than SA(1 s), and the impact of modifying  $\kappa_0$  upon the scatter of ground-shaking being less well modelled within existing GMPEs for PGA than SA(1 s)<sup>45</sup>. The observation that the simulated  $\phi$  values for SA(0.2 s) and SA(1 s) are more similar to the  $\phi$  provided by the considered GMPEs can be partly attributed to  $\kappa_0$  having a more significant impact on PGA than SA(0.2 s) or SA(1 s), and hence by default, variations in  $\kappa_0$  are better modelled in GMPEs for SA(0.2 s) and SA(1 s) than for PGA.

The magnitude-dependency of  $\phi$  for PGA computed from the simulated ground-motions is overall far stronger than the magnitude-dependency observed in the considered empirical GMPEs with heteroscedastic  $\phi$  (Fig. 5.12). For example, the maximum magnitude-dependency of the  $\phi$  for PGA computed from the simulations with the Edwards et al. (2011)  $\kappa_0$  distribution is approximately 200% stronger and 130% stronger than the magnitude-dependency of  $\phi$  for the Bommer et al. (2007) and Ambraseys et al. (2005) GMPEs respectively. The only exception to this observation is over the moment magnitude interval  $M_w$  4.5 -  $M_w$  5.5, within which the magnitude-dependency of  $\phi$  for PGA is far greater for the Boore et al. (2014) GMPE than the simulated ground-motions with any of the considered  $\kappa_0$  distributions (Fig. 5.2). The simulated magnitude-dependencies of  $\phi$  for PGA are likely stronger overall than from the considered empirical GMPEs because the functional forms of the considered GMPEs lack terms modelling variations in  $\kappa_0$ .

More varied results are observed for the magnitude-dependency of  $\phi$  for SA(0.2 s) and SA(1 s) computed from the ground-motion simulations when compared to the considered heteroscedastic GMPEs than for PGA. For SA(0.2 s), the magnitude-dependency of  $\phi$  computed from the simulated ground-motions is lower than for the Ambraseys et al. (2005) or Bommer et al. (2007) GMPEs, but lower than the Boore et al. (2014) GMPE, except over the magnitude interval  $M_w$  4.5 -  $M_w$  5.5, within

---

<sup>44</sup> As discussed above, the larger  $\phi$  computed using the Bora et al. (2017)  $\kappa$  distribution than the other considered  $\kappa$  distributions can be accredited to the larger variability in  $\kappa$  within the Bora et al. (2017)  $\kappa$  distribution.

<sup>45</sup> The influence of  $\kappa$  upon SA(1 s) is better captured by existing GMPEs than the influence of  $\kappa$  upon PGA because modification of  $\kappa$  has a far smaller impact upon the scatter of SA(1 s) than PGA.

which as for PGA and SA(1 s) it is far greater than  $\phi$  computed from the simulated ground-motions. For SA(1 s), the magnitude-dependencies of  $\phi$  computed from the ground-motion simulations can only be compared to the Boore et al. (2014) GMPE due to the other considered GMPEs lacking heteroscedastic  $\phi$  for SA(1 s). Therefore, for SA(1 s), limited comparisons can be made with respect to the magnitude-dependency of  $\phi$  computed from the ground-motion simulations and the considered GMPEs. As for PGA and SA(0.2 s), the magnitude-dependency of  $\phi$  is far smaller for the Boore et al. (2014) GMPE than the magnitude-dependency of  $\phi$  computed from the simulated ground-motions with any of the considered  $\kappa_0$  distributions, except over the magnitude interval  $M_w$  4.5 -  $M_w$  5.5 where the magnitude-dependency of  $\phi$  is far greater for the Boore et al. (2014) GMPE. The magnitude-dependency of  $\phi$  computed from the ground-motion simulations is overall more similar to the Boore et al. (2014) GMPE for SA(1 s) than for PGA or SA(0.2 s). This greater similarity for SA(1 s) can potentially be explained by  $\kappa_0$  describing the decay of specifically high frequency ground-motions; if variations in  $\kappa_0$  have a limited influence on longer period ground-motions, then such variations will likely not have as pronounced an effect for SA(1 s) as they do for PGA. This supports the reasoning above that the absence of terms which model variations in  $\kappa_0$  within the considered GMPEs will result in more pronounced differences between the magnitude-dependencies of  $\phi$  for PGA and SA(0.2 s) compared to SA(1 s).

Variations in  $\kappa_0$  result in the magnitude-dependency of  $\phi$  being marginally smaller for SA(0.2 s) than for SA(1 s). The magnitude-dependency of  $\phi$  would be expected to be greater for SA(0.2 s) than for SA(1 s) because  $\kappa_0$  describes the decay of high-frequency ground-motions. This could be explained by a trade-off between the influence of  $\kappa_0$  and  $\Delta\sigma$  on  $\phi$  at moderate spectral periods, in which  $\kappa_0$  has a stronger influence on  $\phi$  at smaller spectral periods and  $\Delta\sigma$  has a stronger influence on  $\phi$  at larger spectral periods. The presence of such a trade-off is potentially supported by the observations that (1) as the spectral period increases, the magnitude at which peak magnitude-dependency of  $\phi$  occurs for a fixed  $\kappa_0$  and a  $\Delta\sigma$  distribution sampled from Bora et al. (2017) increases and (2) for SA(0.2 s), the peak magnitude-dependency of  $\phi$  computed with a non-fixed  $\kappa_0$  occurs at a greater magnitude than for either PGA or SA(1 s), whilst also being smaller than for either PGA or SA(1 s).

The magnitude-dependency of  $\phi$  for PGA due to solely variation in  $\kappa_0$  being far stronger overall than the magnitude-dependency observed within the considered GMPEs (regardless of heteroscedastic  $\phi$  or homoscedastic  $\phi$ ) is suggestive of (1) future empirical GMPEs requiring additional consideration of  $\kappa_0$  (although there are some existing models which take substantial consideration of this parameter e.g. Laurendeau et al., 2013; Hassani and Atkinson, 2018) and (2) that empirical GMPEs with homoscedastic  $\phi$  are especially inadequate for regions with high variability in  $\kappa_0$ . The latter suggestion is supported by the observation (discussed above) that higher variability in  $\kappa_0$  results in stronger magnitude-dependency for the intra-event standard deviation of high frequency ground-motions (Fig. 5.12).

It should be acknowledged that there is potential for a circular argument associated with the sampled distributions for both  $\kappa_0$  and  $\Delta\sigma$  used within the ground-motion simulations. The sampled distributions have been developed based on models fit to data. These models are then used to examine the influence of  $\kappa_0$  and  $\Delta\sigma$  on the magnitude-dependency of  $\phi$ . If these distributions have been well modelled (i.e.  $\Delta\sigma$ ), then a minimal impact on the magnitude-dependency is observed, whereas if the distribution has been less well modelled (i.e.  $\kappa_0$ ) a considerably greater influence on magnitude-dependency could be observed. However, the observations resulting from variation in  $\kappa_0$  are reasonably well explained. This suggests that  $\kappa_0$  is sufficiently modelled for examining its influence upon the magnitude-dependency of  $\phi$  despite the larger uncertainty generally associated with the modelling of  $\kappa_0$  compared to  $\Delta\sigma$ .

#### **5.4 Conclusions for Investigation of High Frequency Ground-Motion Variability with the Site-Specific Component of Kappa**

Despite the  $\phi$  values computed from the simulated ground-motions being slightly elevated for PGA compared to (1) the  $\phi$  values provided by the considered empirical GMPEs below approximately  $M_w$  2.5 and (2) the corresponding  $\phi$  values for SA(0.2 s) and SA(1 s), this investigation lends support to the notion first proposed by Douglas and Jousset (2011) that  $\kappa_0$  contributes to the magnitude-dependent nature of high frequency ground-motion variability within empirical GMPEs with heteroscedastic  $\phi$ . The analysis undertaken here investigated the influence of  $\kappa_0$  on high frequency ground-motion variability through considering the individual and combined contributions of  $\kappa_0$  and  $\Delta\sigma$ . Comparison of the magnitude-dependency of  $\phi$  computed from the stochastic ground-motion simulations with various  $\kappa_0$  distributions to the magnitude-dependency of  $\phi$  from appropriate empirical GMPEs indicates that consideration of  $\kappa_0$  is required for future empirical GMPEs to better capture the uncertainty of predicted ground-motions. The incorporation of an additional term within the functional form of the GMPE which considered  $\kappa_0$  would help to capture the observed magnitude-dependency of  $\phi$  within the model.

## 6.0 Constructing a North Sea Ground-Motion Prediction Equation Logic Tree

The calculations performed within a conventional approach probabilistic seismic hazard assessment (PSHA) require the input of many models and their associated parameters (See Appendix B). Each of said inputs has an associated uncertainty because of a lack of knowledge with respect to the characteristics of nature (i.e. the characteristics of earthquake ground-motions). This uncertainty caused by a lack of knowledge is termed epistemic uncertainty. For example, there is much epistemic uncertainty as to what the maximum magnitude an earthquake source can produce, or what the ground-shaking intensity will be for a large earthquake at a small distance. Generally, epistemic uncertainty varies significantly with geographical location (Douglas, 2018a). For a region such as coastal California or Japan, where there are high rates of seismicity and therefore extensive earthquake catalogues and vast strong motion networks, epistemic uncertainty is lower because there is an abundance of ground-motion data (and thus a better knowledge of earthquakes in the region) (Douglas, 2018a). For regions where moderate and large earthquakes do not occur frequently, or ground-motion networks are less substantial or only recently operational, this epistemic uncertainty is therefore elevated in comparison (Douglas, 2018a).

The epistemic uncertainty within a (conventional) PSHA<sup>46</sup> is accounted for through the use of logic trees (Kulkarni et al., 1984). Each branch of the logic tree has a set of input models and an associated seismic hazard curve, as well as an assigned weight indicative of the confidence level that the branch is the best selection for the PSHA scenario. Within a logic tree, the mean rate of exceeding a given ground-motion intensity measure is equal to the sum of the rates of exceedance for each branch, multiplied by their respective weights. A detailed overview on the use of logic trees in PSHA is provided by Musson (2012).

The total uncertainty in the outputted seismic hazard (curves) is predominantly the result of the epistemic uncertainty associated with the selection of the ground-motion prediction equations (GMPEs) (e.g. Toro, 2006). The epistemic uncertainty associated with GMPE selection is conventionally accounted for within a conventional approach PSHA through the use of GMPE logic trees.

There are multiple approaches for the development of a GMPE logic tree. The simplest of these is the use of multiple GMPEs, where each GMPE is assigned a weight corresponding to the confidence that the GMPE is the most appropriate. An overview of the methods for selecting the set of GMPEs used in this approach is provided by Kale and Akkar (2017). The next approach is the hybrid empirical method, in which GMPEs derived from observed ground-motions are modified based on the ratio of stochastic ground-motion estimates, resulting in GMPE logic trees applicable to regions with sparse observed ground-motions themselves (Campbell, 2003). Following the hybrid empirical method there is the

---

<sup>46</sup> The constraining of epistemic uncertainty within a PSHA is important because a PSHA aims to represent all possible uncertainties in the prediction of ground-shaking at a selected site (Baker, 2015).

backbone approach, which has been applied frequently within the last decade for PSHAs pertaining to critical facilities (Atkinson et al., 2014). The backbone approach scales the weighting of each considered GMPE according to the uncertainty in the median predicted ground-motion. The scaling of the GMPEs usually corresponds predominantly to the uncertainty in the average stress drop for the region of interest (Douglas, 2018a). The backbone approach results in a set of GMPEs which are explicitly mutually exclusive and collectively exhaustive (MECE<sup>47</sup>), leading to the degree of uncertainty modelled within the GMPE logic tree being more transparent (Douglas, 2018a). The constraining of the epistemic uncertainties in a more transparent process makes the backbone approach ideal for site-specific PSHAs, in particular those pertaining to critical facilities with rigid safety regulations (e.g. nuclear facilities).

Douglas (2018a) proposed a modified backbone approach specifically for regional scale PSHA. This modified approach starts with a small set of backbone GMPEs, which are then branched out to account for potential differences in the average stress drop (i.e. regional dependency), resulting in an expanded set of GMPEs which is assumed to be representative of all ground-motions in the region of interest. Each GMPE in this expanded set has a default weight, which is adjusted accordingly as knowledge of earthquakes in the region of interest increases (e.g. through the acquisition of more ground-motion records). This modified backbone approach explicitly captures reductions in epistemic uncertainty as a greater understanding of ground-motions within the region of interest is incorporated, therefore making this approach ideal for regions with limited ground-motion data (e.g. the North Sea). This approach also likely better captures the epistemic uncertainty associated with ground-motions resulting from future earthquakes than a conventional GMPE logic tree for a region with an abundance of ground-motion data. This is because a region with an abundance of ground-motion data likely has multiple well constrained GMPEs developed from a consistent dataset (e.g. five GMPEs were developed for California in the NGA-West 1 and 2 projects - see Power et al., 2008; Bozorgnia et al., 2014), and therefore a logic tree using these GMPEs is potentially incapable of capturing the epistemic uncertainty associated with future ground-motions because the GMPEs may be too similar (Scherbaum et al., 2005), unlike the expanded set of GMPEs produced using the modified backbone approach (Douglas, 2018a).

Few PSHAs have been undertaken for the North Sea region which are available within the public domain. The most recent North Sea PSHA was undertaken by Bungum et al. (2000). Due to the lack of knowledge associated with the nature of the ground-motions associated with earthquakes in the North Sea, Bungum et al. (2000) used a GMPE logic tree to capture the resulting epistemic uncertainty associated with GMPE choice. This GMPE logic tree comprised the Toro et al. (1997) GMPE and the Ambraseys et al. (1996) GMPE with a 50:50 weighting (Tab. 6.0). Brooks et al. (2020) developed a

---

<sup>47</sup> The different GMPEs on the branches of a PSHA logic tree should be MECE so that the branch weights can be treated as probabilities, which is an implicit assumption when computing mean seismic hazard curves or seismic hazard curves for different percentiles (Bommer and Scherbaum, 2008). This assumption implies that one of the incorporated GMPEs is the true model (but the true model is unknown), and that all the GMPEs are independent of one another. This criterion does likely not hold for logic trees incorporating GMPEs developed from overlapping datasets.

GMPE specifically for the North Sea region<sup>48</sup>, but a GMPE logic tree implementing this GMPE was not developed within this study. The compilation of the high quality dataset used for the development of the Brooks et al. (2020) GMPE was possible due to the collection of an additional two decades of North Sea ground-motion observations since the Bungum et al. (2000) study. For the application of the Brooks et al. (2020) GMPE within a North Sea PSHA, the development of an appropriate GMPE logic tree for the North Sea region is required because using this GMPE alone would not model the high uncertainty in ground-motions in this region.

### **6.1 Identification of an Existing GMPE Logic Tree for Modification to the North Sea Region**

Regional-scale GMPE logic trees have been developed for several regions and sites surrounding the North Sea which potentially have similar seismicity (e.g. the United Kingdom, north-western Europe), and ground-motion records for the North Sea are still relatively sparse compared to for these adjacent regions. Consequently, the modification of an existing GMPE logic tree developed for one of these nearby regions is the most viable means of developing a GMPE logic tree specifically for the North Sea region itself. The identification of the most appropriate existing GMPE logic tree will require consideration of: (1) how effectively each GMPE logic tree captures epistemic uncertainty in the North Sea and (2) the performance of the GMPEs incorporated within each GMPE logic tree in the North Sea. A summary of each considered GMPE logic tree is provided within Tab. 6.0. Although not developed for a regional-scale PSHA, the Tromans et al. (2019) GMPE logic tree was considered because it was developed for a site-specific study in the United Kingdom (the Hinkley Point C nuclear facility). For the PSHA logic trees in which multiple tectonic regimes have been considered, the GMPE logic tree branch pertaining to the tectonic regime which is likely best representative of the total ground-motion in the North Sea was considered.

---

<sup>48</sup> For more details on the development of this GMPE alternatively consult chapters 3 - 4.

**Table 6.0** GMPE logic trees for regions surrounding the North Sea.

GMPE Logic Tree	Site/Region	GMPE 1 [wt.]	GMPE 2 [wt.]	GMPE 3 [wt.]	GMPE 4 [wt.]	GMPE 5 [wt.]	Rationale for GMPE Logic Tree Approach and GMPE Selection
Tromans et al. (2019)	Hinkley Point C (United Kingdom)	Atkinson and Boore (2006, 2011) [0.1]	Bindi et al. (2014a, 2014b)* [0.3]	Boore et al. (2014) [0.3]	Cauzzi et al. (2015) [0.2]	Rietbrock et al. (2013) [0.1]	A multi-GMPE model was chosen over a backbone approach because extensive additional work would be required to select the most appropriate GMPEs and for the scaling of each GMPE if the latter approach was chosen. The preliminary set of GMPEs was determined using the criteria proposed by Cotton et al. (2006) and Bommer et al. (2010). The final set of GMPEs was determined through the expert judgement of the ground-motion modelling team using site-specific technical criteria, including the comparison of the GMPEs amongst themselves and against the ground-motion dataset compiled for the study. A lower weight was assigned to the stochastic GMPEs (Atkinson and Boore, 2014a; 2014b and Rietbrock et al., 2013) and redistributed to the empirical GMPEs due to the significant contributions to the hazard which result from small source-to-site distance ground-motions, for which stochastic GMPEs are often poorly constrained. For the Bindi et al. (2014) GMPE the distance to the surface projection of the rupture ( $R_{j0}$ ) variant was used.
Mosca et al. (2019)	United Kingdom	Atkinson and Boore (2006, 2011) [0.1]	Bindi et al. (2014a, 2014b)* [0.3]	Boore et al. (2014) [0.3]	Cauzzi et al. (2015) [0.2]	Rietbrock et al. (2013) [0.1]	This study adopted the multi-GMPE model of Tromans et al. (2019) rather than a backbone approach. This was because (1) whilst the backbone approach is more transparent in how it captures epistemic uncertainties, calibration is difficult for stable regions with limited strong ground-motion data like the United Kingdom and (2) the modified backbone approach of Douglas (2018a) does not provide scaling factors for a spectral period of 0.2 s, which is required for the most recent version of Eurocode 8. The weights proposed by Tromans et al. (2019) were validated through comparison of the selected GMPEs and the United Kingdom ground-motion dataset used in the investigation.
SHARE – Delavaud et al. (2012); Woessner et al. (2015)  [Branch developed specifically for stable continental regions]	Europe and Turkey	Campbell (2003) [0.2]	Toro (2002) [0.2]	Cauzzi and Faccioli (2008) [0.2]	Akkar and Bommer (2010) [0.2]	Chiou and Youngs (2008) [0.2]	A multi-GMPE model was implemented. The preliminary set of GMPEs was determined using the criteria proposed by Cotton et al. (2006) and Bommer et al. (2010). The final GMPE logic tree was developed using the approach presented by Delavaud et al. (2012), which attempts to capture all possible ground-motions in the region of interest through the parallel undertaking of (1) expert judgement of the preliminary GMPEs guided by a set of predefined rules and (2) the objective testing of each preliminary GMPE using a compiled ground-motion dataset. The results of the expert judgement and GMPE testing were combined to produce several preliminary weighting schemes for the final GMPEs, which were then revised if necessary based on a sensitivity analysis undertaken for each considered tectonic regime's proposed GMPE logic tree.

Continuation of Table 6.0 GMPE logic trees for regions surrounding the North Sea.

GMPE Logic Tree	Site/Region	GMPE 1 [wt.]	GMPE 2 [wt.]	GMPE 3 [wt.]	GMPE 4 [wt.]	GMPE 5 [wt.]	Rationale for GMPE Logic Tree Approach and GMPE Selection
Grünthal et al. (2018)	Germany	Akkar et al. (2014) [0.167]	Bindi et al. (2014a, 2014b) [0.167]	Derras et al. (2014) [0.167]	Bindi et al. (2017) [0.25]	Cauzzi et al. (2015) [0.25]	A multi-GMPE model was implemented. Due to Germany being a complex tectonic environment comprising of both stable and active areas a data-driven and objective regionalisation process (Chen et al., 2016) was used to select appropriate GMPEs, rather than expert judgement, which provides results which are difficult to replicate. Disaggregation results indicated that $M_L$ 4.5 – 5.5 earthquakes at short distances (less than 25 km) had the largest control on the seismic hazard, and consequently GMPEs were sought which performed well within this magnitude range. Models with simple functional forms were favoured because the use of complex functional forms would require the fixing of variables, which introduces additional epistemic uncertainty. For each selected GMPE the hypocentral distance ( $R_{hyp}$ ) variant was used. For the GMPEs which a $R_{hyp}$ variant was not available (Derras et al., 2014; Cauzzi et al., 2015), the procedure of Scherbaum et al. (2004) was used to modify them to use the $R_{hyp}$ metric. Weights were assigned to each GMPE based on how representative each ground-motion dataset considered within the regionalisation process was thought to be of the total ground-motion in Germany.
NGA-East – Goulet et al. (2018). [Applied to listed region by Carlton and Kaynia, 2019]	Oslo, Norway	Carlton and Kaynia (2019) used the 17 NGA-East GMPEs (Goulet et al., 2018) with their pre-assigned weights in a simple logic tree approach. For more details regarding the NGA-East GMPEs and the assigned GMPE weights see Tab. 9-2 of Goulet et al. (2018).					The NGA-East GMPEs (Goulet et al., 2018) were selected because they were developed for central and eastern Northern America (CENA), which is a stable continental region similar to Oslo. The incorporation of 17 period-dependently weighted GMPEs within a logic tree formulation was deemed an appropriate means of capturing the epistemic uncertainty associated with GMPE selection in Oslo.
Bungum et al. (2000)	United Kingdom, Norway and the North Sea	Toro et al. (1997) [0.5]		Ambraseys et al. (1996) [0.5]			Bungum et al. (2000) used the Toro et al. (1997) GMPE, which was developed for CENA and the Ambraseys et al. (1996) GMPE, which was developed for Europe in a multi-GMPE approach to capture the spread of potential ground-motions in the North Sea.

To evaluate how effectively each GMPE logic tree captures epistemic uncertainty in the North Sea, hazard calculations were undertaken for a low hazard North Sea site and a high hazard North Sea site<sup>49</sup> using the OpenQuake seismic hazard software (Pagani et al., 2014). To model the distribution of seismicity in the North Sea, the area source zones used within the Bungum et al. (2000) North Sea PSHA were selected. Hazard curves were computed for peak ground acceleration (PGA) and spectral acceleration (SA) for a period of 1.0 s for the mean, median, 15<sup>th</sup> fractile and 85<sup>th</sup> fractile of predicted ground-motion (Fig. 6.0; Fig. 6.1). Hazard curves were also computed using the Bungum et al. (2000) GMPE logic tree to provide comparison to the GMPE logic trees considered for modification<sup>50</sup>. It should be noted that for this screening of the considered GMPE logic trees that select GMPE

<sup>49</sup> Low hazard site: latitude = 56, longitude = 2; high hazard site: latitude = 66, longitude = 14.

<sup>50</sup> Due to the unavailability of the Ambraseys et al. (1996) GMPE within OpenQuake the Bungum et al. (2000) hazard curves were computed using the CRISIS seismic hazard software (Ordaz et al., 2015).

modifications described within the original logic tree studies were not incorporated within the hazard calculations due to the significant additional work required for their implementation. These omitted modifications are as follows: (1) Tromans et al. (2019) used host-to-target adjustment factors for the incorporated GMPEs to account for differences in the shallow crustal shear-wave velocity ( $V_s$ ) and the high-frequency crustal attenuation ( $\kappa$ ) at the target site and the regions for which the GMPEs were developed and (2) Grunthal et al. (2018) incorporated scaling factors to account for the epistemic uncertainty regarding stress drop (see Fig. 15 of Grunthal et al., 2018 for the scaling factors and their associated weights). The absence of these GMPE modifications will influence the hazard results (see below w.r.t. the uncertainty captured by each model).

For mean PGA, the Tromans et al. (2019) and Grunthal et al. (2018) GMPE logic trees provide the most similar results to one another of the considered GMPEs (more so for the high hazard site) despite sharing only two GMPEs (albeit they are similarly weighted - Tab. 6.0). The mean PGA hazard curve computed using the SHARE GMPE logic tree lies between the NGA-East mean PGA hazard curve and the Tromans et al. (2019) and Grunthal et al. (2018) mean PGA hazard curves. Overall, the NGA-East GMPE logic tree predicts considerably larger values of mean PGA for a given annual frequency of exceedance (AFOE) than the other considered GMPE logic trees. The only exception is within an AFOE range of  $10^{-3}$ - $10^{-1}$  for the high hazard site, where the Bungum et al. (2000) GMPE logic tree provides noticeably larger mean PGA for a given AFOE. At the high hazard site, for an AFOE of  $10^{-3}$ , the predicted mean PGA is approximately 30% larger for the NGA-East GMPE logic tree than the SHARE GMPE logic tree. The noticeably higher mean PGA hazard predicted by the NGA-East GMPE logic tree can be attributed to the GMPEs incorporated within this model having been developed for a magnitude range of  $M_w 4 - 8.2$  for application in central and eastern North America (CENA). Similarly, the larger mean PGA for a given AFOE within the AFOE range of  $10^{-3}$ - $10^{-1}$  for the high hazard site provided by the Bungum et al. (2000) GMPE logic tree can be likely be attributed to the incorporation of a GMPE developed for CENA (the Toro et al., 1997 GMPE – Tab. 6.0).

For mean SA(1.0 s), the Tromans et al. (2019) and Grunthal et al. (2018) GMPE logic trees provide similar results to one another for both the low and high hazard sites as they do for mean PGA. For the high hazard site, below an AFOE of  $10^{-3}$ , the mean SA(1.0 s) for the Bungum et al. (2000) GMPE logic tree is also similar to the results for the Tromans et al. (2019) and Grunthal et al. (2018) GMPE logic trees. For the low hazard site, the 85<sup>th</sup> fractile SA(1.0 s) for the NGA-East GMPE logic tree is reasonably similar to the mean SA(1.0 s) computed using the Bungum et al. (2000) GMPE logic tree. As for mean PGA, this similarity is likely the result of both of these GMPE logic trees incorporating GMPEs developed for CENA. The SHARE and NGA-East GMPE logic trees provide more similar results to one another for mean SA(1.0 s) than for mean PGA, especially within an AFOE range of  $10^{-4}$ - $10^{-2}$  for the high hazard site. For both PGA and SA(1.0 s), the spread of the hazard curves for the SHARE GMPE logic tree is considerably greater than for the other GMPE logic trees.

The relative uncertainty measure popularised by Douglas et al. (2014) was used to measure the epistemic uncertainty associated with each GMPE logic tree for predicting ground-motions in the North Sea. The relative uncertainty,  $U_R = 100 \ln(GM_{85}/GM_{15})$ , where  $(GM_{85})$  is the 85<sup>th</sup> fractile of the predicted ground-shaking for a given return period and  $(GM_{15})$  is the 15<sup>th</sup> fractile of the predicted ground-shaking for a given return period.  $U_R$  is effectively representative of the spread of the fractiles of the distributions of predicted ground-shaking for a given return period using the considered GMPE logic tree, with a larger value for  $U_R$  indicating a greater spread, and therefore a higher epistemic uncertainty being associated with the GMPE logic tree. Within this study  $U_R$  has been computed for PGA and SA(1.0 s) for return periods of 475 years and 2475 years (Tab. 6.2). The computed  $U_R$  is similar overall for the high hazard site and the low hazard site. For simplicity, the GMPE logic trees are therefore only evaluated with respect to  $U_R$  for the high hazard site. The distributions of predicted ground-shaking used to compute  $U_R$  for the high hazard site are displayed in Tab. 6.1.

The absence of select GMPE modifications (see above) will influence the uncertainty associated with the hazard results. The incorporation of the host-to-target adjustment factors within the Tromans et al. (2019) GMPE logic tree would increase the spread of the predicted ground-motions for a given return period. Therefore, the  $U_R$  values computed for the Tromans et al. (2019) GMPE logic tree are artificially reduced by the absence of these host-to-target adjustment factors. The stress drop scaling incorporated within the Grunthal et al. (2018) GMPE logic tree would also increase the spread of predicted ground-motions for a given return period. Therefore, the  $U_R$  values computed for the Grunthal et al. (2018) GMPE logic tree are artificially reduced by the lack of these scaling factors for the stress drop. It should also be noted that the  $U_R$  values computed for the SHARE GMPE logic tree are considerably larger than those computed for similar studies. For example, Douglas et al. (2014) computed values for  $U_R$  between 37 and 52 for PGA and 53 and 64 for SA(1.0 s) using the SHARE GMPE logic tree for PSHAs for Edinburgh and Berlin. These regions likely have similar seismicity to the North Sea, so the differing seismic zonation of the North Sea and the sites selected for the North Sea hazard calculations (larger source-to-site distances overall) could explain the relatively high  $U_R$  values for SHARE observed here.

For PGA,  $U_R$  is smallest for the Tromans et al. (2019) GMPE logic tree for both 475 and 2475 year return periods. For SA(1.0 s),  $U_R$  is smallest for the Grunthal et al. (2018) GMPE logic tree for both 475 and 2475 year return periods. For both PGA and SA(1.0 s), the SHARE GMPE logic tree provides the largest  $U_R$ , as is reflected by the spread of the associated hazard curves (Fig. 6.0; Fig. 6.1). The ratio of  $U_R$  for the two considered ground-motion intensity measures was used to examine if the uncertainty captured by any of the GMPEs is strongly dependent on the spectral period (Tab. 6.2). The uncertainty in a GMPE is only mildly dependent on the spectral period (Douglas et al., 2014), and therefore the results of a PSHA incorporating a GMPE logic tree should also show only a mild dependency on spectral period. The period-dependency of each GMPE logic tree should not be affected by the absence of the GMPE modifications discussed above. The uncertainty captured by the NGA-East GMPE logic

tree demonstrates the weakest period-dependency, which can be attributed to the GMPEs incorporated within this GMPE logic tree having period-dependent weightings (Goulet et al., 2018). The uncertainty captured by the Grunthal et al. (2018) GMPE logic tree demonstrates the strongest period-dependency. The uncertainties captured within a GMPE logic tree are expected to compound as the return period increases, and therefore it would be expected that the  $U_R$  computed for each GMPE logic tree increases with return period to reflect this (Douglas et al., 2014). For both PGA and SA(1.0 s), an increase in  $U_R$  between 475 years and 2475 years is observed for the Tromans et al. (2019), Grunthal et al. (2018) and NGA-East GMPE logic trees but not the SHARE GMPE logic tree.

**Table 6.1** Distributions of predicted PGA and SA(1.0 s) for return periods of 475 years and 2475 years at the high hazard site.

Fractile	PGA (g) for 475 Year RP	PGA (g) for 2475 Year RP	SA01s (g) for 475 Year RP	SA01s (g) for 2475 Year RP
TR19 Mean	0.036	0.095	0.009	0.027
TR19 Median	0.034	0.087	0.010	0.026
TR19 15 <sup>th</sup> Fractile	0.030	0.075	0.008	0.022
TR19 85 <sup>th</sup> Fractile	0.038	0.102	0.010	0.030
SHARE Mean	0.055	0.134	0.016	0.042
SHARE Median	0.055	0.133	0.013	0.036
SHARE 15 <sup>th</sup> Fractile	0.024	0.054	0.008	0.021
SHARE 85 <sup>th</sup> Fractile	0.067	0.145	0.019	0.049
GR18 Mean	0.031	0.079	0.009	0.026
GR18 Median	0.029	0.073	0.009	0.025
GR18 15 <sup>th</sup> Fractile	0.022	0.053	0.008	0.022
GR18 85 <sup>th</sup> Fractile	0.034	0.091	0.009	0.027
NGA-East Mean	0.090	0.223	0.013	0.039
NGA-East Median	0.085	0.219	0.013	0.037
NGA-East 15 <sup>th</sup> Fractile	0.060	0.136	0.010	0.026
NGA-East 85 <sup>th</sup> Fractile	0.100	0.251	0.017	0.048

**Table 6.2**  $U_R$  for the predicted ground-motion for a given return period at the high hazard site.

$U_R$ for GMPE Logic Tree	PGA 475 Years	PGA 2475 Years	SA1s 475 Years	SA1s 2475 Years	SA1s/PGA (475 Years)	SA1s/PGA (2475 Years)
Tromans et al. (2019)	25	31	21	30	0.85	0.97
SHARE	104	99	93	88	0.89	0.88
Grunthal et al. (2018)	45	55	13	18	0.29	0.33
NGA-East	52	61	56	59	1.08	0.96

Several of the GMPEs which performed best when evaluated using North Sea ground-motion records (Tab. 6.3) are incorporated within the considered GMPE logic trees. The Grunthal et al. (2018) GMPE logic tree incorporates the  $R_{hyp}$  variant of the Akkar et al. (2014) GMPE. All distance-metric variants of the Akkar et al. (2014) GMPE were found to perform well in the North Sea GMPE testing, with the  $R_{jb}$

variant being selected as the most appropriate base model for modification to develop a North Sea GMPE (see Brooks et al., 2020 or alternatively consult chapters 3 - 4 for more detail). The Tromans et al. (2019) GMPE logic tree incorporates the Rietbrock et al. (2013) GMPE, which was also found to perform well in the North Sea. The Tromans et al. (2019) GMPE logic tree also incorporates the Boore et al. (2014) GMPE, which was found to perform poor – moderately overall in the North Sea. Both the Grunthal et al. (2018) and Tromans et al. (2019) GMPE logic trees incorporate the Cauzzi et al. (2015) GMPE, which was also found to perform moderately well overall in the North Sea. The SHARE GMPE logic tree incorporates the Toro (2002) GMPE, which was found to be one of the worst performing GMPEs of those evaluated against North Sea ground-motion records. The NGA-East GMPE logic tree does not incorporate any GMPEs evaluated within the North Sea GMPE testing.

Overall, the Tromans et al. (2019) GMPE logic tree is the most appropriate considered GMPE logic tree for modification to develop a North Sea GMPE logic tree. In addition to the site-specific PSHA for which the Tromans et al. (2019) GMPE logic tree was developed the model has been used for the computation of the most recent United Kingdom seismic hazard maps (Mosca et al., 2019). The use of the Tromans et al. (2019) GMPE logic tree within two high profile United Kingdom PSHAs is indicative of it being suitable for use in the adjacent North Sea region. The choice of the Tromans et al. (2019) GMPE logic tree is supported by the hazard calculations undertaken within this investigation: (1) the Tromans et al. (2019) GMPE logic tree incorporates several GMPEs which were found to perform well within the North Sea GMPE testing, suggesting the GMPEs incorporated within the Tromans et al. (2019) GMPE logic tree are appropriate for use in the North Sea, (2) the uncertainty captured by the Tromans et al. (2019) GMPE logic tree demonstrates the second weakest period-dependency of the considered GMPE logic trees and (3) the uncertainty captured by the Tromans et al. (2019) GMPE logic tree increases with an increase in return period, as would be expected within a GMPE logic tree.

**Table 6.3** Results of North Sea GMPE testing. Only the results for GMPEs evaluated within the North Sea GMPE testing which are incorporated within the considered GMPE logic trees are provided here. For more detail on the GMPE testing procedure and the associated results see Chapter 3.

GMPE	PGA	SA(0.1 s)	SA(0.5 s)	SA(1.0 s)
Akkar and Bommer, 2010	Poor fit	Moderate fit	Poor fit	Poor fit
Akkar et al., 2014 ( $R_{jb}$ )	Good fit	Good fit	Moderate fit	Poor fit
Boore et al., 2014	Poor fit	Moderate fit	Poor fit	Poor fit
Bindi et al., 2017 ( $R_{hyp}$ )	Moderate fit	Poor fit	Poor fit	Poor fit
Cauzzi et al., 2015	Poor fit	Moderate fit	Moderate fit	Poor fit
Rietbrock et al., 2013	Moderate fit	Good fit	Moderate fit	Poor fit
Toro et al., 2002	Poor fit	Poor fit	Poor fit	Poor fit

Fit refers to GMPE performance using the North Sea dataset. For more detail on the criteria for each of these descriptions see Tab. 3.1 of Chapter 3.

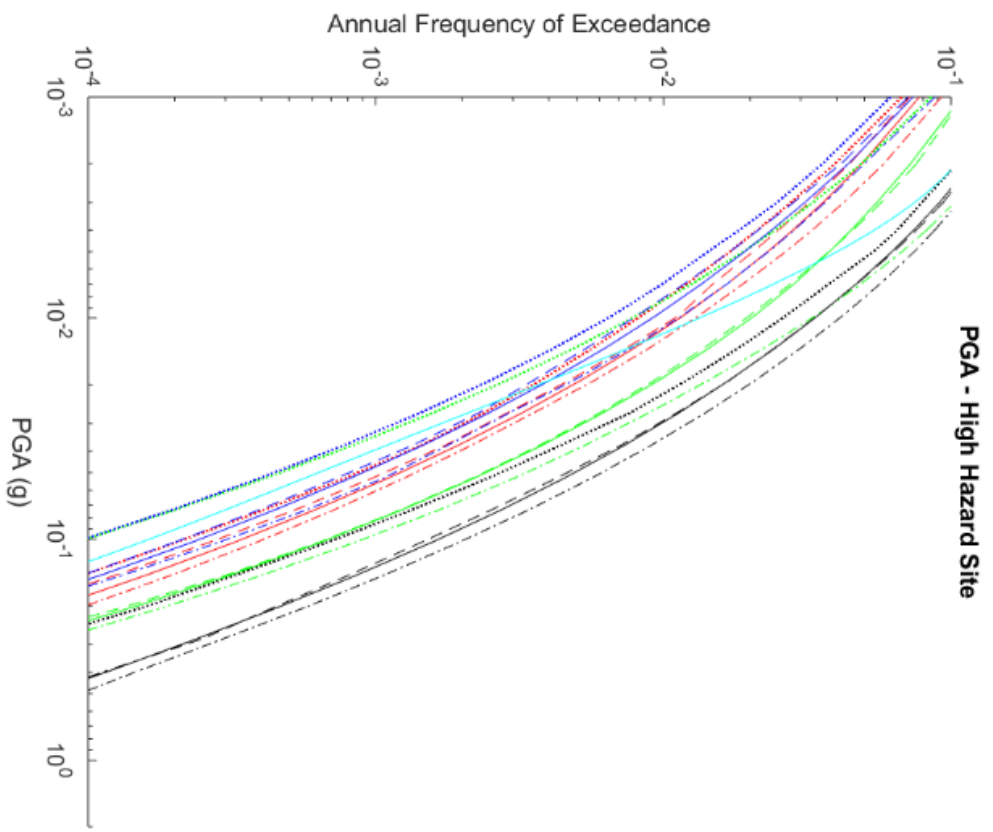
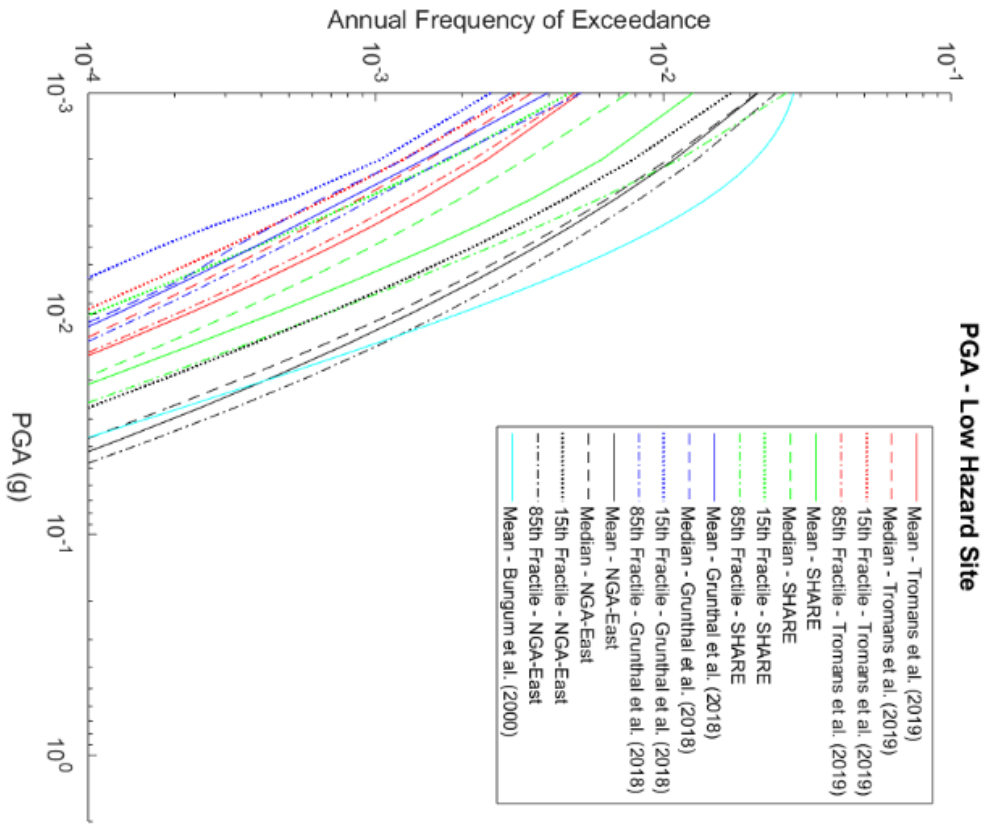


Figure 6.0 PGA seismic hazard curves computed using the considered GMPE logic trees.

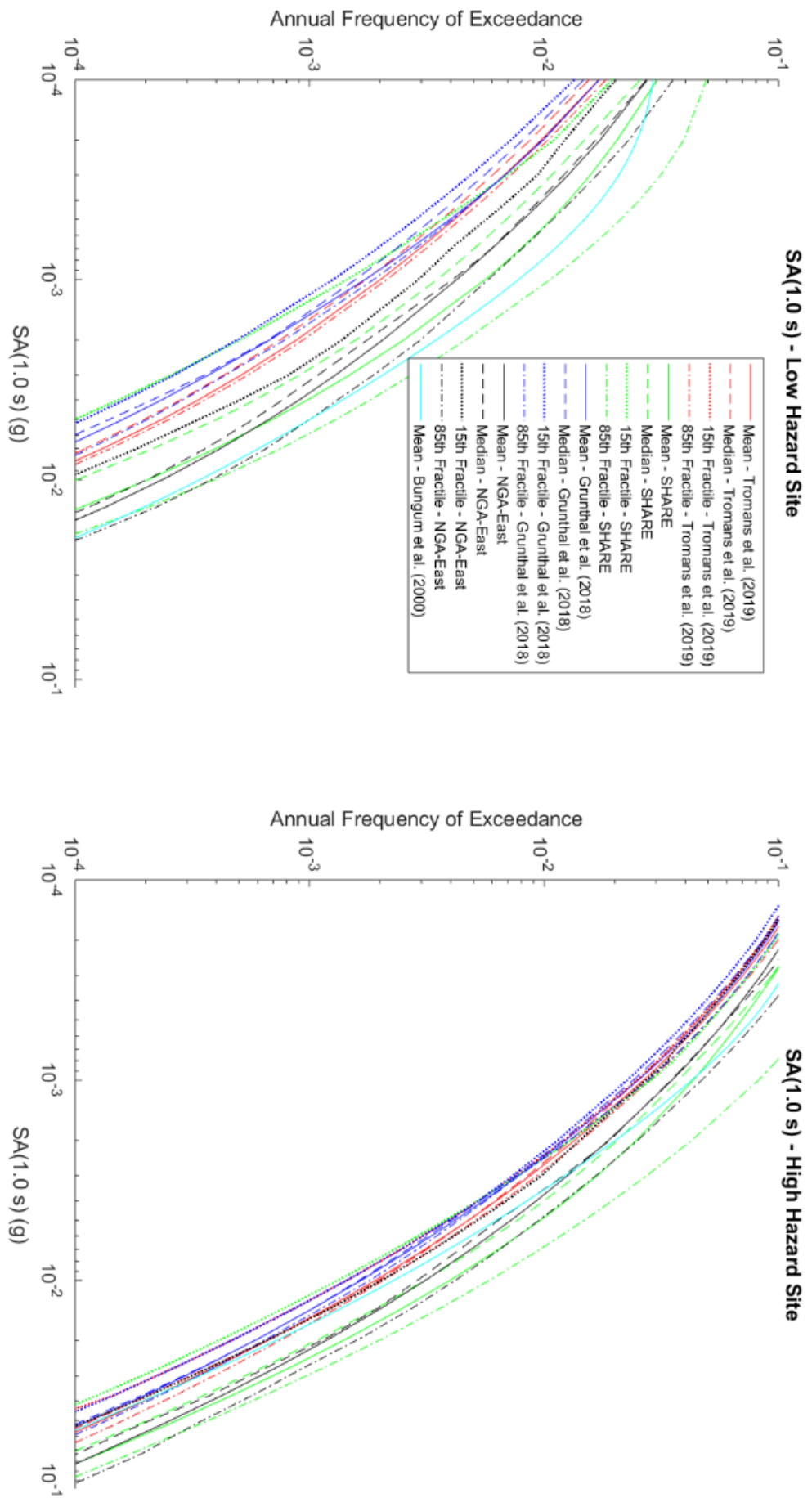


Figure 6.1 SA(1.0 s) seismic hazard curves computed using the considered GMPE logic trees.

## 6.2 Modification of an Existing GMPE Logic Tree for the North Sea Region

The Tromans et al. (2019) GMPE logic tree was modified for use in the North Sea through (1) incorporation of the stress drop scaling factors implemented within the Grunthal et al. (2018) GMPE logic tree and (2) the modification of the default weights assigned to each GMPE by Tromans et al. (2019). As discussed above, the stress drop scaling factors of Grunthal et al. (2018) are expected to increase the spread of the predicted ground-motion for a given return period, resulting in the GMPE logic tree to which they are implemented better accounting for the epistemic uncertainty associated with the average regional stress drop. The modification of the default weight assigned to each GMPE within the Tromans et al. (2019) GMPE logic tree was based on the results of the North Sea GMPE testing. Through giving a greater weighting to GMPEs which performed well when evaluated using North Sea ground-motion data and the opposite for poorly performing GMPEs the predicted ground-motion is more likely to be representative of future North Sea ground-motions. The impact of these two modifications is first demonstrated separately to show their individual impacts on the computed hazard.

### 6.2.1 Implementation of Grunthal et al. (2018) Stress Drop Scaling Factors

The implementation of the stress drop scaling factors of Grunthal et al. (2018) has a moderate effect on the predicted ground-motion for a given return period. For PGA and SA(1.0 s) at both the low hazard site and the high hazard site the stress drop scaling factors result in (1) a larger spread in the predicted ground-motion for a given return period and (2) a moderate overall increase in the predicted ground-motion for a given return period (Fig. 6.2; Fig. 6.3). The larger spread in the predicted ground-motion for a given return period is reflected by the larger post-scaling factor implementation  $U_R$  (Tab. 6.4)<sup>51</sup>. For both PGA and SA(1.0 s) the overall increase in  $U_R$  is (moderately) larger for a return period of 475 years than for a return period of 2475 years. The overall period-dependency of the uncertainty captured by the Tromans et al. (2019) GMPE logic tree is noticeably reduced by the implementation of the stress drop scaling factors. The distributions of predicted ground-shaking used to compute the post-stress drop scaling  $U_R$  are displayed in Tab. 6.5.

---

<sup>51</sup> As for the evaluation of the potential GMPE logic trees for modification to the North Sea,  $U_R$  was computed for return periods of 475 years and 2475 years throughout the modification process.

**Table 6.4**  $U_R$  for the predicted ground-motion for return periods of 475 years and 2475 years using the modified forms of the Tromans et al. (2019) GMPE logic tree at the high hazard site and the low hazard site.

$U_R$ for GMPE Logic Tree	PGA 475 Years	PGA 2475 Years	SA1s 475 Years	SA1s 2475 Years	SA1s/PGA (475 Years)	SA1s/PGA (2475 Years)
Low hazard TR19	30	46	45	45	1.49	0.98
Low hazard TR19 with GR18 mod.	64	77	70	66	1.09	0.86
Low hazard TR19 with mod. weights	30	46	45	45	1.49	0.98
Low hazard TR19 with GR18 mod. and mod. weights	65	67	70	66	1.09	0.99
High hazard TR19	25	31	21	30	0.84	0.97
High hazard TR19 with GR18 mod.	56	52	52	53	0.92	1.02
High hazard TR19 with mod. weights	23	28	21	30	0.93	1.06
High hazard TR19 with GR18 mod. and mod. weights	55	58	52	53	0.95	0.91

**Table 6.5** Distributions of predicted PGA and SA(1.0 s) for return periods of 475 years and 2475 years using the Tromans et al. (2019) GMPE logic tree and the Tromans et al. (2019) GMPE logic tree with the Grunthal et al. (2018) stress drop scaling factors at the high hazard site and the low hazard site.

Fractile	PGA (g) for 475 Year RP	PGA (g) for 2475 Year RP	SA01s (g) for 475 Year RP	SA01s (g) for 2475 Year RP
Low haz. mean	0.002	0.007	0.001	0.004
Low haz. median	0.002	0.005	0.001	0.003
Low haz. 15th fractile	0.002	0.004	0.001	0.002
Low haz. 85th fractile	0.002	0.007	0.001	0.004
Low haz. mean with GR18 mod.	0.003	0.008	0.001	0.004
Low haz. median with GR18 mod.	0.002	0.007	0.001	0.004
Low haz. 15th fractile with GR18 mod.	0.002	0.004	0.001	0.003
Low haz. 85th fractile with GR18 mod.	0.003	0.009	0.001	0.005
High haz. mean	0.036	0.095	0.009	0.027
High haz. median	0.034	0.087	0.010	0.026
High haz. 15th fractile	0.030	0.075	0.008	0.022
High haz. 85th fractile	0.038	0.102	0.010	0.030
High haz. mean with GR18 mod.	0.041	0.108	0.011	0.031
High haz. median with GR18 mod.	0.039	0.105	0.010	0.031
High haz. 15th fractile with GR18 mod.	0.030	0.079	0.008	0.023
High haz. 85th fractile with GR18 mod.	0.052	0.133	0.013	0.038

### 6.2.2 Modification of the Default Tromans et al. (2019) GMPE Weights

For the modification of the default weight assigned to each GMPE within the Tromans et al. (2019) GMPE logic tree two modifications were made. Within this investigation three of the GMPEs within the Tromans et al. (2019) GMPE logic tree were evaluated using North Sea ground-motion data: (1) Rietbrock et al. (2013), (2) Cauzzi et al. (2015) and (3) Boore et al. (2014). The Rietbrock et al. 2013 GMPE was assigned a low weighting by Tromans et al. (2019) due to the GMPE having been derived stochastically, and therefore being less well constrained for larger magnitudes and shorter source-to-site distances. Tromans et al. (2019) redistributed the weight removed from the Rietbrock et al. (2013) GMPE amongst the non-stochastic GMPEs, including the Boore et al. (2014) GMPE (Tab. 6.0). The Rietbrock et al. (2013) GMPE was found to perform well in the North Sea, whereas the Boore et al. (2014) GMPE was found to perform poorly in the North Sea (Tab. 6.3). Based on these results, the weights assigned to the Rietbrock et al. (2013) GMPE and the Boore et al. (2014) GMPE were swapped to provide a simple and rationale modification to the GMPE weightings (Tab. 6.6).

For PGA at the high hazard site and SA(1.0 s) at both the low hazard site and the high hazard site, these modified GMPE weights moderately reduce the overall spread of the predicted ground-motion (Fig. 6.4; Fig. 6.5). For PGA at the low hazard site, the overall spread of the predicted ground-shaking is similar. The overall reduction in the spread of predicted ground-motion for a given return period is partly reflected within the post-GMPE weight modification  $U_R$ . For example, for PGA for return periods of both 475 years and 2475 years at the high hazard site a small reduction in  $U_R$  is observed. These reductions in  $U_R$  result in the overall period-dependency of the uncertainty captured by the Tromans et al. (2019) GMPE logic tree (with the GMPE weight modifications) being reduced (Tab. 6.4). The fractiles used to compute the post-GMPE weight modification  $U_R$  are displayed in Tab. 6.6.

**Table 6.6** Modified GMPE weights for the Tromans et al. (2019) GMPE logic tree.

GMPE 1 [wt.]	GMPE 2 [wt.]	GMPE 3 [wt.]	GMPE 4 [wt.]	GMPE 5 [wt.]
Atkinson and Boore (2006, 2011) [0.1]	Bindi et al. (2014a, 2014b) [0.3]	Boore et al. (2014) [0.1]	Cauzzi et al. (2015) [0.2]	Rietbrock et al. (2013) [0.3]

**Table 6.7** Distributions of predicted PGA and SA(1.0 s) for return periods of 475 years and 2475 years using the Tromans et al. (2019) GMPE logic tree and the Tromans et al. (2019) GMPE logic tree with modified GMPE weights at the high hazard site and the low hazard site.

<b>Fractile</b>	<b>PGA (g) for 475 Year RP</b>	<b>PGA (g) for 2475 Year RP</b>	<b>SA01s (g) for 475 Year RP</b>	<b>SA01s (g) for 2475 Year RP</b>
Low haz. mean	0.002	0.007	0.001	0.004
Low haz. median	0.002	0.005	0.001	0.003
Low haz. 15th fractile	0.002	0.004	0.001	0.002
Low haz. 85th fractile	0.002	0.007	0.001	0.004
Low haz. mean with mod. weights	0.002	0.007	0.001	0.003
Low haz. median with mod. weights	0.002	0.006	0.001	0.003
Low haz. 15th fractile with mod. weights	0.002	0.004	0.001	0.002
Low haz. 85th fractile with mod. weights	0.002	0.007	0.001	0.004
High haz. mean	0.036	0.095	0.009	0.027
High haz. median	0.034	0.087	0.01	0.026
High haz. 15th fractile	0.030	0.075	0.008	0.022
High haz. 85th fractile	0.038	0.102	0.010	0.030
High haz. mean with mod. weights	0.035	0.089	0.009	0.026
High haz. median with mod. weights	0.031	0.080	0.010	0.025
High haz. 15th fractile with mod. weights	0.030	0.073	0.008	0.022
High haz. 85th fractile with mod. weights	0.038	0.097	0.010	0.030

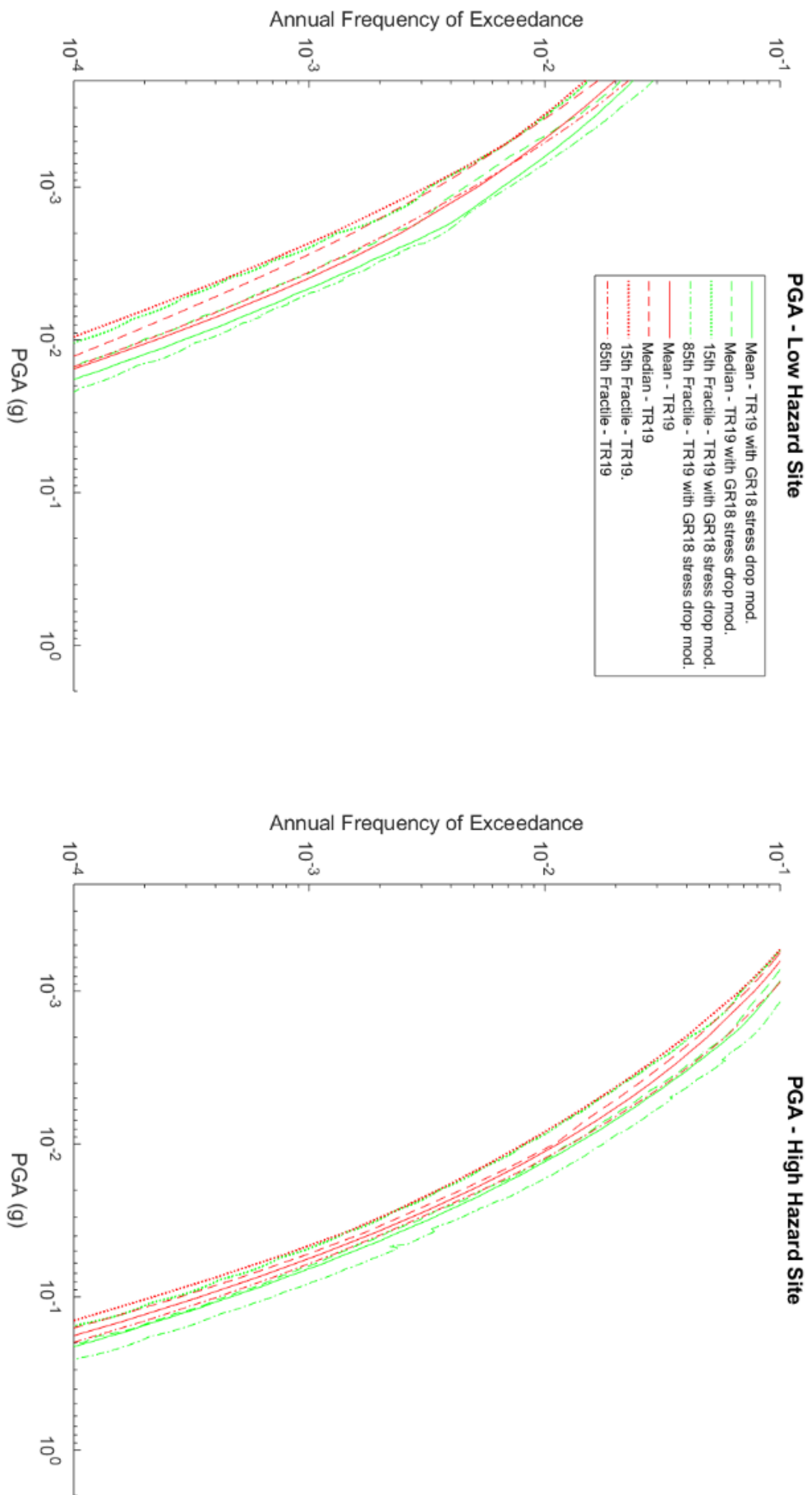


**Figure 6.2** PGA seismic hazard curves computed using the Tromans et al. (2019) GMPE logic tree and the Tromans et al. (2019) with the Grünthal et al. (2018) stress drop scaling factors.

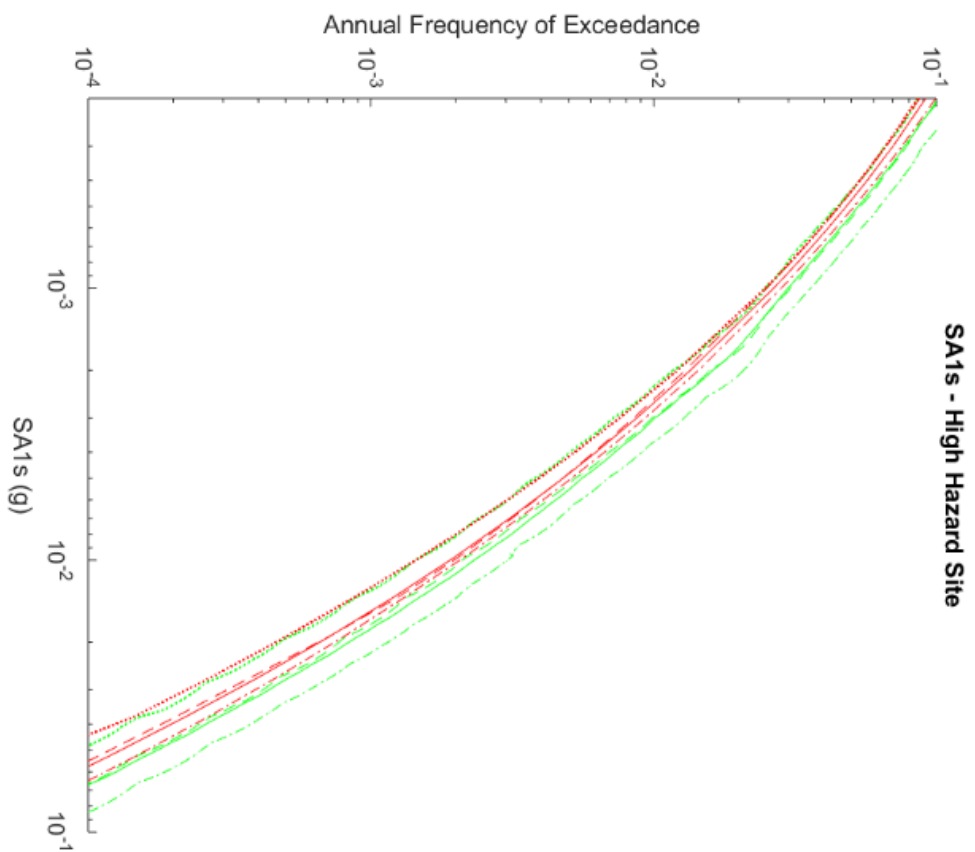
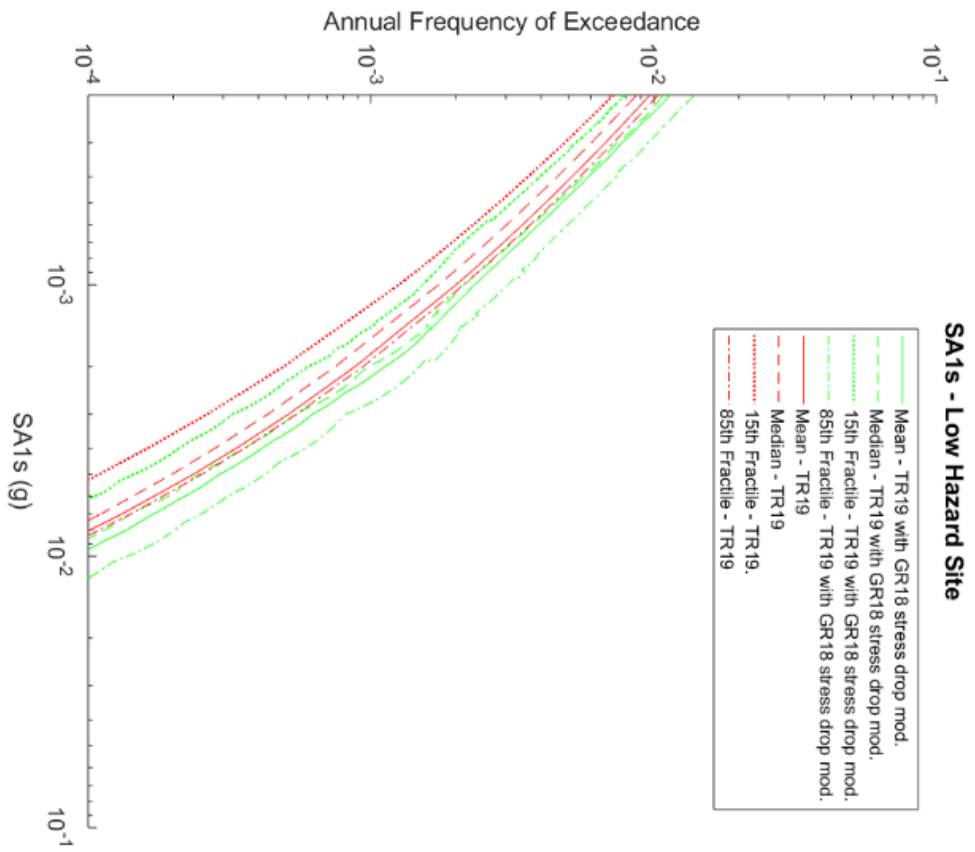


**Figure 6.3** SA(1.0 s) seismic hazard curves computed using the Tromans *et al.* (2019) GMPE logic tree and the Tromans *et al.* (2019) with the Grunthal *et al.* (2018) stress drop scaling factors.

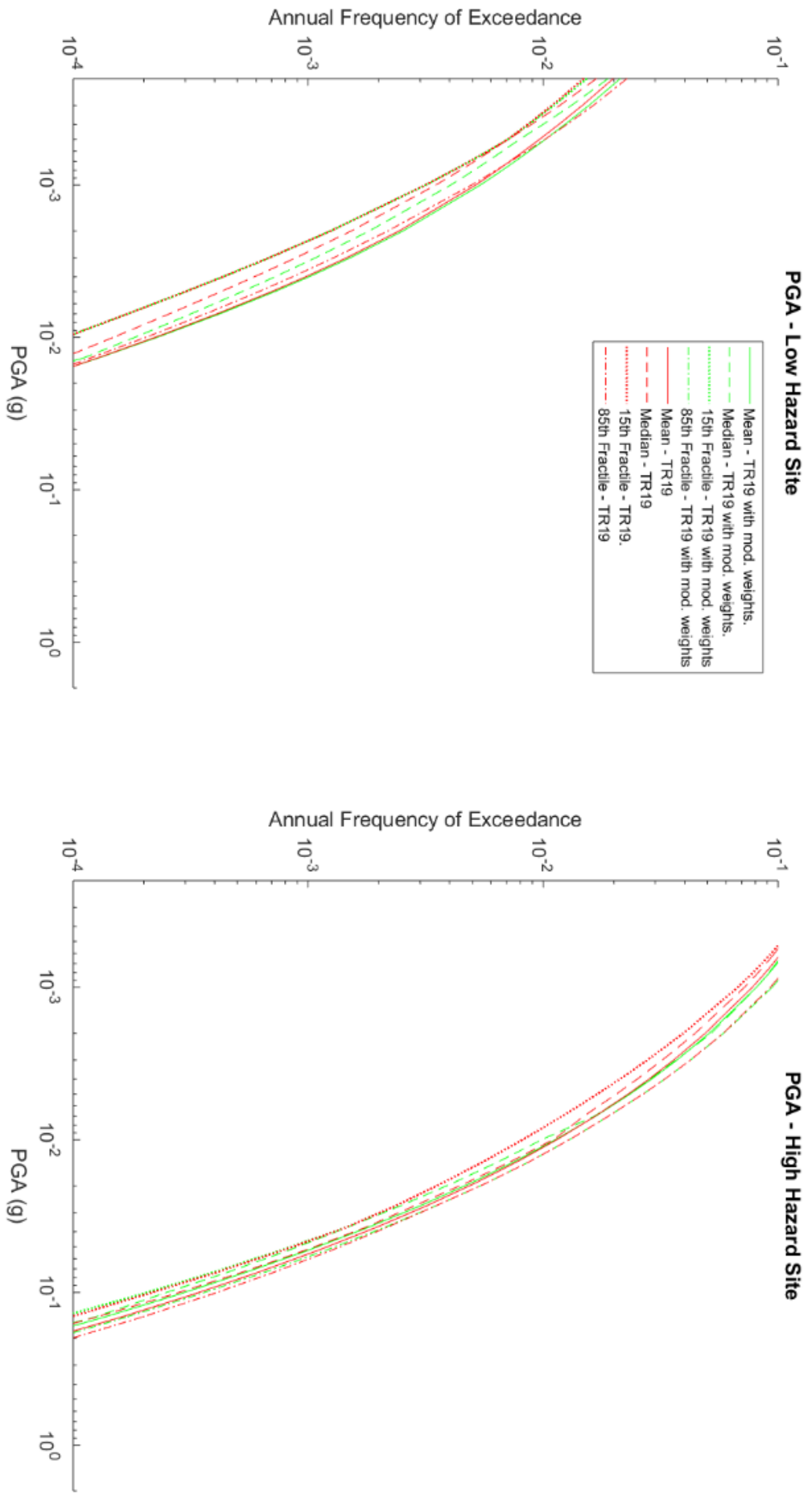


**Figure 6.4** PGA seismic hazard curves computed using the Tromans et al. (2019) GMPE logic tree and the Tromans et al. (2019) with the modified GMPE weights stress drop scaling factors.

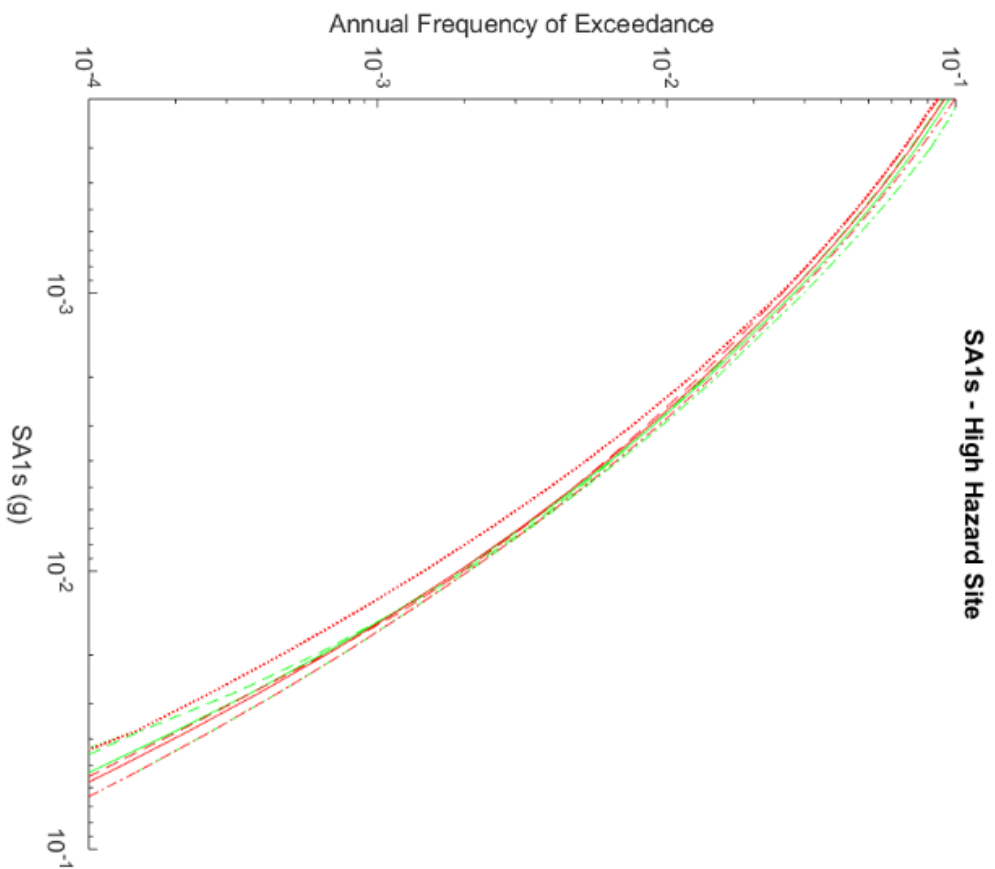
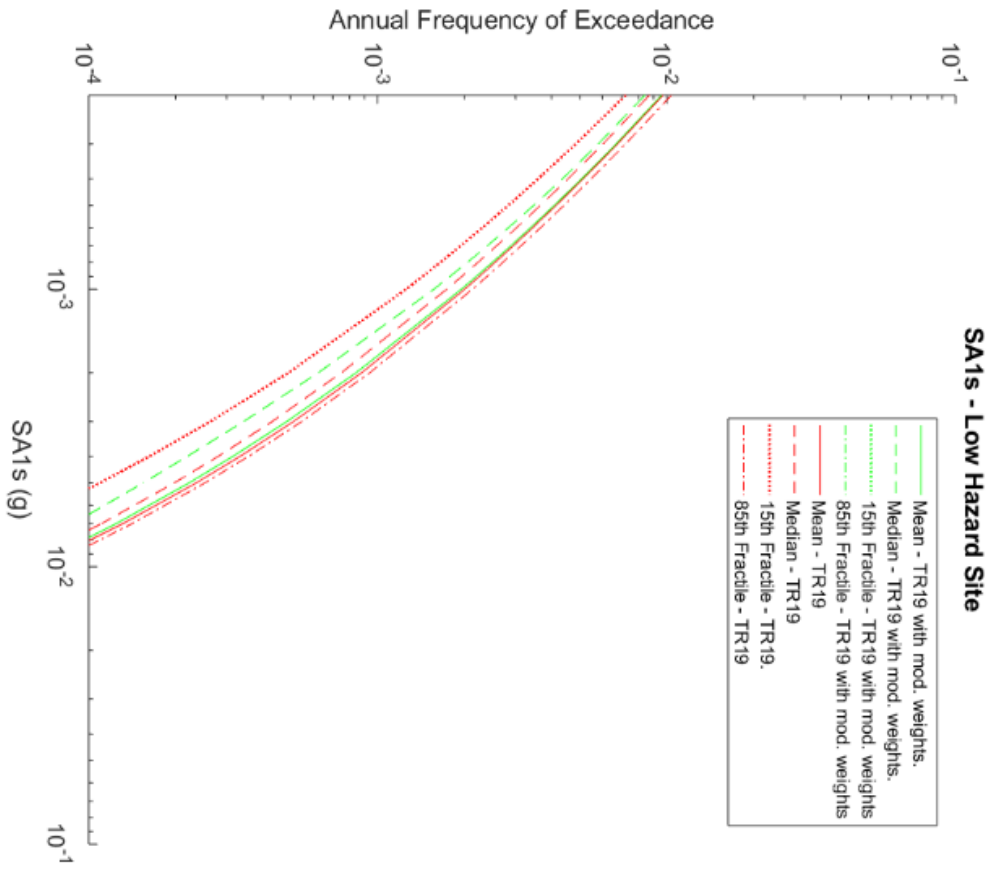


**Figure 6.5** SA(1.0 s) seismic hazard curves computed using the Tromans et al. (2019) GMPE logic tree and the Tromans et al. (2019) with the modified GMPE weights stress drop scaling factors.

### 6.2.3 Implementation of Stress Drop Scaling and Modified Weights

The seismic hazard curves computed with both the Grunthal et al. (2018) stress drop scaling factors and the modified GMPE weights are as expected a hybrid of their separate curves (Fig. 6.6; Fig. 6.7). The hazard curves computed using the GMPE logic trees considered for modification to the North Sea region are provided for comparison. The differences in the  $U_R$  computed using the Tromans et al. (2019) GMPE logic tree with both modifications and the Tromans et al. (2019) GMPE logic tree with only one of the modifications are indicative of an aggregating effect the modifications have upon one another with respect to the captured uncertainty. This is well demonstrated by the  $U_R$  computed for PGA for a return period of 2475 years at the low hazard site using both modifications being smaller than the corresponding  $U_R$  computed using only the Grunthal et al. (2018) stress drop scaling factors (the  $U_R$  computed with both modifications is smaller due to the minimising effect of the modified GMPE weights - Tab. 6.4). This aggregating effect is also well demonstrated by the differences in the overall period-dependency of the uncertainty captured by the Tromans et al. (2019) GMPE logic tree with each modification separately and the two modifications combined. The fractiles used to compute the post-multiple modification  $U_R$  are displayed in Tab. 6.8.

**Table 6.8** Distributions of predicted PGA and SA(1.0 s) for return periods of 475 years and 2475 years using the Tromans et al. (2019) GMPE logic tree and the Tromans et al. (2019) GMPE logic tree with the Grunthal et al. (2018) stress drop scaling factors and the modified GMPE weights at the high hazard site and the low hazard site.

Fractile	PGA (g) for 475 Year RP	PGA (g) for 2475 Year RP	SA01s (g) for 475 Year RP	SA01s (g) for 2475 Year RP
Low haz. mean	0.002	0.007	0.001	0.004
Low haz. median	0.002	0.005	0.001	0.003
Low haz. 15th fractile	0.002	0.004	0.001	0.002
Low haz. 85th fractile	0.002	0.007	0.001	0.004
Low haz. mean with GR18 mod. and mod. weights	0.003	0.009	0.001	0.004
Low haz. median with GR18 mod. and mod. weights	0.002	0.007	0.001	0.004
Low haz. 15th fractile with GR18 mod. and mod. weights	0.002	0.005	0.001	0.003
Low haz. 85th fractile with GR18 mod. and mod. weights	0.003	0.010	0.001	0.005
High haz. mean	0.036	0.095	0.009	0.027
High haz. median	0.034	0.087	0.010	0.026
High haz. 15th fractile	0.030	0.075	0.008	0.022
High haz. 85th fractile	0.038	0.102	0.010	0.030
High haz. mean with GR18 mod. and mod. weights	0.041	0.106	0.011	0.031
High haz. median with GR18 mod. and mod. weights	0.039	0.102	0.010	0.031
High haz. 15th fractile with GR18 mod. and mod. weights	0.030	0.074	0.008	0.023
High haz. 85th fractile with GR18 mod. and mod. weights	0.052	0.133	0.013	0.038

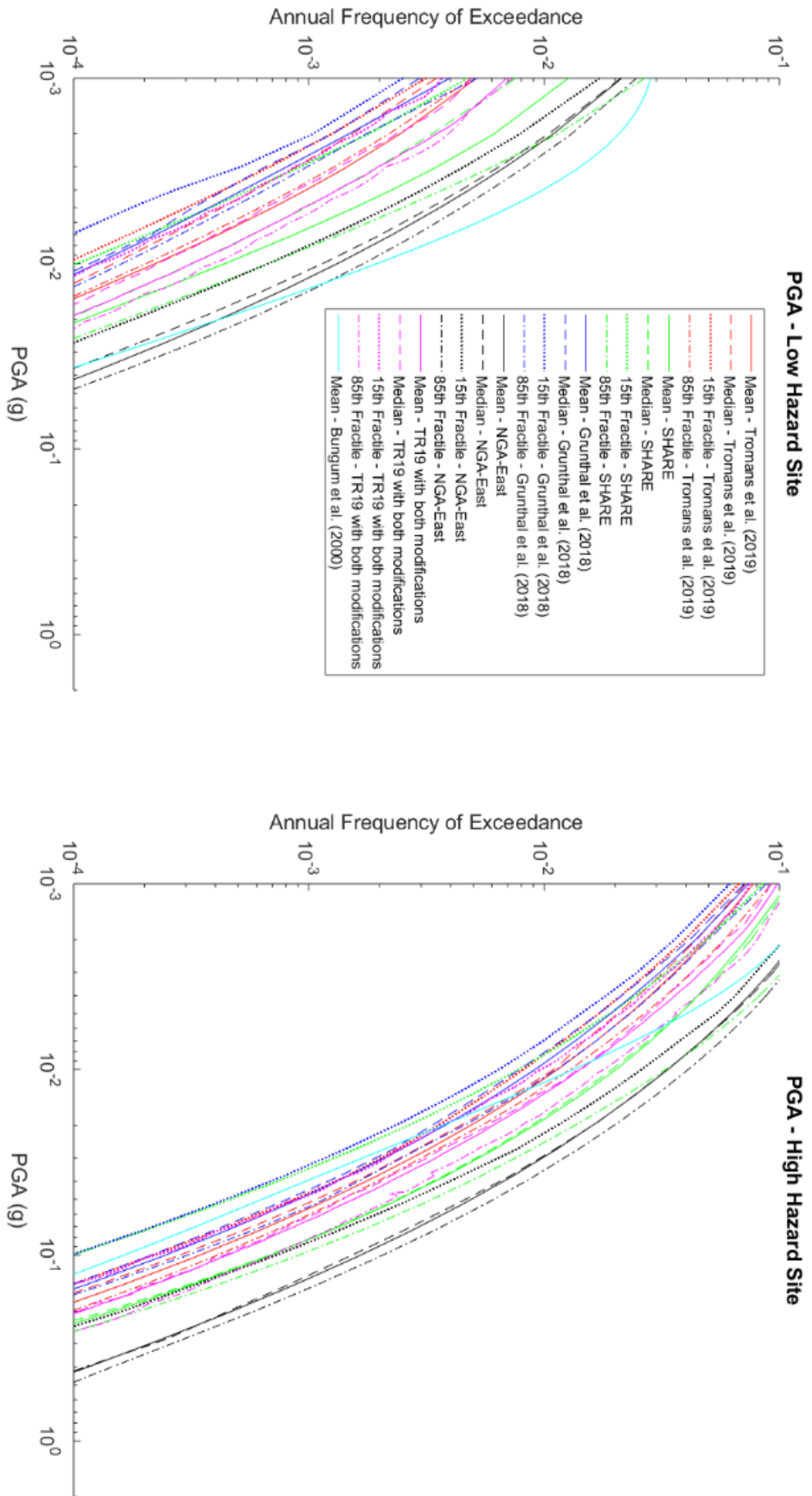


**Figure 6.6** PGA seismic hazard curves computed using the Tromans et al. (2019) GMPE logic tree with both modifications and the GMPE logic trees considered for modification to the North Sea.

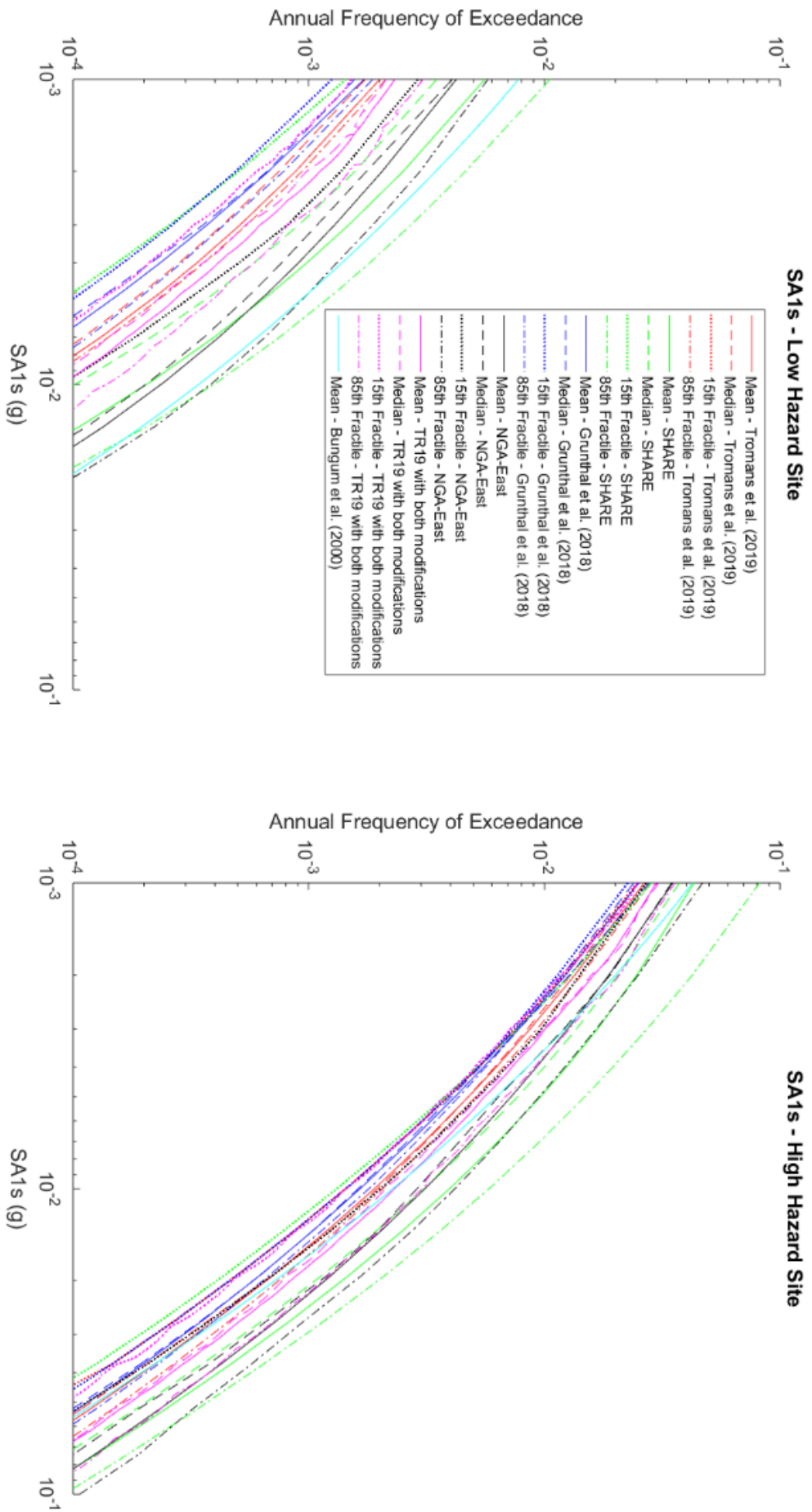


**Figure 6.7** SA(1.0) seismic hazard curves computed using the Tromans et al. (2019) GMPE logic tree and the Tromans et al. (2019) with the modified GMPE weights stress drop scaling factors.

### 6.3 Conclusions for the Construction of a North Sea GMPE Logic Tree

A GMPE logic tree better suited for application to the North Sea region was developed through the modification of the Tromans et al. (2019) GMPE logic tree. The Tromans et al. (2019) GMPE logic tree was modified in two ways. Firstly, the stress drop scaling of Grunthal et al. (2018) was implemented and secondly, the GMPE weights assigned by Tromans et al. (2019) were modified based on the results of the GMPEs evaluated using North Sea ground-motion data. These modifications result in the Tromans et al. (2019) GMPE logic tree providing a moderately larger overall spread of predicted ground-motions for a given return period compared to the Tromans et al. (2019) GMPE logic tree without the modifications. The larger overall spread of predicted ground-motions for a given return period is primarily representative of the captured uncertainty associated with average regional stress drop (the increase in the spread of predicted ground-motion resulting from the stress drop scaling outweighs the reduction caused by the modification of the GMPE weights). This larger overall spread of predicted ground-motions for a given return period therefore improves the suitability of the Tromans et al. (2019) GMPE logic tree for the North Sea region due to better capturing the epistemic uncertainty associated with regional stress drop. The implementation of these modifications reduces the overall period-dependency of the uncertainty captured by the Tromans et al. (2019) GMPE logic tree. For the high hazard site, the overall period-dependency of the uncertainty captured by the Tromans et al. (2019) GMPE logic tree is the second smallest when compared to the GMPE logic trees considered for modification to the North Sea (Tab. 6.9). The only GMPE logic tree which provides a weaker overall period-dependency for the captured uncertainty is the NGA-East GMPE logic tree, which can be attributed to the period-dependent GMPE weightings incorporated within this GMPE logic tree. Ultimately, the modified form of the Tromans et al. (2019) GMPE logic tree developed within this investigation provides a suitable GMPE logic tree for use in the North Sea region through the implementation of simple and measured modifications. The performance of the modified GMPE logic tree could be further improved through the development of GMPE host-to-target adjustment factors for  $V_s$  and kappa similar to those described within Tromans et al. (2019).

**Table 7.9**  $U_R$  for the predicted ground-motion for return periods of 475 years and 2475 years for the Tromans et al. (2019) GMPE logic tree with the combined modifications and the GMPE logic trees considered for modification to the North Sea.

$U_R$ for GMPE Logic Tree	PGA 475 Years	PGA 2475 Years	SA1s 475 Years	SA1s 2475 Years	SA1s/PGA (475 Years)	SA1s/PGA (2475 Years)
Tromans et al. (2019)	25	31	21	30	0.85	0.97
Tromans et al. (2019) with stress drop scaling and GMPE weight mod.	55	58	52	53	0.95	0.91
SHARE	104	99	93	88	0.89	0.88
Grunthal et al. (2018)	45	55	13	18	0.29	0.33
NGA-East	52	61	56	59	1.08	0.96

## 7.0 Reassessment of North Sea Seismic Source Model Parameters

The most recent (publically available and region specific) seismogenic source zone model for the North Sea was developed by Bungum et al. (2000). Within the Bungum et al. (2000) source model, the seismicity of the North Sea is partitioned into 37 source zones, with each zone being assigned an individual  $a$ -value and a homogenous (regional)  $b$ -value (Fig. 7.0). The  $a$ -value is indicative of the overall rate of earthquakes in each zone, and the  $b$ -value represents the ratio of small to large earthquakes in each zone. These source parameters are computed from the linear regression of an earthquake frequency-magnitude distribution (FMD), where the earthquake frequency (count) is in  $\log_{10}$  space (e.g. Fig. 7.1). The relationship between earthquake frequency and magnitude is therefore described by the  $a$ -value and the  $b$ -value:

$$\log_{10} N = a - bm \quad (7.0)$$

where  $N$  is the number of earthquakes greater or equal to magnitude  $m$ . The distribution modelled by this relationship is known as a Gutenberg-Richter (GR) distribution (see Gutenberg and Richter, 1944 for more details). The Bungum et al. (2000) source model uses a regional  $b$ -value due to a scarcity of observed earthquakes for several zones preventing the determination of robust zone-specific  $b$ -values.

Since the development of the Bungum et al. (2000) source model, an additional 20 years of earthquakes have been observed in the North Sea. This additional data permits the determination of better constrained  $a$ - and  $b$ -values for the Bungum et al. (2000) source zones. The computation of more robust  $a$ - and  $b$ - values reduces the epistemic uncertainty of the source model parameters within future North Sea probabilistic seismic hazard assessments (PSHAs). Within this investigation, to reassess the source parameter of Bungum et al. (2000), an expanded catalogue of North Sea earthquakes is prepared and statistically analysed. The updated source parameters are then implemented within a North Sea PSHA for comparative purposes. To permit comparison of the updated  $a$ - and  $b$ -values to those provided by Bungum et al. (2000), the source zonation itself (i.e. the spatial partitioning of the source seismicity) is kept identical to that within Bungum et al. (2000).

### 7.1 Preparation of an Updated North Sea Earthquake Catalogue

The updated North Sea earthquake catalogue is composed of events taken from the earthquake catalogues of (1) the British Geological Survey (BGS)<sup>52</sup>, (2) the Seismic Hazard Harmonization in Europe (SHARE) project<sup>53</sup>, (3) the Norwegian Seismic Array (NORSAR)<sup>54</sup> and (4) the Geological Survey of Denmark and Greenland (GEUS)<sup>55</sup>. The unprocessed BGS catalogue comprised of 1021

---

<sup>52</sup> BGS earthquake catalogue reference: Earthquakes.bgs.ac.uk. (2020)

<sup>53</sup> SHARE earthquake catalogue reference: Efehr.org. (2020).

<sup>54</sup> NORSAR earthquake catalogue reference: NORSAR. (2020)

<sup>55</sup> GEUS earthquake catalogue reference: Geus.dk. (2020).

events from 1927 to 2020, with a longitudinal range of -1.7 to 5.0 and a latitudinal range of 49.3 to 62.9. The unprocessed SHARE catalogue comprised of 262 events from 1900 to 2005<sup>56</sup>, with a longitudinal range of 2.5 to 33.9 and a latitudinal range of 52.9 to 73.3. The unprocessed NORSAR catalogue comprised of 11,150 events from 2000 to 2020<sup>57</sup>, with a longitudinal range of 4.0 to 35.8 and a latitudinal range of 51.3 to 79.0. The unprocessed GEUS catalogue comprised of 3127 events from 1930 to 2020, with a longitudinal range of 0.5 to 17.0 and a latitudinal range of 53.0 to 59.0.

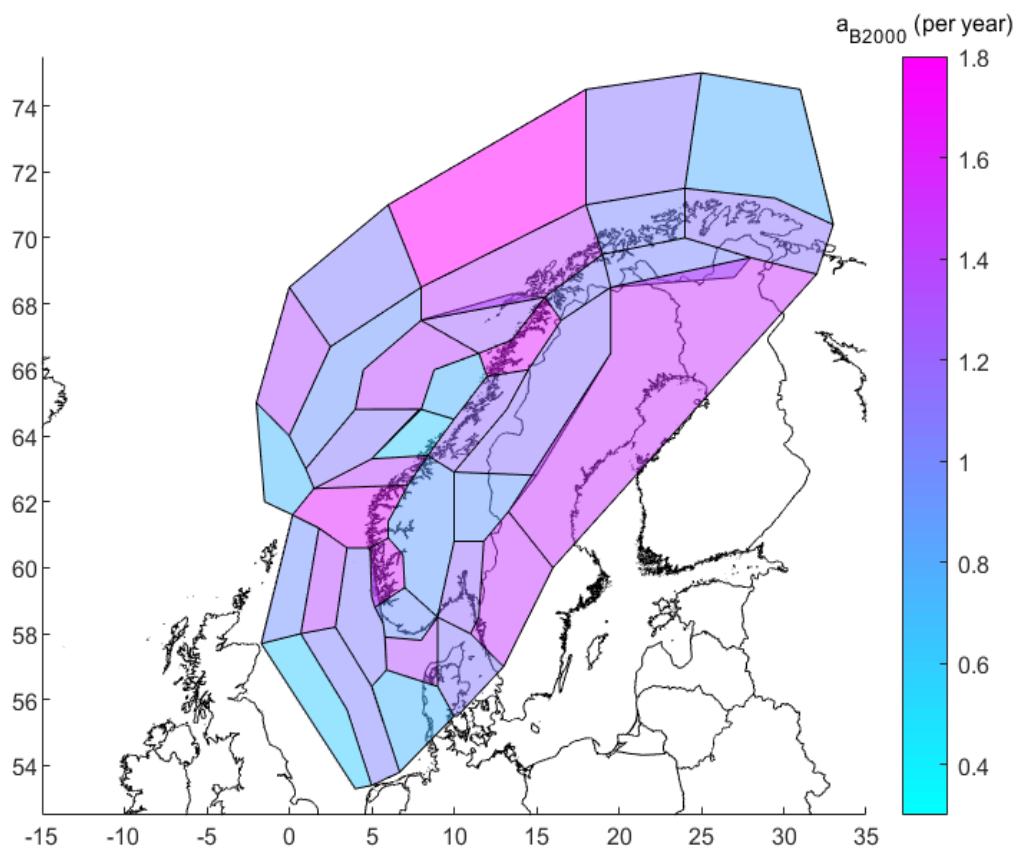


**Figure 7.0** Seismogenic source zonation model of Bungum et al. (2000) with the original  $a$ -values ( $a_{B2000}$ ). The  $a$ -value for each source zone has been normalised by the duration of the Bungum et al. (2000) earthquake catalogue.

The first step in preparation of the updated catalogue was to undertake seismic declustering for each of the four separate earthquake catalogues. Seismicity comprises of two parts: (1) independent earthquakes (i.e. main shocks) caused by isolated tectonic stress loading and (2) earthquakes dependent upon each other (i.e. foreshocks, aftershocks and multiplets), which are triggered by static or dynamic stress perturbations resulting (at least partially) from previous earthquakes (Azak et al., 2017). The non-independent earthquakes are therefore treated as background seismicity, with the purpose of

<sup>56</sup> The publically accessible SHARE earthquake catalogue is limited to pre-2007 earthquakes used for the European-Mediterranean Earthquake Catalogue (EMEC) project (Grünthal and Wahlström, 2012).

<sup>57</sup> The publically accessible NORSAR earthquake catalogue is limited to post-1999 earthquakes.

declustering being to remove this background seismicity, so as to produce a catalogue comprising of solely the independent earthquakes (i.e. the removal of dependent earthquakes which form seismicity clusters). The most commonly applied declustering algorithms are those of Gardner and Knopoff (1974) and Reasenberg (1985) (see the respective publications for more details on these algorithms). For this investigation, the Reasenberg (1985) declustering algorithm was used. The parameters selected for the Reasenberg (1985) are provided in Tab. 7.0. The post-declustering BGS catalogue comprised of 993 events (28 background earthquakes removed). The post-declustering SHARE catalogue comprised of 260 events (1 background earthquake removed). The post-declustering NORSAR catalogue comprised of 9529 events (1621 background earthquakes removed). The post-declustering GEUS catalogue comprised of 3016 events (111 background earthquakes removed).

**Table 7.0** Parameters for the Reasenberg (1985) declustering algorithm.  $\tau_{\min}$  is the minimum look-ahead time for identifying clusters when the first earthquake is not clustered,  $\tau_{\max}$  is the maximum look-ahead time for the building of clusters,  $\rho_1$  is the probability of detecting the next clustered earthquake used for the computation of the look-ahead time ( $\tau$ ),  $x_k$  is the increase of the lower cut-off magnitude during clustering:  $x_{meff} = x_{meff} + x_k M_{max}$ , where  $x_{meff}$  is the effective lower magnitude cut-off and  $M_{max}$  is the largest earthquake in the cluster and  $r_{fact}$  is the number of crack radii surrounding each earthquake within later earthquakes treated as part of the cluster.

Parameter	Value
$\tau_{\min}$ (days)	2.5
$\tau_{\max}$ (days)	15
$\rho_1$	0.90
$x_k$	0.50
$x_{meff}$	1.50
$r_{fact}$	20

Following declustering, the individual catalogues were combined, and duplicate events were removed. Prior to removal of duplicate events, the declustered catalogue comprised of 13,798 events. To remove duplicate events from the compiled earthquake catalogue, and to determine the magnitude of completeness ( $M_c$  - the magnitude above which all earthquakes are reliably recorded in a specified region), the ZMAP software for the statistical analysis of earthquake catalogues (Reyes and Wiemer, 2019) was used. To identify duplicate events, a time of earthquake occurrence threshold of 20 s and a distance threshold of 5 km were used, resulting in the removal of 1463 duplicate events, and the declustered, non-duplicative and combined earthquake catalogue comprising of 12,355 events. A magnitude of completeness of 2.1 was computed (Fig. 7.1) using the maximum curvature solution (Wyss et al., 1999; Wiemer and Wyss 2000), in which the point of maximum curvature is determined

by computing the maximum value of the first derivative of the FMD. Following the removal of earthquakes below the magnitude of completeness, the declustered, non-duplicative catalogue comprised of 8099 events.

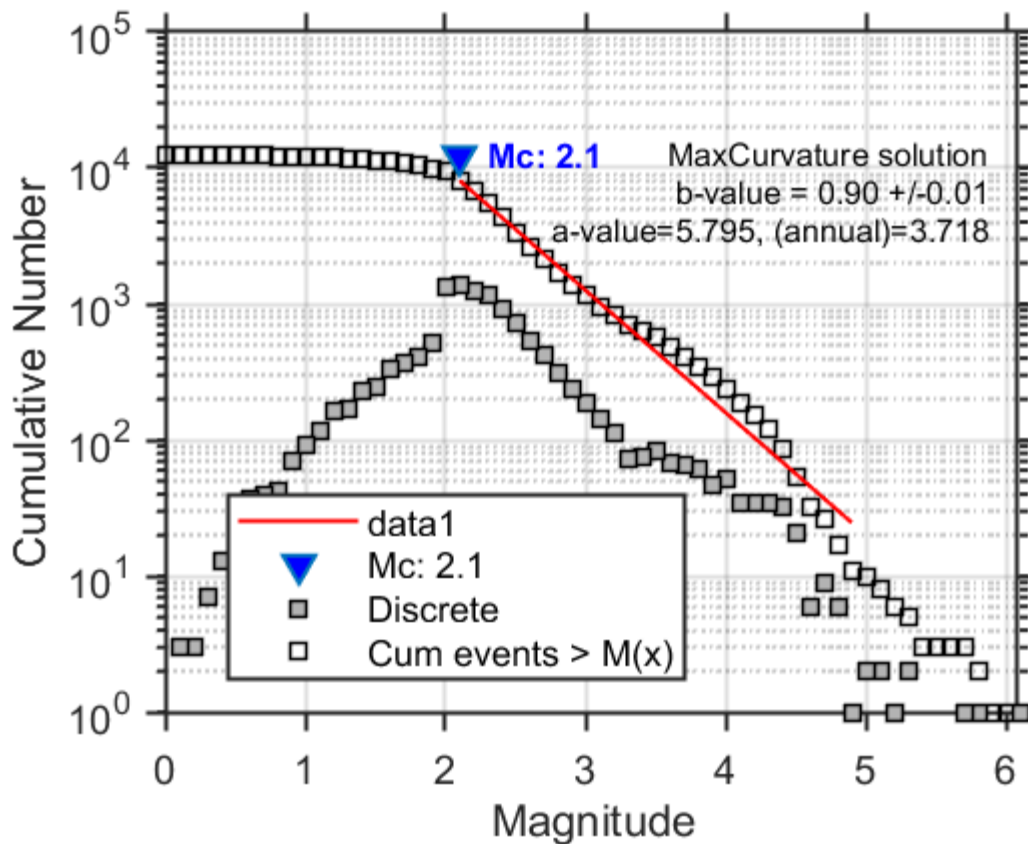


**Figure 7.1** Frequency magnitude distribution of the declustered, non-duplicative and combined North Sea catalogue. This figure was produced by ZMAP.

The Stepp (1972) method was used to assess the completeness of the declustered, non-duplicative and combined (local magnitude ( $M_L$ )  $\geq 2.1$ ) earthquake catalogue. The Stepp (1972) method evaluates the stability of the mean rate of earthquake occurrence ( $\lambda$ ) for each considered magnitude interval in a series of time intervals ( $T_{int}$ ), so as to determine the subinterval of the catalogue required for a stable estimate of  $\lambda$  to be computed for each of said magnitude intervals. This stable estimate of  $\lambda$  is treated as representative of  $\lambda$  if complete reporting of earthquakes within the associated magnitude interval was observed. The Stepp (1972) method relies on the assumption of  $\lambda$  following a Poissonian distribution. Assuming  $\lambda$  is constant, then the standard deviation of  $\lambda$  ( $\delta_\lambda$ ) varies as  $1/\sqrt{T_{int}}$ , with  $\lambda$  therefore being considered as not stable if it deviates from the straight line of a slope of  $1/\sqrt{T_{int}}$  (e.g. Fig. 7.2). The length of  $T_{int}$  for which  $\delta_\lambda$  does not vary from the straight line is therefore treated as the time interval of completeness for the considered magnitude interval. Within this investigation the declustered, non-duplicative and combined ( $M_L \geq 2.1$ ) catalogue was partitioned into 12 time windows and 4 magnitude intervals:  $2.1 \leq M_L < 3.1$ ,  $3.1 \leq M_L < 4.1$ ,  $4.1 \leq M_L < 5.1$  and  $5.1 \leq M_L \leq 6.1$  (Tab. 7.1), with time intervals of completeness of 35 years (1990 - 2020), 40 years (1980 - 2020), 55 years (1965 - 2020) and 95 years

(1925 – 2020) respectively being determined (Fig. 7.2). The declustered, non-duplicative and completeness assessed catalogue comprises of 7922 events, and is henceforth referred to as the updated North Sea earthquake catalogue (UNSEC). The spatial and magnitude distribution of the UNSEC is provided in Fig. 7.3.

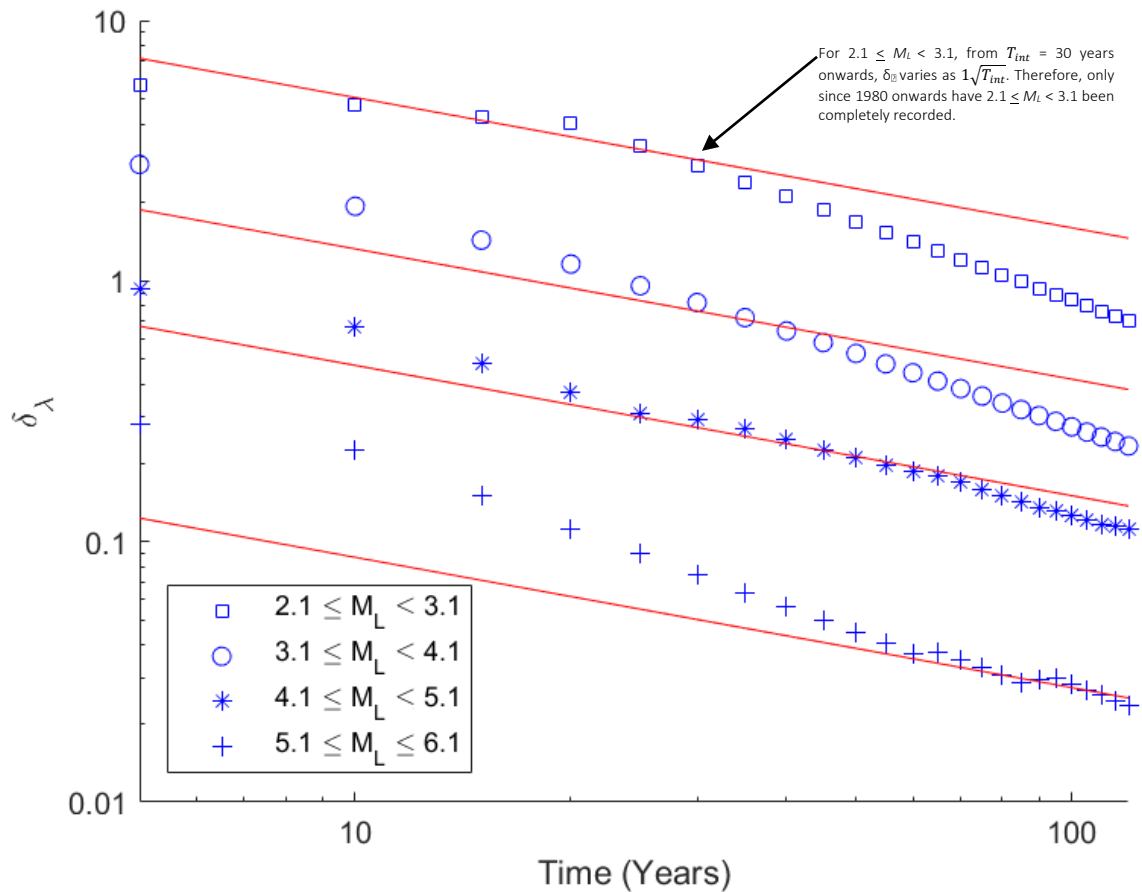


**Figure 7.2** Stepp (1972) plot for the declustered, non-duplicative ( $M_L \geq 2.1$ ) and combined North Sea catalogue.

**Table 7.1** Number of observed earthquakes in each time window for each magnitude interval.  $N$  represents the number of observed earthquakes.

Time Window	$N(2.1 \leq M_L < 3.1)$	$N(3.1 \leq M_L < 4.1)$	$N(4.1 \leq M_L < 5.1)$	$N(5.1 \leq M_L \leq 6.1)$
1900 - 1909	0	11	15	0
1910 - 1919	0	8	5	0
1920 - 1929	0	10	12	1
1930 - 1939	0	11	5	1
1940 - 1949	0	8	3	0
1950 - 1959	0	20	15	1
1960 - 1969	1	16	16	0
1970 - 1979	10	33	11	0
1980 - 1989	257	47	20	0
1990 - 1999	369	75	22	0
2000 - 2009	4238	165	12	0
2010 - 2020	2256	375	44	5

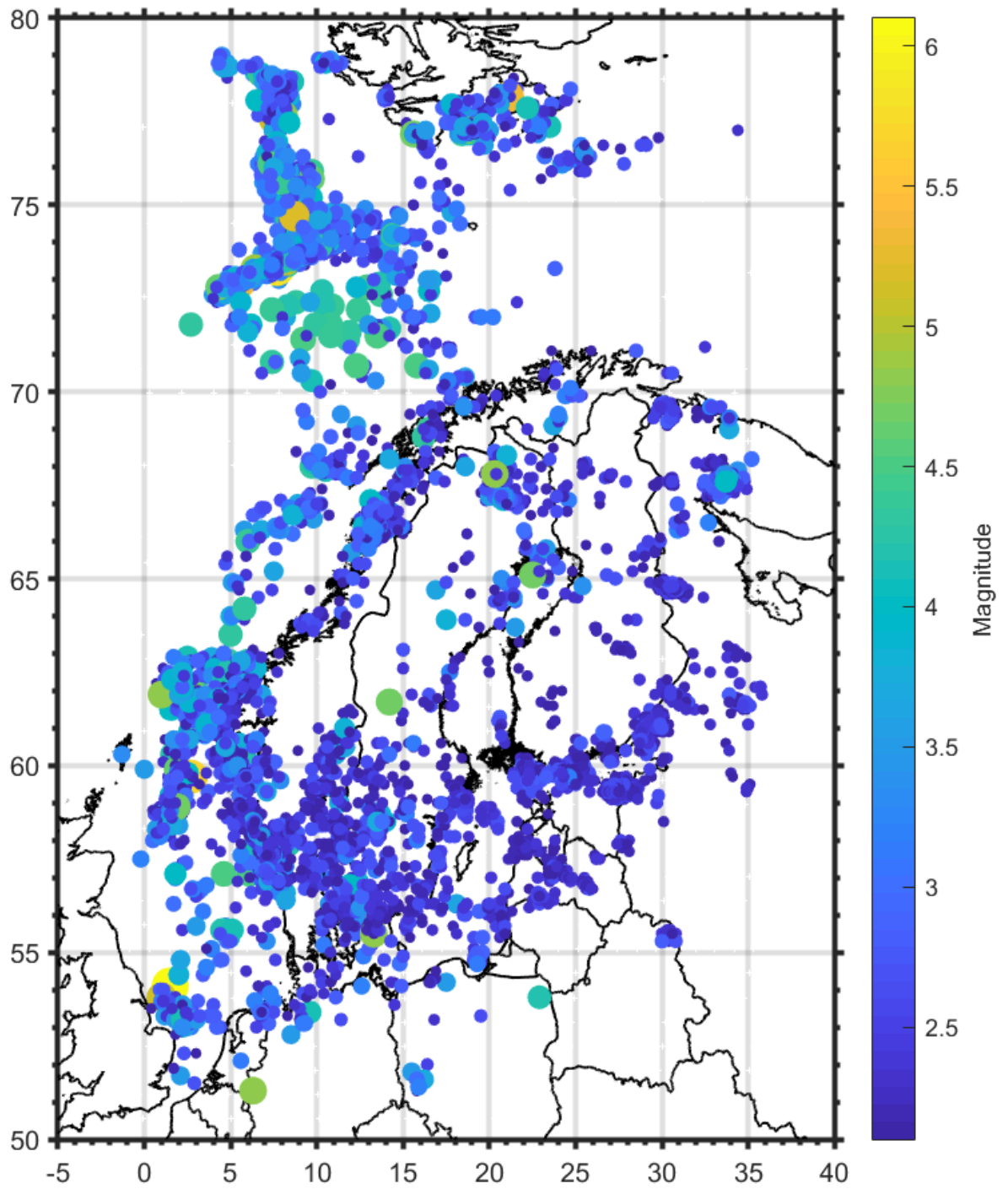


**Figure 7.3** *Magnitude and spatial distribution of the UNSEC.* This figure was produced by ZMAP.

## 7.2 Computation of Updated Source Parameters

Following the preparation of the UNSEC, updated source zone parameters were computed. As discussed above, Bungum et al. (2000) chose to implement a regional  $b$ -value ( $b_{B2000} = 1.05$ ) rather than zone-specific  $b$ -values due to the lack of observed earthquakes in some zones preventing the computation of robust zone-specific  $b$ -values. The additional 20 years of observed earthquakes does not result in a sufficient number of observed earthquakes within each source zone for a robust  $b$ -value to be determined for each of them. Therefore, within this reassessment of source parameters, a regional  $b$ -value ( $b_{upd} = 0.96$ ) was computed, also using ZMAP (Fig. 7.4). The smaller regional  $b$ -value computed within this investigation suggests that large earthquakes are proportionally more common than previously thought in the North Sea, although the difference between  $b_{B2000}$  and  $b_{upd}$  is very small. Updated  $a$ -values ( $a_{upd}$ ) were computed from a FMD comprising of the earthquakes originating within each source zone. Both the updated  $a$ -values computed within this investigation and the original  $a$ -values ( $a_{B2000}$ ) provided by Bungum et al. (2000) were normalised by the durations of their respective earthquake catalogues to permit comparison (Tab. 7.2). For zones with no observed earthquakes (zones 5, 17, 20, 30, 34 and 35) the original  $a$ -values provided by Bungum et al. (2000) were used instead of computing updated  $a$ -values<sup>58</sup>.

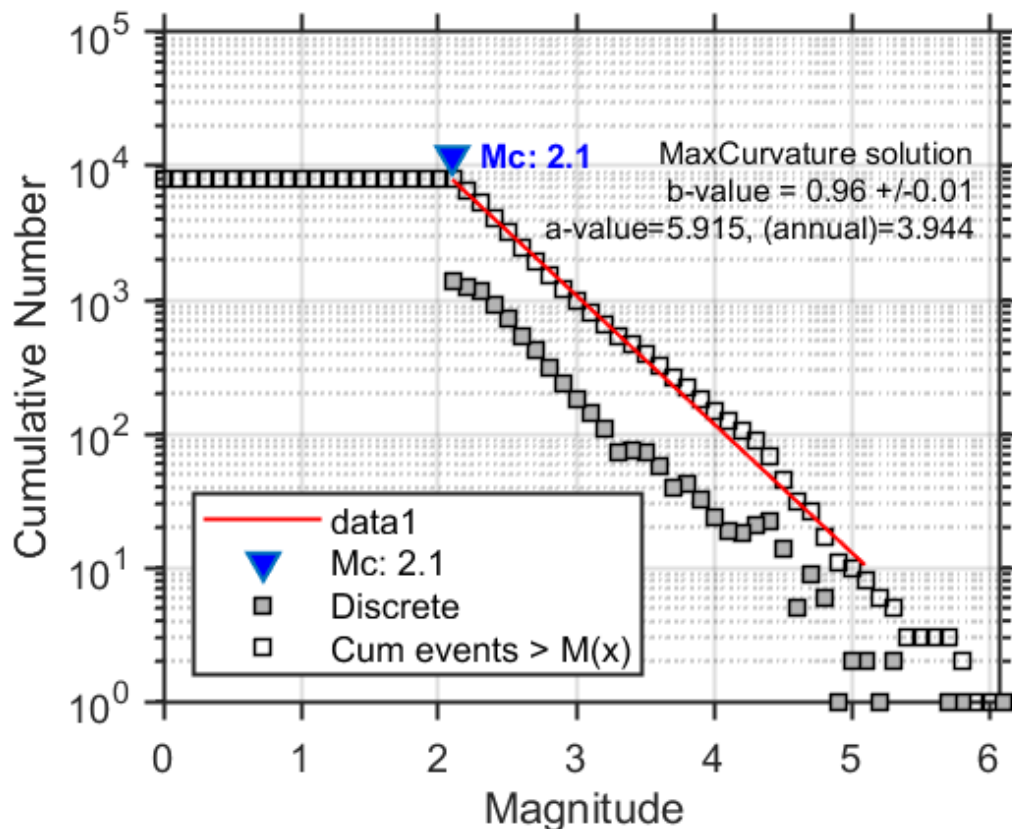


**Figure 7.4** Frequency magnitude distribution of the UNSEC. This figure was produced by ZMAP.

<sup>58</sup> Although  $a$ -values for these zones could still be computed by fixing the regional  $b$ -value, replacement was considered as more appropriate, as the  $a_{B2000}$  values suggest the presence of (limited) seismicity not accounted for in the UNSEC catalogue.

**Table 7.2** Number of observed events for each source zone and (normalised) original and updated *a*-values. Rows shaded grey indicate zones for which no earthquakes were observed within.

Source Zone	Number of Obs. Events	$a_{B2000}$ (per year)	$a_{upd}$ (per year)
1	15	0.947	0.597
2	12	0.606	0.548
3	119	1.361	1.054
4	31	1.034	0.758
5	0	1.053	1.053
6	79	1.635	0.964
7	62	1.559	0.911
8	165	0.938	1.126
9	199	1.332	1.168
10	24	0.880	0.701
11	106	1.174	1.029
12	8	0.899	0.459
13	131	1.462	1.076
14	9	1.140	0.485
15	40	1.395	0.814
16	16	1.087	0.612
17	0	0.620	0.620
18	26	1.179	0.719
19	2	0.750	0.153
20	0	1.390	1.390
21	43	1.615	0.830
22	29	1.217	0.743
23	69	1.423	0.934
24	14	1.024	0.582
25	7	1.024	0.429
26	79	1.125	0.964
27	6	1.116	0.395
28	1	0.774	0.000
29	81	1.789	0.970
30	0	0.918	0.918
31	7	1.072	0.429
32	1106	1.481	1.546
33	16	0.726	0.612
34	0	1.068	1.068
35	0	1.342	1.342
36	5	0.721	0.355
37	131	1.091	1.076

### 7.3 Comparative PSHA Calculations

To assess the significance of the updated source parameters in terms of seismic hazard, comparative PSHA calculations were undertaken within the CRISIS seismic hazard software (Ordaz et al., 2015). These PSHA calculations were undertaken using the Bungum et al. (2000) source zonation model with (1) the updated source parameters and (2) the original source parameters. The ground-shaking was predicted using the Bungum et al. (2000) ground-motion model (GMM). As before the source parameters were normalised by their respective earthquake catalogue lengths to permit comparison of them (or in this case their associated hazard results). The outputs of these PSHA calculations comprise of seismic hazard maps for a return period of 475 years (Fig. 7.6) and seismic hazard curves (Fig. 7.7). The seismic hazard curves were computed for 4 example sites. These 4 example sites cover a large geographical expanse of the North Sea<sup>59</sup>, so as to demonstrate the overall impact of the updated source parameters on potential sites of interest throughout the region.

The outputs of these PSHA calculations are indicative of the updated source parameters having a varied impact on the predicted seismic hazard in the North Sea. For example, at Site 1 and Site 2, for an annual frequency of exceedance (AFOE) of  $10^{-4}$ , the updated source parameters result in increases in the predicted ground-shaking of  $\sim 30\%$  and  $\sim 10\%$  respectively, whereas at Site 3 and Site 4, for the same AFOE, the updated source parameters result in decreases in the predicted ground-shaking of  $\sim 30\%$  and  $\sim 60\%$  respectively. The more significant decrease in predicted ground-shaking for an AFOE of  $10^{-4}$  at Site 4 than for Site 3 can be attributed to the updated source parameters resulting in larger reductions in the seismic hazard originating from the source zones surrounding Site 4 than for Site 3 (Fig. 7.0 vs. Fig. 7.5; Fig. 7.6). Overall, the variations in the predicted seismic hazard resulting from the updated source parameters are moderate but significant, and demonstrate how the predicted seismic hazard is strongly dependent on the adjacent source zones.

Ideally the hazard map computed using the updated source parameters would be compared to the results of the recent seismic hazard assessment for the United Kingdom by Mosca et al. (2020). Unfortunately, a valid comparison is not possible because Mosca et al. (2020)'s seismic hazard maps were computed exclusively for the onshore environment, for which the hazard maps computed using the seismogenic zonation model of Bungum et al., 2000 do not overlap with. However, a simple comparison of the levels of predicted seismic hazard indicates the seismic hazard maps are in good agreement with one another. For a return period of 475 years, Mosca et al. (2020)'s peak ground acceleration (PGA) hazard map (their Fig. 55) provides a maximum PGA of 0.08 g for an onshore site, whereas within this investigation for the same return period, the PGA hazard map computed using the updated source parameters provides a maximum PGA of 0.06 g for an onshore site.

---

<sup>59</sup> Site 1: latitude = 66, longitude = 10; Site 2: latitude = 58, longitude = 4; Site 3: latitude = 60, longitude = 4; Site 4: latitude = 72, longitude = 22.

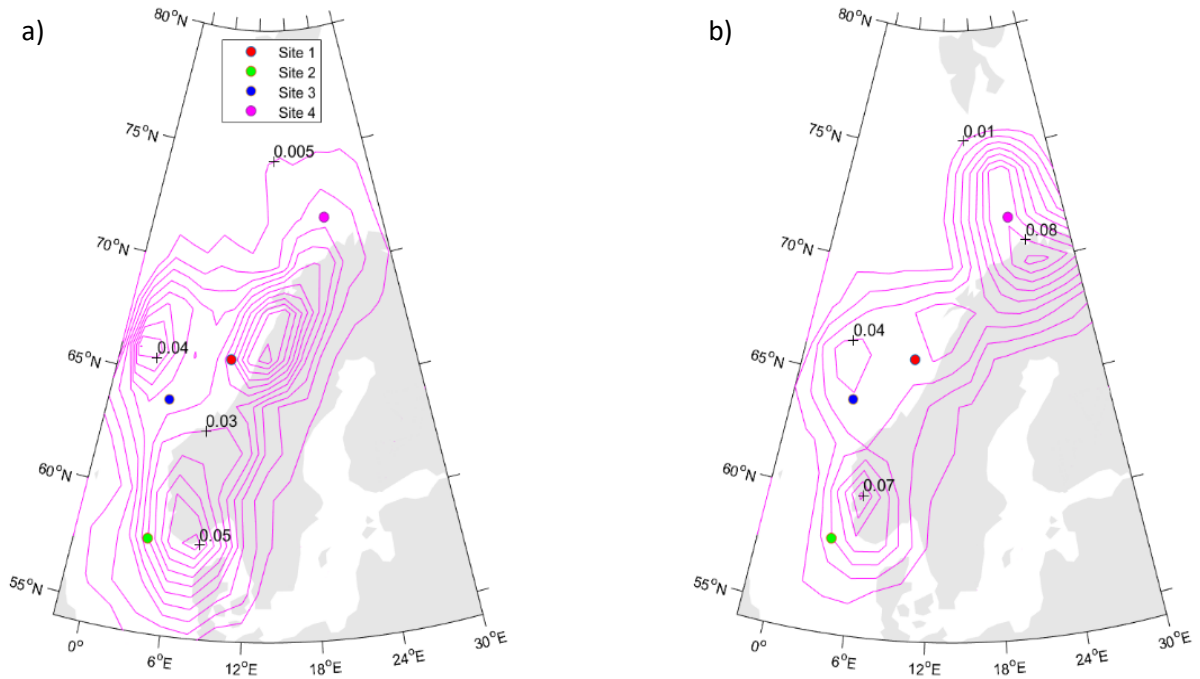


**Figure 7.5** (a) North Sea PGA seismic hazard map computed using the (normalised) updated source parameters computed within this investigation and (b) North Sea PGA seismic hazard map computed using the (normalised) original source parameters of Bungum et al. (2000). PGA is in  $m/s^2$ . Seismic hazard maps were computed for a return period of 475 years using the Bungum et al. (2000) GMM.

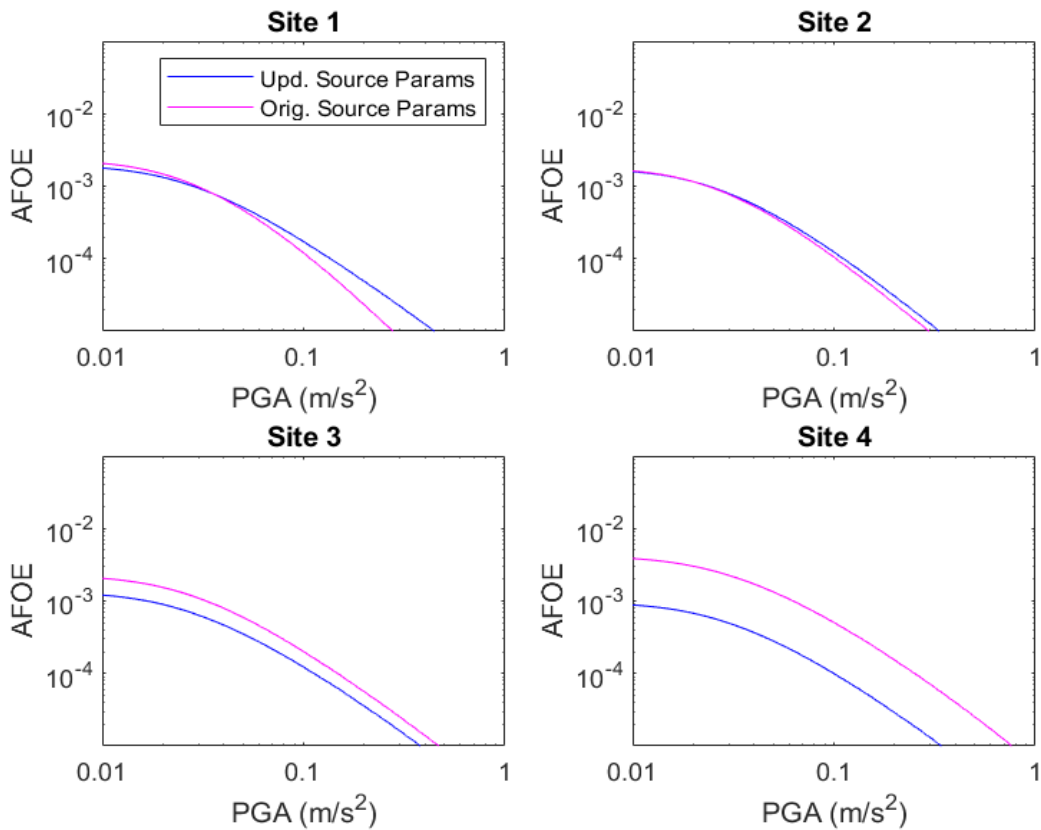


**Figure 7.6** PGA seismic hazard curves for the considered North Sea sites. AFOE = annual frequency of exceedance. Site locations provided in Fig. 7.5.

#### **7.4 Conclusions for Reassessment of North Sea Seismic Source Model Parameters**

Within this investigation the source parameters for each of the 37 source zones within Bungum et al. (2000)'s North Sea source model were reassessed. This reassessment was undertaken in light of 20 years of additional earthquakes having been observed in the North Sea since the publication of Bungum et al. (2000)'s source model for the region. The updated source parameters were computed from a catalogue of North Sea earthquakes. This updated catalogue was compiled from several separate earthquake catalogues which potentially recorded earthquakes in the North Sea. The updated source parameters have a varied impact on the predicted ground-shaking, with moderate but significant results being observed at the considered sites. The impact of the updated source parameters on the predicted ground-shaking suggest that this reassessment of North Sea source zone parameters was potentially important for better capturing North Sea seismic hazard. Therefore, this updated source model could replace the Bungum et al. (2000) source model in future North Sea PSHAs.

#### **7.5 Evaluation of North Sea Probabilistic Seismic Hazard Assessment using Macroseismic Intensities**

Macroseismic intensities are commonly used in the fields of engineering seismology and earthquake engineering to (1) assist in the assessment of magnitudes and locations for historical earthquakes and (2) facilitate public understanding of seismic hazard. Macroseismic intensities can also be used to independently evaluate the results of a PSHA, and therefore determine whether the considered PSHA model appropriately models the seismic hazard within a region, although notable published examples of such evaluations are limited (e.g. Stirling and Peterson, 2006 for USA and New Zealand, Mak and Schorlemmer, 2016 for central and eastern USA and Rey et al., 2018 for France). Here, macroseismic intensities for onshore locations in Norway are used to independently evaluate the updated seismogenic source zonation model for the North Sea developed above. Onshore locations in exclusively Norway, rather than both Norway and the United Kingdom are used to evaluate the updated North Sea source model because the source zonation originally devised by Bungum et al. (2000) results in the simulated seismic hazard being far more strongly felt in Norway.

A significant benefit of using macroseismic intensities rather than ground-motion records to evaluate PSHA results is that macroseismic intensity databases usually span several centuries, rather than a couple of decades as do most ground-motion record databases. The larger time windows often covered by macroseismic intensity databases means the AFOEs for given levels of seismic hazard (at specified sites) can be more rigorously constrained than if ground-motion records were used due to a greater abundance of observations usually being available. However, macroseismic intensities have limitations which should be acknowledged. These limitations are mainly associated with macroseismic records obtained from historical documents. Although macroseismic surveys undertaken today and in the past couple of decades do well to minimise the uncertainty inherently associated with acquiring qualitative

descriptions of ground-shaking from the general populace, historical documents usually only provide a broad description of the felt ground-shaking and earthquake damage (Ambraseys et al. (1983). Furthermore, historical macroseismic observations are often restricted to sites where macroseismic observations could be sufficiently archived, such as town halls, churches and other focal points within communities due to literacy being largely limited amongst the general populace prior to the beginning of 20<sup>th</sup> century (Ambraseys et al., 1983). These limitations are observed for Norwegian macroseismic intensities.

To overcome such limitations, a kriging-with-a-trend technique (Olea, 1999; Ambraseys and Douglas, 2004; Rey et al., 2018) can be used to estimate the felt intensity at sites for earthquakes for which no macroseismic records exist. The kriging-with-a-trend algorithm uses the existing macroseismic intensities to model the attenuation of felt intensity with distance from the earthquake epicentre. This results in the generation of isoseismal contours for each earthquake, from which the intensity at a given site can be estimated, resulting in an expanded set of macroseismic intensities for each site. The generated isoseismal contours are shaped by the existing macroseismic intensities. The expanded sets of macroseismic intensities generated using the kriging-with-a-trend algorithm can then be used to compute hazard curves for each sites. These hazard curves are then compared to hazard curves computed for the same sites using the updated seismogenic source model within a conventional PSHA. This process is detailed below, and largely follows the methodology used by Rey et al. (2018) to assess the suitability of the European Seismic Hazard Model 2013 (ESHM13 – see Woessner et al., 2015 for more details on this model) for predicting seismic hazard France using French macroseismic intensities and the kriging-with-a-trend technique discussed above. From this point forward, macroseismic intensities are referred to as macroseismic data points (MDPs).

## **7.6 Methodology for Evaluation of North Sea PSHA using Macroseismic Intensities**

The process for evaluating North Sea PSHA using MDPs can be divided into four steps. The first of these steps is the compilation of a dataset of MDPs for Norwegian locations. This data was acquired from the University of Bergen's macroseismic intensity database (Nnsn.geo.uib.no, 2020), which archives macroseismic intensities for both contemporary and historical earthquakes felt in Norway. The downloaded dataset comprises of 6,030 MDPs for 184 North Sea region earthquakes and 1272 locations (Fig. 7.7), and covers from 1657 to 2016. The macroseismic intensity for each MDP are provided in European Macroseismic Scale (EMS-98 – see Grünthal, 1998 for more details). It should be noted that for the earthquakes listed in the University of Bergen's macroseismic database only epicentral areas are provided, rather than latitudinal and longitudinal coordinates of the epicentres. Therefore, the coordinates for each earthquake's epicentre were estimated from their epicentral areas. Fortunately, the epicentral area provided for each earthquake is reasonably specific, and therefore not too much

approximation was required, with the only exception being the earthquakes listed as originating within the North Sea itself due to its broad geographical boundaries<sup>60</sup>.

The second step was the identification of appropriate Norwegian sites to evaluate North Sea PSHA for, and the use of the kriging-with-a-trend algorithm to generate additional MDPs at each of these sites. The selected sites were chosen because they provide good geographical coverage of Norway (Fig. 7.7), and therefore the seismic hazard present at each site is likely varied too. The kriging algorithm was used to generate (EMS-98 scale) isoseismal contours for each of the earthquakes within the MDP dataset (e.g. Fig. 7.8). Each set of isoseismal contours was visually checked because (1) offshore earthquakes result in poor azimuthal coverage of the existing MDPs relative to earthquake epicentre, resulting in poorly constrained isoseismal contours for offshore earthquakes and (2) the built-in contouring functions within MATLAB (which the kriging algorithm kindly provided by John Douglas was written in) occasionally generate complicated sets of contours which are not realistic. If the generated isoseismal contours were deemed defective following visual inspection, estimations of macroseismic intensities at the considered sites for the corresponding earthquakes were not made using them (e.g. the isoseismal contours for the offshore 09/03/1866 earthquake were overly-complex and therefore this earthquake was discarded). However, existing MDPs for these earthquakes were considered. If an MDP for an earthquake already existed for the selected site, then the estimated MDP for the same earthquake was discarded.

---

<sup>60</sup> For these earthquakes, the most seismically active point in the North Sea was fixed as their epicentral coordinates. The most seismically active point in the North Sea (latitude = 61, longitude = 3) was approximated from a simple plot of the epicentres of observed North Sea earthquakes (see Fig. 2.6 in Chapter 2). The chosen point lies to the east of the Viking Graben, which is known to generate a large amount of seismicity in the North Sea (Ritsema and Gürpınar, 1983), and therefore can be considered as an appropriate proxy for the epicentres of these earthquakes.

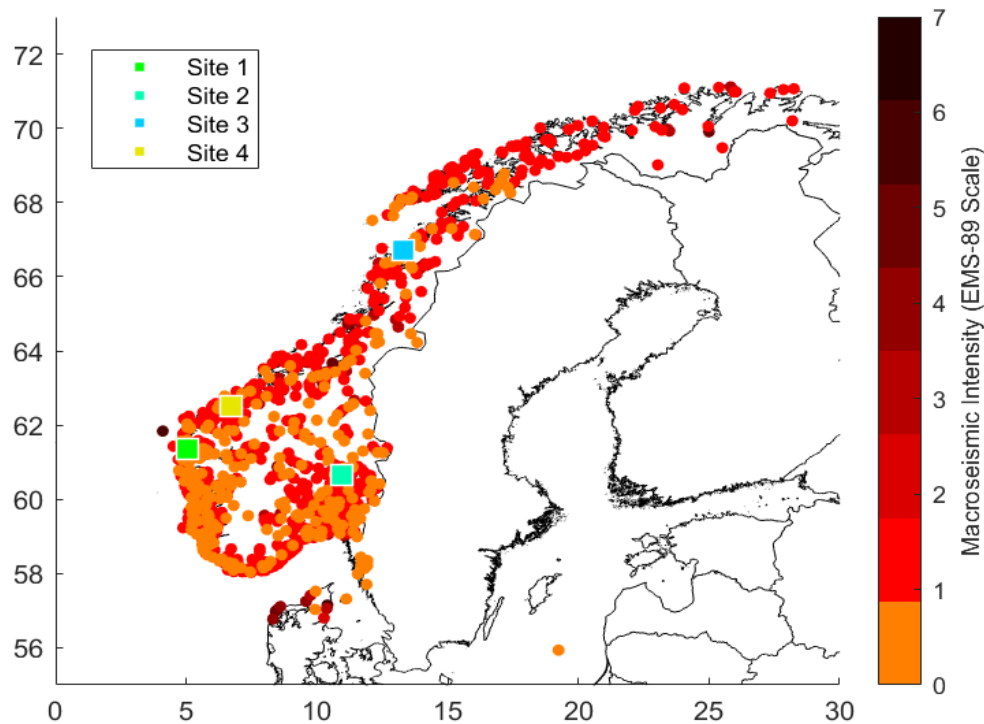


**Figure 7.7** Spatial distribution of MDPs within the compiled dataset.

The third step was to determine the period of completeness for the expanded set of MDPs at each of the selected sites. Periods of completeness were determined for each site's set of MDPs by plotting the cumulative number of MDPs with an intensity  $\geq 1$  versus time (Fig. 7.9), with stable rates of occurrence over time indicating complete periods of earthquake observations (Rey et al., 2018). For sites 1, 2, 3 and 4, periods of completeness of 1975 – 2016 (41 years), 1976 – 2016 (40 years), 1976 – 2016 (40 years) and 1973 – 2016 (43 years) were determined respectively (Tab. 7.3). These periods of completeness are reasonably small, and will result in large AFOEs being computed for a given intensity at each site. Therefore, in the next stage, a larger period of completeness of 1759 – 2016 (257 years) is also considered to provide more moderate AFOEs for a given intensity at each site. A time window of 257 years corresponds to the first macroseismic record reporting an intensity of less than 4 within the MDP dataset.

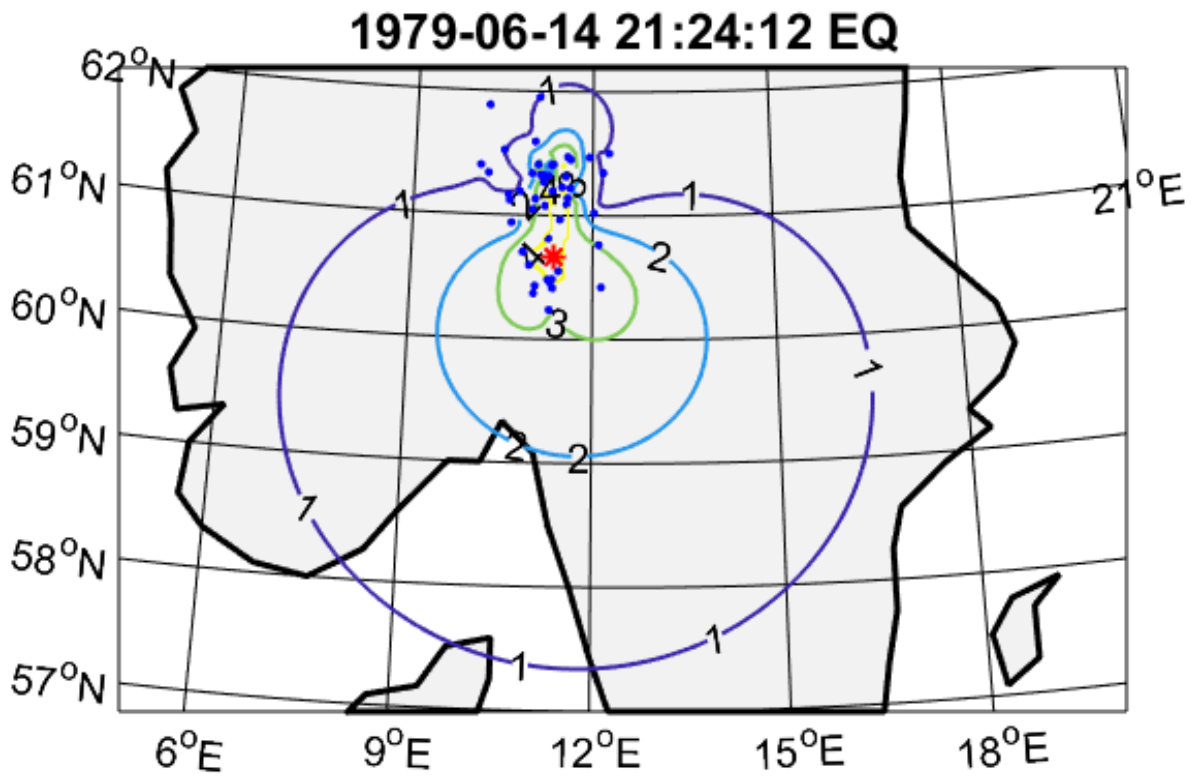


**Figure 7.8** Isoseismal contours (EMS-98 scale) generated for the 1979/06/14 21:24:12 and 2009-11-10 02:29:57 earthquakes. Red asterisk represents the earthquake epicentres. Blue dots represent existing MDPs for the earthquakes.

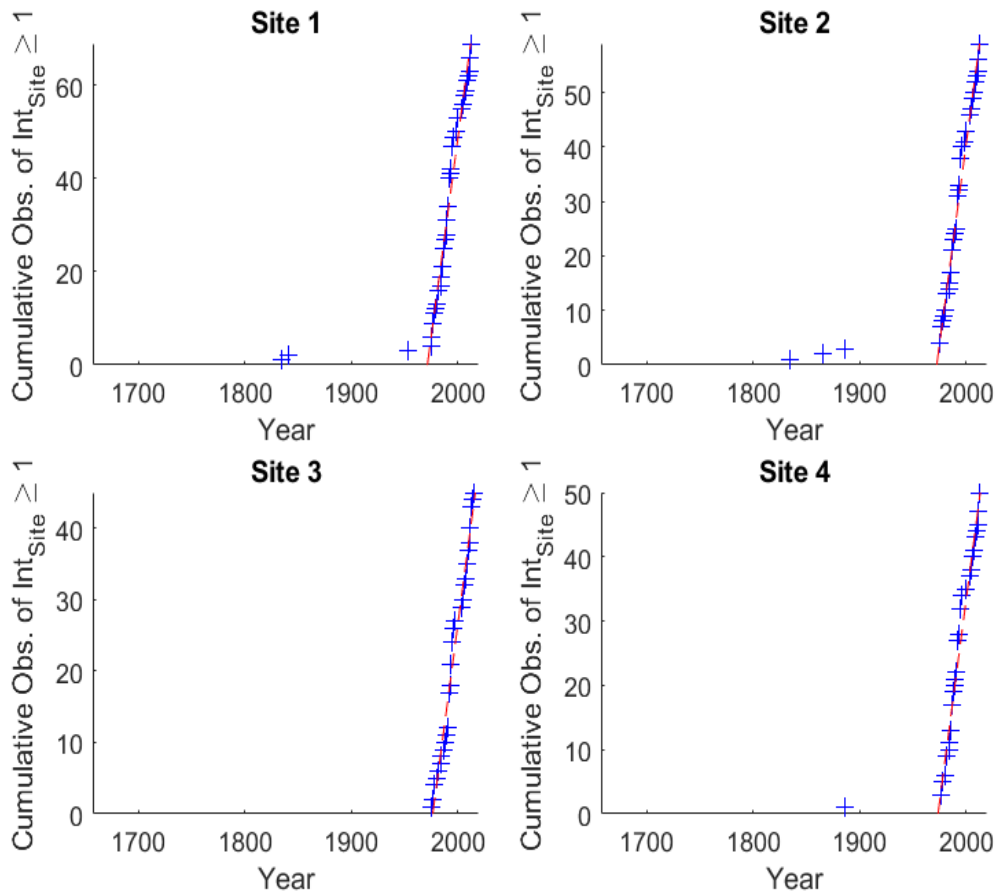


**Figure 7.9** Plots of cumulative number of MDPs (intensity  $\geq 1$ ) against time. Red dashed line indicates periods for which approximately stable rates of occurrence are observed.

**Table 7.3** Periods of completeness and number of MDP for a given intensity at each site.

Site	Period of MDP Completeness	Equivalent Window (Years)	Int. $\geq 1$	Int. $\geq 2$	Int. $\geq 3$	Int. $\geq 4$	Int. $\geq 5$	Int. $\geq 6$
1	1975-2016	41	66	41	26	10	0	0
2	1976-2016	40	56	27	17	7	0	0
3	1976-2016	40	45	28	15	6	0	0
4	1973-2016	43	49	31	24	5	2	1

The final step was to (1) compute AFOEs for each observed intensity at each site from the time-windowed sets of MDPs and (2) compute hazard curves from a North Sea PSHA (Fig. 7.10). For the PSHA calculations the updated North Sea seismogenic source zonation model was used and three ground-motion models (GMMs) were considered: (1) the Bungum et al. (2000) GMPE logic tree, (2) the Akkar et al. (2014) GMPE and (3) the Musson (2013) intensity prediction equation (IPE). The Bungum et al. (2000) GMPE logic tree was selected because it was used in the most recent publically

available North Sea PSHA (Bungum et al., 2000)<sup>61</sup>. The Akkar et al. (2014) GMPE was selected because it was identified as the most appropriate base model for the development of a North Sea specific GMPE within this investigation (see chapters 3 - 4 for more details on this GMPE). The Musson (2013) IPE was selected because it predicts the expected intensity (EMS-98 scale) at a location as a function of magnitude and distance, and was developed from United Kingdom MDPs (No IPEs have been developed specifically for Norway, and the United Kingdom is region with overall similar seismicity to the neighbouring North Sea – Mallard et al., 2003). For the Bungum et al. (2000) and Akkar et al. (2014) GMMs, the predicted ground-motion had to be converted from PGA to intensity, which was done so using the empirical relationship between PGA and intensity (EMS-98 scale) determined by Zanini et al. (2019 – see their equation 6). This empirical relationship was developed using a set of 220 MDPs for Italy, which has considerably elevated seismicity compared to the North Sea region, but the moment magnitude ( $M_w$ ) range of the 22 earthquakes associated with these MDPs is  $3.2 \leq M_w \leq 6.1$ , which is a similar  $M_w$  range to that of earthquakes observed in the North Sea (Bungum et al., 2000), and therefore this relationship can be deemed appropriate for use here. The intensity hazard curves computed using these GMMs for the selected sites are provided in Fig. 7.10, along with the hazard curves computed from the time-windowed MDP sets. These hazard curves are compared in the following section to provide a means of independently evaluating North Sea PSHA.

### **7.7 Results for Evaluation of North Sea PSHA using Macroseismic Intensities**

The most prominent observation for the hazard curves is that the AFOEs computed using the MDPs with either the site-specific time windows (~40 years) or the 257-year time window provide near-constant over-predictions for a given-intensity compared to the AFOEs computed using the GMMs (Fig. 7.10). The only exception is for site 3, where the AFOEs for a given intensity computed using the Akkar et al. (2014) GMPE are similar to the AFOEs computed using the MDPs with the 257-year time window. Assuming each set of time-windowed MDPs are representative of the seismic hazard expected at each site, the larger AFOEs for a given intensity from the MDPs suggests that the considered North Sea PSHA models under-predict the true seismic hazard. Similar observations to the above were made by Rey et al. (2018), who observed within half of the French municipalities (sites) they considered that ESHM13 under-predicted the seismic hazard compared to that suggested by the MDPs. Such under-prediction could potentially be caused by high macroseismic intensities being observed from small earthquakes, which are below the minimum magnitude considered within the PSHA calculations. It should be acknowledged that the site-specific time windows provide considerably higher AFOEs than the 257-year time-window, and therefore that only the AFOEs computed using the 257-year time-window are considered within the discussion below as they provide more realistic AFOEs.

---

<sup>61</sup> The Bungum et al. (2000) GMPE logic tree was developed for North Sea sites, including coastal locations, but not inshore locations such as Site 1 (Oslo). However, this GMM is still considered for Site 1 to permit additional comparison of its performance compared to the AFOEs for a given intensity computed from the MDPs.

The Bungum et al. (2000) GMPE logic tree provides AFOEs for a given intensity which give the worst match to the AFOEs computed from the MDPs, suggesting this GMM under-predicts the seismic hazard more significantly than the Akkar et al. (2014) or Musson (2013) GMMs for the considered sites. The Akkar et al. (2014) GMPE provides AFOEs for a given intensity most similar to the AFOEs computed from the MDPs, although only for site 3 are close matches observed. The Musson (2013) IPE provides AFOEs which for lower intensities are between the AFOEs computed using the Bungum et al. (2000) and Akkar et al. (2014) GMMs, but for larger intensities are sometimes higher than the AFOEs computed by either of these GMMs. For example, at sites 1 and 2, the AFOEs for intensities 1 – 3 computed using the Musson (2013) IPE are either less than or approximately equal to the AFOEs computed using the Akkar et al. (2014) GMPE, but for intensities 4 - 6 the AFOEs computed using the Musson (2013) IPE begin to exceed the AFOEs computed using the Akkar et al. (2014) GMPE (similar results are observed for Site 4, but from an intensity of 5 upwards instead). These observations suggest that (1) the Akkar et al. (2014) GMPE is the most suitable of the considered GMMs for North Sea PSHA because this GMM provides intensity hazard curves most similar to the AFOEs computed using the MDPs and (2) the moderate overlap of the Akkar et al. (2014) GMPE and the Musson (2013) IPE suggests that the empirical relations between PGA and EMS-98 scale intensity determined by Zanini et al. (2019) are appropriate for use in the North Sea region<sup>62</sup>, although there is the caveat that the converted intensities are dependent upon the GMM used for the prediction of the PGA values which are to be converted to intensity. It should also be noted that the considerable under-prediction of the Bungum et al. (2000) GMM compared to both the other GMMs and the MDPs supports the development of a GMM specifically for the North Sea, as undertaken in chapters 3 - 4.

### **7.8 Conclusions for Evaluation of North Sea PSHA using Macroseismic Intensities**

MDPs for onshore Norwegian locations were used to independently evaluate a North Sea PSHA procedure which incorporated an updated North Sea seismogenic source zone model and considered several GMMs. To provide additional MDPs for the selected sites a kriging-with-a-trend technique was implemented. The hazard curves computed from (1) the macroseismic intensities recorded at each considered site and (2) the PSHA calculations with each GMM are noticeably different, with the AFOEs for a given intensity generally being greater for those computed from the MDPs than those computed within the PSHA calculations. However, the Akkar et al. (2014) GMM provides reasonably similar results to the MDPs for site 3, and provides more similar results to the MDPs for the other considered sites at most intensities too. Additionally, the good agreement of the Akkar et al. (2014) GMPE and the Musson (2013) IPE suggests that empirical relations of Zanini et al. (2019) are appropriate for the conversion of PGA to EMS-98 scale intensity in the North Sea region. Overall, despite the AFOEs

---

<sup>62</sup> There is insufficient data to confirm this suggestion through developing an original empirical relationship between pairs of observed PGA and macroseismic intensity for earthquakes observed in Norway.

computed from the MDPs being disappointingly elevated compared to those provided by the PSHA calculations, some useful insights into North Sea PSHA are gained.

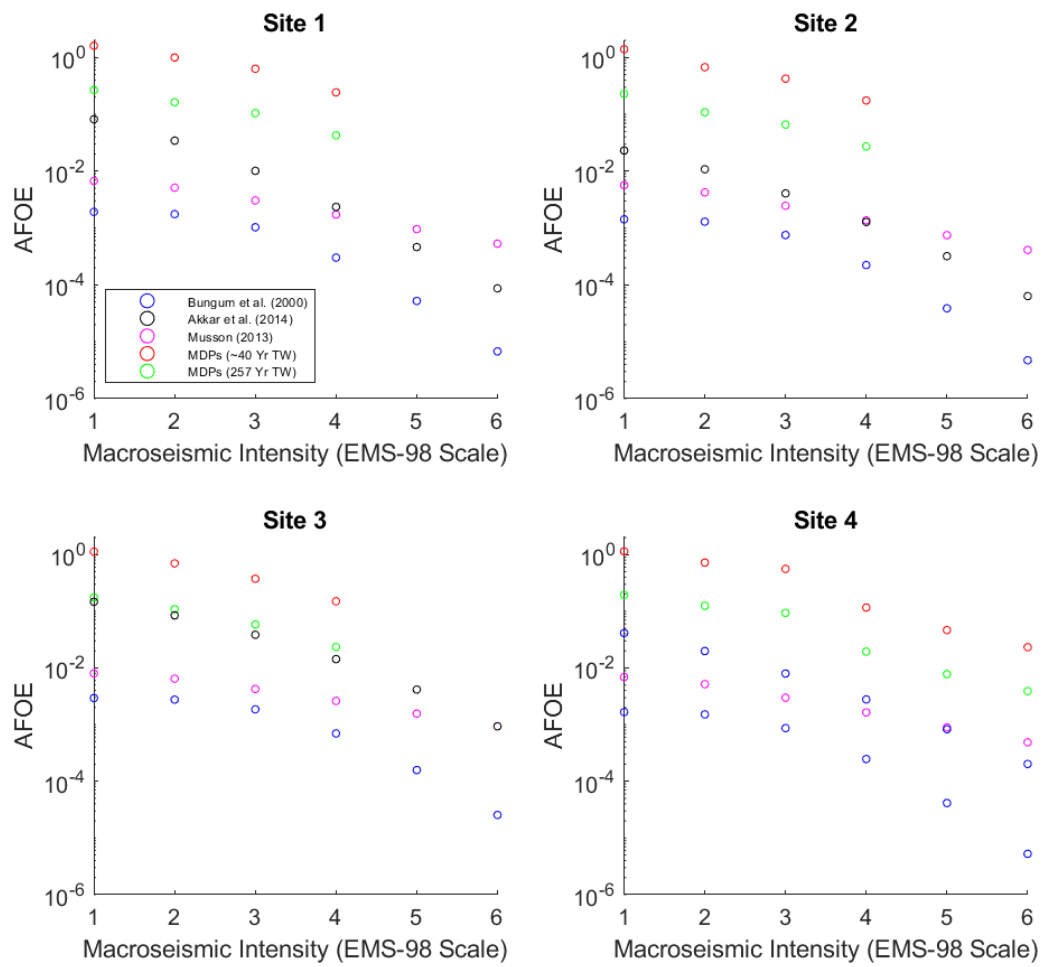


**Figure 7.10** Intensity hazard curves computed from the MDPs and the North Sea PSHA calculations.

## 8.0 Assessing the Seismic Risk for Critical Infrastructure in the North Sea

Within the prior chapters of this investigation the North Sea probabilistic seismic hazard assessment (PSHA) of Bungum et al. (2000) was reassessed and subsequently modified to provide improved seismic hazard estimates for the region. These improved seismic hazard estimates can be used to determine the probabilities of certain levels of ground-motion intensity being experienced by infrastructure in the region. When the probabilities of specified levels of ground-motion intensity and the seismic capacity (the capability of a structure to resist damage – Boore and Bommer, 2005) are considered together the seismic risk for a structure can be assessed. The likelihood of a structure failing to perform satisfactorily under a predefined limit state (e.g. collapse) when subjected to a specified level of ground-motion intensity is defined as the seismic fragility (Erberik, 2015). In accordance with this definition, seismic fragility analysis (SFA) is the assessment of the seismic vulnerability of a structure subjected to earthquake ground-motions.

The following overview of seismic fragility analysis is summarised from Erberik (2015).

Fragility analysis produces two key outputs, (1) the damage probability matrix and (2) the fragility curve. The damage probability matrix (DPM) is a table which provides discrete values of limit (damage) state probabilities for specified levels of a ground-motion intensity measure (e.g. Fig. 8.0). Each column of a DPM represents a constant level of ground-motion intensity, and each row denotes the probability of the considered structure reaching a limit state when subjected to this given level of ground-motion intensity. Fragility curves are continuous functions representing the probability of exceeding limit states for specified levels of ground-motion intensity (e.g. Fig. 8.0). The primary purpose of fragility curves is to determine the seismic performance of new or existing structures. For new structures, the fragility information is used for design optimisation. For existing structures, the fragility information is used for condition assessment. When fragility curves are derived to represent a specific type of structure, they can be used for regional seismic damage studies, as is undertaken below. Seismic damage studies are undertaken because they can be implemented in (1) pre-earthquake mitigation procedures and (2) post-earthquake decision making processes.

Information from fragility curves can be converted to construct DPMs and vice versa. Fig. 8.0 demonstrates how a DPM can be generated from a given set of fragility curves. The vertical axis, simply labelled as “probability” refers to the probability of exceeding a limit state. The horizontal axis represents the range of considered ground-motion intensity levels. The columns of the DPM are generated by intersecting the fragility curve set with vertical lines (the dashed lines in Fig. 8.0) at specified ground-motion intensity levels, and calculating the corresponding limit state probabilities, which are the corresponding portions between any two limit states in these vertical alignments.

Seismic fragility analysis is effectively the comparison of seismic demand and seismic capacity, so as to estimate whether the seismic capacity is exceeded for a predefined performance level when the

structure is subjected to a specified level of ground-motion intensity. Due to the probabilistic nature of seismic fragility analysis, both the seismic demand and seismic capacity are defined by probability functions in terms of certain random variables to quantify the uncertainties involved in the process.

The general framework of seismic fragility analysis is presented in Fig. 8.1. The elements enclosed by dashed lines can be regarded as a single component within the seismic fragility analysis. Each component of seismic fragility analysis is briefly explained below.

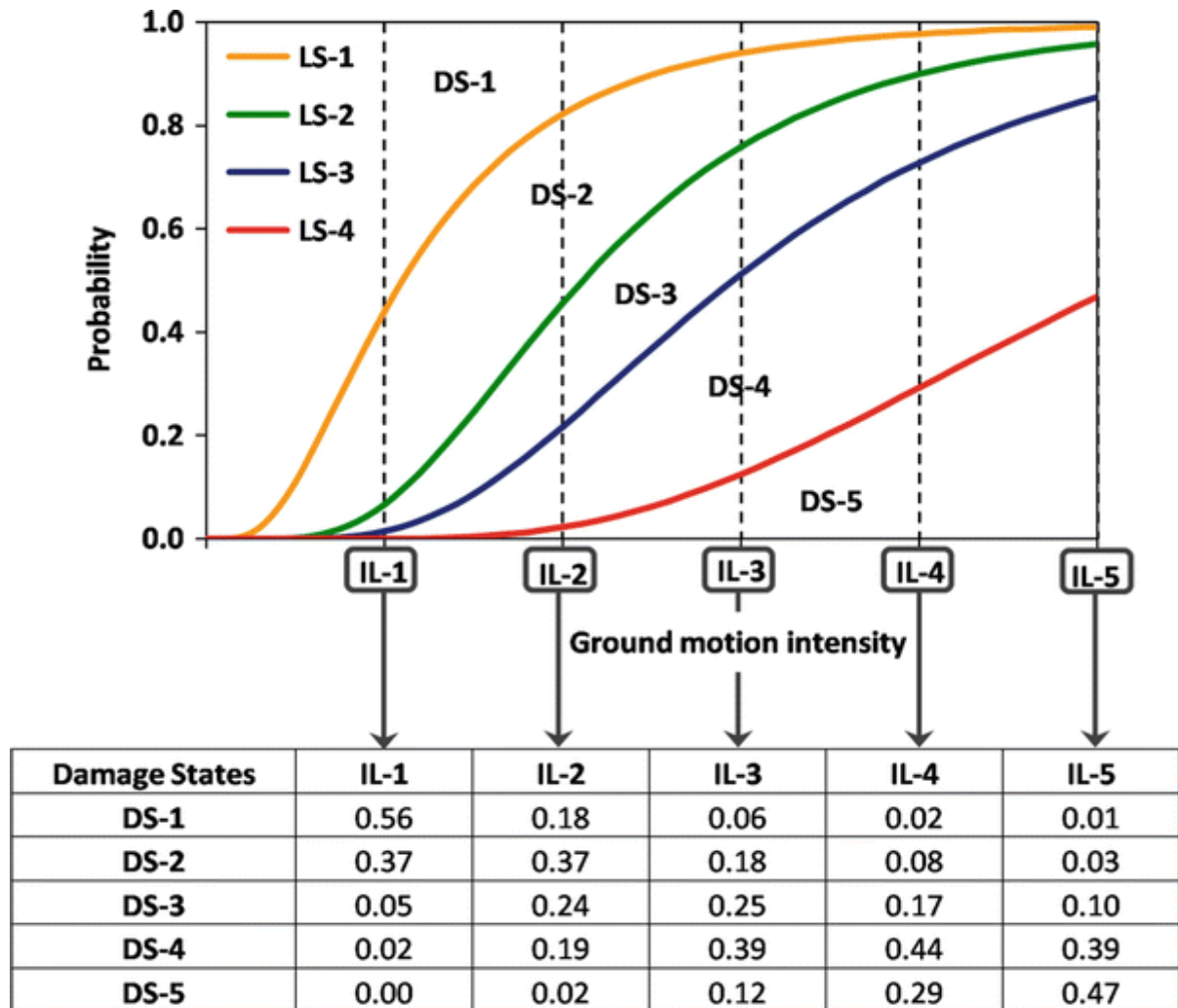


Figure 8.0 Conversion from fragility curves to DPM. Taken from Erberik (2015).

### Step 1 of SFA: Analytical Model and Structural Simulations

The first component of seismic fragility analysis is the development of the analytical model which is used in the structural simulations. The analytical model can range from a single-degree-of-freedom (SDOF) system to a detailed finite element model. Large numbers of structural simulations are required to construct the response statistics. Therefore, the use of a simple analytical model such as a SDOF system is highly advantageous due to reducing computational demand. However, the use a simple analytical model often results in only the general behaviour of the structure being captured, with local structural characteristics potentially being omitted. Therefore, simple analytical models are best

implemented to generate the response characteristics for a class of structure (e.g. reinforced concrete frame structures) for the prediction of regional damage or loss estimation, rather than for structures with specific construction details like historical masonry buildings, where more complex analytical modelling such as finite element analysis is considered.

Following the formulation of the analytical model, dynamic analysis (a type of structural simulation in which structures are subjected to dynamic loading, here in the form of seismic excitation) is undertaken. Due to the probabilistic nature of seismic fragility analysis, the major structural parameters within the analytical model are treated as random variables, each assigned a probability density function. Normal or lognormal probability distributions are commonly used for simplicity. The major structural parameters can be mechanical properties such as stiffness or strength, or geometric properties like length, height or cross-sectional dimensions. To generate the population of analytical simulations a sampling method is required, with this usually being the well-known Monte Carlo sampling method (Metropolis and Ulam, 1949) due to its robustness and simplicity.

### **Step 2 of SFA: Characterisation of Ground-Motion Intensity**

The characterisation of the ground-motion intensity is important for dynamic analysis (structural simulations) due to the dynamic loading being represented by seismic excitation. Within the dynamic analyses, actual or synthetic ground-motion records are used. Ground-motion records are generally selected to cover the whole range of considered intensity levels. Synthetic ground-motion records<sup>63</sup> are usually considered when there is a lack of ground-motion records associated with appropriate earthquakes (i.e. earthquakes in the region, or similar to those which occur in the region).

A key part of ground-motion characterisation is the selection of the appropriate ground-motion intensity measure (GMIM). The most commonly used GMIM are single (peak) value parameters such as peak-ground acceleration (PGA) and peak-ground velocity (PGV), which can be obtained from the ground-motion records. Spectral parameters are often used due to single-degree-of-freedom (SDOF) systems experiencing a larger response for the natural period(s) of the considered structure (Erberik, 2015)<sup>64</sup>. If a spectral parameter such as spectral acceleration (SA) is used, the spectral ordinate usually corresponds to the first natural period of the considered structure ( $T_1$ ), so as to account for the maximum possible level of ground-motion intensity experienced by the structure (Ajamy et al., 2018). The limit states are defined in terms of the most appropriate structural response parameter(s) for each considered structure.

### **Step 3 of SFA: Generation of Response Statistics**

Following the development of the analytical model, the characterisation of the ground-motion intensity and the subsequent dynamic analyses, the generation of response statistics is undertaken. The generation of response statistics requires the undertaking of numerous dynamic analysis. The generated response

---

<sup>63</sup> See Chapter 5 for more details on the stochastic simulation of ground-motions.

<sup>64</sup> See Chapter 3 for more details on ground-motion records.

statistics are plotted upon scatter plots, in which the vertical axis represents the response parameter and the horizontal axis represents the GMIM (Fig. 8.2a). An example response parameter considered here is drift (lateral displacement). Fig. 8.2a demonstrates the uncertainty associated with ground-motion characterisation and the dynamic analyses. Despite the observed scatter, the general trend in Fig. 8.2a is that as the ground-motion intensity increases, the seismic demand (represented by the response parameter) also increases.

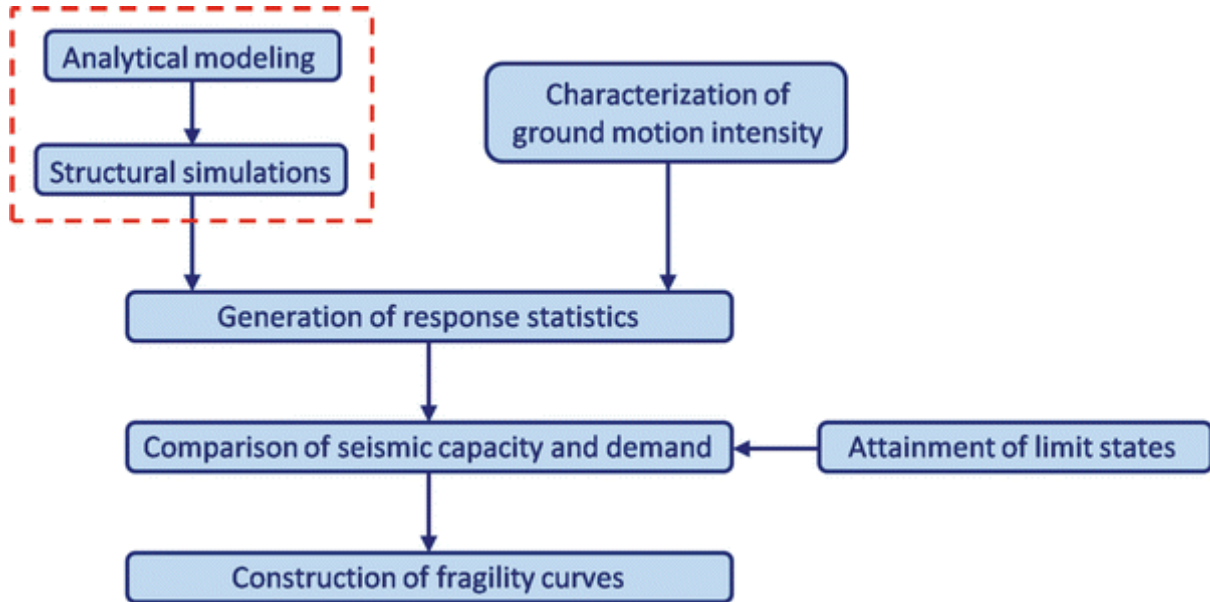


Figure 8.1 General framework of fragility analysis. Taken from Erberik (2015).

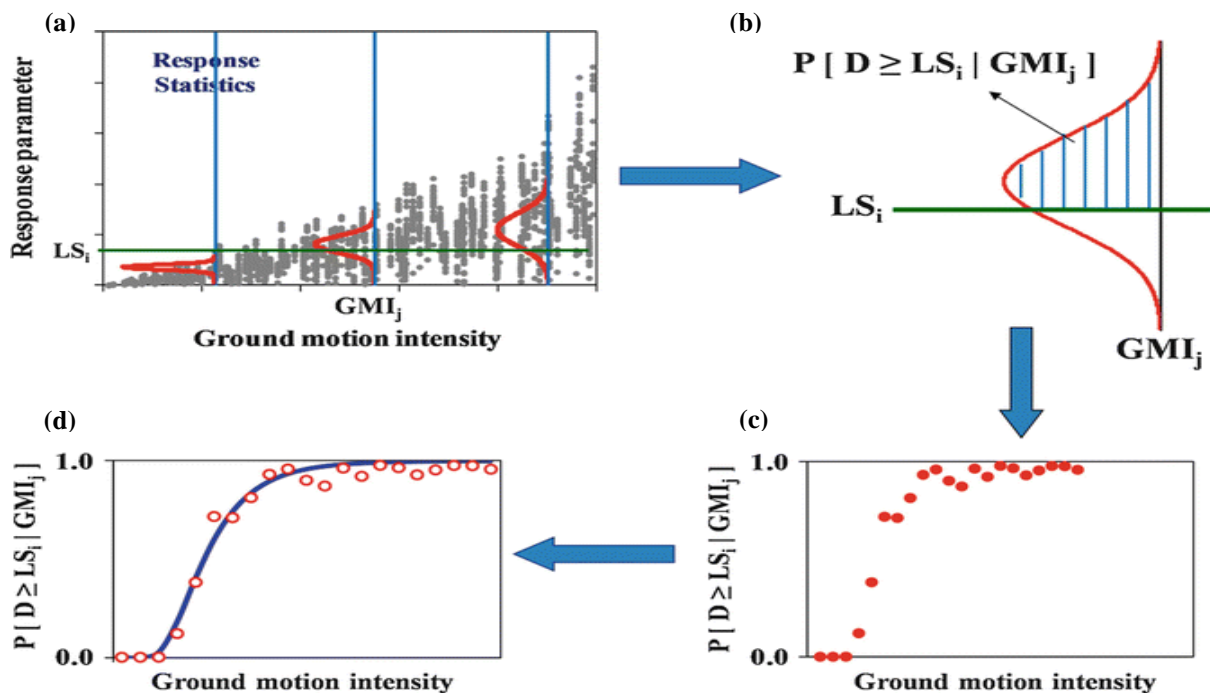


Figure 8.2 Schematic representation of the fragility curve generation procedure: (a) response statistics, (b) probability of exceeding a limit state at a specific ground-motion intensity, (c) discrete fragility information for a predetermined limit state and (d) continuous fragility function. Taken from Erberik (2015).

#### **Step 4 of SFA: Comparison of Seismic Capacity and Demand, and the Attainment of Limit States**

To generate fragility curves, limit states must be defined as functions of the considered response parameter. Limit state values can be defined from previous studies if the considered structure type has been investigated previously. More commonly however, the local characteristics of the structure require the determination of new limit states. In the absence of field observations or experimental findings, the determination of new limit states requires the use of analytical approaches. The most common of such methods is non-linear static analysis, more specifically the pushover method<sup>65</sup>, with this being because the progression of structural damage can be determined using this type of analysis. Conventionally, two or more limit states are defined in a seismic fragility analysis. For example, in the Federal Emergency Management Agency (FEMA) documentation for the seismic rehabilitation of buildings (FEMA, 1997), three limit states are defined: (1) “Immediate Occupancy”, (2) “Life Safety” and (3) “Collapse Prevention” in terms of inter-story drift (the relative lateral displacement between adjacent floors).

#### **Step 5 of SFA: Construction of Fragility Curves**

Each vertical line within the scattered response statistics data in Fig. 8.2a represents a specific ground-motion intensity level, each with its own statistical distribution. If a limit state is added to the same plot the probabilities of exceeding the considered limit state at specified levels ground-motion intensity can be determined. This process is demonstrated in Fig. 8.2b, where  $LS_i$  represents the  $i$ th limit state and  $GMI_j$  represents the  $j$ th ground-motion intensity level. Therefore, the shaded area within the given distribution represents the probability of exceeding the  $i$ th limit state at the  $j$ th ground-motion intensity level, i.e.  $P[D \geq LS_i | GMI_j]$ . The obtained probability represents one data point in Fig. 8.2c. Additional data points are computed by repeating this process for different ground-motion intensity levels (over the considered range) for the same limit state, from which curve fitting can be used to determine a continuous function, i.e. a fragility curve (Fig. 8.2d). The continuous fragility function is generally represented by a cumulative lognormal distribution (Fig. 8.2d).

### **8.1 Critical Offshore Infrastructure in the North Sea**

Here, existing structure-specific fragility curves are convolved with the seismic hazard estimates computed from the improved PSHA calculations to assess the engineering vulnerability of critical offshore North Sea infrastructure in terms of seismic risk (the likelihood of infrastructure sustaining a certain level of damage in a future earthquake). The engineering vulnerability of North Sea infrastructure (and the associated seismic risk) is important to consider because structural damage can be detrimental to: (1) the environmental health of the region i.e. oil spills and industrial chemical leaks, (2) the personal health of personnel operating on or in proximity to the damaged infrastructure and (3)

---

<sup>65</sup> A pushover analysis is performed by subjecting a structure to a monotonically increasing pattern of lateral forces with corresponding changes in elastic and inelastic behaviour until an ultimate condition is reached (see Fajfar, 2000 for more details).

the operations and financial status of the corporations and governments which are dependent upon the infrastructure (Sakai et al. 2017; Romeo, 2013). The offshore infrastructure considered in this investigation comprise of: (1) oil and gas platforms and (2) wind turbine facilities.

Offshore oil and gas platforms can be broadly classified as floating or fixed platforms, where the water depth determines which platform type is used. Fixed steel jacket (FSJ) platforms are a specific subtype of fixed platforms (Fig. 8.3). FSJ platforms have globally widespread use because of their relatively simple design and the availability of hydrocarbons within shallow waters during the onset of offshore exploration (Kammula and Sriramula, 2014). Despite the diminished availability of shallow water hydrocarbons and the subsequent transition of exploration to deeper waters, FSJ platforms remain in widespread service, with 7,500 distributed throughout the world (Ferreira, 2003), and 556 having been installed in the North Sea as of 2012 (Oil and Gas UK, 2012).

Of the 556 FSJ platforms installed in the North Sea as of 2012, at least 10% have been decommissioned (Oil and Gas UK, 2012). The decommissioning process will result in over 700 hydrocarbon fields around the world ceasing production between 2018 and 2022 (Wood Mackenzie, 2017). Due to the onset of the decommissioning industry, the implications for the seismic risk for offshore platforms undergoing disassembly should be considered. Despite the global onset of decommissioning many operators are looking to operate FSJ platforms beyond their initial design life of ~25 years (Kammula and Sriramula, 2014). As of 2008, approximately half of the 288 FSJ platforms present in the United Kingdom Continental Shelf (UKCS) of the North Sea have exceeded their design life (Stacey et al., 2008), and therefore if not decommissioned will require assessment of their structural health<sup>66</sup>. Considering the widespread use of FSJ platforms in the North Sea and the extension of their use beyond their initial design life, it is necessary to assess the engineering risk for FSJ platforms. Therefore, FSJ platforms are the platform type considered within this investigation, for which appropriate fragility curves are identified.

Wind turbines are becoming increasingly deployed due to the rising demand for renewable energy. Wind turbines are especially viable within the offshore environment due to the inherent abundance of wind resources, the lack of visual or noise complaints and the available space (Jonkman et al., 2009). However, the offshore environment provides additional site effects which are not accounted for in the seismic design of onshore wind turbines, with these primarily being (1) the presence of the water layer and (2) the supersaturation of seafloor sediments. Both of these additional site effects have been found to considerably reduce the vertical component of incident P-waves, especially at the resonant frequency of the water column (Boore and Smith, 1999; Hatayama, 2004). Larger period ground-motions have been shown to be unaffected directly by the presence of the water layer (Boore and Smith, 1999). Considering that larger period ground-motions are more important for the seismic design of

---

<sup>66</sup> More recent design life statistics were sought for North Sea FSJ platforms but were not available in the public domain. The total number of FSJ platforms which have exceeded their design life in the region is likely substantially higher now.

conventional offshore structures (Zhang and Zheng, 2019), the water layer is of minimal importance for estimating the ground-shaking at offshore sites (Boore and Smith, 1999). A more detailed overview of offshore site effects is provided in Chapter 4. The type of offshore wind turbine facility considered within this investigation is referred to within the literature as an “NREL offshore 5-MW baseline wind turbine”, or more simply a “5-MW offshore turbine”.

The 5-MW turbine classification was developed by the U.S. office of energy (Jonkman et al., 2009) to provide a reference model for use in the general (including seismic) engineering of offshore wind turbine facilities, having been created from the aggregation of publically available design specifications provided by leading turbine manufacturers. The 5-MW wind turbine is specified as a conventional three-blade, marine environment turbine with a maximum water depth of 20 – 30 m (Fig. 8.4). Due to this maximum water depth restriction, 5-MW wind turbines in the northern North Sea (where seismic hazard was reassessed in this investigation) are restricted to coastal locations (Fig. 8.5). Considering the widespread use of the 5-MW specification within engineering studies, corresponding fragility curves are readily available. Appropriate fragility curves for 5-MW wind turbines are subsequently identified below.

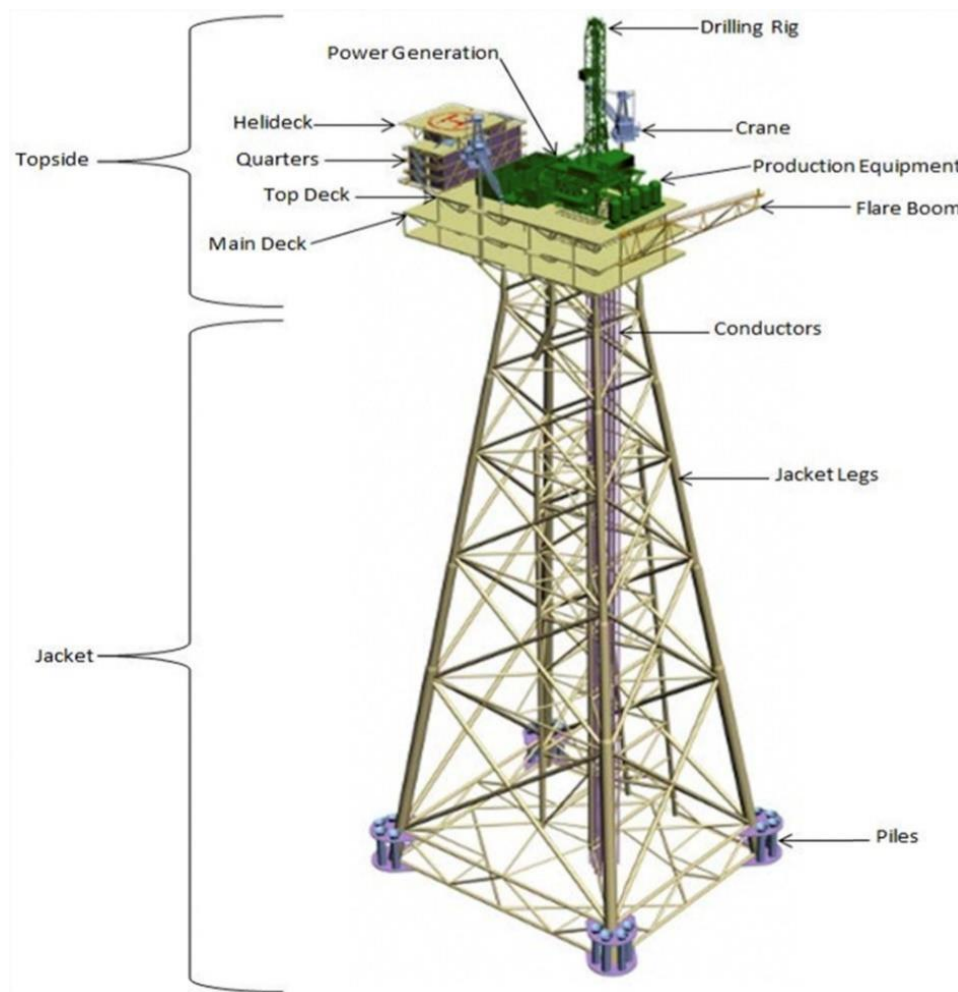


**Figure 8.3** Simple schematic diagram of a fixed-steel jacket platform. Taken from Bull and Love (2019).

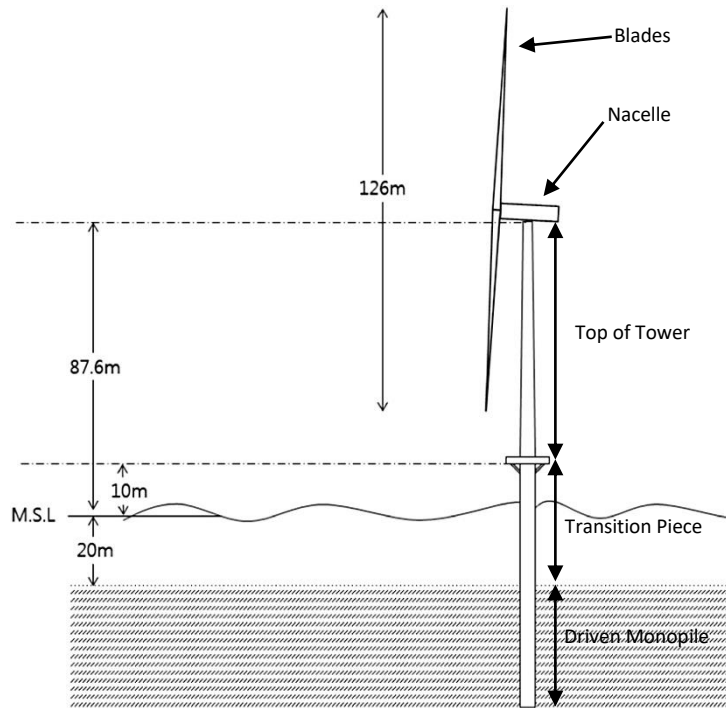


**Figure 8.4** Simple two-dimensional schematic of a 5-MW offshore wind turbine. M.S.L = mean sea level. Adapted from Kim et al. (2014).

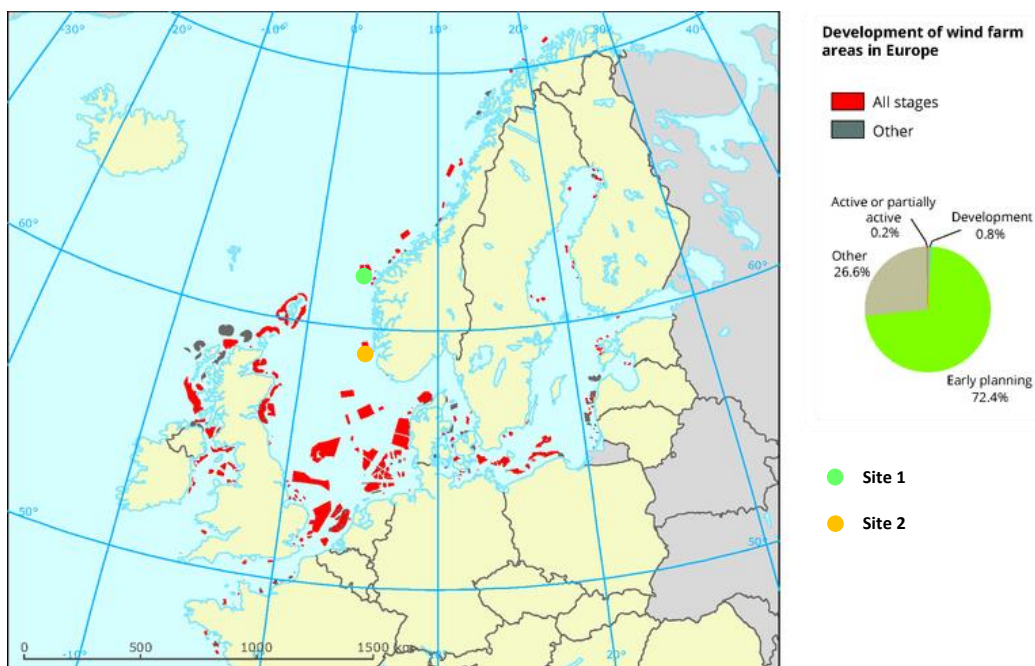


**Figure 8.5** Spatial distribution of offshore wind farm development in northwestern Europe. The locations for which seismic hazard estimates are computed below are also provided. Adapted from eea.europa.eu. (2015). This image has been modified and is available for reuse under the creative commons license (CC BY 2.5 DK) as per [https://creativecommons.org/licenses/by/2.5/dk/deed.en\\_GB](https://creativecommons.org/licenses/by/2.5/dk/deed.en_GB):

## 8.2 Identification of Appropriate Fragility Curves

Fragility curves have been developed specifically for FSJ platforms by (1) Ajamy et al. (2018) and (2) Zarrin et al. (2017) (Fig. 8.6a). For the fragility curves of Ajamy et al. (2018) three damage (limit) states were defined: (1) extensive, (2) complete and (3) ultimate collapse. The first two damage states are defined as levels of damage that are considered for seismic performance in fixed platforms, in accordance with the American Society of Civil Engineers (ASCE), the Federal Emergency Management Agency (FEMA) and the National Institute of Building Science (NIBS) seismic design guidelines (ASCE, 2007; FEMA 350, 2000; FEMA 351, 2000; NIBS, 1999). The NIBS damage state definitions for steel moment frames (from which FSJ platforms are largely constructed) are provided in Tab. 8.0. The seismic demand (the structural response resulting from a given level of ground-motion intensity) was defined in terms of the maximum inter-level drift ratio (IDR), and the ground-motion intensity was characterised in terms of SA, with a spectral period corresponding to  $T_1 = \sim 2$  s. These fragility curves incorporate the site effects resulting from the marine environment through consideration of the interaction between the seafloor (soil) foundations and the pile structures (which attach the FSJ platforms to the soil foundations – Fig. 8.3) within the analytical model considered in the non-linear dynamic analyses. An important advantage offered by the Ajamy et al. (2018) fragility curves is that for each damage state, the aleatory uncertainty and the epistemic uncertainty associated with estimating the seismic demand for a given level of ground-motion intensity are considered. The aleatory uncertainty is associated with the inherent randomness in ground-shaking, structural capacity and soil-pile structure interaction, and the epistemic uncertainty is associated primarily with analytical model selection within non-linear dynamic analysis.

The fragility curves of Zarrin et al. (2017) are appropriate due to characterising the seismic demand in terms of maximum inter-story drift ratio, the ground-motion intensity in terms of SA, and having considered a (complete) collapse damage state ( $DS_{Z17}$ ), with the collapse damage state being defined in terms of seismic performance using the FEMA 351 (2000) seismic performance guidelines. The spectral ordinate considered within the characterisation of the ground-motion as SA is not explicitly stated, but due to corresponding to  $T_1$  for FSJ platforms can be assumed to be reasonably similar to that considered by Ajamy et al. (2018).

**Table 8.0** *Damage state definitions for steel moment frames as defined by the National Institute of Building Science.* The final damage state, “ultimate collapse” is not defined within these guidelines but is considered by Ajamy et al. (2018) for FSJ platforms, and so is listed here. Taken from NIBS (1999).

Damage State	Definition	Damage State Abbreviation
Slight structural damage	Minor deformations in connections or hairline cracks in few welds.	DS1 <sub>A18</sub>
Moderate structural damage	Some steel members have yielded exhibiting observable permanent rotations at connections; few welded connections may exhibit major cracks through welds or few bolted connections may exhibit broken bolts or enlarged bolt holes.	DS2 <sub>A18</sub>
Extensive structural damage	Most steel members have exceeded their yield capacity, resulting in significant permanent lateral deformation of the structure. Some of the structural members or connections may have exceeded their ultimate capacity exhibited by major permanent member rotations at connections, buckled flanges and failed connections. Partial collapse of portions of structure is possible due to failed critical elements and/or connections.	DS3 <sub>A18</sub>
Complete structural damage	Significant portion of the structural elements have exceeded their ultimate capacities or some critical structural elements or connections have failed resulting in dangerous permanent lateral displacement, partial collapse or collapse of the building.	DS4 <sub>A18</sub>
Ultimate Collapse	Collapse of the entire structure due to considerable reductions in stiffness and strength (Yeter et al., 2020).	DS5 <sub>A18</sub>

For (5-MW) offshore wind turbines, fragility curves have been developed by (1) Mo et al. (2017) and (2) Kim et al. (2014), and therefore are considered here (Fig. 8.6b). For the Mo et al. (2017) fragility curves, four damage states (Tab. 8.1) were defined for 6 sets of operating conditions (see Table 8 of Mo et al., 2017), which consider the seismic demand in terms of displacement at the nacelle (the nacelle is the cover which houses the power generating components), rotation at the tower top and stress at the transition piece of a 5-MW wind turbine (Fig. 8.4). The ground-motion intensity was characterised in terms of PGA. Here, the damage states under the most demanding operational conditions (wind speed = 24 m/s, turbine state = normal operations) were considered. As for the FSJ fragility curves developed by Ajamy et al. (2018), the fragility curves of Mo et al. (2017) account for offshore site effects, with this being through consideration of the interaction between seafloor foundations and the monopile structure within the analytical model considered in the non-linear dynamic analyses. The fragility curves of Kim et al. (2014) are appropriate due to having been developed specifically for 5-MW wind turbines, having characterised the ground-motion intensity in terms of PGA and having considered allowable stress and yield stress damage states (DS1<sub>K14</sub> and DS2<sub>K14</sub> respectively – albeit for stress in the tower component rather than the transition piece) and allowable displacement and yield displacement of the nacelle damage states (DS3<sub>K14</sub> and DS4<sub>K14</sub> respectively) (Tab. 8.1).

The allowable and yield stress values for the corresponding damage states from the Mo et al. (2017) and Kim et al. (2014) studies are noticeably different. For example, the Mo et al. (2017) yield stress state requires a stress of 305 MPa, whereas the Kim et al. (2014) yield stress state requires a stress of 408 MPa (Tab. 8.1). These differing yield stress values can be largely explained by being for different (albeit structurally proximal) parts of a 5-MW wind turbine (Fig. 8.4). The critical responses for the

(allowable) nacelle displacement damage states are more similar ( $DS1_{M17} = 2.08$  m vs.  $DS3_{K14} = 2.04$  m) than for  $DS3_{M17}$  vs  $DS1_{K14}$  and  $DS4_{M17}$  vs  $DS2_{K14}$  due to considering the same part of a 5-MW wind turbine. Therefore, direct comparison between  $DS1_{M17}$  and  $DS3_{K14}$  is a more suitable for evaluating how consideration of different fragility curves influences the seismic risk to 5-MW wind turbines in the North Sea (see below) than the other comparable damage states.

**Table 8.1** Damage state definitions for a 5-MW offshore wind turbine. M17 = Mo et al. (2017). K14 = Kim et al. (2014).

Damage State Abbreviation	Critical Response	Description
$DS1_{M17}$	2.08 m	1.25%H Nacelle displacement
$DS2_{M17}$	$2.5^\circ$	$2.5^\circ$ Rotation at tower top
$DS3_{M17}$	250 MPa	Allowable stress at the transition piece
$DS4_{M17}$	305 MPa	Yield stress at the transition piece
$DS1_{K14}$	204 MPa	Allowable stress
$DS2_{K14}$	408 MPa	Yield stress
$DS3_{K14}$	2.04 m	Allowable (nacelle) displacement
$DS4_{K14}$	4.30 m	Yield (nacelle) displacement

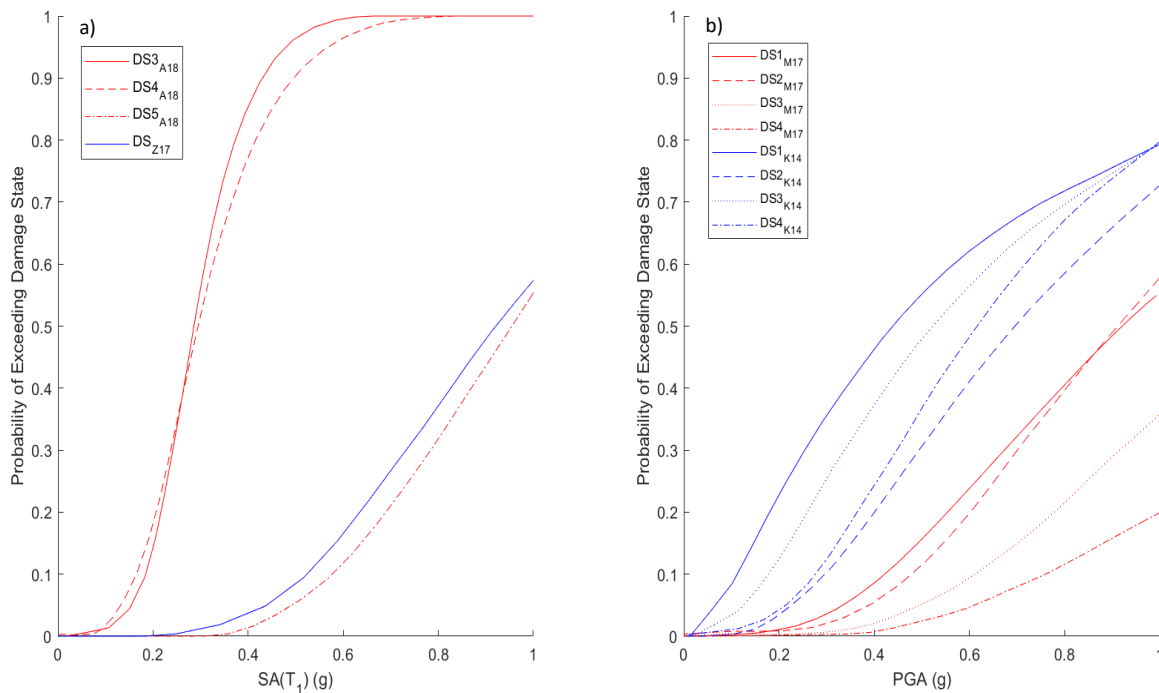


**Figure 8.6** Considered fragility curves for (a) FSJ platforms and (b) 5-MW offshore wind turbines.

### 8.3 Convolution of Seismic Hazard and Seismic Fragility

The convolution of the fragility curves for each considered type of structure with the North Sea seismic hazard estimates permits the computation of the corresponding seismic risk in terms of the (mean) annual frequency of exceeding (AFOE) each damage state (Kennedy and Short, 1994; Cornell, 1996;

Cornell et al., 2002). The reciprocal of the AFOE for each damage state is the damage return period (DRP).

Here, the improved North Sea PSHA calculations are used to provide estimates of the seismic hazard in the region. Seismic hazard curves are computed for two North Sea sites (Fig. 8.7). Both of these sites are located along coastal Norway (Fig. 8.5), and lie adjacent to the Viking Graben, along which many platforms are situated due to geological faults facilitating hydrocarbon production (Pang et al., 2003), whilst also being situated in shallow water depths which are appropriate for the construction of 5-MW wind turbines (in the northern North Sea – again see Fig. 8.5). Here, two ground-motion models (GMMs) are considered: (1) the Bungum et al. (2000) GMM and (2) the Joyner-Boore distance ( $R_{jb}$ ) variant of the Akkar et al. (2014) ground-motion prediction equation (GMPE), which was identified as the base model for a new North Sea GMPE<sup>67</sup>. For each GMM, hazard estimates are calculated from PSHAs using (1) the original parameters for the Bungum et al. (2000) North Sea source zone model and (2) the updated parameters for the same source zone model computed in Chapter 7. The improved seismic hazard estimates were computed using the Akkar et al. (2014) GMPE and the updated source zone parameters, with this PSHA formulation henceforth being referred to as AK2014<sub>Upd</sub>. The original seismic hazard estimates were computed using the Bungum et al. (2000) GMM and the original source zone parameters, with this PSHA formulation henceforth being referred to as B2000<sub>Orig</sub>. Comparison of the AK2014<sub>Upd</sub> and B2000<sub>Orig</sub> PSHA formulations will demonstrate the impact of the improved North Sea PSHA calculations on seismic risk estimates for the region.

The convolution of the seismic hazard and the seismic fragility information to provide the mean AFOE for each damage state,  $\lambda_{DS}$  can be expressed using the total probability theorem (Benjamin and Cornell, 1970; Cornell et al., 2002):

$$\lambda_{DS} = \int P(DS|x) * |dH(x)| \quad (8.0)$$

where the first element  $P(DS|x)$  is the probability of exceeding the damage state,  $DS$  for a given level of ground-motion intensity  $x$ , and the second term  $|dH(x)|$  is the absolute value of the derivative of the site's seismic hazard curve (see Cornell et al., 2002 for more detail on the probabilistic basis for equation 8.0). The first element  $P(DS|x)$  is provided by the fragility curve. The mean AFOEs for each damage state are provided in Tab. 8.2 for FSJ platforms and Tab. 8.3 for 5-MW wind turbines.

---

<sup>67</sup> See Chapter 7 for more details on the reassessment of the Bungum et al. (2000) source model parameters and chapters 3 - 4 for more details on the identification and development of this North Sea GMPE.

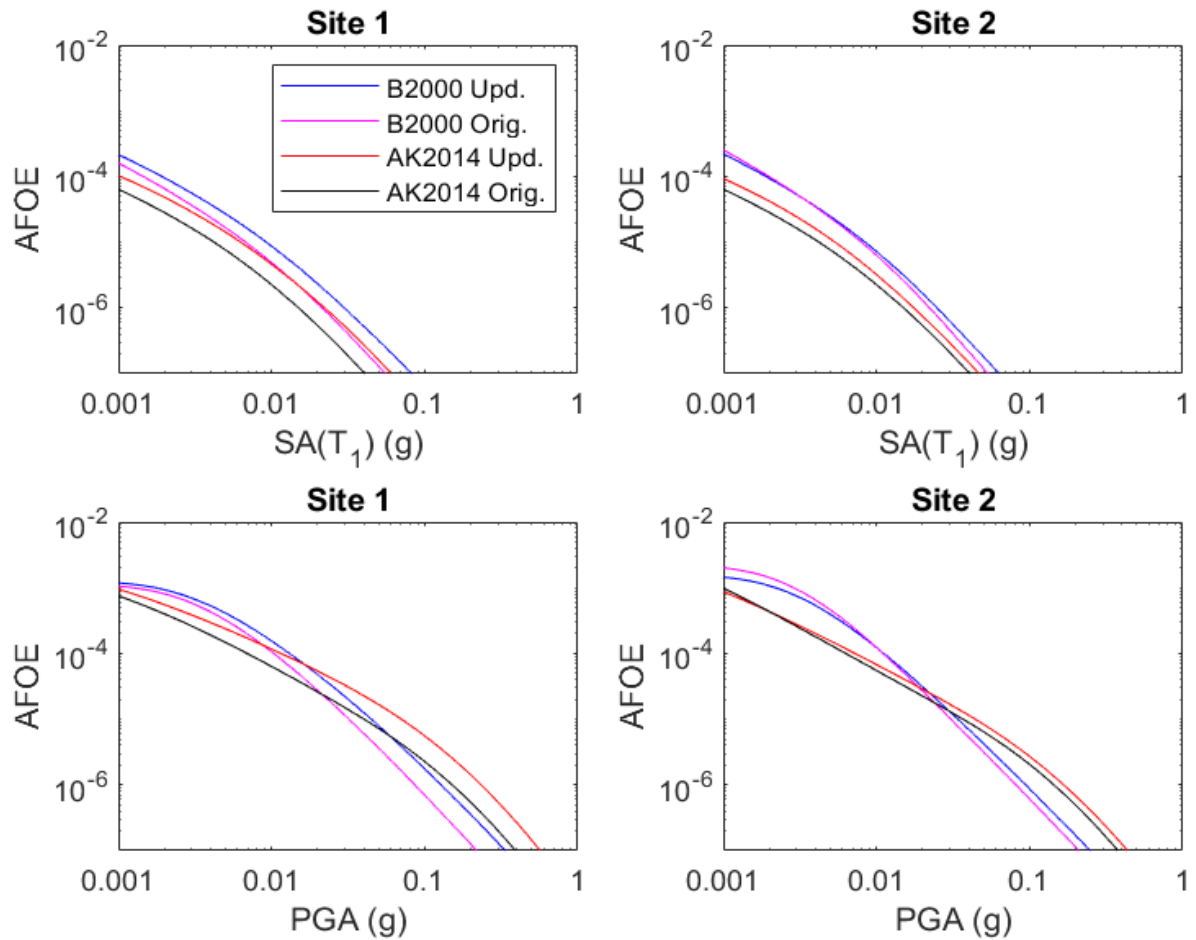


**Figure 8.7** Seismic hazard curves for sites in the North Sea. B2000 = Bungum et al. (2000) GMM. AK2014 = Akkar et al. (2014) GMPE. Upd. = updated source zone parameters. Orig. = original source zone parameters.

**Table 8.2** Mean AFOEs for each damage state considered for FSJ platforms in the North Sea.

Damage State	B2000 <sub>Orig</sub> for Site 1	AK2014 <sub>Upd</sub> for Site 1	B2000 <sub>Orig</sub> for Site 2	AK2014 <sub>Upd</sub> for Site 2
DS3 <sub>A18</sub>	3.21E-04	1.78E-04	5.73E-04	1.70E-04
DS4 <sub>A18</sub>	1.24E-04	6.73E-05	2.14E-04	6.27E-05
DS5 <sub>A18</sub>	8.76E-06	4.98E-06	1.46E-05	4.57E-06
DS <sub>Z17</sub>	1.33E-05	7.51E-06	2.21E-05	6.90E-06

**Table 8.3** Mean AFOEs for each damage state considered for 5-MW wind turbines in the North Sea.

Damage State	B2000 <sub>Orig</sub> for Site 1	AK2014 <sub>Upd</sub> for Site 1	B2000 <sub>Orig</sub> for Site 2	AK2014 <sub>Upd</sub> for Site 2
DS1 <sub>M17</sub>	7.82E-06	4.83E-05	1.93E-05	6.06E-05
DS2 <sub>M17</sub>	7.69E-06	4.35E-05	1.90E-05	5.40E-05
DS3 <sub>M17</sub>	2.85E-06	1.54E-05	7.03E-06	1.90E-05
DS4 <sub>M17</sub>	1.49E-06	8.69E-06	3.68E-06	1.08E-05
DS1 <sub>K14</sub>	7.19E-05	6.29E-04	1.79E-04	8.13E-04
DS2 <sub>K14</sub>	5.07E-05	2.62E-04	1.25E-04	3.21E-04
DS3 <sub>K14</sub>	6.77E-05	4.97E-04	1.68E-04	6.32E-04
DS4 <sub>K14</sub>	5.96E-05	3.58E-04	1.47E-04	4.42E-04

#### 8.4 Results for Convolution of Seismic Hazard and Seismic Fragility

The convolving of the seismic hazard and seismic fragility information results in mean AFOEs that are small compared to those available in the literature for the same fragility information and different seismic hazard curves. For example, Ajamy et al. (2018) computed a mean AFOE for DS5<sub>A18</sub> for an FSJ platform in the Persian Gulf of 3.42E-04, corresponding to a DRP of 2925 years. Within this investigation the mean AFOEs for DS5<sub>A18</sub> range from 4.57E-06 to 1.46E-05, result in DRPs of ranging from ~70,000 years to ~220,000 years. These larger DRPs suggest that the engineering risk for FSJ platforms located in the North Sea is far lower than for FSJ platforms in the Persian Gulf. The larger DRPs computed here for DS5<sub>A18</sub> can be attributed to the estimates of North Sea seismic hazard (Fig. 8.7) used here being considerably lower than Ajamy et al. (2018)'s estimates of seismic hazard in the Persian Gulf (see Fig. 3 for their Persian Gulf location hazard curve). Despite the AFOEs for each damage state being lower than those available in the literature due to the limited seismic hazard in the North Sea, these values are in good agreement with those expected for the countries bordering the region, as reported by Gkimpraxis et al. (2020), who report mean AFOEs for a collapse damage state (in a four storey concrete reinforced building) in the United Kingdom and northwestern Europe of less than or equal to 1E-06, and of 1.1E-05 to 5E-05 for Norway (see Figure 10 of Gkimpraxis et al., 2020 for more details).

The relative magnitudes of the mean AFOEs for each damage state are largely as expected i.e. the more severe damage states have lower mean AFOEs than the less severe damage states. This pattern is representative of more severe damage states having lower probabilities of being exceeded for a given level of ground-motion intensity (i.e. the area under a fragility curve integrated within equation 8.0 is smaller for a more severe damage state), and is observed for all considered PSHA formulations. For

FSJ platforms, the largest mean AFOEs are for DS3<sub>A18</sub>, followed by DS4<sub>A18</sub>, DS<sub>Z17</sub> and then DS5<sub>A18</sub>. For 5-MW wind turbines, the mean AFOEs are larger for the allowable stress states (DS3<sub>M17</sub>, DS1<sub>K14</sub>) than for the yield stress states (DS4<sub>M17</sub>, DS2<sub>K14</sub>).

It should also be noted that reasonably similar mean AFOEs are computed for similar damage states. For example, for the ultimate collapse states for FSJ platforms (DS5<sub>A18</sub>, DS<sub>Z17</sub>) and the allowable stress states (DS3<sub>M17</sub>, DS1<sub>K14</sub>) and yield stress states (DS4<sub>M17</sub>, DS2<sub>K14</sub>) for 5-MW wind turbines, similar (within approximately 1 order of magnitude) mean AFOEs are observed. The ultimate collapse states for FSJ platforms (DS5<sub>A18</sub>, DS<sub>Z17</sub>) are the most similar, which can be attributed to the corresponding fragility curves being more similar than the curves for the other comparable damage states (Fig. 8.6). The seismic risk (in terms of mean AFOE for each damage state) is inherently influenced by the selected fragility curve, but the similar results for approximately equivalent damage states computed here demonstrates that comprehensive analytical modelling of (offshore) infrastructure can result in similar seismic risk estimates.

Most importantly, the chosen PSHA calculations influences the mean AFOEs for each damage state. As would be expected, the seismic hazard at each site varies due to the influence of path and site effects (Sanchez-Sesma, 1987) and the selection of the source model and GMM. Therefore, the mean AFOE for each damage state will also vary with each site with consideration of different PSHA calculations.

For FSJ platforms at both site 1 and site 2, the mean AFOEs for all damage states computed using the AK2014<sub>Upd</sub> calculations are marginally smaller (although within 1 order of magnitude) than those computed using the B2000<sub>orig</sub> calculations. For 5-MW wind turbines at both site 1 and site 2, the mean AFOEs for all damage states computed using the AK2014<sub>Upd</sub> calculations are marginally larger (although again within 1 order of magnitude) than those computed using the B2000<sub>orig</sub> calculations. This suggests that (the considered fragility curves of) 5-MW wind turbine are potentially more vulnerable to the levels of ground-motion intensity for which the AK2014<sub>Upd</sub> hazard curves provide higher AFOEs than (the considered fragility curves of) FSJ platforms are (compared to if the B2000<sub>orig</sub> calculations are considered instead).

Overall, the impact of the AK2014<sub>Upd</sub> calculations leads to either marginal increases or decreases in the mean AFOEs for each damage state at the considered sites, with the occurrence of an increase or decrease being dependent on the considered infrastructure. The decreases in the mean AFOEs for FSJ platform damage states resulting from the AK2014<sub>Upd</sub> calculations suggests that the assessed seismic risk for FSJ platforms generally decreases at appropriate locations (for their construction/operation in the northern North Sea) compared to when the original PSHA calculations of Bungum et al. (2000) are implemented. The increases in the mean AFOEs for 5-MW wind turbine damage states resulting from AK2014<sub>Upd</sub> calculations suggests the assessed seismic risk generally increases for 5-MW wind turbines compared to when the original PSHA calculations are considered.

## 8.5 Consideration of the Maximum Credible Earthquake in the North Sea

The 1931 Dogger Bank is the largest recorded earthquake in the North Sea region with a local magnitude ( $M_L$ ) of 6.1 (Ritsema and Gürpınar, 1983). Earthquakes of a similar size are too infrequent in the North Sea region for their annual recurrence rate to be well estimated (Mallard et al., 2003). Therefore, the seismic risk associated with a similar North Sea earthquake is considered within a deterministic (as opposed to probabilistic) seismic hazard scenario to provide a consideration of the maximum credible earthquake (MCE – see Baker, 2015) in the region i.e. determine the seismic hazard assuming such an earthquake has occurred. The expected ground-shaking in terms of PGA and SA for feasible sites (for the deployment of either an FSJ platform or a 5-MW wind turbine) at select distances from an earthquake similar to the 1931 Dogger Bank earthquake has been computed using the Akkar et al. (2014) GMPE (Fig. 8.8; Tab. 8.4). The probabilities for each damage state resulting from these estimated levels of ground-motion intensity are discussed below. The source parameters for the considered earthquake are as follows:  $M_L = 6.5$ , focal depth = 20 km. An  $M_L$  of 6.5 is chosen to provide a credible maximum size for a North Sea earthquake. For each site a shear-wave velocity in the upper 30 m of the subsurface ( $V_{S30}$ ) of 600 m/s is assumed. Setting  $V_{S30} = 600$  m/s is appropriate based on site investigations for offshore North Sea sites undertaken by Rognlien (1987)<sup>68</sup>. The Akkar et al. (2014) GMPE considers moment magnitude ( $M_w$ ), as opposed to  $M_L$ , but for small to moderate size earthquakes (as are expected in the North Sea),  $M_w$  and  $M_L$  can generally be treated as approximately equal (Kramer et al., 2014).

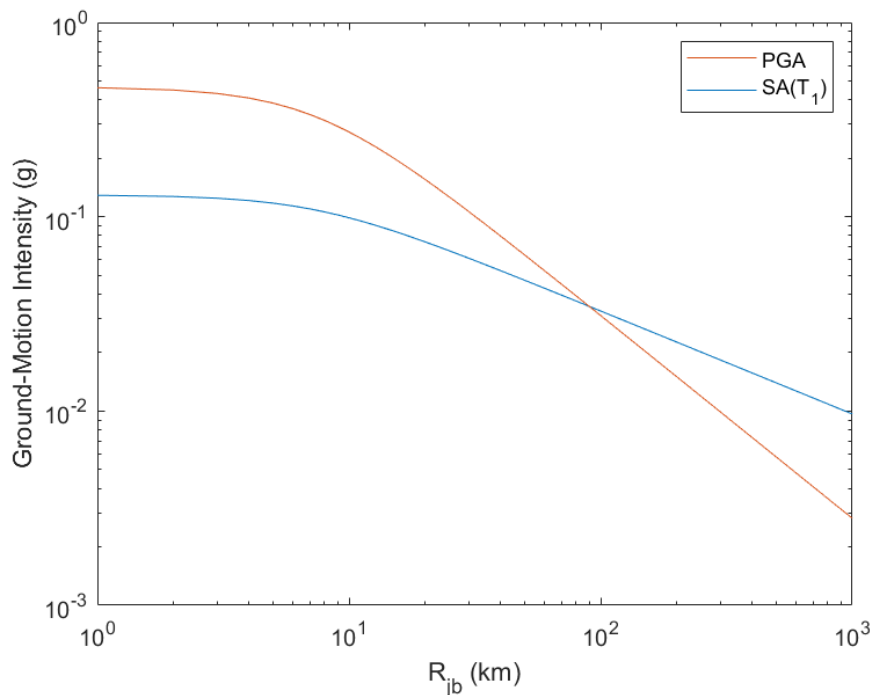


**Figure 8.8** Ground-motion intensity vs.  $R_{jb}$  for an  $M_L$  6.5 earthquake using the Akkar et al. (2014) GMPE.

<sup>68</sup> See Chapter 4 for the computation of offshore site response in the North Sea using the subsurface site profiles provided by Rognlien (1987).

**Table 8.4** Ground-motion intensities at select distances for an  $M_L$  6.5 earthquake using the Akkar et al. (2014) GMPE. GMIM = ground-motion intensity measure.

GMIM (g)	$R_{jb} = 1$ km	$R_{jb} = 25$ km	$R_{jb} = 50$ km	$R_{jb} = 100$ km	$R_{jb} = 200$ km
PGA	0.461	0.127	0.063	0.031	0.015
SA( $T_1$ )	0.129	0.067	0.047	0.033	0.023

Based on the ground-motion intensities predicted using the Akkar et al. (2014) GMPE (Tab. 8.4) the seismic risk for FSJ platforms is only significant if the MCE for the North Sea occurs almost directly beneath the platform. For example, the probability of exceeding  $DS_{3A18}$  or  $DS_{4A18}$  is considerably high (both  $> 85\%$ ) if the MCE occurs at a (source-to-site) distance of 1 km, but if the MCE occurs at a distance of 25 km, the probabilities for the same damage states are both less than 5% (Tab. 8.5). This suggests that FSJ platforms in the North Sea are only seismically vulnerable in this scenario if the MCE for the region occurs in close proximity ( $R_{jb} < 25$  km) to the platform. For 5-MW wind turbines in the North Sea, the probabilities of exceedance given the occurrence of an MCE are only significant ( $> 5\%$ ) for  $DS_{1K14}$  at distances of 1 km and 25 km, suggesting that 5-MW wind turbines are considerably resilient to the ground-shaking expected from an MCE in the North Sea, even if occurring in immediate proximity to structure.

The greater probabilities of exceedance for the FSJ platform damage states than for the 5-MW damage states appear to suggest that 5-MW wind turbines are considerably more seismically resilient than FSJ platforms. However, this is specifically the seismic resilience for the ground-shaking resulting from an MCE in the North Sea. Aside from for  $DS_{1K14}$ , the probabilities of exceedance for each 5-MW damage state are generally very small ( $< 1\%$ ) below  $\sim 0.2$  g. The ground-shaking (in terms of PGA) resulting from an MCE in the North Sea are below this threshold of  $\sim 0.2$  g for all considered distances (Tab. 8.4). Therefore, for scenarios in which larger levels of (PGA) ground-shaking are expected (i.e. regions with greater seismic hazard), the comparative differences in the seismic resilience of FSJ platforms and 5-MW wind turbines will potentially be different.

**Table 8.5** Probability of exceeding each FSJ damage state (PoE) for the expected SA at each site from an  $M_L$  6.5 earthquake using the Akkar et al. (2014) GMPE.

Damage State	PoE ( $R_{jb} = 1$ km)	PoE ( $R_{jb} = 25$ km)	PoE ( $R_{jb} = 50$ km)	PoE ( $R_{jb} = 100$ km)	PoE ( $R_{jb} = 200$ km)
$DS_{3A18}$	$\sim 94\%$	$\sim 2\%$	$> 1\%$	$> 1\%$	$> 1\%$
$DS_{4A18}$	$\sim 86\%$	$\sim 3\%$	$> 1\%$	$> 1\%$	$> 1\%$
$DS_{5A18}$	$\sim 4\%$	$> 1\%$	$> 1\%$	$> 1\%$	$> 1\%$
$DS_{Z17}$	$\sim 5\%$	$> 1\%$	$> 1\%$	$> 1\%$	$> 1\%$

**Table 8.6** Probability of exceeding each 5-MW wind turbine damage state (PoE) for the expected PGA at each site from an  $M_L$  6.5 earthquake using the Akkar et al. (2014) GMPE.

Damage State	PoE ( $R_{jb} = 1$ km)	PoE ( $R_{jb} = 25$ km)	PoE ( $R_{jb} = 50$ km)	PoE ( $R_{jb} = 100$ km)	PoE ( $R_{jb} = 200$ km)
DS1 <sub>M17</sub>	> 1%	> 1%	> 1%	> 1%	> 1%
DS2 <sub>M17</sub>	> 1%	> 1%	> 1%	> 1%	> 1%
DS3 <sub>M17</sub>	> 1%	> 1%	> 1%	> 1%	> 1%
DS4 <sub>M17</sub>	> 1%	> 1%	> 1%	> 1%	> 1%
DS1 <sub>K14</sub>	~ 10%	~ 5%	~ 3%	~ 1%	> 1%
DS2 <sub>K14</sub>	> 1%	> 1%	> 1%	> 1%	> 1%
DS3 <sub>K14</sub>	~ 3%	~ 2%	~ 1%	> 1%	> 1%
DS4 <sub>K14</sub>	~ 1%	> 1%	> 1%	> 1%	> 1%

## 8.6 Consideration of the 2001 Ekofisk Earthquake

The unintentional injection of large volumes of water into the overburden of the Ekofisk field's reservoir resulted in an  $M_L$  4.2 earthquake, with the ground-shaking from this earthquake being strongly felt on the Ekofisk platforms despite no physical damage being observed (Ottemöller et al., 2005; see Chapter 2 for an overview of the Ekofisk earthquake). Considering that no physical damage was observed for FSJ platforms in the vicinity of the Ekofisk earthquake, comparison of the probabilities of exceeding each FSJ damage state (given the occurrence of an  $M_L$  4.2 earthquake) to this observation will prove insightful as to how appropriate the considered FSJ fragility curves are for platforms in the North Sea. As for the MCE scenario, the expected ground-shaking has been computed using the Akkar et al. (2014) GMPE for select distances (Fig. 8.9; Tab. 8.7).

**Table 8.7** Ground-motion intensities at select distances for an  $M_L$  4.2 earthquake using the Akkar et al. (2014) GMPE. GMIM = ground-motion intensity measure.

GMIM (g)	$R_{jb} = 1$ km	$R_{jb} = 25$ km	$R_{jb} = 50$ km	$R_{jb} = 100$ km	$R_{jb} = 200$ km
PGA	5.17E-02	5.04E-03	1.46E-03	4.02E-04	1.10E-04
SA( $T_1$ )	8.46E-04	1.56E-04	6.33E-05	2.48E-05	9.67E-06

The probabilities of exceedance for all FSJ damage state given the occurrence of an  $M_L$  4.2 earthquake are very small (< 1% - Tab. 8.8). These very small probabilities of exceedance (even for DS3<sub>A18</sub> - the least severe FSJ damage state) are in good agreement with the lack of no (observed) physical damage for platforms in the immediate vicinity of the Ekofisk earthquake. This is suggestive of the FSJ fragility curves being appropriate for modelling the seismic risk for platforms in the North Sea.

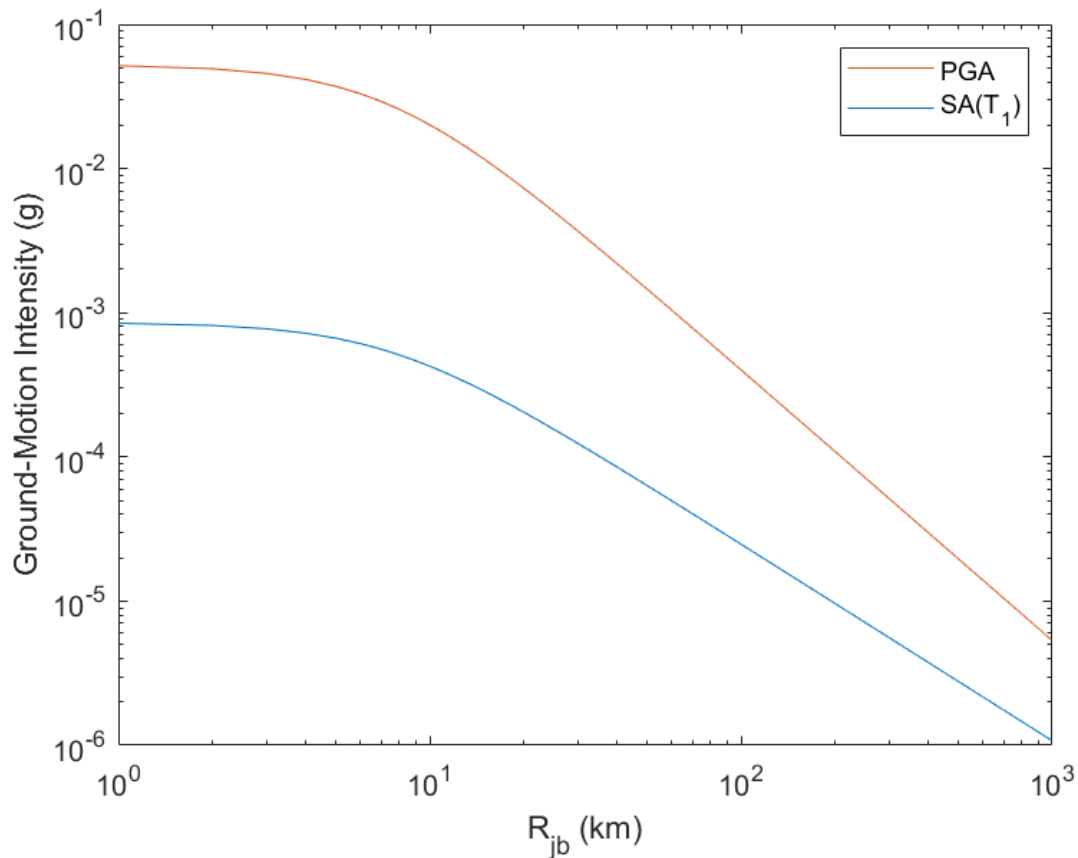


**Figure 8.9** Ground-motion intensity vs.  $R_{jb}$  for an  $M_L$  4.2 earthquake using the Akkar et al. (2014) GMPE.

**Table 8.8** Probability of exceeding each FSJ damage state (PoE) for the expected PGA at each site from an  $M_L$  4.2 earthquake using the Akkar et al. (2014) GMPE.

Damage State	PoE ( $R_{jb} = 1$ km)	PoE ( $R_{jb} = 25$ km)	PoE ( $R_{jb} = 50$ km)	PoE ( $R_{jb} = 100$ km)	PoE ( $R_{jb} = 200$ km)
DS3 <sub>A18</sub>	> 1%	> 1%	> 1%	> 1%	> 1%
DS4 <sub>A18</sub>	> 1%	> 1%	> 1%	> 1%	> 1%
DS5 <sub>A18</sub>	> 1%	> 1%	> 1%	> 1%	> 1%
DS <sub>Z17</sub>	> 1%	> 1%	> 1%	> 1%	> 1%

### 8.7 Conclusions for Assessing the Seismic Risk for Critical Infrastructure in the North Sea

Here, North Sea PSHA calculations were convolved with appropriate fragility curves to compute the seismic risk present to offshore infrastructure in the North Sea. The seismic risk present in the North Sea was found to decrease for FSJ platforms and increase for 5-MW wind turbines when the updated PSHA formulation for the region was implemented rather than the PSHA formulation of Bungum et al. (2000). For FSJ platforms, the occurrence of an MCE is only of significance in terms of seismic resilience if the MCE occurs close to the platform. For 5-MW wind turbines, the occurrence of an MCE

only provides significant probabilities of exceedance for the least severe damage state ( $DS1_{K14}$ ) at small source-to-site distances. The very small probabilities of exceedance for the FSJ platform damage states given the occurrence of an ML 4.2 earthquake are suggestive of the considered fragility curves being good representations of the seismic risk for platforms in the North Sea. In conclusion, when the updated North Sea seismic hazard estimates are considered, the seismic risk increases for 5-MW wind turbines and decreases for FSJ platforms, but 5-MW wind turbines are more seismically resilient than FSJ platforms in the instance of a “worst case” earthquake.

## 9.0 Conclusions for Reassessment of North Sea Seismic Hazard and Potential Future Work

Within this investigation North Sea probabilistic seismic hazard assessment (PSHA) was reassessed. This reassessment was in light of (1) the availability of additional ground-motion data, (2) significant PSHA advancements and (3) the determined engineering significance of the 2001 Ekofisk event (and its implications for the potentially evolving state of induced seismicity in the North Sea) since the most recent publically available North Sea PSHA by Bungum et al. (2000).

This reassessment of North Sea PSHA comprised of: (1) identifying an appropriate existing ground-motion prediction equation (GMPE) for use in the North Sea, (2) improving the performance of this base GMPE through relaxation of the ergodic assumption with respect to path and site effects, (3) the improvement of the Bungum et al. (2000) seismogenic source model and (4) evaluation of the updated PSHA formulation using macroseismic data.

The base model GMPE (the  $R_b$  variant of Akkar et al., 2014) was identified using ground-motion residual analysis (Tab. 3.8). The relaxation of the ergodic assumption with respect to path and (onshore) site effects resulted in small but significant improvements to the performance of the base model GMPE in the North Sea.

To relax the ergodic assumption with respect to site, k-means clustering and principal component analysis were used to constrain North Sea site effects, resulting in the computation of cluster amplification functions for onshore sites in the region with similar geotechnical conditions. These cluster amplification functions provide moderate but significant reductions in the site-to-site variability for the expected ground-motions incident at onshore sites in the North Sea (Fig. 4.4), thus improving the performance of the base model GMPE in the region.

To relax the ergodic assumption with respect to path, a tomographic inversion analysis was used to better constrain North Sea path effects. Through better constraining path effects, a small but significant and consistent reduction in the variability of the intra-event GMPE residuals was observed over each considered spectral period (Fig. 4.13). The validity of these reductions was supported by statistical tests in the form of a checkerboard reconstruction analysis and the replication of similar path effects using random segments of the same input dataset. The constrained path effects were successfully implemented as path corrections for forward modelling through the modification of a Monte Carlo PSHA program, and resulted in varied but reasonable impacts on the predicted intensities of ground-shaking (Fig. 4.18; Fig. 4.19).

The validity of the improvements to the base model GMPE undertaken in this investigation are inherently limited by the small size of the considered ground-motion dataset, but this is well accounted for through (1) the use of only 2 clusters in the computation of cluster amplification functions and (2) a low resolution grid within the tomographic inversion analysis. These challenges highlight the

difficulties associated with GMPE development in regions with small to moderate seismicity (where fewer ground-motions are observed than in more seismically active regions).

The seismogenic source model of Bungum et al. (2000) was updated using 20 years of additional earthquake observations. The updated source model was found to have a varied impact on the predicted ground-shaking within PSHA calculations, with moderate yet significant differences being observed for the considered sites compared to when the original source model was used (Fig. 7.6). The consideration of 20 years of additional earthquake observations suggests that this source model better captures the seismicity present in the North Sea, and therefore could replace the Bungum et al. (2000) source model.

An updated North Sea PSHA formulation (comprising of the Akkar et al., 2014 GMPE and the updated source model) was evaluated using macroseismic data. A kriging-with-a-trend technique was used to generate additional macroseismic data so as to provide comparative seismic hazard curves for each considered site. The annual frequencies of exceedance for a given intensity of ground-shaking were generally greater for those computed from the macroseismic data than from the PSHA formulations, but the PSHA formulation with the Akkar et al. (2014) GMPE provides more similar results (overall) to the macroseismic data than the PSHA formulations which use the other considered GMPEs (Fig. 7.10).

The updated North Sea PSHA calculations were also found to influence the (assessed) seismic risk for critical infrastructure deployed in the region. The updated hazard estimates were convolved with appropriate fragility curves to compute mean annual frequencies of exceeding predefined damage states. The seismic risk was found to decrease for offshore platforms and increase for offshore wind turbines when the updated hazard estimates were used rather than the Bungum et al. (2000) hazard estimates (Tab. 8.2; Tab. 8.3). The ground-shaking resulting from (1) a maximum credible earthquake (MCE) in the North Sea ( $M_L$  6.5) and (2) an earthquake similar to the 2001 Ekofisk earthquake were estimated using the base model GMPE. For offshore platforms the occurrence of an MCE resulted in significant probabilities of exceedance for most of the considered damage states if the MCE occurred in immediate proximity to the platform (Tab. 8.5). For offshore wind turbines the probabilities of exceedance were also only noticeable for the smallest source-to-site distances, although only for the least severe damage state (Tab. 8.6). In summary, the updated North Sea seismic hazard estimates result in increases to the seismic risk for offshore wind turbines and decreases for offshore platforms, but offshore wind turbines are more seismically resilient than offshore platforms in the instance of an MCE in the North Sea. It should also be noted that the very small ( $< 1\%$ ) probabilities of exceedance for the platform damage states given the occurrence of an earthquake similar to the 2001 Ekofisk earthquake (Tab. 8.8) suggest that the offshore platform fragility curves appropriately model the seismic risk for platforms in the North Sea.

## 9.1 Potential Future Work for the Reassessment of North Sea Seismic Hazard

North Sea PSHA has been thoroughly reassessed in this investigation. A large part of this reassessment has focussed on the development of a North Sea GMPE. A lack of readily-available data inherently limited the scope of this analysis. For the North Sea GMPE, the processed ground-motion dataset contained few near-source ( $< 50$  km source-to-site distance) or larger magnitude ( $M_L > 4.0$ ) records due to the limited offshore seismic monitoring in the region. This lack of large magnitude, offshore records increased the uncertainty associated with evaluating each GMPE's performance for predicting higher levels of seismic hazard in the North Sea. Furthermore, the considered ground-motion dataset is limited to magnitudes below those which are of high interest in PSHA for offshore infrastructure in the North Sea. The constraints of the considered dataset therefore represent a significant weakness in the GMPE testing procedure. To improve the evaluation and development of GMPEs in the North Sea, more high quality ground-motion data for large magnitude, small source-to-site distance earthquakes are therefore required. This provides impetus for the installation of more accelerometers on the North Sea seabed, so as to improve seismic monitoring in the region and thus facilitate North Sea GMPE development. The installation of more seabed accelerometers could also potentially result in ground-motions from earthquakes induced by hydrocarbon production in the North Sea being recorded. This would aid the development of a North Sea GMPE developed specifically for the prediction of ground-motions from earthquakes induced by hydrocarbon production. The development of a North Sea GMPE for hydrocarbon production induced seismicity would improve the prediction of ground-shaking resulting from an earthquake similar to the 2001 Ekofisk earthquake, which was deemed to be of engineering significance for offshore infrastructure in the North Sea by Ottemöller et al. (2005) and a driving force for the reassessment of North Sea PSHA in this investigation.

As discussed above, the limited size of the ground-motion dataset also influenced the resolution of the grid considered within the tomographic inversion analysis undertaken to constrain North Sea path effects. An expanded North Sea ground-motion dataset (achieved through the installation of seabed accelerometers) would enable the resolution of this grid to be increased, and therefore constrain smaller particularities in North Sea attenuation. This would help to further relax the ergodic assumption with respect to path, and thus further improve North Sea seismic hazard estimates.

Improved seismic monitoring of the North Sea seabed would also provide (additional) offshore sites for clustering in the Kotha et al. (2018) site classification method. The lack of geotechnical information for (onshore) North Sea sites highlighted the requirement of abundant *a posteriori* information to maximise the usefulness of the Kotha et al. (2018) site classification method. Through the inclusion of offshore sites in the clustering and geotechnical information for each site, the cluster amplification functions could be applied to both onshore and offshore sites in the North Sea which were not included in the original analysis, and for which no ground-motions have been observed to be assigned the appropriate cluster amplification function, therefore significantly expanding the applicability and effectiveness of

these site effect corrections. These site effect corrections could then be implemented within the modified Monte Carlo PSHA program which the path effect corrections have already been incorporated within. The provision of geotechnical information for offshore sites would also mean the Rognlien (1987) site transfer functions could potentially be implemented too. In summary, considerable advancements in the constraining of North Sea site effects could be accomplished if geotechnical information was acquired for each (accelerometer) site in the region.

## **9.2 Concluding Remarks for Investigation**

In this investigation the seismic hazard in the North Sea was comprehensively reassessed, resulting in an updated North Sea PSHA formulation. This PSHA formulation comprised of a North Sea GMPE and an updated source model. The development of the North Sea GMPE was constrained by the limitations of the considered ground-motion dataset and the lack of geotechnical information for North Sea sites. However, the path and site effect corrections developed for the North Sea GMPE were considerate of said limitations, and resulted in incremental but significant improvements to the performance of the base model GMPE. Significant future work pertaining to North Sea GMPE development could be undertaken if (1) seismic monitoring of the North Sea seabed was improved and (2) geotechnical subsurface profiles were acquired for each accelerometer site in the region. The updated source model resulted in reasonable modifications to the seismic hazard in the North Sea. The updated PSHA formulation was moderately well validated when evaluated using macroseismic data.

The updated seismic hazard estimates result in moderate but significant modifications to the (assessed) seismic risk for critical offshore infrastructure present in the North Sea. These seismic risk estimates are likely more appropriate than those which could previously be computed using the Bungum et al. (2000) hazard estimates due to the additional ground-motion data and PSHA advancements considered within this study (which were not available when the Bungum et al., 2000 PSHA was undertaken).

Ultimately, the improved North Sea PSHA formulation (and the associated seismic risk estimates) devised in this study help to better assess the structural health of offshore North Sea infrastructure, and therefore minimise the likelihood of levels of seismic damage which could result in significant detriment to (1) the environmental health of the North Sea, (2) the health of personnel operating on or near the damaged infrastructure or (3) the operations and/or financial status of corporations and governments which rely upon this infrastructure.

## 10.0 References

- Abrahamson, N.A. (1988). Statistical properties of peak ground accelerations recorded by the SMART1 array. *Bulletin of the Seismological Society of America*, **78**, pp.26-41.
- Abrahamson, N.A. and Sykora D. (1993). Variation of ground motions across individual sites. In: *Proceedings of the 4th DOE Natural Phenomena Hazards Mitigation Conference*. Atlanta, Georgia, October 19-22, National Technical Information Service, U.S. Department of Commerce, Springfield, VA, Vol. 1, pp.192-198.
- Abrahamson, N.A., Silva, W.J. and Kamai, R. (2014). Summary of the ASK14 ground motion relation for active crustal regions. *Earthquake Spectra*, **30**(3), pp.1025-1055.
- Ajamy, A., Asgarian, B., Ventura, C. and Zolfaghari, M. (2018). Seismic fragility analysis of jacket type offshore platforms considering soil-pile-structure interaction. *Engineering Structures*, **174**, pp.198-211.
- Aki, K. (1967). Scaling Law of Seismic Spectrum. *Journal of Geophysical Research*. **72**, pp.1217-1231.
- Aki, K. and Richards, P. (2002). *Quantitative seismology*. Sausalito, Calif.: University Science Books.
- Akkar, S. and Bommer, J.J. (2010). Empirical equations for the prediction of PGA, PGV and spectral accelerations in Europe, the Mediterranean region and the Middle East. *Seismological Research Letters*, **81**(2), pp.195-206.
- Akkar, S. and Çağnan, Z. (2010). A local ground motion predictive model for Turkey and its comparison with other regional and global ground motion models. *Bulletin of the Seismological Society of America*, **100**(6), pp.2978-2995.
- Akkar, S., Sandikkaya, M.A. and Bommer, J.J. (2014). Empirical ground motion models for point- and extended-source crustal earthquake scenarios in Europe and the Middle East. *Bulletin of Earthquake Engineering*, **12**(1), pp.359-387.
- Ambraseys, N. and Douglas, J. (2003). Near-field horizontal and vertical earthquake ground motions. *Soil Dynamics and Earthquake Engineering*, **23**(1), pp.1-18.
- Ambraseys, N. and Douglas, J. (2004). Magnitude calibration of north Indian earthquakes. *Geophysical Journal International*, **159**(1), pp.165-206.
- Ambraseys, N., Banda, E., Irving, J. *et al.* (1983). Notes on historical seismicity. *Bulletin of the Seismological Society of America*, **73**, pp.1917-1920.
- Ambraseys, N., Douglas, J., Sarma, S. and Smit, P. (2005). Equations for the Estimation of Strong Ground Motions from Shallow Crustal Earthquakes Using Data from Europe and the Middle East: Horizontal Peak Ground Acceleration and Spectral Acceleration. *Bulletin of Earthquake Engineering*, **3**(1), pp.1-53.

- Ambraseys, N., Simpson, K. and Bommer, J.J. (1996). Prediction of Horizontal Response Spectra in Europe. *Earthquake Engineering & Structural Dynamics*, **25**(4), pp.371-400.
- Ambraseys, N., Smit, P., Douglas, J., Margaris, B., Sigbjörnsson, R., Olafsson, S., Suhadolc, P. and Costa, G. (2004). Internet site for European strong-motion data. *Bollettino di Geofisica Teorica ed Applicata*, **45**(3), pp.113-129.
- Ameri, G., Drouet, S., Traversa, P., Bindi, D. and Cotton, F. (2017). Toward an empirical ground motion prediction equation for France: accounting for regional differences in the source stress parameter. *Bulletin of Earthquake Engineering*, **15**(11), pp.4681-4717.
- Anderson, J. and Brune, J. (1999). Probabilistic Seismic Hazard Analysis without the Ergodic Assumption. *Seismological Research Letters*, **70**(1), pp.19-28.
- Anderson, J. and Hough, S. E. (1984). A Model for the Shape of the Fourier Amplitude Spectrum of Acceleration at High Frequencies. *Bulletin of the Seismological Society of America*, **74**, pp.1969-1993.
- Anderson, J. and Humphrey, J. (1991). A Least Squares Method for Objective Determination of Earthquake Source Parameters. *Seismological Research Letters*, **62**(3-4), pp.201-209.
- Arabasz, W., Nava, S., McCarter, M., Pankow, K., Pechmann, J., Ake, J. and McGarr, A. (2005). Coal-Mining Seismicity and Ground-Shaking Hazard: A Case Study in the Trail Mountain Area, Emery County, Utah. *Bulletin of the Seismological Society of America*, **95**(1), pp.18-30.
- ASCE (2007). Seismic rehabilitation of existing buildings. ASCE/SEI41-06, *American Society of Civil Engineers/Structural Engineering Institute*, Reston, VA.
- Atakan, K. and Havskov, L. (1996). Local site effects in the northern North Sea based on single-station spectral ratios of OBS recordings. *Terra Nova*, **8**(1), pp.22-33.
- Atkinson G., Bommer J.J. and Abrahamson N.A. (2014). Alternative approaches to modelling epistemic uncertainty in ground motions in probabilistic seismic-hazard analysis, *Seismological Research Letters*, **85**(6), pp.1141-1144.
- Atkinson, G. (2015). Ground-Motion Prediction Equation for Small-to-Moderate Events at Short Hypocentral Distances, with Application to Induced-Seismicity Hazards. *Bulletin of the Seismological Society of America*, **105**(2A), pp.981-992.
- Atkinson, G. and Assatourians, K. (2017). Are Ground-Motion Models Derived from Natural Events Applicable to the Estimation of Expected Motions for Induced Earthquakes? *Seismological Research Letters*, **88**(2A), pp.430-441.
- Atkinson, G. and Boore, D.M. (1995). Ground Motion Relations for Eastern North America. *Bulletin of the Seismological Society of America*, **85**, pp.17-30.

- Atkinson, G. and Boore, D.M. (2006). Earthquake ground motion prediction equations for eastern North America. *Bulletin of Seismological Society of America*, **96**(6), pp.2181-2205.
- Atkinson, G. and Boore, D.M. (2011). Modifications to existing ground-motion prediction equations in light of new data. *Bulletin of Seismological Society of America*, **10**(3), pp.1121-1135.
- Atkinson, G., Wald, D., Worden, C. and Quitariano, V. (2018). The Intensity Signature of Induced Seismicity. *Bulletin of the Seismological Society of America*, **108**(3A), pp.1080-1086.
- Asareh, M.A., (2015). Dynamic behavior of operational wind turbines considering aerodynamic and seismic load interaction. University of Missouri Doctoral Dissertations, 2375.
- Baisch, S., Koch, C. and Muntendam-Bos, A., 2019. Traffic Light Systems: To What Extent Can Induced Seismicity Be Controlled? *Seismological Research Letters*, **90**(3), pp.1145-1154.
- Baker, J. (2015) Introduction to Probabilistic Seismic Hazard Analysis. *White Paper Version 2.1*, pp. 77.
- Baker, J. and Cornell, C.A. (2005). A vector-valued ground motion intensity measure consisting of spectral acceleration and epsilon. *Earthquake Engineering & Structural Dynamics*, **34**(10), pp.1193-1217.
- Ball, F. and Downs, G. (1966). *Report of investigations, study of possible connection between operation of RMA disposal well and earthquake in Derby, Colorado, area*. Report of Investigations, Injection Well Earthquake Relationship, Rocky Mountain Arsenal, Denver, Colorado. Omaha: U.S. Army Corps of Engineers.
- Beauval, C., Tasan, H., Laurendeau, A., Delavaud, E., Cotton, F., Gueguen, P. and Kuehn, N. (2012). On the Testing of Ground-Motion Prediction Equations against Small-Magnitude Data. *Bulletin of the Seismological Society of America*, **102**(5), pp.1994-2007.
- Benjamin, J.R. and Cornell, C.A. (1970). *Probability, statistics, and decision for civil engineers*. McGraw-Hill, New York.
- Beresnev, I. A., Wen, K.L. and Yeh, Y.T. (1994). Source, path, and site effects on dominant frequency and spectral variation of strong ground motion recorded by SMART1 and SMART2 arrays in Taiwan. *International Journal of Earthquake Engineering Structural Dynamics*, **23**, pp.583-597.
- BGS & Ove Arup and Partners (1997). UK continental shelf seismic hazard. Health and Safety Executive Offshore Technology Report OTH 93 416, HMSO, London;

- Bindi, D., Cotton, F., Kotha, S., Bosse, C., Stromeyer, D. and Grünthal, G. (2017). Application-driven ground motion prediction equation for seismic hazard assessments in non-cratonic moderate-seismicity areas. *Journal of Seismology*, **21**(5), pp.1201-1218.
- Bindi, D., Massa, M., Luzi, L., Ameri, G., Pacor, F., Puglia, R. and Augliera, P. (2014a). Pan-European ground motion prediction equations for the average horizontal component of PGA, PGV, and 5%-damped PSA at spectral periods up to 3.0 s using the RESORCE dataset. *Bulletin of Earthquake Engineering*, **12**(1), pp.391-430.
- Bindi, D., Parolai, S., Grosser, H., Milkereit, C. and Durukal, E. (2007). Empirical ground-motion prediction equations for northwestern Turkey using the aftershocks of the 1999 Kocaeli earthquake. *Geophysical Research Letters*, **34**(L08305).
- Biot, M. (1941). General Theory of Three-Dimensional Consolidation. *Journal of Applied Physics*, **12**(2), pp.155-164.
- Bolt, B.A. (1973). Duration of strong ground motion. In: Proceedings of the 5th world conference on earthquake engineering, pp.1304-1313.
- Bommer, J.J. and Abrahamson, N.A. (2006). Why Do Modern Probabilistic Seismic-Hazard Analyses Often Lead to Increased Hazard Estimates? *Bulletin of the Seismological Society of America*, **96**(6), pp.1967-1977.
- Bommer, J.J. and Scherbaum, F. (2008). The use and misuse of logic trees in probabilistic seismic hazard analysis. *Earthquake Spectra*, **24**(4), pp.997-1009.
- Bommer, J.J., Abrahamson, N.A., Strasser, F., Pecker, A., Bard, P., Bungum, H., Cotton, F., Fäh, D., Sabetta, F., Scherbaum, F. and Studer, J. (2004). The Challenge of Defining Upper Bounds on Earthquake Ground Motions. *Seismological Research Letters*, **75**(1), pp.82-95.
- Bommer, J.J., Dost, B., Edwards, B., Stafford, P., van Elk, J., Doornhof, D. and Ntinalexis, M. (2015). Developing an Application-Specific Ground-Motion Model for Induced Seismicity. *Bulletin of the Seismological Society of America*, **106**(1), pp.158-173.
- Bommer, J.J., Douglas, J., Scherbaum, F., Cotton, F., Bungum, H. and Fäh, D. (2010). On the selection of ground-motion prediction equations for seismic hazard analysis. *Seismological Research Letters*, **81**, pp.783-793.
- Bommer, J.J., Oates, S., Cepeda, J., Lindholm, C., Bird, J., Torres, R., Marroquín, G. and Rivas, J. (2006). Control of hazard due to seismicity induced by a hot fractured rock geothermal project. *Engineering Geology*, **83**(4), pp.287-306.

- Bommer, J.J., Stafford, P. and Ntinalexis, M. (2016). *Empirical Ground-Motion Prediction Equations for Peak Ground Velocity from Small-Magnitude Earthquakes in the Groningen Field Using Multiple Definitions of the Horizontal Component of Motion*. NAM.
- Bommer, J.J., Stafford, P. and Ntinalexis, M. (2017a). *Empirical Ground-Motion Prediction Equations for Peak Ground Velocity from Small-Magnitude Earthquakes in the Groningen Field Using Multiple Definitions of the Horizontal Component of Motion - Updated Model for Application to Smaller Earthquakes*. NAM.
- Bommer, J.J., Stafford, P., Alarcon, J. and Akkar, S. (2007). The Influence of Magnitude Range on Empirical Ground-Motion Prediction. *Bulletin of the Seismological Society of America*, **97**(6), pp.2152-2170.
- Bommer, J.J., Stafford, P., Edwards, B., Dost, B., van Dedem, E., Rodriguez-Marek, A., Kruiver, P., van Elk, J., Doornhof, D. and Ntinalexis, M. (2017b). Framework for a Ground-Motion Model for Induced Seismic Hazard and Risk Analysis in the Groningen Gas Field, The Netherlands. *Earthquake Spectra*, **33**(2), pp.481-498.
- Boore, D.M. (1986). Short-period P- and S-wave Radiation from Large Earthquakes: Implications for Spectral Scaling Relations. *Bulletin of the Seismological Society of America*, **76**, pp.43-64.
- Boore, D.M. (2003). Simulation of Ground Motion Using the Stochastic Method. *Pure and Applied Geophysics*, **160**(3), pp.635-676.
- Boore, D.M. (2005). *SMSIM—Fortran Programs for Simulating Ground Motions from Earthquakes: Version 2.3—A Revision of OFR 96-80-A*. USGS Open-File Report 00-509, modified version, describing the program as of 19 May 2019 (Version 7.05).
- Boore, D.M. and Atkinson, G. (2008). Ground motion prediction equations for the average horizontal component of PGA, PGV, and 5%-damped PSA at spectral periods between 0.01s and 10.0s. *Earthquake Spectra*, **24**(1), pp.99-138.
- Boore, D.M. and Atkinson, G. (2008). Ground-Motion Prediction Equations for the Average Horizontal Component of PGA, PGV, and 5%-Damped PSA at Spectral Periods between 0.01 s and 10.0 s. *Earthquake Spectra*, **24**(1), pp.99-138.
- Boore, D.M. and Boatwright, J. (1984). Average Body-wave Radiation Coefficients. *Bulletin of the Seismological Society of America*. **74**, pp.1615-1621.
- Boore, D.M. and Bommer, J.J. (2005). Processing of strong-motion accelerograms: needs, options and consequences. *Soil Dynamics and Earthquake Engineering*, **25**, pp.93-115.

- Boore, D.M. and Joyner, W.B. (1984). A Note on the Use of Random Vibration Theory to Predict Peak Amplitudes of Transient Signals. *Bulletin of the Seismological Society of America*, **74**, pp.2035-2039.
- Boore, D.M. and Joyner, W.B. (1997). Site amplifications for Generic Rock Sites. *Bulletin of the Seismological Society of America*, **87**, pp.327-341.
- Boore, D.M. and Kishida, T. (2016). Relations between Some Horizontal-Component Ground-Motion Intensity Measures Used in Practice. *Bulletin of the Seismological Society of America*, **107**(1), pp.334-343.
- Boore, D.M. and Smith, C.E. (1999). Analysis of earthquake recordings obtained from the Seafloor Earthquake Measurement System (SEMS) instruments deployed off the coast of southern California. *Bulletin of the Seismological Society of America*, **89**(1), pp.260–274.
- Boore, D.M., Stewart, J., Seyhan, E. and Atkinson, G. (2014). NGA-West2 Equations for Predicting PGA, PGV, and 5% Damped PSA for Shallow Crustal Earthquakes. *Earthquake Spectra*, **30**(3), pp.1057-1085.
- Bora, S., Cotton, F., Scherbaum, F., Edwards, B. and Traversa, P. (2017). Stochastic source, path and site attenuation parameters and associated variabilities for shallow crustal European earthquakes. *Bulletin of Earthquake Engineering*, **15**(11), pp.4531-4561.
- Bormann, P. and Dewey, J. (2012). *The New IASPEI Standards for Determining Magnitudes from Digital Data and their Relation to Classical Magnitudes*. IASPEI, pp.6-7.
- Bossu, R. (1996). Etude de la sismicité intraplaque de la région de Gazli (Ouzbékistan) et la localisation de la déformation sismique. PhD Thesis. L'Université Joseph Fourier, Grenoble.
- Bourne, S., Oates, S., Bommer, J., Dost, B., van Elk, J. and Doornhof, D. (2015). A Monte Carlo Method for Probabilistic Hazard Assessment of Induced Seismicity due to Conventional Natural Gas Production. *Bulletin of the Seismological Society of America*, **105**(3), pp.1721-1738.
- Bowden, D. and Tsai, V. (2017). Earthquake ground motion amplification for surface waves. *Geophysical Research Letters*, **44**(1), pp.121-127.
- Bozorgnia, Y. and Campbell, K. (2004). The Vertical-to-Horizontal Response Spectral Ratio and Tentative Procedures for Developing Simplified V/H and Vertical Design Spectra. *Journal of Earthquake Engineering*, **8**(2), pp.175-207.
- Bozorgnia, Y. and Campbell, K. (2016). Ground Motion Model for the Vertical-to-Horizontal (V/H) Ratios of PGA, PGV, and Response Spectra. *Earthquake Spectra*, **32**(2), pp.951-978.
- Bozorgnia, Y. and Niazi, M. (1993). Distance scaling of vertical and horizontal response spectra of the Loma Prieta earthquake. *Earthquake Engineering and Structural Dynamics*, **22**, pp.695-707.

- Bozorgnia, Y. and others (2014). NGA-West2 research project. *Earthquake Spectra*, **30**(3), pp.973-987.
- Bozorgnia, Y., Niazi, M. and Campbell, K.W. (1995). Characteristics of free-field vertical ground motion during the Northridge earthquake. *Earthquake Spectra*, **11**, pp.515-525.
- Bozorgnia, Y., Niazi, M. and Campbell, K.W. (1996). Relationship between vertical and horizontal ground motion for the Northridge earthquake. In: *Proceedings of the Eleventh World Conference on Earthquake Engineering*. June 23 1996 – June 28 1996, Acapulco, Mexico.
- Bragato, P.L. and Slejko, D. (2005). Empirical ground motion attenuation relations for the eastern Alps in the magnitude range 2.5–6.3. *Bulletin of the Seismological Society of America*, **95**(1) pp.252-276.
- Brooks, C. and Douglas, J. (2020) Influence of the Site-Specific Component of Kappa on the Magnitude-Dependency of Within-Event Aleatory Variabilities in Ground-Motion Models. *Seismological Research Letters*, **92**(1), pp.238-245.
- Brooks, C., Douglas, J. and Shipton, Z. (2020). Improving earthquake ground-motion predictions for the North Sea. *Journal of Seismology*, **24**(2), pp.343-362.
- Brune, J.N. (1970). Tectonic Stress and the Spectra of Seismic Shear Waves from Earthquake. *Journal of Geophysical Research*, **75**, pp.4997-5009.
- Brune, J.N. (1971). Correction. *Journal of Geophysical Research*, **76**, pp.5002.
- BS EN 1998 (2004). *Eurocode 8: Design of structures for earthquake resistance*.
- Bull, A. and Love, M. (2019). Worldwide oil and gas platform decommissioning: A review of practices and reefing options. *Ocean & Coastal Management*, **168**, pp.274-306.
- Bungum, H. and Selnes, P. B. (1988). Earthquake loading on the Norwegian Continental Shelf. *Summary Report*.
- Bungum, H., Lindholm, C., Dahle, A., Woo, G., Nadim, F., Holme, J., Gudmestad, O., Hagberg, T. and Karthigeyan, K. (2000). New Seismic Zoning Maps for Norway, the North Sea, and the United Kingdom. *Seismological Research Letters*, **71**(6), pp.687-697.
- Bureau, G. J. (1981). Near-source peak ground acceleration. *Earthquake Notes*, **52**, pp.81.
- Burton, P. and Neilson, G. (1980). *Annual Catalogues of British Earthquakes Recorded on LOWNET*. Seismological Bulletin. London: Institute of Geological Sciences.
- Bydlon, S., Gupta, A. and Dunham, E. (2017). Using Simulated Ground Motions to Constrain Near-Source Ground-Motion Prediction Equations in Areas Experiencing Induced Seismicity. *Bulletin of the Seismological Society of America*, **107**(5), pp.2078-2093.

- Bydlon, S., Withers, K. and Dunham, E. (2019). A Ground Motion Prediction Equation for Mw 3-5.8 Earthquakes in Oklahoma and Kansas Using a Composite Recorded/Simulated Ground Motion Catalogue. *Bulletin of the Seismological Society of America*, **109**(2), pp.652-671.
- Campbell, K.W. (1982). A study of the near-source behaviour of peak vertical acceleration. *EOS*, **63**, pp.1037.
- Campbell, K.W. (1985). Strong Motion Attenuation Relations: A Ten-Year Perspective. *Earthquake Spectra*, **1**(4), pp.759-804.
- Campbell, K.W. (1991). A random-effects analysis of near-source ground motion for the Diablo Canyon Power Plant site, San Luis Obispo County, California: Dames & Moore Report prepared for Lawrence Livermore National Laboratory, July 25.
- Campbell, K.W. (2003). Prediction of strong ground motion using the hybrid empirical method and its use in the development of ground-motion (attenuation) relations in eastern North America. *Bulletin of the Seismological Society of America*, **93**, pp.1012-1033.
- Campbell, K.W. and Bozorgnia, Y. (2003) Updated near-source ground-motion (attenuation) relations for the horizontal and vertical components of peak ground acceleration and acceleration response spectra. *Bulletin of the Seismological Society of America*, **93**(1), 314–331.
- Campbell, K.W. and Bozorgnia, Y. (2008). NGA Ground-motion Model for the Geometric Mean Horizontal Component of PGA, PGV, PGD and 5% Damped Linear Elastic Response Spectra for Periods Ranging from 0.01 to 10 s. *Earthquake Spectra*, **24**(1), pp.139-171.
- Campbell, K.W. and Bozorgnia, Y. (2014). NGA-West2 ground motion model for the average horizontal components of PGA, PGV, and 5%-damped linear acceleration response spectra. *Earthquake Spectra*, **30**(3), pp.1087-1115.
- Carder, D. (1966). *Evaluation of seismicity in the Denver area*. in Report of Investigations, Injection Well Earthquake Relationship, Rocky Mountain Arsenal, Denver, Colorado. Omaha: U.S. Army Corps of Engineers.
- Carlton, B.D. and Kaynia A.M. (2019). PSHA of Oslo, Norway, using smoothed gridded seismicity source zones and NGA East ground motion models. In: *Earthquake Geotechnical Engineering for Protection and Development of Environment and Constructions: Proceedings of the 7<sup>th</sup> International Conference on Earthquake Geotechnical Engineering*. June 17-20, 2019, Rome, Italy, pp.1621-1628.
- Cartwright, D.E. and Longuet-Higgins, M.S. (1956). The Statistical Distribution of the Maxima of a Random Function, *Proceedings of the Royal Society of London* **237**, pp.212-232.

- Castellaro, S., Mulargia, F. and Rossi, P. (2008). Vs30: Proxy for Seismic Amplification? *Seismological Research Letters*, **79**(4), pp.540-543.
- Cauzzi, C and Faccioli, E. (2008). Broadband (0.05 to 20 s) prediction of displacement response spectra based on worldwide digital records. *Journal of Seismology*, **12**, pp.453-475.
- Cauzzi, C., Faccioli, E., Vanini, M. and Bianchini, A. (2015). Updated predictive equations for broadband (0.01–10 s) horizontal response spectra and peak ground motions, based on a global dataset of digital acceleration records. *Bulletin of Earthquake Engineering*, **13**(6), pp.1587-1612.
- Cesca, S., Dahm, T., Juretzek, C. and Kühn, D. (2011). Rupture process of the 2001 May 7 Mw 4.3 Ekofisk induced earthquake. *Geophysical Journal International*, **187**(1), pp.407-413.
- Chandler, A., Lam, N. and Tsang, H. (2006). Near-surface attenuation modelling based on rock shear-wave velocity profile. *Soil Dynamics and Earthquake Engineering*, **26**(11), pp.1004-1014.
- Chen, B., Wang, D., Li, H., Sun, Z. and Li, C. (2017). Vertical-to-horizontal response spectral ratio for offshore ground motions: Analysis and simplified design equation. *Journal of Central South University*, **24**(1), pp.203-216.
- Chen, Y., Weatherill, G., Pagani, M. and Cotton, F. (2016). Insights into data-driven tectonic regionalisation in seismic hazard analysis. Japan Geoscience Union Meeting, Tokyo.
- Chin, B. H., and Aki, K. (1991). Simultaneous study of the source, path, and site effects on strong ground motion during the 1989 Loma Prieta earthquake: a preliminary result of pervasive nonlinear site effects. *Bulletin of the Seismological Society of America*, **81**, pp.1859-1884.
- Chiou, B.S.J. and Youngs, R. R. (2008). An NGA model for the average horizontal component of peak ground motion and response spectra. *Earthquake Spectra*, **24**, pp.173-215.
- Chiou, B.S.J. and Youngs, R. R. (2014). Update of the Chiou and Youngs NGA model for the average horizontal component of peak ground motion and response spectra. *Earthquake Spectra*, **30**(3), pp.1117-1153.
- Chiou, B.S.J., Youngs, R., Abrahamson, N. and Addo, K. (2010). Ground-Motion Attenuation Model for Small-To-Moderate Shallow Crustal Earthquakes in California and Its Implications on Regionalization of Ground-Motion Prediction Models. *Earthquake Spectra*, **26**(4), pp.907-926.
- Chiu, K. and Snyder, D. (2015). Regional seismic wave propagation (Lg & Sn phases) in the Amerasia Basin and High Arctic. *Polar Science*, **9**(1), pp.130-145.
- Clough, R. and Penzien, J. (1993). *Dynamics of Structures*. 2nd edition. New York: McGraw Hill Publishing Company.

- Cooley, J. and Tukey, J. (1965). An algorithm for the machine calculation of complex Fourier series. *Mathematics of Computation*, **19**(90), pp.297-297.
- Coppersmith, K.J. (2016). Report on Mmax Expert Workshop, Mmax panel chairman Kevin Coppersmith, June 2016.
- Cornell, C.A. (1996). Calculating building seismic performance reliability: a basis for multi-level design norms. In: *Proceedings of 11th world conference on earthquake engineering*, Acapulco.
- Cornell, C.A., Banon, H. and Shakal, A.F. (1979). Seismic motion and response prediction alternatives. *Earthquake Engineering Structural Dynamics*, **7**(4), pp.295-315.
- Cornell, C.A., Jalayer, F., Hamburger, R.O. and Foutch, D.A. (2002). Probabilistic Basis for 2000 SAC Federal Emergency Management Agency Steel Moment Frame Guidelines. *Journal of Structural Engineering*, **128**(4), pp.526-533.
- Cotton, F., Scherbaum, F., Bommer, J.J. and Bungum, H. (2006). Criteria for selecting and adjusting ground-motion models for specific target regions: application to central Europe and rock sites. *Journal of Seismology*, **10**, pp.137-156.
- Dahm, T., Cesca, S., Hainzl, S., Braun, T. and Krüger, F. (2015). Discrimination between induced, triggered, and natural earthquakes close to hydrocarbon reservoirs: A probabilistic approach based on the modeling of depletion-induced stress changes and seismological source parameters. *Journal of Geophysical Research: Solid Earth*, **120**(4), pp.2491-2509.
- Dahm, T., Krüger, F., Stammer, K., Klinge, K., Kind, R., Wylegalla, K. and Grasso J. (2007). The 2004  $M_w$  4.4 Rotenburg, Northern Germany, Earthquake and Its Possible Relationship with Gas Recovery. *Bulletin of the Seismological Society of America*, **97**(3), pp.691-704.
- Data-ogauthority.opendata.arcgis.com (2020). *Oil and Gas Authority Open Data*. [online] Available at: <https://data-ogauthority.opendata.arcgis.com/> [Accessed 18 February 2020].
- Davis, S. D., Pennington, W. D. and Carlson, S. M. (1989). A compendium of earthquake activity in Texas, *University of Texas Bureau of Economic Geology Circular*.
- Davis, S.D. and Frohlich, C. (1993). Did (or will) fluid injection cause earthquakes? Criteria for a rational assessment. *Seismological Research Letters*, **64**, pp.207-224.
- Davis, S.D. and Pennington, W.D. (1989). Induced seismic deformation in the Cogdell oil field of west Texas. *Bulletin of the Seismological Society of America*, **79**(5), pp.1477-1495.
- Davis, S.D., Nyffenegger, P.A. and Frohlich, C. (1995). The 9 April 1993 Earthquake in South-Central Texas: Was it induced by fluid withdrawal? *Bulletin of the Seismological Society of America*, **85** (6), pp.1888-1895.

- Dawood, H. and Rodriguez-Marek, A. (2013). A Method for Including Path Effects in Ground-Motion Prediction Equations: An Example Using the Mw 9.0 Tohoku Earthquake Aftershocks. *Bulletin of the Seismological Society of America*, **103**(2B), pp.1360-1372.
- Delavaud, E., Cotton, F., Akkar, S. and others. (2012). Toward a ground-motion logic tree for probabilistic seismic hazard assessment in Europe. *Journal of Seismology*, **16**, pp.451-473.
- Dempsey, D. and Suckale, J. (2017). Physics-based forecasting of induced seismicity at Groningen gas field, the Netherlands. *Geophysical Research Letters*, **44** (15), pp.7773-7782.
- Denton, P. (2007). *Earthquake Magnitude*. Edinburgh: British Geological Survey.
- Derras, B., Bard, P. Y. and Cotton, F. (2014). Towards fully data driven ground-motion prediction models for Europe. *Bulletin of Earthquake Engineering*, **12**(1), pp.495-516
- Diao, H., Hu, J. and Xie, L. (2014). Effect of seawater on incident plane P and SV waves at ocean bottom and engineering characteristics of offshore ground motion records off the coast of southern California, USA. *Earthquake Engineering and Engineering Vibration*, **13**(2), pp.181-194.
- Dost, B., Caccavale, M., van Eck, T. and Kraaijpoel, D. (2013). *Report on the Expected PGV and PGA Values for Induced Earthquakes in the Groningen Area*. KNMI.
- Douglas, J. (2003). What is a poor quality strong-motion record? *Bulletin of Earthquake Engineering*, **1**, pp.141-156.
- Douglas, J. (2018a). Capturing Geographically-Varying Uncertainty in Earthquake Ground-motion Models or What We Think We Know May Change. In: *Recent Advances in Earthquake Engineering in Europe. ECEE 2018. Geotechnical, Geological and Earthquake Engineering*. June 18 2018 – June 21 2018, Thessaloniki, Greece, pp.153-181.
- Douglas, J. (2018b). Calibrating the backbone approach for the development of earthquake ground motion models. In: *Best Practice in Physics-based Fault Rupture for Seismic Hazard Assessment of Nuclear Installations: Issues and Challenges Towards Full Seismic Risk Analysis*. May 14 2018 – May 16 2018, Cadarache, France.
- Douglas, J. and Edwards, B. (2016). Recent and future developments in earthquake ground motion estimation. *Earth-Science Reviews*, **160**, pp.203-219.
- Douglas, J. and Jousset, P. (2011). Modeling the Difference in Ground-Motion Magnitude-Scaling in Small and Large Earthquakes. *Seismological Research Letters*, **82**(4), pp.504-508.
- Douglas, J., Edwards, B., Convertito, V., Sharma, N., Tramelli, A., Kraaijpoel, D., Cabrera, B., Maercklin, N. and Troise, C. (2013). Predicting Ground Motion from Induced Earthquakes in Geothermal Areas. *Bulletin of the Seismological Society of America*, **103**(3), pp.1875-1897.

- Douglas, J., Ulrich, T., Bertil, D. and Rey, J. (2014). Comparison of the Ranges of Uncertainty Captured in Different Seismic-Hazard Studies. *Seismological Research Letters*, **85**(5), pp.977-985.
- Earthquake.usgs.gov. (2018). *Focal Mechanisms*. [online] Available at: <https://earthquake.usgs.gov/learn/topics/beachball.php> [Accessed 29 Jun. 2018].
- Earthquakes.bgs.ac.uk (2020a). *British Geological Survey Earthquake Database Search*. [online] Available at: <http://earthquakes.bgs.ac.uk/earthquakes/dataSearch.html> [Accessed 20 August 2020].
- Earthquakes.bgs.ac.uk (2020b). *Earthquakes Booklet - How We Measure Them*. [online] Available at: [http://earthquakes.bgs.ac.uk/education/eq\\_guide/eq\\_booklet\\_how\\_we\\_measure.htm](http://earthquakes.bgs.ac.uk/education/eq_guide/eq_booklet_how_we_measure.htm) [Accessed 19 December 2020].
- Edwards, B., Allmann, B., Fäh, D. and Clinton, J. (2010). Automatic computation of moment magnitudes for small earthquakes and the scaling of local to moment magnitude. *Geophysical Journal International*, **183**(1), pp.407-420.
- Edwards, B., Fäh, D. and Giardini, D. (2011). Attenuation of seismic shear wave energy in Switzerland. *Geophysical Journal International*, **185**(2), pp.967-984.
- Edwards, B., Zurek, B., van Dedem, E., Stafford, P., Oates, S., van Elk, J., deMartin, B. and Bommer, J. (2018). Simulations for the development of a ground motion model for induced seismicity in the Groningen gas field, The Netherlands. *Bulletin of Earthquake Engineering*, **17**(8), pp.4441-4456.
- eea.europa.eu (2015). *Development of wind farm areas in Europe*. [online] Available at: <https://www.eea.europa.eu/data-and-maps/figures/development-of-wind-farm-areas> [Accessed 2 February 2021].
- Efehr.org (2020). *EFEHR | Earthquake Catalogue Europe*. [online] Available at: <http://www.efehr.org/en/Documentation/specific-hazard-models/europe/earthquake-catalogue/> [Accessed 20 August 2020].
- EQE International Ltd (2002). Seismic hazard - UK continental shelf. Health and Safety Executive Offshore Technology Report 2002/005
- Erberik, M. A. (2015). Seismic Fragility Analysis. In: Beer, M., Kougiumtzoglou, I., Patelli, E. and Au IK. (eds) *Encyclopedia of Earthquake Engineering*. Springer, Berlin, Heidelberg.
- Eroglu Azak, T., Kalafat, D., Şeşetyan, K. and Demircioğlu, M. (2017). Effects of seismic declustering on seismic hazard assessment: a sensitivity study using the Turkish earthquake catalogue. *Bulletin of Earthquake Engineering*, **16**(8), pp.3339-3366.

- Europe-geology.eu (2019). *EGDI / Metadata*. [online] Available at: <http://www.europe-geology.eu/metadata/> [Accessed 28 Apr. 2019].
- Evans, D.G. and Steeples, D.W. (1987). Microearthquakes near the Sleepy Hollow oil-field, Southwestern Nebraska. *Bulletin of the Seismological Society of America*, **77** (1), pp.132-140.
- Eyidoğan, H., Nábělek, J. and Toksöz, M.N. (1985). The Gazli, USSR, 19 March 1984 Earthquake: The mechanism and tectonic implications. *Bulletin of the Seismological Society of America*, **75** (3), pp.661-675.
- Fajfar, P. (2000). A Nonlinear Analysis Method for Performance Based Seismic Design. *Earthquake Spectra*, **16**(3), pp.573-592.
- FEMA (1997). NEHRP guidelines for the seismic rehabilitation of buildings. FEMA Publication 273. Federal Emergency Management Agency, Washington, DC.
- FEMA 350. (2000). Recommended seismic design criteria for new steel moment-frame buildings. SAC Joint Venture, Federal Emergency Management Agency, Washington DC.
- FEMA 351. (2000). Recommended seismic evaluation and upgrade criteria for existing welded steel moment-frame buildings. SAC Joint Venture, Federal Emergency Management Agency, Washington DC.
- Ferreira, D.D. (2003). *Fiscal treatment decommissioning and bonds: anticipating impacts of financial assurance requirements for offshore decommissioning, a decision model for the oil industry*. Doctoral dissertation, State University Campinas, Brazil.
- Finn, W.D.L. and Bhatia, S.K. (1981). Prediction of seismic pore-water pressures. In: *Proceedings, 10th International Conference on Soil Mechanics and Foundation Engineering*, Volume 3, pp.201-206.
- Ford, G. (2018). *Bulletin of British Earthquakes 2017*. Earthquake Bulletin. Edinburgh: British Geological Survey.
- Ford, G., Marrow, P., Musson, R., Newmark, R., Redmayne, D., Ritchie, M., Ross, K. and Walker, A. (1987). *Bulletin of British Earthquakes 1985*. Bulletin of British Earthquakes. Edinburgh: British Geological Survey.
- Fossen, H. and Hurich, C. (2005). The Hardangerfjord Shear Zone in SW Norway and the North Sea: a large-scale low-angle shear zone in the Caledonian crust. *Journal of the Geological Society*, **162**(4), pp.675-687.
- Foulger, G., Wilson, M., Gluyas, J., Julian, B. and Davies, R. (2017). Global review of human-induced earthquakes. *Earth-Science Reviews*.

- Frankel, A., Mueller, C., Barnhard, T., Perkins, D., Leyendecker, E., Dickman, N., Hanson, S. and Hopper, M. (1996). *National Seismic Hazard Maps: Documentation June 1996*. U.S. Geological Survey. Open-File Report 96-532.
- Frohlich, C., DeShon, H., Stump, B., Hayward, C., Hornbach M. and Walter J.I. (2016). A historical review of induced earthquakes in Texas. *Seismological Research Letters*, **87**, pp.1022-1038.
- Gallipoli, M. and Mucciarelli, M. (2009). Comparison of Site Classification from VS30, VS10, and HVSR in Italy. *Bulletin of the Seismological Society of America*, **99**(1), pp.340-351.
- Gardner, J.K. and Knopoff, L. (1974). Is the sequence of earthquakes in Southern California, with aftershocks removed, Poissonian? *Bulletin of the Seismological Society of America*, **64**(5), pp.1363-1367.
- Gautier, D. (2003). *Carboniferous-Rotliegend Total Petroleum System Description and Assessment Results Summary*. U.S. Geological Survey Bulletin 2211. Reston: United States Geological Survey, p.5.
- Gautier, D. (2013). *Kimmeridgian shales total petroleum system of the North Sea graben province*. Virginia: Bibliogov, p.9.
- Gestermann, N., Plenefisch, T., Schwaderer, U. and Joswig, M. (2015). Induced Seismicity at the Natural Gas Fields in Northern Germany. In: *Schatzalp Induced Seismicity Workshop*. March 10 – March 13 2015, Davos, Switzerland: BGR.
- Geus.dk (2020). *Registered Earthquakes in Denmark*. [online] Available at: <<https://www.geus.dk/natur-og-klima/jordskaelv-og-seismologi/registrerede-jordskaelv-i-danmark/>> [Accessed 20 August 2020].
- Gkimpraxis, A., Tubaldi, E. & Douglas, J. (2020). Evaluating alternative approaches for the seismic design of structures. *Bulletin of Earthquake Engineering*, **18**, pp.4331-4361.
- Gkimpraxis, A., Tubaldi, E. and Douglas, J. (2019) Comparison of methods to developed risk-targeted seismic design maps. *Bulletin of Earthquake Engineering*, **17**, pp.3727-3752.
- Global Earthquake Model Foundation. (2019). *OPENQUAKE Tools & Data*. [online] Available at: <https://www.globalquakemodel.org/tools-products> [Accessed 21 Mar. 2019].
- Goda, K., Wagener, T. and Aspinall, W. (2014). Anatomy of Natural Hazard Analysis: Uncertainty Propagation and Visualization. In: *Second International Conference on Vulnerability and Risk Analysis and Management (ICVRAM)*. 13 July 2014 – 16 July 2014. Liverpool, United Kingdom.
- Goulet, C., Bozorgnia, Y., Abrahamson, N., Kuehn, N., Al Atik, L., Youngs, R., Graves, R. and Atkinson, G. (2018). Central and Eastern North America Ground-Motion Characterization:

- NGA-East Final Report. Pacific Earthquake Engineering Research Center, Berkeley, CA. PEER Report No. 2018/08.
- Grasso, J. (1992). Mechanics of seismic instabilities induced by the recovery of hydrocarbons. *Pure and Applied Geophysics PAGEOPH*, **139** (3-4), pp.507-534.
- Grasso, J. and Feignier, B. (1990), Seismicity Induced by Gas Depletion: H. Lithology Correlated Events, Induced Stresses and Deformations, *Pure Applied Geophysics*, **134**, pp.427-450.
- Grasso, J. and Wittlinger, G. (1990), Ten Years of Seismic Monitoring over a Gas Field Area, *Bulletin of the Seismological Society of America*, **80**, pp.450-473.
- Gregersen, S. and Vaccari, F. (1993). Lg-Wave Modelling for the North Sea. *Geophysical Journal International*, **114**(1), pp.76-80.
- Grigoli, F., Cesca, S., Rinaldi, A.P., Manconi, A., López-Comino, J.A., Clinton, J.F, Westaway, R., Cauzzi, C., Dahm, T. and Wiemer, S. (2018). The November 2017 MW 5.5 Pohang earthquake: a possible case of induced seismicity in South Korea. *Science*, **360**, pp.1003-1006.
- Grimaz, S. and Slejko, D. (2014). Seismic hazard for critical facilities. *Bollettino di Geofisica Teorica ed Applicata*, **55**(1), pp.3-16.
- Grunthal, G. (1988). European Macroseismic Scale 1998 (EMS-98). *Conseil de L'Europe, Cahiers du Centre Europeen de Geodynamique et de Seismologie*, vol. 15.
- Grünthal, G. and Wahlström, R. (2012). The European-Mediterranean Earthquake Catalogue (EMEC) for the last millennium. *Journal of Seismology*, **16**, pp.535–570.
- Gupta, A., Baker, J. and Ellsworth, W. (2017). Assessing Ground-Motion Amplitudes and Attenuation for Small-to-Moderate Induced and Tectonic Earthquakes in the Central and Eastern United States. *Seismological Research Letters*, **88**(5), pp.1379-1389.
- Gutenberg, B. and Richter, C.F. (1944). Frequency of earthquakes in California. *Bulletin of the Seismological Society of America*, **34**(4), pp.185-188.
- Hanks and Kanamori, H. (1979). A moment magnitude scale. *Journal of Geophysical Research*, **84**(B5), p.2348.
- Hanks, T.C. (1979).  $b$  Values and  $w^{\gamma}$  Seismic Source Models: Implications for Tectonic Stress Variations along Active Crustal Fault Zones and the Estimation of High-frequency Strong Ground Motion. *Journal of Geophysical Research*, **84**, pp.2235-2242.
- Hanks, T.C. and McGuire, R.K. (1981). The Character of High-frequency Strong Ground Motion. *Bulletin of the Seismological Society of America*. **71**, pp.2071-2095.

- Hassani, B. and Atkinson, G. (2018). Adjustable Generic Ground-Motion Prediction Equation Based on Equivalent Point-Source Simulations: Accounting for Kappa Effects. *Bulletin of the Seismological Society of America*, **108**(2), pp.913-928.
- Hatayama, K. (2004). Theoretical evaluation of effects of sea on seismic ground motion. In: *Proceedings of the 13th world conference on earthquake engineering*. August 1 2004 – August 6 2004, Vancouver, B.C., Canada. No. 3229.
- Havskov, J. and Ottemöller, L. (2010). *Routine data processing in earthquake seismology*. Dordrecht: Springer, p.119.
- Hearn, T., Wang, S., Pei, S., Xu, Z., Ni, J. and Yu, Y. (2008). Seismic amplitude tomography for crustal attenuation beneath China. *Geophysical Journal International*, **174**(1), pp.223-234.
- Hsieh, P. and Bredehoeft, J. (1981). A reservoir analysis of the Denver earthquakes: A case of induced seismicity. *Journal of Geophysical Research: Solid Earth*, **86** (B2), pp.903-920.
- Hudson, D.E. (1979). Reading and interpreting strong motion accelerograms. Earthquake Engineering Research Institute, Berkeley, California, USA (Monograph).
- Husid, R. (1967). *Gravity effects on the earthquake response of yielding structures*. Earthquake Engineering Research Laboratory, California Institute of Technology, Pasadena.
- Idriss, I.M. (1985). Evaluating seismic risk in engineering practice. In: *Proceedings of the Eleventh International Conference on Soil Mechanics and Foundation Engineering*. August 12 1985 – August 16 1985, San Francisco, USA.
- Idriss, I.M., Sadigh, K. and Power, M.S. (1982). Dependence of peak horizontal accelerations and velocities on earthquake magnitude at close distances to the source (abs.). *Earthquake Notes*, **53**, 45.
- Isc.ac.uk (2020). *ISC-GEM Catalogue*. [online] Available at: <<http://www.isc.ac.uk/iscgem/download.php>> [Accessed 20 August 2020].
- ISO19901-2 (2004). *Petroleum and natural gas industries - specific requirements for offshore structures - part 2: seismic design procedures and criteria*. International Organisation for Standardisation, Geneva.
- ISO19901-2 (2016). *Petroleum and natural gas industries - specific requirements for offshore structures - part 2: seismic design procedures and criteria*. International Organisation for Standardisation, Geneva.
- Izadi, G. and Elsworth, D. (2013). The effects of thermal stress and fluid pressure on induced seismicity during stimulation to production within fractured reservoirs. *Terra Nova*, **25**(5), pp.374-380.

- Jacob, K.H. (1991). Seismic zonation and site response: Are building code soil-factors adequate to account for variability of site conditions across the US? In: *Proceedings, 4th International Conference on Microzonation*. Volume 1, pp.695-702.
- Jibson, R. (1987). Summary of research on the effects of topographic amplification of earthquake shaking on slope stability. *Open-File Report 87-268*, U.S. Geological Survey, Menlo Park, California.
- Jibson, R.W., Harp, E.L. and Michael, J.A. (1998). A method for producing digital probabilistic seismic landslide hazard maps: an example from the Los Angeles, California, area. US Geological Survey O-F report, pp.98-113.
- Jolliffe, I. (2013). *Principal Component Analysis*. Berlin: Springer Science & Business Media.
- Jonkman, J.M., Butterfield, S., Musial, W. and Scott, G. (2009). *Definition of a 5MW Reference Wind Turbine for Offshore System Development*. National Renewable Energy Laboratory (NREL).
- Joyner, W.B., and Boore, D.M. (1981). Peak horizontal acceleration and velocity from strong-motions records including records from the 1979 Imperial Valley, California, earthquake. *Bulletin of the Seismological Society of America*. **71**, pp.2011-2038.
- Kale, Ö. and Akkar, S. (2017). A ground-motion logic-tree scheme for regional seismic hazard studies. *Earthquake Spectra*, **33**(3), pp.837-856.
- Kammula, V. and Sriramula, S. (2014). Seismic Fragility of Aging Offshore Platforms. In: Beer, M., Kougoumtzoglou, I., Patelli, E., and Au, I. K. (eds) *Encyclopedia of Earthquake Engineering*. Springer, Berlin, Heidelberg.
- Kaynia, A. (2019). Seismic considerations in design of offshore wind turbines. *Soil Dynamics and Earthquake Engineering*, **124**, pp.399-407.
- Kemp, A. (2005). Optimizing Oil and Gas Depletion in the Maturing North Sea with Growing Import Dependence. *Oxford Review of Economic Policy*, **21**(1), pp.43-66.
- Kennedy, R.P. and Short, S.A. (1994). Basis for seismic provisions of DOE-STD-1020. Rep. No. UCRLCR-111478, Lawrence Livermore National Laboratory, Livermore, Calif., and Rep. No. BNL-52418, Brookhaven National Laboratory, Upton, N.Y.
- Kennett, B. (2009). *Seismic Wave Propagation in Stratified Media*. Canberra: ANU Press.
- Kennett, B. and Mykkeltveit, S. (1984). Guided wave propagation in laterally varying media -- II. Lg-waves in north-western Europe. *Geophysical Journal International*, **79**(1), pp.257-267.
- Kim, D., Lee, S. and Lee, I. (2014). Seismic fragility analysis of 5 MW offshore wind turbine. *Renewable Energy*, **65**, pp.250-256.

- King, J.L. and Tucker, B.E. (1984). Dependence of sediment-filled valley response on the input amplitude and the valley properties. *Bulletin of the Seismological Society of America*, **74**(1), pp.153-165.
- Kjørhaug, R. and Kaynia, A. (2015). Vertical earthquake response of megawatt-sized wind turbine with soil-structure interaction effects. *Earthquake Engineering & Structural Dynamics*, **44**(13), pp.2341-2358.
- Kotha, S., Bindi, D. and Cotton, F. (2017). Site-Corrected Magnitude- and Region-Dependent Correlations of Horizontal Peak Spectral Amplitudes. *Earthquake Spectra*, **33**(4), pp.1415-1432.
- Kotha, S., Cotton, F. and Bindi, D. (2018). A new approach to site classification: Mixed-effects Ground Motion Prediction Equation with spectral clustering of site amplification functions. *Soil Dynamics and Earthquake Engineering*, **110**, pp.318-329.
- Kotha, S., Cotton, F. and Bindi, D. (2019). Empirical Models of Shear-Wave Radiation Pattern Derived from Large Datasets of Ground-Shaking Observations. *Scientific Reports*, **9**(1).
- Kotha, S., Weatherill, G., Bindi, D. and Cotton, F. (2020). A regionally-adaptable ground-motion model for shallow crustal earthquakes in Europe. *Bulletin of Earthquake Engineering*.
- Kottke, A.R. and Rathje, E.M. (2008). *Technical manual for Strata*. Pacific Earthquake Engineering Research Center, Berkeley, CA. PEER Report No. 2008/10.
- Kramer, S. (2014). *Geotechnical Earthquake Engineering*. Pearson, Harlow.
- Kristiansen, T.G., Barkved, O. and Patillo, P.D. (2000). Use of passive seismic monitoring in well and casing design in the compacting and subsiding valhall field, North Sea. *Society of Petroleum Engineering SPE*, 65134
- Ktenidou, O., Roumelioti, Z., Abrahamson, N., Cotton, F., Pitilakis, K. and Hollender, F. (2017). Understanding single-station ground motion variability and uncertainty ( $\sigma$ ): lessons learnt from EUROSEISTEST. *Bulletin of Earthquake Engineering*, **16**(6), pp.2311-2336.
- Kulkarni, R.B., Youngs, R.R. and Coppersmith, K.J. (1984). Assessment of confidence intervals for results of seismic hazard analysis. In: *Proceedings of Eighth World Conference on Earthquake Engineering*. 21 July 1984 – 28 July 1984. San Francisco, USA. Volume 1, pp.263-270.
- Laurendeau, A., Cotton, F., Ktenidou, O., Bonilla, L. and Hollender, F. (2013). Rock and Stiff-Soil Site Amplification: Dependency on VS30 and Kappa ( $\kappa_0$ ). *Bulletin of the Seismological Society of America*, **103**(6), pp.3131-3148.
- Lévêque, J., Rivera, L. and Wittlinger, G. (1993). On the use of the checker-board test to assess the resolution of tomographic inversions. *Geophysical Journal International*, **115**(1), pp.313-318.

- Liu, L. and Pezeshk, S. (1999), An Improvement on the Estimation of Pseudoresponse Spectral Velocity Using RVT Method. *Bulletin of the Seismological Society of America*, **89**, pp.1384-1389.
- Mahani, A. and Kao, H. (2018). Ground Motion from M 1.5 to 3.8 Induced Earthquakes at Hypocentral Distance < 45 km in the Montney Play of Northeast British Columbia, Canada. *Seismological Research Letters*, **89**(1), pp.22-34.
- Mak, S. and Schorlemmer, D. (2016). A comparison between the forecast by the United States National Seismic Hazard Maps with recent ground-motion records. *Bulletin of the Seismological Society of America*, **106**(4), pp.1817-1831.
- Mallard, D., Skipp, W. and Aspinall, W. (2003). *An appraisal of existing seismic hazard estimates for the UK Continental Shelf*. Sudbury: HSE Books.
- Manandhar, S., Cho, H. and Kim, D. (2016). Effect of bedrock stiffness and thickness of weathered rock on response spectrum in Korea. *KSCE Journal of Civil Engineering*, **20**(7), pp.2677-2691.
- McGarr, A. (1991), On a Possible Connection between Three Major Earthquakes in California and Oil Production. *Bulletin of the Seismological Society of America*, **81**, pp. 948-970.
- McGarr, A. and Fletcher, J. (2005). Development of Ground-Motion Prediction Equations Relevant to Shallow Mining-Induced Seismicity in the Trail Mountain Area, Emery County, Utah. *Bulletin of the Seismological Society of America*, **95**(1), pp.31-47.
- McGuire, R.K. and Hanks, T.C. (1980). RMS Accelerations and Spectral Amplitudes of Strong Ground Motion during the San Fernando, California, Earthquake. *Bulletin of the Seismological Society of America*, **70**, pp.1907-1919.
- McNamara, D., Petersen, M., Thompson, E., Powers, P., Shumway, A., Hoover, S., Moschetti, M. and Wolin, E. (2018). Evaluation of Ground-Motion Models for USGS Seismic Hazard Forecasts: Induced and Tectonic Earthquakes in the Central and Eastern United States. *Bulletin of the Seismological Society of America*, **109**(1), pp.322-335.
- Mereu, R.F., Brunet, J., Morrissev, K., Price, B. and Yapp, A. (1986). A study of the microearthquakes of the gobles oil field area of Southwestern Ontario. *Bulletin of the Seismological Society of America*, **76** (5), pp.1215-1223.
- Metropolis, N. and Ulam, S. (1949). The Monte Carlo method. *Journal of the American Statistical Association*, **44**(247), pp.335-341.
- Montalvo-Arrieta, J.C., Pérez-Campos, X., Ramos-Zuñiga, L.G., Paz-Martínez, E.G., Salinas-Jasso, J.A., Navarro de León, I. and Ramírez-Fernández, J.A. (2018). El Cuchillo seismic sequence of October 2013-July 2014 in the Burgos Basin, Northeastern Mexico: hydraulic fracturing or

- reservoir-induced seismicity? *Bulletin of the Seismological Society of America*, **108**, pp.3092-3106.
- Mosca, I., Sargeant, S., Baptie, B., Musson R.M.W. and Pharaoh, T. (2020). *National seismic hazard maps for the UK: 2020 update*. British Geological Survey Open Report, OR/20/053.
- Mulders, F.M.M. (2003). Modelling of stress development and fault slip in and around a producing gas reservoir. PhD thesis. TU Delft, Netherlands.
- Musson R.M.W. (2008). *The seismicity of the British Isles to 1600*. BGS, Earth Hazards and Systems, Internal Report OR/08/049, pp. 90.
- Musson, R.M.W. (2009). The use of Monte Carlo simulations for seismic hazard assessment in the UK. *Annals of Geophysics*, **43**, pp.1-9.
- Musson, R.M.W. (2012). On the Nature of Logic Trees in Probabilistic Seismic Hazard Assessment. *Earthquake Spectra*, **28**(3), pp.1291-1296.
- Musson, R.M.W., Pappin, J., Lubkowski, Z., Booth, E. and Long, D. (1993). *U.K. Continental Shelf seismic hazard*, Health and Safety Executive Report No. OTH 93 416.
- Nakamura, Y. (1989). A method for dynamic characteristics estimation of subsurface using microtremor on the ground surface. *Q. Rep. Railway Tech. Res. Inst.*, **30**(1), pp.25-33.
- Niazi, M. and Bozorgnia, Y. (1989). Behaviour of vertical ground motion parameters in the near-field. *Seismological Research Letters*, **60**(4).
- Niazi, M. and Bozorgnia, Y. (1990). Observed ratios of PGV/PGA and PGD/PGA for deep soil sites across SMART-1 array, Taiwan. In: *Proceedings of the Fourth US National Conference on Earthquake Engineering*. May 20 1990 – May 24 1990, Palm Springs, CA. Volume 1, pp.367-374.
- Niazi, M. and Bozorgnia, Y. (1991). Behaviour of near-source peak vertical and horizontal ground motions over SMART-1 array, Taiwan. *Bulletin of the Seismological Society of America*, **81**, pp.715-732.
- Niazi, M. and Bozorgnia, Y. (1992). Behaviour of near-source vertical and horizontal response spectra at SMART-1 array, Taiwan. *Earthquake Engineering and Structural Dynamics*, **21**, pp.37-50.
- NIBS (1999). Standardized Earthquake Loss Estimation Methodology (HAZUS 99 technical manual). *Report prepared for Federal Emergency Management Agency*, Washington, DC.
- Nicholson, C. and Wesson, R.L. (1990). Earthquake hazard associated with deep well injections a report of the U.S. /Environmental Protection Agency. Technical report. United States Geological Survey Bulletin 1951.

- Nlog.nl (2016). *Groningen gasfield / NLOG*. [online] Available at: <https://www.nlog.nl/en/groningen-gasfield> [Accessed 19 Aug. 2019].
- Nnsn.geo.uib.no (2020). *Macroseismic Data*. [online] Available at: <http://nnsn.geo.uib.no/midop/> [Accessed 26 November 2020].
- Nogoshi, M. and Igarashi, T. (1971). On the Amplitude Characteristics of Microtremor (Part 2). *Zisin (Journal of the Seismological Society of Japan. 2nd ser.)*, **24**(1), pp.26-40.
- Noreng, O. (1980). *Oil Industry and Government Strategy in the North Sea*. Abingdon: ROUTLEDGE, p.70.
- NORSAR. (2020). *Seismic Bulletins*. [online] Available at: <https://www.norsar.no/seismic-bulletins/> [Accessed 20 August 2020].
- Northsearegion.eu (2017). *Offshore renewable energy developments - Offshore Wind*. [online] Available at: <https://northsearegion.eu/northsee/e-energy/offshore-renewable-energy-developments-offshore-wind/> [Accessed 19 February 2021].
- Novakovic, M., Atkinson, G. and Assatourians, K. (2018). Empirically Calibrated Ground-Motion Prediction Equation for Oklahoma. *Bulletin of the Seismological Society of America*. In Press.
- Oil and Gas UK (2012). *The Decommissioning of Steel Piled Jackets in the North Sea Region*.
- Olea, R.A. (1999). *Geostatistics for engineers and earth scientists*. Kluwer Academic Publishers, Dordrecht.
- Ordaz, M., Martinelli, F., Aguilar, A., Arboleda, J., Meletti, C. and D'Amico, V. (2015). CRISIS 2015. Program for computing seismic hazard.
- Ottmøller, L., Nielsen, H.H., Atakan, K., Braunmiller, J., and Havskov, J. (2005). The 7 May 2001 induced seismic event in the Ekofisk oil field, North Sea. *Journal of Geophysical Research*, **110** (B10).
- Pacor, F. and Luzi, L. (2014). Engineering Characterization of Earthquake Ground Motions. In: Beer, M., Kougoumtzoglou, I., Patelli, E. and Au, I. K. (eds) *Encyclopedia of Earthquake Engineering*. Springer, Berlin, Heidelberg.
- Pacor, F., Paolucci, R., Ameri, G., Massa, M. and Puglia, R. (2011). Italian strong motion records in ITACA: overview and record processing. *Bulletin of Earthquake Engineering*, **9**(6), pp.1741-1759.
- Pagani, M, Monelli, D., Weatherill, G., Danciu, L., Crowley, H., Silva, V., Henshaw, P., Butler, L., Nastasi, M., Panzeri, L., Simionato, M. and Vigano, D. (2014). OpenQuake-engine: an open hazard (and risk) software for the global earthquake model. *Seismological Research Letters*, **85**, pp.692-702.

- Pang, X., Lerche, I., Zhou, H. and Jiang, Z. (2003). Hydrocarbon Accumulation Control by Predominant Migration Pathways. *Energy Exploration & Exploitation*, **21**(3), pp.167-186.
- Pennington, W.D., Davis, S.D., Carlson, S.M., Dupree, J. and Ewing, T.E. (1986). The evolution of seismic barriers and asperities caused by the depressurising of fault planes in oil and gas of South Texas. *Bulletin of the Seismological Society of America*, **76** (4), pp.939-948.
- Phillips, W., Fairbanks, T., Rutledge, J. and Anderson, D. (1998). Induced microearthquake patterns and oil-producing fracture systems in the Austin chalk. *Tectonophysics*, **289** (1-3), pp.153-169.
- Pitilakis, K., Riga, E. and Anastasiadis, A. (2013). New code site classification, amplification factors and normalized response spectra based on a worldwide ground-motion database. *Bulletin of Earthquake Engineering*, **11**(4), pp.925-966.
- Plenefisch, T., Gestermann, N., Ceranna, L., Wegler, U., Vasterling, M. and Bischoff, M. (2014). Seismicity in the vicinity of the natural gas fields of Völkersen und Söhlingen (Northern Germany) - looking for imperceptible seismic events. *Geophysical Research Abstracts*, **16**, EGU2014-5756-1.
- Pollyea, R., Mohammadi, N., Taylor, J. and Chapman, M. (2018). Geospatial analysis of Oklahoma (USA) earthquakes (2011–2016): Quantifying the limits of regional-scale earthquake mitigation measures. *Geology*, **46**(3), pp.215-218.
- Power, M., Chiou, B., Abrahamson, N., Bozorgnia, Y., Shantz, T. and Roblee, C. (2008). An overview of the NGA project. *Earthquake Spectra*, **24**(1), pp.3-21.
- Pratt, W.E., Johnson, D.W. (1926). Local subsidence of the Goose Creek oil field. *Journal of Geology*, **34**, pp.577-590.
- Principia Mechanical Ltd (1986). North Sea seismicity. UK Dept. of Energy Offshore Technology Report No. OTH 86 219, HMSO, London.
- Rashedi, H. and Mahani, A. (2017). Data Analysis of Induced Seismicity in Western Canada. *CSEG RECORDER*, **42**(01), pp.26-28.
- Rawlinson, N., Fichtner, A., Sambridge, M. and Young, M.K. (2014). Seismic tomography and the assessment of uncertainty, *Adv. Geophysics*, **55**, pp.1-76.
- Rayleigh, C.B., Healy, J.H. and Bredehoeft, J.D. (1976). An experiment in Earthquake control at Rangely, Colorado. *Science* **191** (4233), pp.1230-1237.
- R-Crisis (2019). *R-CRISIS*. [online] Available at: <http://www.r-crisis.com/> [Accessed 18 Mar. 2019]
- Reasenber, P. (1985). Second-order moment of central California seismicity, 1969-82, *Journal of Geophysical Research*, **90**, pp.5479-5495.

- Repository.lboro.ac.uk (2020). *Types of Seismic Waves*. [online] Available at: <[https://repository.lboro.ac.uk/articles/figure/Types\\_of\\_seismic\\_waves/7309127/1](https://repository.lboro.ac.uk/articles/figure/Types_of_seismic_waves/7309127/1)> [Accessed 19 December 2020].
- Rey, J., Beauval, C. and Douglas, J. (2018). Do French macroseismic intensity observations agree with expectations from the European Seismic Hazard Model 2013? *Journal of Seismology*, **22**, pp.589-604.
- Reyes, C. and Wiemer, S. (2019). ZMAP7, a refreshed software package to analyse seismicity. *Geophysical Research Abstracts*, **21**, EGU2019-13153.
- Rhoades, D.A. (1997). Estimation of attenuation relations for strong-motion data allowing for individual earthquake magnitude uncertainties. *Bulletin of the Seismological Society of America*, **87**, pp.1674-1678.
- Richter, C.F. (1935). An instrumental earthquake magnitude scale. *Bulletin of the Seismological Society of America*, **25**, p.1-31.
- Rietbrock, A., Strasser, F. and Edwards, B. (2013). A Stochastic Earthquake Ground Motion Prediction Model for the United Kingdom. *Bulletin of the Seismological Society of America*, **103** (1), pp.57 -77.
- Ritsema, A. and Gürpınar, A. (1983). *Seismicity and seismic risk in the offshore North Sea area*. Dordrecht: D. Reidel Pub. Co., pp.53-75.
- Rognlien, B. (1987). Soil response on selected sites on the Norwegian Continental Shelf. *ELOCS Report* 4-1.
- Romeo, R. (2013). Seismic Risk Analysis of an Oil-Gas Storage Plant. In: *Proceedings of the International Conference on Seismic Design of Industrial Facilities*. September 26 2013 - September 27 2013, pp.17-26.
- Rothe, G.H. and Lui, C.Y. (1983). Possibility of induced seismicity in the vicinity of the Sleepy Hollow oil field, Southwestern Nebraska. *Bulletin of the Seismological Society of America*, **73** (5), pp.1357-1367.
- Rutledge, J., Phillips, W. and Schuessler, B. (1998). Reservoir characterization using oil-production-induced microseismicity, Clinton County, Kentucky. *Tectonophysics*, **289** (1-3), pp.129-152.f
- Sadigh, K. (1983). Considerations in the development of site-specific spectra. In: *Proceeding of Conference XXII; Site-Specific Effects of Soil and Rock on Ground Motions and the Implications for Earthquake Resistant Design*, U.S. Geol. Surv. Open-File Rept. 83-845, 423-458.

- Sadigh, K., Egan, J. and Youngs, R. (1986). Specification of ground motion for seismic design of long period structures (abstract). *Earthquake Notes*, **57**, no. 1, 13.
- Sakai, H., Pulido, N., Hasegawa, K. and Kuwata, Y. (2017). A new approach for estimating seismic damage of buried water supply pipelines. *Earthquake Engineering & Structural Dynamics*, **46**(9), pp.1531-1548.
- Sanchez-Sesma, F. (1987). Site effects on strong ground motion. *Soil Dynamics and Earthquake Engineering*, **6**(2), pp.124-132.
- Sargeant, S. and Ottemöller, L. (2009). *Lg* wave attenuation in Britain. *Geophysical Journal International*, **179**(3), pp. 1593-1606.
- Scherbaum, F., Bommer, J.J., Bungum, H., Cotton, F. and Abrahamson, N.A. (2005). Composite ground-motion models and logic trees: Methodology, sensitivities, and uncertainties. *Bulletin of the Seismological Society of America*, **95**(5), pp.1575-1593.
- Schnabel, P.B., Lysmer, J. and Seed, H.B. (1972). SHAKE: a computer program for earthquake response analysis of horizontally layered sites. *EERC Report*, 72-12, pp.88.
- Segall, P. (1985). Stress and subsidence resulting from subsurface fluid withdrawal in the epicentral region of the 1983 Coalinga Earthquake. *Journal of Geophysical Research*, **90**(B8), p.6801.
- Segall, P. (1989). Earthquakes triggered by fluid extraction. *Geology*, **17** (10), p.942.
- Segall, P., Grasso, J. and Mossop, A. (1994). Poroelastic stressing and induced seismicity near the Lacq gas field, southwestern France. *Journal of Geophysical Research*, **99** (B8), p.15423.
- Shahjouei, A. and Pezeshk, S. (2016). Alternative Hybrid Empirical Ground-Motion Model for Central and Eastern North America Using Hybrid Simulations and NGA-West2 Models. *Bulletin of the Seismological Society of America*, **106**(2), pp.734-754.
- Sharma, N., Convertito, V., Maercklin, N. and Zollo, A. (2013). Ground-Motion Prediction Equations for The Geysers Geothermal Area based on Induced Seismicity Records. *Bulletin of the Seismological Society of America*, **103**(1), pp.117-130.
- Sigbjörnsson, R. and Ambraseys, N. (2003). Uncertainty Analysis of Strong-Motion and Seismic Hazard. *Bulletin of Earthquake Engineering*, **1**(3), pp.321-347.
- Snoke J.A. (1989). Earthquake mechanisms. In: *Geophysics. Encyclopedia of Earth Science*. Springer, Boston, Massachusetts.
- Srinivasan, C., Sharma, M.L., Kotadia, J. and Willy, Y.A. (2008). Peak ground horizontal acceleration attenuation relationship for low magnitudes at short distances in south Indian region. In: *Proceedings of Fourteenth World Conference on Earthquake Engineering*. October 12 2008 – October 17 2008, Beijing, China. Paper no. 02-0135.

- Stacey, A., Birkinshaw, M. and Sharp, J. V. (2008). Life extension issues for ageing offshore installations. In: *American Society of Mechanical Engineers, proceedings of the international conference on offshore mechanics and arctic engineering*, vol 5, pp.199-216.
- Stevenson, J. (2003). Historical Development of the Seismic Requirements for Construction of Nuclear Power Plants in the U.S. and Worldwide and their Current Impact on Cost and Safety. In: *International Conference on Structural Mechanics in Reactor Technology*. August 17 2003 – August 22 2003, Prague, Czech Republic, pp.1-2.
- Stirling, M. and Petersen, M. (2006). Comparison of the historical record of earthquake hazard with seismic-hazard models for New Zealand and the continental United States. *Bulletin of the Seismological Society of America*, **96**(6), pp.1978-1994.
- Strachan, N., Hoefnagels, R., Ramírez, A., van den Broek, M., Fidje, A., Espegren, K., Seljom, P., Blesl, M., Kober, T. and Grohnheit, P. (2011). CCS in the North Sea region: A comparison on the cost-effectiveness of storing CO<sub>2</sub> in the Utsira formation at regional and national scales. *International Journal of Greenhouse Gas Control*, **5**(6), pp.1517-1532.
- Strasser, F., Abrahamson, N. and Bommer, J.J. (2009). Sigma: Issues, Insights, and Challenges. *Seismological Research Letters*, **80**(1), pp.40-56.
- Strasser, F., Bommer, J. and Abrahamson, N. (2007). Truncation of the distribution of ground-motion residuals. *Journal of Seismology*, **12**(1), pp.79-105.
- Suckale, J. (2009). Induced seismicity in hydrocarbon fields, *Advances in Geophysics*, **51**, ch. 2, pp.55-106
- Sumy, D., Neighbors, C., Cochran, E. and Keranen, K. (2017). Low stress drops observed for aftershocks of the 2011 M<sub>w</sub> 5.7 Prague, Oklahoma, earthquake. *Journal of Geophysical Research: Solid Earth*, **122**(5), pp.3813-3834.
- Tocher D. 1958. Earthquake energy and ground breakage. *Bulletin of the Seismological Society of America*, **48**, pp.147-153
- Toro, G. (2002). *Modification of the Toro et al. (1997) Attenuation Equations for Large Magnitudes and Short Distances*. Risk Engineering, Inc.
- Toro, G. (2006). The Effects of Ground-Motion Uncertainty on Seismic Hazard Results: Examples and Approximate Results. Poster presented at: *2006 SSA Annual Meeting*. April 18 2006, San Francisco, USA.
- Toro, G., Abrahamson, N. and Schneider, J. (1997). Model of Strong Ground Motions from Earthquakes in Central and Eastern North America: Best Estimates and Uncertainties. *Seismological Research Letters*, **68**(1), pp.41-57.

- Trifunac, M.D. and Brady, A.G. (1975). A study of the duration of strong earthquake ground motion. *Bulletin of the Seismological Society of America*, **65**, pp.581-626.
- Trifunac, M.D. and Todorovska, M. (2001). Evolution of accelerographs, data processing, strong motion arrays and amplitude and spatial resolution in recording strong earthquake motion. *Soil Dynamics and Earthquake Engineering*, **21**, pp.537-555.
- United States Geological Survey (2003). *Rupture in South-Central Alaska— The Denali Fault Earthquake of 2002*. Menlo Park, California: United States Geological Survey.
- Urlainis, A., Shohet, I. and Levy, R. (2015). Probabilistic Risk Assessment of Oil and Gas Infrastructures for Seismic Extreme Events. *Procedia Engineering*, **123**, pp.590-598.
- van Eck, T., Goutbeek, F., Haak, H. and Dost, B. (2006). Seismic hazard due to small-magnitude, shallow-source, induced earthquakes in The Netherlands. *Engineering Geology*, **87**(1-2), pp.105-121.
- van Eijs, R., Mulders, F., Nepveu, M., Kenter, C. and Scheffers, B. (2006). Correlation between hydrocarbon reservoir properties and induced seismicity in the Netherlands. *Engineering Geology*, **84**(3-4), pp.99-111.
- van Thienen-Visser, K. and Breunese, A. J. (2015). Induced seismicity of the Groningen gas field: History and recent developments. *The Leading Edge*, **34**, pp.664-671.
- van Thienen-Visser, K., Sijacic, D., van Wees, J., Kraaijpoel, D. and Roholl, J. (2016). *Groningen field 2013 to present Gas production and induced seismicity*. Utrecht: TNO.
- Verdon, J. (2014). Significance for secure CO<sub>2</sub> storage of earthquakes induced by fluid injection. *Environmental Research Letters*, **9**(6), p.064022.
- Verdon, J., Baptie, B. and Bommer, J. (2019). An Improved Framework for Discriminating Seismicity Induced by Industrial Activities from Natural Earthquakes. *Seismological Research Letters*, **90**(4), pp.1592-1611.
- Walling, M.A. and Abrahamson, N.A (2012). Non-Ergodic Probabilistic Seismic Hazard Analyses, Paper presented at: *WCEE, 24 – 28 September, Lisboa, Portugal*.
- Watabe, M., Tohido, M., Chiba, O. and Fukuzawa, R. (1990). Peak accelerations and response spectra of vertical strong motions from near-field records in USA. In: *Proceedings of the Eighth Japan Earthquake Engineering Symposium*. Volume 1, pp.301-306.
- Weatherill, G. and Burton, P. (2010). An alternative approach to probabilistic seismic hazard analysis in the Aegean region using Monte Carlo simulation. *Tectonophysics*, **492**(1-4), pp.253-278.

- Wells, D. and Coppersmith, K.J. (1994). New empirical relationships among magnitude, rupture length, rupture width, rupture area, and surface displacement. *Bulletin of the Seismological Society of America*, **84**(4), pp.974-1002.
- Wiemer, S., and Wyss, M. (2000). Minimum magnitude of complete reporting in earthquake catalogs: examples from Alaska, the western United States, and Japan. *Bulletin of the Seismological Society of America*, **90**, pp.859-869.
- Wilson, M., Davies, R., Foulger, G., Julian, B., Styles, P., Gluyas, J. and Almond, S. (2015). Anthropogenic earthquakes in the UK: A national baseline prior to shale exploitation. *Marine and Petroleum Geology*, **68**, pp.1-17.
- Wiprut, D. and Zoback, M. (2000). Fault reactivation and fluid flow along a previously dormant normal fault in the northern North Sea. *Geology*, **28**(7), pp.595-598.
- Woessner, J., Laurentiu, D., Giardini, D. *et al.* (2015). The 2013 European Seismic Hazard Model: key components and results. *Bulletin of Earthquake Engineering*, **13**, pp.3553–3596.
- Wong, I. (2013). How big, how bad, how often: are extreme events accounted for in modern seismic hazard analyses? *Natural Hazards*, **72**(3), pp.1299-1309.
- Wood Mackenzie (2017). *US\$32 Billion of Decommissioning Worldwide Over the Next Five Years: Is the Industry Ready?* Wood Mackenzie Reports.
- Wyss, M., Hasegawa, A., Wiemer, S. and Umino, N. (1999). Quantitative mapping of precursory seismic quiescence before the 1989, m7.1 off-Sanriku earthquake, Japan. *Annali Di Geofisica*, **42**, pp.851-869.
- Yang, W. (2014). *Reflection Seismology*. Elsevier.
- Yenier, E., Atkinson, G. and Sumy, D. (2017). Ground Motions for Induced Earthquakes in Oklahoma. *Bulletin of the Seismological Society of America*, **107**(1), pp.198-215.
- Yerkes, R. and Castle, R. (1976). Seismicity and faulting attributable to fluid extraction. *Engineering Geology*, **10** (2-4), pp.151-167.
- Yeter, B., Tekgoz, M., Garbatov, Y. and Soares, C. G. (2020). Fragility analysis of an ageing monopile offshore wind turbine subjected to simultaneous wind and seismic load. *Safety in Extreme Environments*, **2**, pp.155–170.
- Youngs, R. R., Abrahamson, N., Makdisi, F. I. and Sadigh, K. (1995). Magnitude-dependent variance of peak ground acceleration. *Bulletin of the Seismological Society of America*, **85**(4), pp.1161-1176.
- Zalachoris, G. and Rathje, E. (2019). Ground Motion Model for Small-to-Moderate Earthquakes in Texas, Oklahoma, and Kansas. *Earthquake Spectra*, **35**(1), pp.1-20.

- Zanini, M., Hofer, L. and Faleschini, F. (2019). Reversible ground motion-to-intensity conversion equations based on the EMS-98 scale. *Engineering Structures*, **180**(1), pp.310-320.
- Zarrin, M., Behrouz, A. and Abyani, M. (2017). Probabilistic Seismic Collapse Analysis of Jacket Offshore Platforms. *Journal of Offshore Mechanics and Arctic Engineering*, **140**.
- Zhang, Q. and Zheng, X. (2019). Offshore earthquake ground motions: Distinct features and influence on the seismic design of marine structures. *Marine Structures*, **65**, pp.291-307.
- Zoback, M. and Zinke, J. (2002). Production-induced Normal Faulting in the Valhall and Ekofisk Oil Fields. *Pure and Applied Geophysics*, **159**(1), pp.403-420.

## **Appendix A: Basic Earthquake Terminology**

It is important to define and explain the basic terminology used in earthquake engineering. Basic earthquake terminology includes (1) earthquake generation and seismic waves, (2) earthquake magnitude, (3) earthquake stress drop, (4) earthquake distance metrics and (5) earthquake focal mechanisms.

### **A.1 Earthquake Generation and Seismic Waves**

The following overview of earthquake generation is largely summarised from Snoke (1989).

Earthquakes occur in areas subjected to deformation induced by regional tectonic stresses (plate tectonics). Once the accumulated stress at a single point surpasses the strength of the rock, a brittle fracture and/or slip on pre-existing zones of weakness occurs, resulting in a rupture. The region on which this rupture occurs is referred to as an earthquake fault, and pre- and post-rupture the fault is in static equilibrium. Rupturing results in the release of the accumulated stress on the fault. During a rupture, the accumulated strain energy on the fault is released as a combination of radiated (elastic) seismic waves, frictional heating of the fault surface and the cracking of the surrounding rock, resulting in the occurrence of an earthquake. The gradual accumulation of strain energy on a fault, followed by its release in the form of an earthquake generating rupture summarises the elastic rebound theory of Reid (1911), which is the most common model for the origin of (crustal) earthquakes.

The seismic waves generated during an earthquake can be split into (1) body waves and (2) surface waves. Ground-motions refer to the movement of the ground at a given site due to incident seismic waves. The following overview of seismic waves is summarised from Yang (2014).

Body waves are seismic waves which travel through the body of the earth and are reflected and transmitted at interfaces of differing seismic velocity and/or density. Body waves comprise of P-waves and S-waves. P-waves can be referred to as pressure-waves (due to being formed from alternating compressions and rarefactions of the medium through which they propagate), longitudinal/compressional waves (due to particle compression along the direction of P-wave propagation – Fig. A.0) or primary-waves (due to being the first waves recorded by a seismograph – Fig. A.1). S-waves can be referred to as shear waves (due to inducing shear in the medium through which they propagate), transverse waves (due to particle motion being transverse to the direction of S-wave propagation – Fig. A.0) and secondary waves (due to being slower than P-waves and therefore recorded second by a seismograph – Fig. A.1). The offset in arrival times between P-waves and S-wave at the same seismograph can be used to estimate the distance from the location to the earthquake. If distances for a single earthquake can be computed at 3 separate locations with good azimuthal coverage, then the earthquake's location can be determined using triangulation. Unlike P-waves, S-waves cannot propagate through the molten outer core of the earth due to their shearing motion not being transmittable through fluids with low or zero viscosity.

Surface waves are those which only travel through the earth's crust, and are produced when body waves propagate toward surface. Consequently, surface waves are more often produced by shallow earthquakes than by deep earthquakes. Surface waves comprise of lower frequency vibrations than body waves, and therefore arrive later than both P-waves and S-waves at the same seismograph (Fig. A.1). However, the lower frequency vibrations of surface waves result in them being largely responsible for the damage resulting from earthquakes due to having the largest amplitudes of any seismic waves (Fig. A.1). Surface waves comprise of Love waves and Rayleigh waves. For Love waves, movement is perpendicular to the direction of propagation (transverse motion<sup>69</sup> - Fig. A.0), resulting in side-to-side movement being observed in the ground through which Love waves are propagating. Love waves are the fastest type of surface waves. For Rayleigh waves, motion occurs as rolling similar to the movement of an ocean wave (Fig. A.0). The rolling motion causes both vertical and horizontal movement of the ground through which Rayleigh waves propagate, resulting in most felt shaking from an earthquake being due to Rayleigh waves.

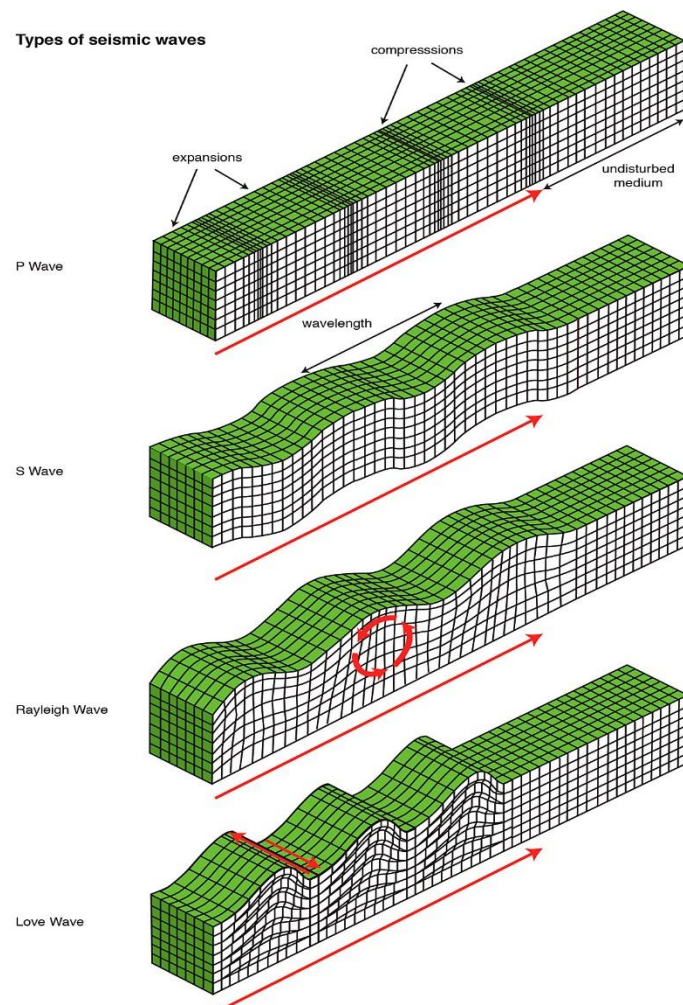


**Figure A.0** Motion for each main type of seismic wave. Taken from [http://Repository.lboro.ac.uk/articles/figure/Types\\_of\\_seismic\\_waves/7309127](http://Repository.lboro.ac.uk/articles/figure/Types_of_seismic_waves/7309127) (2020).

<sup>69</sup> Love waves effectively have the same motion as S-waves, but with horizontal displacement rather than vertical displacement.

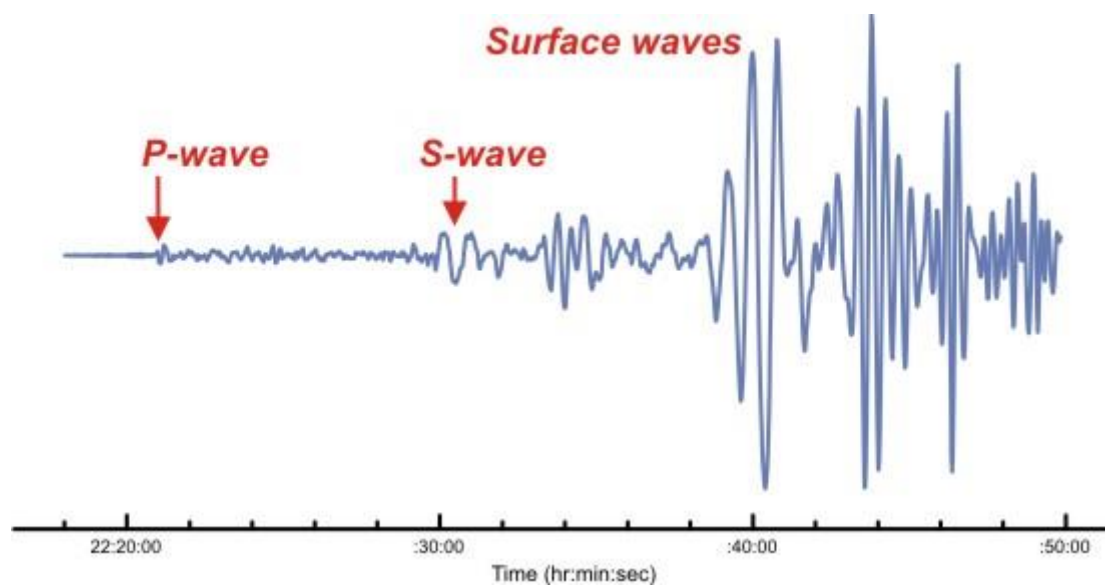


**Figure A.1** Seismogram for an arbitrary earthquake demonstrating arrival time offset for P-waves, S-waves and surface waves. Adapted from Earthquakes.bgs.ac.uk (2020b). Contains British Geological Survey materials @NERC 2020.

## A.2 Earthquake Magnitude

The magnitude of an earthquake is a number which quantifies the amplitude (size) of the event (Denton, 2007). Earthquake magnitude scales are logarithmic (i.e. a one-unit increase in earthquake magnitude corresponds to a ten-fold increase in earthquake amplitude). Several magnitude scales have been developed. In the present day the moment magnitude ( $M_w$ ) scale is widely used because it can measure the amplitude of larger earthquakes, unlike the historic Richter scale, which frequently underestimates the size of larger earthquakes (Richter, 1935). Furthermore,  $M_w$  is more closely connected to the physical size of the earthquake, rather than other scales which are comparatively arbitrary (Denton, 2007).

The Richter scale determines the size of an earthquake using the amplitude of ground-motion displacement measured by a seismograph, and was originally determined for earthquakes in southern California (Denton, 2007):

$$M_L = \log_{10}(d) + 2.56\log_{10}(R) - 1.67 \quad (\text{A.0})$$

where  $d$  represents the measured horizontal ground-motion displacement (measured in micrometres) and  $R$  represents the distance from the earthquake epicentre to the seismograph which measured the ground-motion displacement (measured in km). It should be noted that  $d$  does not represent the true horizontal ground-motion displacement because it is amplified by the instrument itself (see Chapter 3 for more details on seismographs). This scale is still applicable for measuring earthquakes occurring at shallow depths for distances of less than 600 km, and so is commonly referred to as the local magnitude ( $M_L$ ) scale (Denton, 2007).

For earthquakes in regions with attenuation parameters different to those in southern California, the Richter scale equation can be written as (Bormann and Dewey, 2012)<sup>70</sup>:

$$M_L = \log_{10}(d) + C(R) - D \quad (\text{A.1})$$

Where  $d$  and  $R$  are the same as in equation A.0, aside that  $d$  can represent the measured vertical ground-motion displacement as well as the horizontal ground-motion displacement.  $C$  and  $D$  are calibrated to fit the different regional attenuation values, as well as to account for systematic differences which may occur between ground-motion displacements measured on horizontal seismographs and vertical seismographs (Bormann and Dewey, 2012).

The  $M_W$  scale uses the size of the area of fault rupture (the seismic moment,  $M_0$ ) of an earthquake to determine the magnitude of the earthquake (Denton, 2007). To determine  $M_W$ , one must therefore first calculate  $M_0$  for the earthquake:

$$M_0 = \mu * \text{rupture area} * \text{slip length} \quad (\text{A.2})$$

where  $\mu$  is the shear modulus of the earth's crust ( $\sim 3 \times 10^{10}$  N/m). In practice,  $M_0$  is computed from the spectral analysis of a seismogram<sup>71</sup>. Following the calculation of  $M_0$ , the corresponding  $M_W$  can be calculated (Hanks and Kanamori, 1978):

$$M_W = 2/3 \log_{10}(M_0) - 6.06 \quad (\text{A.3})$$

Importantly, although  $M_L$  often over-predicts for larger earthquakes the constants used for the definition of  $M_W$  (equation A.3) mean that for smaller earthquakes the  $M_L$  and  $M_W$  scales should match reasonably well (Denton, 2007).

### A.3 Earthquake Stress-Drop

Alongside magnitude scales, stress drop parameters are used to estimate the size of an earthquake source. Within this investigation, the static stress drop is considered, and is summarised from Boore (2003). The static stress-drop of an earthquake can be defined as the difference between the average shear stress across a fault before and after a rupture:

$$\Delta\sigma = c\mu \frac{D_z}{L} \quad (\text{A.4})$$

where  $\Delta\sigma$  represents the static stress-drop,  $D_z$  represents the average slip throughout the faulted area,  $L$  represents the length of the fault area,  $\mu$  represents the elastic shear modulus and  $c$  represents a geometric constant (which is close to 1 if  $L$  is measured correctly) (Ruff, 1999). In practical applications

---

<sup>70</sup> To determine local magnitudes in the United Kingdom and the North Sea, the BGS would utilise equation (A.1).

<sup>71</sup> A seismogram is the graphical output of a seismograph. See Chapter 3 for more details on seismographs, seismograms and the signal processing of seismograms, including (Fourier) spectral analysis.

such as the stochastic simulation of ground-motions, static stress drop is often estimated using the Brune stress drop model<sup>72</sup>.

A commonly used scaling dependency in seismology is the relationship between seismic moment and corner frequency. As first recognised by Aki (1967), a constant static stress-drop is suggested by the seismic moment being inversely proportional to the cubed corner frequency (Fig. A.2). This does not definitively mean that static stress-drop is always constant and independent of earthquake size, although the static stress-drop is usually found to be constant for earthquakes of varying sizes, with this self-similar scaling applying down towards a moment magnitude close to zero (Aki, 1967).

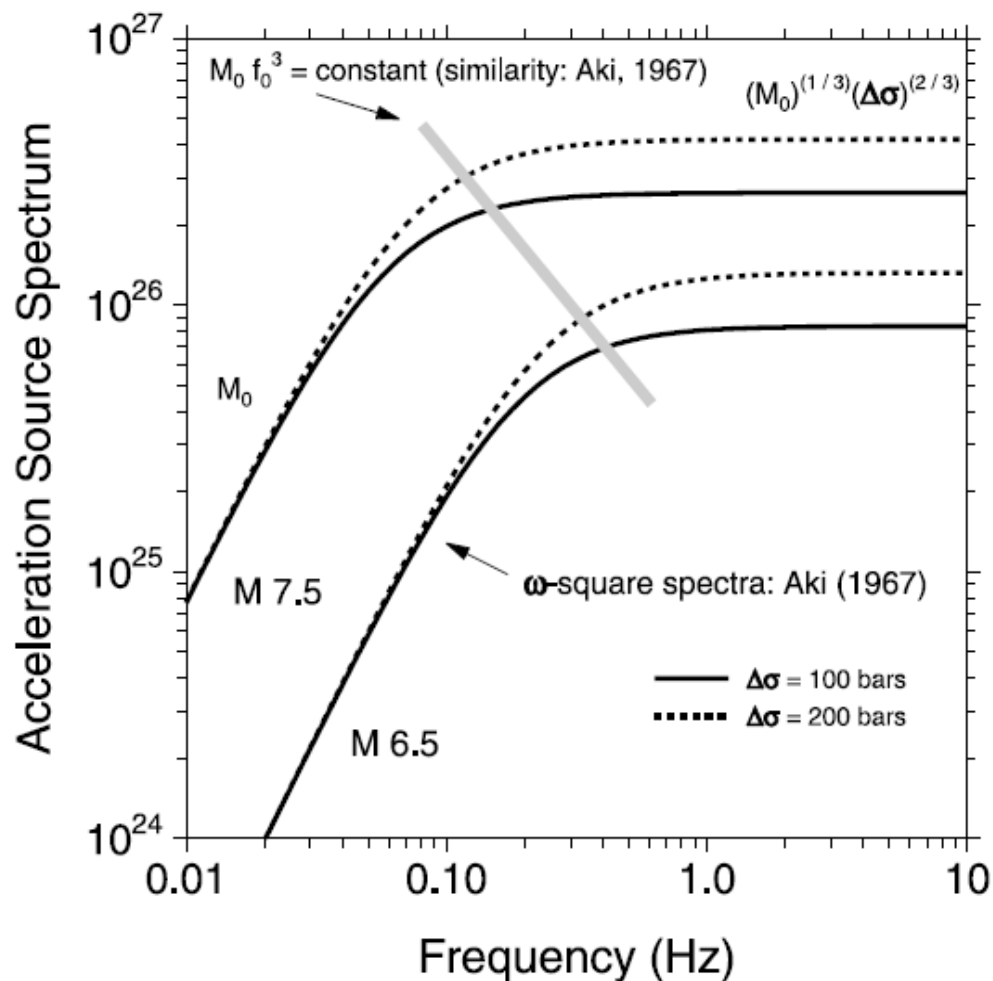


**Figure A.2** Source scaling for single corner frequency  $\omega^2$  model spectral shape. For constant stress drop  $M_0 f_0$  is a constant (Aki, 1967) The dependence of the corner frequency ( $f_0$ ) on the seismic moment ( $M_0$ ) (represented by the shaded line) determines the scaling of the spectral shapes. Taken from Boore (2003).

<sup>72</sup> See Chapter 5 for more details on both stochastic ground-motion simulations and the Brune stress drop model.

#### A.4 Earthquake Distance Metrics

There are four variants of earthquake distance which are commonly used in engineering seismology: (1) epicentral distance, (2) hypocentral distance, (3) Joyner-Boore distance and (4) rupture distance. Epicentral distance refers to the horizontal distance from the epicentre (i.e. the point on the surface directly above the hypocentre - the point where the earthquake rupture starts) of an earthquake to a site of interest (Fig. A.3). Hypocentral distance refers to the distance from the hypocentre of an earthquake to a site of interest (Fig. A.3). Joyner-Boore distance refers to the shortest horizontal distance from the vertical surface projection of a rupture plane to a site of interest (Fig. A.3). Rupture distance refers to the shortest distance from a rupture plane to a site of interest (Fig. A.3). It should be noted that within the field of engineering seismology that the distance from the earthquake to a site of engineering interest (measured using one of the four variants discussed above) is conventionally referred to as the source-to-site distance.

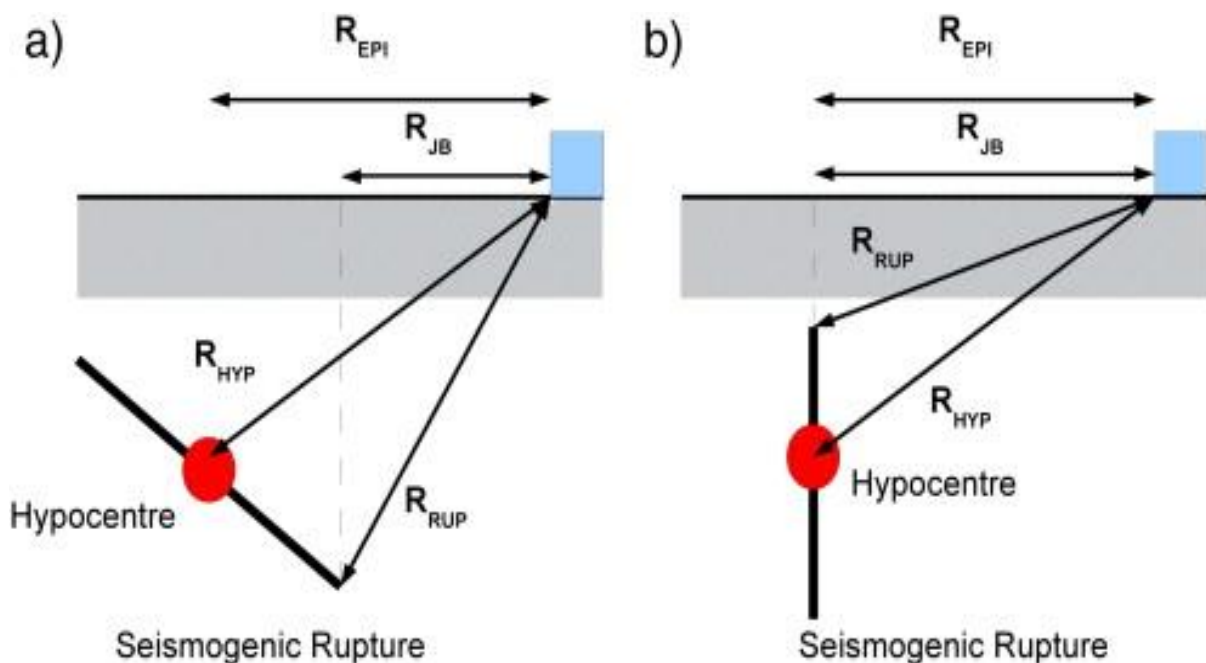


**Figure A.3** Schematic diagram for the four common source-site distance metrics for a) dipping fault, and b) a vertical fault.  $R_{epi}$  = epicentral distance,  $R_{hyp}$  = hypocentral distance,  $R_{jb}$  = Joyner–Boore distance and  $R_{rup}$  = rupture distance. Taken from Weatherill and Burton (2010).

#### A.5 Earthquake Focal Mechanism Terminology

The focal mechanism of an earthquake refers to the direction of slip and the orientation of the fault on which the earthquake occurs. The following explanation of earthquake focal mechanism terminology is summarised from Earthquake.usgs.gov (2018).

Focal mechanisms are determined from the interpretation of seismograms. Such mechanisms are often displayed on maps as symbols resembling beach balls (Fig. A.4). These beach ball symbols are projections on a horizontal plane of the lower half of an arbitrary sphere (focal sphere) encapsulating the earthquake source. A line is set where the fault plane intersects the focal sphere. The stress field

orientation at the time of fault rupture is a key factor in determining the direction of slippage on the fault plane.

The beach ball symbols illustrate this stress field orientation. In these beach ball symbols, the grey quarters contain the tension axis (T) (Fig. A.4), which represents the minimum compressive stress direction (compression), whereas the white quarters contain the pressure axis (P), which represents the maximum compressive stress direction (dilation). Figure A.4 illustrates the various focal mechanisms which can be determined. The first three examples (strike-slip, normal and reverse) represent fault motion which is either mostly horizontal (strike slip) or mostly vertical (normal and reverse). The last example (oblique-reverse) represents fault motion which comprises largely of both horizontal and vertical motion.

It should be noted that the determination of several earthquake focal mechanisms within a geological region enables the identification of geological faults, as well as insight into the regional stress field orientation (Snoke. 1989).

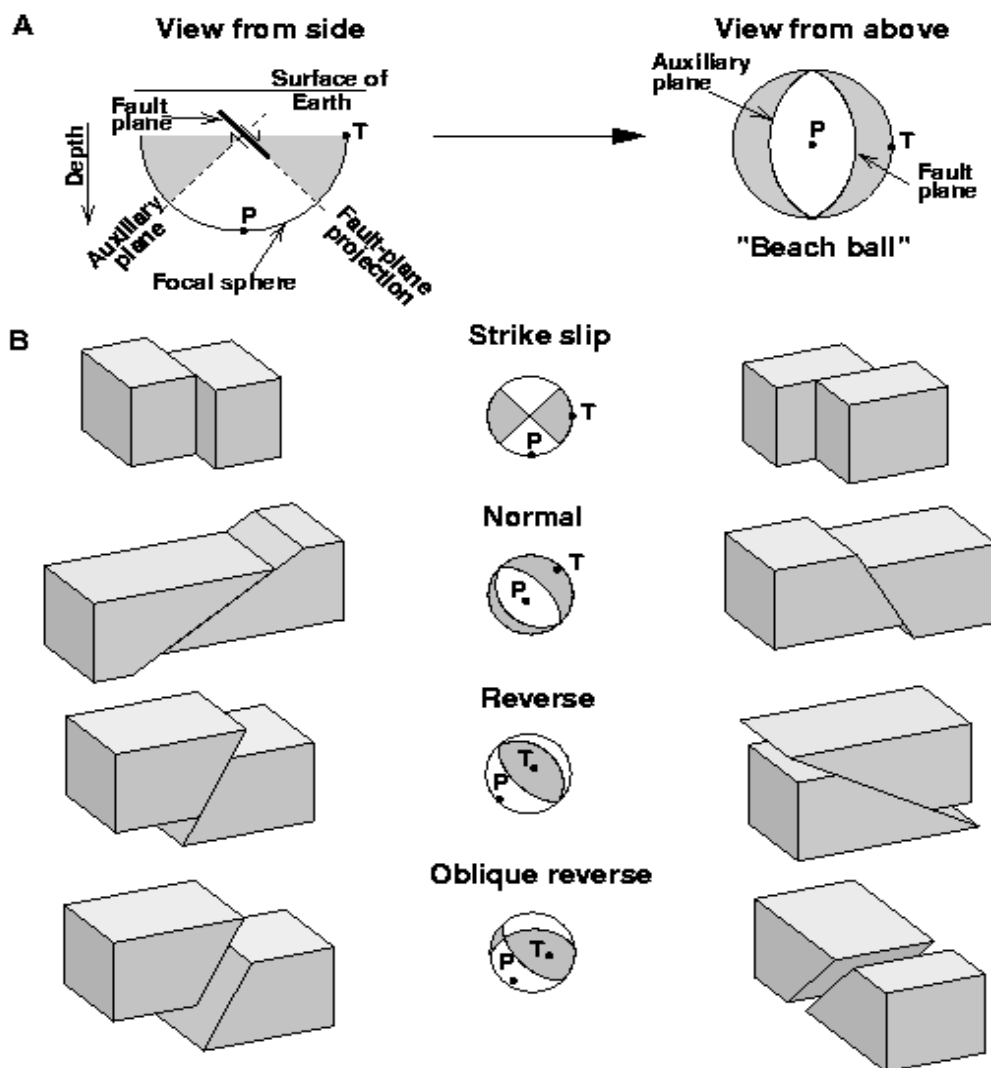


**Figure A.4** Schematic diagram for earthquake focal mechanisms. Taken from Earthquake.usgs.gov (2018).

## Appendix B: Overview of Probabilistic Seismic Hazard Assessment

The following description of probabilistic seismic hazard assessment (PSHA) is largely summarised from Baker (2015), which should be consulted for further details. This description summarises a conventional approach PSHA. Please consult section B.8 for a description of the Monte Carlo PSHA approach.

The principal aim of an earthquake engineering analysis is to ensure a specified structure can withstand a given level of ground-shaking and maintain a certain level of structural integrity. In the context of this investigation the structures such analyses are considered for are high value offshore facilities in the North Sea e.g. oil and gas platforms and offshore wind turbines.

To determine the intensity of ground-shaking incorporated within such an analysis, the large uncertainties associated with the location, magnitude and subsequent ground-shaking of potential earthquakes in the North Sea must be accounted for. PSHA is used because this method permits the assimilation of these uncertainties to provide probability distributions for future ground-shaking intensities that could occur in the North Sea.

A key output of a PSHA is a seismic hazard curve (Fig. B.0). A seismic hazard curve provides the annual frequency of exceedance for a given level of ground-shaking. The return period for a given level of ground-shaking is defined as the reciprocal of the corresponding annual rate of exceedance<sup>73</sup>. The seismic hazard curve is an essential input for calculating the engineering risk presented by ground-shaking. The lower levels of ground-shaking are exceeded relatively frequently, whereas the higher levels of ground-shaking occur rarely. A seismic hazard curve could be obtained experimentally if one could actually observe earthquakes over thousands of years. In the case of assessing the risk associated

---

<sup>73</sup> For example, if a given level of ground-shaking has a 0.005 annual rate of exceedance, then the return period is equal to  $1/0.005 = 200$  years. This does not indicate that the given level of ground-shaking is exceeded every 200 years, but that mean time between exceedances is every 200 years.

For a given annual rate of exceedance, the probability of exceeding a given level of ground-shaking within a specified time window can be calculated if the probability distribution of time between the occurrence of earthquakes is known. This distribution is assumed to be Poissonian. The use of a Poissonian distribution assumes that the occurrences of earthquakes are independent.

Under the assumption of a Poissonian distribution, the probability of observing at least one event over a period of time  $t$  is equal to:

$$P(\text{at least one event in time } t) = 1 - e^{-\lambda t} \quad (\text{B.0})$$

where  $\lambda$  is the annual rate of occurrence of an event. If  $\lambda t$  (equal to the expected number of occurrences) is small (less than  $\sim 0.1$ ), the probability can be approximated as:

$$P(\text{at least one event in time } t) \approx \lambda t \quad (\text{B.1})$$

Using the above calculations, PSHA results are converted between annual rates of exceedance, probabilities of exceedance and return periods. It should be noted that (1) the conversion between annual rates of exceedance and probabilities of exceedance is usually made assuming a Poissonian distribution for the time between the occurrence of earthquakes and (2) probabilities of exceedance and annual rates of exceedance are only considered as equivalent if the probability level of interest is small (less than  $\sim 0.1$ ).

with flooding, one can in fact use such an observationally focused approach, but for earthquakes (including those in the North Sea) this can't be undertaken due to an insufficient number of observations to extrapolate to relatively infrequent, higher ground-shaking intensity events. Furthermore, one must consider the uncertainties in location, size and associated ground-shaking, whereas in flooding only the size of the flood event must be considered. Consequently, one must obtain the required seismic hazard data through the mathematical amalgamation of models for the locations and sizes of potential future earthquakes with predictions for the ground-shaking resulting from such earthquakes (i.e. by using PSHA).

There are five stages to undertaking a conventional approach PSHA (which are discussed below):

1. Identify all earthquake sources within the specified region (i.e. the North Sea) capable of producing significantly damaging ground-motions.
2. Determine the rates at which earthquakes of various magnitudes are expected to occur within the specified region.
3. Determine the distribution of source-to-site distances for potential earthquakes in the specified region.
4. Determine the distribution of predicted ground-shaking in the specified region as function of magnitude, distance and other input parameters.
5. Assimilate uncertainties in future earthquakes size, distance and ground-shaking for the specified region to compute the annual rate of exceeding a given level of ground-shaking.

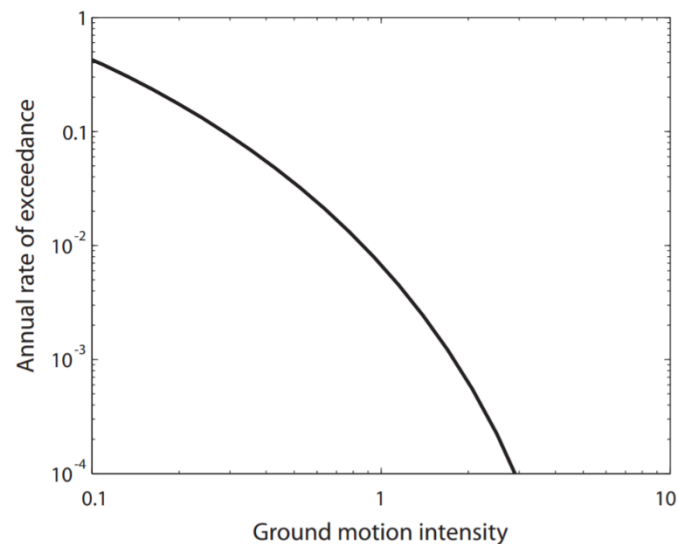


**Figure B.0** *Seismic hazard curve for an arbitrary return period.* Taken from Baker (2015).

### **B.1 Identification of Earthquake Sources**

One must consider all earthquake sources in the specified region capable of producing significantly damaging ground-motions. Such potential sources comprise of faults (Fig. B.1) (planar surfaces

determined through observations of past earthquake locations, as well as geological and seismological evidence), or in the case that specific faults are not identifiable, areal regions within which earthquakes could occur (Fig. B.2). Following the identification of possible earthquake sources in the specified region, one can determine the distributions of magnitudes and distances associated with each source identified.

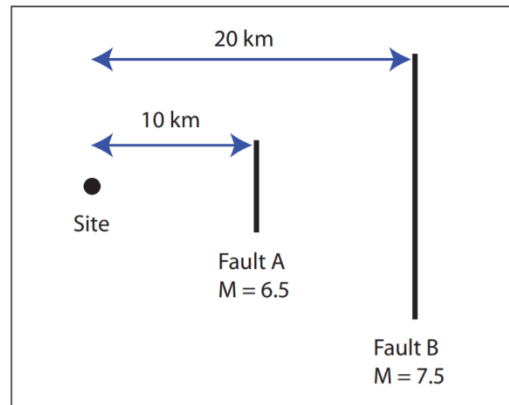


**Figure B.1** Fault sources with different associated magnitudes and source-to-site distances. Taken from Baker (2015).

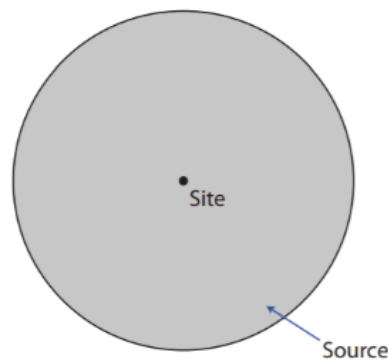


**Figure B.2** Areal earthquake source with a site located within it. Taken from Baker, 2015).

## B.2 Identification of Earthquake Magnitudes

Earthquake sources are capable of producing earthquakes of various magnitudes (i.e. sizes). The number of earthquakes within a region greater than a given size is known to follow a distribution of:

$$\log_{10} N = a - bm \tag{B.2}$$

where  $N$  is the number of earthquakes larger than or equal to magnitude  $m$ , and  $a$  and  $b$  are constants. This distribution was first observed by Gutenberg and Richter (1944), and is known as the Gutenberg-Richter recurrence law (Fig. B.3). The constants  $a$  and  $b$  are estimated from statistical analysis of observed earthquakes in the specified region and the consideration of regional geological evidence (Gutenberg and Richter, 1944). The  $a$ -parameter is indicative of the overall rate of earthquakes (the

activity rate), and the  $b$ -parameter indicates the ratio of small to large earthquakes (usually equalling approximately 1). The  $a$ -parameter is often normalised over the duration of the catalogue to provide an annual activity rate.

This recurrence law (equation B.2) can be used to compute the cumulative distribution function (CDF) for earthquakes in the specified region that are larger than a given minimum magnitude  $m_{min}$ :

$$\begin{aligned}
 F_M(m) &= P(M \leq m | M > m_{min}) \\
 &= \frac{\text{Rate of earthquakes with } m_{min} < M \leq m}{\text{Rate of earthquakes with } m_{min} < M} \\
 &= \frac{\lambda_{m_{min}} - \lambda_m}{\lambda_{m_{min}}} \\
 &= \frac{10^{a-bm_{min}} - 10^{a-bm}}{10^{a-bm_{min}}} \\
 &= 1 - 10^{-b(m-m_{min})}, m > m_{min}
 \end{aligned} \tag{B.3}$$

where  $F_M(m)$  is the CDF for magnitude  $M$ . The probability density function (PDF) can be determined through taking the derivative of the CDF:

$$\begin{aligned}
 f_M(m) &= \frac{d}{dm} F_M(m) \\
 &= \frac{d}{dm} [1 - 10^{-b(m-m_{min})}] \\
 &= b \ln(10) 10^{-b(m-m_{min})}, m > m_{min}
 \end{aligned} \tag{B.4}$$

where  $f_M(m)$  is the PDF for magnitude  $M$ . This PDF clearly relies on the Gutenberg-Richter recurrence law (equation B.2), which theoretically predicts magnitudes with no upper limit, however the finite size of faults limits the maximum magnitude of an earthquake in reality. Consequently, if a maximum magnitude  $m_{max}$  is determined for the specified region, then equation B.3 becomes

$$F_M(m) = \frac{1 - 10^{-b(m-m_{min})}}{1 - 10^{-b(m_{max}-m_{min})}}, m_{min} < m < m_{max} \tag{B.5}$$

and equation B.4 becomes

$$f_M(m) = \frac{b \ln(10) 10^{-b(m-m_{min})}}{1 - 10^{-b(m_{max}-m_{min})}}, m_{min} < m < m_{max} \tag{B.6}$$

The restricted magnitude distribution associated with having a maximum magnitude for a specified region is known as a bounded Gutenberg-Richter distribution (Fig. B.3). Within the North Sea, the maximum magnitude event observed so far was the local magnitude ( $M_L$ ) 6.1 Dogger Bank earthquake of 1931 (Ritsema and Gürpınar, 1983), and thus for the North Sea region a bounded Gutenberg-Richter

scale with a maximum magnitude of approximately  $M_L$  6.5 is appropriate (as is used within Bungum et al., 2000's PSHA study for the North Sea).

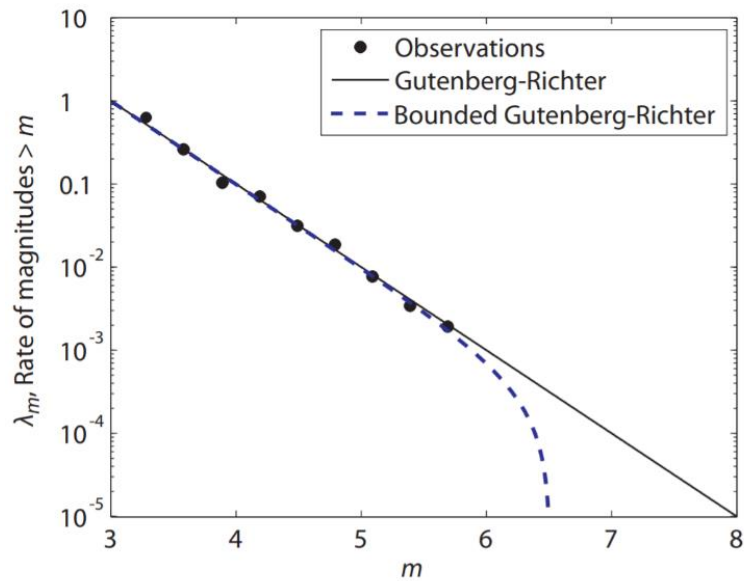


**Figure B.3** A Gutenberg-Richter distribution, a bounded Gutenberg-Richter distribution and observed data for an arbitrary region. Taken from Baker (2015).

For further use within the PSHA process, the continuous distribution of potential magnitudes must be converted into discrete sets of magnitudes (Fig. B.4). For example, for a source with a minimum considered magnitude of 5, a maximum magnitude of 8 and a  $b$  parameter of 1 in an arbitrary region, Tab. B.0 shows the magnitude bins, associated CDF values and the associated probabilities of occurrence for these discrete magnitude bins as columns 1, 2 and 3 respectively. The associated probability for each magnitude bin is computed as follows:

$$P(M = m_j) = F_M(m_j + 1) - F_M(m_j) \quad (\text{B.7})$$

where  $m_j$  are the discrete set of magnitudes, arranged so that  $m_j < m_j + 1$  to the discrete value  $m_j$ .

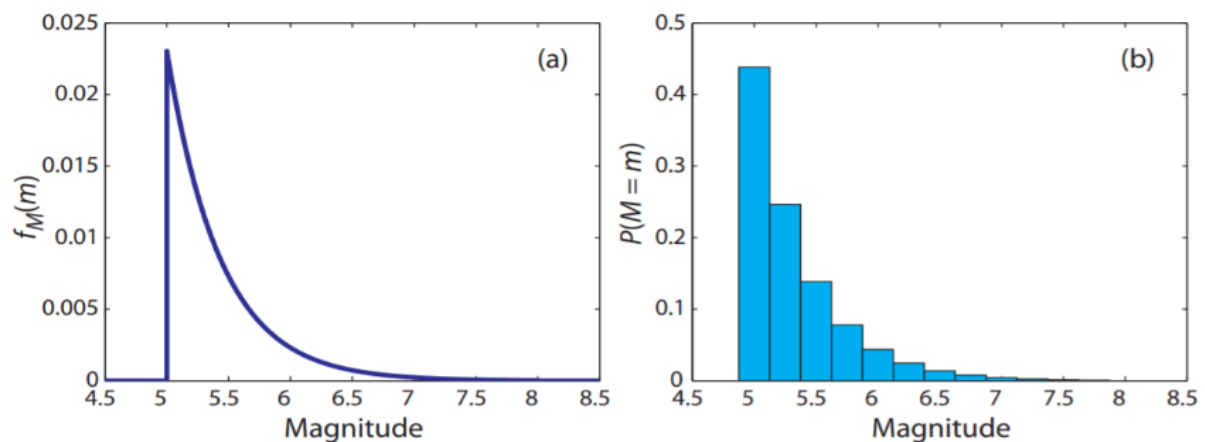


**Figure B.4** Conversion of a continuous magnitude distribution (a) into a discrete magnitude distribution (b) for a hypothetical source with a truncated Gutenberg-Richter distribution with a minimum considered magnitude of 5, a maximum magnitude of 8 and a  $b$  parameter of 1. Taken from Baker (2015).

**Table B.0** Magnitude probabilities for a hypothetical source with a minimum considered magnitude of 5, a maximum magnitude of 8 and a  $b$  parameter of 1. Taken from Baker (2015).

$m_j$	$F_M(m_j)$	$P(M = m_j)$
5.00	0.0000	0.4381
5.25	0.4381	0.2464
5.50	0.6845	0.1385
5.75	0.8230	0.0779
6.00	0.9009	0.0438
6.25	0.9447	0.0246
6.50	0.9693	0.0139
6.75	0.9832	0.0078
7.00	0.9910	0.0044
7.25	0.9954	0.0024
7.50	0.9978	0.0014
7.75	0.9992	0.0008
8.00	1.0000	0.0000

### B.3 Identification of Earthquake Distances

To predict the ground-shaking at a specified site, it is necessary to model the distribution of source-to-site distances. For an earthquake source it is generally assumed that an earthquake is equally likely to occur anywhere along a fault or within a specified area. Consequently, considering that the earthquake locations are assumed to be uniformly distributed over a source, it is relatively simple to determine the source-to-site distance distribution using solely the geometry of the identified earthquake source. For example, if we consider an area earthquake source in the North Sea with a site situated within it (e.g. an oil and gas platform or an offshore wind turbine facility), in which the source is equally likely to produce an earthquake anywhere within 100 km of the site (Fig. B.5), a probabilistic description of the source-to-site distances can be computed. The probability of an earthquake epicentre situated at a distance less than  $r$  is equal to the area of a circle of radius  $r$  divided by the area of a circle of a radius of 100 km:

$$\begin{aligned}
 F_R(r) &= P(R \leq r) \\
 &= \frac{\text{area of circle with radius } r}{\text{area of circle with radius } 100} \\
 &= \frac{\pi r^2}{\pi(100)^2} \\
 &= \frac{r^2}{10,000}
 \end{aligned} \tag{B.8}$$

It should be noted that equation B.8 is only valid for source-to-site ( $r$ ) values between 0 and 100 km. When considering for other distances, the following more comprehensive description is given:

$$F_R(r) = \begin{cases} 0 & \text{if } r < 0 \\ \frac{r^2}{10,000} & \text{if } 0 < r < 100 \\ 1 & \text{if } r > 100 \end{cases} \quad (\text{B.9})$$

As with determining the magnitude distribution, the PDF can be computed by taking the derivative of the CDF (Fig. B.6):

$$f_R(r) = \frac{d}{dr} F_r(r) = \begin{cases} \frac{r}{5000} & 0 < r < 100 \\ 0 & \text{otherwise} \end{cases} \quad (\text{B.10})$$

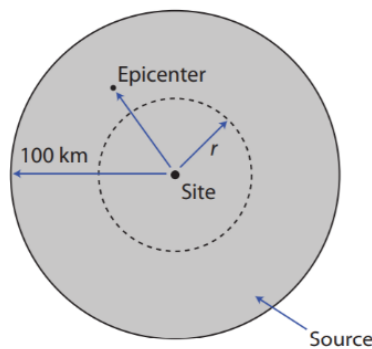


**Figure B.5** Example area source with a specified site. Taken from Baker (2015).

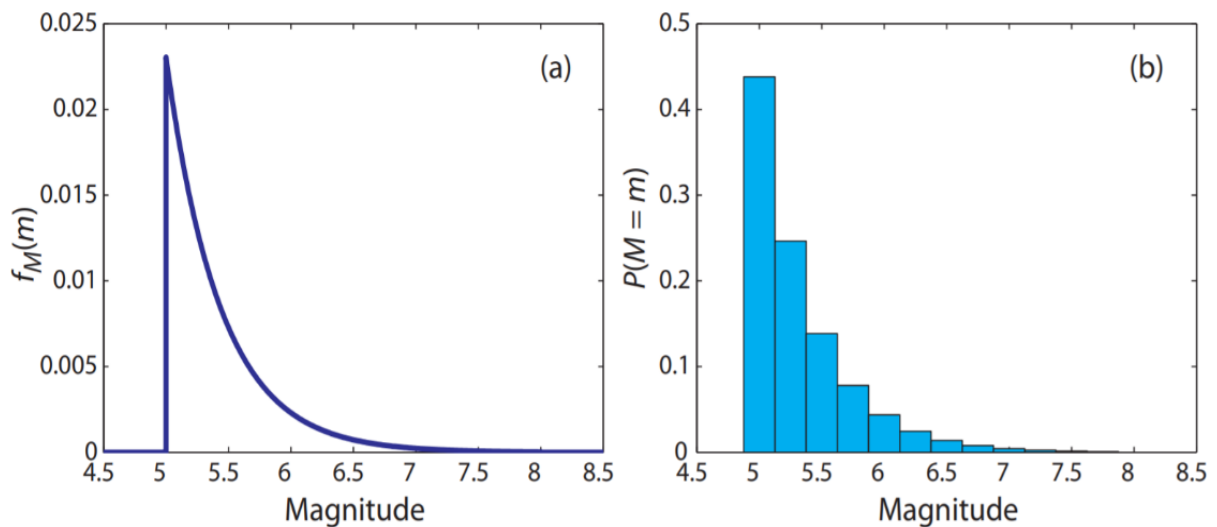


**Figure B.6** CDF (a) and PDF (b) for an area source. Taken from Baker (2015).

#### B.4 Predicting the Distribution of Ground-shaking from Potential Earthquakes

Following the quantification of the magnitudes and source-to-site distances as probability distributions, the associated potential ground-motions from such earthquakes must be predicted. To predict the intensities of ground-shaking, a ground-motion model (GMM) is required. The most commonly used

type of GMM is a ground-motion prediction equation (GMPE)<sup>74</sup>. GMPEs predict ground-motion intensities as a function of magnitude, distance and other input parameters such as faulting mechanism and the localised near surface site conditions. GMPEs are developed through non-linear statistical regression of observed ground-motion intensities for the considered input parameters for a specified area (e.g. Fig. B.7), or through the stochastic method in which a point-source model is derived from observed ground-motion intensities and used to simulate ground-motion records, to which a GMPE is then fitted to (see Chapter 5 for an overview of the stochastic method).

As is apparent from Fig. B.7, there is noticeable scatter for the observed ground-motion intensities, and thus it is necessary for GMPEs to provide probability distributions for ground-motion intensities too.

To fully describe these probability distributions, GMPEs generally take the following form:

$$\ln IM = \overline{\ln IM}(M, R, \theta) + \sigma(M, R, \theta) \cdot \varepsilon \quad (\text{B.11})$$

where  $\ln IM$  is the natural log of the ground-motion intensity measure of interest (in the case of Fig. B.7. spectral acceleration for a period of 1 second), which can be modelled as a random variable since it fits well to a normal (Gaussian) distribution. The terms  $\overline{\ln IM}(M, R, \theta)$  and  $\sigma(M, R, \theta)$  represent the outputs of the GMPE as the predicted mean and standard deviation of  $\ln IM$  respectively. As discussed above, these terms are functions of both the magnitude ( $M$ ) and the distance ( $R$ ) inputs, as well as other parameters, collectively referred to as  $\theta$ . Additionally, there is  $\varepsilon$ , which is a standard normal random variable representative of the observed variation in  $\ln IM$  (i.e. it is the number of standard deviations by which an observed logarithmic ground-motion varies from the mean logarithmic ground-motion predicted by the GMPE for the same spectral period – Baker and Cornell, 2005).

The latter term of equation B.11 results in the calculation of a “scattered” value of the predicted ground-motion. The calculation of a scattered value accounts for the aleatory variability<sup>75</sup> observed in recorded ground-motions (the same size earthquake at the same source-to-site distance does not always result in the same observed ground-motion, and therefore this randomness must be accounted for in the ground-shaking predicted by the GMPE).

An example of a relatively simple GMPE is Cornell et al. (1979)’s model. For predicting peak ground acceleration (PGA – one of the most commonly used ground-motion intensity measures<sup>76</sup>), the equation is:

$$\overline{\ln PGA} = -0.152 + 0.859M - 1.803 \ln(R + 25) \quad (\text{B.12})$$

<sup>74</sup> Other forms of GMM include GMPE logic trees (see below) and intensity prediction equations (IPEs – see Chapter 7 for more details this type of models).

<sup>75</sup> Aleatory variability represents the natural randomness in a variable.

<sup>76</sup> For more information on ground-motion intensity measures please consult Chapter 3.

Within this model the standard deviation of  $\ln PGA$  is 0.57, and is constant for all magnitudes and distances. Due to  $\ln PGA$  following a normal distribution, the probability of a specified level of PGA being exceeded can be computed using the mean and standard deviation for this GMPE:

$$P(PGA > x|m,r) = 1 - \Phi\left(\frac{\ln x - \overline{\ln PGA}}{\sigma \ln PGA}\right) \quad (\text{B.13})$$

where  $\Phi()$  represents the standard normal CDF.

Additionally, when one considers that the CDF is equivalent to an integral of the PDF, it can also be written that:

$$P(PGA > x|m,r) = \int_x^\infty f_{PGA}(u) du \quad (\text{B.14})$$

where  $f_{PGA}(u)$  is the PDF of  $PGA$ , given  $m$  and  $r$ . Unlike  $\Phi()$ ,  $f_{PGA}(u)$  can be written out analytically. Substituting in this PDF gives the following equation, which can be evaluated with a PSHA program such as the *CRISIS* seismic hazard software (R-Crisis, 2019):

$$P(PGA > x|m,r) = \int_x^\infty \frac{1}{\sigma \ln PGA \sqrt{2\pi}} \exp\left(-\frac{1}{2}\left(\frac{\ln u - \overline{\ln PGA}}{\sigma \ln PGA}\right)^2\right) du \quad (\text{B.15})$$

The relationship between the predicted mean output of a GMPE and the PDF is illustrated within Fig. B.7. The predicted mean PGA +/- one standard deviation as a function of distance is shown, as predicted by the Campbell and Bozorgnia (2008) GMPE (of which the updated 2014 model has been considered for use in the North Sea within this investigation), with the PDF for a distance of 10 km superimposed upon this plotted function.

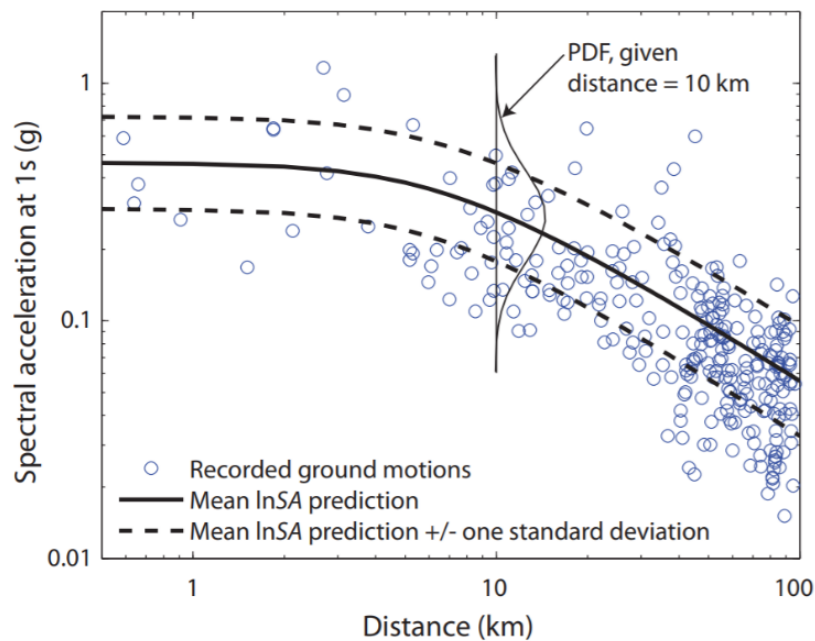


**Figure B.7** Observed spectral accelerations for a period of 1 second from the 1999 Chi-Chi, Taiwan earthquake and a predicted distribution computed using the Campbell and Bozorgnia 2008 GMPE. Taken from Baker (2015).

## B.5 Assimilating Uncertainties in Earthquakes Size, Source-to-Site Distance and Predicted Ground-shaking

Following the acquisition of the distributions discussed above for magnitude, distance and predicted ground-shaking, one can assimilate this information using the total probability theorem to compute the annual rate of exceeding a given level of ground-shaking. If one considers the probability of exceeding a ground-motion intensity level  $x$ , given the occurrence of a future earthquake from one source, the total probability theorem can be written as:

$$P(IM > x) = \int_{m_{min}}^{m_{max}} \int_0^{r_{max}} P(IM > x|m, r) f_M(m) f_R(r) dr dm \quad (B.16)$$

where  $P(IM > x|m, r)$  is from the GMPE selected and  $f_M(m)$  and  $f_R(r)$  are the PDFs for magnitude and distance respectively. The integration of these terms combines the probabilities of exceedance with respect to all considered magnitudes and distances considered within the PSHA.

Equation B.16 determines the probability of exceedance of a specified ground-motion intensity level given the occurrence of an earthquake from one source, and thus does not consider how frequently earthquakes occur at the source of interest. To determine the rate of  $IM > x$ , rather than the probability of  $IM > x$  given the occurrence of an earthquake from the source:

$$\lambda(IM > x) = \lambda(M > m_{min}) = \int_{m_{min}}^{m_{max}} \int_0^{r_{max}} P(IM > x|m, r) f_M(m) f_R(r) dr dm \quad (B.17)$$

where  $\lambda(M > m_{min})$  represents the rate of occurrence of earthquakes greater than a minimum magnitude ( $m_{min}$ ) from the considered source and  $\lambda(IM > x)$  is the rate of  $IM > x$ .

When considering situations with more than one source (as is the case within the North Sea), the rate of  $IM > x$  is the sum of  $IM > x$  for all sources considered:

$$\lambda(IM > x) = \sum_{i=1}^{n_{sources}} \lambda(M_i > m_{min}) \int_{m_{min}}^{m_{max}} \int_0^{r_{max}} P(IM > x|m, r) f_{M_i}(m) f_{R_i}(r) dr dm \quad (B.18)$$

where  $n_{sources}$  is the total number of sources considered and  $M_i$  and  $R_i$  represent the magnitude and distance distributions respectively for source  $i$ .

Equation B.17 (or equivalently equation B.18) is the key equation associated with a conventional approach PSHA. This equation assimilates the probabilities of earthquakes occurring from selected sources, the possible magnitudes and distances associated with these earthquakes and the distribution of ground-shaking intensity which could result from their occurrence. The output of this equation is the rate of a given level of ground-shaking being exceeded, which is an important input in an earthquake engineering analysis. PSHA is therefore useful within this investigation for evaluating the seismic hazard which offshore infrastructure within the North Sea is exposed to over its lifetime.

## **B.6 The Outputs of a PSHA Calculation**

Alongside the seismic hazard curve, two other important outputs of PSHA are the uniform hazard response spectrum (UHRS - Fig. B.8) and the seismic hazard contour map (Fig. B.9). Like the seismic hazard curve, these outputs can be considered within an earthquake engineering analysis.

The UHRS is an important output of PSHA because a common goal of the process is to identify a design response spectrum<sup>77</sup>. To produce a UHRS, the PSHA calculations discussed above are carried out for spectral accelerations over a range of periods, usually with 5% damping. Following this, a target annual rate of exceedance is selected, with every spectral period for the computed accelerations corresponding to this chosen target rate selected. Finally, these spectral accelerations are plotted against their corresponding periods to produce a UHRS (Fig. B.8). As is suggested by the method for computing UHRS, every ordinate has an equal rate (annual frequency) of exceedance, thus leading to the term uniform hazard response spectra. However, it should be emphasised that despite this terminology, the UHRS incorporates separate spectral acceleration values at different periods, which may have come from more than a single earthquake. The plotting of the ordinates within a UHRS for the same spectral period over different return periods will produce a seismic hazard curve (Fig. B.8).

The seismic hazard contour map is computed through selecting a target probability of exceedance for a specified return period. The hazard contours join points of equal ground-motion intensity for this target probability of exceedance over the specified return period to illustrate the spatial distribution of seismic hazard within a region (e.g. see Fig. B.9 for such a map for the North Sea region). Such contour maps can be used to determine the seismic hazard which sites of interest within a PSHA are exposed to depending on their geographical locations.

## **B.7 Epistemic Uncertainty within PSHA**

The total uncertainty associated with a seismic hazard calculation comprises of both epistemic uncertainty and aleatory uncertainty (variability). Aleatory uncertainty refers to random variation in repeated observations of a phenomenon, as is considered above. Epistemic uncertainty refers to the lack of knowledge and the resulting uncertainty associated with model and/or parameter choice. Most epistemic uncertainty within a PSHA is due to a lack of knowledge with respect to earthquakes in the site/region of interest. A lack of knowledge with respect to earthquakes is usually due to (1) limited seismic monitoring in the region or (2) naturally low regional seismicity resulting in few observable earthquakes. Epistemic uncertainty is often reduced within a PSHA through implementing logic trees for model and parameter selection e.g. a GMPE logic tree can be implemented to reduce the epistemic uncertainty associated with GMPE selection (see Chapter 6 for more details on GMPE logic trees).

---

<sup>77</sup> The design response spectrum is the UHRS deemed most appropriate for the structure considered within the earthquake engineering analysis.

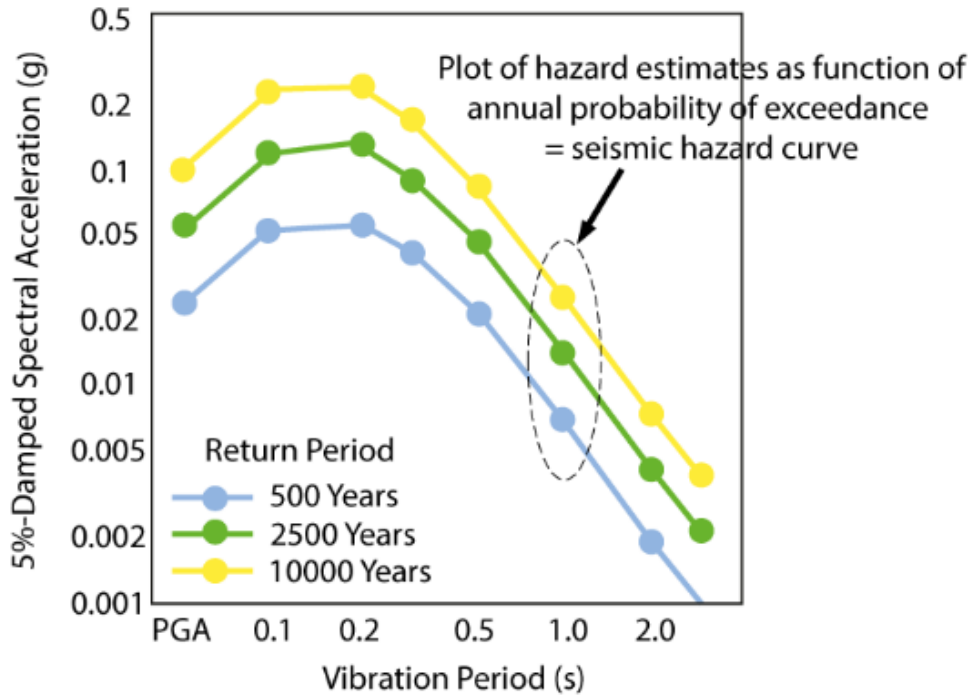


**Figure B.8** Arbitrary uniform hazard spectrum for three return periods. Adapted from Goda et al. (2014).

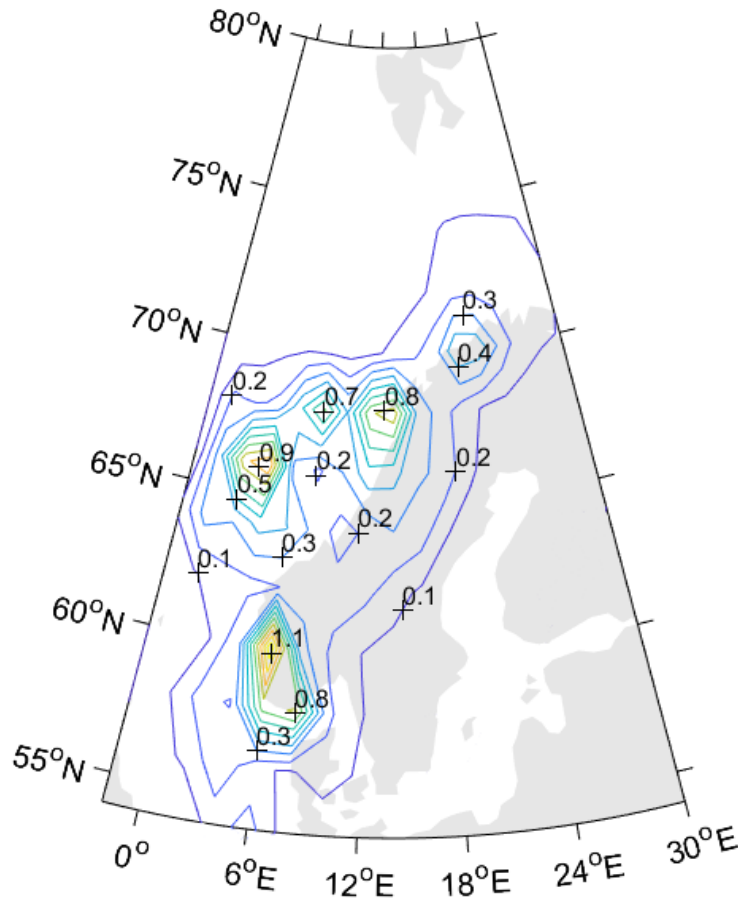


**Figure B.9** PGA seismic hazard contour map for the Norwegian economic sector of the North Sea computed using the Bungum et al. (2002) logic tree approach (see section X.7 for more information on logic trees in PSHA). Return period is 475 years. PGA in  $m/s^2$ . Reproduced from Bungum et al. (2002) (see their Fig. 4) using their North Sea source zone data, which was kindly provided by Conrad Lindholm.

## Appendix C: Site Effects and Site Response Analysis

Following the occurrence of an earthquake, the generated seismic waves will propagate throughout the earth. As these seismic waves propagate away from the source (the fault on which stored elastic strain energy was released) they will be modified due to various physical phenomena. The physical phenomena which modify seismic waves due to local geotechnical conditions are referred to as site effects. Due to differing geotechnical conditions, site effects result in the amplitudes of ground-shaking from the same earthquake varying significantly (Sanchez-Sesma, 1987). Therefore, site effects are evaluated using site response analysis. Within this appendix, brief overviews of (1) site effects and (2) site response analysis are provided.

### C.1 Site Effects

The following overview of site effects is summarised from Kramer (2014).

The local geotechnical conditions at an onshore<sup>78</sup> site can vary primarily due to (1) the stiffness of the subsurface layers, (2) the total thickness of the soil to bedrock, (3) basin geometry and (4) the topography.

The stiffness of the subsurface layers greatly influences the amplitude of the ground-shaking felt at a site. If the subsurface layers comprise of (less stiff) soil or soft rock, ground-motions are amplified more than if the subsurface layers comprise of (more stiff) hard rock (Bowden and Tsai, 2017). For a site underlain by low stiffness subsurface layers, the long period incident ground-motions will be more amplified than the short period incident ground-motions, with the opposite being observed for high stiffness sites (Fig. C.0). This observation can be explained by a simplified form of the amplification function<sup>79</sup>:

$$|a_f(\omega)| = \frac{1}{\sqrt{\cos^2(kH) + (\xi kH)^2}} = \frac{1}{\sqrt{\cos^2\left(\frac{\omega H}{V_s}\right) + \left[\xi\left(\frac{\omega H}{V_s}\right)\right]^2}} \quad (\text{C.0})$$

where  $a_f$  is the amplification factor for ground-motion of a given angular frequency ( $\omega$ ),  $V_s$  is the S-wave velocity within the layer the ground-motions are propagating into,  $H$  is the layer thickness,  $\xi$  is the damping ratio for the system and  $k$  is the wave number ( $= \omega/V_s$ ). This function demonstrates that amplification by a damped layer varies with frequency, and that the amplification reaches a local maximum<sup>80</sup> whenever  $kH = \pi/2 + n\pi$  ( $n$  represents the  $n$ th natural frequency of the considered subsurface layer). The frequencies corresponding to the local maxima are the natural frequencies of the

---

<sup>78</sup> Additional site effects are experienced for offshore sites such as those considered in a seismic hazard assessment for the North Sea. These offshore site effects include (1) the presence of the water layer and (2) the supersaturation of near-surface sediments on the seafloor. See Chapter 4 for an overview of these offshore site effects.

<sup>79</sup> Amplification functions are used to describe the modification of amplitude for a ground-motion incident at a subsurface layer.

<sup>80</sup> The maxima will never reach infinity because if  $\xi > 0$  the denominator will always be less than 1.

considered subsurface layer. Low stiffness layers (approximated for by a low  $V_s$ ) have lower natural frequencies, resulting in greater resonance (and therefore amplification) for large period ground-motions than for short period ground-motions, with the opposite occurring for high stiffness layers.

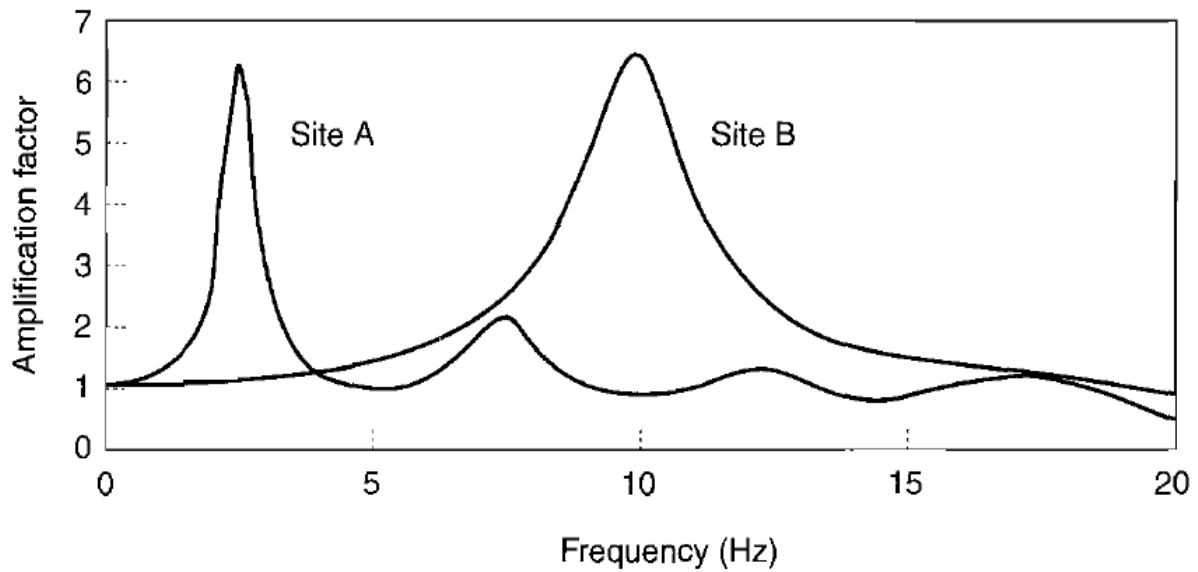


**Figure C.0** Amplification factor against frequency for a low stiffness site (Site A) and a high stiffness site (Site B). Taken from Kramer (2014).

If an elastic bedrock is considered, the amplification at a given site will also be influenced by the seismic impedance of the bedrock. For a ground-motion upwardly propagating from a bedrock layer to a soil layer, the seismic impedance ratio depends on the relative difference between the stiffness of the bedrock ( $V_{sb}$ ) and the stiffness of the soil ( $V_{bb}$ ):

$$I = \frac{\gamma_b V_{sb}}{\gamma_s V_{ss}} \quad (\text{C.1})$$

where  $I$  is the impedance ratio and  $\gamma_b$  and  $\gamma_s$  are the unit weights of the bedrock and soil layers respectively. The impedance ratio is greater when the bedrock is stiffer as opposed to when the bedrock is softer, and a greater impedance ratio results in greater amplification of ground-motions because the stiffer bedrock acts as a rigid interface which traps the majority of seismic waves within the soft soil layer, leading to a build-up of seismic energy as seismic waves constructively interfere (Manandhar et al., 2016). For example, Jacob (1991) determined that if equivalent soil conditions are observed, harder bedrocks can provide amplification factors approximately 50% greater than those associated with softer bedrocks.

A greater total soil to bedrock thickness provides a larger cavity volumetrically for seismic waves to be trapped in, resulting in ground-motions which are both larger in amplitude and of longer duration due to the trapped seismic waves experiencing constructive interference and reflection respectively. The characteristic site period (the period of vibration at which the greatest amplification is expected) is also related to the thickness of the soil layer:

$$T_s = \frac{4H_{ss}}{V_{ss}} \quad (\text{C.2})$$

where  $T_s$  is the characteristic site period and  $H_{ss}$  is the thickness of the soil layer, with a greater soil layer thickness resulting in a larger site period. Therefore, for sites with thicker soil layers, larger periods experience greater amplification, and for sites with thinner soil layers, smaller periods experience greater amplification. It should be noted that the frequency corresponding to the characteristic site period is referred to as the fundamental frequency,  $\omega_0$ .

Basin geometry can also strongly influence the ground-shaking at a site. The curvature of a basin, within which soft alluvial soils have often been deposited in large volumes, can trap body waves, of which some propagate through the surface to form large amplitude and long duration surface waves. If only vertically propagating seismic waves are considered within a site response analysis, the seismic hazard at sites located within basins (as many cities are located upon) can be underestimated due to neglecting the potential generation of highly damaging surface waves. For example, King and Tucker (1984) observed that one-dimensional site response analysis could estimate the ground-shaking towards the centre of the Chusal Valley in Afghanistan, but not at the edges. This was explained by the computed amplification factors for the central locations being markedly different than those computed for the peripheral locations, demonstrating the influence of basin geometry and the accompanying alluvial deposits on ground-shaking.

Local topography can also exert control over ground-motions incident at a site. The Pacoima Dam seismograph recorded considerably greater than expected amplitudes of ground-shaking for the  $M_L$  6.4, 1971 San Fernando earthquake. The Pacoima Dam seismograph was situated on the crest of a narrow ridge. Numerous studies have since attributed these elevated ground-shaking amplitudes to the dynamic response of the ridge itself. For example, Jibson (1987) measured the ground-shaking for five earthquakes in Japan at various points along the crest of a ridge, and found that the average ground-shaking on the peak of the ridge was 2.5 times greater than the average ground-shaking at the base of the ridge. Similar amplification patterns for ridges have also been observed for earthquakes in Italy and Chile (Finn, 1981). For other topographic features (e.g. gullies, lakes), the expected response of incident seismic waves is more difficult to predict due to having to account for the geometry of the topographic feature, the angles of incidence and frequencies of the incoming seismic waves.

## **C.2 Site Response Analysis**

To estimate the expected ground-shaking intensities at a given site, site response analysis is used. The following overview of the basic theory behind linear-elastic site response and subsequently of equivalent-linear elastic site response analysis are summarised from Kottke and Rathje (2008), which should be consulted for more details.

### C.2.1 Linear-Elastic Site Response Analysis

For linear-elastic and one-dimensional wave propagation, the soil layer is assumed to behave as a Kelvin-Voigt solid, in which the dynamic response is described using a purely elastic spring and a purely viscous dashpot. The solution to the one-dimensional wave equation for a single angular frequency ( $\omega$ ) provides displacement ( $u$ ) as a function of depth ( $z$ ) and time ( $t$ ):

$$u(z, t) = Ae^{i(\omega t + k^* z)} + Be^{i(\omega t - k^* z)} \quad (C.3)$$

In this equation,  $A$  and  $B$  are the respective amplitudes of the upward ( $-z$ ) and downward ( $+z$ ) waves respectively (Fig. C.1). The complex (dynamic) wave number,  $k^*$  is related to the shear modulus ( $G$ ), damping ratio ( $D$ ) and density ( $p$ ) of the soil layer:

$$k^* = \frac{\omega}{V_s^*} \quad (C.4)$$

$$V_s^* = \sqrt{\frac{G^*}{p}} \quad (C.5)$$

$$G^* = G(1 - 2D^2 + i2D\sqrt{1 - D^2}) \cong G(1 + i2D) \quad (C.6)$$

where  $G^*$  and  $V_s^*$  are the complex shear modulus and complex S-wave velocity respectively. If the damping ratio is assumed to be small ( $\sim 10\%$ ), then the approximation of  $G^*$  is appropriate.

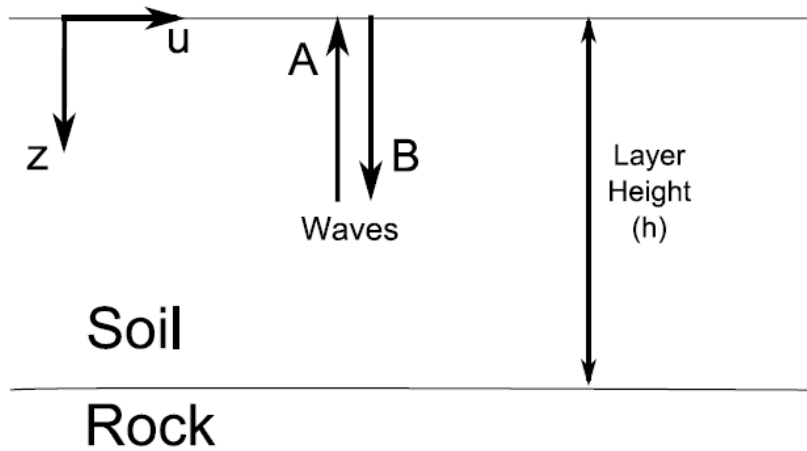


**Figure C.1** Notation for the one-dimensional wave form equation (equation C.3). Taken from Kottke and Rathje (2008).

Equation C.3 is only applicable for a single layer with homogenous soil properties in which the wave amplitudes ( $A$  and  $B$ ) can be computed from the layer boundary conditions. For a scenario with multiple layers (Fig. C.2), the wave amplitudes are calculated using recursive formulas through maintaining compatibility of displacement and shear stress at the layer boundaries:

$$A_{m+1} = \frac{1}{2}A_m(1 + \alpha_m^*)e^{ik_m^*h_m} + \frac{1}{2}B_m(1 - \alpha_m^*)e^{ik_m^*h_m} \quad (C.7)$$

$$B_{m+1} = \frac{1}{2}A_m(1 - \alpha_m^*)e^{ik_m^*h_m} + \frac{1}{2}B_m(1 + \alpha_m^*)e^{ik_m^*h_m} \quad (C.8)$$

where  $m$  is the layer number,  $h_m$  is the layer thickness and  $\alpha_m^*$  is the complex impedance ratio. The complex impedance ratio is given by:

$$\alpha_m^* = \frac{k_m^* G_m^*}{k_{m+1}^* G_{m+1}^*} = \frac{p_m V_{s,m}^*}{p_{m+1} V_{s,m+1}^*} \quad (\text{C.9})$$

and calculates the relative amplitudes of the upwardly and downwardly propagating waves. At the surface of the soil layer ( $m = 1$ ), and the shear stress must equal zero, which therefore means the amplitudes of the upwardly and downwardly propagating waves ( $A_1 = B_1$ ). The wave amplitudes within the soil profile are computed for each angular frequency (assuming stiffness and damping have been defined for each layer), and are used to compute the response at the site surface. This calculation is undertaken by setting  $A_1 = B_1 = 1.0$  at the surface and recursively computing the wave amplitudes ( $A_{m+1} = B_{m+1}$ ) in successive layers downward to the input (base) layer of the site subsurface profile. The transfer function between the ground-motion in the target layer ( $m$ ) and in the rock layer ( $n$ ) is defined as:

$$TF_{m,n}(\omega) = \frac{u_m(\omega)}{u_n(\omega)} = \frac{A_m + B_m}{A_n + B_n} \quad (\text{C.10})$$

with the transfer function representing the ratio of the amplitude of (displacement, velocity or acceleration) ground-motion between two layers within the site subsurface profile for a given angular frequency.

1	$A_1 \uparrow \downarrow B_1$	$\rho_1 h_1 G_1 D_1$
2	$A_2 \uparrow \downarrow B_2$	$\rho_2 h_2 G_2 D_2$
$m$	$A_m \uparrow \downarrow B_m$	$\rho_m h_m G_m D_m$
$m + 1$	$A_{m+1} \uparrow \downarrow B_{m+1}$	$\rho_{m+1} h_{m+1} G_{m+1} D_{m+1}$
$n$	$A_n \uparrow \downarrow B_n$	$\rho_n h_n G_n D_n$

**Figure C.2** Nomenclature for one-dimensional wave propagation. Taken from Kottke and Rathje (2008).

A transfer function for the geotechnical conditions provided in Tab. C.0 is provided in Fig. C.3. The frequencies at which the peaks in the transfer function occur are controlled by the natural frequencies of the site profile. The frequency at which the largest peak in the transfer function occurs represents the site's fundamental frequency, and represents the frequency at which the largest amplification is experienced at the site. As would be expected, an increase in the damping ratio of the considered system decreases the peaks of the transfer function, resulting in lower amplification.

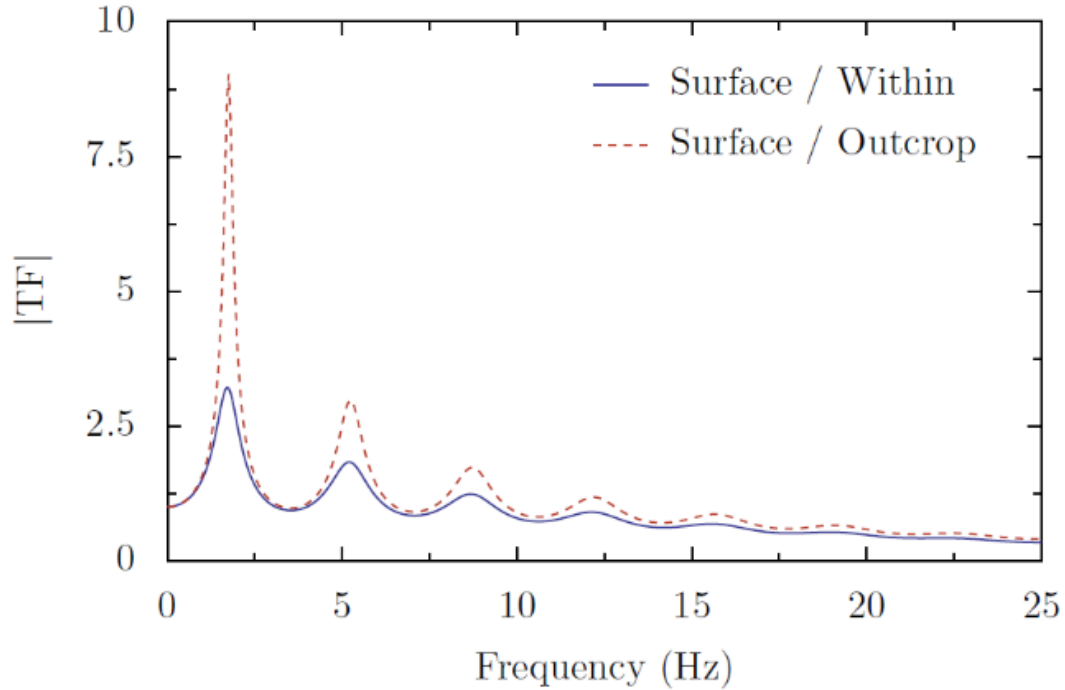


**Figure C.3** Transfer function for a site with given geotechnical properties, considering different inputs. These geotechnical conditions are provided in Tab. C.0. See below for an explanation of “within” and “outcrop” motion terminology. Taken from Kottke and Rathje (2008).

**Table C.0** Geotechnical Conditions for site considered within Fig. C.3. Taken from Kottke and Rathje (2008).

<i>Geotechnical Property</i>	<i>Rock Layer</i>	<i>Soil Layer</i>
$p$ (g/cm <sup>3</sup> )	2.24	1.93
$h$ (m)	Inf.	50
$V_s$ (m/s)	1500	350
$D$	1%	7%

The ground-shaking at the target layer is computed by multiplying the Fourier amplitude spectrum<sup>81</sup> (FAS) of the ground-motion inputted at the rock layer by the transfer function for the site:

$$Y_m(\omega) = TF_{m,n}(\omega) \cdot Y_n(\omega) \quad (\text{C.11})$$

where  $Y_m$  is the FAS at the top of the target layer and  $Y_n$  is the inputted FAS at layer  $n$ .

It should be noted that the inputted FAS in equation C.11 is typically representative of the ground-motion at the site surface, where the upwardly and downwardly propagating wave amplitudes are equal ( $A_n = B_n$ ), rather than at the base of the soil deposit where these amplitudes are not equal ( $A_n \neq B_n$ ). This change in the boundary conditions ( $A_n = B_n$  at the surface,  $A_n \neq B_n$  at the base of the soil deposit – see Fig. C.4) must be accounted for. The ground-motions at a free surface are referred to as “outcrop”

<sup>81</sup> See Chapter 3 for more details on Fourier amplitude spectra.

motions. Outcrop motions are described by twice the amplitude of the upwardly propagating wave (2A). Equation C.10 can be modified to transfer an outcrop motion to a layer motion. To do so, equation C.10 is multiplied by a transfer function which makes the outcrop motion a “within” motion at the base of the soil profile. Within motions refer to ground-motions recorded at depth (e.g. recorded in a borehole), for which the transfer function given by equation C.10 alone cannot be used. A second transfer function is therefore required to translate from an outcrop motion to a within motion. The combined transfer function is as follows:

$$TF_{m,n}(\omega) = \underbrace{\frac{A_m+B_m}{A_n+B_n}}_{\text{within} \rightarrow \text{layer}_n} \cdot \underbrace{\frac{A_n+B_n}{2 \cdot A_n}}_{\text{outcrop} \rightarrow \text{within}} = \underbrace{\frac{A_m+B_m}{2 \cdot A_n}}_{\text{outcrop} \rightarrow \text{layer}_n} \quad (\text{C.12})$$

Equation C.12 was used to compute the transfer functions provided in Fig. C.3. In one instance the inputted ground-motion is specified as an outcrop motion, and in the other instance the inputted ground-motion is specified as a within motion. As would be expected, the within-to-outcrop (surface/within) transfer function provides greater amplification than the outcrop-to-outcrop (surface/outcrop) transfer function.

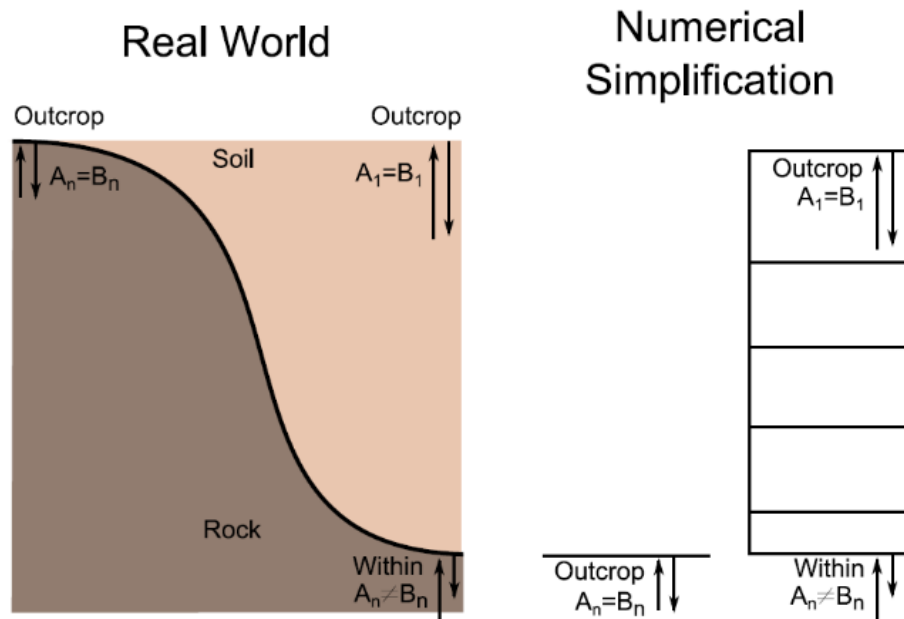


**Figure C.4** Diagram explaining outcrop motion and within motion conditions. Outcrop = upwardly and downwardly propagating ground-motions are equal ( $A_n = B_n$ ). Within = upwardly and downwardly propagating ground-motions are not equal ( $A_n \neq B_n$ ). Taken from Kottke and Rathje (2008).

### C.2.2 Equivalent-Linear Elastic Site Response Analysis

Whilst the response analysis discussed above treats the soil layer as linear-elastic, soil behaves in a nonlinear manner, in which the dynamic (complex) properties of soil (shear modulus and damping ratio) vary with shear strain, and in turn influence the intensity of ground-shaking at the considered site. In equivalent-linear site response (ELSR) analysis, the nonlinear behaviour of soil in response to ground-motion is approximated for by modifying its linear-elastic properties according to the level of induced

strain. The strain compatible values of  $G$  and  $D$  are calculated iteratively based on the computed level of this induced strain. A transfer function is implemented to compute the shear strain in the target layer based on the outcropping input motion. This strain transfer function computes the shear strain at the middle of the target layer ( $z = h_m/2$ ), and is used to determine the strain compatible soil properties. It should be noted that unlike the transfer functions discussed above, which only amplify the FAS for the inputted ground-motion, the strain transfer function (1) amplifies the ground-motion and (2) converts the acceleration into strain. The strain transfer function based on an outcropping input motion:

$$TF_{mn}^{strain}(\omega) = \frac{\gamma(\omega, z=h_m/2)}{\ddot{u}_{n,outcrop}(\omega)} = \frac{ik_m[A_m e^{(ik_m^* h_m/2)} - B_m e^{-(ik_m^* h_m/2)}]}{-\omega^2(2 \cdot A_n)} \quad (C.13)$$

The “strain FAS” within the target layer is computed by applying the strain transfer function to the FAS of the input motion. The maximum strain within the target layer is derived from the strain FAS<sup>82</sup>. However, the use of the maximum strain within the target layer to compute the strain-compatible soil properties is not appropriate because the maximum strain only occurs for an instant in time. Due to this, an effective strain ( $\gamma_{eff}$ ) is computed from the maximum strain. Typically,  $\gamma_{eff}$  is 65% of the maximum strain. Fig. C.5 provides an example of a strain time-series and the associated  $\gamma_{eff}$ .

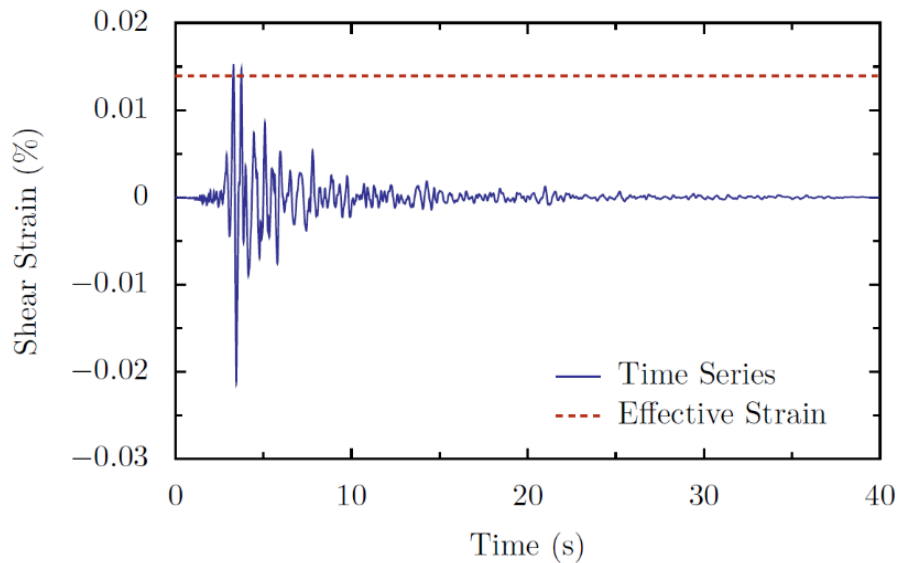


**Figure C.5** Comparison of strain time-series and corresponding effective stress for a target layer within an ELSR analysis. Taken from Kottke and Rathje (2008).

ELSR analysis requires that strain-dependent nonlinear soil properties are defined. The initial (low strain) shear modulus ( $G_{max}$ ) is defined as:

$$G_{max} = \rho_{site} V_{sm}^2 \quad (C.14)$$

where  $\rho_{site}$  is the density of the site and  $V_{sm}$  is the measured S-wave velocity of the site.

<sup>82</sup> The maximum strain is computed from the strain FAS through either conversion to the time-domain or alternatively random vibration theory (see Section 2.2 Kottke and Rathje, 2008 for more details).

Characterising the nonlinear behaviour of  $G$  and  $D$  is achieved through modulus reduction and the use of damping curves which describe the variation of  $G = G_{max}$  and  $D$  with shear strain<sup>83</sup>. Using these initial dynamic properties of the soil, ELSR analysis can be undertaken in the following steps:

1. The wave amplitudes ( $A$  and  $B$ ) are computed for each layer in the soil deposit profile.
2. The strain transfer function is computed for each layer.
3. The maximum strain within each layer is computed by applying the strain transfer function to the FAS of the inputted ground-motion and taking the maximum response.
4. A value of  $\gamma_{eff}$  is computed for each layer based on the corresponding maximum strain.
5. The strain compatible soil properties ( $G$  and  $D$ ) are recomputed for each layer based on the current iteration of  $\gamma_{eff}$ .
6. The recomputed strain compatible soil properties are compared to the previous iteration, and an error is calculated. If the error for all layers is below a defined threshold, the calculation ends. The dynamic response of the soil deposit is now computed.

Within this investigation, the STRATA site response software (Kottke and Rathje, 2008) is used to undertake ELSR analysis for offshore sites in the North Sea (see Chapter 4 for more details).

---

<sup>83</sup> See Section 2.1.3 of Kottke and Rathje (2008) for more details on (1) the nonlinear behaviour of  $G$  and  $D$  and (2) the characterisation of these dynamic properties within ELSR analysis.

## Appendix D: Induced Seismicity Mechanisms Associated with Hydrocarbon Production

An increase in the occurrence of earthquakes due to increased hydrocarbon production is well established (e.g. Grasso, 1992; Suckale, 2009). Such seismicity is caused by stress variations in the hydrocarbon reservoir and the surrounding rock (Suckale, 2009). There are three primary mechanisms by which hydrocarbon production can induce an earthquake within or surrounding a hydrocarbon field: (1) fluid injection, (2) fluid extraction and (3) mass transfer (Grasso, 1992). These mechanisms can initiate seismicity on both local and regional scales through causing small but significant stress changes ( $\leq 1$  MPa) (Grasso, 1992), with the resulting earthquakes typically being small to moderate in size (local magnitude ( $M_L$ )  $\leq 4.5$ ) (Suckale, 2009). Many other types of human activity are known to be capable of inducing earthquakes, with examples ranging from the impoundment of dams to quarrying and the extraction of groundwater (e.g. Foulger et al., 2017). However, such cases are not considered in this investigation. Overviews of the three primary mechanisms for induced seismicity resulting from hydrocarbon production are provided below.

### D.1 Fluid Injection (Mechanism 1)

Fluid is injected for several reasons in hydrocarbon production: (1) the replacement of fluids previously extracted in a mature hydrocarbon field, (2) to encourage hydrocarbon production by generating local fractures to provide fluid migration pathways, (3) to force fluid migration towards currently producing wells and (4) for reservoir pressure conservation (Suckale, 2009). The injection of fluids can result in localised hydraulic fracturing within the reservoir (Grasso, 1992). As fluid percolates through the local fractures it bears a component of the effective normal stress equal to the pressure of the injected fluid (Grasso, 1992; Suckale, 2009). The injected fluid does not possess shear strength, and thus the effective normal stress and associated frictional resilience to shear are reduced. If the localised fractures are then exposed to shear stresses exceeding the product of the effective normal stress and the corresponding coefficient of friction then slippage is induced in the reservoir due to the reservoir rock approaching the envelope of mechanical failure and initiating an earthquake (Suckale, 2009). However, the seismic slip generated by local fracture propagation is not the principal cause of earthquakes associated with fluid injection. These earthquakes are induced by slippage on pre-existing planes of weakness adjacent to the local fractures, where reductions in effective normal stress also occur (Grasso, 1992). These stress changes associated with earthquakes induced by hydrocarbon production can be described using a Coulomb failure criterion:

$$\tau > \mu(S_n - P_p) + \tau_0 \quad (\text{D.0})$$

where  $\tau$  is the shear stress acting on (a patch of) the fault,  $\mu$  is the coefficient of friction,  $S_n$  is the normal stress,  $P_p$  is the pore pressure,  $\tau_0$  is the cohesion, and failure occurs if the shear stress exceeds the fault strength (Zoback and Zinke, 2002; Baisch et al., 2019). In summary, through raising the pore pressure, there is a reduction in the effective normal stress ( $S_n - P_p$ ) acting on pre-existing planes of weakness,

resulting in seismic slip occurring at levels of shear stress below those at which seismic slip would normally be capable of occurring at (Zoback and Zincke, 2002).

#### **D.1.1 The Rangely Oil Field, U.S.A.**

A Coulomb failure criterion for fluid injection related seismicity is validated by the well-known controlled experiment conducted at the Rangely oil field of the Uinta Basin, Colorado, by Raleigh et al., (1976). This experiment was undertaken in 1969 when a network of short period, vertical component seismometers was established. Prior to the experiment, secondary recovery of hydrocarbons through water injection had been performed at Rangely field since 1957, with 976 earthquakes observed in the Uinta Basin close to the injection site between November 1962 and January 1970 (Suckale, 2009). From October 1969 to May 1973, two cycles of fluid injection were carried out in the field, with it being observed that the rate of seismicity altered rapidly with fluid pressure alterations (Fig. D.0; Rayleigh et al., 1976). The earthquakes were found to cluster around a fault partially situated within a zone of significantly elevated pore pressure (Fig. D.1) which was built up by secondary recovery (Rayleigh et al., 1976). Consequently, Rayleigh et al. (1976) confirmed that a decrease in effective normal stress could generate earthquakes, and therefore that a Coulomb failure criterion could explain this fluid injection related seismicity. Correlations for hydraulic fracturing type fluid-injection have also been observed in areas such as Seventy-Six oil field, Kentucky, U.S. (Rutledge et al., 1998). However, definitive correlations between fluid injection and seismicity are seemingly related exclusively to fluid injection of the hydraulic-fracturing subclass (Suckale, 2009). Additionally, it should be noted that correlations as definitive as those observed in the highly-controlled Rangely field experiment are the exception, rather than the rule. Other investigations into the link between fluid injection and seismicity suggest far more intricate relationships which incorporate temporal and spatial components (e.g. the 2001 Ekofisk event) (Ottemöller et al., 2005; Suckale, 2009).

#### **D.1.2 Rocky Mountain, U.S.A.**

The link between hydraulic-fracturing class fluid injection and seismicity was not unanimously accepted prior to the Rayleigh et al. (1976) experiment. Prior to this study, the U.S. Military injected high-pressure waste fluids into the Rocky Mountain Arsenal basement rock near Denver, Colorado, during which a swarm of over 1500 earthquakes was observed between April 1962 and August 1967 (Rayleigh et al., 1976; Grasso, 1992). Carder (1966) showed that the energy released by these earthquakes could not be provided by the work done solely through fluid injection. The Rocky Mountain earthquakes are therefore widely considered to have been triggered by fluid injection, rather than induced. This is because the stress perturbations associated with fluid injection likely resulted in the release of strain energy predominantly accumulated by tectonic deformation, rather than by fluid injection related stress changes directly (Ball and Downs, 1966; Hsieh and Bredehoeft, 1981).

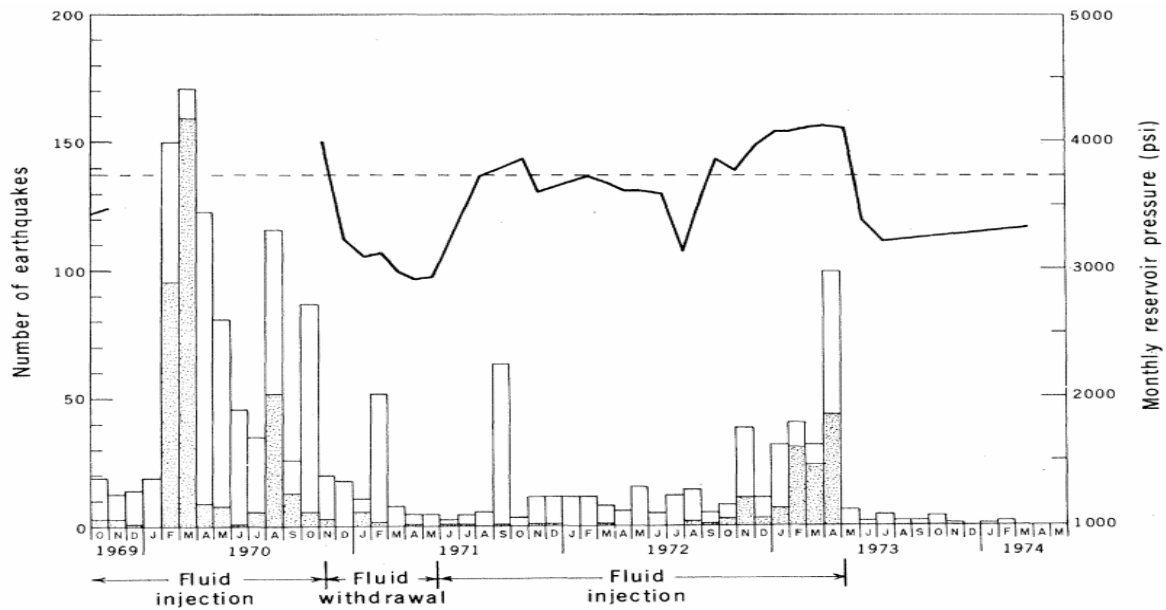


**Figure D.0** Frequency of earthquakes at Rangely field and temporal association with fluid injection. Stippled bars indicate earthquakes  $\leq 1$  km of the experimental injection wells. Clear areas indicate all others. Pressure history shown by heavy line; predicted critical pressure by dashed line. Taken from Rayleigh et al. (1976).

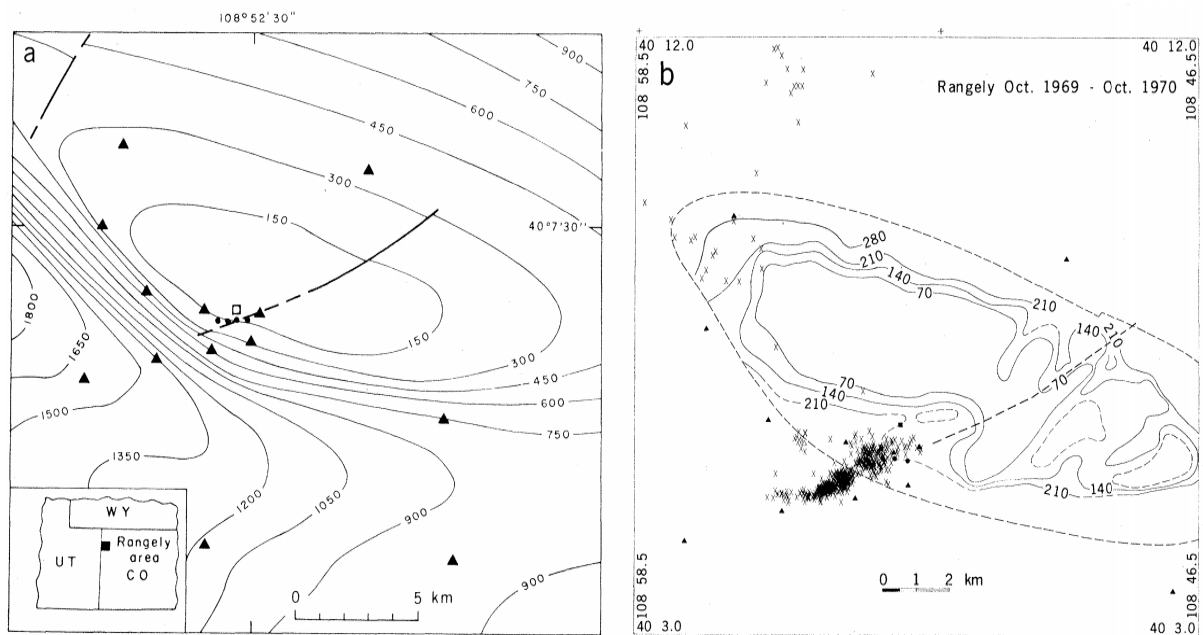


**Figure D.1** (a) Structure contour map of the Rangely anticline. Subsurface faults shown as dashed lines. The contour interval is 150 m, indicating depth below sea level to the Weber sandstone. (•) Experimental wells used for varying fluid pressure in Weber sandstone. (□) Well used for measurement of stress. (Δ) Seismic stations. (b) Earthquakes located at Rangely between October 1969 and November 1970. The contours are bottom-hole 3-day shut-in pressures as of September 1969; the interval is 70 bars. (x) Earthquakes; (Δ) Seismic stations; (•) experimental wells. The heavy, dashed line indicates the fault mapped in the subsurface. Taken from Rayleigh et al. (1976).

Despite hydrocarbon production related fluid injection being predominantly linked with microseismicity ( $M_L \leq 3$ ) (e.g. Mereu et al., 1986; Evans and Steeples, 1987; Phillips et al., 1988), moderate to large magnitude earthquakes associated with fluid injection have been observed, although the correlation between such fluid injection and seismic activity is not readily apparent (e.g. the 2001 Ekofisk event) (Ottemöller et al., 2005; Suckale, 2009). This lack of clear correlation is attributed to four factors: (1) Hydrocarbon field injection and depletion commonly occur at separate wells, resulting in complex underground flow pathways which complicate how spatial variations in pore-pressure are linked to fluid injection activity, (2) common incompleteness of accurate injection history data (e.g. for the investigation of the seismicity of the Gobles field of Ontario, Canada, Mereu et al. (1986) could not obtain detailed pressure variations), (3) the often occurring time lapse between fluid injection and the onset of seismicity (e.g. the Sleepy Hollow field of Nebraska, U.S. – see Rothe and Lui, 1983; the Cogdell field of Texas, U.S. – see Davis and Pennington, 1989) and (4) large uncertainties in hypocentre location for many of the investigated earthquakes (e.g. Evans and Steeples, 1987) (Suckale, 2009).

The largest observed seismic event thought to be linked to fluid injection in a hydrocarbon production context is that of the 1978  $M_L$  5.3 earthquake of the Cogdell Canyon Reef field of West Texas, U.S (Davis et al., 1989; Suckale, 2009). This earthquake formed part of a sequence of seismic events which occurred from 1974 to 1982, with this seismic sequence being attributed to water injection for secondary recovery which was initiated in the field in 1956 (Nicholson and Wesson, 1990).

## **D.2 Fluid Extraction (Mechanism 2)**

Within hydrocarbon reservoirs, fluid extraction is directly caused by the production of oil or gas, rather than the application of enhanced recovery techniques (e.g. hydraulic fracturing) or reservoir maintenance methods (e.g. reservoir pressure conservation) as is the case for fluid injection (see above) (Grasso, 1992). Fluid extraction reduces the pore pressure within reservoir rock, consequently increasing the effective normal stress acting upon the reservoir, and so would be expected to prevent recurrent faulting within the reservoir (Segall, 1985; Segall, 1989; Suckale, 2009). However, such instabilities have been found to originate either above or below reservoir level, rather than within the lower pressure, depleted segments of the reservoir itself (Grasso and Wittlinger, 1990; Grasso, 1992). Therefore, seismicity caused by fluid extraction can occur through either (1) induced stress changes relating to hydrocarbon production and associated structure-scale mechanical deformation or (2) fluid extraction leading to the strengthening of pre-existing faults (Pennington et al., 1986; Segall, 1989; Mulders, 2003). Consequently, the requirement of nearby pre-existing faults means the geological setting (either local or regional scale) is highly important for fluid injection related seismicity (Suckale, 2009). Seismicity induced by fluid extraction is therefore less frequent than seismicity induced by fluid injection (Baisch et al., 2019). Investigation of the significant subsidence within the Goose Creek Oil field, Texas, U.S. by Pratt and Johnson (1926) first resulted in recognition of the link between reservoir depletion and the occurrence of significant mechanical deformation within and around the reservoir.

### D.2.1 The Lacq Field, France

A well-studied example of a region exhibiting such seismicity is the Lacq field of Aquitaine, France, in which a gas pressure drop of 45% (~300 bars) over 10 years of production resulted in seismic ruptures above the reservoir, and an additional 10 years of production corresponding to a 70% (~ 450 bars) drop in gas pressure triggered seismic ruptures 1 km below the reservoir (Grasso and Wittlinger, 1990). The north Pyrenean foreland in which the Lacq field is situated has been aseismic for several centuries, with the first  $M_L > 3$  event observed in November 1969, approximately 10 years after hydrocarbon production was initiated in the field, and one event of at least such size having been observed each year since (Fig. D.2) (Grasso and Wittlinger, 1990). Furthermore, the epicentres of all  $M_L > 3$  events recorded are situated within the Lacq field (Grasso and Wittlinger, 1992). In addition to the correlation between fluid depletion and seismicity, such observations provide compelling evidence for the Lacq field's recent uptake in seismicity being induced by fluid extraction, rather than by tectonic means (Grasso and Wittlinger, 1990). Throughout other sites where data collection has not been as extensive as the Lacq field, depletions of 30 MPa at depths of 3 – 5 km have been observed to still induce  $M_L 3 - 4$  earthquakes under highly differing tectonic strain regimes, ranging from stable (e.g. Texas) to compressional (e.g. Canada) (Grasso, 1992).

The Lacq reservoir was shown by Grasso and Feigner (1990) to bear a radial, axisymmetric distribution of stresses, contrasting significantly with the regional scale stress pattern. This radial, axisymmetric reservoir stress pattern is supportive of the theory of poroelasticity (established by Biot, 1941). Within a hydrocarbon reservoir, poroelasticity explains how large decreases in pore pressure result in the contraction of the reservoir rock, and the elastic coupling between the reservoir and the encompassing rock causes the surrounding crust to be placed under stress, which is observed as field subsidence through differential compaction of the reservoir (Segall, 1985). These stress perturbations were estimated by Segall et al. (1994) to be 0.2 MPa or less, with an effective normal stress change of 0.1 MPa being capable of inducing a seismic event. Such stress perturbations are capable of inducing seismic events through causing seismic slip on preferentially oriented planes of weakness (Yerkes and Castle, 1976; Segall et al., 1994). Such fracture planes are known to occur on pre-existing discontinuities, which are either tectonic or lithological in nature (Grasso and Feignier, 1990). The theory of poroelasticity is well supported by the observed linear relationship between pressure reduction and subsidence within the Lacq field (Fig. D.2) (Segall et al., 1994), and thus an analytical poroelastic model can be applied to evaluate the degree of stress variation in the rock overlying the depleted reservoir (Grasso, 1992). However, as noted by Grasso (1992), the theory of poroelasticity fails to explain the spatial and temporal variations in seismicity within the Lacq field, including the decline in seismicity within the field since the 1980s, and the spatial clustering (swarming) of induced earthquakes observed by Grasso and Wittlinger (1990).

A two-step temporal mechanism for modelling stress changes (and thus seismicity) within a depleted reservoir was proposed by Grasso (1992), and applied within the Lacq field. This model helps account for some of the noted spatial and temporal inconsistencies resulting from the application of a simplistic poroelastic model. Within the Lacq field where Grasso (1992) tested this two stage mechanism, slip on three faults provides a good fit for both the observed differential subsidence and the simple poroelastic model (Fig. D.3) (Grasso, 1992).

### **D.2.2 Fluid Extraction Induced Seismicity on Pre-existing Faults**

Fluid extraction can also result in induced earthquakes through interaction with pre-existing faults (i.e. fault reactivation). This was first proposed by Pennington et al. (1986), the main concept of the model being that a reduction in pore pressure increases the effective normal stress acting upon the fault (Fig. D.4). Consequently, the strength of the fault is raised, which prevents slip from occurring in the localised region of fluid extraction. The locking up of the fault causes strain to accrue, which is the result of either continuous aseismic slip upon local (still-slipping) segments of the fault or differential compaction. The accumulation of this strain results in stress increasing on the locked segments of the fault. Over time this stress will continue to gradually build up to form high stress barriers (asperities), which fail upon the stress exceeding the maximum shear strength of the fault portion to produce seismic slip, and thus earthquakes. Grasso (1992) noted that this mechanism has been observed in the Grozny field, Russia, where reservoir depletion over 6 years caused a 30 MPa pressure drop. This pressure drop stabilised the tectonic instabilities near the reservoir whilst elevating stresses at locked fault portions, generating seismicity (Grasso, 1992).

An additional principle of this mechanism, as stated by Pennington et al. (1986) is that the cycle of fault locking and seismic slipping repeats whilst the fault is active and a reduction in pore pressure continues. Importantly, this means that as fluid extraction progresses, future earthquakes induced by this mechanism are expected to be of greater magnitudes. Pennington et al. (1986) also propose that an increase in effective confining pressure could potentially lead to greater stress drop earthquakes, and hence greater surface accelerations, which would result in the seismic hazard from such earthquakes being elevated. As noted by Mulders (2003), the magnitude of such earthquakes are also controlled by the size of the affected faults, the mechanical properties of the rock matrices and the size of the depletion-associated pressure drop. The hydrocarbon fields of Imogene and Fashing of Texas, U.S. have both exhibited seismicity but without exhibiting differential subsidence. Pennington et al. (1986) proposed that their mechanism could explain this seismicity; both fields possess structural traps comprising of normal faults and have undergone significant pressure reductions following production. This mechanism was later confirmed as being responsible for the seismicity within these fields by Davis et al. (1995).

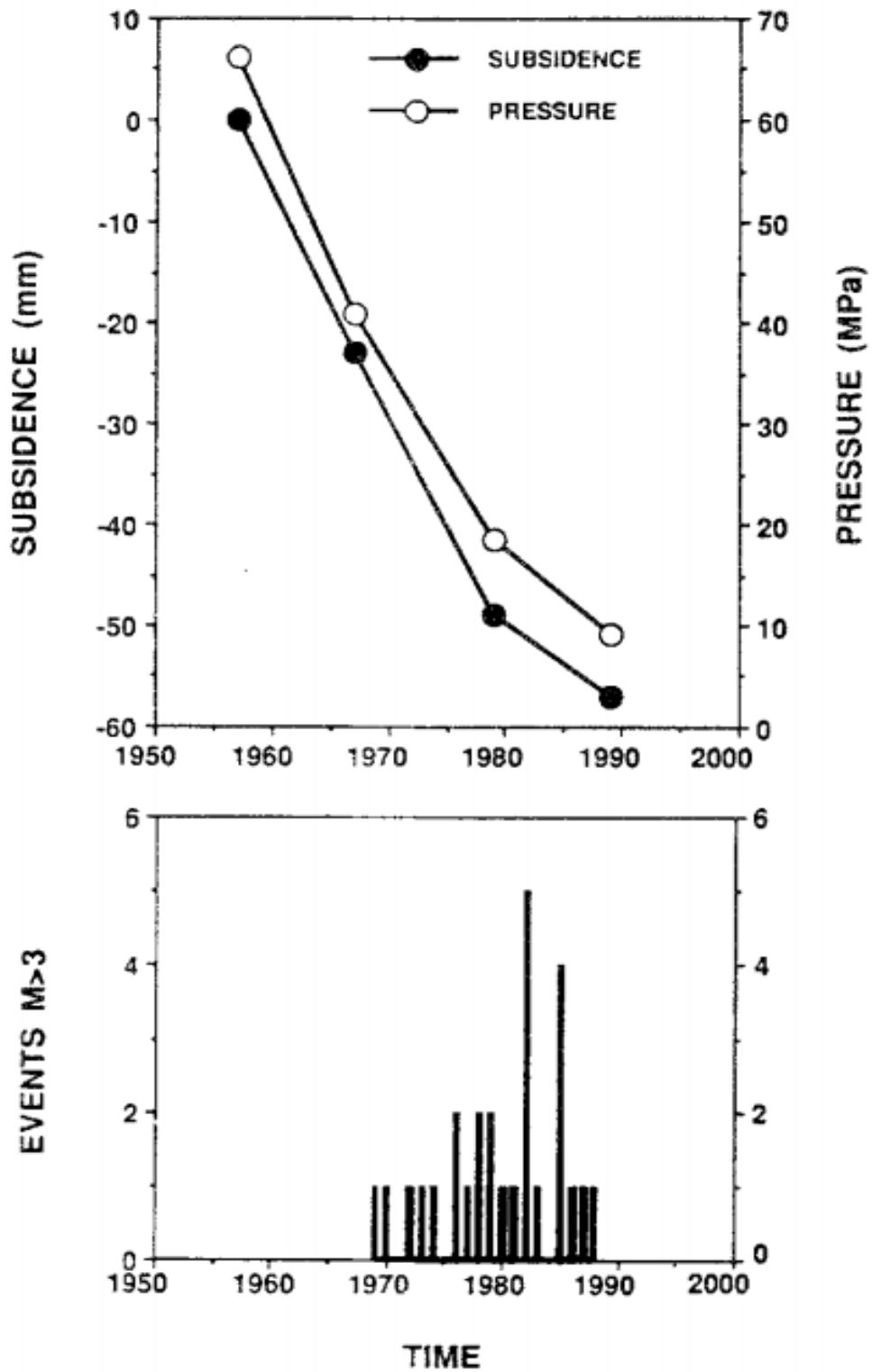


**Figure D.2** Seismic and aseismic deformation of the Lacq gas field as a function of pressure decrease within the gas reservoir. Taken from Grasso (1992).

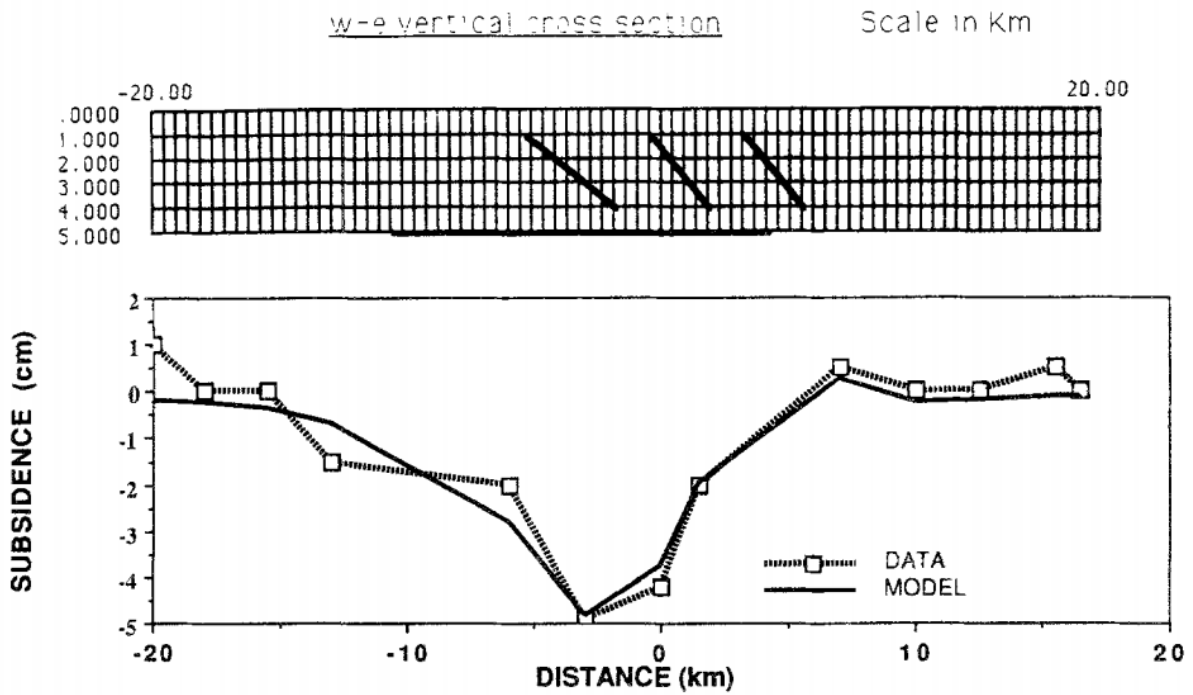


**Figure D.3** Comparison between observed and calculated surface displacements due to fault slips for the Lacq field. Calculated surface displacements from Grasso (1992) two-part mechanism for temporal strain modelling. Adopted from Grasso (1992).

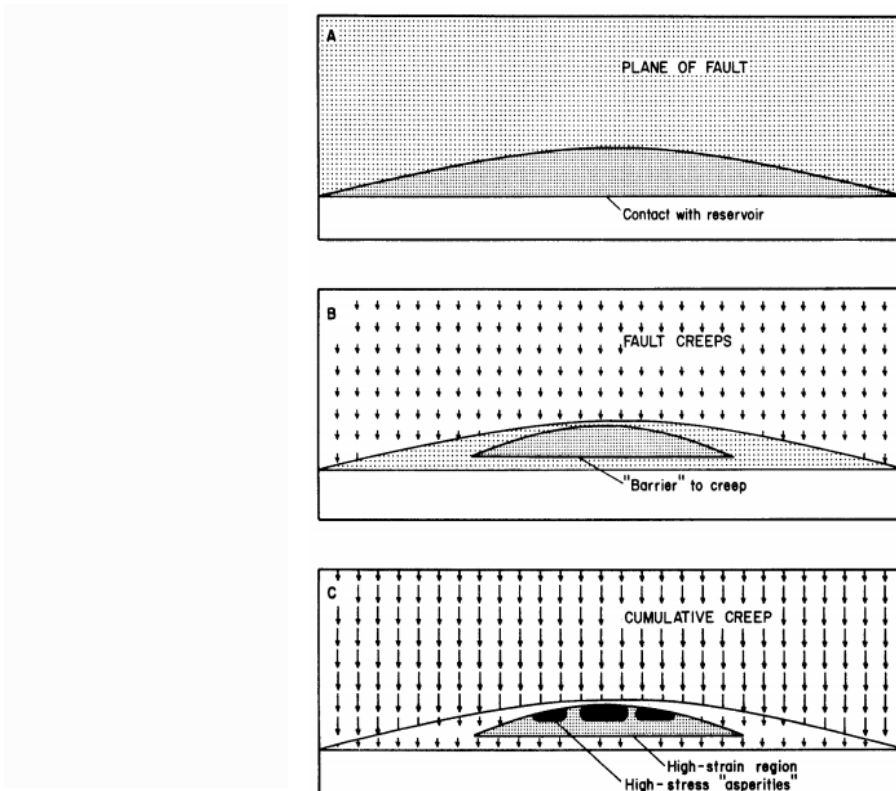


**Figure D.4** Mechanism for fluid extraction inducing seismicity due to depletion in proximity to pre-existing faults. Diagram illustrates this mechanism on the fault foot wall: (A) Before fluid extraction by production, (B) Production has lowered fluid pressures along fault to produce barriers for creep, (C) Accrual of strain on the barriers results in high stress which accumulates to exceed the strength of the fault segment, resulting in failure and seismicity. Taken from Pennington et al. (1986).

### D.3 Mass Transfer (Mechanism 3)

In addition to seismicity caused by production-induced pressure depletions, fluid extraction can also induce earthquakes through more complex fluid manipulations (Grasso, 1992). Such occurrences are observed within reservoirs on the margins of which fluids are injected to encourage hydrocarbon migration towards production wells, resulting in seismicity occurring in the region between the fluid depletion zone and the fluid injection zone (Fig. D.5) (Davis and Pennington, 1989). The increase in poroelastic stress transfer associated with fluid extraction compounds onto the fluid injection effect, resulting in fracture generation due to large imbalances, and the occurrence of seismicity adjacent to these generated fractures (Davis and Pennington, 1989; Grasso, 1992). Seismicity caused by this cumulative mechanism (or similar) has been observed in multiple fields, including Cogdell field, Texas, U.S. (Davis and Pennington, 1989) and Gobles field, Ontario, Canada (Mereu et al., 1986). Some important examples of potentially mass transfer related seismicity are provided in sections D.3.1 and D.3.2.

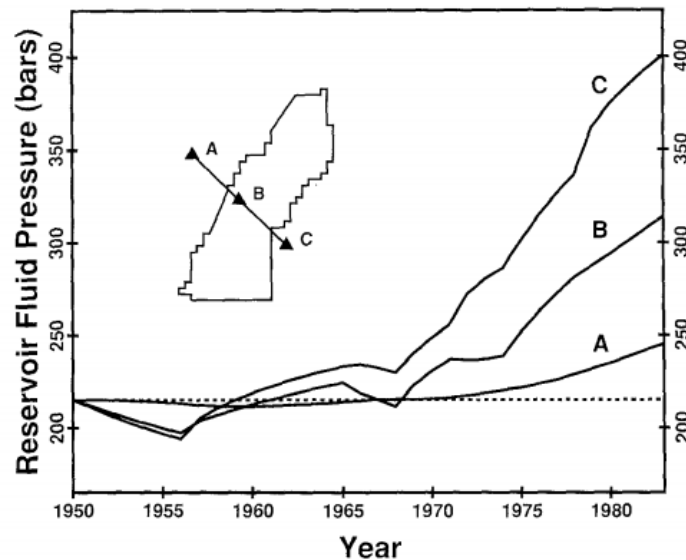


**Figure D.5** Calculated fluid pressure histories of three selected points in the Cogdell field. Inset figure indicates locations of points used to compute pressure histories. Point A represents a point well located outside of the Coalinga field, point B represents a point in the production region, and point C represents the outer region of the field i.e. injection region. The majority of the earthquakes observed by the U.S. Geological Survey Network originated closest to point B. The dashed line represents the initial hydrostatic conditions of the reservoir. Taken from Davis and Pennington (1989).

Thermal stresses resulting from water injection for enhanced recovery also contribute to mass transfer related seismicity. These thermal stresses were first proposed by Grasso (1992) to contribute to induced seismicity through thermoelasticity in a way similar to that of poroelasticity. The contribution of thermoelasticity to mass transfer related seismicity was confirmed by Izadi and Elseworth (2013). They concluded that whilst the most important mechanism for mass transfer related seismicity is the augmentation of fluid pressure, as time passes and fluid migration occurs within fractures, reductions in effective stress can be caused by thermal quenching, further contributing to the induced seismicity.

### **D.3.1 Coalinga, U.S.A.**

Three large ( $M_S > 5$ ) earthquakes observed near Coalinga, California, U.S.A in a seismic sequence lasting from 1976 to 1987 are considered cases of significant seismicity induced by hydrocarbon production (Grasso, 1992). The Coalinga, Kettleman North Dome and Montebello oil fields which these earthquakes occurred within are all situated upon recently uplifted anticlines (McGarr, 1991). As a result of this uplift being recent McGarr (1991) determined that these earthquakes were most likely not tectonic in origin despite originating at greater depths than at which oil production was occurring. McGarr (1991) proposed an additional mechanism related to mass transfer to explain the occurrence of these large earthquakes, which are not adequately accounted for exclusively by the three induced seismicity mechanisms discussed above. In this proposed mechanism the removal of load from the upper layers of the reservoir by fluid extraction results in hydromechanical perturbations within the upper crust. The mass extraction of fluid lowers the mean density of the upper crust, thus inducing isostatic imbalance in which horizontal compaction of the upper crust occurs. To resolve this imbalance the ductile lower crust deforms, consequently increasing the load on the seismogenic portion of the upper crust. This seismogenic layer then undergoes failure to restore local static equilibrium, generating seismicity. McGarr (1991)'s proposed mechanism well explains the occurrence of large earthquakes in hydrocarbon fields with growing anticline reservoirs which have experienced mass fluid extraction.

### **D.3.2 Gazli Gas Field, Uzbekistan**

The mass transfer mechanism has been proposed as an explanation for the unresolved seismic sequence observed within the Gazli gas field of Uzbekistan (Grasso 1992). The Gazli seismic sequence was recorded from 1976 to 1984, with four large earthquakes (April 1976 -  $M_S$  7.0; May 1976 -  $M_S$  7.0; June 1978 -  $M_S$  5.7; March 1984 -  $M_S$  7.0) recorded during this time (Suckale, 2009). The association of this seismic sequence with hydrocarbon production was first put forward by Simpson and Leith (1985) on the rationale that: (1) the region was previously aseismic for several centuries, (2) the seismic sequence does not concur with conventional aftershock patterns, (3) the Gazli gas field reservoir has experienced significant pressure depletion since production has begun and (4) source modelling of the March 1984 ( $M_S$  7.0) earthquake by Eyidoğan et al. (1985) suggested the rupture propagated downward, which Simpson and Leith (1985) interpreted as being indicative of an abnormal near-surface stress distribution (Suckale, 2009). Despite this seemingly compelling evidence for the seismic sequence being induced by hydrocarbon production, some studies have made this claim contentious. For example, Eyidoğan et al. (1985) propose the large magnitude events are suggestive of a major fault to the north of the Gazli field, with the continuous uplift since the Quaternary suggestive of the long term migration of seismic activity, which is episodic in nature, and thus correlates with the previously aseismic nature of the area since medieval times. Most importantly, Bossu (1996) evaluated the isostatic imbalance model proposed by McGarr (1991) for this unusual seismic sequence. Bossu (1996) concluded that the interfering processes of water injection and gas extraction would result in only small pressure changes

(~0.06 bars) comparable to those which generate tidal stresses, and thus not be capable of inducing an earthquake through mass fluid transfer (Suckale, 2009).

#### **D.4 General Characteristics of Induced Seismicity Resulting from Hydrocarbon Production**

Regardless of the induced seismicity mechanism, earthquakes resulting from hydrocarbon production have been observed to have several common characteristics. Suckale (2009) outlines these as follows:

1. Magnitude range: Within most hydrocarbon fields, induced earthquakes are limited to being small to moderate in magnitude ( $< M_L 4.5$ ).
2. Correlation with production: It is often difficult to determine the correlation between the occurrence of earthquakes and hydrocarbon production due to the incompleteness of production data. Even in areas where production data is complete, a clear correlation between the occurrence of earthquakes and production data is uncommon, however a clear exception to this is the (highly controlled) Rangely field experiment discussed above.
3. Location: Induced seismicity usually occurs either directly above or below the corresponding hydrocarbon reservoir (e.g. the Lacq field – see Grasso and Wittlinger, 1990; the Ekofisk field - see Ottemöller et al., 2005).
4. Spatial clustering: The majority of studies on induced seismicity in hydrocarbon fields show that earthquakes resulting from hydrocarbon production frequently form spatial clusters (i.e. earthquake swarms) (e.g. Rangely – see Raleigh et al., 1976; Sleepy Hollow – see Evans and Steeples, 1987). Additionally, many of these production induced earthquakes can be associated with pre-existing faults (e.g. the Lacq field – see above).
5. Temporal patterns: There is typically a time-lapse of several years (or decades) between the onset of hydrocarbon production and significant increases in the seismic activity within a hydrocarbon field (e.g. the 28 year-delay between gas production and seismicity within the Groningen field – van Eck et al., 2016). Such a delay is in accordance with the poroelastic modelling (discussed above) of Segall (1985). However, the level of seismic monitoring within many hydrocarbon fields only increases as seismicity occurs, and consequently the onset of induced seismicity within a hydrocarbon field could actually be far earlier than estimated within many studies.
6. Faulting: The faulting within hydrocarbon fields in which induced earthquakes are observed is primarily determined by the pre-existing stress field (e.g. the Lacq field – see Segall, 1989). This is because production related stress perturbations are comparatively small. However, as observed in many cases hydrocarbon production can lead to the reactivation of pre-existing faults (e.g. the Groningen field – see Van Eijs et al., 2006) or the formation of new faults (e.g. Goose Creek – see Pratt and Johnson, 1926).

## Appendix E: Statistical Methods Used for Constraining Site Effects in the North Sea

The Kotha et al. (2018) site classification scheme derives site classes using two statistical techniques: (1) principal component analysis (PCA) and (2) k-means clustering. Explanations of these two statistical techniques are provided below.

### E.1 Principal Component Analysis

The following description of PCA is summarised from Jolliffe (2013), which should be consulted for further details on this statistical technique.

PCA is a statistical technique enabling the reduction of a multi-dimensional dataset to a handful of principal dimensions which are representative of the contribution by each variable within the dataset to the total variability of the dataset. In a simple example comprising a dataset with two variables ( $V_1$  and  $V_2$ ) and six data points ( $DP_1 \dots DP_6$ ) (Fig. E.0; Tab. E.0) the procedure is as follows:

1. Firstly, PCA plots the variables present within the dataset against each other for every data point, and then fixes the dataset to the origin of the plot using the centre of the data (Fig. E.0; Fig. E.1). This centred plot maintains the relative position of each data point to every other data point in the dataset.
2. Next, the plotted data points are projected onto a line, with the largest total sum of squared distances from each projected data point to the origin (SSD) used to determine the best fit of the line (Fig. E.1). Due to the Pythagorean theorem, the use of the largest SSD value results in the minimisation of the distance between each data point and its projection onto the line (e.g. for data point 4 the distance  $b_4$  – see Fig. E.1), resulting in the best fit of the line to the centred data points. This fitted line represents the first principal component (PC1). The line of the first principal component can therefore be defined as the line with which maximum variability of the projected values occurs on. The projected values on this line associated with the maximum variability are referred to as the principal component scores (Fig. E.1). The principal component scores represent the standardised (centred) data points in the principal component space.
3. In PCA the SSD for each principal component is also referred to as that principal component's eigenvalue. The variability contributed to the dataset by a principal component is equal to:

$$\text{Variance of Principal Component} = \frac{\text{principal component's eigenvalue}}{n - 1} \quad (\text{E.0})$$

where n represents the total number of samples in the dataset.

- The gradient of the PC1 line is approximately 0.342 (see Fig. E.1), indicating that the majority of the data is spread out over the first variable,  $V_1$ . The gradient indicates if one moves 2.940 ( $1/0.342$ ) units along the x-axis, a corresponding increase of 1 unit along the y-axis is observed. Dividing the x and y components of the PC1 line's gradient vector by the gradient vector of the PC1 line itself ( $\sqrt{2.940^2 + 1^2} = 3.093$ ) yields the eigenvector for PC1. The eigenvector for PC1 of the arbitrary dataset is thus given by:

$$\text{Eigenvector for PC1} = \sim \begin{bmatrix} 2.940/3.093 \\ 1/3.093 \end{bmatrix} = \sim \begin{bmatrix} 0.950 \\ 0.323 \end{bmatrix} \quad (\text{E.1})$$

The values of each principal component's eigenvector are referred to as the principal coefficient scores. The principal coefficient scores represent weights which the standardised (i.e. centred) original dataset data points can be multiplied by to transform them into the principal component scores.

- Following the determination of the first principal component's parameters, the process is repeated for the second principal component (PC2). One difference however is that the fit of the line representing PC2 is simply drawn perpendicular to the line of PC1, rather than using the largest sum of squares between the data points and the origin as for PC1 (Fig. E.1). The largest sum of squares between the data points and the origin is still required however as it is representative of the eigenvalues for PC2. For a dataset with more than two variables (as is often the case in PCA) the process of determining principal component parameters is continued for as many principal components as necessary. The maximum number of principal components for a dataset is theoretically equal to the number of variables in the dataset.
- After determining the parameters for each principal component, the number of principal components which can effectively explain the entire dataset's variability can be computed. The variability of the dataset explained by each principal component can be determined using equation E.0. Dividing the variability explained by each principal component by the sum of the principal component variability values provides the contribution of each principal component to the dataset's total variability. Rather subjectively, to determine the number of principal components to use for further analysis, one must decide how much of the variability in the dataset should be explained by the number of principal components chosen e.g. is it acceptable to only use two principal components if they can explain 70% of the total dataset variability?
- Once the number of principal components required to represent the whole dataset is known, a PCA plot (Fig. E.2) can be constructed (assuming the variability is captured sufficiently in at

most 3 principal components). The PCA plot is an important output of the PCA technique, especially for implementing Kotha et al. (2018)'s site classification methodology within this investigation because it enables the k-means clustering of the multidimensional intra-event residual data by reducing the data to a two-dimensional format, from which k-means clustering can be applied, and cluster site amplification functions can be computed (see Chapter 4 for more detail on this site classification methodology and below for more detail on k-means clustering).

**Table E.0** Simple arbitrary dataset for explanation of the PCA statistical technique.

<i>DP</i>	$V_1$	$V_2$
1	10	6
2	11	4
3	8	5
4	3	3
5	2	2.8
6	1	1

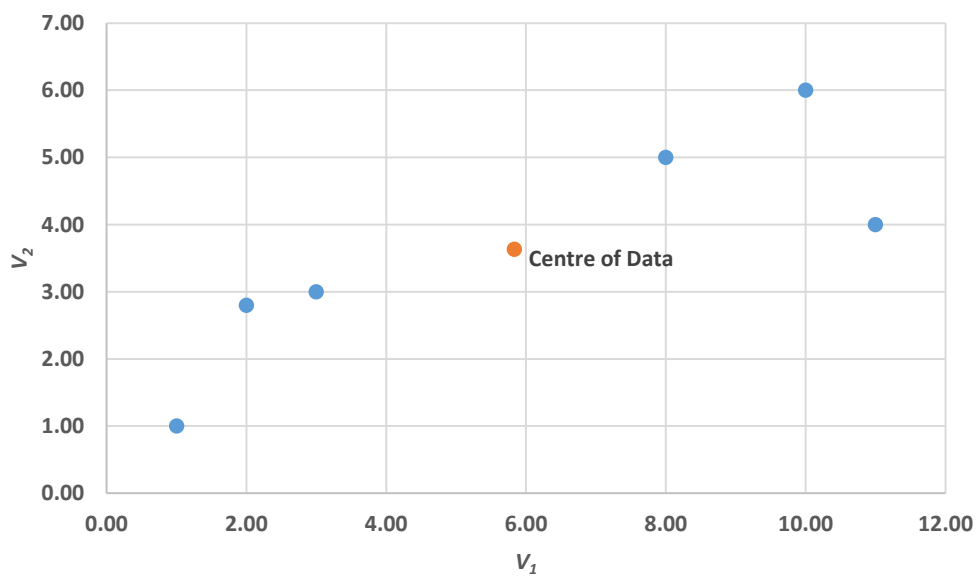


**Figure E.0** Plot of the arbitrary dataset used in the PCA methodology demonstration.

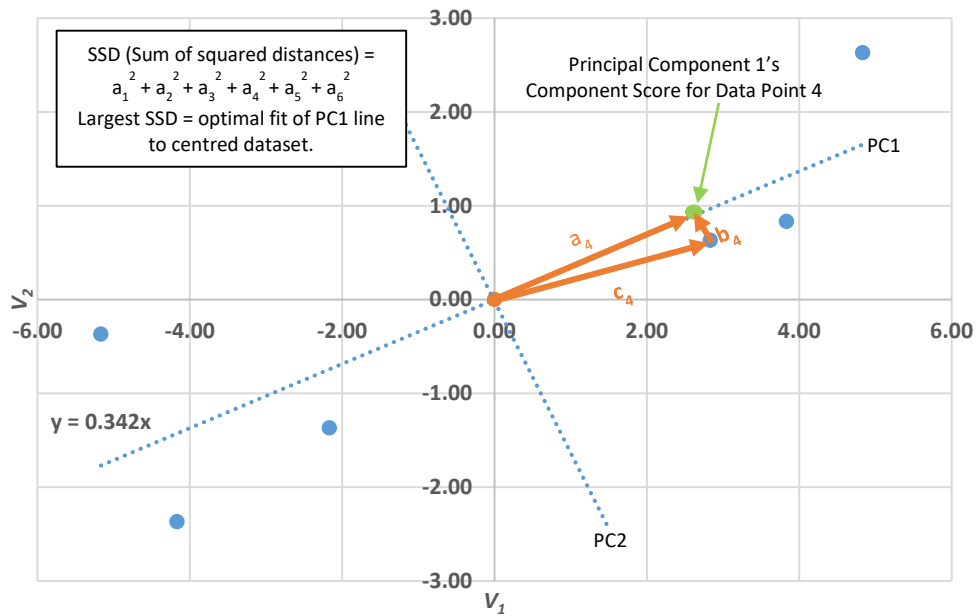


**Figure E.1** Plot illustrating how principal components and the lines representing them are determined in PCA following the centering of the dataset. Distance  $a_4$  represents the distance between the projection of data point 4 onto the PC1 line and the origin. The Green data point represents the projection of data point 4 onto the PC1 line i.e. the principle component 1 score for data point 4. The principal components are determined from the arbitrary dataset used in the PCA methodology demonstration (see Tab. E.0).

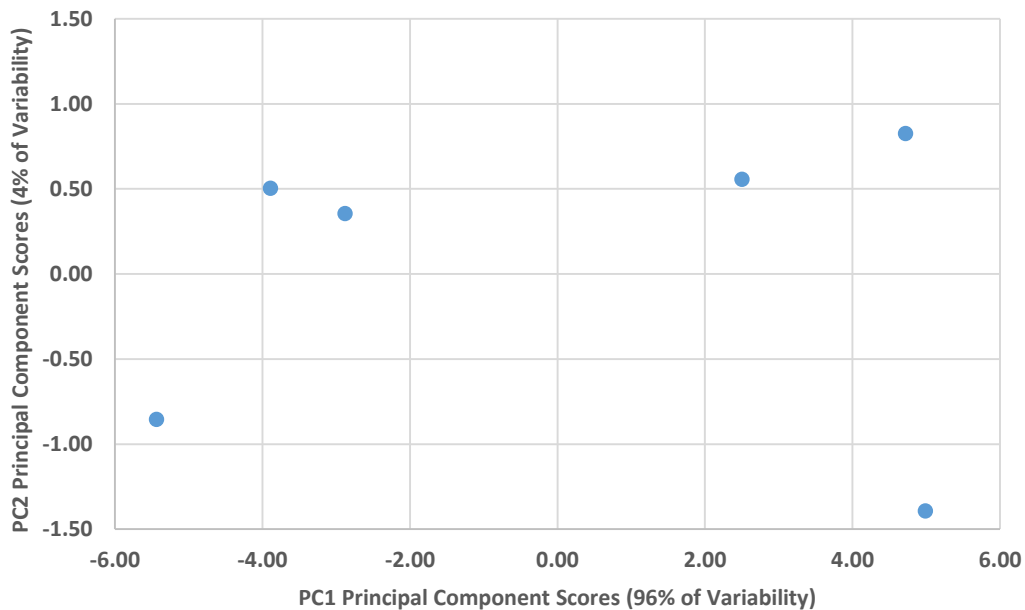


**Figure E.2** PCA Plot of PC1 and PC2. Principal components scores are determined from the arbitrary dataset used in the PCA methodology demonstration (see Tab. E.0).

## E.2 K-Means Clustering

The following description of k-means clustering is summarised from Aggarwal (2014).

The k-means clustering technique is a type of unsupervised machine learning used to cluster data. The k-means algorithm determines  $k$  cluster centroids, and each data point in the inputted dataset is assigned to the closest one of these centroids. Each centroid defines a cluster. The value of  $k$  (i.e. the number of clusters the dataset can be segregated into) can be determined through various methods (see below). In the following example, using the outputs of the PCA demonstration, the k-means clustering technique is demonstrated:

1. In k-means clustering the input dataset comprises a set of observations for each data point  $x^1 \dots x^m, x^m \in \mathbb{R}^n$ . In this demonstration of k-means clustering, the observations for each data point are the PC1 and PC2 principal component scores from the PCA demonstration (Tab. E.1).

The principal component scores for each data point do not have labels,  $y^i$ . The lack of labels for the dataset justifies the use of an unsupervised learning algorithm. The aim of this k-means clustering demonstration is therefore to predict  $k$  centroids and a label  $c^i$  for every data point. It should be noted that in the following demonstration  $k = 3$ .

2. In the first step of the k-means algorithm,  $k$  centroids  $\mu_1 \dots \mu_k \in \mathbb{R}^n$  are randomly assigned, and every data point is assigned to its nearest centroid using its smallest squared Euclidean distance to each centroid (Fig. E.3). Essentially, if  $c^i$  is the selection of centroids in set  $C$ , each data point  $x$  is assigned to a cluster using:

$$\text{For every set, } i: \quad c^i = \arg \min_j \|x^i - \mu_j\|^2 \quad (\text{E.2})$$

3. Following the assignment of each data point to a cluster centroid, the cluster centroids are recalculated. The new cluster centroids are determined by taking the mean of all the data points assigned to each of the previous cluster centroids:

$$\text{For every set, } j: \quad \mu_j = \frac{\sum_{i=1}^m 1_{\{c^i=j\}} x^i}{\sum_{i=1}^m 1_{\{c^i=j\}}} \quad (\text{E.3})$$

The k-means algorithm subsequently iterates between assigning each data point to its nearest cluster centroid and then recalculates the cluster centroids using the means of all data points assigned to that cluster centroid. This process continues until conditional criteria are achieved e.g. the sum of distances between cluster centroids and the data points in each cluster are minimised, or the set number of iterations is complete. Usually, such criteria are for the clustered data points to not alternate which cluster they are allocated to following further iterations of the k-means algorithm (e.g. Fig. E.3 compared to Fig. E.4 and Fig. E.5). For the k-means algorithm, convergence is said to have occurred once this condition has been met.

4. To determine the optimal value for  $k$ , a variety of methods are available. One of the simplest way of doing so is using a silhouette plot (e.g. Fig. E.6). A silhouette plot uses silhouette values to indicates how effectively the data points have been clustered.

Silhouette values indicate how similar an object (i.e. a clustered data point) is to the cluster it has been assigned to compared to the other clusters computed. Silhouette values can vary from -1 to 1. A negative silhouette value indicates a relatively poor fit of the data point to the cluster, whereas a positive silhouette value indicates a relatively good fit of the data point to the cluster.

The silhouette value  $s$  of a clustered object can be computed as follows (summarised from Rousseeuw, 1987):

$$\text{For each data point } i \in C_i: \quad a(i) = \frac{1}{|C_i|-1} \sum_{j \in C_i, i \neq j} d(i, j) \quad (\text{E.4})$$

where  $a(i)$  is the average (Euclidean) distance between data point  $i$  and all other data points in the same cluster, with  $d(i, j)$  being the distance between data points  $i$  and  $j$  in the cluster  $C_i$ . Therefore,  $a(i)$  is representative of the average dissimilarity of data point  $i$  to all other data points within the cluster to which data point  $i$  has been assigned, with a smaller value indicating a better fit.

$$\text{Then, for each data point } i \in C_i: \quad b(i) = \min_{i \neq j} \frac{1}{|C_j|} \sum_{j \in C_j} d(i, j) \quad (\text{E.5})$$

where  $b(i)$  is the smallest average distance of data point  $i$  to the data points assigned to the other clusters (the clusters that data point  $i$  has not been assigned to). It should be noted that the computation of  $b(i)$  inherently requires more than one cluster. Therefore, silhouette plots are constructed under the assumption that more than one cluster has been computed (i.e.  $k > 1$ ).

Following the computation of  $a(i)$  and  $b(i)$  for data point  $i$  the corresponding silhouette value  $s(i)$  can be computed:

$$s(i) = \frac{b(i)-a(i)}{\max\{a(i),b(i)\}} \quad (\text{E.6})$$

which can also be expressed as:

$$s(i) = \begin{cases} 1 - a(i)/b(i), & \text{if } a(i) < b(i) \\ 0, & \text{if } a(i) = b(i) \\ b(i)/a(i) - 1, & \text{if } a(i) > b(i) \end{cases} \quad (\text{E.7})$$

which therefore shows that:

$$-1 \leq s(i) \leq 1 \quad (\text{E.8})$$

The resulting silhouette values are plotted to provide a visual representation of how well the data has been clustered, as demonstrated in Fig. E.6 for the arbitrary dataset. This silhouette plot shows positive silhouette values for all of the data points in the arbitrary dataset, indicating that  $k = 3$  is a viable number of clusters for the data to be partitioned into. To determine whether more or less clusters optimises the clustering of the data, additional silhouette plots can be constructed from the same data clustered with different  $k$  values, and the resulting silhouette values can be compared. It should also be noted that whilst fewer clusters may provide larger (positive) silhouette values (as is preferable), the  $k$  value ultimately used for dataset clustering can often be influenced by the context of the investigation, which can demand more clusters than deemed optimal by the silhouette plots. Consequently, the determining of the optimal number of clusters often must take into account both (1) the requirements of the investigation and (2) the desire for improved silhouette values (i.e. better clustering), which introduces notable subjectivity into the determination of the optimal  $k$  value (as observed in this study – see below).

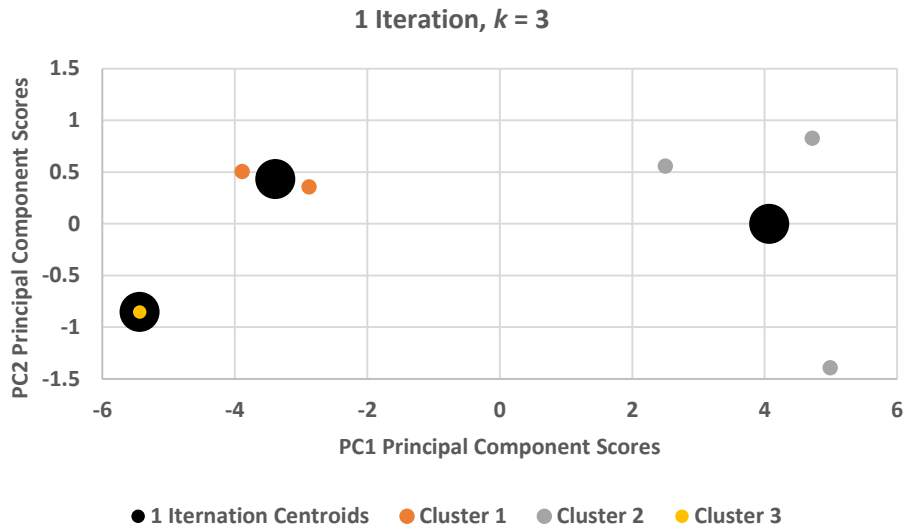


**Figure E.3** Clustered PCA Plot of PC1 and PC2 for 1 iteration of the  $k$ -means algorithm.

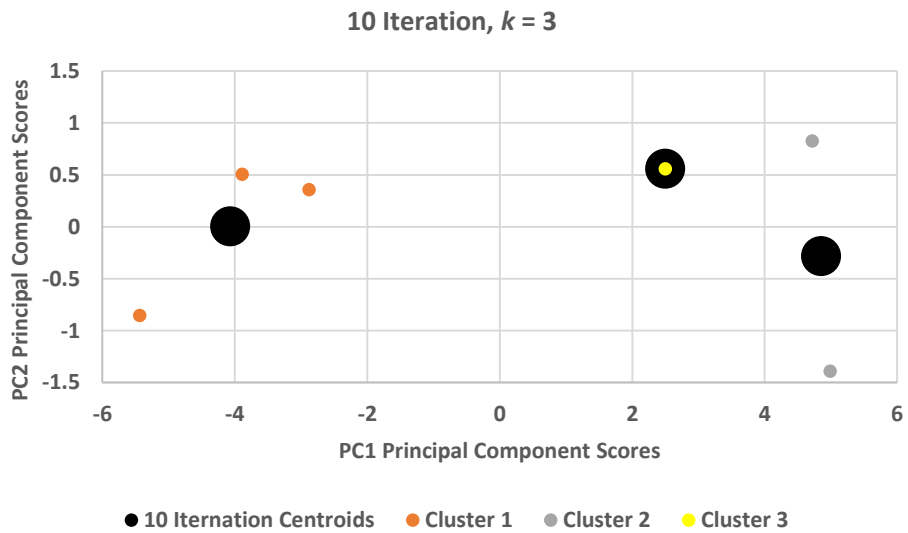


**Figure E.4** Clustered PCA Plot of PC1 and PC2 for 10 iterations of the  $k$ -means algorithm.

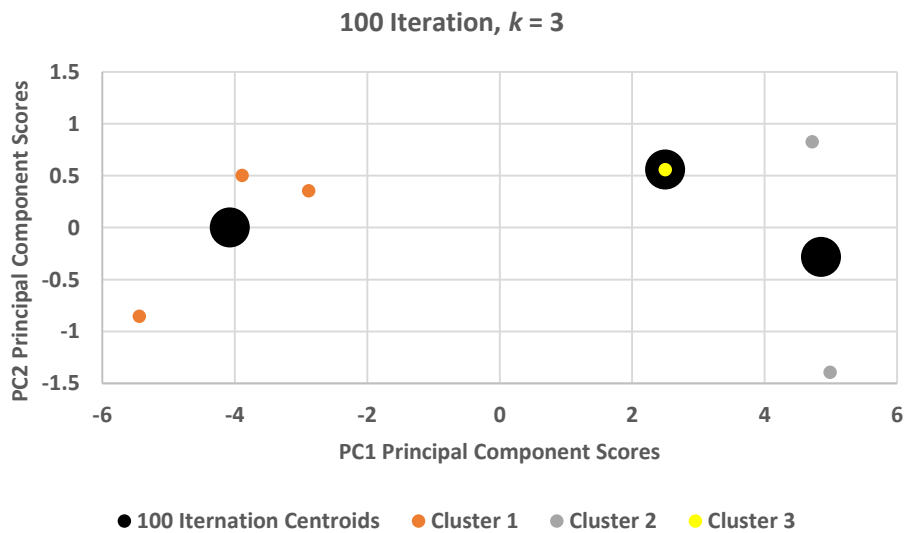


**Figure E.5** Clustered PCA Plot of PC1 and PC2 for 100 iterations of the  $k$ -means algorithm.

**Table E.1** Principal component scores for the arbitrary dataset following PCA.

<i>DP</i>	<i>PC1 Component Score</i>	<i>PC2 Component Score</i>
1	4.7200	0.8269
2	4.9889	-1.3929
3	2.5002	0.5581
4	-2.8812	0.3568
5	-3.8902	0.5049
6	-5.4375	-0.8538

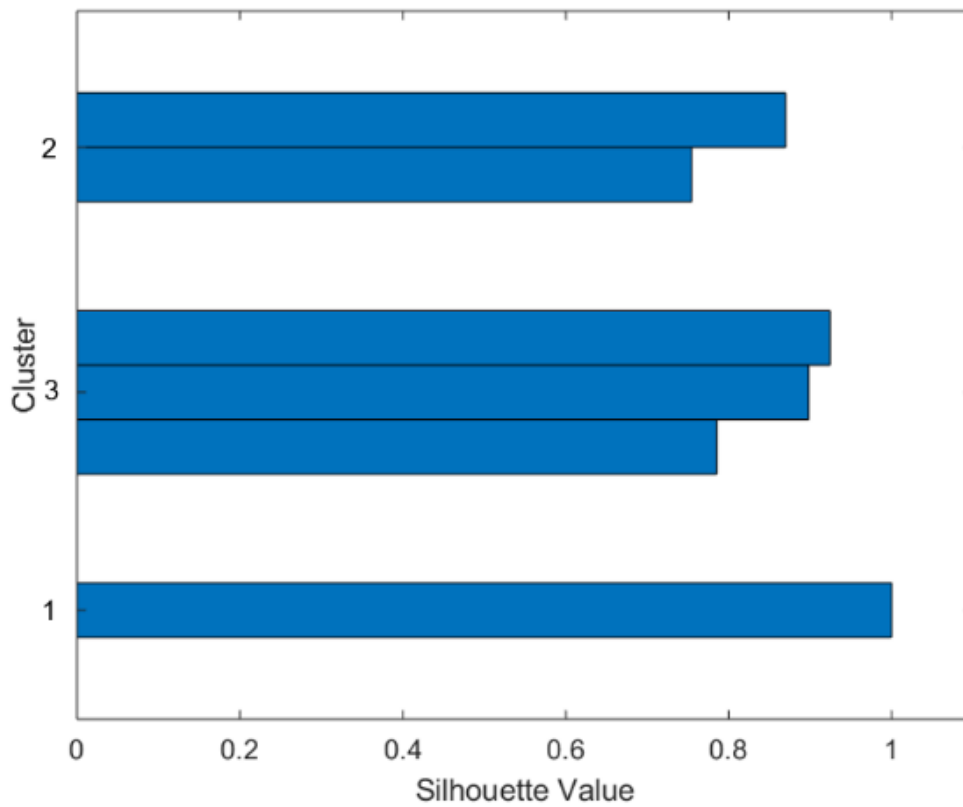


**Figure E.6** Silhouette plot of the clustered principal component scores (iterations = 100,  $k = 3$ ).